RISING STARS: AFRICA

EDITED BY: Tebello Nyokong, Aziz Amine, Emmanuel Oluwadare Balogun,
Shivani Mishra and Eno E. Ebenso

PUBLISHED IN: Frontiers in Chemistry

frontiers Research Topics

ISSN 1664-8714
ISBN 978-2-88974-362-9
DOI 10.3389/978-2-88974-362-9

About Frontiers

Frontiers is more than just an open-access publisher of scholarly articles: it is a pioneering approach to the world of academia, radically improving the way scholarly research is managed. The grand vision of Frontiers is a world where all people have an equal opportunity to seek, share and generate knowledge. Frontiers provides immediate and permanent online open access to all its publications, but this alone is not enough to realize our grand goals.

Frontiers Journal Series

The Frontiers Journal Series is a multi-tier and interdisciplinary set of open-access, online journals, promising a paradigm shift from the current review, selection and dissemination processes in academic publishing. All Frontiers journals are driven by researchers for researchers; therefore, they constitute a service to the scholarly community. At the same time, the Frontiers Journal Series operates on a revolutionary invention, the tiered publishing system, initially addressing specific communities of scholars, and gradually climbing up to broader public understanding, thus serving the interests of the lay society, too.

Dedication to Quality

Each Frontiers article is a landmark of the highest quality, thanks to genuinely collaborative interactions between authors and review editors, who include some of the world's best academicians. Research must be certified by peers before entering a stream of knowledge that may eventually reach the public - and shape society; therefore, Frontiers only applies the most rigorous and unbiased reviews.
Frontiers revolutionizes research publishing by freely delivering the most outstanding research, evaluated with no bias from both the academic and social point of view. By applying the most advanced information technologies, Frontiers is catapulting scholarly publishing into a new generation.

What are Frontiers Research Topics?

Frontiers Research Topics are very popular trademarks of the Frontiers Journals Series: they are collections of at least ten articles, all centered on a particular subject. With their unique mix of varied contributions from Original Research to Review Articles, Frontiers Research Topics unify the most influential researchers, the latest key findings and historical advances in a hot research area! Find out more on how to host your own Frontiers Research Topic or contribute to one as an author by contacting the Frontiers Editorial Office: frontiersin.org/about/contact

RISING STARS: AFRICA

Topic Editors:
Tebello Nyokong, Rhodes University, South Africa
Aziz Amine, University of Hassan II Casablanca, Morocco
Emmanuel Oluwadare Balogun, Ahmadu Bello University, Nigeria
Shivani Mishra, University of South Africa, South Africa
Eno E. Ebenso, North-West University, South Africa

Citation: Nyokong, T., Amine, A., Balogun, E. O., Mishra, S., Ebenso, E. E., eds. (2022). Rising Stars: Africa. Lausanne: Frontiers Media SA.
doi: 10.3389/978-2-88974-362-9

Table of Contents

frontiers in Chemistry

EDITORIAL
published: 27 January 2022
doi: 10.3389/fchem.2022.851125

Editorial: Rising Stars: Africa

Emmanuel O. Balogun[1,2]*, *Tebello Nyokong*[3], *Aziz Amine*[4], *Shivani Mishra*[5] and *Eno Ebenso*[5]

[1]Department of Biochemistry, Ahmadu Bello University, Zaria, Nigeria, [2]Africa Centre of Excellence for Neglected Tropical Diseases and Forensic Biotechnology (ACENTDFB), Ahmadu Bello University, Zaria, Nigeria, [3]Department of Chemistry, Rhodes University, Grahamstown, South Africa, [4]Faculty of Sciences and Techniques, Hassan II University of Casablanca, Casablanca, Morocco, [5]Nanotechnology and Water Sustainability Research Unit, College of Science, Engineering and Technology, University of South Africa, Johannesburg, South Africa

Keywords: medicinal chemistry, green chemistry, synthesis, nanoscience—nanotechnology, electrocatalysis, inorganic chemistry, infectious diseases

Editorial on the Research Topic

Rising Stars: Africa

OPEN ACCESS

Edited and reviewed by:
Michael Kassiou,
The University of Sydney, Australia

****Correspondence:***
Emmanuel O. Balogun
eobalogun@abu.edu.ng

Specialty section:
This article was submitted to Medicinal and Pharmaceutical Chemistry, a section of the journal Frontiers in Chemistry

Received: *09 January 2022*
Accepted: *11 January 2022*
Published: *27 January 2022*

Citation:
Balogun EO, Nyokong T, Amine A, Mishra S and Ebenso E (2022) Editorial: Rising Stars: Africa. Front. Chem. 10:851125. doi: 10.3389/fchem.2022.851125

With a total population of about 1.34 billion, Africa accounts for 17.2% of the world population (https://www.worldometers.info/world-population/#region). However, this population does not match research output as Africa contributes less than 1% to global research efforts in terms of scholarly publications from various disciplines of science and engineering as well as the social sciences (Duermeijer et al., 2018). No African country spends up to 0.9% of the gross domestic product (GDP) on research and development (R&D), whereas the four top countries (United States, China, Japan, and Germany) in terms of volume of R&D investment, each commits over 3% of their GDPs to R&D amounting to 613, 525, 173, and 132 billion US$, respectively. Commendably, South Africa is the only African country with annual spending of over $6 billion on R&D, followed by Morocco with $1.5 billion; all other countries in Africa commits less than $1 billion to R&D (OECD, 2022). This annual spending on R&D correlates well with research output. For instance, while 422,808 articles were published by researchers in United States in year 2018; about 13,000 publications emanated from South Africa, and less than 1,000 papers from most African countries. The top performing African countries are Algeria, Egypt, Kenya, Morocco, Nigeria, South Africa, and Tunisia. Noteworthy, there is presently a remarkable improvement of Africa's contribution to global research output. A recent in-depth analysis using Elsevier's SciVal tool revealed a consistent positive upturn in Africa's research productivity. In fact, Africa has been adjudged as having the highest research productivity growth rate of approximately 39% in the past 5 years and this is simultaneously matched with increases in number of authors at an average growth rate of 43% (Duermeijer et al., 2018). Indeed, there are numerous talented African early career scientists who have demonstrated abilities to emerge as regional and global research leaders in their fields. Many of them have received awards, fellowships, and grants that have provided the opportunity to build independent research career and networks across institutions in Africa and shows the potentials to undertake cutting-edge scientific research that will address challenges that are peculiar to the African continent as well as contributing to solve global challenges. These recent advances are highly commendable and encouraging as continuing on this path will help Africa to build a thriving knowledge-based economy and place her as a critical hub for the new industrial revolution. To achieve this goal, the numerous challenges against productive science must be tackled. These challenges include: 1) lack of research facilities, 2) inadequate manpower and skills, 3) lack of national and regional funding mechanisms, 4) poor access to channels for dissemination of research to the global community, and 5) very weak intranational and intracontinental collaborations. To address these limitations, stakeholders comprised of institutions, national governments, and publishers must deploy resources within their means to enhance the successes recorded by African scientists and researchers. This synergy will propel the continent to solve the numerous

FIGURE 1 | Map of Africa showing the distribution of authors by country of affiliated institution. Authors are from six countries shown in the map. Values represent number of authors and the proportion as percentages in parentheses.

problems that suppress its economic growth and development. Towards contributing to scientific research in Africa, Frontiers, a leading publisher through one of its journals, *Frontiers in Chemistry* initiated a research topic called "Rising Stars: Africa," which is a collection to "showcase the compelling work of recognized researchers in the early stages of their independent careers, from the breadth of the African continent." We believe that this effort will help to tackle challenges #4 and #5 (listed above). The research topic was edited by top African scientists who were carefully selected based on their achievements and contributions to diverse fields of chemistry, which reflects the variety and excellence of the published articles. The works in this collection showcase efforts made by Africans across the chemical sciences and with potential applications to solve compelling problems faced by Africa particularly with regards to infectious diseases, poverty, environmental pollution, energy, and lack of potable water. In this topic, we provide a compilation of the recent progress made by African-led research groups in diverse fields of chemistry, towards addressing African problems. In total there are 14 accepted contributions comprised of 11 original research articles and three review papers all in covering multiple fields: analytical chemistry, biochemistry, chemical synthesis, electrochemistry, green chemistry, immunochemistry, inorganic chemistry, medicinal chemistry, nanotechnology, and physical chemistry. Based on country of affiliations, the contributing African authors are from six countries (listed in order of number of authors); South Africa, Nigeria, Zimbabwe, Algeria, Kenya, and Democratic Republic of Congo (**Figure 1**).

The articles address numerous regional and global problems that fall under one of these three broad categories- Climate change, environmental pollution, and infectious diseases. The number of papers in these categories were four, three, and seven, respectively, which may reflect the present magnitude of the impacts of these problems on Africa.

Climate change (CC) is a product of ecosystem imbalance and is described as a significant variation in the usual pattern of Earth's average weather conditions, global warming, changing precipitation patterns, and extreme weather and climate events such as flood and drought, are prominent manifestations

(Balogun et al., 2016; WMO 2021). Since emission of carbon dioxide CO_2 is a major cause CC, strategies to reduce CO_2 release and/or atmospheric accumulation will help to mitigate the impacts of CC. In this compilation, Tshuma et al described their effort to develop metal-organic frameworks (MOFs), one of the potent techniques for CO_2 capture and storage (CCS). The successfully developed two MOFs- [Cd2 (bpydc)2 (DMF) 2·2DMF]n (JMS-3) and [Zn (bpydc) (DMF)·DMF]n (JMS-4) from 2,2'-bipyridine-4,4'-dicarboxylate (bpdc) linker and tested their CO_2 storage and H_2 adsorption capacity as potential CCS material. Their results revealed that JMS-3a (active form) has better CO_2 and $\mathbf{H}_2$ adsorption capacity (1.36 and 2.88 mmol·g-1average) than JMS-4a (active form) (0.98 and 2.29 mmol·g-1). However, JMS-3a is not stable under different chemical environments that are normally employed in the catalytic hydrogenation of CO_2. Thus, making JMS-4a a better potential candidate for application in CCS. The work of Ocansey et al. reported here is highly innovative towards reducing atmospheric CO_2. There effort was not only in the line of utilizing MOFs for CCS, they have established a catalytic system for enhanced conversion of CO_2 to useful industrial product, formic acid *via* iridium (III) tetrazole Complex-mediated hydrogenation of CO_2. The iridium (III) tetrazole Complex catalyst was highly efficient with just 1 μmol producing up to 180 mM concentrated formate solution. Formic acid has wide range applications due to its antibacterial pesticidal property. The worth of annual global consumption of formic acid stands at $680 million. Furthermore, since the use of fossil fuels for energy generation is a chief source of CO_2 release, tapping and conversion of solar energy has gained wide acceptance as an eco-friendly means of reducing fossil fuel burning. This is made possible by the invention of solar cells, which trap photons from the Sun and convert them to electricity. To create better efficiency solar cells, scientists exploited the intense light absorption and chemical stability of metallophthalocyanines (molybdenum disulfide, MoS_2 and copper phthalocyanine, CuPc) to produce solar cells (Manamela et al.). The work by Manamela et al. was the first to demonstrate that combination of MoS_2 and CuPc can efficiently function as a photovoltaic (PV) system. The currently used PV technologies are silicon-based solar cells (SBSCs), which makes this technology too costly for wide penetration most especially for most African countries. To curb this problem, dyes have been used as sensitizers in the fabrication of highly efficient dye-sensitized solar cells (DSSCs) and even the best photosensitizer dye, tricarboxy–terpyridyl ruthenium complex is still far less efficient than the conventional SBSCs. With consideration for low cost and sustainability, organic PVs have been considered and developed from natural sources. In this collection, Sanusi et al., successfully extracted an apigenin derivative from Hibiscus rosa-sinensis plant and validated it as a model for testing the performance of organic PVs as light harvesters in solar cells.

Environmental pollution is the release of harmful or potentially harmful substances (contaminants), which may be solid, liquid or gas into the environment. It is caused by man's activities through exploration, industrialization, mining, and urbanization. Environmental pollution is the greatest problem facing humanity because it annually causes over nine million human deaths and about $4.6 trillion loss to global economy. Recently, water remediation technology using multi-walled carbon nanotubes (MWCNTs) was developed as an adsorbent of contaminants from water bodies. To improve the efficiency of MWCNTs, Makhado and Hato synthesised sodium alginate/poly (acrylic acid)/oxidized-multi-walled carbon nanotubes hydrogel nanocomposite (SA/p (AAc)/o-MWCNTs HNC) and tested its efficacy on methylene blue contaminated water. They found that SA/p (AAc)/o-MWCNTs HNC had high adsorptive capacity of 1,596.0 mg/g, and importantly, it can be repeatedly used for several cycles without significant reduction in the adsorption capacity. In addition to the use of adsorptive materials for cleaning contaminated water bodies, chemical methods involving photocatalysis (PC) and photoelectrocatalysis (PEC) are in use as safe and efficient techniques. While these techniques are effective for colourless contaminants, their efficiency is compromised when the contaminant is a dye because dyes prevent penetration of light, which is a necessity for PC and PEC actions. To alleviate this problem, Nwachukwu and Arotiba conducted a review of possible solutions to this problem and suggested the use of perovskite oxide–based PC and PEC for highly effective remediation of contaminated water because perovskite possess exceptional optical and electrochemical properties, which makes them capable of efficient light absorption even in the visible region. In addition, perovskite have long-term stability. For effective remediation of contaminated soil and water it is important to have a robust quantitative analytical method. In the context of Africa, the method should be simple, cheap, and highly efficient. The present analytical tools such as chromatography and mass spectrometry do not fulfil the stated criteria. Therefore, Zouaoui et al. developed a molecularly imprinted chitosan film grafted on a 4-Aminophenylacetic Acid on gold electrode as a microsensor for accurate detection and quantification of glyphosate, which is a generally used herbicide and a common contaminant of soil and water. Their microsensor is very sensitive. It can detect the contaminant at a concentration as low as 1×10^{-12} mg/ml (Zouaoui et al.).

Africa, particularly the sub-Saharan countries bear the highest impacts of infectious diseases. The five topmost killer infectious diseases in Africa are acute respiratory infections, HIV/AIDS, diarrhoea, malaria, and tuberculosis. They are responsible for more than six million deaths per year. These diseases are a major reason why life expectancy in sub-Saharan Africa is as low as 46 years compared to 85 years for Japan (Boutayeb, 2010). The economic impact of diseases to Africa is estimated as $2.4 trillion/year (WHO 2019). For Africa to overcome this problem, concerted efforts are needed with respect to intervention development for new, cheap, simple, and effective diagnostics, vaccines, and/or drugs. At present, most diagnostic techniques such as the enzyme-linked Immunosorbent Assays (ELISA) are expensive, time-consuming, expensive, requires bulky equipment, and highly skilled personnel for performing the analysis and result interpretation. Owing to these, the use of electrochemical immunoassay (EI) was developed to overcome the ELISA drawbacks. Using C-reactive protein, Adesina and Mashazi fabricated immunosensor for impedimetric detection by covalently immobilising oriented antibody on gold electrodes. In addition to significantly increased sensitivity, results from the immunosensor can be digitized. Tuberculosis is one of the major infectious diseases in Africa. Although isoniazid and pyrazinamide are first line drugs for treatment, toxic side effects and reduced efficacy are associated drawbacks. Towards solving this problem, Ngilirabanga et al. employed a novel approach to co-crystallize the drugs isoniazid and pyrazinamide with glutaric acid. Their results showed that there was an improvement of desirable physicochemical properties (increased solubility and stability) of the drug co-crystals, which may consequently improve their pharmacological and therapeutic properties. Two papers, a Review by Marzuq et al. and a research article by Anyam et al. provided a comprehensive insight into efforts by African scientists to combat tropical infectious diseases through search for novel natural compounds for development of chemotherapy. Marzuq et al. catalogued medicinal chemistry information on 93 compounds from different natural sources that have been described to possess antiparasitic activities against the pathogens of malaria, trypanosomiasis, and leishmaniasis. Such detail information on the different novel drug candidate compounds in a single piece, will enhance antiparasitic drug development. The discovery of medicinal phytochemicals complements high-tech drug discovery programs involving screening of combinatorial libraries and rational drug discovery (Balogun et al., 2019), which may not be practicable in the continent due to limited technologically advanced facilities. Resistance to drugs by pathogenic organisms is a major problem in disease management by chemotherapy. Drug resistance may result from genetically encoded resistance factors such as drug degrading enzymes or drug efflux transport proteins, or through formed extracellular matrices that enable agglutination to form a community (most especially bacteria) and colonise surfaces. The last scenario reduces the accessibility of an administered drug to the bacteria, therefore, preventing the drug effect. With this background, Openda et al. developed a photodynamic antimicrobial chemotherapy technique (PACT) in which metal-conjugated porphyrins are loaded onto carbon nanomaterials and used to treat *Staphylococcus aureus* followed by exposure to light. They reported that the treatment was effective on both planktonic and biofilm forms. The mechanism of action of PACT is based on nanomaterial-mediated rapid transport of conjugated photosensitiser dyes across barriers and metal-enhanced photosensitiser property of the dyes (such as porphyrins), i.e., ability to generate injurious reactive species upon exposure to light. Recent advances in PACT were adequately reviewed by Oyim et al. where they concluded on the possibility of adding PACT systems to the current therapeutic arsenals for combating microbial resistance, especially where the conventional antimicrobials have failed. Finally, it is important continue investigations toward development of more sensitive analytical techniques for detection and quantitation of pollutants, contaminants, or drugs in both the environment and in living systems. In this regard, based on the specific electrocatalytic behaviour of chemical substances, Chundu et al. successfully developed and fabricated an electrochemical sensor for accurate detection and quantification of various analytes. This was achieved through co-polymerization of different monomeric forms of phthalocyanine and conjugated to graphene oxide, and finally linked to glassy carbon electrode. They validated the sensor by using it detect and quantify ascorbic acid and tryptophan, two coexisting physiologically important molecules.

In conclusion, this research topic has provided an excellent platform for African scientists to share their research and achievements with the global research community. We believe this will promote collaborations amongst scientists in the continent towards bringing solutions to the myriads of problems that affect the continent and the world at large.

The guest editors acknowledge the authors for their commendable efforts, as well as the reviewers for their time and dedication. We sincerely thank the editorial staff of this issue for this bold idea and valuable assistance throughout the editing process.

AUTHOR CONTRIBUTIONS

All authors listed have made a substantial, direct, and intellectual contribution to the work and approved it for publication.

FUNDING

EB is supported by the Fogarty International Center of the National Institutes of Health, United States of America under Award Number K43TW012015.

REFERENCES

Balogun, E. O., Inaoka, D. K., Shiba, T., Tsuge, C., May, B., Sato, T., et al. (2019). Discovery of Trypanocidal Coumarins with Dual Inhibition of Both the Glycerol Kinase and Alternative Oxidase of Trypanosoma Brucei Brucei. *FASEB j.* 33 (11), 13002–13013. doi:10.1096/fj.201901342r

Balogun, E. O., Nok, A. J., and Kita, K. (2016). Global Warming and the Possible Globalization of Vector-Borne Diseases: a Call for Increased Awareness and Action. *Trop. Med. Health* 44, 38. doi:10.1186/s41182-016-0039-0

Boutayeb, A. (20102010). "The Impact of Infectious Diseases on the Development of Africa," in *The Impact of Infectious Diseases on the Development of Africa. Handbook of Disease Burdens and Quality of Life Measures*. Editors VR Preedy and RR Watson (New York, NY: Springer), 1171–1188. doi:10.1007/978-0-387-78665-0_66

Duermeijer, C., Amir, M., and Schoombee, L. (2018). Africa Generates Less Than 1% of the World's Research; Data Analytics Can Change that. Available at: https://www.elsevier.com/connect/africa-generates-less-than-1-of-the-worlds-research-data-analytics-can-change-that (Accessed January 4, 2022).

OECD (2022). Gross Domestic Spending on R&D (Indicator). *Res. Develop.*. doi:10.1787/d8b068b4-en

WHO (2019). Diseases Cost the African Region $2.4 Trillion a Year, Says WHO. Available at: https://www.afro.who.int/news/diseases-cost-african-region-24-trillion-year-says-who (Accessed January 4, 2022).

WMO (2021). Climate Change Triggers Mounting Food Insecurity, Poverty and Displacement in Africa. Available at: https://public.wmo.int/en/media/press-release/climate-change-triggers-mounting-food-insecurity-poverty-and-displacement-africa (Accessed January 05, 2022).

Conflict of Interest: The authors declare that the research was conducted in the absence of any commercial or financial relationships that could be construed as a potential conflict of interest.

frontiers in Chemistry

ORIGINAL RESEARCH
published: 05 November 2020
doi: 10.3389/fchem.2020.581226

Synthesis and Characterization of 2D Metal-Organic Frameworks for Adsorption of Carbon Dioxide and Hydrogen

Piwai Tshuma [1], Banothile C. E. Makhubela [2*], Christophe A. Ndamyabera [3], Susan A. Bourne [3] and Gift Mehlana [1*]

[1] Department of Chemical Technology, Faculty of Science and Technology, Midlands State University, Gweru, Zimbabwe, [2] Center for Synthesis and Catalysis Department of Chemical Sciences, Faculty of Science, University of Johannesburg, Johannesburg, South Africa, [3] Department of Chemistry, Faculty of Science, University of Cape Town, Cape Town, South Africa

Edited by:
Tebello Nyokong,
Rhodes University, South Africa

Reviewed by:
Zhiyong Guo,
Fuzhou University, China
Seong Huh,
Hankuk University of Foreign Studies,
South Korea

***Correspondence:**
Banothile C. E. Makhubela
bmakhubela@uj.ac.za
Gift Mehlana
mehlanag@staff.msu.ac.zw

Specialty section:
This article was submitted to
Supramolecular Chemistry,
a section of the journal
Frontiers in Chemistry

Received: 08 July 2020
Accepted: 28 September 2020
Published: 05 November 2020

Citation:
Tshuma P, Makhubela BCE, Ndamyabera CA, Bourne SA and Mehlana G (2020) Synthesis and Characterization of 2D Metal-Organic Frameworks for Adsorption of Carbon Dioxide and Hydrogen. Front. Chem. 8:581226. doi: 10.3389/fchem.2020.581226

The reaction of $Cd(NO_3)_2{\cdot}4H_2O$ and $Zn(NO_3)_2{\cdot}6H_2O$ with the bipyridyl dicarboxylate ligand H_2bpydc (2,2′-bipyridine-4,4′-dicarboxylic acid) afforded two porous metal organic frameworks $[Cd(bpydc)_2(DMF)_2{\cdot}2DMF]_n$ (JMS-3) and $[Zn(bpydc)(DMF){\cdot}DMF]_n$ (JMS-4). X-ray diffraction studies revealed that both JMS-3 and JMS-4 crystallize in the monoclinic crystal. The MOFs possess 2D interdigited networks with (**sql**) topology. Sorption studies showed that the activated phase of JMS-3 had CO_2 volumetric uptakes of 26.50 and 30.89 cm^3 (STP) g^{-1} (1.18 and 1.39 mmol g^{-1}) whist JMS-4 gave 10.96 and 16.08 cm^3 (STP) g^{-1} (0.49 and 0.71 mmol g^{-1}) at 298 and 273 K respectively.

Keywords: carbon dioxide, topology, metal-organic framework, adsorption, catalysis

INTRODUCTION

One of the most threatening environmental issues is the atmospheric increase in the concentration of CO_2. Climate change and global warming has been attributed to the gradual increase in CO_2 in the atmosphere (Poloni et al., 2014; Saeidi et al., 2014; Cuéllar-Franca and Azapagic, 2015; Gunasekar et al., 2016; Hu et al., 2019). Different strategies meant to reduce CO_2 emissions such as the use of renewable energy and CO_2 capture and storage (CCS) (Liang et al., 2013) have been proposed and adopted. Although CCS is an attractive method of dealing with CO_2 emissions, it is of paramount importance to find ways recycling greenhouse gas as well as harnessing renewable sources of energy for industrial applications.

Recent studies have demonstrated that metal-organic frameworks (MOFs) are good candidates for CCS. MOFs are crystalline materials constructed using metal centers and organic linkers (Dhakshinamoorthy et al., 2012; Chughtai et al., 2015). These materials have shown remarkable H_2 and CO_2 capture and storage at high pressure. Notably, MOFs have been shown to outperform other materials, such as zeolites, silica and metal oxides, in terms of adsorption capacities for CO_2 as well as in separation of gases materials (Choi et al., 2009; Li et al., 2011; Anbia and Hoseini, 2012; Ding et al., 2019; Kidanemariam et al., 2019). These high adsorption capacities are attributed to high porosity, large surface area, tunable functionalities as well as uniform-structured cavities (Liu et al., 2014) which makes them promising candidates for diverse applications in gas storage (Yang et al., 2012), separation (Mehlana et al., 2014), catalysis (Valvekens et al., 2013), and sensing (Mehlana et al., 2015a,b; Mehlana et al., 2016). In order to improve the gas adsorption capacity of MOFs toward CO_2, strategies such as pore size control (Sun et al., 2006; Lin et al., 2011), incorporation of open metal sites (Britt et al., 2009; Liang et al., 2013) grafting of amines into the frameworks and introduction of nitrogen-rich organic linkers (Demessence et al., 2009; Andirova et al., 2016) have been proposed.

As part of our ongoing work to develop novel materials that can be used for carbon dioxide capture and conversion using the bipyridyl dicarboxylate linker, herein, we present two novel MOFs of $[Cd_2(bpydc)_2(DMF)_2{\cdot}2DMF]_n$ and $[Zn(bpydc)(DMF){\cdot}DMF]_n$ which were successfully synthesized using 2,2′-bipyridine-4,4′-dicarboxylate (bpdc) linker (Tshuma et al., 2020a,b). Topological analysis revealed that the MOFs possess a 2D network with square lattice topology. The MOFs JMS-3 and JMS-4 (where JMS denotes Johannesburg and Midlands State) showed a crystalline to crystalline transformation upon activation. Chemical stability studies of the activated phases revealed that JMS-3a is not stable in a number of solvents while JMS-4a showed greater stability. Both JMS-3a and JMS-4a showed appreciable CO_2 and H_2 adsorption capacity. This makes both JMS-3a and JMS-4a potential candidates for CO_2 storage and conversion.

EXPERIMENTAL SECTION

Materials and Reagents

$Cd(NO_3)_2{\cdot}4H_2O$, $Zn(NO_3)_2{\cdot}6H_2O$), N,N- dimethylformamide (DMF) and H_2bpydc were purchased from Sigma-Aldrich and used without further purification unless otherwise mentioned.

Analytical Methods

Single crystal X-ray diffraction (SCXRD) data collection was done on a Bruker KAPPA APEX II DUO Diffractometer equipped with graphite monochoromated Mo Kα radiation (λ = 0.71073 Å). The XPERT-PRO diffractometer (Cu Kα radiation) was used to collect Powder X-ray diffraction (PXRD) data. A current flow of 40 mA and voltage of 40 kV was used to generate the X-rays. The Perkin Elmer Fourier BX II fitted with an ATR probe was used to collect Fourier Transform Infrared (FITR) spectra of the samples. The thermal profiles of the JMS-3a and JMS-4a were recorded on a TA Discovery Instrument TA-Q50. In a typical experiment, samples weighing between 2 and 5 mg were heated at 10°C min^{-1} within a temperature range of 25–600°C under nitrogen purge gas flow of 50 $mLmin^{-1}$. Adsorption studies were performed using a Micrometrics 3Flex Surface Analyser. The samples were prepared by using a Micrometrics Flowprep with the flow of nitrogen over the samples for 4 h at 60°C. The samples were activated at 150°C under vacuum for 2 h before the analysis to remove all the solvent molecules.

SYNTHESIS

Synthesis of $[Cd_2(bpdc)_2(DMF)_2{\cdot}2DMF]_n$ (JMS-3) and $[Zn(bpdc)(DMF){\cdot}DMF]_n$ (JMS-4)

JMS-3: About 25 mg (0.098 mmol) of H_2bpydc was predissolved in DMF (10 mL) followed by addition of $Cd(NO_3)_2{\cdot}4H_2O$ (117 mg, 0.38 mmol). The resulting solution was sealed in a glass vial and heated at 115°C for 8 h to yield colorless block shaped crystals. Elemental Analysis, Found % C 43.3, %H 4, %N 11.4, calculated, % C 43.1, %H 3.99, %N 11.2.

JMS-4: A mixture of H_2bpydc (27 mg, 0.105 mmol) and $Zn(NO_3)_2{\cdot}6H_2O$ (112 mg, 0.377 mmol) were dissolved in DMF at room temperature. The reaction mixture was placed in a sealed glass vial and heated at 100°C for 6 h to obtain colorless block crystals. Elemental Analysis, Found % C, 47.5 %H 4.2, %N 12.1, calculated, % C 47.6, %H 4.4, %N 12.3

Crystallographic Data Collection and Refinement

JMS-3 and JMS-4's single crystal data were collected on a Bruker KAPPA APEX II DUO diffractometer equipped with graphite monochoromated Mo Kα radiation (λ = 0.71073 Å). The SAINT program was used for unit cell refinement and data reduction. The structures of the two MOFs were solved by direct methods (program SHELXS2018) (Sheldrick, 2018) and refined anisotropically on F^2 full-matrix least-squares with SHELXL (Sheldrick, 2018) using the X-SEED (Barbour, 2001) interface. All non-hydrogen atoms were refined anisotropically The hydrogen atoms were placed in idealized positions using the riding model and assigned temperature factors relative to the parent atom. The

TABLE 1 | Crystal data and refinement parameters for JMS-3 and JMS-4.

	JMS-3	JMS-4
Empirical formula	$C_{36}H_{40}N_8Cd_2O_{12}$	$C_{18}H_{20}N_4Zn_1O_6$
Formula weight ($gmol^{-1}$)	1001.58	453.75
Temperature/K	293(2)	150(2)
Crystal system	monoclinic	monoclinic
Space group	P2(1)/c	P2(1)
a/Å	18.4447(13)	9.3824(6)
b/Å	15.0567(11)	14.7232(9)
c/Å	16.0209(11)	14.7089(9)
α/°	90	90
β/°	113.878(1)	101.203(2)
γ/°	90	90
Volume/$Å^3$	4068.4(5)	1993.2(2)
Z	4	4
Calculated density (g/cm^3)	1.635	1.5119
μ(Mo-Kα) /mm^{-1}	1.12	1.27
F(000)	2016	936
Crystal size/mm^3	0.38 × 0.36 × 0.21	0.26 × 0.20 × 0.17
Radiation	MoKα (λ = 0.71073)	MoKα (λ = 0.71073)
2θ Max/°	56.82	52.94
Reflections collected	95569	54023
No. unique data	10205	4105
Goodness of fit on S	1.021	1.085
Final R indexes [I>=2σ (I)]	0.0638	0.0546
Final wR_2 indexes [all data]	0.0829	0.1052
Largest diff. peak/hole/e $Å^{-3}$	0.69/−0.57	1.15/−0.80

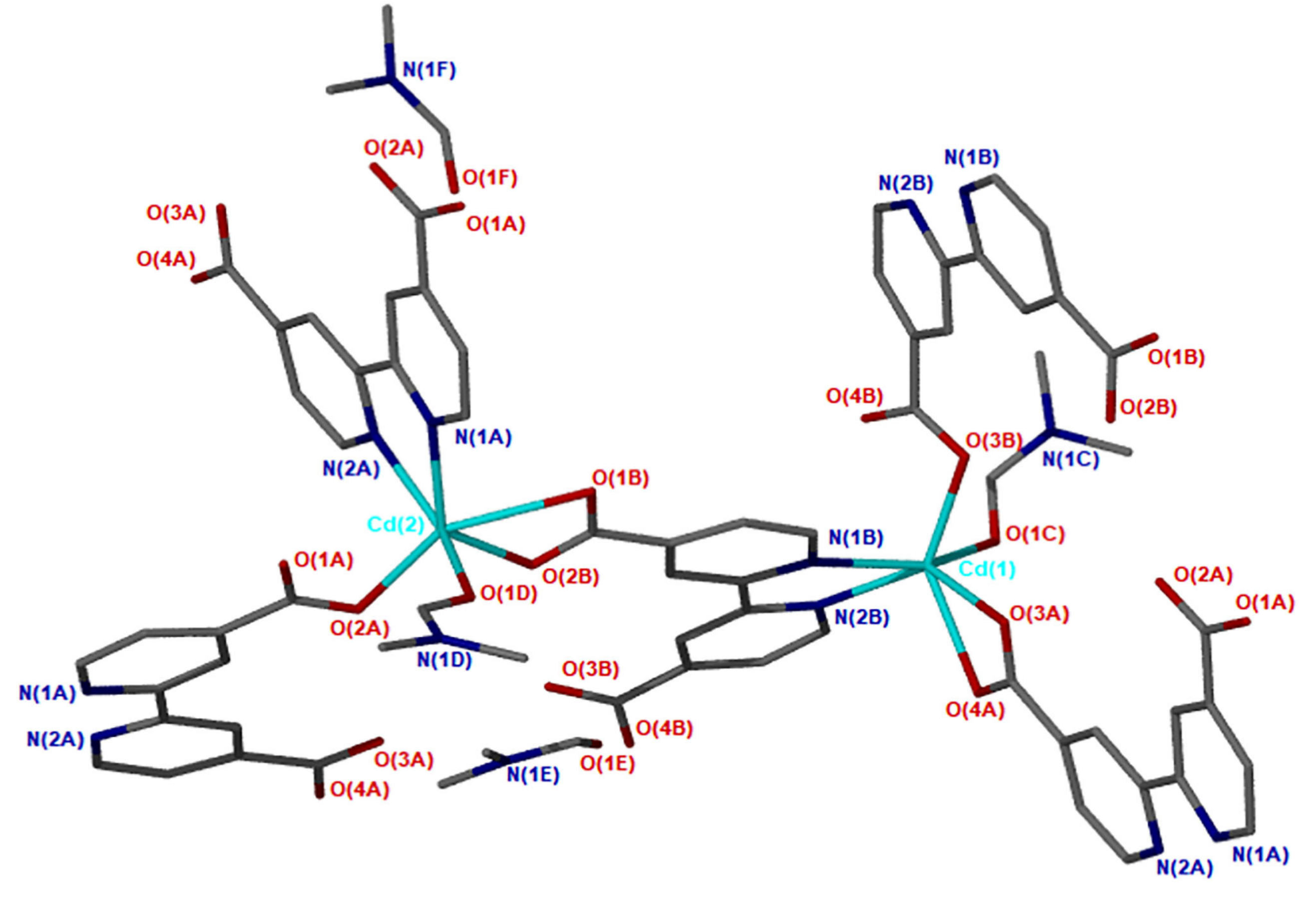

FIGURE 1 | Coordination environment of Cd(II) in JMS-3.

crystallographic data for JMS-3 and JMS-4 with CCDC numbers 2010231 and 2010232, respectively, is given in **Table 1**.

RESULTS AND DISCUSSION

Structural Description

X-ray diffraction analysis using the single crystal method revealed that JMS-3 crystallizes in the monoclinic system and space group $P2_1/c$. The asymmetric unit of JMS-3, comprises of two crystallographic independent Cd(II) centers, two deprotonated bpydc linkers, two coordinated DMF molecules and two uncoordinated DMFs. As shown in **Figure 1**, each cadmium metal center is bound to three bpydc linkers. The carboxylate moiety assumes both bidentate and monodentade binding mode. Two nitrogen atoms of the third linker are chelated to Cd(II). A DMF molecule is also bound to each of the Cd(II) centers. The Cd–N bond length around Cd ranges from 2.318(2) to 2.366 (3) while Cd-O ranges from 2.239 (2) to 2.588(2) Å (see **Supplementary Table 1**). The bond length around the two metal centers are different. This explains why the structure contains two crystallographically independent Cd(II) centers. The Cd(II) metal center assumes a distorted octahedral geometry with bond angles ranging from 54.19(8) to 152.57(9) and 84.89(8) to 154.73(8)° for Cd1 and Cd2, respectively. The packing diagram of JMS-3 displays 2D networks which are interdigited (**Figure 2A**). Coordinated and uncoordinated DMF molecules are trapped in the rectangular channels as illustrated in **Figure 2B**. Weak intermolecular and intramolecular C-H…O bonding exist between the host framework and guest molecules. These are suggested to reinforce the geometry and impart stability in the MOF. Guest molecules occupy 53.8% of the unit cell volume, as estimated in PLATON (Spek, 2009).

JMS-4 crystallizes in the $P2_1$ space group. The asymmetric unit comprises of one zinc metal center, one deprotonated bpydc linker and two DMF molecules. The Zn(II) is coordinated to one bpydc linker through two monodentate Zn(II)-O bonds to the carboxylate moiety, two bipyridyl nitrogen atoms in a chelating fashion and one DMF molecule. This gives rise to a trigonal bipyramidal coordination as illustrated in **Figure 3**. The Zn–N ranges from 2.1019(2) to 2.177(3) Å while the Zn-O bond length ranges from and 1.976(2) to 2.104(2), respectively. These bond lengths are given in **Supplementary Table 2** and are consistent with literature reports. Analysis of the bond angles around the zinc center shows that they are within a range of 76.40(10) to 159.71(10)°. **Figure 4** shows the packing diagram of JMS-4 with 2D layers packing in a similar fashion to that of JMS-3.

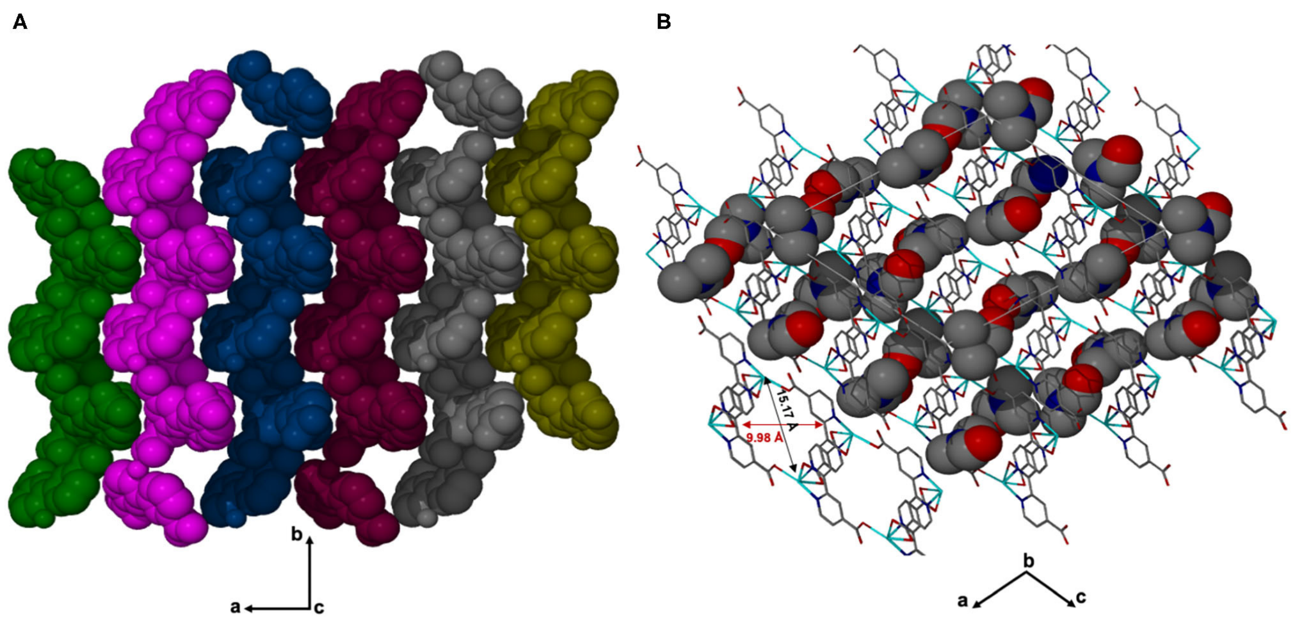

FIGURE 2 | **(A)** Structure of JMS-3 displaying interdigited channels, viewed along *c*-axis. **(B)** The 2D network of JMS-3 guest molecules are drawn with van der Waals radii.

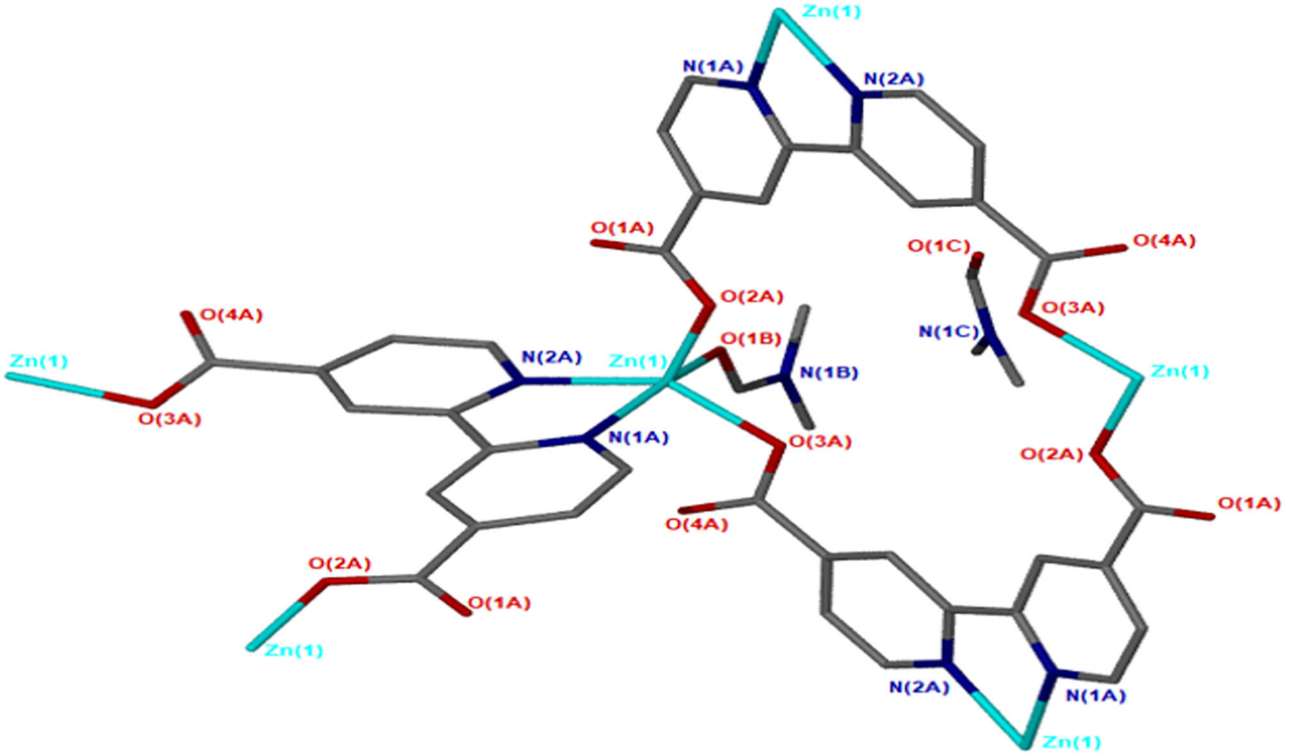

FIGURE 3 | Coordination geometry of Zn(II) in JMS-4.

The observed rectangular channels which are occupied by both coordinated and uncoordinated DMF molecules (10.342 × 9.036 Å) run along *b*-axis. PLATON (Spek, 2009) estimates that the volume occupied by both the coordinated and uncoordinated DMF molecules accounts for 52.3% of the unit cell volume. There are no noticeable interactions between the 2D network

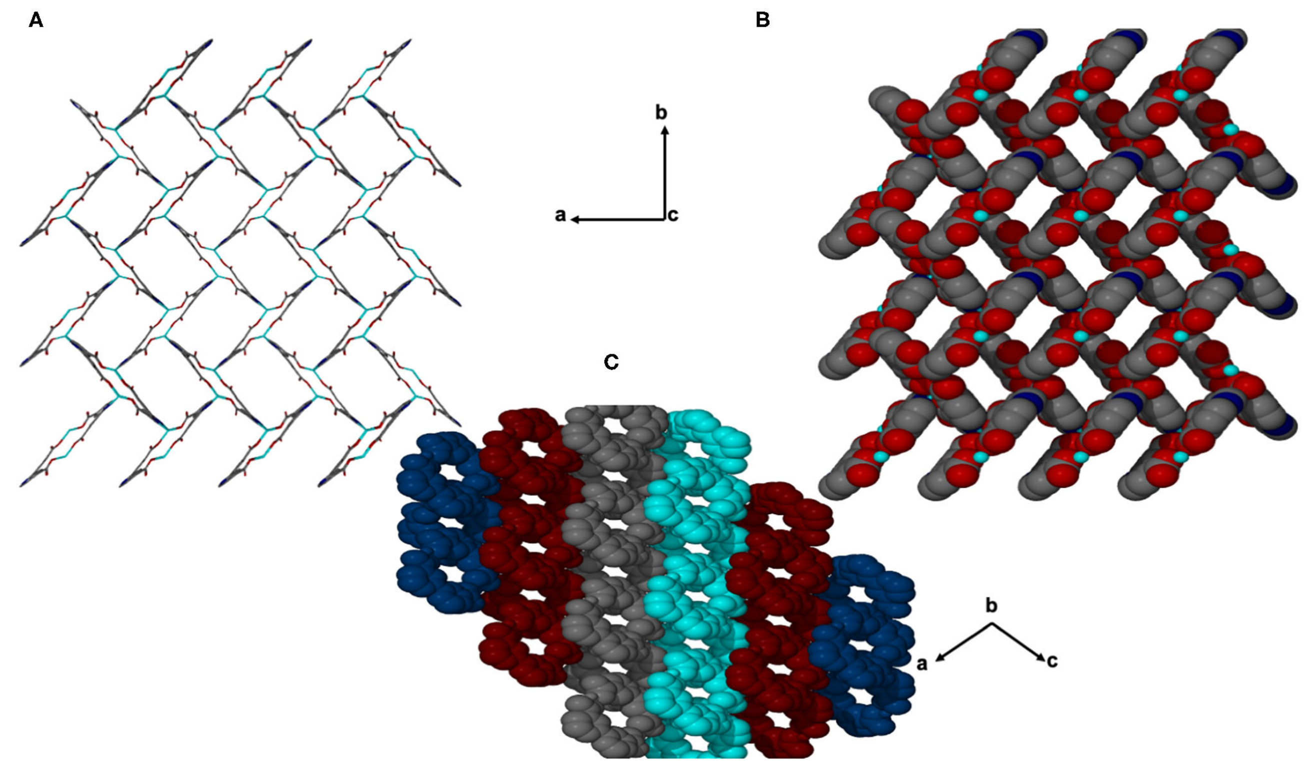

FIGURE 4 | Channels of JMS-4 **(A)** stick form, **(B)** space filling viewed along c axis, and **(C)** Packing diagram drawn in Van der waals radii displaying the interdigited chains.

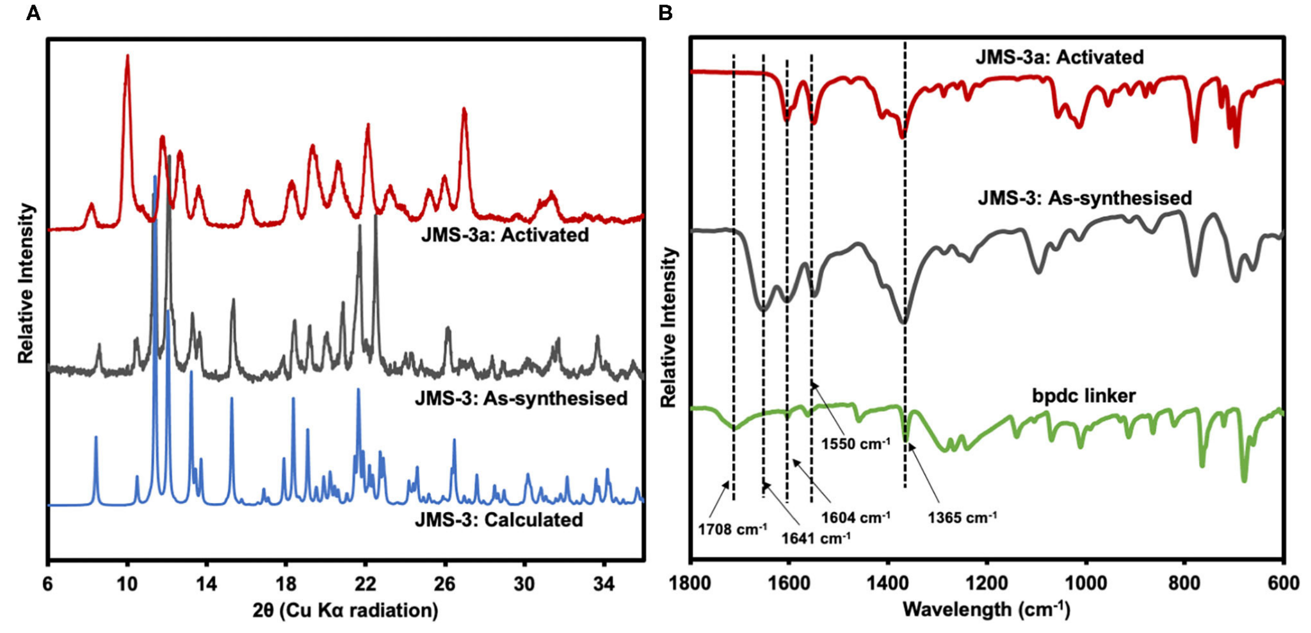

FIGURE 5 | **(A)** PXRD patterns of calculated, as-synthesized and activated JMS-3. **(B)** IR spectra of the linker, as synthesized and activated JMS-3.

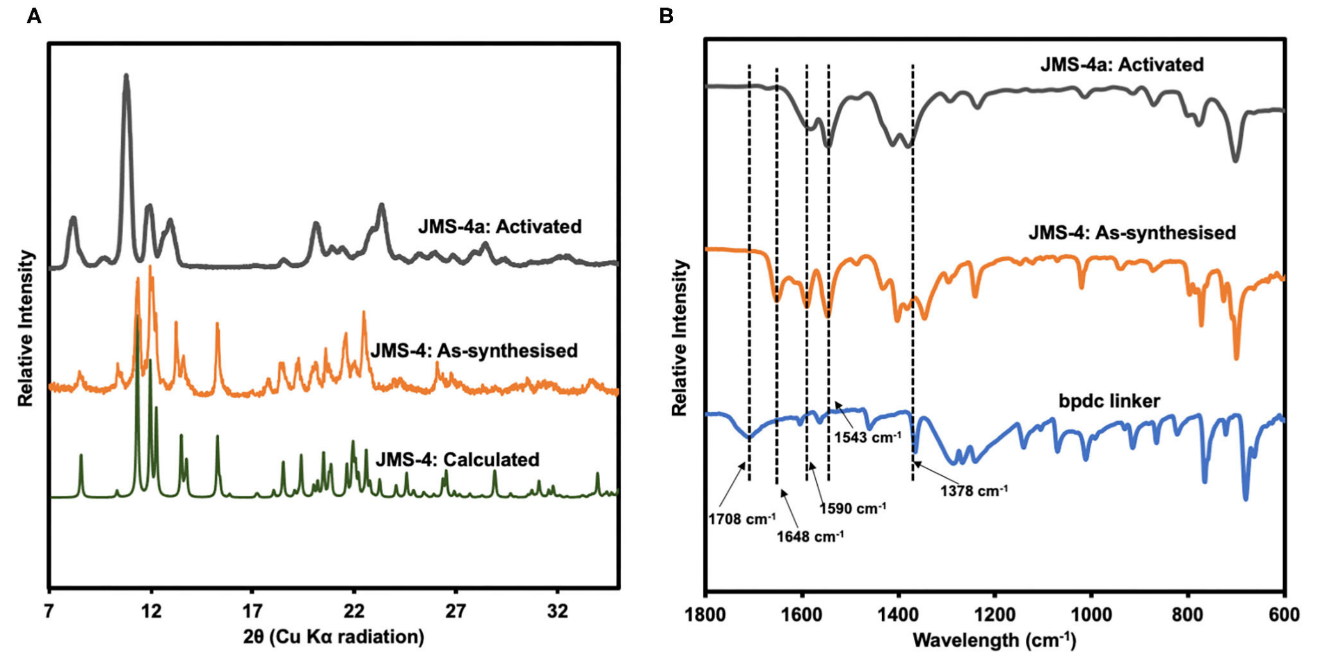

FIGURE 6 | (A) PXRD patterns of calculated, experimental and activated JMS-4, **(B)** IR spectrum of the linker, as-synthesized and activated JMS-4.

and the uncoordinated guest DMF molecules. However, weak intermolecular hydrogen bonding between the 2D layers and π…π interactions of the aromatic rings stabilizes the structure.

Thermal Analysis and PXRD Studies

Thermal analysis of JMS-3 by TGA illustrated in **Supplementary Figure 1** exhibits an initial mass loss of 28.6% between 100 and 150°C. The observed weight loss is attributed to the extrusion of four DMF molecules (calculated 29.2%). The MOF was activated by replacing the DMF molecules by methanol followed by heating at 24 h at 80°C to give JMS-3a. As shown in **Figure 5A**, a comparison of the experimental PXRD of JMS-3 with the calculated pattern, reveals a good match confirming phase purity of the as-synthesized MOF. Upon removal of the guest DMF molecules, JMS-3 undergoes a structural transformation as evidenced by the appearance of new diffraction peaks around 10, 16, and 27 two-theta positions.

FTIR results presented in **Figure 5B** shows that the band at 1708 cm^{-1} in the linker shifts to 1,604 cm^{-1} in JMS-3, which is evidence that the carboxylate moiety is coordinated to the Cd(II) center. These results are consistent with single crystal X-ray data. Successful activation of the MOF is evidenced by the disappearance of the FTIR band at 1,641 cm^{-1}, which is attributed to the carbonyl stretch of DMF molecules. The band located at 1,550 cm^{-1} is attributed to the C-C of the benzene ring. The carboxylate asymmetric and symmetric carboxylate stretches were observed at 1,604 and 1,365 cm^{-1}, respectively, with a magnitude of separation of 239 cm^{-1}. After activation of JMS-3, the position of the bands does not change suggesting that the integrity of the carboxylate functional group is retained (Lu et al., 2016).

The thermal behavior of JMS-4 was examined by TGA. An initial weight loss of 32.5% observed in the TGA curve in **Supplementary Figure 2** is attributed to the loss of two DMF molecules modeled in the asymmetric unit (calculated 32.2%). Framework decomposition occurs around 350°C. No significant weight loss occurs below 350°C on the TGA curve of the activated framework (JMS-4a), indicating solvent molecules have been completely removed, although due to humidity, about 4% loss was still observed on the activated sample curve.

PXRD studies confirmed the phase purity of JMS-4 as evidenced by excellent agreement between the calculated and experimental diffraction patterns (**Figure 6A**). Upon activation of JMS-4 a new phase is obtained. The IR spectrum of as-synthesized JMS-4 (**Figure 6B**) shows a band at 1,648 cm^{-1} assignable to carbonyl stretch of DMF molecules. This band disappears upon activation. The bands at 1,590 and 1,378 cm^{-1} are assigned to the asymmetric and symmetric stretches of the carboxylate group respectively, with a magnitude of separation of 212 cm^{-1}. Upon activation, the FTIR analysis suggests that the integrity of carboxylate moiety with respect to its binding mode is not altered (Lu et al., 2016).

Topological Analysis

Topological analysis of JMS-3 and JMS-4 was perfomed using Topos computer programme (Coelho, 2007). As shown in **Figure 7A**, the compound was reduced to a simple net by considering each metal center as a 4 connected node. Each cadmium center is connected to the other cadimium center by the linear bpydc bridges to produce a square-lattice (**sql**) topology (Mehlana et al., 2013, 2017). The packing in **Figure 7B** is a zig-zag 2D layered network. The packing is in an offset position with approximately equi-distances between the layers (Mehlana et al., 2015a; Tella et al., 2017). Although the two MOFs have diffrenent geometries around the metal center and crystallize in different space groups, they exhibit the same **sql** topology.

Non-isothermal Desorption Kinetics

The kinetics of DMF desorption in JMS-3 and JMS-4 were investigated to determine the activation energy required to remove the guest molecules. The Ozawa method, which relies on the use of several heating rates and the temperature being

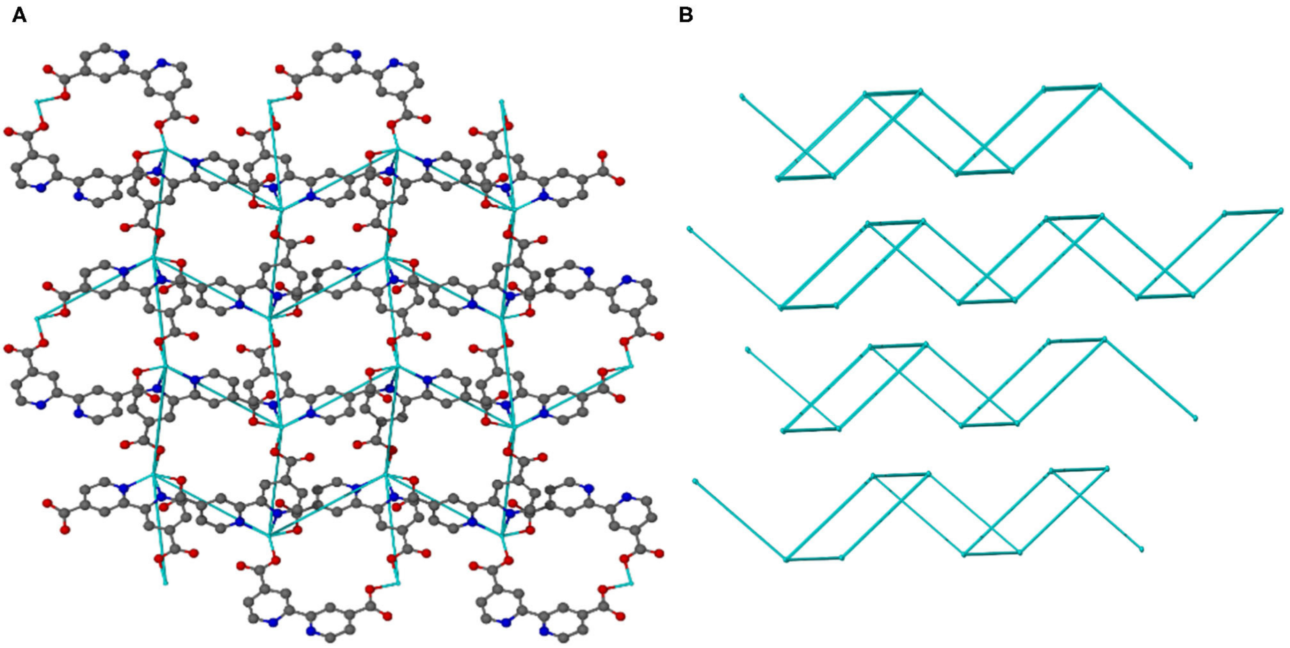

FIGURE 7 | (A) 4-connected 2D net of JMS-3 and **(B)** Zig-zag packing in JMS-3.

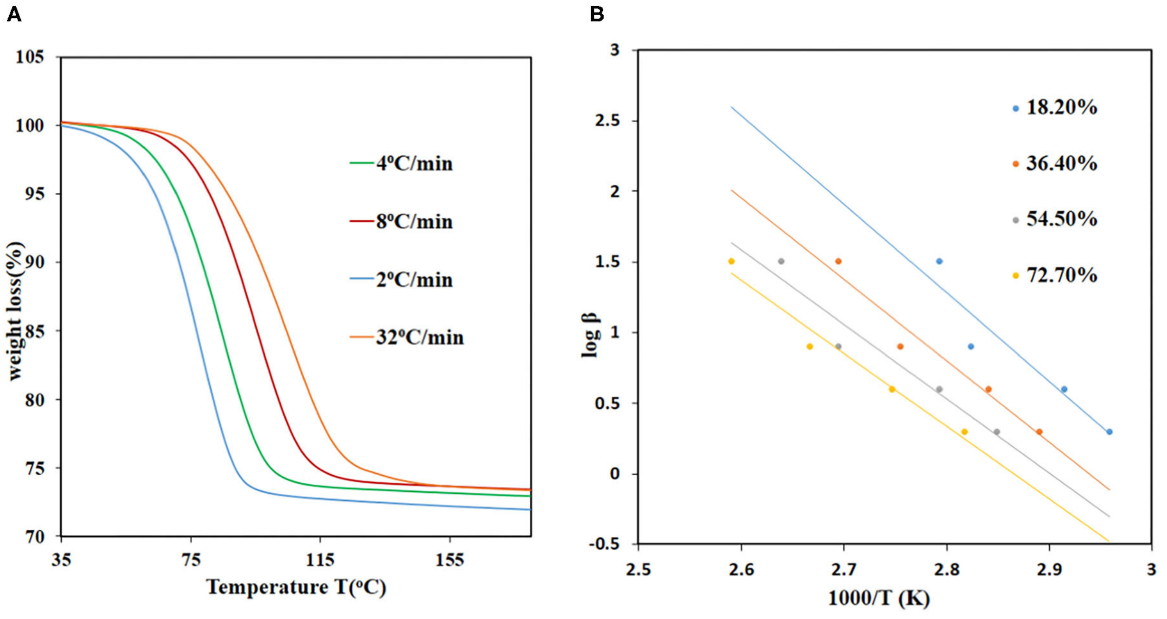

FIGURE 8 | Desorption kinetics for JMS-4: **(A)** TGA traces obtained using different heating rates as a function of temperature, **(B)** log β vs. 1/T, the gradient of the slope were used to calculate the activation energies.

recorded at specific conversion levels for each heating rate was used (Ozawa, 1965). The method made makes use of the equation below:

$$\log \beta\alpha = \log\left(\frac{A\alpha.\mathrm{Eax}}{g(a)R}\right) - 2.315 - 0.457\left(\frac{Eaa}{RTa}\right),$$

Where β_α – heating rate
A_α – frequency factor
$E_{a\alpha}$ – activation energy
T_a – temperature at each conversion level
g_α – kinetic model

The equation can be used to calculate the activation energies at each conversion level. The TGA data was converted to extent-of-reaction (α) vs. temperature and the information obtained from the curves used to plot graphs of log β_α vs. $1/T_a$. The activation energies for JMS-3 ranged from 68.9 to 90.1 kJ mol^{-1} within a conversion range 16.7–83.3% conversion levels, respectively, while the activation energies ranging from 68.9 to 91.6 kJ/mol for JMS-4 within a conversion range of 22–80%. **Figure 8A** shows the desorption kinetic profiles of JMS-4 at different heating rates from the non-isothermal runs while **Figure 8B** depicts plots of log β vs, 1/T, the slope of which is ensued the activation energies at the different conversion levels. The kinetic profiles of JMS-3 is presented in **Supplementary Figure 3**. The two MOFs exhibited similar average activation energies of 81.65 and 82.35 kJ/mol for JMS-3 and JMS-4, respectively. The observed energies are consistent with the modeled DMF molecules being coordinated to the metal center and the structural features of the MOFs.

Chemical Stability Studies

To test the chemical stability, the activated MOFs, **JMS-3a** and **JMS-4a** were soaked in different organic solvents for 36 h. As shown in the PXRD pattern of the recovered samples (**Figure 9A**), **JMS-3a** is not stable under different chemical environments. A new phase, which is uniform throughout is obtained. Contrary to **JMS-3a,** the structure of **JMS-4a** is maintained as shown by an excellent agreement between the PXRD paterrns of the activated phase and the ones obtained after soaking the materials in different solvents for 36 h (**Figure 9B**).

Carbon Dioxide and Hydrogen Adsorption Studies

CO_2 adsorption isotherms of JMS-3a and MOF JMS-4a carried at temperatures (298, 273, and 195 K) and 1 atm pressure (**Figure 10**) revealed a Type-1 isotherm, which is typical of microporous materials (Alhamami et al., 2014). JMS-3a gave volumetric uptakes of 26.50 and 30.89 cm^3 (STP) g^{-1} (1.18 and 1.39 $mmolg^{-1}$) whist JMS-4a gave 10.96 and 16.08 cm^3 (STP) g^{-1} (0.49 and 0.71 $mmolg^{-1}$) at 298 and 273 K, respectively. At 195 K, the MOFs show a rapid uptake of CO_2 at low pressure with volumetric uptake of 34.66 and 38.84 cm^3 (STP)g^{-1} (1.52 and 1.74 $mmolg^{-1}$) for JMS-3a and JMS-4a, respectively, confirming inherent permant porosity of the MOFs. CO_2 sorption studies at 273 K revealed a surface area of 151 and 36 m^2g^{-1} for JMS-3a and JMS-4a, respectively. The use of CO_2 sorption for BET calculation is controversial, however, Bae et al. demonstrated that this method maybe applied to ultramicroporous materals at 273 K (Kim et al., 2016). JMS-3a perform exceptionally well for CO_2 capture at 273 and 298 K, probably due to its high suface area compared to JMS-4a. Upon activation, the PXRD pattern of JMS-3a (**Figure 3**) shows that structural transformation is not much

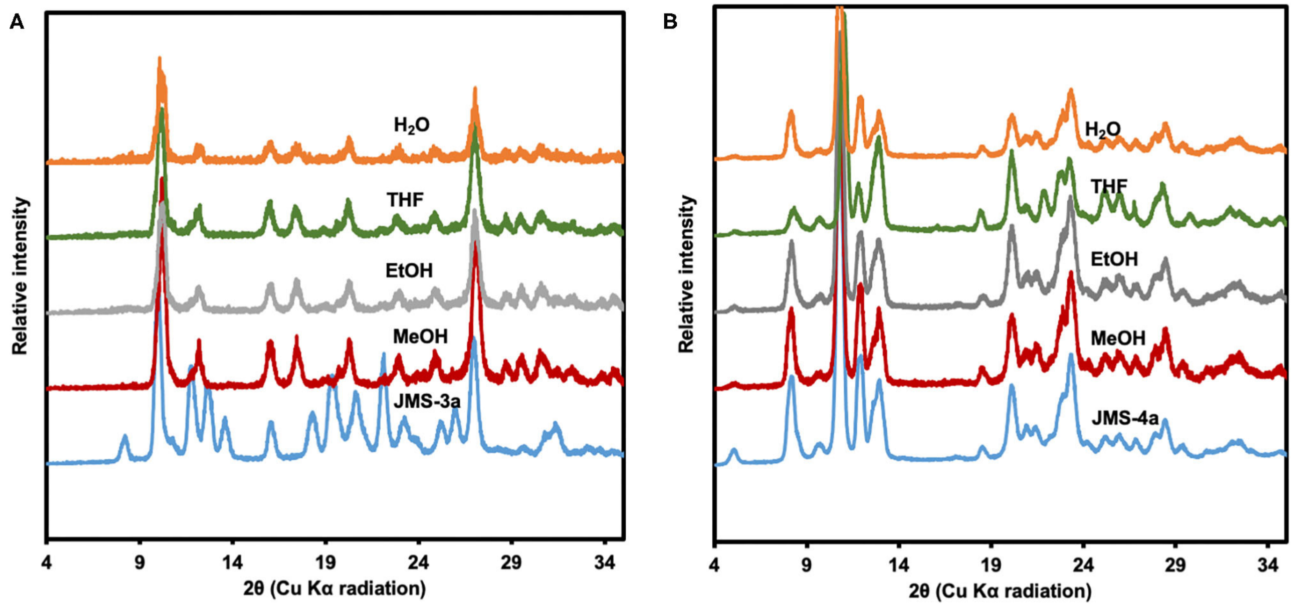

FIGURE 9 | (A) PXRD patterns of JMS-3a **(B)** JMS-4 soaked in several solvents for 36 h.

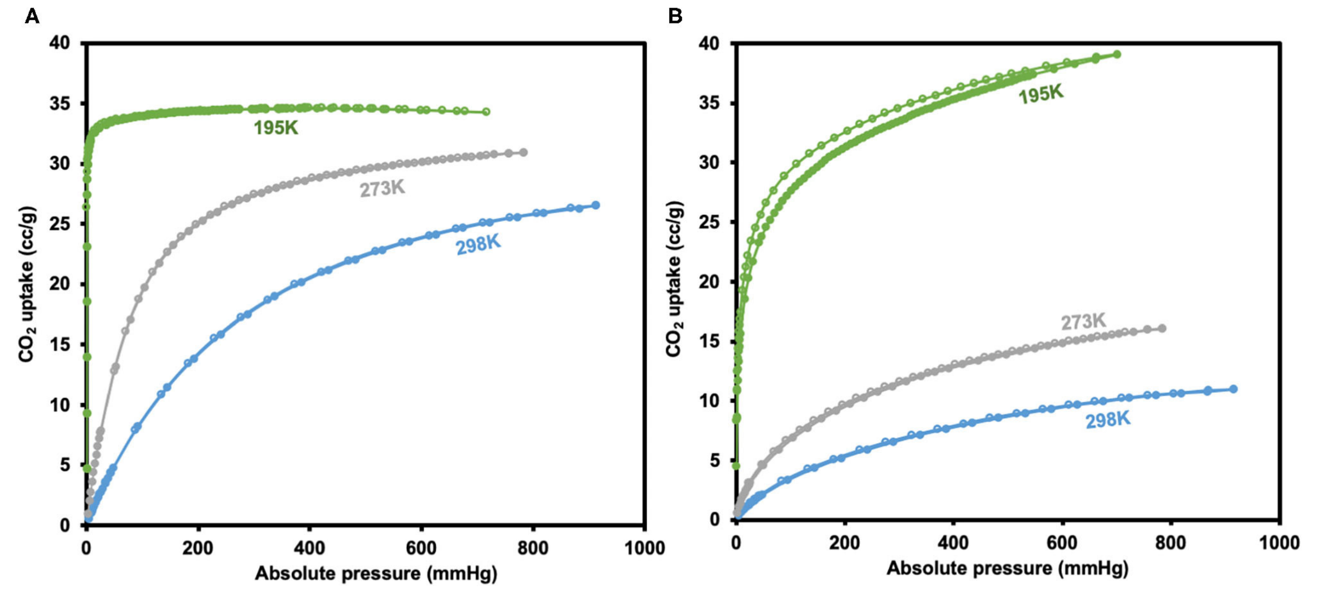

FIGURE 10 | CO_2 adsorption-desorption isotherms for JMS-3a **(A)** and JMS-4a **(B)** (closed circles represent adsorption and open circles desorption).

as compared to JMS-4a (**Figure 7**). The adsorption branches of the isotherm carried out at 273 and 298 K were used to obtain a precise prediction over the quantity of CO_2 adsorbed at the saturation point (Ugale et al., 2018). The estimated values of isosteric heat (Q_{st}) of adsorption for JMS-3a were found to be 33–34 kJ mol^{-1} at loading values ranging from 0.12 to 0.99 mmol g^{-1}(**Supplementary Figure 4**). CO_2 isotherms for JMS-4a between 273 and 298 K revealed isosteric heats of adsorption values of 29–31 kJ mol^{-1} at loading values of 0.32–0.45 mmol g^{-1} (**Supplementary Figure 5**). The observed CO_2 uptake indicate moderate to strong interaction of CO_2 with the MOFs and are comparable to other MOFs reported in literature as illustrated in **Table 2**.

Hydrogen sorption studies in **Figure 11** reveals a storage capacity of up to 65 and 51 cm^{3}g^{-1} for JMS-3a and JMS-4a at 800 mmHg and 77K, corresponding to sorption of 0.58 and 0.46 wt.% (2.88 and 2.29 mmolg^{-1}), and displays a significant hysteresis loop. The hydrogen adsorption values are comparable to that of [$Cd_2(Tzc)_2$]n (0.55 wt.%) and [Zn(hfipbb)(bpt)]$_n$ (0.44 wt.%) but less than that of [Zn(TCPB)2]$_n$ (0.80 wt.%) under similar conditions.

TABLE 2 | A comparison of CO_2 adsorption capacity for various Cd and Zn based MOFs at 1 atm.

MOF material	Temp (K)	CO_2 uptake (mmolg^{-1})	Qst (kJmol^{-1})	References
[{Cd_2(L-glu)$_2$(bpe)}]$_n$	273 298	0.92 0.64	40.8	Ugale et al., 2017
[$Cd_2(Tzc)_2$]n	195	2.45	-	Zhong et al., 2011
[Zn(TCPB)$_2$]$_n$	195 273	6.29 2.89	-	Lin et al., 2012
[Zn(hfipbb)(bpt)]$_n$	195	1.71	35.8	Chatterjee and Oliver, 2018
	273 298	0.96 0.62		
[$Cd_2(bpdc)_2$]$_n$	195	1.52	34.4	This work
	273 298	1.39 1.18		
[Zn(bpdc)]$_n$	195	1.74	30.7	This work
	273 298	0.71 0.49		

L-glu, L-glutamate dianion; bpe, 1.2-bis(4-pyridyl)ethylene; Tzc, tetraazolate-5-carboxylate; TCPB, 1,3,5-tri(4-carboxyphenoxy)benzene; hfipbb, 4,4′-(hexafluoroisooropylidene)bis (benzoate) and bpt, 4-amino-3,5-bis(4-pyridyl)-1,2,4-triazole. Reports in this table include adsorption capacities in mmolg^{-1}. (Some have been converted to these units from the originally reported units).

CONCLUSIONS

The structures of two MOFs JMS-3 and JMS-4 were reported. These MOFs were analyzed by diffraction and spectroscopic methods. Although the two MOFs crystallized in different space groups, topological analysis revealed that they both exhibit an **sql** net. Desorption kinetic studies for the removal of the DMF molecules revealed that the activation energy required in both systems was comparable (an average of 79 kJ mol^{-1} for JMS-3 and 81 kJ mol^{-1} for JMS-4). The activated phases JMS-3a and JMS-4a were exposed to ethanol, methanol, water and THF to test their chemical stability. As opposed to JMS-3a, JMS-4a did not reveal any structural changes when soaked in these solvents that are normally employed in the catalytic hydrogenation of CO_2. This makes JMS-4a a potential candidate for application in CO_2 conversion reactions. Future work will focus on encapsulating molecular catalysts in JMS-4a for CO_2 hydrogenation studies.

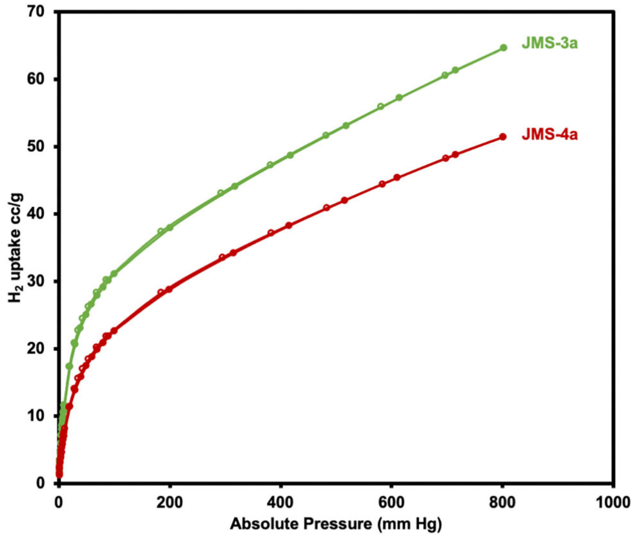

FIGURE 11 | Adsorption and desorption isotherms of JMS-3a and JMS-4a at 77K for H_2 studies.

DATA AVAILABILITY STATEMENT

The datasets presented in this study can be found in online repositories. The names of the repository/repositories accession number(s) can be found in the article/**Supplementary Material**.

AUTHOR CONTRIBUTIONS

PT and CN carried out the experimental work. BM, SB, and GM supervised the experimental work. The first draft of the manuscript was written by PT and was then revised by all the co-authors.

FUNDING

This work was supported by FLAIR research grant.

ACKNOWLEDGMENTS

The authors would like to thank the Royal Society and the African Academy of Sciences (AAS) for funding this project through the Future-Leaders African Independent Research (FLAIR) Program. PT gratefully acknowledges the financial support she received from Organization for Women in Science for the Developing World. The University of Johannesburg Center of Synthesis, Catalysis and Spectrum is also acknowledged for availing their facilities.

SUPPLEMENTARY MATERIAL

The Supplementary Material for this article can be found online at: https://www.frontiersin.org/articles/10.3389/fchem.2020.581226/full#supplementary-material

REFERENCES

Alhamami, M., Doan, H., and Cheng, C. H. (2014). A review on breathing behaviors of metal-organic-frameworks (MOFs) for gas adsorption. *Materials* 7, 3198–3250. doi: 10.3390/ma7043198

Anbia, M., and Hoseini, V. (2012). Development of MWCNT@MIL-101 hybrid composite with enhanced adsorption capacity for carbon dioxide. *Chem. Eng. J.* 191, 326–330. doi: 10.1016/j.cej.2012.03.025

Andirova, D., Cogswell, C. F., Lei, Y., and Choi, S. (2016). Effect of the structural constituents of metal organic frameworks on carbon dioxide capture. *Microporous Mesoporous Mater.* 219, 276–305. doi: 10.1016/j.micromeso.2015.07.029

Barbour, L. J. (2001). X-Seed - a software tool for supramolecular crystallography. *J. Supramolecul. Chem.* 1, 189–191. doi: 10.1016/S1472-7862(02)00030-8

Britt, D., Furukawa, H., Wang, B., Glover, T. G., and Yaghi, O. M. (2009). Highly efficient separation of carbon dioxide by a metal-organic framework replete with open metal sites. *Proc. Natl. Acad. Sci. U.S.A.* 106, 20637–20640. doi: 10.1073/pnas.0909718106

Chatterjee, N., and Oliver, C. L. (2018). A dynamic, breathing, water-stable, partially fluorinated, two-periodic, mixed-ligand Zn(II) metal-organic framework modulated by solvent exchange showing a large change in cavity size: gas and vapor sorption studies. *Crystal Growth Design* 18, 7570–7578. doi: 10.1021/acs.cgd.8b01391

Choi, S., Drese, J. H., and Jones, C. W. (2009). Adsorbent materials for carbon dioxide capture from large anthropogenic point sources. *ChemSusChem* 2, 796–854. doi: 10.1002/cssc.200900036

Chughtai, A. H., Ahmad, N., Younus, H., Laypkov, A., and Verpoort, F. (2015). Metal-organic frameworks: versatile heterogeneous catalysts for efficient catalytic organic transformations. *Chem. Soc. Rev.* 44, 6804–6849. doi: 10.1002/chin.201546250

Coelho, A. (2007). *TOPAS-Academic, Version 4.1 (Computer Software), Coelho* Software, Brisbane.

Cuéllar-Franca, R. M., and Azapagic, A. (2015). Carbon capture, storage and utilisation technologies: a critical analysis and comparison of their life cycle environmental impacts. *J. CO2 Utilization* 9, 82–102. doi: 10.1016/j.jcou.2014.12.001

Demessence, A., Alessandro, D. M. D., Foo, M. L., and Long, J. R. (2009). Strong CO_2 binding in water-stable, triazole-bridged metal-organic framework functionalised with ethylenediamine. *J. Am. Chem. Soc.* 131, 8784–8786. doi: 10.1021/ja903411w

Dhakshinamoorthy, A., Alvaro, M., and Garcia, H. (2012). Commercial metal-organic frameworks as heterogeneous catalysts. *Chem. Commun.* 48, 11275–11288. doi: 10.1039/c2cc34329k

Ding, M., Flaig, R. W., Jiang, H. L., and Yaghi, O. M. (2019). Carbon capture and conversion using metal-organic frameworks and MOF-based materials. *Chem. Soc. Rev.* 48, 2783–2828. doi: 10.1039/C8CS00829A

Gunasekar, G. H., Park, K., Jung, K. D., and Yoon, S. (2016). Recent developments in the catalytic hydrogenation of CO_2 to formic acid/formate using heterogeneous catalysts. *Inorganic Chem. Front.* 3, 882–895. doi: 10.1039/C5QI00231A

Hu, Z., Wang, Y., Shah, B. B., and Zhao, D. (2019). CO_2 capture in metal-organic framework adsorbents: an engineering perspective. *Adv. Sustain. Syst.* 3:1800080. doi: 10.1002/adsu.201800080

Kidanemariam, A., Lee, J., and Park, J. (2019). Recent innovation of metal-organic frameworks for carbon dioxide photocatalytic reduction. *Polymers* 11:2090. doi: 10.3390/polym11122090

Kim, K. C., Yoon, T. U., and Bae, Y. S. (2016). Applicability of using CO_2 adsorption isotherms to determine BET surface areas of microporous materials. *Microporous Mesoporous Mater.* 224, 294–301. doi: 10.1016/j.micromeso.2016.01.003

Li, J. R., Ma, Y., Colin McCarthy, M., Sculley, J., Yu, J., Jeong, H. K., et al. (2011). Carbon dioxide capture-related gas adsorption and separation in metal-organic frameworks. *Coordination Chem. Rev.* 255, 1791–1823. doi: 10.1016/j.ccr.2011.02.012

Liang, Z., Du, J., Sun, L., Xu, J., Mu, Y., Li, Y., et al. (2013). Design and synthesis of two porous metal–organic frameworks with *Nbo* and *Agw* topologies showing high CO_2 adsorption capacity. *Inorganic Chem.* 52, 10720–10722. doi: 10.1021/ic4017189

Lin, X. M., Li, T. T., Wang, Y. W., Zhang, L., and Su, C. Y. (2012). Two ZnIImetal-organic frameworks with coordinatively unsaturated metal sites: structures, adsorption, and catalysis. *Chem. J.* 7, 2796–2804. doi: 10.1002/asia.201200601

Lin, Z. J., Liu, T. F., Xu, B., Han, L. W., Huang, Y. B., and Cao, R. (2011). Pore-size tuning in double-pillared metal-organic frameworks containing cadmium clusters. *Cryst. Eng. Comm*. 13, 3321–3324. doi: 10.1039/c1ce05099k

Liu, J., Chen, L., Cui, H., Zhang, J., Zhang, L., and Su, C. Y. (2014). Applications of metal-organic frameworks in heterogeneous supramolecular catalysis. *Chem. Soc. Rev.* 6011–6061. doi: 10.1039/C4CS00094C

Lu, S. M., Wang, Z., Li, J., Xiao, J., and Li, C. (2016). Base-free hydrogenation of CO_2 to formic acid in water with an iridium complex bearing a: N, N′-Diimine Ligand." *Green Chem.* 18, 4553–4558. doi: 10.1039/C6GC00856A

Mehlana, G., Bourne, S. A., and Ramon, G. (2014). The role of C–H…π interactions in modulating the breathing amplitude of a 2D square lattice net: alcohol sorption studies. *CrystEngComm* 16:8160. doi: 10.1039/C4CE00496E

Mehlana, G., Bourne, S. A., Ramon, G., and Öhrström, L. (2013). Concomitant Metal Organic Frameworks of Cobalt(II) and 3-(4-Pyridyl) benzoate: optimized synthetic conditions of solvatochromic and thermochromic systems. *Crystal Growth Design* 13, 633–644. doi: 10.1021/cg301312v

Mehlana, G., Chitsa, V., and Mugadza, T. (2015a). Recent advances in metal–organic frameworks based on pyridylbenzoate ligands: properties and applications. *RSC Adv.* 5, 88218–88233. doi: 10.1039/C5RA15575D

Mehlana, G., Ramon, G., and Bourne, S. A. (2016). A 4-fold interpenetrated diamondoid metal-organic framework with large channels exhibiting solvent sorption properties and high iodine capture. *Micropor. Mesoporous Mater.* 231, 21–30. doi: 10.1016/j.micromeso.2016.05.016

Mehlana, G., Wilkinson, C., Dzesse, C. N. T., Ramon, G., and Bourne, S. A. (2017). Structural diversity observed in two-dimensional square lattice metal-organic frameworks assembled from Zn(II) and 3-(4-Pyridyl)Benzoate. *Crystal Growth Design* 17, 6445–6454. doi: 10.1021/acs.cgd.7b01101

Mehlana, G., Wilkinson, C., Ramon, G., and Bourne, S. (2015b). Reversible thermochromic and mechanochromic behaviour in a 3D hydrogen bonded discrete complex. *Polyhedron* 98, 224–229. doi: 10.1016/j.poly.2015.06.016

Ozawa, T. (1965). A new method of analyzing thermogravimetric data. *Chem. Soc. Jpn.* 1881–1886. doi: 10.1246/bcsj.38.1881

Poloni, R., Lee, K., Berger, R. F., Smit, B., and Neaton, J. B. (2014). Understanding trends in CO_2 adsorption in metal-organic frameworks with open-metal sites *J. Phys. Chem. Lett.* 5, 861–865. doi: 10.1021/jz500202x

Saeidi, S., Amin, N. A. S., and Rahimpour, M. R. (2014). Hydrogenation of CO2 to value-added products - a review and potential future developments. *J. CO_2 Utilization* 5, 66–81. doi: 10.1016/j.jcou.2013.12.005

Sheldrick, G. M. (2018). Crystal structure refinement with SHELXL. *Acta Crystallogr. Section C* 71, 3–8.

Spek, A. L. (2009). Structure validation in chemical crystallography. *Acta Crystallographica* 65(Pt 2), 148–155. doi: 10.1107/S090744490804362X

Sun, D., Ma, S., Ke, Y., Collins, D. J., and Zhou, H. C. (2006). An interweaving MOF with high hydrogen uptake. *J. Am. Chem. Soc.* 128, 3896–3897. doi: 10.1021/ja058777l

Tella, A. C., Mehlana, G., Alimi, L. O., and Bourne, S. A. (2017). Solvent-free synthesis, characterization and solvent-vapor interaction of Zinc(II) and copper(II) coordination polymers containing nitrogen-donor ligands. *Zeitschrift Fur Anorganische Und Allgemeine Chem.* 643, 523–530. doi: 10.1002/zaac.201600460

Tshuma, P., Makhubela, B. C. E., Bingwa, N., and Mehlana, G. (2020a). Palladium(II) immobilized on metal-organic frameworks for catalytic conversion of carbon dioxide to formate. *Inorganic Chem.* 59, 6717–6728. doi: 10.1021/acs.inorgchem.9b03654

Tshuma, P., Makhubela, B. C. E., Öhrström, L., Bourne, S. A., Chatterjee, N., Beas, I. N., et al. (2020b). Cyclometalation of Lanthanum(Iii) based MOF for catalytic hydrogenation of carbon dioxide to formate. *RSC Adv.* 10, 3593–3605. doi: 10.1039/C9RA09938G

Ugale, B., Dhankhar, S. S., and Nagaraja, C. M. (2017). Construction of 3D homochiral metal-organic frameworks (MOFs) of Cd(II): selective CO_2 adsorption and catalytic properties for the knoevenagel and henry reaction. *Inorganic Chem. Front.* 4, 348–359. doi: 10.1039/C6QI00506C

Ugale, B., Singh Dhankhar, S., and Nagaraja, C. M. (2018). Exceptionally stable and 20-connected lanthanide metal-organic frameworks for selective CO_2 capture and conversion at atmospheric pressure. *Crystal Growth Design* 18, 2432–2440. doi: 10.1021/acs.cgd.8b00065

Valvekens, P., Vermoortele, F., and De Vos, D. (2013). Metal–organic frameworks as catalysts: the role of metal active sites. *Catal. Sci. Tech.* 3:1435. doi: 10.1039/c3cy20813c

Yang, Q., Guillerm, V., Ragon, F., Wiersum, A. D., Llewellyn, P. L., Zhong, C., et al. (2012). CH_4 storage and CO_2 capture in highly porous zirconium oxide based metal–organic frameworks. *Chem. Commun.* 48, 9831–9833. doi: 10.1039/c2cc34714h

Zhong, D. C., Zhang, W. X., Cao, F. L., Jiang, L., and Lu, T. B. (2011). A three-dimensional microporous metal-organic framework with large hydrogen sorption hysteresis. *Chem. Commun.* 47, 1204–1246. doi: 10.1039/C0CC03506H

Conflict of Interest: The authors declare that the research was conducted in the absence of any commercial or financial relationships that could be construed as a potential conflict of interest.

frontiers in Chemistry

ORIGINAL RESEARCH
published: 13 November 2020
doi: 10.3389/fchem.2020.591353

Chiral-at-Metal: Iridium(III) Tetrazole Complexes With Proton-Responsive P-OH Groups for CO_2 Hydrogenation

Edward Ocansey, James Darkwa and Banothile C. E. Makhubela*

Research Centre for Synthesis and Catalysis, Department of Chemical Science, University of Johannesburg, Auckland Park, South Africa

A rise in atmospheric CO_2 levels, following years of burning fossil fuels, has brought about increase in global temperatures and climate change due to the greenhouse effect. As such, recent efforts in addressing this problem have been directed to the use of CO_2 as a non-expensive and non-toxic single carbon, C_1, source for making chemical products. Herein, we report on the use of tetrazolyl complexes as catalyst precursors for hydrogenation of CO_2. Specifically, tetrazolyl compounds bearing P–S bonds have been synthesized with the view of using these as P^N bidentate tetrazolyl ligands (**1**–**3**) that can coordinate to iridium(III), thereby forming heteroatomic five-member complexes. Interestingly, reacting the *P*,*N*′-bidentate tetrazolyl ligands with $[Ir(C_5Me_5)Cl_2]_2$ led to serendipitous isolation of chiral-at-metal iridium(III) half-sandwich complexes (**7**–**9**) instead. Complexes **7**–**9** were obtained via prior formation of non-chiral iridium(III) half-sandwich complexes (**4**–**6**). The complexes undergo prior P–S bond heterolysis of the precursor ligands, which then ultimately results in new half-sandwich iridium(III) complexes featuring monodentate phosphine co-ligands with proton-responsive P-OH groups. Conditions necessary to significantly affect the rate of P–S bond heterolysis in the precursor ligand and the subsequent coordination to iridium have been reported. The complexes served as catalyst precursors and exhibited activity in CO_2 and bicarbonate hydrogenation in excellent catalytic activity, at low catalyst loadings (1 μmol or 0.07 mol% with respect to base), producing concentrated formate solutions (*ca* 180 mM) exclusively. Catalyst precursors with proton-responsive P-OH groups were found to influence catalytic activity when present as racemates, while ease of dissociation of the ligand from the iridium center was observed to influence activity in spite of the presence of electron-donating ligands. A test for homogeneity indicated that hydrogenation of CO_2 proceeded by homogeneous means. Subsequently, the mechanism of the reaction by the iridium(III) catalyst precursors was studied using ^1H NMR techniques. This revealed that a chiral-at-metal iridium hydride species generated *in situ* served as the active catalyst.

Keywords: chiral-at-metal 1, tetrazole 2, iridium(III) complexes 3, CO_2 Hydrogenation 4, $NaHCO_3$ reduction, CO_2 utilization, green chemistry

Edited by:
Emmanuel Oluwadare Balogun,
Ahmadu Bello University, Nigeria

Reviewed by:
Tomoo Mizugaki,
Osaka University, Japan
Mohsen Ahmadi,
Leibniz Institute for Plasma Research and Technology e.V. (INP), Germany

***Correspondence:**
Banothile C. E. Makhubela
bmakhubela@uj.ac.za

Specialty section:
This article was submitted to Catalysis and Photocatalysis, a section of the journal Frontiers in Chemistry

Received: *04 August 2020*
Accepted: *12 October 2020*
Published: *13 November 2020*

Citation:
Ocansey E, Darkwa J and Makhubela BCE (2020) Chiral-at-Metal: Iridium(III) Tetrazole Complexes With Proton-Responsive P-OH Groups for CO_2 Hydrogenation. Front. Chem. 8:591353. doi: 10.3389/fchem.2020.591353

INTRODUCTION

The utilization of fossil fuels as a source of energy has contributed toward human development (Saeidi et al., 2014). However, this dependence on fossil fuels has contributed to the gradual buildup of greenhouse gases such as CO_2 in the atmosphere. This increase in the amount of greenhouse gases is a major contributor to the greenhouse effect that has caused increase in global temperatures and climate change (Huang and Tan, 2014; Saeidi et al., 2014). Increase in the amount of CO_2 as a greenhouse gas in the atmosphere has necessitated the development of economical, safe, and efficient systems to capture and utilize it as a resource instead of disposing it as waste. Thus, CO_2 serves as an attractive single carbon (C_1) building block for making various compounds including formic acid, methanol, formamides, formaldehyde to name a few (Ma et al., 2009). Although CO_2 is currently a C_1 source in some industrial processes, like in the production of urea and salicylic acid, its thermodynamic stability still hinders its widespread utilization. Therefore, CO_2 valorization requires electro- or photo-reduction or reacting it with high-energy substrates in the presence of catalysts. Catalytic hydrogenation of CO_2 provides an avenue for CO_2 fixation so as to unlock its full potential as a C_1 source, thereby promoting its valorization (Jessop et al., 1995).

Various homogeneous and heterogeneous catalysts have been reported for the hydrogenation of CO_2 to a variety of products. However, one of the best catalysts for the hydrogenation of CO_2 is the trihydridoiridium P^N^P pincer complex, by Nozaki and co-workers (Tanaka et al., 2009), which served as an excellent catalyst. Despite the impressive catalytic activity shown by the Nozaki iridium catalyst (*ca* TONs as high as 3,500,000), it requires a strong base to achieve such high catalytic activity and productivity (200,000 h^{-1}). Also, a strong base is used during the catalytic process, meaning isolation of the product (i.e., formic acid) requires use of a strong acid in order to convert the product formate to formic acid. Use of acids in chemical processes is not ideal as they are highly corrosive to equipment and they generate unwanted acid effluent. There is also the challenge of forming unwanted inorganic salts as by-products (Yasaka et al., 2010) Therefore, the development of highly active catalysts for the hydrogenation of carbon dioxide that use mild organic bases such as DBU is desirable (Makuve et al., 2019; Malaza and Makhubela, 2020).

Another class of catalysts for CO_2 hydrogenation are iridium half-sandwich complexes. They have been shown to be effective catalysts for both CO_2 hydrogenation and formic acid dehydrogenation (Leitner et al., 1994; Himeda et al., 2007, 2008; Boddien et al., 2011, 2012; Papp et al., 2011). In fact, Himeda and co-workers have demonstrated that the electron-donating ability of *N,N′*-bidentate ligands in half-sandwich iridium complexes enhances the catalytic activity of these complexes for the CO_2 hydrogenation reaction through electronic effects (Himeda et al., 2007). More recently in 2017, Himeda and co-workers reported (cyclopentadienyl)iridium(III) complexes with pyridyl-diazole ligands that have hydroxyl electron-donating functional groups and an electron-rich diazole ring. The presence of the hydroxyl groups under basic conditions deprotonate to form strongly electron-donating oxyanions that activate dihydrogen through second sphere coordination effects, leading to the formation of the catalytically active iridium hydride in the CO_2 hydrogenation reaction (Rakowski Dubois and Dubois, 2009; Wang et al., 2012; Suna et al., 2014). This is generally referred to as proton-responsive catalytic reactions. Both computational and experimentally observed studies have confirmed the participation of proton-responsive groups in the catalytic cycle of iridium hydride species in CO_2 hydrogenation reactions (Suna et al., 2017). This, therefore, clearly indicates that the choice of ligand plays a vital role in the catalytic activity of complexes in CO_2 hydrogenation reactions.

We postulated, at the beginning of this project, that iridium tetrazole complexes featuring NH groups are likely to display proton-responsive behavior and thus act as highly active CO_2 hydrogenation catalysts. This formed the basis of our investigation and the current report (Ocansey et al., 2020). We are aware of several tetrazole MOFs, with possible proton-responsive NH groups, that have mostly been utilized in the synthesis of MOF for CO_2 capture or CO_2-assisted cycloaddition reactions, but none, to the best of our knowledge, has been used as CO_2 hydrogenation catalyst (Pachfule and Banerjee, 2011; Cui et al., 2012; Poloni and Smit, 2012; Go et al., 2013; Zhao et al., 2016). Such CO_2 adsorption by the tetrazoles can be attributed to hydrogen bonding between CO_2 molecules and polarizing groups in the tetrazole (Poloni and Smit, 2012; Zhao et al., 2016). We believe that it is this polarizing effect in our (cylopentadienyl)irirdium(III) tetrazole complexes that makes them very good catalysts for CO_2 hydrogenation catalysts.

Another attribute of the (cylopentadienyl)irirdium(III) tetrazole complexes as CO_2 hydrogenation catalysts is their chirality at the iridium center. There are prominent examples of optically active half-sandwich piano stool complexes that are chiral-at-metal complexes where the configuration may be stable or labile in solution. Such compounds allow the monitoring of the stereochemical course of substitution reactions as well as being used in organic synthesis in ligand transformation reactions as a result of their chirality (Brunner, 2001). Complexes with chirality at the metal center have been used as effective catalysts in the enantioselective Friedel–Crafts addition of indoles to α,β-unsaturated 2-acyl imidazoles (Huo et al., 2014) and trichloromethylation of 2-acyl imidazoles and 2-acyl pyridines (Huo et al., 2015). In addition, these chiral complexes have been used as hydrogenation catalysts in the hydrogenation of acyclic aromatic N-aryl imines (Imamoto et al., 2006), α-dehydroamino esters, enamides, dimethyl itaconate (Kurihara et al., 2009), and imines (Murata et al., 1999), and in transfer hydrogenation of β,β′-disubstituted nitroalkenes (Chen et al., 2013) and ketones (Tian et al., 2016) with high enantioselectivities and at low catalyst loadings. Despite the impressive array of hydrogenation reactions these complexes are capable of, they have rarely been evaluated as catalysts for CO_2 hydrogenation. Knowing the role of proton-responsive groups on hydrogenation catalysts and the electron-rich nature along with CO_2 affinity of tetrazole compounds led to the present study in search of highly active CO_2 hydrogenation catalysts.

EXPERIMENTAL

All reactions were carried out in air unless otherwise stated. All solvents used were reagent grade, purchased from Sigma-Aldrich, and dried under nitrogen before use. 1-Phenyl-1*H*-tetrazole-5-thiol, chlorodiphenylphosphine, chlorobis(3,5-dimethylphenyl)phosphine, bis(3,5-di(trifluoromethyl)phenyl)chloro phosphine, and sodium methoxide were purchased from Sigma-Aldrich and used without further purification. Iridium(III) chloride was purchased from Heraeus South Africa and used as received. $[Ir(C_5Me_5)Cl_2]_2$ (White et al., 1992) was synthesized according to literature procedures. NMR spectra were recorded on a Bruker 400-MHz NMR spectrometer (^{1}H at 400 MHz, ^{13}C{^{1}H} at 100 MHz, and ^{13}P{^{1}H} NMR 161.99 MHz). Spectrometer chemical shifts were reported relative to the internal standard tetramethylsilane (δ 0.00 ppm) and referenced to the residual proton and carbon signals at 7.24 and 77.0 ppm, respectively, of $CDCl_3$. Infrared spectra were obtained neat using a Perkin Elmer Spectrum BX II fitted with an ATR probe. Melting points were obtained using a Gallenkamp Digital Melting-point Apparatus 5A 6797. Elemental analysis was performed on a Thermos Scientific FLASH 2000 CHNS-O Analyzer. Mass spectrometry was performed using Waters Synapt G2 mass spectrometer with both ESI positive and Cone Voltage 15 V. XRD spectra were obtained from a Bruker APEX-II CCD Diffractometer.

Synthesis of 5-((bis(3,5-Dimethylphenyl)Phosphino)Thio)-1-Phenyl-1H-Tetrazole (1)

Into a Schlenk tube containing 10-ml THF solution of 50 mg (0.281 mmol) 1-Phenyl-1*H*-tetrazole-5-thiol, 16.6 mg (0.31 mmol) NaOMe was added and the mixture stirred under argon at 0–5°C for 1 h. This was then followed by the dropwise addition of 77.5 mg (0.28 mmol) chlorobis(3,5-dimethylphenyl)phosphine. The reaction mixture was then stirred at room temperature for 16 h. After the reaction time had elapsed, the reaction mixture was filtered via canula and the filtrate dried *in vacuo* to yield the product. Appearance white solid (Yield = 91 mg, 78%). Solubility: Soluble in chloroform, DCM, DMSO; FT-IR (ν_{max}/cm^{-1}): 1,685.85 (C=N). Melting point range: 91–92°C. ^{1}H NMR ($CDCl_3$, 30°C, δ-ppm): 7.89 (d, ^3J = 12 Hz, 2H, H_{arom}), 7.62–7.58 (m, 4H, H_{arom}), 7.15 (s, 2H, H_{arom}); 2.28 (s, 12H, H_{CH3}); ^{13}C{^{1}H} NMR ($CDCl_3$, 30°C, δ-ppm): 155.4, 136.21, 135.29, 134.99, 133.62, 133.44, 133.22, 133.08, 132.84, 132.54 132.07, 131.89, 129.96, 129.74, 129.52, 128.94, 128.77, 128.44, 124.20, 21.70 ^{31}P{^{1}H} NMR ($CDCl_3$, 30°C, δ-ppm): 22.87; HR-ESI-MS $[M\text{-}Ph]^+ = 341.0990$; Elemental analysis; Anal. calcd. for $C_{23}H_{23}N_4PS$: C, 66.01%; H, 5.54%, N, 13.39% S, 7.66%; Found C, 66.25%; H, 5.18%; N, 13.77%; S, 7.88%.

Synthesis of 5-((Diphenylphosphino)Thio)-1-Phenyl-1H-Tetrazole (2)

Into a Schlenk tube containing 10-ml THF solution of 500 mg (2.81 mmol) 1-phenyl-1*H*-tetrazole-5-thiol, 166.7 mg (3.086 mmol) NaOMe was added and the mixture stirred under argon at 0–5°C for 1 h. This was then followed by the dropwise addition of 0.50 ml (2.81 mmol) of chlorodiphenylphosphine. The reaction mixture was then stirred at room temperature for 16 h. After the reaction time had elapsed, the reaction mixture was filtered via canula and the filtrate dried *in vacuo* to yield the product. Appearance colorless oil (Yield = 720 mg, 71%). Solubility: Soluble in chloroform, DCM, methanol, DMSO; FT-IR (ν_{max}/cm^{-1}): 1,591.30 (C=N). ^{1}H NMR ($CDCl_3$, 30°C, δ-ppm): 7.88 (d, ^3J = 7.6 Hz, 4H, H_{arom}), 7.73–7.47 (m, 11H, H_{arom}); ^{13}C{^{1}H} NMR ($CDCl_3$, 30°C, δ-ppm): 163.67, 133.91, 133.77, 133.59, 132.52, 132.44, 132.32, 132.18, 131.54, 131.34 130.07, 129.96, 129.38, 129.02, 128.80, 128.68, 128.54, 124.19, 124.09 ^{31}P{^{1}H} NMR ($CDCl_3$, 30°C, δ-ppm): 18.54 HR-ESI-MS; $[M+O]^- = 377.0410$; $[M\text{-}PPh_2]^- = 177.0222$; Elemental analysis; Anal. calcd. for $C_{19}H_{15}N_4PS$: C, 62.97%; H, 4.17%; N, 15.46%; S, 8.85%; Found C, 62.46%; H, 4.51%; N, 15.88%; S, 9.01%.

Synthesis of 5-((bis(3,5-bis(Trifluoromethyl)Phenyl)Phosphino)Thio)-1-Phenyl-1H-Tetrazole (3)

Into a Schlenk tube containing 10-ml THF solution of 50 mg (0.281 mmol) 1-phenyl-1*H*-tetrazole-5-thiol, 16.6 mg (0.31 mmol) NaOMe was added and the mixture stirred under argon at 0–5°C for 1 h. This was then followed by the dropwise addition of 138.21 mg (0.28 mmol) bis(3,5-di(trifluoromethyl)phenyl)chlorophosphine. The reaction mixture was then stirred at room temperature for 16 h. After the reaction time had elapsed, the reaction mixture was filtered via canula and the filtrate dried *in vacuo* to yield the product. Appearance white solid (Yield = 148 mg, 83%). Solubility: Soluble in chloroform, DCM, DMSO; FT-IR (ν_{max}/cm^{-1}): 1,684.85 (C=N). Melting point range: 95–96°C. ^{1}H NMR ($CDCl_3$, 30°C, δ-ppm): 8.43–8.40 (m, 4H, H_{arom}), 8.26 (s, 2H, H_{arom}), 7.85 (m, 2H, H_{arom}); 7.58 (m, 2H, H_{arom}); ^{13}C{^{1}H} NMR ($CDCl_3$, 30°C, δ-ppm): 161.29, 134.21, 134.09, 133.99, 133.52, 133.44, 133.32, 133.08, 132.54, 131.54 131.07, 130.00, 129.96, 129.44, 129.12, 128.90, 128.77, 128.54, 124.19, ^{31}P{^{1}H} NMR ($CDCl_3$, 30°C, δ-ppm): 13.30 HR-ESI-MS; $[M]^+ = 634.5455$; Elemental analysis; Anal. calcd. for $C_{23}H_{11}F_{12}N_4PS$: C, 43.55%; H, 1.75%, N, 8.83%; S, 5.05%; Found C, 43.46%; H, 1.53%; N, 9.02%; S, 4.99%.

Synthesis of $[IrCp^*Cl_2(P(Ph)_2OH)]$ (5)

Into a Schlenk tube, 86 mg (0.24 mmol) 5-((diphenylphosphino)thio)-1-phenyl-1H-tetrazole (**2**) was added to 95 mg (0.12 mmol) of $[Ir(C_5Me_5)Cl_2]_2$ using 5.00 ml of methanol as solvent. The reaction mixture was then stirred for 24 h under argon at room temperature. After the reaction time had elapsed, the precipitate formed was filtered off in air, and the filtrate dried with the crude product obtained being washed with 10 ml 1:1 (v:v diethylether: hexane) and subsequently dried *in vacuo* for 6 h to yield (**5**). Appearance: Orange solid, (Yield = 94 mg, 52%). Solubility: Soluble in chloroform, DCM, methanol; FT-IR (ν_{max}/cm^{-1}): 3,050.47 (s, P-OH). Melting point range: 167°C (Decomp); ^{1}H NMR ($CDCl_3$, 30°C, δ-ppm): 7.67–7.62

(m, 9H, H_{arom}), 7.44–7.24 (m, 6H, H_{arom}), 1.46 (s, 15H, H_{Cp*}); $^{13}C\{^1H\}$ NMR ($CDCl_3$, 30°C, δ-ppm): 132.54; 132.42; 131.41; 128.01; 127.0; 127.84; 93.01; 9.28; $^{31}P\{^1H\}$ NMR ($CDCl_3$, 30°C, δ-ppm) = 76.92; HR-ESI-MS $[M\text{-}Cl]^+$ = 565.1045; Elemental analysis; Anal. calcd. for $C_{22}H_{26}Cl_2IrOP$: C, 44.00%; H, 4.36%; Found C, 44.46%; H, 4.51%.

Synthesis of $[IrCp^*Cl(P(Ph)_2OH)S\text{-}Tz]$ (8)

The residue obtained from the procedure above in the synthesis of **5** was washed with 10 ml 1:1 (v:v diethylether: hexane) and dried *in vacuo* to yield (**8**). Appearance: Yellow solid, (Yield = 77 mg, 43%). Solubility: Soluble in chloroform, DCM; FT-IR (ν_{max}/cm^{-1}): 2,968.50 (s, P-OH), 1,499.68 (C=N). Melting point range: 218°C (Decomp); ^1H NMR ($CDCl_3$, 30°C, δ-ppm): 8.05 (m, 2H, H_{arom}), 7.80 (m, 2H, H_{arom}), 7.64 (m, 2H, H_{arom}), 7.44 (m, 6H, H_{arom}), 7.14 (m, 3H, H_{arom}), 1.40 (s, 15H, H_{Cp*}); $^{13}C\{^1H\}$ NMR ($CDCl_3$, 30°C, δ-ppm): 133.64; 133.55; 133.40; 133;20; 132.91; 132.78; 132.68; 132.42; 132.12; 131.31; 129.09; 128.44; 127.84; 96.41; 9.48; $^{31}P\{^1H\}$ NMR ($CDCl_3$, 30°C, δ-ppm) = 56.83; HR-ESI-MS $[M\text{-}Cl]^+$ = 707.1599; Elemental analysis; Anal. calcd. for $C_{29}H_{31}ClIrN_4OPS$: C, 46.92%; H, 4.21%, N, 7.55%, S, 4.31%; Found C, 47.11%; H, 4.61%; N, 7.82%; S, 4.12%.

Synthesis of $[IrCp^*Cl(P(Ph\text{-}CF_3)_2OH)S\text{-}Tz]$ (9)

Into a Schlenk tube, 70 mg (0.11 mmol) of 5-((bis(3,5-bis(trifluoromethyl)phenyl)phosphino)thio)-1-phenyl-1H-tetrazole **(3)** was added to 44 mg (0.05 mmol) of $[Ir(C_5Me_5)Cl_2]_2$ using 5.00 ml of $CHCl_3$ as solvent. The reaction mixture was then stirred for 24 h at room temperature. After the reaction time had elapsed, the solvent was dried with the crude product obtained being washed with 10 ml 1:1 (v:v diethylether: hexane) and subsequently dried *in vacuo* for 6 h to yield **(9)**. Appearance: Orange solid (Yield = 37 mg, 67%). Solubility: Soluble in chloroform, DCM, THF; FT-IR (ν_{max}/cm^{-1}): 2,974 (s, P-OH), 1,617.72 (C=N). Melting point range: 192°C (Decomp); ^1H NMR ($CDCl_3$, 30°C, δ-ppm): 8.63–8.40 (m, 4H, H_{arom}), 8.31 (s, 2H, H_{arom}), 7.85 (m, 2H, H_{arom}); 7.63 (m, 2H, H_{arom}); $^{13}C\{^1H\}$ NMR ($CDCl_3$, 30°C, δ-ppm): 160.11, 135.99, 134.69, 133.82, 133.52, 133.44, 133.08, 132.99, 132.42, 131.54, 131.07, 130.00, 129.96, 129.44, 129.36, 129.00, 128.66, 128.00, 123.01, 96.52, 9.43; $^{31}P\{^1H\}$ NMR ($CDCl_3$, 30°C, δ-ppm) = 55.15; HR-ESI-MS $[M\text{-}Cl]^+$ = 979.1093; Elemental analysis Anal. calcd. for $C_{33}H_{27}ClF_{12}IrN_4OPS$: C, 39.08%; H, 2.68%, N, 5.52%, S, 3.16%; Found C, 40.12%; H, 3.01%; N, 5.61%; S, 3.33%.

General CO_2 Hydrogenation Reaction

Into a stainless steel reactor, 1 μmol of an appropriate catalyst was dissolved in 10 ml of appropriate solvent. 1.44 mmol of the appropriate base was added and the resulting solution was pressurized with the required CO_2:H_2 ratios. The reaction mixture was then stirred at the appropriate temperature for the required time at 1,500 rpms. After the reaction time had elapsed, the reactor was cooled and the gasses slowly vented. 0.4 ml of the contents of the reactor was sampled and added to 0.2 ml of D_2O and 5 μl of DMF (as standard). Amounts of product (formate) obtained was calculated by integral relations between singlet formate peak at 8.3 ppm and the singlet DMF formamide peak at 7.9 ppm in the ^1H NMR spectrum of the sample.

SYNTHESIS AND CHARACTERIZATION OF TETRAZOLE-BASED LIGANDS 1–3

Synthesis of three thio-tetrazole compounds **1**–**3** (**Scheme 1**) was achieved by first reacting 1-phenyl-1*H*-tetrazole-5-thiol with a slight excess of NaOMe, to deprotonate the hydrogen in the thiol functional group, followed by the addition of the appropriate chlorodialkylphosphine and subsequent separation of NaCl. All three compounds were isolated in excellent yields as colorless oil for **2**, and as whitish solids for **1** and **3** that are air and moisture sensitive. They are soluble in most organic solvents (such as chloroform and dichloromethane) and were characterized by NMR spectroscopy. The easiest way to monitor this reaction was by$^{31}P\{^1H\}$ NMR spectroscopy. The phosphorus peak for chlorodiphenylphosphine is around 85 ppm, while the peaks for compounds **1**, **2**, and **3** are 22.9 ppm, 18.0 ppm, and 13.3 ppm, respectively. To confirm that compounds **1**–**3** were unoxidized, we prepared the oxidized forms of **1**–**3**, which have phosphorus peaks at 29 ppm, 31.0 ppm, and 25 ppm, respectively. Mass spectra of the ligands also confirmed their formation for which molecular ions or masses of fragmented moieties are observed (**Supplementary Figures 15–17**).

SYNTHESIS AND CHARACTERIZATION OF TETRAZOLYL IRIDIUM COMPLEXES

Reacting compounds **1**–**3** with $[Ir(C_5Me_5)Cl_2]_2$ in a 2:1 ratio yielded interestingly complexes **4**–**9** (**Scheme 2**), all of which contain portions of the original compounds used to ligate $(C_5Me_5)Ir$ fragment, thus suggesting that the original compounds expected to be the ligand in a product had hydrolyzed. For example, monitoring the reaction between compound **2** and 0.5 eq $[Ir(C_5Me_5)Cl_2]_2$ by $^{31}P\{^1H\}$ NMR spectroscopy showed that the reaction yielded Iridium **5** within 1 h, and only after 4 h was **8** observed as a second product (**Figure 1**). It was only after 24 h that the reaction mixture showed complexes **5** and **8** formed in nearly the same amounts, clearly demonstrating that the rate of formation of **8** is much slower than that of **5**. All iridium complexes were obtained as yellow solids in excellent yields and readily soluble dichloromethane and chloroform, but some of these compounds are insoluble in methanol. The structures of these complexes were confirmed by mass spectrometry for which peaks pertaining to $[M\text{-}Cl]^+$ in addition to the corresponding isotopic peaks are observed. For example, complex **5** is soluble in methanol while complex **8** is insoluble in methanol. Therefore, carrying out the complexation reaction in methanol provides an easy route to separate the different iridium complexes that are formed.

To confirm that the products from the reactions of **1**–**3** with $[Ir(C_5Me_5)Cl_2]_2$ are the results of a water-assisted hydrolysis

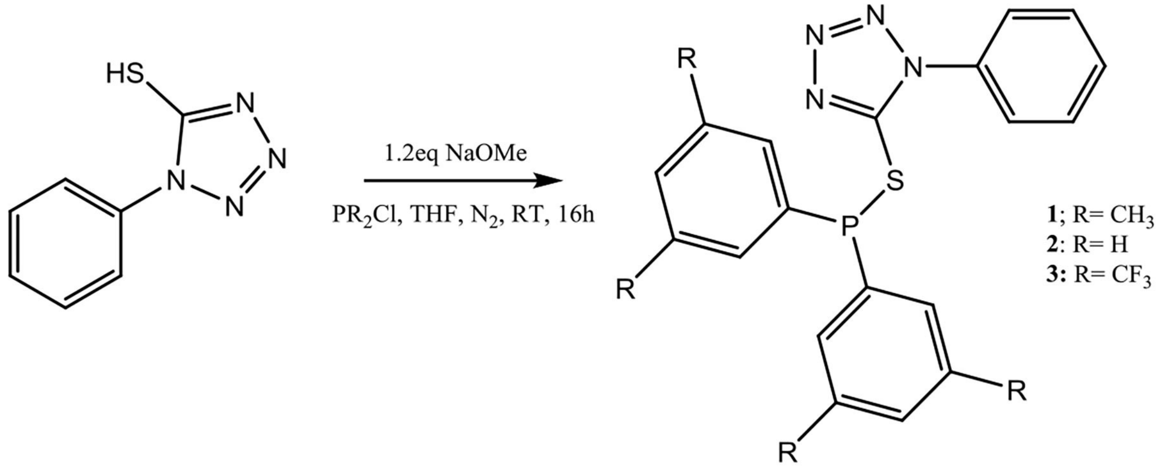

SCHEME 1 | Synthesis of thio-tetrazole ligands **1–3**.

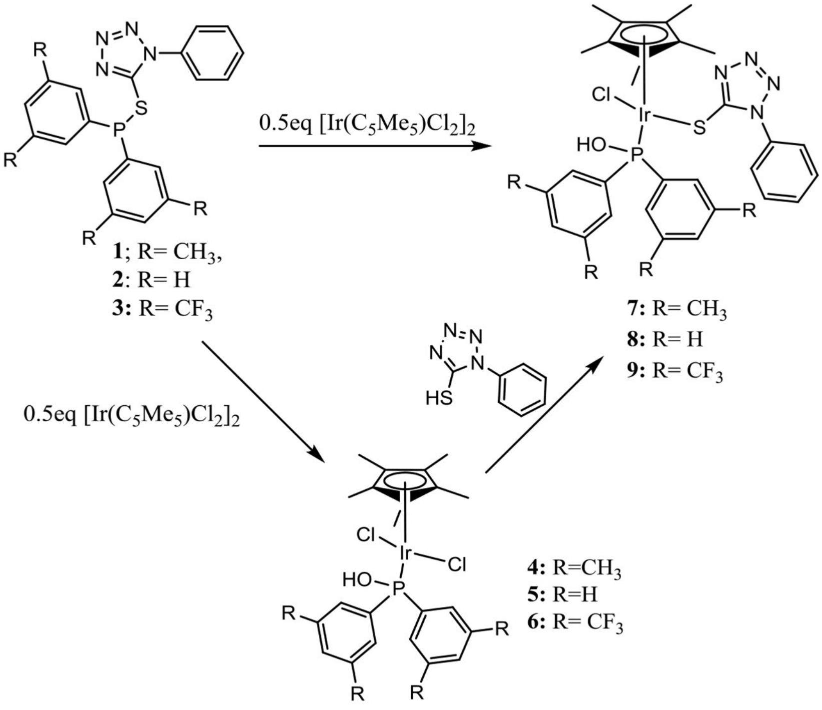

SCHEME 2 | Synthesis of tetrazolyl iridium complexes.

of the P–S bonds present in the ligands, the progress of the reaction between **2** and $[Ir(C_5Me_5)Cl_2]_2$ was monitored *in situ* with $^{31}P\{^1H\}$ NMR spectroscopy in D_2O. We observed distinct $^{31}P\{^1H\}$ NMR peaks that can be attributed to deuterated and non-deuterated analogs of **5** and **8** (**Supplementary Figure 1**).

Interestingly, there is very little oxidation of the phosphorus atom in **2** as observed from the *in situ* $^{31}P\{^1H\}$ NMR studies in the presence of D_2O (**Supplementary Figure 1**). This indicates that the presence of adventitious water in these reactions only hydrolyzes the P–S bond in compound **2** leading to the formation of **5** and subsequently the reaction of **5** with *in situ* generated 1-phenyl-1*H*-tetrazole-5-thiol to form **8**. This reaction route was also confirmed by the reaction of isolated **5** with phenyl-1*H*-tetrazole-5-thiol that forms **8** in <5 min.

Changing the metal precursor from $[Ir(C_5Me_5)Cl_2]_2$ to $[Ir(C_5Me_5)(H_2O)_3][SO_4]^{2-}$ in the reaction with **2** resulted in the formation of new species where $^{13}P\{^1H\}$ NMR peaks at 77 ppm and 57 ppm are observed. Considering **5** and **8** have

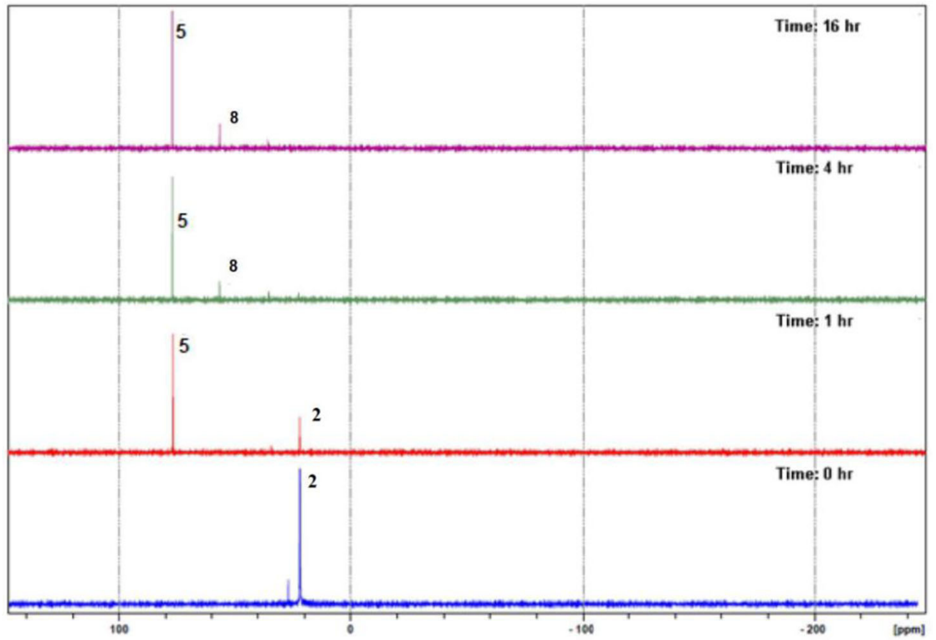

FIGURE 1 | *In situ* $^{31}P\{^{1}H\}$ NMR spectroscopy monitoring of the reaction between **2** and $[Ir(C_5Me_5)Cl_2]_2$.

$^{13}P\{^{1}H\}$ NMR peaks around 77 ppm and 57 ppm, respectively, we propose the formation of aqua/sulfato-**5** at 77 ppm and aqua/sulfato-**8** at 57 ppm where the chloride ligands in **5** and **8** are substituted with aqua or sulfato ligands in each complex. Observing similar P–S heterolysis with different iridium precursors indicated that P–S heterolysis may also be assisted by the presence of the metal. Similar metal-assisted bond hydrolysis has been reported in literature (Ahmad et al., 2019). In order to confirm what effects substituents on the phenyl groups bonded to the phosphorus atom have on coordination mode for the monodentate Iridium(III) complexes, two new ligands with electron-withdrawing (**3**) and electron-donating groups (**1**) on the phenyl groups were reacted with $[Ir(C_5Me_5)Cl_2]_2$ (**Scheme 2**).

The progress of each reaction was monitored by $^{31}P\{^{1}H\}$ NMR spectroscopy. **Figure 2** shows the changes that occurred in the course of the reaction between **3** and $[Ir(C_5Me_5)Cl_2]_2$, where a new Iridium phosphorus intermediate (**6**) with a peak around 65 ppm was converted in less than 2 h to complex **9** with a peak 55 ppm. However, in the case of the reaction of ligand **1** with $[Ir(C_5Me_5)Cl_2]_2$, even after heating the reaction mixture at 50°C for 24 h, we observed various phosphine species (**Supplementary Figure 2**). The phosphorus peak at 77 ppm was assigned to **4**, the peak at 58 ppm was assigned to **7**, but the peak at 33.8 ppm remains unidentified. We were, however, unable to separate the complexes in the reaction mixture as they are all soluble in similar solvents. It is, nevertheless, evident that ligands **1**, **2**, and **3** react with $[Ir(C_5Me_5)Cl_2]_2$ in the following order: ligand with electron-withdrawing substituent **>** ligand with no substituent > ligand with electron-donating substituent. This indicates that the electron-withdrawing ability of substituents attached to the phosphorus atom plays an important role in the heterolysis and in subsequent stabilization of iridium-phosphorus in bonds **7**, **8**, and **9**. The latter can be explained by the fact that the π-acid strength of the phosphorus atom follows the order $3,5\text{-}(CH_3)_2\text{-}C_6H_3)P(OH) < (C_6H_5)P(OH) < 3,5\text{-}(CF_3)_2\text{-}C_6H_3)P(OH)$. The electron-withdrawing (CF_3) group concentrates electron density away from the phosphorus atom, which favors increased π back-donation to the phosphorus, thereby reinforcing the Ir–P bond more in **9** than in **8** and **7**.

SINGLE CRYSTAL X-RAY STRUCTURES OF COMPLEX 8

Enantiopure crystals for **8** were grown by slow evaporation from a solution of **8** in $CHCl_3$, and the crystallographic data of this complex are shown in **Supplementary Table 2**. Complex **8** crystallizes in the monoclinic crystal system with space group $P2_1/n$ with piano-stool geometry around the iridium center. The iridium center is an iridium(III) center with a negatively charged sulfur moiety as ligand. Interestingly, hydrogen bonding is observed between the hydroxyl protons bonded to the phosphorus atom in complex **8** and one of the nitrogen atoms in the tetrazole ring (**Figure 3**).

It is interesting to note that re-growing crystals of **8** results in racemic co-crystallization of enantiomers of **8** that have chirality at the metal center in the triclinic space group *P-1*. As expected, the complexes have piano-stool geometry around both iridium centers with a negatively charged sulfur containing moiety as ligand (**Figure 4**). Similarly, hydrogen bonding is

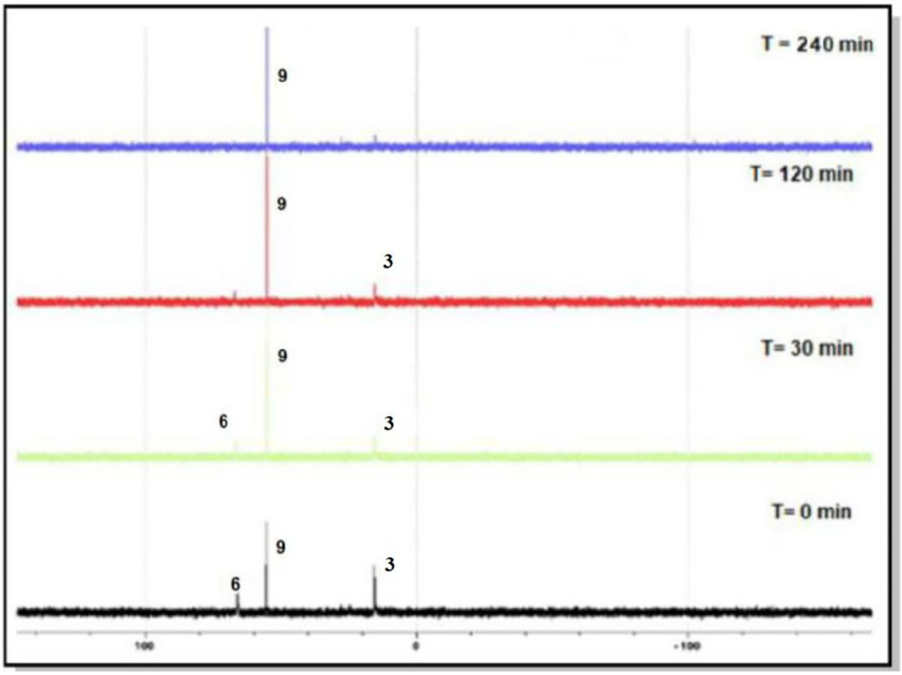

FIGURE 2 | Reaction between **3** and $[Ir(C_5Me_5)Cl_2]_2$ monitored by $^{31}P\{^1H\}$ NMR spectroscopy.

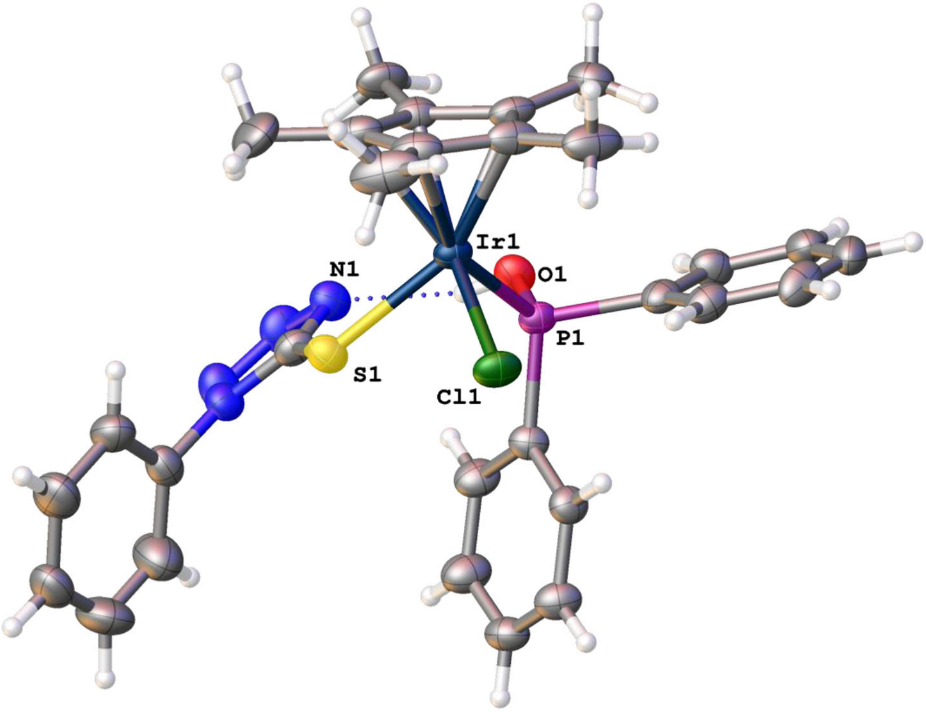

FIGURE 3 | Molecular structures of enantiopure complex **8**.

observed between the hydroxyl protons and a nitrogen atom in the tetrazole ring. **Supplementary Tables 1, 2** show selected bond lengths and angles and crystallographic data, respectively, for enantiopure complex **8** and racemic complex **8**. The bond angles and distances obtained for racemic and enantiomer **8** are in similar ranges for reported Ir–S or Ir–P complexes (Hughes

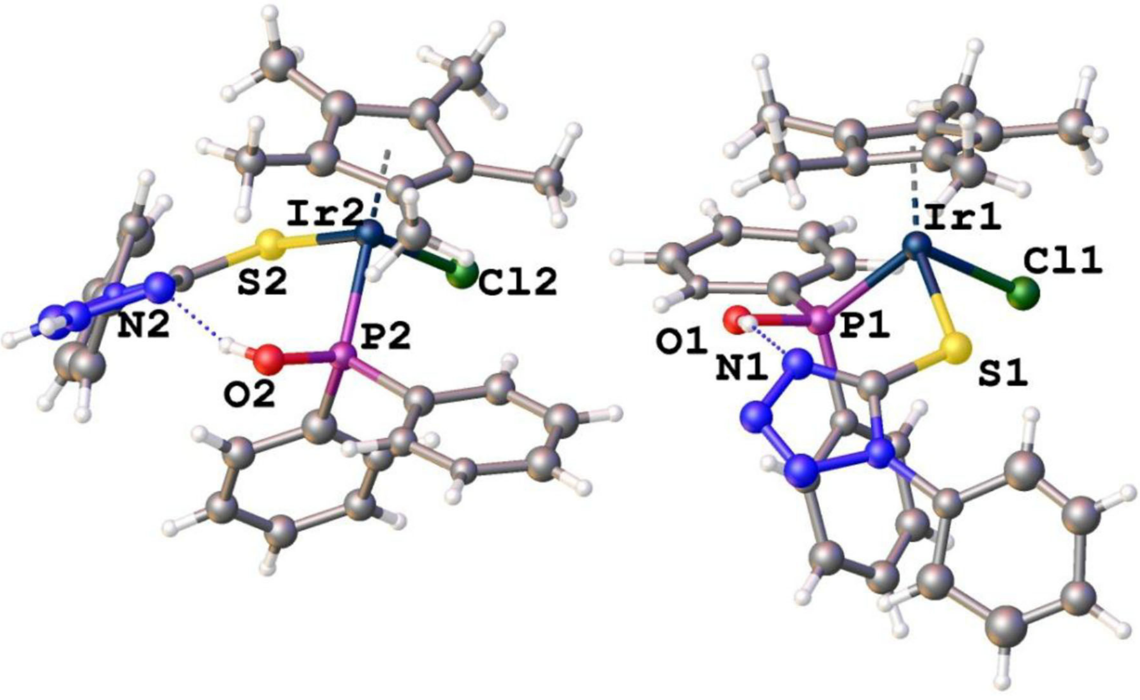

FIGURE 4 | Molecular structures of racemic complex **8** (solvent molecules removed for clarity).

et al., 2001; Ludwig et al., 2012). The high $R_{\text{int}} = 0.1542$ for racemic complex **8** is possibly the result of twinning.

EVALUATION OF CHIRAL-AT-METAL IRIDIUM COMPLEXES IN CO_2 HYDROGENATION

Using either ethanol or DMSO as solvents for CO_2 hydrogenation, there was only trace amounts of formate detected in the ^1H NMR spectrum of the reaction mixture using **5**, **8**, or **9** (the product obtained is a DBU salt of formic acid and was not separated). However, changing the solvent to water resulted in the formation of a modest amount of formate (0.027 mmol) using **8**. This increase in TONs is probably because water has been shown to enhance the rate of CO_2 hydrogenation possibly due to hydrogen-bonding interaction between water and an oxygen atom in CO_2 during the insertion of CO_2 in the catalytically active metal hydride species (Suna et al., 2017). However, adding THF resulted in an eight-fold increase in TON that indicates the importance of THF as solvent for the reaction. Increasing the temperature of the reaction also resulted in an increase in the amount of formate formed. At 160°C, 0.656 mmol of formate was produced compared to 0.197 at 90°C (**Table 1**). Varying the ratios of both CO_2 and H_2 gave the ideal ratio of CO_2:H_2 at 40 bar. Changing the ratio of H_2:CO_2 from 3:1 to 1:1 generally resulted in an improvement in TONs. This suggests that the rates of formation of the catalytically active iridium hydride species and the insertion of CO_2 into the iridium–hydride bond proceed at similar rates. Furthermore, addition of different bases affect the TONs of the reaction (**Table 1**). The best base for the reaction is DBU (**Table 1**, entries 11 and 12). We also observed that the amount of product formed is higher than the amount of base used. This is possible because 1 eq of DBU is known to stabilize multiple equivalences of formate via homoconjugation during the CO_2 hydrogenation reaction (Munshi et al., 2002; Getty et al., 2009; Jeletic et al., 2014; Zhang et al., 2015).

Reducing the amount of catalyst used and reaction time resulted in lower amounts of formate produced. As such, the optimum reaction conditions for catalyst **8** in CO_2 hydrogenation were as follows: 10 ml of a 4:1 mixture of H_2O:THF, temperature of 160°C, 1:1 mixture of CO_2:H_2 at 40 bar, DBU as base, 1 μmol catalyst loading, a 24-h reaction time, and stirring rate of 1,500 rpm. The progress of the reaction could be followed by sampling the reaction mixture after 24 h and running the ^1H NMR (**Supplementary Figure 3**) and the $^{13}C\{^1H\}$ NMR (**Supplementary Figure 4**) spectra. The NMR spectra indicated the formation of bicarbonate ion during the course of the CO_2 hydrogenation, an observation that has also been reported in the literature as a product from CO_2 and wet DBU (Heldebrant et al., 2005). Hydrogenation of $NaHCO_3$ using **8** also resulted in the production of formate (**Table 2**). This indicates that the hydrogenation of bicarbonate, in addition to CO_2, is an additional viable route to the production of formate in CO_2 hydrogenation under the conditions used in our study. Comparing other iridium half-sandwich catalysts with P-OH groups to catalyst **8** (TON 1 561) for CO_2 hydrogenation, it

TABLE 1 | Optimization of reaction conditions for the CO_2 hydrogenation reaction using **8**.

Entry	Solvent (10 ml)	Temperature (°C)	Pressure (H_2: CO_2) (bar)	Base (1.44 mmol)	mmol Product	TON
1	H_2O	90	10:30	K_2CO_3	0.027	5
2	H_2O:THF(4:1)	90	10:30	K_2CO_3	0.197	39
3	DMSO	90	10:30	K_2CO_3	Trace	–
4	Ethanol	90	10:30	K_2CO_3	Trace	–
5	H_2O:THF(4:1)	140	10:30	K_2CO_3	0.329	66
6	H_2O:THF(4:1)	160	10:30	K_2CO_3	0.656	131
7	H_2O:THF(4:1)	160	13.3:26.6	K_2CO_3	0.652	130
8	H_2O:THF(4:1)	160	20:20	K_2CO_3	0.744	149
9	H_2O:THF(4:1)	160	26.6:13.3	K_2CO_3	0.576	115
10	H_2O:THF(4:1)	160	20:20	Et_3N	0.451	90
11	H_2O:THF(4:1)	160	20:20	DBU	2.350	470
12	H_2O:THF(4:1)	160	20:20	DBU	1.561	1,561
13[a]	H_2O:THF(4:1)	160	20:20	DBU	0.057	281
14[b]	H_2O:THF(4:1)	160	20:20	DBU	0.704	704

*Reactions were performed in 10 ml of appropriate neat solvent or mixture, 1.44 mmol of base at appropriate temperature and pressure with stirring (1,500 rpm), and complex **8** (5 μmol) for 24 h using DMF as standard. TON = calculated mmol of [HCO_2^-]/mmol of catalyst. (a) 1 μmol of catalyst used for 24 h; (b) 0.2 μmol of catalyst used in 24-h reaction time; (c) 1 μmol of catalyst used for 16 h.*

TABLE 2 | Chiral-at-metal complexes for CO_2 hydrogenation.

Entry	Catalyst	mmol Product (mmol)[a]	[HCO_2^-] (mM)	TON (TON)[b]
1	5	1.878 (1.305)	188	1,878 (1,305)
2	8	1.561 (0.752)	156	1,561 (752)
3	8[c]	0.601	60	601
4	9	1.391 (1.172)	139	1,391 (1,172)
5	[Cp*Ir(L1)(Cl)]Cl[d]	0.26	26	1,300
6	[Cp*Ir(L2)(Cl)]Cl[d]	0.91	91	4,600
7	[Cp*Ir(BiBzImH$_2$)Cl]Cl[e]	17.5	350	1,750
8	[Cp*IrCl(NHC-py^{OtBU})]OTf[f]	5.55	222	740
9	[Cp*IrCl(NHC-py^{OH})]OTf[f]	6.45	258	860

*Reactions performed in 10 ml of a 4:1 H_2O:THF mixture, 0.216 ml DBU at 160°C under 40 bar CO_2:H_2 (1:1) with stirring (1,500 rpm) in the presence of a complex (1 μmol) for 24 h. (a) Calculated mmol of [HCO_2^-] in the presence of excess mercury (500 Hg:1 cat); (b) calculated TON of [HCO_2^-] when reaction carried out in the presence of excess mercury (500 Hg:1 cat); (c) performed in 10 ml of a 4:1 H_2O:THF mixture, 1.44 mmol of $NaHCO_3$ at 160°C under 50 bar H_2 with stirring (1,500 rpm) in the presence of a complex (1 μmol) for 24 h. (d) Reference (Suna et al., 2017). **L1** = 2-(1H-imidazol-2-yl)pyridine, **L2** =2-(1H-pyrazol-3-yl)pyridine performed in 10 ml of a 2.0 M $KHCO_3$ aqueous solution (pH 8.5) at 50°C under 1.0 MPa H_2/CO_2 (1:1) with stirring (1,500 rpm) in the presence of a complex (20 μm) for 24 h. (e) Reference (Gunasekar et al., 2018). The reaction was carried out in a 50-ml 1 M KOH solution of MeOH/H_2O (1:1) mixture under 4.0 MPa total pressure (CO_2/H_2 = 1) using 0.2 mM catalyst at 80°C for 38 h. (f) Reference (Siek et al., 2017). Reactions were performed in 25 ml of an aqueous solution of 0.3 mM catalyst and 1 M $NaHCO_3$ at 115°C and 300 psig of H_2/CO_2 (1:1) for 18 h.*

is evident that catalyst **5** (TON 1 878) performs better than catalyst **8** (**Table 2**). The performance of these two catalysts indicates that electron-donating substituents on the tetrazolyl results in lower catalytic activity. Nevertheless, it is also possible that increased catalytic activity could be the result of the ease with which chlorides dissociate from the iridium center and the subsequent iridium dihydride species formation. Such secondary hydrido species formation for **8** would be more unfavorable for the following reasons. Since **8** exists as an enantiomer, the P-OH group could play the role of a proton-responsive group, where the enantiomer of **8** with P-OH and chloride ligands oriented away from each other would require a significant amounts of energy in forming the iridium hydride species, but the other enantiomer with both P-OH and Cl groups oriented toward each other would require considerably less energy. Interestingly, catalyst **9**, which has a more electron-deficient iridium center, because of the electron-withdrawing nature of the CF_3 substituents, also has a similar TON (1,391) to that of **8**. This suggests that the CF_3 groups are too far from the metal center to significantly influence catalytic activity. This assertion is further supported by $^{31}P\{^{1}H\}$ NMR peaks for both **8** and **9** around 55 ppm, in contrast to more electron-deficient phosphine metal complex peaks that are expected more downfield.

When the catalytic activity of **5–9** are compared to other highly active proton-responsive iridium(III) half-sandwich precatalysts for CO_2 hydrogenation (Siek et al., 2017; Suna et al., 2017; Gunasekar et al., 2018), it is evident that these chiral-at-metal catalysts with proton-responsive P-OH groups are equally as active for CO_2 hydrogenation as shown by their high TONs. For example, more concentrated formate solutions (around 180 mM) are produced from **5**, **8**, and **9** catalyzed CO_2 hydrogenation in our study compared to 26–91 mM for N^N bidentate iridium half-sandwich catalysts reported in literature. These concentrated formate solutions are obtained due to higher temperatures and pressures used. However, these catalysts do not require highly basic solutions and/or significantly extended reaction times in order to obtain similar formate solutions.

MECHANISM OF ACTION OF CHIRAL-AT-METAL COMPLEXES FOR CO_2 HYDROGENATION

A mercury drop test indicated that CO_2 was hydrogenated via a homogeneous/cocktail of catalysts approach (**Table 2**). As such, plausible reaction mechanisms for the CO_2 hydrogenation reaction involving the chiral-at-metal Iridium complexes were investigated. In the presence of excess base and water, complex **8** would be expected to undergo an aquation reaction, with the chloro ligand being replaced with a water ligand while deprotonating the OH group on the phosphorus donor occurs to yield **A** (**Scheme 3**). *In situ* ^1H NMR experiments involving the reaction of complex **8** with two equivalence of DBU demonstrated the disappearance of the hydroxyl protons at 11.6 ppm indicating deprotonation (**Supplementary Figure 5**). This indicated that during the hydrogenation of CO_2, the P-OH group could possibly function as a proton-responsive group to assist in the heterolytic cleavage of H_2.

Pressurizing **8** in a THF/water mixture with two equivalence of DBU and 5 bar of D_2 at 100°C for 1 h resulted in the

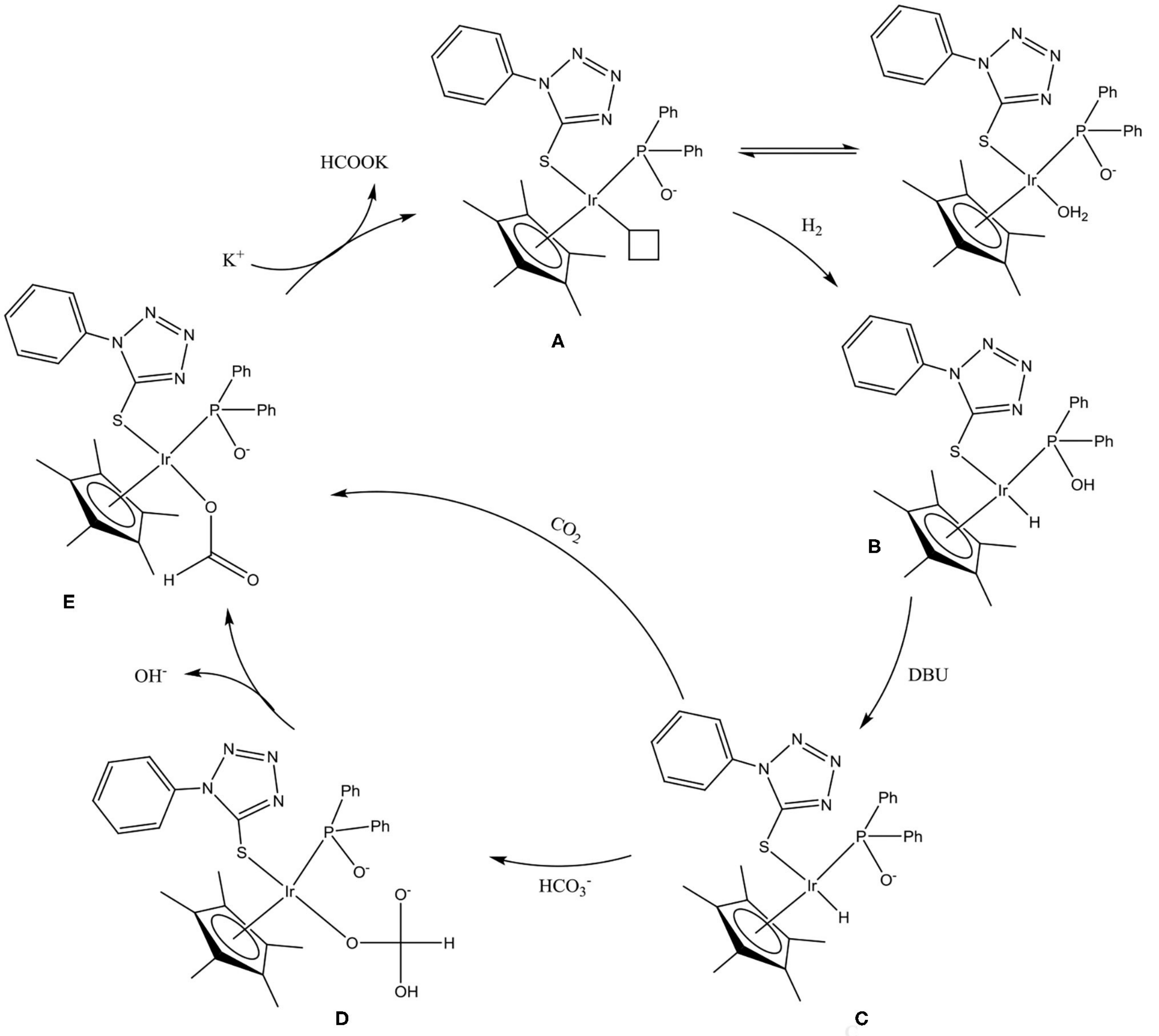

SCHEME 3 | Plausible reaction mechanism for chiral-at-metal Iridium complexes in CO_2 hydrogenation. **(A)** Deprotonated iridium-aqua complex, **(B)** Iridium-hydride complex, **(C)** Deprotonated iridium-hydride species, **(D)** Iridium-carbonato species, and **(E)** Iridium-formato species.

appearance of doublet hydride peaks around −15.5 ppm as well as corresponding shifts in peaks in the aromatic region (**Figure 5**). This was due to the exchange of hydrogen and deuterium present in solution yielding proton signals in the ^1H NMR spectrum. The observed splitting of hydride signal was as a result of the proximity of the NMR active phosphorus atom. Similar splitting for such hydride protons have also been observed in literature (Feller et al., 2016). In addition, there was a corresponding shift in the $^{31}P\{^1H\}$ NMR from around 57 ppm to 72 ppm upon formation of the iridium hydride species (**Supplementary Figure 6**).

Due to the presence of excess base in solution, the iridium hydride species could be expected to exist as **C** (**Scheme 3**) since the proton on the P-OH group is deprotonated. Subsequently, insertion of *in situ* generated bicarbonate ions into the iridium–hydride bond yields intermediate **D**, which, upon dissociation of a hydroxyl group, yields the iridium–formato species **E**. However, direct insertion of CO_2 into the metal–hydride bond is also possible during the formation of the iridium–formato species as a result of the observation of formate when other non-carbonate bases are used for the reaction. Introducing CO_2 to a solution of **C** results in the disappearance of the hydride signal. Such direct CO_2 insertion in metal–hydride bonds have been reported in mechanisms involving interactions between CO_2 and the metal–hydride bonds prior to the formation of the metal–formato species (Wang et al., 2012; Suna et al., 2017).

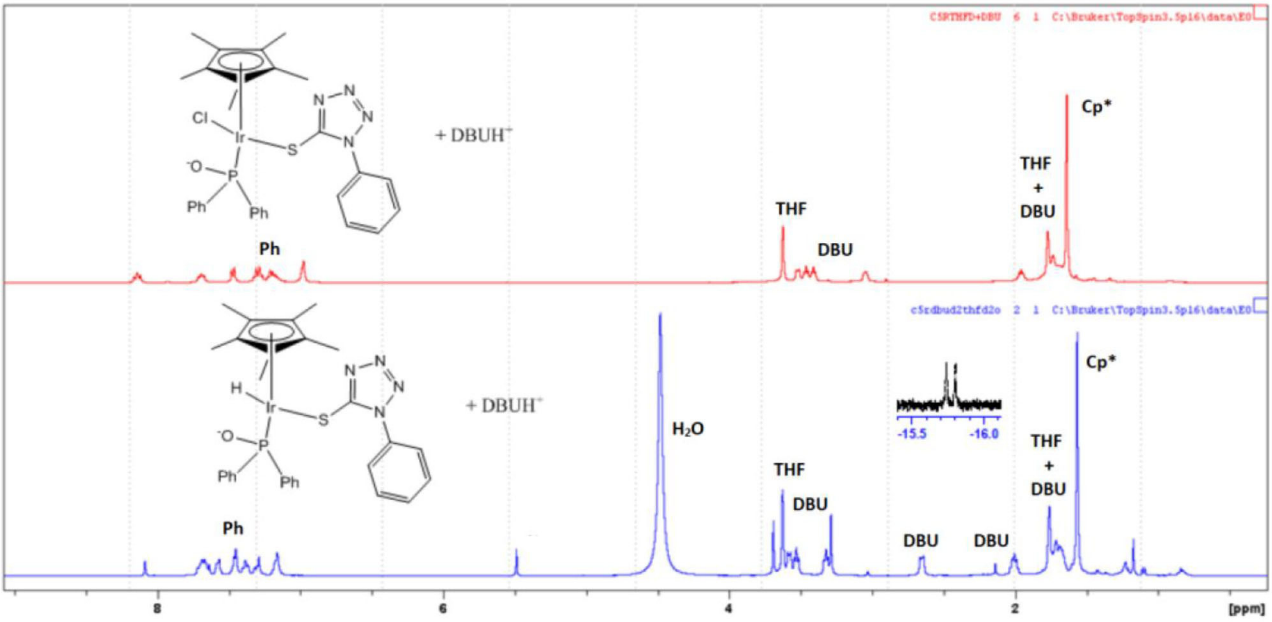

FIGURE 5 | Formation of chiral-at-metal iridium hydride species using **8**.

The final step of the reaction is then reductive elimination of formate using the base in order to regenerate species **A** (**Scheme 3**).

CONCLUSION

Unintended iridium complexes (**4–9**) were obtained as a result of the heterolysis of P–S tetrazolyl ligands (**1–3**) during complexation with $[Ir(C_5Me_5)Cl_2]_2$. The heterolysis is ascribed to the presence of water and electron-withdrawing groups on the phosphorus moiety, which were found to facilitate the heterolysis of the P–S bond in the ligand during complexation with $[Ir(C_5Me_5)Cl_2]_2$. The iridium complexes hydrogenate CO_2 as well as $NaHCO_3$ in a 4:1 water:THF solvent mixture, and DBU as abase. A key factor in the activity of these iridium complexes as excellent CO_2 hydrogenation catalysts is the ability to be proton responsive. We observed such proton-responsive enhanced catalytic ability from chiral-at-the-metal complexes that have the P-OH proton-responsive functional groups. Complex **8** was used to establish that the mechanism of the CO_2 hydrogenation reaction for the iridium complexes proceeded with the iridium precatalysts first undergoing aquation, followed by H_2 heterolysis that is driven by proton-responsive P-OH groups to form an iridium hydride intermediate. This iridium hydride species is the catalytically active species that hydrogenates either bicarbonate species or CO_2 to yield the formate product.

DATA AVAILABILITY STATEMENT

The raw data supporting the conclusions of this article will be made available by the authors, without undue reservation. The crystallographic datasets presented in this study can be found in online repositories. The names of the repository/repositories and accession number(s) can be found below: Cambridge Crystallographic Data Center, CCDC numbers 1840199 and 1993265.

AUTHOR CONTRIBUTIONS

JD and BM conceptualized the research. EO designed and carried out the experiments with guidance from BM and JD. EO, JD, and BM discussed and analyzed the experimental data and finalized the manuscript. All authors contributed to the article and approved the submitted version.

FUNDING

We acknowledge the National Research Foundation of South Africa (NRF) (Grant Numbers: 117989 and 112943), Sasol SA, and the University of Johannesburg Center for Synthesis and Catalysis for financial support.

ACKNOWLEDGMENTS

We would also like to thank UJ Faculty of Science Spectrum for use of NMR facility.

SUPPLEMENTARY MATERIAL

The Supplementary Material for this article can be found online at: https://www.frontiersin.org/articles/10.3389/fchem.2020.591353/full#supplementary-material

Electronic supporting information (ESI) is available free of charge. CCDC number **1840199** contains the supplementary crystallographic data for racemic complex **8**. CCDC number 1993265 contains the supplementary crystallographic data for enantiopure complex **8.** These data can be obtained free of charge from the Cambridge Crystallographic Data Center from the Director, CCDC, 12 Union Road, Cambridge, CB2 1EZ, UK (fax: +44 1223 336063; deposit@ccdc.cam.ac.uk or https://www.ccdc.cam.ac.uk/structures/).

REFERENCES

Ahmad, G., Rasool, N., Rizwan, K., Altaf, A. A., Rashid, U., Hussein, M. Z., et al. (2019). Role of pyridine nitrogen in palladium-catalyzed imine hydrolysis: a case study of (E)-1-(3-bromothiophen- 2-yl)-N-(4-methylpyridin-2-yl)methanimine. *Molecules* 24, 2609. doi: 10.3390/molecules24142609

Boddien, A., Federsel, C., Sponholz, P., Mellmann, D., Jackstell, R., Junge, H., et al. (2012). Towards the development of a hydrogen battery. *Energy Environ. Sci.* 5, 8907–8911. doi: 10.1039/c2ee22043a

Boddien, A., Gärtner, F., Federsel, C., Sponholz, P., Mellmann, D., Jackstell, R., et al. (2011). CO_{2-} "Neutral" hydrogen storage based on bicarbonates and formates. *Angew. Chem. Int. Ed.* 50, 6411–6414. doi: 10.1002/anie.201101995

Brunner, H. (2001). Stability of the metal configuration in chiral-at-metal half-sandwich compounds. *Eur. J. Inorg. Chem.* 2001, 905–912. doi: 10.1002/1099-0682(200104)2001:4<905::AID-EJIC905>3.0.CO;2-V

Chen, L. A., Xu, W., Huang, B., Ma, J., Wang, L., Xi, J., et al. (2013). Asymmetric catalysis with inert chiral-At-metal iridium complex. *J. Am. Chem. Soc.* 135, 10598–10601. doi: 10.1021/ja403777k

Cui, P., Ma, Y., Li, H., Zhao, B., Li, J., and Cheng, P. (2012). Multipoint interactions enhanced CO_2 uptake: a zeolite-like zinc – tetrazole framework with 24-nuclear zinc cages. *J. Am. Chem. Soc.* 134, 18892. doi: 10.1021/ja3063138

Feller, M., Gellrich, U., Anaby, A., Diskin-Posner, Y., and Milstein, D. (2016). Reductive cleavage of CO_2 by metal-ligand-cooperation mediated by an iridium pincer complex. *J. Am. Chem. Soc.* 138, 6445–6454. doi: 10.1021/jacs.6b00202

Getty, A. D., Tai, C. C., Linehan, J. C., Jessop, P. G., Olmstead, M. M., and Rheingold, A. L. (2009). Hydrogenation of carbon dioxide catalyzed by ruthenium trimethylphosphine complexes : a mechanistic investigation using high-pressure NMR spectroscopy. *Organometallics* 28, 5466–5477. doi: 10.1021/om900128s

Go, M. J., Lee, K. M., Oh, C. H., Kang, Y. Y., Kim, S. H., Park, H. R., et al. (2013). New titanium catalysts containing tetrazole for cycloaddition of CO_2 to epoxides. *Organometallics* 32, 4452–4455. doi: 10.1021/om400605k

Gunasekar, G. H., Yoon, Y., Baek, I. H., and Yoon, S. (2018). Catalytic reactivity of an iridium complex with a proton responsive N-donor ligand in CO2 hydrogenation to formate. *RSC Adv.* 8, 1346–1350. doi: 10.1039/C7RA12343D

Heldebrant, D. J., Jessop, P. G., Thomas, C. A., Eckert, C. A., and Liotta, C. L. (2005). The reaction of 1,8-diazabicyclo[5.4.0]undec-7-ene (DBU) with carbon dioxide. *J. Org. Chem.* 70, 5335–5338. doi: 10.1021/jo0503759

Himeda, Y., Onozawa-Komatsuzaki, N., Miyazawa, S., Sugihara, H., Hirose, T., and Kasuga, K. (2008). pH-Dependent catalytic activity and chemoselectivity in transfer hydrogenation catalyzed by iridium complex with 4,4′-dihydroxy-2,2′-bipyridine. *Chem. A Eur. J.* 14, 11076–11081. doi: 10.1002/chem.200801568

Himeda, Y., Onozawa-komatsuzaki, N., Sugihara, H., and Kasuga, K. (2007). Simultaneous tuning of activity and water solubility of complex catalysts by acid - base equilibrium of ligands for conversion of carbon dioxide. *Organometallics*, 26, 702–712. doi: 10.1021/om060899e

Huang, C. H., and Tan, C. S. (2014). A review: CO_2 utilization. *Aerosol Air Qual. Res.* 14, 480–499. doi: 10.4209/aaqr.2013.10.0326

Hughes, R. P., Lindner, D. C., Smith, J. M., Zhang, D., Incarvito, C. D., Lam, K. C., et al. (2001). Water, water, everywhere. Synthesis and structures of perfluoroalkyl rhodium and iridium(III) compounds containing water ligands. *J. Chem. Soc. Dalt. Trans.* 2001, 2270–2278. doi: 10.1039/b102482p

Huo, H., Fu, C., Harms, K., and Meggers, E. (2014). Asymmetric catalysis with substitutionally labile yet stereochemically stable chiral-at-metal iridium(III) Complex. *J. Am. Chem. Soc.* 136, 2990–2993. doi: 10.1002/chin.201437026

Huo, H., Wang, C., Harms, K., and Meggers, E. (2015). Enantioselective, catalytic trichloromethylation through visi- ble-light-activated photoredox catalysis with a chiral iridium complex. *J. Am. Chem. Soc.* 137, 9551–9554. doi: 10.1021/jacs.5b06010

Imamoto, T., Iwadate, N., and Yoshida, K. (2006). Enantioselective hydrogenation of acyclic aromatic N-aryl imines catalyzed by an iridium complex of (S,S)-1,2-Bis(tert-butylmethylphosphino)ethane. *Org. Lett.* 8, 2289–2292. doi: 10.1021/ol060546b

Jeletic, M. S., Helm, M. L., Hulley, E. B., Mock, M. T., Appel, A. M., and Linehan, J. C. (2014). A cobalt hydride catalyst for the hydrogenation of CO_2: pathways for catalysis and deactivation. *ACS Catal.* 4, 3755–3762. doi: 10.1021/cs5009927

Jessop, P. G., Iktariya, T., Noyori, R., Ikariya, T., and Noyori, R. (1995). Homogeneous hydrogenation of carbon dioxide. *Chem. Rev.* 95, 259–272. doi: 10.1021/cr00034a001

Kurihara, K., Yamamoto, Y., and Miyaura, N. (2009). A chiral bidentate phosphoramidite (Me-BIPAM) for Rh-catalyzed asymmetric hydrogenation of α-dehydroamino esters, enamides, and dimethyl itaconate. *Tetrahedron Lett.* 50, 3158–3160. doi: 10.1016/j.tetlet.2008.12.086

Leitner, W., Dinjus, E., Gaßner, F., and Gaher, F. (1994). Activation of carbon dioxide, Rhodium-catalysed hydrogenation of carbon dioxide to formic acid. *J. Organomet. Chem.* 475, 257–266. doi: 10.1016/0022-328X(94)84030-X

Ludwig, G., Korb, M., Rüffer, T., Lang, H., and Steinborn, D. (2012). Chlorido[1-diphenylphosphanyl-3-(phenyl-sulfanyl)propane-k2 P,S](η5-pentamethylcyclopentadienyl)iridium(III) chloride monohydrate. *Acta Crystallogr. Sect. E Struct. Rep. Online* 68, 112–122. doi: 10.1107/S1600536812021964

Ma, J., Sun, N., Zhang, X., Zhao, N., Xiao, F., Wei, W., et al. (2009). A short review of catalysis for CO_2 conversion. *Catal. Today* 148, 221–231. doi: 10.1016/j.cattod.2009.08.015

Makuve, N., Mehlana, G., Tia, R., Darkwa, J., and Makhubela, B. C. E. (2019). Hydrogenation of carbon dioxide to formate by α-diimine RuII, RhIII, IrIII complexes as catalyst precursors. *J. Organomet. Chem.* 899, 120892. doi: 10.1016/j.jorganchem.2019.120892

Malaza, S. S. P., and Makhubela, B. C. E. (2020). Direct and indirect CO_2 hydrogenation catalyzed by Ir(III), Rh(III), Ru(II), and Os(II) half-sandwich complexes to generate formates and N,N-diethylformamide. *J. CO_2 Util.* 39,101149. doi: 10.1016/j.jcou.2020.02.019

Munshi, P., Main, A. D., Linehan, J. C., Tai, C. C., and Jessop, P. G. (2002). Hydrogenation of carbon dioxide catalyzed by ruthenium trimethylphosphine complexes: the accelerating effect of certain alcohols and amines. *J. Am. Chem. Soc.* 124, 7963–7971. doi: 10.1021/ja0167856

Murata, K., Ikariya, T., and Cp, P. E. N. (1999). New chiral rhodium and iridium complexes with chiral diamine ligands for asymmetric transfer hydrogenation of aromatic ketones. *J. Org. Chem.* 64, 2186–2187. doi: 10.1021/jo990213a

Ocansey, E., Darkwa, J., and Makhubela, B. (2020). Iridium and palladium CO_2 hydrogenation in water by catalysts precursors with electron-rich tetrazole ligands. *Organometallics* 39, 3088–3098. doi: 10.1021/acs.organomet.0c00276

Pachfule, P., and Banerjee, R. (2011). Porous nitrogen rich cadmium-tetrazolate based metal organic framework (MOF) for H2 and CO2 Uptake. *Cryst. Growth Des.* 11, 5176–5181. doi: 10.1021/cg201054f

Papp, G., Csorba, J., Laurenczy, G., and Joó, F. (2011). A charge / discharge device for chemical hydrogen storage and generation. *Angew. Chem. Int. Ed.* 50, 10433–10435. doi: 10.1002/anie.201104951

Poloni, R., and Smit, B. (2012). Ligand-assisted enhancement of CO_2 capture in metal – organic frameworks. *J. Am. Chem. Soc.* 134, 6714. doi: 10.1021/ja2118943

Rakowski Dubois, M., and Dubois, D. L. (2009). The roles of the first and second coordination spheres in the design of molecular catalysts for H_2 production and oxidation. *Chem. Soc. Rev.* 38, 62–72. doi: 10.1039/B801197B

Saeidi, S., Amin, N. A. S., and Rahimpour, M. R. (2014). Hydrogenation of CO_2 to value-added products - a review and potential future developments. *J. CO_2 Util.* 5, 66–81. doi: 10.1016/j.jcou.2013.12.005

Siek, S., Burks, D. B., Gerlach, D. L., Liang, G., Tesh, J. M., Thompson, C. R., et al. (2017). Iridium and ruthenium complexes of N-heterocyclic carbene- and pyridinol-derived chelates as catalysts for aqueous carbon dioxide hydrogenation and formic acid dehydrogenation: The role of the alkali metal. *Organometallics* 36, 1091–1106. doi: 10.1021/acs.organomet.6b00806

Suna, Y., Ertem, M. Z., Wang, W., Kambayashi, H., Manaka, Y., Muckerman, J. T., et al. (2014). Positional effects of hydroxy groups on catalytic activity of proton-responsive half-sandwich cp* iridium (III) complexes. *organometallics* 33, 6519–6530. doi: 10.1021/om500832d

Suna, Y., Himeda, Y., Fujita, E., Muckerman, J. T., and Ertem, M. Z. (2017). Iridium complexes with proton-responsive azole-type ligands as effective catalysts for CO_2 hydrogenation. *ChemSusChem* 10, 4535–4543. doi: 10.1002/cssc.201701676

Tanaka, R., Yamashita, M., and Nozaki, K. (2009). Catalytic hydrogenation of carbon dioxide using Ir(III)-pincer complexes. *J. Am. Chem. Soc.* 131, 14168–14169. doi: 10.1021/ja903574e

Tian, C., Gong, L., and Meggers, E. (2016). Chiral-at-metal iridium complex for efficient enantioselective transfer hydrogenation of ketones. *Chem. Commun.* 52, 4207–4210. doi: 10.1039/C6CC00972G

Wang, W.-H., Hull, J. F., Muckerman, J. T., Fujita, E., and Himeda, Y. (2012). Second-coordination-sphere and electronic effects enhance iridium(III)-catalyzed homogeneous hydrogenation of carbon dioxide in water near ambient temperature and pressure. *Energy Environ. Sci.* 5, 7923–7926. doi: 10.1039/c2ee21888g

White, C., Yates, A., Maitlis, P. M., Heinekey, D. M., (1992). "(η^5-Pentamethylcyclopentadienyl)rhodium and iridium compounds," in *Inorganic Syntheses*, ed R. N. Grimes (New York, NY: Wiley Online Library), 228.

Yasaka, Y., Wakai, C., Matubayasi, N., and Nakahara, M. (2010). Controlling the equilibrium of formic acid with hydrogen and carbon dioxide using ionic liquid. *J. Phys. Chem.* 114, 3510–3515. doi: 10.1021/jp908174s

Zhang, Y., Macintosh, A. D., Wong, J. L., Bielinski, E. A., Williard, P. G., Mercado, B. Q., et al. (2015). Iron catalyzed CO_2 hydrogenation to formate enhanced by Lewis acid co-catalysts. *Chem. Sci.* 6, 4291–4299. doi: 10.1039/C5SC01467K

Zhao, Y., Li, Y., Cui, C., Xiao, Y., Li, R., Wang, S., et al. (2016). Tetrazole – viologen-based flexible microporous metal organic framework with high CO_2 selective uptake. *Inorg. Chem.* 55, 4–9. doi: 10.1021/acs.inorgchem.6b00320

Conflict of Interest: The authors declare that the research was conducted in the absence of any commercial or financial relationships that could be construed as a potential conflict of interest.

frontiers in Chemistry

ORIGINAL RESEARCH
published: 16 November 2020
doi: 10.3389/fchem.2020.595908

Mechanochemical Synthesis and Physicochemical Characterization of Isoniazid and Pyrazinamide Co-crystals With Glutaric Acid

Jean Baptiste Ngilirabanga[1], **Marique Aucamp**[1], **Paulo Pires Rosa**[2] **and Halima Samsodien**[1]*

[1] School of Pharmacy, University of the Western Cape, Cape Town, South Africa, [2] Faculty of Pharmaceutical Sciences, State University of Campinas, Saö Paulo, Brazil

The present work reports two novel pharmaceutical co-crystals; 2:1 isoniazid-glutaric acid (INHGA) and 2:1 pyrazinamide-glutaric acid (PGA). Isoniazid and pyrazinamide are key first-line drugs used for the treatment of tuberculosis. The co-crystals were produced *via* solid-state and solvent assisted grinding methods. Thermal characteristics of the samples were obtained using the differential scanning calorimetry, hot stage microscopy, and thermogravimetric analyses. The morphology of the powder samples by scanning electron microscopy, structural analysis by Fourier transform infrared spectroscopy and powder X-rays diffraction ensured co-crystal formation. Thermal analyses confirmed the co-crystals with new melting transitions ranging between their respective starting materials. Unique morphologies of the co-crystal particles were clear in SEM micrographs. The formation of intermolecular interactions with the co-crystal former was confirmed by the FT-IR spectral band shifting and was supported by distinct PXRD patterns of co-crystals thereby authenticating the successful co-crystal formation. *In vitro* solubility evaluation of the synthesized co-crystals by HPLC suggested a remarkable increase in solubility of both INH and PZA in their respective co-crystals.

Keywords: antitubercular, co-crystallization, mechanochemistry, solid-state grinding, liquid-assisted grinding, characterization, saturation solubility

Edited by:
Shivani Mishra,
University of South Africa, South Africa

Reviewed by:
Yohann Corvis,
Université de Paris, France
Andrei I. Khlebnikov,
Tomsk Polytechnic University, Russia

***Correspondence:**
Halima Samsodien
hsamsodien@uwc.ac.za

Specialty section:
This article was submitted to
Medicinal and Pharmaceutical
Chemistry,
a section of the journal
Frontiers in Chemistry

Received: 17 August 2020
Accepted: 12 October 2020
Published: 16 November 2020

Citation:
Ngilirabanga JB, Aucamp M, Pires Rosa P and Samsodien H (2020) Mechanochemical Synthesis and Physicochemical Characterization of Isoniazid and Pyrazinamide Co-crystals With Glutaric Acid. Front. Chem. 8:595908. doi: 10.3389/fchem.2020.595908

INTRODUCTION

For centuries, infectious diseases have been the leading cause of death in human existence. Among known infectious diseases, tuberculosis (TB), an infection caused by *Mycobacterium tuberculosis*, and HIV/AIDS caused by the human immunodeficiency virus (HIV) holds the leading rates on infection (Raviglione and Sulis, 2016) with TB ranked the second killer disease worldwide after HIV. TB is also known as the oldest infectious disease in history (Pinheiro et al., 2014), yet still a danger which the battle against is far from over. Compared to the 2012–2013 WHO report, approximately 8.6 million TB infections were recorded and 1.3 million deaths associated with TB, 10 million new cases, and 1.5 million deaths were reported in 2018. Nonetheless, 58 million lives have been saved over the period of 10 years (2010–2018) using the current TB treatment strategies (Baddeley et al., 2013).

It is estimated that one-fourth of the population worldwide are infected by latent *Mycobacterium tuberculosis* (Mtb). This serves as a reservoir for the active and deadly form of the infection, making it even harder to control the infection. The threat is further aggravated by the appearance of drug resistance making treatment very complicated and in some cases resulting in treatment failure (Somoskovi et al., 2001; Hu et al., 2017; Howard et al., 2018) and co-infection with HIV/AIDS (Pawlowski et al., 2012; Mesfin et al., 2014; Bell and Noursadeghi, 2018; Duarte et al., 2018; Letang et al., 2020).

Despite the advent of drug resistance and several other drawbacks and inconveniences for patients, the fact remains that antibiotics have remarkably contributed to the control of TB and other various infections, saving many lives by reducing the associated morbidity and mortality rate of bacterial infections (Aminov, 2010).

As anti-tubercular drugs, isoniazid, chemically known as isonicotinic acid hydrazide (INH) and pyrazinamide known as pyrazinecarboxamide (PZA) are two key drugs in the first-line treatment of TB. Both drugs are used in a single combined dose concomitant with rifampicin (RIF) and ethambutol (ETB) or streptomycin. INH and PZA are prodrugs in nature; both activated after administration, the process triggered by the bacterial enzymes. The mechanisms of action were thoroughly explained by Unissa et al. (2016), and INH is the most used drug in TB treatment. Its potential is well-understood not only by its activity but also through the meaning of multidrug-resistance TB (MDR-TB).

However, despite its remarkable activity which seems to relate to molecular targets of the prokaryotic cells, toxicity and different side effects (dryness of the mouth, flu-like syndrome, allergic reactions, peripheral neuritis, mental abnormalities, methaemoglobinemia, and hepatotoxicity), have been linked to the use of INH (Sarceviča et al., 2016).

PZA is also a very effective antimycobacterial agent that offers to the combinations its unique sterilizing activity against persistent tubercle bacilli during the initial intensive phase of treatment. The use of PZA is also associated with shortening the duration of TB treatment, from 9 to 6 months (Somoskovi et al., 2001; Chiş et al., 2005). PZA shows prodigious but pH-dependent *in-vivo* activity. It is effective against *M. tuberculosis* only under acidic conditions. However, like many other drugs, different side effects have been attributed to the prolonged use of PZA (Schaberg et al., 1996).

Regardless of their substantial contribution, there is evidence of different strains being resistant to all available antitubercular drugs as well as different inconveniences (side effects) to patients caused by the use of high doses required to achieve a better therapeutic effect. Additionally, while INH and RIF are essential in the TB treatment regimen, these two drugs present interaction issues, and the presence of PZA catalyzes their interactions. Such interactions were also reported during the use of the fixed-dose combinations containing these three substances with ETB (Battini et al., 2018). Such interactions may lead to the reduced activity of the dose, treatment failure, and the appearance of drug resistance or even advert effects (Scripture and Figg, 2006; Palleria et al., 2013; Michael et al., 2016).

Due to these setbacks, there is an intense need for new drugs and novel treatment strategies to improve the treatment of the infection. The possibility of enhancing the efficacy of existing drugs is considered a cost-effective approach to address the mentioned challenges (Aitipamula et al., 2013). Today, co-crystallization is one of the strategies used to fine-tune the physicochemical properties of drugs (Patel et al., 2012; Gadade and Pekamwar, 2016). Co-crystallization uses principles of crystal engineering to modify the physicochemical properties of the active pharmaceutical ingredients (APIs) while maintaining intrinsic drug activity (Duggirala et al., 2016). Based on this and the fact that a wider range of compounds readily available to be explored, co-crystallization has become a preferred approach over salt formation, amorphous forms, hydrates/solvates and polymorphism.

Pharmaceutical co-crystals which consist of an API and a pharmaceutically regarded as safe compound bind together in the crystal lattice (in a very defined stoichiometry), through intermolecular (non-covalent) interactions among which hydrogen bonding being the most encountered bonding type (Sekhon, 2009; Gadade and Pekamwar, 2016; Masodkar et al., 2018). Different pharmaceutical co-crystals have been reported. These include that of indomethacin-saccharin (Chun et al., 2013), pyrazinamide-diflunisal (Évora et al., 2011), isoniazid-4-aminosalicylic acid co-crystal (Grobelny et al., 2011), dimethylglyoxime with N-heterocyclic aromatic compounds and acetamide (Abidi et al., 2017), etc.

Grinding crystalline materials also known as mechanochemistry has become a method of choice for co-crystal preparation (Shan and Zaworotko, 2008; Brown, 2012; Lin, 2016). In this work, mechanochemical reaction as a co-crystal formation approach, was used to produce two novel supramolecular co-crystals of the two antitubercular drugs INH and PZA with glutaric acid (GA). Both drugs have shown the affinity to form co-crystals with carboxylic acids. Some of the co-crystals have been reported (Grobelny et al., 2011; Cherukuvada and Nangia, 2012; Luo and Sun, 2013; Diniz et al., 2018). Two of the PZA polymorphic co-crystals with dicarboxylic acids were previously reported and were synthesized *via* solution crystallization, and their structures were solved (Aitipamula et al., 2014). Other co-crystal polymorphs were listed by Gadade and Pekamwar (2016).

MATERIALS AND METHODOLOGY

Materials

All materials used in this project were of analytical grade. Isoniazid (purity $\geq$ 99.6%) and pyrazinamide (purity $\geq$ 98.6%) and glutaric acid (purity $\geq$ 99.9%) (structures depicted in **Figure 1**). Solvents used were purchased from Sigma-Aldrich Chemie GmbH (Steinheim, Germany) and were used as received unless otherwise stated.

Synthesis

Both 2:1 co-crystals INHGA (2:1) and PGA (2:1) were synthesized using solid-state grinding and solvent-assisted grinding processes. Initially, the screening for the co-crystal was

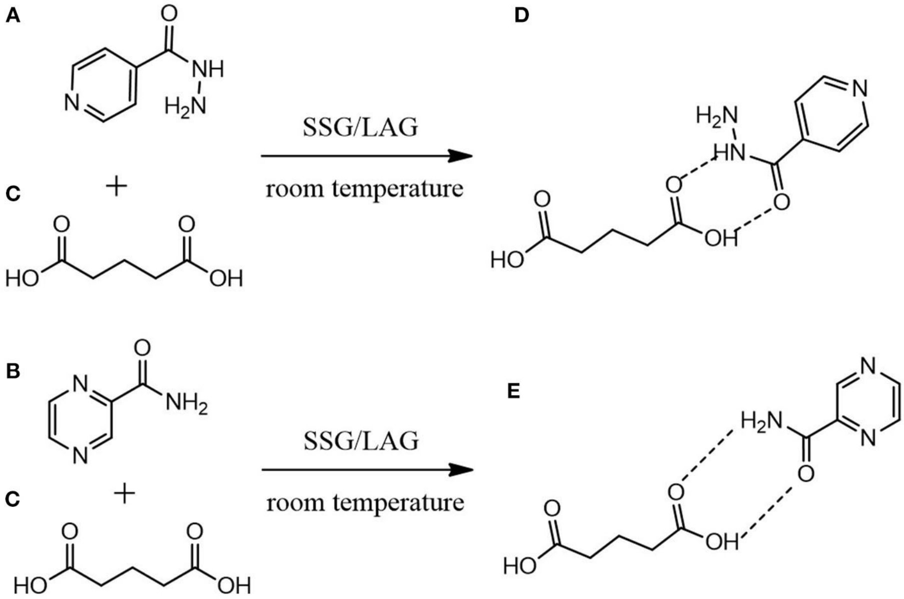

FIGURE 1 | Proposed molecular mechanistic for the formation of **(D)** INHGA (2:1) and **(E)** PGA (2:1) co-crystals of **(A)** isoniazid and **(B)** pyrazinamide with **(C)** glutaric acid as a co-former using solid-state grinding (SSG) and liquid-assisted grinding (LAG).

carried out using solid-state grinding, a method during which the mixtures INH:GA and PZA:GA in different molar ratios (1:1; 2:1; 1:2) were subjected to milling using a mortar and pestle. Both co-crystals were reproduced by the milling process assisted by a few drops of the solvent (ethanol 96%) added to the mixtures throughout the grinding process. The reproducibility of samples was ensured by repeating experiments in triplicate.

Physicochemical Characterization

Pure APIs, co-former and the co-crystal samples were characterized by hot stage microscopy (HSM), differential scanning calorimetry (DSC), thermogravimetric analysis (TGA), Fourier transform infrared spectroscopy (FT-IR), scanning electron microscopy (SEM), and powder X-ray diffraction (PXRD). All analyses were performed in triplets.

Hot Stage Microscopy (HSM)

Thermo-microscopic analyses were carried out on an optical microscope Olympus (SZX-ILLB200) equipped with a Linkam temperature-controlled stage (THMS600/720), connected to a T95-PE system controller (Linkam Scientific Instruments Ltd., Tadworth, Surrey, UK). The hot-stage was calibrated using USP melting point standards. Images were recorded with an Olympus UC30 camera attached to the specified microscope (Olympus Optical, Japan) using Stream Essentials software. Samples were submerged *in silicon* oil and subjected to heating over a temperature range of 30–350°C at a constant heating rate of 10°C/min.

Differential Scanning Calorimetry (DSC)

The DSC measurements were carried out on a DSC 8000 Perkin Elmer instrument (Waltham, USA), incorporating a cooling system and a Perkin Elmer nitrogen gas generator. Samples (2.5–5 mg) were crimped in the aluminum pans sealed with pierced lids. The instrument was calibrated by measuring the onset temperatures of the melting of indium (m.p. 156.6°C) and zinc (m.p. 419.5°C) while the heat flow was calibrated from the enthalpy of melting of indium (28.62 J/g). The samples were heated to 20–30°C above the melting range of the sample's highest melting component, at a heating rate of 10°C/min. All analyses were performed under continuous 99.8% dry nitrogen purging with a flow rate of 20 mL/min.

Thermogravimetry (TGA)

A Perkin-Elmer 4000 PC thermal system (Waltham, USA) was used. The calibration of the instrument was performed using three different references; alumel (m.p. = 154.2°C), Perk alloy (m.p. = 596°C) and iron (m.p. = 780°C) at 1 and 2°C/min. The programmed TG technique was carried out over a temperature range between 30–400°C at a predetermined heating rate of 10°C/min. Samples were continuously purged by a stream of 99.8% dry nitrogen gas (20 mL/min) and solvent stoichiometry of the compounds was determined from the percentage mass loss.

Fourier Transform Infrared Spectrophotometry (FT-IR)

Infra-red spectra of the individual drugs and the co-crystal samples were obtained using a Perkin-Elmer 100 FTIR instrument (Waltham, USA) fitted with UATR® and controlled with Spectrum software version 6.3.5.0176 for the analysis. Analyses of powder or crystalline samples were done over the range of 650–4,000 cm^{-1} at a 2 cm^{-1} resolution.

Scanning Electron Microscopy (SEM)

The morphology of untreated INH, PZA, GA, and co-crystal samples were conducted using an AURIGA Field Emission High-Resolution Scanning Electron Microscope (HRSEM), Zeiss (Germany). Powder samples were mounted onto aluminum stubs using carbon tape. Accelerating voltage of 5 kV was used for images and 20 kV for EDS. The lament current was set at 2,359 amps. Carbon tabs were placed on the aluminum stubs to hold samples. Working distance (WD) for images is displayed on each image. SmartSEM 90 and AZTEC software were used for imaging and EDS, respectively.

Powder X-Ray Diffraction (PXRD)

PXRD data were recorded on a D8 Advance powder X-ray diffractometer (Bruker AXS GmbH, Germany) with CuKα radiation (Cu-Kα_1 = 1.54056 Å). The tube voltage and current applied were 35 kV and 40 mA, respectively. A V20 variable slit was used. Samples were placed on the sample holder which has 1 mm thickness and 1.5 cm in diameter. With a scan rate of 2° per min, sample scan was performed in a continuous scan in locked coupled mode, within a range of 2θ 5 to 50°. Origin Pro 8.5. was used to plot PXRD patterns.

In vitro Solubility Studies

Excess amounts of the individual drugs INH, PZA, and their respective co-crystals were added to USP aqueous buffer solutions at pH 1.2 (0.1N hydrochloric acid), 0.2M potassium phosphate buffer (pH 6.8 and pH 7.4), and deionized water (18.s MΩ). The mixtures were continuously shaken in an incubator shaker at 37°C (± 0.5°C) and at 100 rpm for 24 h. Samples were filtered using 0.20 μm PVDF syringe filters and analyzed using an HPLC. INH and PZA in both co-crystal preparations were quantified using an Agilent HPLC system setting with FXB Pump (Flexar Binary Pump), an automated injector equipped with a UV detector (LC 200a Series PDA Detector), and a Flexar autosampler. Isocratic elution using acetonitrile: water mixed in 30:70 (v/v) solution was applied at a flow rate of 10 mL/min. A reversed-phase Luna C_{18} HPLC column 250 mm × 4.6 mm, 5μm was used. Injection volume was 10 μL and absorbance of elution was recorded at 262 and 270 nm following suitable dilutions.

RESULTS AND DISCUSSION

Thermal analysis by DSC confirmed the melting onsets of the individual drugs INH, PZA, and the co-former GA, respectively at 172.0, 189.7, and 98.6°C. The GA DSC curve showed an additional broad peak at 74.0°C corresponding to the polymorphic transition (polymorph-β to α) (Bruni et al., 2013). The 2:1 co-crystal of isoniazid-glutaric acid (INHGA) exhibited a single sharp endothermic melt at 106.9°C (**Figure 2**). This melting temperature falls in the range between then INH and GA melting points.

The melting onset of the 2:1 pyrazinamide-glutaric acid (PGA) co-crystal obtained from dry and/or solvent assisted co-grinding, was found at 102.4°C. The melting point ranges between melting temperatures of the PZA and co-former GA. **Table 1** summarizes all the essential thermal properties of the samples.

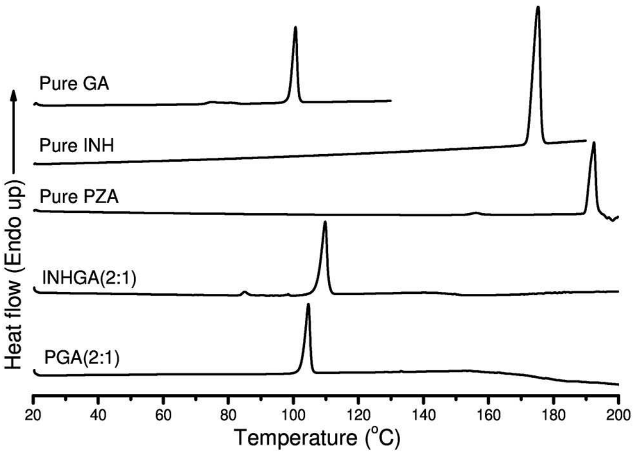

FIGURE 2 | The DSC curves of pure pentanedioic acid (GA), isoniazid (INH), pyrazinamide (PZA), and two potential co-crystals INHGA (2:1) and PGA (2:1).

TABLE 1 | Thermal properties for pure INH, PZA, GA, and the two co-crystals INHGA (2:1) and PGA (2:1) from DSC analyses.

Sample	Melting onset temperature (°C)	$\Delta_{fus}H$ (J/g)
INH	172.0	206.704
INHGA (2:1)	106.9	99.451
GA	98.6	96.711
PGA (2:1)	102.4	99.889
PZA	189.7	227.915

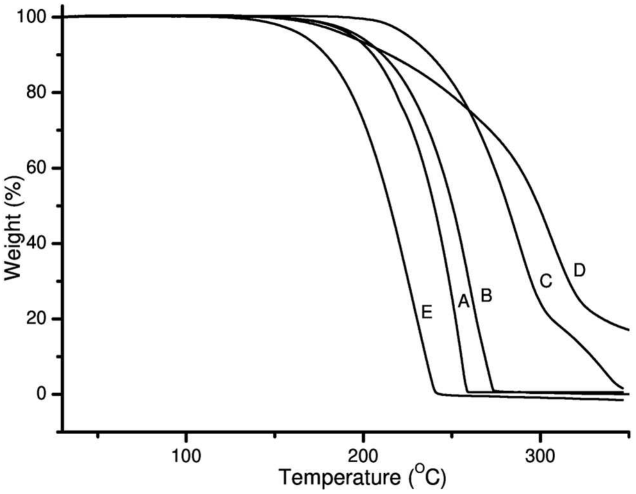

FIGURE 3 | TGA thermograms of (A) PZA, (B) GA, (C) INH, (D) INHGA (2:1) and (E) PGA (2:1) co-crystal.

These unique melting points were the first indication of the successful co-crystallization experiments, although further confirmation by other analytical techniques is warranted since the change in melting points among multicomponent solid forms may occur either due to formation of non-covalent

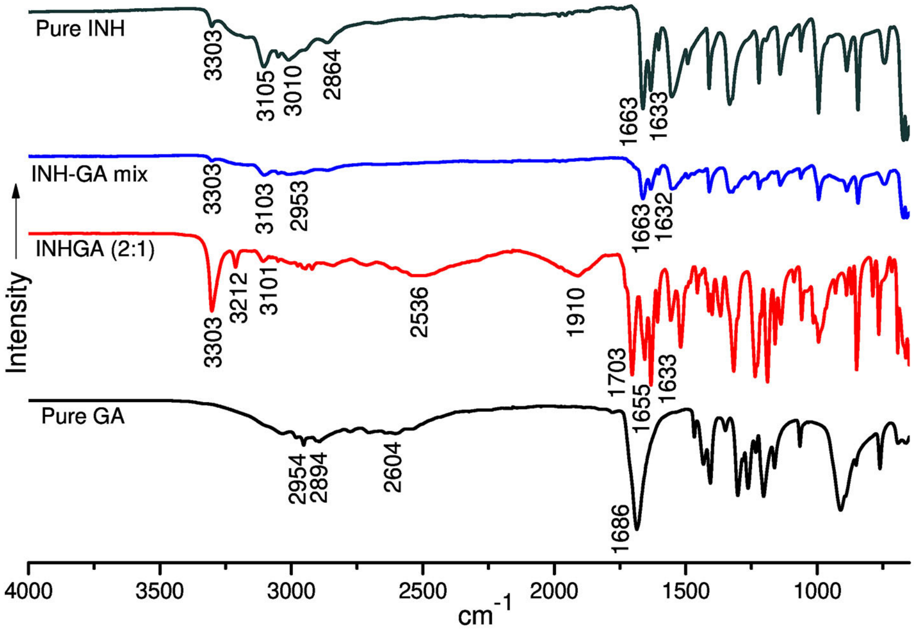

FIGURE 4 | The FTIR spectra of isoniazid (INH), pentanedioic acid (GA), and INH-GA as a physical mixture and the (2:1) co-crystal.

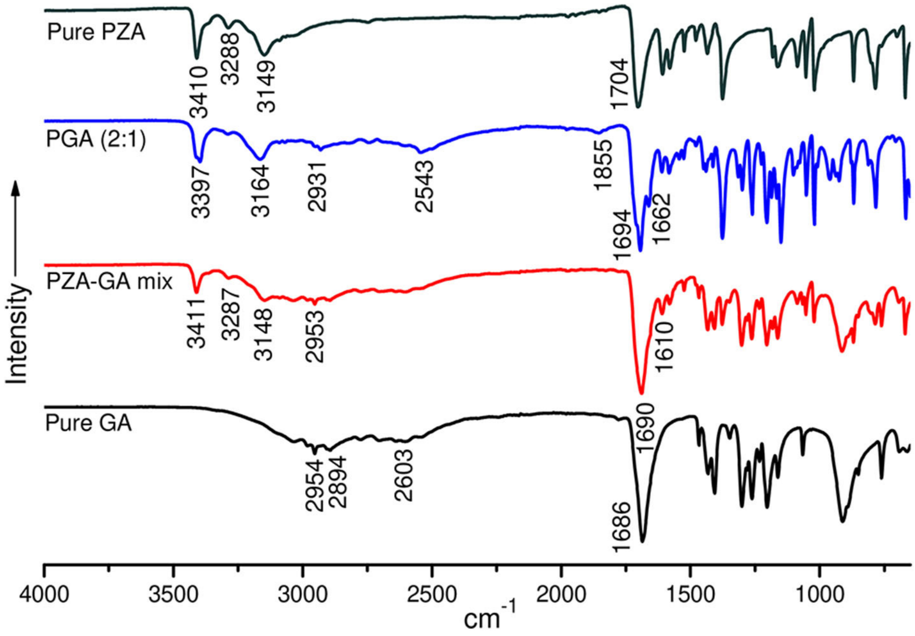

FIGURE 5 | FTIR spectra of pure pyrazinamide (PZA), PGA (2:1) co-crystal, 2:1 physical mixture, and pure pentanedioic acid (GA).

bonding interaction between API and co-formers, alteration in packing arrangements (e.g., polymorphic transition, the formation of eutectic solid mixtures or solid solution). The fact that a single peak was established during DSC analysis certainly identifies an interaction between the two parent compounds.

HSM and TGA experiments were carried out to further understand the thermal behavior of the co-crystal samples. The results obtained were subsequently compared to the DSC data. In both cases, the co-crystals remain stable until melting temperatures are reached. Results obtained from HSM (**Supplementary Figure 2**) and TGA analyses showed no thermal

TABLE 2 | Summary of the different band shifting in the spectra of the INHGA (2:1) and their functional groups.

Functional groups	INH	INHGA (2:1)	GA	Comments
Stretching N–H	3,303 cm^{-1}	3,303 cm^{-1}	–	Increased intensity in INHGA (2:1)
Asym C–H	3,107 cm^{-1}	3,101 cm^{-1}	–	Shifting of C-H in INHGA (2:1)
Stretching O–H	–	–	2,954 cm^{-1}	O-H band subsided in the INHGA (2:1)
C–H	3,010 cm^{-1}	–	–	Disbanded in INHGA (2:1)
O–H	–	2,536 cm^{-1}	2,894 cm^{-1} 2,604 cm^{-1}	The band shifted and less intensified
	–	1,910 cm^{-1}		A new band in the INHGA (2:1)
Carbonyl C=O	1,663 cm^{-1}	1,704 cm^{-1}	1,683 cm^{-1}	Shifting in INHGA (2:1)
Stretching C=N	–	1,633 cm^{-1}	1,632 cm^{-1}	The band is more intensified in INHGA (2:1)

TABLE 3 | Summary of the different band shifting in the spectra of PGA (2:1) and their assignments.

Functional groups	PZA	PGA (2:1)	GA	Comments
N–H	3,409 cm^{-1}	3,398 cm^{-1}		Broadening and shift in PGA (2:1)
Sym-N-H	3,288 cm^{-1}			Subsided
Stretching C–H	3,148 cm^{-1}	3,159 cm^{-1}		Bands shifted in PGA (2:1)
Carboxylic O–H		2,931 cm^{-1} 2,543 cm^{-1}	2,954 cm^{-1} 2,604 cm^{-1}	Band shifted significantly
Carbonyl C=O	1,704 cm^{-1}	1,694 cm^{-1}		Significant band shifting
Carbonyl C=O		1,662 cm^{-1}	1,686 cm^{-1}	Significant band shifting

changes before melting occurs and correlate with DSC outcomes. Based on the HSM analysis, GA melted between 98 and 101°C range. Co-crystals INHGA (2:1) and PGA (2:1) showed a melt in the temperature ranges 106–111and 102–108°C, respectively, thus matching the DSC results.

TGA thermograms of pure PZA, GA, INH, and both co-crystals are shown in **Figure 3**. The TGA thermogram generated from pure PZA showed a stepwise mass loss with initial 24.8% loss occurring before and over melting range (from 150 to 205°C), suggesting the presence of moisture in PZA sample. The second mass loss occurred due to the decomposition of the sample over 205–245°C temperature range with 74.1% of mass loss (**Figure 3A**). GA generated a TGA thermogram (**Figure 3C**) showing only a decomposition mass loss over 150–250°C.

On the other hand, the TGA thermogram of pure INH exhibited a stepwise mass loss with decomposition (onset at 229°C). The first step indicated 81.3% loss of the initial sample weight followed by 18% loss (**Figure 3C**).

The mass loss recorded by TGA prior to the melting range was insignificant (0.0%) for both co-crystals INHGA (2:1), and PGA (2:1), thus confirming that they are anhydrous and solvent-free. The TGA curves are further characterized by single steps of weight loss upon decomposition of the samples which took place at a high temperature above melting points with a decomposition and/or evaporation phenomenon at ∼180 and 198°C for INHGA (2:1), and PGA (2:1), respectively (**Figures 3A,B**). A total mass loss of 92.0 and 98.2% was recorded for the respective co-crystals.

Structural studies by FTIR were conducted to confirm the formation of the co-crystals by monitoring spectral changes of band positions in the spectra of INHGA (2:1) and PGA (2:1) co-crystal samples in comparison to pure INH and PZA and co-former GA. Such changes only occur as a result of intermolecular interaction between co-formers and confirm if a co-crystal was formed (Ali et al., 2012; Kumar, 2017). **Figures 4**, **5** illustrate IR spectra of INH, PZA, GA, and both INHGA (2:1) and PGA (2:1) co-crystals.

FTIR spectra of the individual drugs INH, PZA, and GA were obtained first and were used as references to analyze the co-crystal spectra. The INH spectrum exhibits two stretching amide ν(N-H) bands at 3,303 and 3,107 cm^{-1}, stretch ν(C-H) at 3,010 cm^{-1}, while amide stretching carbonyl at 1,663 cm^{-1} and C=C at 1,633 cm^{-1} in agreement with the literature (Gunasekaran et al., 2009; Ravikumar et al., 2013). The FTIR spectrum generated by GA is mainly characterized by a series of hydroxyl O-H stretching bands at 2,954, 2,894, and 2,604 cm^{-1} and the stretching carbonyl C=O at 1,686 cm^{-1}.

The analysis of the IR spectrum of INHGA (2:1) co-crystal indicated that the INH carbonyl ν(C=O) stretch band shifted to 1,656 cm^{-1} while the GA stretching carbonyl ν(C=O) at 1,686 cm^{-1} shifted to 1,704 cm^{-1} due to H-bonding N-H···C=O. Further, less intensified GA carboxyl ν(O-H) at 2,604 cm^{-1} significantly shifted to 2,536 cm^{-1} as a result of H-bonding to N-H of INH. A new broad absorption peak at 1,910 cm^{-1} in the INHGA (2:1) spectrum further indicated the H-bonding effect. Other shifts identified are illustrated in **Table 2**.

The FTIR spectra of pure PZA, GA, and PGA (2:1) co-crystal samples are presented in **Figure 5** and **Table 3**. The significant differences in the N–H, O-H, and C=O stretching vibrations confirmed the generation of the indistinguishable co-crystal.

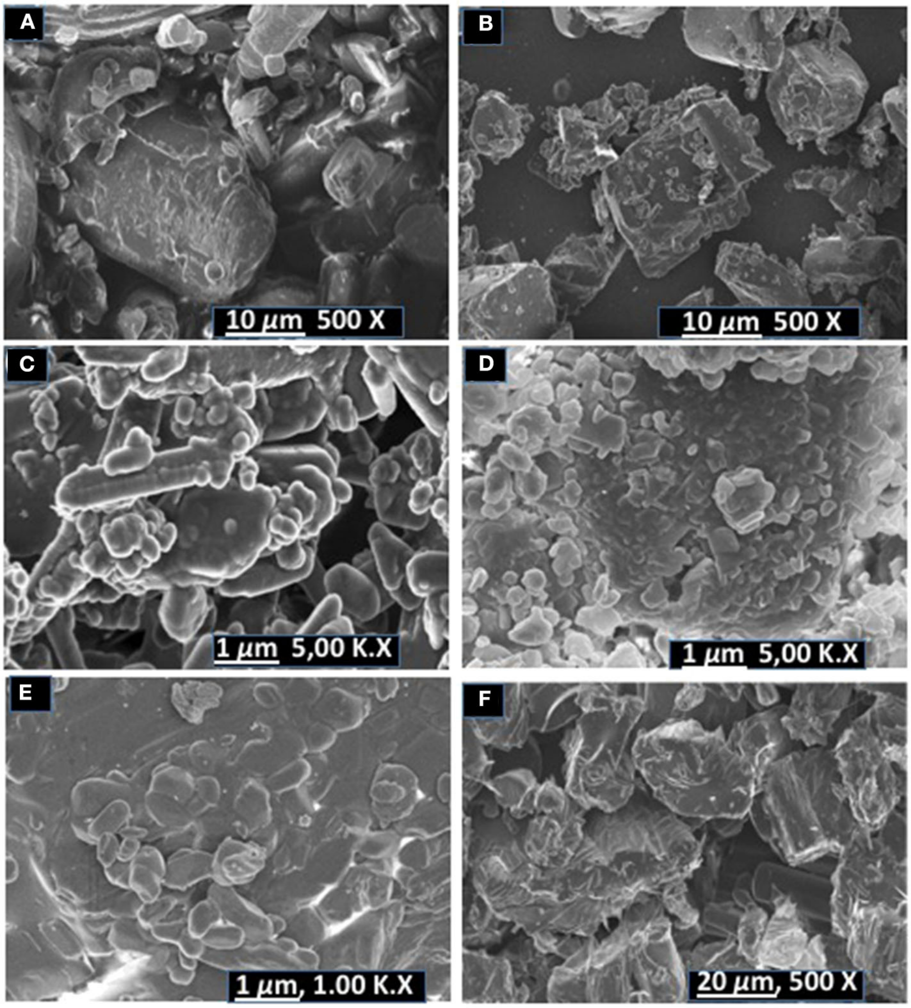

FIGURE 6 | SEM micrographs of **(A)** pyrazinamide, **(B)** isoniazid, **(C)** PGA (2:1) co-crystal, **(D)** INHGA (2:1) co-crystal **(E)** pentanedioic acid, and **(F)** isoniazid-pentanedioic acid physical mixture.

The PZA IR spectrum exhibited characteristic bands at 3,410, 3,288, and 3,149 cm^{-1}, respectively, corresponding to asymmetric and symmetric amides stretching ν(N-H) and ν(=C-H) stretching. The absorption band at 1,704 cm^{-1} is assigned to stretching carbonyl ν(C=O) (Chiş et al., 2005; Gunasekaran et al., 2009).

Displacement of the PZA asymmetric stretching ν(N-H) band to 3,398 cm^{-1} and subsidence of the symmetric ν(N-H) stretching band in the spectra of PGA (2:1) co-crystal samples confirmed the contribution of amide N-H in H-bonding with GA carbonyl. The shifting of both PZA and GA carbonyl stretching ν(C=O) to 1,699 and 1,662 cm^{-1} positions in PGA, respectively, further suggested C=O···N-H bonding. The displacement of GA ν(O-H) stretching vibration at 2,954/2,604 to 2,931/2,543 cm^{-1} in the spectrum of PGA (2:1) co-crystal suggested O-H···N-H H-bonding to PZA amide ν(N-H).

SEM analysis was carried out to evaluate changes in the morphology of the co-crystal samples vs. pure untreated components. SEM micrographs are shown in **Figure 6**.

INH exhibited dusty irregularly shaped particles with sharp edges. GA exhibited round shapes and also have smooth surfaces. The INHGA (2:1) (**Figure 6D**) co-crystal exhibited a mixture of fragmented hexagonal and irregularly shaped particles with sharp surfaces, different from both INH (**Figure 6B**) and GA, and dusty aggregates due to the grinding exercise. The physical mixture sample is composed of the short-range order of particles from INH and GA (**Figure 6F**).

The SEM images of untreated PZA, GA, and PGA (2:1) are presented in **Figures 6A,C,E**. Pure PZA powder is composed of large and differently shaped crystals whereas PGA (2:1) powder from dry grinding is made of small amassed aggregates of round shapes (see supporting information). Rod-like particles mixed with round irregularly shaped aggregates with smooth edges were observed for the PGA (2:1) co-crystal sample obtained from solvent assisted grinding.

The co-crystals were further confirmed by PXRD analyses. In the absence of single X-ray diffraction data for the structure elucidation, PXRD is a non-destructive tool to confirm the new phases of the powder samples (Corvis et al., 2010; Padrela et al., 2012). PXRD authenticated the successful co-crystallization as previously confirmed by FTIR and other thermal analyses used. The patterns for the individual drugs and the co-crystal products are depicted in **Figures 7**, **8**.

Differences in patterns is a clear confirmation of the successful co-crystal formation. The INH PXRD pattern exhibits peaks at $2\theta = 11.9$, 14.3, 15.6, 16.7, 19.6, 25.3, 26.9, and 27.3°. The main diffraction peaks in GA pattern appear at $2\theta = 13.8$, 19.7, 22.2, and 28.0°. The INHGA (2:1) PXRD pattern exhibited new diffraction peaks at $2\theta = 18.7$, 2, and 27.4° (**Figure 7**), thus confirming the new phase and the successful co-crystal formation.

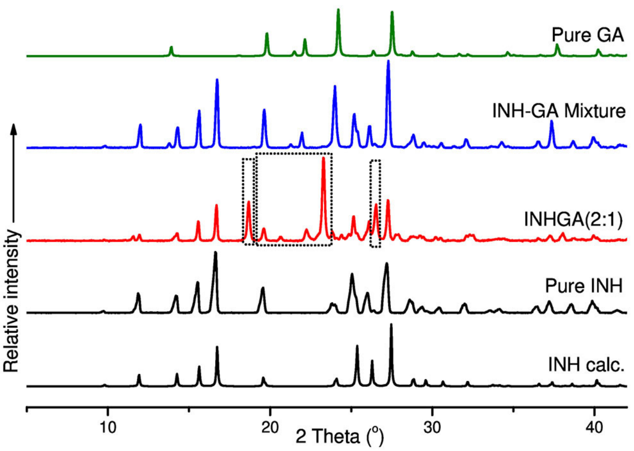

FIGURE 7 | PXRD patterns of pure and calculated isoniazid, pentanedioic acid, INHGA (2:1) co-crystal, and INH-GA physical mixture.

The PZA PXRD pattern showed peaks at $2\theta = 7.7$, 15.5, 17.6, 27.0, and 27.3° whereas the pattern generated by co-crystal sample PGA (2:1) exhibited new peaks at $2\theta = 10$, 16.5, 20.4, 25.2, and 29.8° (**Figure 8**) and was, therefore, confirmed as a new phase.

In vitro solubility measurements were obtained using HPLC. After the necessary dilutions, samples were analyzed using HPLC at optimum wavelength of 262 and 270 nm detection for INH and PZA, respectively. The calibration curves for the two individual drugs INH and PZA were reported with a regression-squared value of 0.9997 and 0.09999, respectively (**Supplementary Figure 3**).

An increase in solubility of 1.7 and 1.3 times, was measured at acidic pH values 1.2 (0.1 N HCl) and 5.8 (PBS) for INHGA (2:1) co-crystal. At pH 7.4, the solubility increase was less significant (1.03-times increase) whereas the aqueous solubility of the co-crystal had slightly decreased. This suggested the influence of pH on the solubility of the co-crystal and the pure INH.

PGA (2:1) on the other hand, has shown a solubility of 1.5, 1.8, and 1.3-times higher than those recorded for pure PZA, respectively, in the aqueous medium, potassium phosphate buffer at pH 5.8, and 7.4 (**Figure 9**). Despite an increase in solubility of PGA (2:1) co-crystal in aqueous solution, the co-crystal exhibited reduced solubility in acidic medium pH 1,2 (0.1 N HCl), suggesting increased stability of PZA by co-crystallization. The solubility of the co-crystals may be increased or decreased

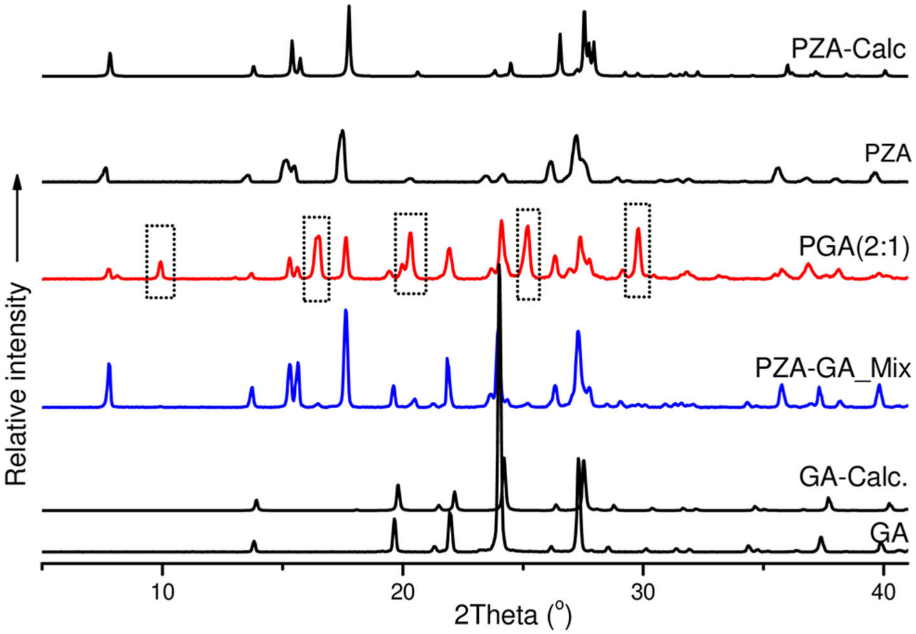

FIGURE 8 | PXRD patterns of pure and calculated pyrazinamide, pure and calculated pentanedioic acid, PZA-GA physical mixture and PGA (2:1) co-crystal.

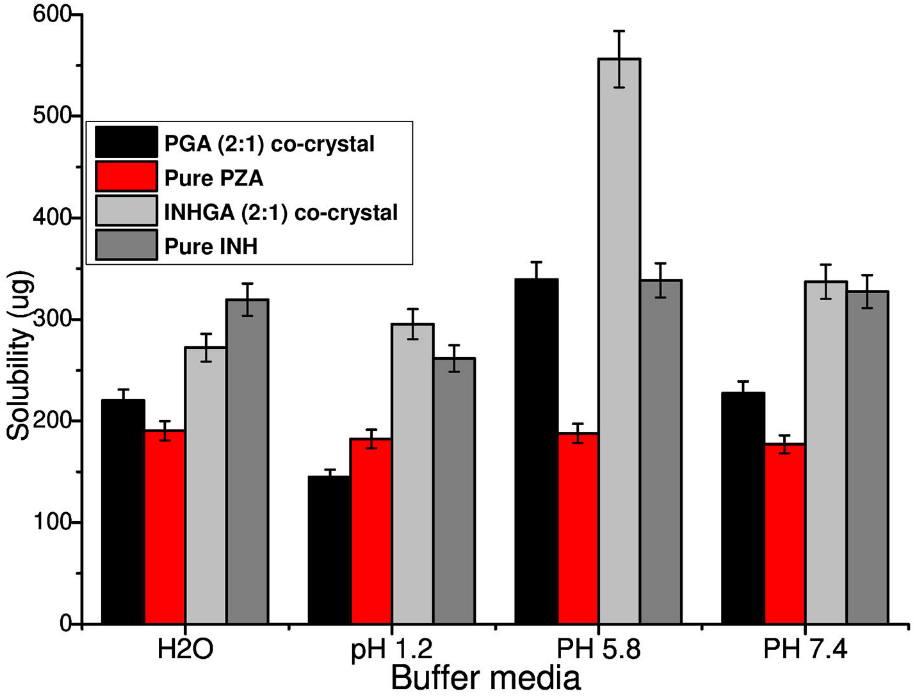

FIGURE 9 | Histogram comparing the solubility of untreated isoniazid (INH) and pyrazinamide (PZA) to their respective co-crystals INHGA (2:1) and PGA (2:1).

depending on the crystal density and strength of the hydrogen bond synthons. The higher the crystal packing, the more stable a co-crystal is and the less soluble it becomes (Rajesh Goud et al., 2014; Sugandha et al., 2014). Even though no pH-dependence was observed in pure PZA solubility measurements, its co-crystal with glutaric acid PGA suggested otherwise. The observed increase of solubility may further be attributed to reduced melting points of co-crystals in comparison to the pure APIs.

CONCLUSION

Co-crystals INHGA (2:1) and PGA (2:1) co-crystal were successfully prepared using co-grinding; a simple, safe, and cost-effective method. Characterization established different properties signifying both to be novel co-crystals. Solubility studies conducted suggested an enhanced solubility of both drugs as co-crystals, in different pH environments. The co-crystal formation is known to stabilize unstable drugs (Ranjit and Sarma, 2018), therefore reduced solubility of the co-crystal INHGA (2:1) in the aqueous medium is plausibly due to an increased stability. Notably, increased solubility and stability of the co-crystals vs. individual APIs infer what pharmaceutical formulators desire.

DATA AVAILABILITY STATEMENT

All datasets generated for this study are included in the article/**Supplementary Material**.

AUTHOR CONTRIBUTIONS

JN: methodology, validation, formal analysis, investigation and data curation, writing original draft, visualization, and writing—review and editing. MA: resources and data curation and writing—review and editing. PP: resources, data curation, and writing—review and editing. HS: conceptualization, resources, writing—review and editing, supervision, project administration, and funding acquisition. All authors contributed to the article and approved the submitted version.

FUNDING

The work reported in this publication was supported by the South African Medical Research Council under a Self-Initiated Research Grant. The views and opinions expressed are those of the author(s) and do not necessarily represent the official views of the SA MRC. This work was also based on the research supported in part by the National Research Foundation of South Africa for the Grant No. TTK1207031917.

SUPPLEMENTARY MATERIAL

The Supplementary Material for this article can be found online at: https://www.frontiersin.org/articles/10.3389/fchem.2020.595908/full#supplementary-material

REFERENCES

Abidi, S. S. A., Azim, Y., Gupta, A. K., and Pradeep, C. P. (2017). Mechanochemical synthesis and structural characterization of three novel cocrystals of dimethylglyoxime with N-heterocyclic aromatic compounds and acetamide. *J. Mol. Struct.* 1150, 103–111. doi: 10.1016/j.molstruc.2017.08.080

Aitipamula, S., Chow, P. S., and Tan, R. B. H. (2014). Polymorphism in cocrystals: a review and assessment of its significance. *CrystEngComm* 16, 3451–3465. doi: 10.1039/c3ce42008f

Aitipamula, S., Wong, A. B. H., Chow, P. S., and Tan, R. B. H. (2013). Novel solid forms of the anti-tuberculosis drug, isoniazid: ternary and polymorphic cocrystals. *CrystEngComm* 15, 5877–5887. doi: 10.1039/c3ce40729b

Ali, H. R. H., Alhalaweh, A., Mendes, N. F. C., Ribeiro-Claro, P., and Velaga, S. P. (2012). Solid-state vibrational spectroscopic investigation of cocrystals and salt of indomethacin. *CrystEngComm* 14, 6665–6674. doi: 10.1039/c2ce25801c

Aminov, R. I. (2010). A brief history of the antibiotic era: lessons learned and challenges for the future. *Front. Microbiol.* 1:134. doi: 10.3389/fmicb.2010.00134

Baddeley, A., Dean, A., Monica-Dias, H., Falzon, D., Floyd, K., Garcia, I., et al. (2013). *Global Tuberculosis Report 2013*. World Health Organization.

Battini, S., Mannava, M. K. C., and Nangia, A. (2018). Improved stability of tuberculosis drug fixed-dose combination using isoniazid-caffeic acid and vanillic acid cocrystal. *J. Pharm. Sci.* 107, 1667–1679. doi: 10.1016/j.xphs.2018.02.014

Bell, L. C. K., and Noursadeghi, M. (2018). Pathogenesis of HIV-1 and *Mycobacterium tuberculosis* co-infection. *Nat. Rev. Microbiol.* 16, 80–90. doi: 10.1038/nrmicro.2017.128

Brown, S. P. (2012). Applications of high-resolution 1H solid-state NMR. *Solid State Nucl. Magn. Reson.* 41, 1–27. doi: 10.1016/j.ssnmr.2011.11.006

Bruni, G., Maietta, M., Maggi, L., Mustarelli, P., Ferrara, C., Berbenni, V., et al. (2013). Preparation and physicochemical characterization of acyclovir cocrystals with improved dissolution properties. *J. Pharm. Sci.* 102, 4079–4086. doi: 10.1002/jps.23721

Cherukuvada, S., and Nangia, A. (2012). Fast dissolving eutectic compositions of two anti-tubercular drugs. *CrystEngComm* 14, 2579–2588. doi: 10.1039/c2ce06391c

Chiş, V., Pîrnău, A., Jurcă, T., Vasilescu, M., Simon, S., Cozar, O., et al. (2005). Experimental and DFT study of pyrazinamide. *Chem. Phys.* 316, 153–163. doi: 10.1016/j.chemphys.2005.05.004

Chun, N.-H., Wang, I.-C., Lee, M.-J., Jung, Y.-T., Lee, S., Kim, W.-S., et al. (2013). Characteristics of indomethacin-saccharin (IMC-SAC) co-crystals prepared by an anti-solvent crystallization process. *Eur. J. Pharm. Biopharm.* 85, 854–861. doi: 10.1016/j.ejpb.2013.02.007

Corvis, Y., Négrier, P., Lazerges, M., Massip, S., Léger, J. M., and Espeau, P. (2010). Lidocaine/ l -menthol binary system: cocrystallization versus solid-state immiscibility. *J. Phys. Chem. B* 114, 5420–5426. doi: 10.1021/jp101303j

Diniz, L. F., Souza, M. S., Carvalho, P. S., da Silva, C. C. P., D'Vries, R. F., and Ellena, J. (2018). Novel isoniazid cocrystals with aromatic carboxylic acids: crystal engineering, spectroscopy and thermochemical investigations. *J. Mol. Struct.* 1153, 58–68. doi: 10.1016/j.molstruc.2017.09.115

Duarte, R., Lönnroth, K., Carvalho, C., Lima, F., Carvalho, A. C. C., Muñoz-Torrico, M., et al. (2018). Tuberculosis, social determinants and co-morbidities (including HIV). *Pulmonology* 24, 115–119. doi: 10.1016/j.rppnen.2017.11.003

Duggirala, N. K., Perry, M. L., Almarsson, Ö., and Zaworotko, M. J. (2016). Pharmaceutical cocrystals: along the path to improved medicines. *Chem. Commun.* 52, 640–655. doi: 10.1039/C5CC08216A

Évora, A. O. L., Castro, R. A. E., Maria, T. M. R., Rosado, M. T. S., Silva, M. R., Beja, A. M., et al. (2011). Pyrazinamide-diflunisal: a new dual-drug co-crystal. *Cryst. Growth Des.* 11, 4780–4788. doi: 10.1021/cg200288b

Gadade, D. D., and Pekamwar, S. S. (2016). Pharmaceutical cocrystals: regulatory and strategic aspects, design and development. *Adv. Pharm. Bull.* 6, 479–494. doi: 10.15171/apb.2016.062

Grobelny, P., Mukherjee, A., and Desiraju, G. R. (2011). Drug-drug co-crystals: temperature-dependent proton mobility in the molecular complex of isoniazid with 4-aminosalicylic acid. *CrystEngComm* 13, 4358–4364. doi: 10.1039/c0ce00842g

Gunasekaran, S., Sailatha, E., Seshadri, S., and Kumaresan, S. (2009). FTIR, FT Raman spectra and molecular structural confirmation of isoniazid. *Indian J. Pure Appl. Phys*, 47, 12–18.

Howard, N. C., Marin, N. D., Ahmed, M., Rosa, B. A., Martin, J., Bambouskova, M., et al. (2018). *Mycobacterium tuberculosis* carrying a rifampicin drug resistance mutation reprograms macrophage metabolism through cell wall lipid changes. *Nat. Microbiol.* 3, 1099–1108. doi: 10.1038/s41564-018-0245-0

Hu, Y., Xu, L., He, Y. L., Pang, Y., Lu, N., Liu, J., et al. (2017). Prevalence and molecular characterization of second-line drugs resistance among multidrug-resistant *Mycobacterium tuberculosis* isolates in Southwest of China. *BioMed. Res. Int.* (2017) 2017:4563826. doi: 10.1155/2017/4563826

Kumar, S. (2017). Pharmaceutical cocrystals: an overview. *Indian J. Pharm. Sci.* 79, 858–871. doi: 10.4172/pharmaceutical-sciences.1000302

Letang, E., Ellis, J., Naidoo, K., Casas, E. C., Sánchez, P., Hassan-Moosa, R., et al. (2020). Tuberculosis-HIV co-infection: progress and challenges after two decades of global antiretroviral treatment roll-out. *Arch. Bronconeumol.* 56, 446–454. doi: 10.1016/j.arbr.2019.11.013

Lin, S.-Y. (2016). Mechanochemical approaches to pharmaceutical cocrystal formation and stability analysis. *Curr. Pharm. Des.* 22, 5001–5018. doi: 10.2174/1381612822666160726111253

Luo, Y. H., and Sun, B. W. (2013). Pharmaceutical co-crystals of pyrazinecarboxamide (PZA) with various carboxylic acids: crystallography, hirshfeld surfaces, and dissolution study. *Cryst. Growth Des.* 13, 2098–2106. doi: 10.1021/cg400167w

Masodkar, S. R., Pande, S. D., and Atram, S. C. (2018). Development and characterization of telmisartan tablet by the use of co-crystallization technique. *World J. Pharm. Pharmaceut. Sci.* 7, 651–669. doi: 10.20959/wjpps20185-11428

Mesfin, Y. M., Hailemariam, D., Biadglign, S., and Kibret, K. T. (2014). Association between HIV/AIDS and multi-drug resistance tuberculosis: a systematic review and meta-analysis. *PLoS ONE* 9:e82235. doi: 10.1371/journal.pone.0082235

Michael, O. S., Sogaolu, O. M., Fehintola, F. A., Ige, O. M., and Falade, C. O. (2016). Adverse events to first line anti-tuberculosis drugs in patients co-infected with hiv and tuberculosis. *Ann Ib Postgrad Med.* 14, 21–29.

Padrela, L., De Azevedo, E. G., and Velaga, S. P. (2012). Powder X-ray diffraction method for the quantification of cocrystals in the crystallization mixture. *Drug Dev. Ind. Pharm.* 38, 923–929. doi: 10.3109/03639045.2011.633263

Palleria, C., Di Paolo, A., Giofrè, C., Caglioti, C., Leuzzi, G., Siniscalchi, A., et al. (2013). Pharmacokinetic drug-drug interaction and their implication in clinical management. *J. Res. Med. Sci.* 18, 601–610.

Patel, J. R., Carlton, R. A., Needham, T. E., Chichester, C. O., and Vogt, F. G. (2012). Preparation, structural analysis, and properties of tenoxicam cocrystals. *Int. J. Pharm.* 436, 685–706. doi: 10.1016/j.ijpharm.2012.07.034

Pawlowski, A., Jansson, M., Sköld, M., Rottenberg, M. E., and Källenius, G. (2012). Tuberculosis and HIV co-infection. *PLoS Pathog.* 8:e1002464. doi: 10.1371/journal.ppat.1002464

Pinheiro, M., Silva, A. S., Pisco, S., and Reis, S. (2014). Interactions of isoniazid with membrane models: implications for drug mechanism of action. *Chem. Phys. Lipids* 183, 184–190. doi: 10.1016/j.chemphyslip.2014.07.002

Rajesh Goud, N., Khan, R. A., and Nangia, A. (2014). Modulating the solubility of sulfacetamide by means of cocrystals. *CrystEngComm* 16, 5859–5869. doi: 10.1039/C4CE00103F

Ranjit, T., and Sarma, B. (2018). Drug-drug and drug-nutraceutical cocrystal/salt as alternative medicine for combination therapy: a crystal engineering approach. *Crystals* 8:101. doi: 10.3390/cryst8020101

Raviglione, M., and Sulis, G. (2016). Tuberculosis 2015: burden, challenges and strategy for control and elimination. *Infect. Dis. Rep.* 8:6570. doi: 10.4081/idr.2016.6570

Ravikumar, N., Gaddamanugu, G., and Anand Solomon, K. (2013). Structural, spectroscopic (FT-IR, FT-Raman) and theoretical studies of the 1:1 cocrystal of isoniazid with p-coumaric acid. *J. Mol. Struct.* 1033, 272–279. doi: 10.1016/j.molstruc.2012.10.029

Sarceviča, I., Kons, A., and Orola, L. (2016). Isoniazid cocrystallisation with dicarboxylic acids: vapochemical, mechanochemical and thermal methods. *CrystEngComm* 18, 1625–1635. doi: 10.1039/C5CE01774B

Schaberg, T., Rebhan, K., and Lode, H. (1996). Risk factors for side-effects of isoniazid, rifampin and pyrazinamide in patients hospitalized for pulmonary tuberculosis. *Eur. Respir. J.* 9, 2026–2030. doi: 10.1183/09031936.96.09102026

Scripture, C. D., and Figg, W. D. (2006). Drug interactions in cancer therapy. *Nat. Rev. Cancer* 6, 546–558. doi: 10.1038/nrc1887

Sekhon, B. S. (2009). Pharmaceutical co-crystals - a review. *Ars Pharmaceut.* 50, 99–117. Available online at: http://hdl.handle.net/10481/27459

Shan, N., and Zaworotko, M. J. (2008). The role of cocrystals in pharmaceutical science. *Drug Discov. Today* 13, 440–446. doi: 10.1016/j.drudis.2008.03.004

Somoskovi, A., Parsons, L. M., and Salfinger, M. (2001). The molecular basis of resistance to isoniazid, rifampin, and pyrazinamide in *Mycobacterium tuberculosis*. *Respir. Res.* 2, 164–168. doi: 10.1186/rr54

Sugandha, K., Kaity, S., Mukherjee, S., Isaac, J., and Ghosh, A. (2014). Solubility enhancement of ezetimibe by a cocrystal engineering technique. *Cryst. Growth Des.* 14, 4475–4486. doi: 10.1021/cg500560w

Unissa, A. N., Subbian, S., Hanna, L. E., and Selvakumar, N. (2016). Overview on mechanisms of isoniazid action and resistance in *Mycobacterium tuberculosis*. *Infect. Genet. Evol.* 45, 474–492. doi: 10.1016/j.meegid.2016.09.004

Conflict of Interest: The authors declare that the research was conducted in the absence of any commercial or financial relationships that could be construed as a potential conflict of interest.

frontiers in Chemistry

ORIGINAL RESEARCH
published: 04 December 2020
doi: 10.3389/fchem.2020.612418

Electrically Enhanced Transition Metal Dichalcogenides as Charge Transport Layers in Metallophthalocyanine-Based Solar Cells

Lebogang Manamela [1], Juvet N. Fru [2], Pannan I. Kyesmen [2], Mmantsae Diale [2] and Nolwazi Nombona [1]*

[1] Department of Chemistry, University of Pretoria, Pretoria, South Africa, [2] Department of Physics, University of Pretoria, Pretoria, South Africa

Transitional metal dichalcogenides (TMDs), such as molybdenum disulfide (MoS_2) have found application in photovoltaic cells as a charge transporting layer due to their high carrier mobility, chemical stability, and flexibility. In this research, a photovoltaic device was fabricated consisting of copper phthalocyanine (CuPc) as the active layer, exfoliated and Au-doped MoS_2, which are n-type and p-type as electron and hole transport layers, respectively. XRD studies showed prominent peaks at (002) and other weak reflections at (100), (103), (006), and (105) planes corresponding to those of bulky MoS_2. The only maintained reflection at (002) was weakened for the exfoliated MoS_2 compared to the bulk, which confirmed that the material was highly exfoliated. Additional peaks at (111) and (200) planes were observed for the Au doped MoS_2. The interlayer spacing (d_{002}) was calculated to be 0.62 nm for the trigonal prismatic MoS_2 with the space group *P6m2*. Raman spectroscopy showed that the $E^{1}_{2}g$ (393 cm^{-1}) and A_{1g} (409 cm^{-1}) peaks for exfoliated MoS_2 are closer to each other compared to their bulk counterparts (378 and 408 cm^{-1}, respectively) hence confirming exfoliation. Raman spectroscopy also confirmed doping of MoS_2 by Au as the Au-S peak was observed at 320 cm^{-1}. Exfoliation was further confirmed by SEM as when moving from bulky to exfoliated MoS_2, a single nanosheet was observed. Doping was further proven by EDS, which detected Au in the sample suggesting the yield of a p-type Au-MoS_2. The fabricated device had the architecture: Glass/FTO/Au-MoS_2/CuPc/MoS_2/Au. A quadratic relationship between *I-V* was observed suggesting little rectification from the device. Illuminated *I-V* characterization verified that the device was sensitive and absorbed visible light. Upon illumination, the device was able to absorb photons to create electron-hole pairs and it was evident that semipermeable junctions were formed between Au-MoS_2/CuPc and CuPc/MoS_2 as holes and electrons were extracted and separated at respective junctions generating current from light. This study indicates that the exfoliated and Au-MoS_2 could be employed as an electron transporting layer (ETL) and hole transporting layer (HTL), respectively in fabricating photovoltaic devices.

Keywords: phthalocyanines, charge transporting layer, exfoliation, N-type, TMDS

OPEN ACCESS

Edited by:
Tebello Nyokong,
Rhodes University, South Africa

Reviewed by:
Isaac Akinbulu,
University of Lagos, Nigeria
Ahmet Turgut Bilgicli,
Sakarya University, Turkey

***Correspondence:**
Nolwazi Nombona
nolwazi.nombona@up.ac.za

Specialty section:
This article was submitted to Inorganic Chemistry, a section of the journal Frontiers in Chemistry

Received: *02 October 2020*
Accepted: *13 November 2020*
Published: *04 December 2020*

Citation:
Manamela L, Fru JN, Kyesmen PI, Diale M and Nombona N (2020) Electrically Enhanced Transition Metal Dichalcogenides as Charge Transport Layers in Metallophthalocyanine-Based Solar Cells. Front. Chem. 8:612418. doi: 10.3389/fchem.2020.612418

INTRODUCTION

Climate change and global warming occur mainly due to the release of CO_2 and other greenhouse gases into the atmosphere (Hewage et al., 2019). These greenhouse gases trap heat on the earth's surface and atmosphere increasing the average temperature of the globe. The release of these harmful gases is mainly due to the burning of fossil fuels for energy generation. This suggests the need for the implementation of better technologies to mitigate this issue of climate change (Perera, 2018).

Solar cells are devices that have been developed to capture photons from the sun to produce electricity (Wang et al., 2014; Yu and Sivula, 2017). The major advantage of using solar cells is that they are small devices that can be used anywhere unlike current electrical technologies. Adding on to their advantages, the cost of the solar cell can be reduced by making use of cheap materials and they only require the abundant and free solar energy as a source (Shah and Wallace, 2004; Guo et al., 2008). A typical solar cell consists of an active layer, an electron transporting layer (ETL) (most often an n-type semiconductor), and a hole transporting layer (HTL) (most often a p-type semiconductor) sandwiched between two electrodes (Markvart and Castaner, 2018). The active layer absorbs photons from the sunlight and generate an electron-hole pair. The electron transporting layer acts as a semipermeable membrane which only extracts and separates the electrons from the holes (Markvart and Castaner, 2018). The electron is then taken to the cathode and through an external circuit generating electricity, and finally gets to the anode where it recombines with the hole. The hole would, at the same time, have been extracted by the hole transporting layer, separated from the electron, and ultimately taken to the anode for recombination with the electron that has completed the circuit (Ragoussia and Torres, 2015; Marinova et al., 2016). An efficient solar cell is designed such that the time the charges take to reach their respective membranes (p and n-type semiconductors) is smaller than the lifetime of the electron-hole pair (Shieh et al., 2010; Zhu et al., 2018). However, the abovementioned mechanism does not occur as smoothly. Some solar cells experience frequent electron-hole recombination as their semiconducting materials have low carrier charge mobility. Some solar cells have materials that have low thermal and chemical stability resulting in a reduced lifetime of the solar cell (Dharmadasa et al., 2019).

Solar cells that are currently being extensively studied are nanocrystal based, polymer, perovskite and dye-sensitized solar cells (Luceño-Sánchez et al., 2019). The advantages of these solar cells are their low cost of production, flexibility, lightness, and their ever-improving efficiencies (Yan and Saunders, 2014). Generally, these solar cells have low cost of fabrication as compared with widely used solar cells (silicon-based). However, their efficiencies are relatively low. Perovskite solar cells have efficiencies comparable to silicon solar cells (Ke and Kanatzidis, 2019). They are however disadvantageous as they suffer from chemical and thermal stability (Dharmadasa et al., 2019). This study will utilize the metallophthalocyanines (MPc), CuPc, as a photoactive layer. This is due to its intense light absorption in the visible to near-infrared and they have high chemical and thermal stability compared to the widely used perovskite and polymer photon absorbers. Transition metal dichalcogenides (TMDs) will be employed in this study as charge carrier agents.

TMDs are semiconducting materials with the molecular formula MX_2, were M is a transition metal (Mo, W, Sn, etc.) and X a chalcogen (S, Se, Te) (Brent et al., 2017). For each TMD, the layer of M atoms is sandwiched between two layers of X atoms and these atoms are held together by covalent bonds. TMDs naturally occur as bulk materials which simply means that many layers of MX_2 are held together by weak van der Waals forces. In this bulk form, these materials have a bandgap of $\sim$1.2 eV (Choi et al., 2017). When bulky, TMDs can be converted to mono- or few-layers by separating the nanosheets, consequently changing the bandgap to $\sim$1.8 eV (Yun et al., 2012). TMDs have interesting properties, such as high surface area, catalytic active sites and the bandgap can be manipulated (Li and Zhu, 2015). TMDs have high charge carrier mobility (Ke and Kanatzidis, 2019; Zhou and Zhao, 2019), which means that they are able, under an electric field, to move electrons and holes quickly through their surface (Li and Zhu, 2015). This implies that the electrons and the holes will not recombine quickly after electron-hole pair generation resulting in an improved performance of the solar cell. In addition, 2D MoS_2 materials are advantageous over their bulk, 0D and 1D counterparts because of their excellent electronic, charge storage and catalytic properties including quantum confinement, high absorption coefficient, high surface-to-volume ratio and tunable bandgap (Nawz et al., 2020). These properties have led to TMDs being used in a variety of applications, such as solar cells, lubricants, transistors, and hydrogen evolution catalysis (Mandyam et al., 2020). MoS_2 is intrinsically n-type and is mostly used as an ETL. However, it can undergo p-type doping with gold (Au) to fit its purpose as the HTL.

The CuPc molecule contains 18-π electrons and the delocalization of these electrons renders it useful for various applications, such as solar cell and other opto-electronic devices. CuPc is chemically and thermally stable (Li et al., 2017). This material is characterized by an intense light absorption in the visible to near infrared making it a good candidate as a photoactive layer in solar cell devices. CuPc, to the best of our knowledge, has not been formerly investigated in photovoltaics as the sole photoactive layer. This material has been applied as an active layer together with a polymer or an organic molecule to form an active layer blend. Kim et al. (2016) fabricated several MPc-based solar cells. The photoactive layers of these solar cells were a blend of MPc and 3,4,9,10-perylenetetracarboxylic bisbenzimidazole (PTCBI) (MPc:PTCBI). The PdPc based solar cell showed the highest efficiency as it reached a PCE of 1.3%. An explanation provided for this result was that PdPc had the longest excitonic diffusion as compared to the other MPc's (ZnPc and CuPc). The results for PdPc-based solar cells showed drastic enhancement of performance when PTCBI was substituted by C_{60} fullerenes. The PCE nearly doubled, as it was reported to be 2.2%. Ali et al. (2020) report the fabrication of an organic solar sell with the active layer being CuPc/C_{60}. Derouiche et al. (2010) fabricated a solar cell with the active layer consisting of CuPc:PCBM. For the first time, the use of CuPc individually as the active layer will be reported. This type of solar cell will be cost-effective in comparison to traditional polymer based solar cells that are more complex in their fabrication.

TMD nanosheets have been used in several electronic applications, such as solar cells and field effect transistors. Li et al. (2015) fabricated an ultrathin p-n junction using p-type and n-type MoS_2. The p-type MoS_2 was obtained from doping MoS_2 with gold. The fabricated p-n junction device showed solar to electricity conversion for MoS_2 with thicknesses that are <8 nm. The film thickness that gave the most efficiency was found to be 3 nm. It was further concluded that ultrathin films were desired since they were flexible, light and transparent, an advantage over the most widely used silicon semiconductor. Ye et al. (2015) fabricated a p-n bilayer photodetector using doped and undoped MoS_2 (n- and p-type, respectively). They learned that the device has the potential to separate photogenerated charges and observed an improvement in response and sensitivity to the visible light. As such, the device exhibited a desired performance under illumination. Gu et al. (2013) used ultrathin MoS_2 nanosheets as hole transporting layers in an organic solar cell. The fabricated organic solar cell showed an improved power conversion efficiency (PCE) when compared to the device that used traditional MoO_3 as the hole transporting layer. Singh et al. (2019) fabricated a perovskite solar cell and used MoS_2 as the ETL. The solar cell demonstrated a PCE of 13.1% which is comparable to PCE's obtained when "state-of-the-art" compact TiO_2 and SnO_2 are used as ETL. This shows that p- and n-type MoS_2 nanosheets improve charge transport, response and sensitivity of the device to visible light, implying that these materials can add value in photovoltaic devices. The p- and the n-type MoS_2 have been used in the same p-n junction device and they have also been used as either the ETL or HTL in a single solar cell device, as earlier stated. However, to the best of our knowledge, these materials have never been used together in one solar cell as the HTL and the ETL, respectively. Also, MoS_2 and CuPc have been used together previous in several applications including FET and sensing. However, to the best of our knowledge, there is no solar cell that consist of both CuPc and MoS_2.

In this study, for the first time, CuPc and MoS_2 were used in a solar cell. n- and p-type MoS_2 were used together in a solar cell as an ETL and HTL, respectively and CuPc was used as a photoactive layer. A cost effective device with the architecture Glass/FTO/Au-MoS_2/CuPc/MoS_2/Au was fabricated. Au-MoS_2 was deposited onto the FTO/Glass by spin coating followed by annealing. The next step was the physical vapor deposition which was used to deposit CuPc. This was followed by the deposition of MoS_2 by spin coating and lastly, the gold contact by physical vapor deposition. **Figure 1** illustrates how the device is structured. Under illumination, the device produced photogenerated electron-hole pairs and it was evident that semipermeable junctions were formed between Au-MoS_2/CuPc and CuPc/MoS_2 as holes and electrons were extracted and separated at respective junctions generating current from light. This study showed that both exfoliated and doped MoS_2 could be employed as ETL and HTL, respectively, when fabricating photovoltaic devices.

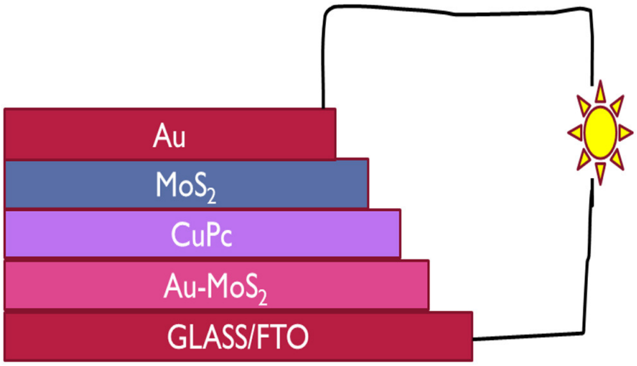

FIGURE 1 | The architecture of the device fabricated in this study with CuPc as the active layer, MoS_2 and Au-MoS_2 the ETL and HTL, respectively sandwitched between the two electrodes, FTO and Au contact.

METHODS AND MATERIALS

Synthesis of MoS_2 nanosheets was carried out in an ultrasonic bath from Labotech (using model 704). Spin coating was carried out using a Laurell technology spin coater model WS-650MZ-23NPPB. Samples were centrifuged using a thermo scientific Labofuge 700 centrifuge.

Acetone, dimethylformamide (DMF), isopropyl alcohol and N-methyl-2-pyrrolidone (NMP) were all purchased from Radchem (Pty) LTD. Copper phthalocyanine (CuPc), fluorine-doped tin oxide (FTO), gold (III) chloride ($AuCl_3$), nickel phthalocyanine (NiPc) were purchased from Sigma-Aldrich. Molybdenum disulphide (MoS_2) was purchased from Protea laboratory solution (Pty) LTD.

Synthesis of MoS_2 Nanosheets

MoS_2 nanosheets were synthesized following a previously reported procedure (Wang et al., 2014). The liquid-based exfoliation method was followed to obtain a large quantity of MoS_2. Briefly, 0.5 g of MoS_2 powder was added into 10 mL N-methyl-2-pyrrolidone (NMP) which was the exfoliating agent. The concentration of the resulting mixture was 5 $mg{\cdot}mL^{-1}$. The mixture was then sonicated for 6 h at 5°C. The mixture was left to settle for 72 h. The upper three-quarters of the mixture was decanted into a centrifuge tube and centrifuged at 3,000 rpm for 30 min and the supernatant was collected and deposited as a thin film on a glass substrate for characterization.

Doping of MoS_2 With Gold

Doping of the MoS_2 by gold was done following a procedure previously reported (Ubani et al., 2016). In summary, 20 mM of aqueous gold solution was prepared by dissolving 0.3 g of $AuCl_3$ in distilled water. Ten microliters of the gold solution was spin-coated on TMD coated glass substrate, at 2,500 rpm for 1 min. The resulting sample was annealed at 100°C for 10 min to obtain the Au doped TMDs.

Solar Cell Fabrication

FTO-coated glass substrates were cleaned thoroughly by sonication in 2-propanol, then in acetone, and lastly in distilled water for 10 min in each solvent. Subsequently, a MoS_2 dispersed in an organic solvent was spin-coated on FTO at 1,500 rpm. Thereafter, aqueous $AuCl_3$ (20 mM) was spin-coated on top of the MoS_2 layer. The FTO substrate was annealed at 100°C for 10 min. The sample was placed in a physical vapor deposition bell jar where a layer of a CuPc was deposited. The thickness of the MPc film was maintained at 200 nm. Another TMD layer was deposited by spin coating on top of the MPc film. The resulting sample was annealed at 210°C for 60 min. A gold contact of thickness 100 nm was deposited on the substrate using physical vapor deposition.

Characterization

X-ray diffraction (XRD) analysis was conducted using a Bruker D2 PHASER-e diffractometer using Cu-Kα radiation (0.15418 nm) to identify the phase orientation and crystallographic structure of the material prepared. Raman spectroscopy measurements were recorded on a WiTec alpha300 RAS+ Confocal Raman microscope with 532 nm excitation laser at 5 mW. Scanning electron microscopy (SEM) was carried out on a crossbeam 540 FEG SEM microscope from Zeiss. The crossbeam 540 FEG was coupled with energy dispersive X-ray spectroscopy which was used for the determination of elemental composition of the samples. UV-vis absorption measurements were taken on a CARY 100 BIO UV-Vis spectrophotometer. Current-voltage (I–V) measurements were conducted on a B2900 solar management unit (SMU). Illuminated I–V measurement were performed using a Model 91150V solar simulator with solar output conditions of 1,000 W/m^2 at 25°C and AM 1.0 G reference spectral filtering, which is the air mass coefficient used universally for measuring performance of a solar cell.

RESULTS AND DISCUSSION

Characterization of MoS_2 Nanosheets

Bulk MoS_2 underwent XRD characterization before exfoliation and the results were recorded. After exfoliation, the materials were spin-coated onto a microscope glass substrate, annealed and taken for XRD characterization. **Figure 2A** shows the XRD pattern of the bulk MoS_2 which was indexed according to JCPDS card number 06-0097 (Štengl et al., 2014). This XRD spectrum confirms the crystal structure of MoS_2. The XRD pattern shows a diffracted peak at $2\theta = 14.4°$ (002) and other low intensity peaks at $2\theta = 29°$ (004), $2\theta = 33°$ (001), $2\theta = 34°$ (101), $2\theta = 39.56°$ (103), and $2\theta = 49.8°$ (105). The peaks (002), (100), (103), and (105) are layer dependent and they can be used as an important tool to detect exfoliation. Complete disappearance of the reflections (100), (103), and (105) illustrates that exfoliation has taken place. A reduction in intensity of the (002) is also important (Ravula et al., 2015) as it indicates exfoliation.

After exfoliation, the sample was characterized and the resulting XRD pattern is shown in **Figure 2B**. This XRD diffractogram did not have all the peaks exhibited by the diffractogram of the bulky material. Only one peak was maintained. This peak is at $2\theta = 14.3°$ and is indexed as the (002) peak. A direct evidence of exfoliation is the disappearance of the (100), (103), and (105) which was the case in this study. This maintained peak has a lower intensity when compared to the (002) peak for the bulky material and this was also reported elsewhere (Ma et al., 2018). The (002) peak provides useful information for determining if the MoS_2 is bulky or if it is mono- or few-layered. Maintaining the peak with other disappearing shows that exfoliation has taken place (Park et al., 2017). A decrease in intensity of the peak suggests that exfoliation has indeed taken place and single layers are dominating the sample (Sun et al., 2014). The two XRD spectra have the (002) peak with the exfoliated MoS_2 spectrum having a lower intensity. The difference observed between the spectra is the presence of additional peaks in the bulk MoS_2 spectrum while the exfoliated material has only the (002) peak. As such, the difference between the two XRD spectra is due to the difference in the number of layers in the two materials.

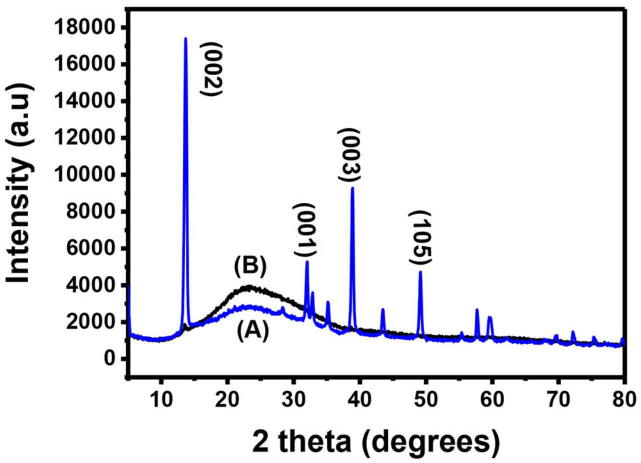

FIGURE 2 | XRD spectra for **(A)** bulky and **(B)** exfoliated MoS_2.

The interlayer $d_{(002)}$ spacing is calculated according to the (002) peak ($2\theta = 14.3°$).

$$\lambda = 2d\sin\theta$$
$$d = \lambda/(2\sin\theta)$$
$$d = \frac{0.154}{2\sin 7.15}$$
$$d = 0.62\ nm$$

The interlayer $d_{(002)}$ for the exfoliated MoS_2 was calculated to be 0.62 nm. MoS_2 single layer has its elements bonded in this manner: S-Mo-S. Each single-layer of MoS_2 consists of two hexagonal planes of S atoms and an intercalated hexagonal plane of Mo atoms bound with the S atoms in a trigonal prismatic arrangement (D_{3h}-MoS_6). The symmetry space group of bulk MoS_2 is $P3m1$, which is the point group D_{6h}. The space group of the single layer is $P6m2$ which is the point group D_{3h}. As a result, systems with even number of layers belong to the space group $P3m1$, and systems with odd number of layers to the

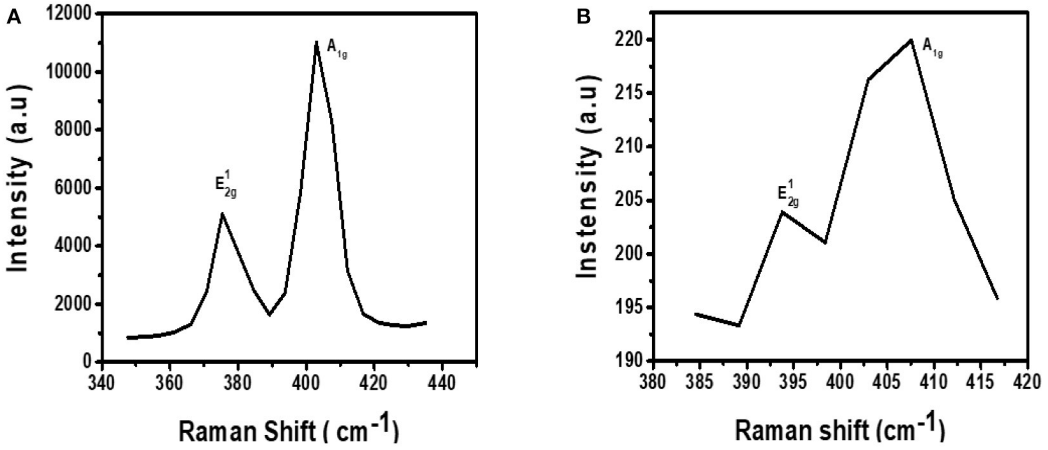

FIGURE 3 | Raman spectra for **(A)** bulky MoS_2 and **(B)** exfoliated MoS_2.

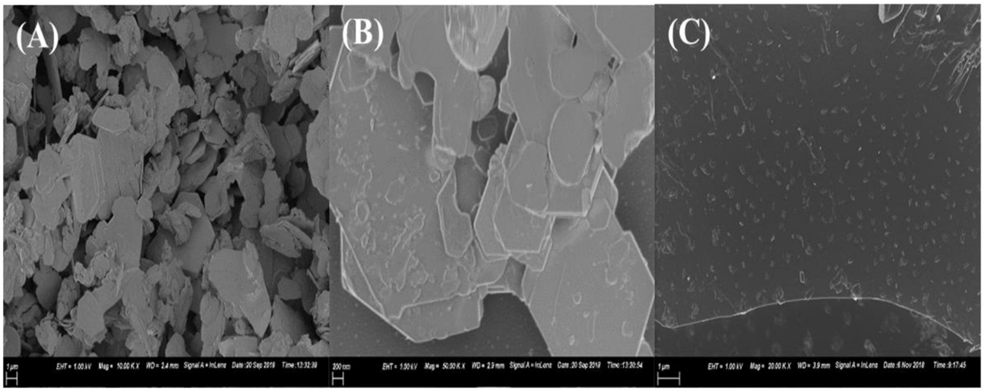

FIGURE 4 | SEM micrograph of **(A)** bulky MoS_2, **(B)** MoS_2 exfoliated for 3 h, **(C)** MoS_2 exfoliated for 6 h.

*P*6*m*2 space group (Molina-Sanchez and Wirt, 2011; Štengl et al., 2014). The peaks shown by **Figure 2** closely agrees with the reports for hexagonal 2H-MoS_2 D_{3h} with space group *P*6*m*2 (Sun et al., 2014).

The Raman fingerprint for MoS_2 is evidenced by vibrations at ∼380 and ∼410 cm^{-1}. These vibrations are known as the E^1_{2g} and A_{1g} peak, respectively. The E^1_{2g} peak gives information about the in-plane opposite vibrations of sulfur and molybdenum atoms while the A_{1g} gives information about the out-of-phase vibrations of the sulfur atoms. Raman spectroscopy can further be used to confirm if exfoliation has indeed taken place (Kaushik et al., 2018). This confirmation can be done by comparing the Raman spectra of the exfoliated and the bulk MoS_2 material. When moving from bulk to few layers of MoS_2 sheets, the distance between the two Raman peaks, E^1_{2g} and A_{1g}, reduces indicating exfoliation has taken place.

Figure 3A shows the Raman spectrum for MoS_2 before it was subjected to exfoliation. As expected from the Raman fingerprint of MoS_2, the bulky material exhibited the E^1_{2g} and A_{1g} peaks at 378 and 408 cm^{-1}, respectively. The distance between the two peaks was found to be 30 cm^{-1}.

Figure 3B shows the Raman spectrum for exfoliated MoS_2. The spectrum contains two peaks and they are found at Raman shifts 393 and 409 cm^{-1}. The distance between the two peaks was calculated to be 16 cm^{-1}. This was a reduction from 30 cm^{-1} for bulky material. As such, it can be concluded that exfoliation has indeed taken place. Also, the Raman spectrum for the exfoliated material is characterized by low intensity relative to the spectrum for bulk material. This observation is similar to a previous study done by Munkhbayar et al. (2018), where they investigated the effects of exfoliation of MoS_2 on Raman peak intensity. They observed that the intensity increases with the number of exfoliated layers suggesting a reduced intensity upon exfoliation.

MoS_2 was taken for morphology characterization using scanning electron microscopy (SEM). The aim was to confirm if indeed going from bulky to exfoliated TMDs, the formation of few-layered nanosheets can be observed. **Figure 4A** shows the SEM micrograph for bulky MoS_2. The morphology observed is

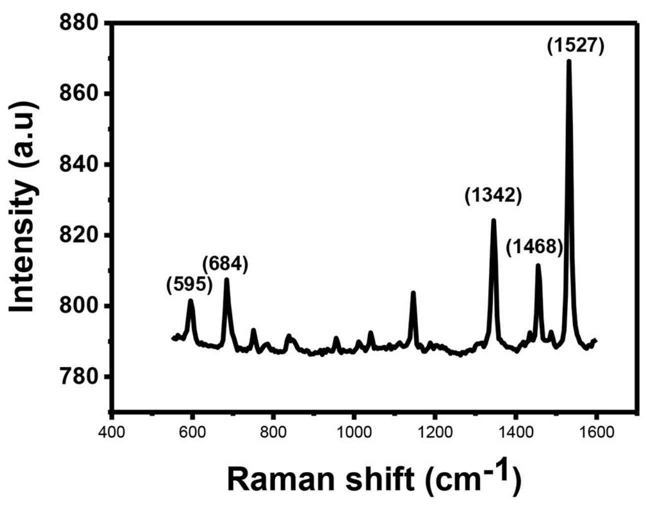

FIGURE 5 | Raman spectrum for CuPc.

that of nanoflakes. Isolating each nanoflake, it can be observed that they are made up of several layers stacked together. These layers are held together by weak van der Waals forces which are easily overcome by exfoliation. Thereafter, the bulky MoS_2 underwent exfoliation in NMP for 3 h and the sample was taken for SEM characterization. **Figure 4B** shows the SEM micrograph for the resulting material at a higher magnification. The morphology observed was nanosheets. However, the nanosheets were still stacked together into a few layers of different size and the layers were fewer as compared to the micrograph of the bulky material. This suggest that exfoliation has occurred. However, more time was needed for the nanosheets to be separated. The material was exfoliated further for a total of 6 h. **Figure 4C** shows the micrograph for the resulting material. The micrograph shows a monolayer nanosheet morphology indicating that exfoliation has taken place completely and single-layered materials were dominating the sample.

Characterization of CuPc

Figure 5 shows Raman spectra for the CuPc. The spectrum show that CuPc has a peak observed at 595 cm^{-1} known as the A_{1g} peak. This peak is related to the deformation of the benzene rings. The second peak observed is found at ~684 cm^{-1}. This peak is called the B_{1g} and it is associated with benzene breathing. There are other several peaks with lower intensities found between 800 and 1,200 cm^{-1} which provide information about C-N stretching, isoindole in-plane bending, C-H bending and out of plane C-H bending (Kumar et al., 2017).

The peaks found between 1,300 and 1,600 cm^{-1} are useful for the determination of the central metal ion. Within this range, there is a coupling of two Raman spectra. The two coupled Raman spectra are $B_{1g} + E_g$ and $A_{1g} + B_{2g}$. The peaks observed in this range are located at the Raman shifts of ~1,342, ~1,468 and anywhere between 1,500 and 1,600 cm^{-1} depending on the central metal atom. The peak that is located at ~1,342 cm^{-1} provides information about pyrrole stretching. This peak is called the B_{2g} peak and it gives information about stretching of bonds, such as Cα-Nβ, Nα-Cα-Cβ, and C–C–H. The peak observed at Raman shift of ~1,468 cm^{-1} provides information about the isoindole ring stretching while the peak observed at Raman shifts between 1,500 and 1,600 cm^{-1} results due to clustering of B_{1g} and A_{1g} together into one vibration. Accurate assignment of these vibrations is important as both the vibrations are sensitive to the size of the metal ion at the center of the phthalocyanine. The peak gives information about the vibrations observed on the Cα-Nβ-Cα bridge bond. B_{1g} peak also gives information about vibrations that occur as a result of benzene stretching. The $B_{1g} + A_{1g}$ peak for CuPc is observed at 1,527 cm^{-1}.

The metallophthalocyanine was deposited by physical vapor deposition on a glass substrate and the thin film was taken for UV-Vis characterization. **Figure 6** illustrates the UV-Vis spectrum of CuPc thin film. The UV-Vis spectra of CuPc exhibits three prominent absorption peaks. These absorption peaks are at wavelengths ~350, ~620, and ~700 nm. The absorption peak that occurs at the wavelength ~350 nm is associated with the Soret band of the phthalocyanine ring. This Soret band is associated with π *to* π^* electronic transitions (b_{2u} to e_g) (Zou et al., 2018). While, on the other hand, the absorption peaks observed at ~620 and ~700 nm are associated with the Q band of the dimer and the monomer of the CuPc molecule. The Q band occurs as a result of electronic excitation of the π electrons from the HOMO to the LUMO of the Pc ring (a_1 to e_g) (Zou et al., 2018). From the UV-Vis spectrum of CuPc, the Q band fall within the range of visible light (Xu et al., 2010; Güzel et al., 2015). This suggests that this material can absorb visible light from the sun making them viable candidates for being used as photoactive layers in solar cells.

Characterization of the CuPc/TMD Junction

To confirm that the layers in the junction are not disturbed and new bonds were not formed, Raman spectroscopy was conducted on the samples. For MoS_2, the range of the Raman spectrum to be considered is 380–420 cm^{-1} while for CuPc the range to be considered is between 1,300 and 1,600 cm^{-1}. As such, the spectrum was broken down into these ranges to visualize both the materials' vibrations individually. **Figure 7A**, which is the first part of the spectrum to be isolated, was the MoS_2 range. From this range, the characteristic, E^1_{2g} and A_{1g}, peaks, were observed. This shows that the material has S and Mo atoms and it further imparts on the fact that these elements are bonded together in a manner that MoS_2 atoms bond, meaning that the nanosheets were not disturbed upon coating over the CuPc film and no new bonds have been formed by either the Mo or the S atoms and the old bonds of MoS_2 have not been broken as well. **Figure 7B** shows the spectrum range of CuPc. The peaks of CuPc at this range were maintained. This shows that the CuPc material after being coated with MoS_2 remained intact and the atoms of CuPc have not formed new bonds and the old bonds of the materials have not been broken.

Characterization of Doped MoS_2

After doping MoS_2 by Au, the thin film sample underwent XRD characterization. The results of these characterizations are shown in **Figure 8**. It is expected that the peaks of both Au and MoS_2 nanosheets be observed on the XRD spectrum. **Figure 8A** shows the XRD spectra of Au-MoS_2 with a few peaks which overlap with those of the substrate shown in **Figure 8B**. The weak intensity peak observed at 15.1° is indexed (002), this is a 0.8 shift from 14.3 when compared to undoped MoS_2. This shift indicates changes in the stoichiometric composition by doping or/and a difference in the ionic radii between the main element and the dopant (Connolly, 2012). This peak occurs as a result of exfoliation of MoS_2 into 2D nanosheets and now appears sharp. It has been found that heat treatment causes MoS_2 to become more crystalline (Zubavichus et al., 1999; Sonto-Puente et al., 2007). The peak observed at 32.5 is indexed (100). It is not clear why this peak is observed but it has been reported previously by Qiao et al. (2017). This peak might be the (100) peak of MoS_2 as it was also reported to be maintained after exfoliation (Niemeyer, 2015). The peaks for Au where indexed using the JCPDS. File no. 89-3697. The peaks observed at 37.8 and 44.5, indexed (111) and (200), respectively, matched with Au peaks observed from the JCPDS file no. 89-3697 (Shi et al., 2013). XRD confirmed that MoS_2 nanosheets were successfully doped with Au.

Raman spectroscopy is a powerful tool for determining if doping has successfully taken place. It can provide information about which type of doping has taken place (n or p-type doping). Generally, n-type doping of MoS_2 results in softening of the A_{1g} peak resulting in a relative decrease in intensity (Shi et al., 2013). This type of doping is also evidenced by a reduction in the distance between E^1_{2g} and A_{1g} (Shi et al., 2013). On the other hand, p-type doping generally increases the distance between the two peaks as they will move apart (Shi et al., 2013). This p-type doping also results in a Raman spectrum with an increased intensity of the A_{1g} peak (Shi et al., 2013;

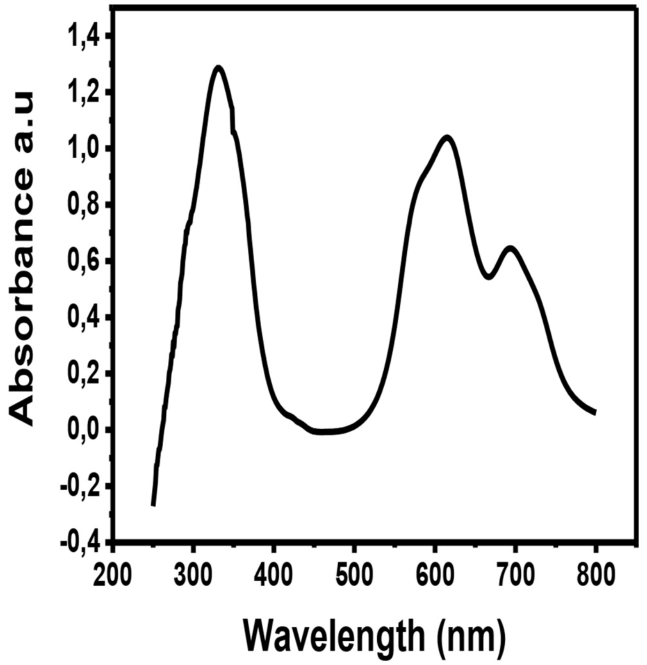

FIGURE 6 | UV-Vis spectrum of CuPc.

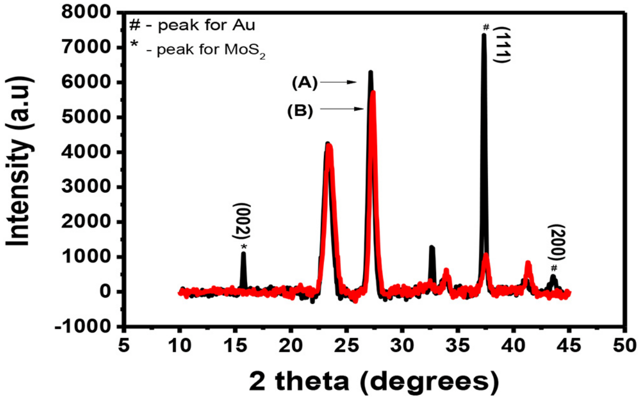

FIGURE 8 | XRD spectra for **(A)** (black) Au-MoS_2 deposited on a glass substrate and **(B)** (red) the substrate.

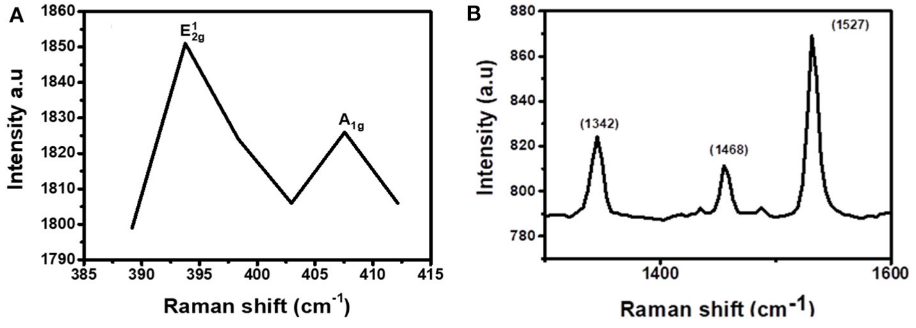

FIGURE 7 | Raman spectrum for CuPc/MoS_2 bilayer separated into two regions, **(A)** 385–415 cm^{-1} (exfoliated MoS_2 region) and **(B)** 1,250–1,650 cm^{-1} (CuPc region).

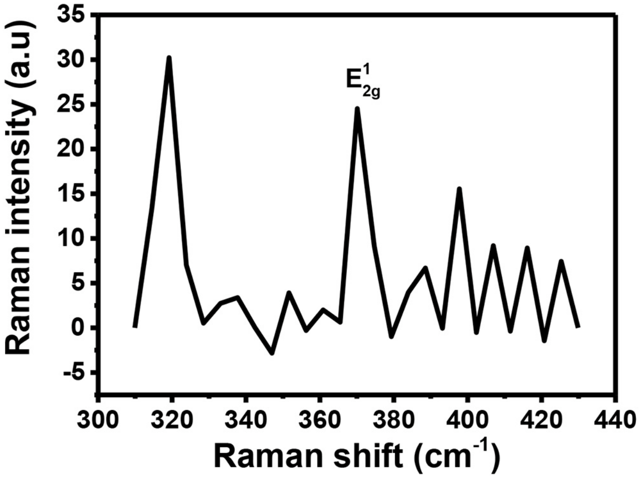

FIGURE 9 | The Raman spectrum for Au-MoS_2.

Singha et al., 2015). There are other cases where doping has been successfully executed on MoS_2 but for such cases, when comparing the Raman spectra for the doped and the pristine MoS_2, no significant change is observed (Laskar et al., 2014; Chuang et al., 2015). However, in our study, most of the expected results mentioned above were not observed upon applying p-type doping on MoS_2 using Au. **Figure 9** shows the Raman spectrum recorded for Au-MoS_2. From this spectrum, it is observed that only the E^1_{2g} peak is present. The E^1_{2g} peak observed is found to be blue-shifted to 374 cm^{-1} with respect to the peak of the pristine MoS_2. It has been reported previously that Au-S modes are observed between 250 and 325 cm^{-1} (Birte et al., 2014). From the **Figure 9**, there is a peak that is observed at 320 cm^{-1}. The reason this peak was detected might be because of the Au-S bond in this molecule. Noisy peaks are observed at 380 cm^{-1} $\leq$ which may suggest that some level of crystallinity might have been lost during the doping process. The peaks were observed at relatively low intensities.

After MoS_2 underwent Au doping, the sample was taken for EDS to see the elements present in the sample. **Figure 10** shows the EDS spectrum for Au-MoS_2. The presence of Au and elements of MoS_2 was enough to confirm that doping has occurred. This technique confirmed that all the elements making up Au-MoS_2 are present. These elements are detected at different eV regions of the spectrum. The Au peak occurs at 2.12 eV, the Mo peaks at 2.29 and 8.40 eV, and lastly, S peak at 2.31 eV. Other elements are detected but do not form part of the sample. These are normal surface contaminants and elements of the glass substrate used.

Characterization of Solar Cell Devices

Dark and Illuminated Current and Voltage (I-V) Measurements of Fabricated Solar Cell Devices

Figure 11 shows the *I-V* characterization results for the device with the architecture Glass/FTO/Au-MoS_2/CuPc/MoS_2/Au. **Figure 11A** shows the *I-V* curve of the device under (1) dark and (2) illuminated conditions. **Figure 11B** shows a semi-log of *I-V* curve of the device under (1) dark and (2) illuminated conditions.

Considering **Figure 11A**, curve 1 shows that under dark conditions, when voltage is 1 V, the recorded current is 0.01 A. The shape this curve exhibits is quadratic implying that a quadratic relationship between *I-V* is observed and this type of dependence has been reported before (Fru et al., 2020). This indicates that the device is not purely ohmic and there is a slight rectification exhibited by the device. The fact that this device is slightly rectifying is confirmed by the first curve (1) on **Figure 11B** which is a semi-log curve of *I-V* of the device under dark conditions. The curve is asymmetric as it shows that the forward biased and the reverse biased current are not the same. The forward biased current is slightly higher than the reverse-biased current. This shows that there is rectification in the device. However, the difference between the current values for forward biased and reverse biased is small suggesting that the device could only perform at a little rectification.

A plot of *I-V* under these illuminated conditions is given in curve 2 of **Figure 11A**. This curve shows that a voltage of 1 V, the current is ∼0.015 A. This implies that more current is generated under illuminated *I-V* measurements than in dark *I-V* measurements. This is also viewed for the semi-log plot of *I-V* of the device under illuminated conditions (**Figure 11B**, curve 2). A conclusion drawn from this is that the device is sensitive and can absorb visible light to generate, separate, and extract free charges. The active layer of this device, CuPc, has been shown by UV-Vis studies that it has a high sensitivity to the visible region of the electromagnetic spectrum. As such, this material is a good photon absorber and suitable for use as the photoactive layer in solar cells. Charge separation occurs at the junction between the CuPc active layer and the charge transport layers. At the MoS_2/CuPc junction, electrons are allowed to move across the junction while holes are blocked. At the Au-MoS_2/CuPc junction, holes move across while electrons are blocked. The separated photogenerated charges flow through the external and constitute a photogenerated current.

Despite being able to generate the electron-hole pair upon photon absorption, followed by separation of the electrons and holes at the heterojunctions, and ultimately the traveling of the electrons across the external circuit, the fabricated device showed that the relationship between *I-V* is quadratic. From the quadratic curve of *I-V*, it is not possible to measure solar cell parameters, such as fill factor and PCE. However, comparing a device exhibiting an ohmic and quadratic relationship of *I-V*, the device showing the quadratic relationship is most promising to become a solar cell. The semi-log plot for *I-V* indicates that the device shows little rectification of current. This is an important property in demonstrating that the fabricated device shows great promise in being further developed for solar cell application.

From this study, it can be seen that MoS_2 and CuPc are compatible materials that can work together in photovoltaic systems. The deposition technique for each of the two materials also allowed them to be put against each other without interfering with the chemistry of each, proving their compatibility.

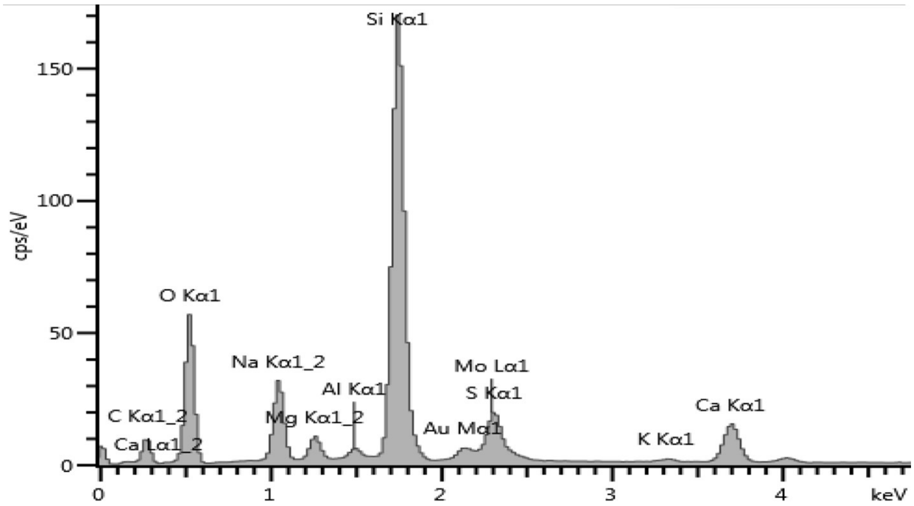

FIGURE 10 | EDS spectrum of Au-MoS_2 on a glass substrate.

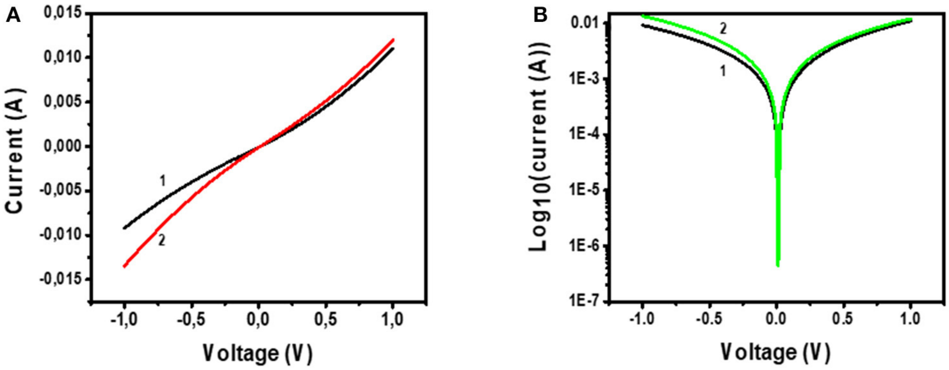

FIGURE 11 | (A) I-V measurements of Glass/FTO/Au-MoS_2/CuPc/MoS_2/Au device under (1) dark conditions and (2) illuminated conditions. **(B)** Voltage against $\log_{10}$(Current) for Glass/FTO/Au-MoS_2/CuPc/MoS_2/Au device measured in (1) dark and (2) illuminated conditions.

Illuminated *I*-V measurements verified that the fabricated device was responsive and sensitive to visible light. CuPc was able to generate the electron-hole pair and each was transported across their respected junctions to their charge carriers. The MoS_2 and Au-MoS_2 were able to extract electrons and holes, respectively from the CuPc upon generation. The Au-MoS_2 was stable and compatible with the CuPc as a clear junction was observed between the two materials. The compatibility of these materials show that they can be used together in photovoltaic devices.

CONCLUSIONS

Mono to few-layered TMDs (MoS_2) was successfully synthesized using a liquid-assisted exfoliation method from their bulky counterparts. To achieve this step, sonication time as well as the solvent to be used for exfoliation were carefully put into consideration. Successful synthesis of MoS_2 was confirmed by several characterization techniques including XRD, Raman spectroscopy and SEM. The interlayer spacing for the trigonal prismatic (D_{3h} point group) MoS_2 was found to be 0.62 nm and has a space group of *P*6*m*2. The MoS_2 nanosheets underwent p-type doping using gold *via* a wet chemical approach. The process was successfully conducted and the resulting materials was Au-MoS_2. Successful doping of these MoS_2 nanosheets was confirmed using XRD, Raman spectroscopy and EDS. A photovoltaic device with the architecture Glass/FTO/Au-MoS_2/CuPc/MoS_2/Au was successfully fabricated for the first time in this study. The device fabricated utilized Au-MoS_2 and pristine MoS_2 as hole transporting layer (HTL) and electron transporting layer (ETL), respectively. For photoactive layer, this device used CuPc. The use of only CuPc as the active layer and n- and p-type MoS_2 as the (ETL) and (HTL), respectively, resulted in the fabrication of a simple and cost-effective device. The resulting device was tested for solar cell properties and performance using dark and illuminated *I-V* characterization. The device fabricated in this study underwent dark *I-V* measurements and it showed a small amount of rectification. A conclusion drawn from this is that the device was rectifying, but not enough to perform solar cell measurements, as the dark *I-V* curve showed rectification but it was too little to allow the calculation of several solar cell parameters, such as PCE and fill factor. However, the device was not completely passive as the relationship between current and voltage was not ohmic (linear) but quadratic instead. This shows that the 2D MoS_2, Au-MoS_2, and CuPc are promising materials for solar cell application. From illuminated *I-V* characterization, the device had its measurements (curves) not aligned with the curves for measurements taken under dark conditions. The maximum current values recorded for the devices under illuminated conditions were higher than the current values recorded under dark conditions. As such, the fabricated device was found to be sensitive to solar radiation and hence the photoactive material (CuPc) used in the device is an adequate photon absorber and can generate electron-hole pairs sunlight. The photogenerated charge carriers were successfully separated at the junctions by the respective charge-transporting layers suggesting that the MoS_2 (ETL) and Au-MoS_2 (HTL) are suitable for such an application as they resulted in the device's rectification of current and could be employed in making other photovoltaic devices.

DATA AVAILABILITY STATEMENT

The original contributions presented in the study are included in the article/supplementary materials, further inquiries can be directed to the corresponding author/s.

AUTHOR CONTRIBUTIONS

LM conducted the lab work as part of his research thesis. JF and PK assisted LM with some of the experiments and in the preparation of the manuscript. MD was the co-supervisor of LM. NN was the supervisor of LM. All authors contributed to the article and approved the submitted version.

FUNDING

This work was funded by the National Research Foundation (NRF), South Africa (Grant #TTK170504229661).

ACKNOWLEDGMENTS

The author would like to acknowledge the University of Pretoria, Chemistry and Physics department for their generous support. The author would also like to acknowledge colleagues from the NN research group for their support.

REFERENCES

Ali, A. M., Said, D. A., Khayyat, M., Boustimi, M., and Seoudi, R. (2020). Improving the efficiency of the organic solar cell (CuPc/C60) via PEDOT: PSS as a photoconductor layer doped by silver nanoparticles. *Results Phys*. 16:102819. doi: 10.1016/j.rinp.2019.102819

Birte, V., Patric, O., Sandra, L., Chanaka, K., Amala, D., and Thomas, B. (2014). Structural information on the Au-S interface of thiolate-protected goldclusters: a Raman spectroscopy study. *J. Phys. Chem*. 18, 9604–9611. doi: 10.1021/jp502453q

Brent, J. R., Savjani, N., and O'Brien, P. (2017). Synthetic approaches to two-dimensional transition metal dichalcogenide nanosheets. *Prog. Mater. Sci*. 89, 411–478. doi: 10.1016/j.pmatsci.2017.06.002

Choi, W., Choudhary, N., Han, G. H., Park, J., Akinwande, D., and Lee, Y. H. (2017). Recent development of two-dimensional transition metal dichalcogenides and their applications. *Biochem. Pharmacol*. 20, 116–130. doi: 10.1016/j.mattod.2016.10.002

Chuang, M., Yang, S., and Chen, F. (2015). Metal nanoparticle-decorated two-dimensional molybdenum sulfide for plasmonic-enhanced polymer photovoltaic devices. *Materials* 8, 5414–5425. doi: 10.3390/ma8085252

Connolly, J. R. (2012). *Diffraction Basics, Part 2, Introduction to X-Ray Powder Diffraction*. Available online at: http://www.xray.cz/xray/csca/kol2011/kurs/dalsi-cteni/Connolly-2005/06-Diffraction-II.pdf

Derouiche, H., Miled, H. B., and Mohamed, A. B. (2010). Enhanced performance of a CuPc: PCBM based solar cell using bathocuproine BCP or nanostructured TiO_2 as hole-blocking layer. *Phys. Status Solidi A* 207, 479–483. doi: 10.1002/pssa.200925424

Dharmadasa, M., Rahaq, Y., and Alam, A. E. (2019). Perovskite solar cells : short lifetime and hysteresis behaviour of current–voltage characteristics. *J. Mater. Sci. Mater. Electron*. 30, 12851–12859. doi: 10.1007/s10854-019-01759-2

Fru, J. N., Nombona, N., and Diale, M. (2020). Synthesis and characterisation of methylammonium lead tri-bromide perovskites thin films by sequential physical vapor deposition. *Phys. B Phys. Condens. Matter*. 578, 411884. doi: 10.1016/j.physb.2019.411884

Gu, X., Cui, W., Li, H., Wu, Z., Zeng, Z., Lee, S., et al. (2013). A solution-processed hole extraction layer made from ultrathin MoS_2 nanosheets for efficient organic solar cells. *Adv. Energy Mater*. 3, 1262–1268. doi: 10.1002/aenm201300549

Guo, Q., Jun Kim, S., Kar, M., Shafarman, W. N., Birkmire, R. W., Stach, E. A., et al. (2008). Development of $CuInSe_2$ nanocrystal and nanoring inks for low-cost solar cells. *Nano Lett*. 8, 2982–2987. doi: 10.1021/nl802042g

Güzel, E., Koca, A., Gül, A., and Koçak, M. B. (2015). Microwave-assisted synthesis, electrochemistry and spectroelectrochemistry of amphiphilic phthalocyanines. *Synth. Metals* 199, 372–380. doi: 10.1016/j.synthmet.2014.11.032

Hewage, L., Willhelm, U., and Mesthrige, W. J. (2019). Global research on carbon emissions: a scientometric review. *Sustainability* 2, 1–25. doi: 10.3390/su11143972

Kaushik, V., Wu, S., Jang, H., Kang, J., and Kim, K. (2018). Scalable exfoliation of bulk MoS_2 to single- and few-layers using toroidal taylor vortices. *Nanomaterials* 8, 587–598. doi: 10.3390/nano8080587

Ke, W., and Kanatzidis, M. G. (2019). Prospects for low-toxicity lead-free perovskite solar cells. *Nat. Commun*. 10, 1–4. doi: 10.1038/s41467-019-08918-3

Kim, I., Haverinen, H. M., Wang, Z., Madakuni, S., Kim, Y., Li, J., et al. (2016). Efficient organic solar cells based on planar metallophthalocyanines. *Chem. Mater*. 85, 4256–4260. doi: 10.1021/cm901320p

Kumar, S., Kaur, N., Sharma, K., and Mahajan, A. (2017). Improved Cl_2 sensing characteristics of reduced graphene oxide when decorated with copper phthalocyanine nano flowers. *RSC Adv*. 7, 25229–25236. doi: 10.1039/C7RA02212C

Laskar, M. R., Nath, D. N., Ma, L., Lee, E. W., Lee, C. H., Kent, T., et al. (2014). p-type doping of MoS_2 thin films using Nb. *Appl. Phys. Lett*. 104:092104. doi: 10.1063/1.4867197

Li, H., Lee, D., Qu, D., Liu, X., Ryu, J., Seabaugh, A., et al. (2015). Ultimate thin vertical p–n junction composed of two-dimensional layered molybdenum disulfide. *Nat. Commun.* 6:6564. doi: 10.1038/ncomms7564

Li, X., and Zhu, H. (2015). Two-dimensional MoS_2: properties, preparation, and applications. *J. Mater*. 1, 33–44. doi: 10.1016/j.jmat.2015.03.003

Li, Y., Wang, B., Yu, Z., Zhou, X., Kang, D., Wu, Y., et al. (2017). The effects of central metals on ammonia sensing of metallophthalocyanines covalently bonded to graphene oxide hybrids. *RCS Adv.* 7, 34215–34225. doi: 10.1039/C7RA06081E

Luceño-Sánchez, J. A., Díez-Pascual, A. M., and Capilla, R. P. (2019). Materials for photovoltaics: state of art and recent development. *Int. J. Mol. Sci.* 20, 967–1018. doi: 10.3390/ijms20040976

Ma, H., Shen, Z., and Ben, S. (2018). Understanding the exfoliation and dispersion of MoS_2 nanosheets in pure water. *J. Colloid Interface Sci.* 517, 204–212. doi: 10.1016/j.jcis.2017.11.013

Mandyam, S. V., Kim, H. K., and Drndic, M. (2020). Large area few-layer TMD film growths and their applications. *J. Phys. Mater.* 3:024008. doi: 10.1088/2515-7639/ab82b3

Marinova, N., Valero, S., and Delgado, J. L. (2016). Organic and perovskite solar cells: working principles, materials and interfaces. *J. Colloid Interface Sci.* 488, 373–389. doi: 10.1016/j.jcis.2016.11.021

Markvart, T., and Castaner, L. (2018). *Principles of Solar Cell Operation. McEvoy's Handbook of Photovoltaics: Fundamentals and Applications*. Limassol: Academic Press.

Molina-Sanchez, A., and Wirt, L. (2011). Phonons in single and few-layer MoS_2 and WS_2. *Phys. Rev. B.* 84:155413. doi: 10.1103/PhysRevB.84.155413

Munkhbayar, G., Palleschi, S., Perrozzi, F., Nardone, M., Davaasambuu, J., and Ottaviano, L (2018). A study of exfoliated molybdenum disulfide (MoS_2) based on raman and photoluminescence spectroscopy. *Solid State Phenom.* 271, 40–46. doi: 10.4028/www.scientific.net/SSP.271.40

Nawz, T., Safdar, A., Hussai, M., Lee, D. S., and Siyar, M. (2020). Graphene to advanced MoS_2: a review of structure, synthesis, and optoelectronic device application. *Crystals* 10:902. doi: 10.3390/cryst10100902

Niemeyer, W. D. (2015). SEM/EDS analysis for problem solving in the food industry. *Proc. SPIE* 9636:96360G. doi: 10.1117/12.2196962

Park, M., Nguyen, T. P., Choi, K. S., and Park, J. (2017). MoS_2-nanosheet/graphene-oxide composite hole injection layer in organic light-emitting diodes. *Electron. Mater. Lett.* 13, 344–350. doi: 10.1007/s13391-017-1612-3

Perera, F. (2018). Pollution from fossil-fuel combustion is the leading environmental threat to global pediatric health and equity: Solutions exist. *Int. J. Environ. Res. Public Health.* 16, 1–17. doi: 10.3390/ijerph15010016

Qiao, X., Zhang, Z., and Tian, F. (2017). Enhanced catalytic reduction of p-nitrophenol on ultrathin MoS_2 nanosheets decorated noble-metal nanoparticles. *Cryst. Growth Des.* 17, 3538–3547. doi: 10.1021/acs.cgd.7b00474

Ragoussia, M., and Torres, T. (2015). New generation solar cells: concepts, trends and perspectives. *Chem. Commun.* 51, 3957–3972. doi: 10.1039/C4CC09888A

Ravula, S., Essner, J. B., and Baker, G. A. (2015). Kitchen-inspired nanochemistry: dispersion, exfoliation, and hybridization of functional MoS_2 nanosheets using culinary hydrocolloids. *Chem. Nano. Mater.* 1, 167–177. doi: 10.1002/cnma.201500022

Shah, V. G., and Wallace, D. B. (2004). "Low-cost solar cell fabrication by drop-on-demand ink-jet printing," in *IMAPS 37th Annual International Symposium on Microelectronics*. Plano, TX.

Shi, Y., Huang, J., Jin, L., Hsu, Y., Yu, S. F., Li, L., et al. (2013). Selective decoration of Au nanoparticles on monolayer MoS_2 single crystals. *Sci. Rep.* 3:1839. doi: 10.1038/srep01839

Shieh, J., Liu, C., Meng, H., Tseng, S., and Chao, Y. (2010). The effect of carrier mobility in organic solar cells. *J. Appl. Phys.* 107, 1–9. doi: 10.1063/1.3327210

Singh, R., Giri, A., Pal, M., Thiyagarajan, K., Kwak, J., Lee, J., et al. (2019). Perovskite solar cells with an MoS_2 electron transport layer. *J. Mater. Chem.* 7, 7151–7158. doi: 10.1039/C8TA12254G

Singha, S. S., Nandi, D., and Singha, A. (2015). Tuning the photoluminescence and ultrasensitive trace detection properties of few-layer MoS_2 by decoration with gold nanoparticles. *RSC Adv.* 5, 24188–24193. doi: 10.1039/C5RA01439E

Sonto-Puente, M., Flores-Aquino, E., Avalos-Borja, M., Fuentes, S., and Cruz-Reyes, J. (2007). Synthesis, characterization and cyclohexene hydrogenation activity of high surface area molybdenum disulfide catalysts. *Catal. Lett.* 113, 170–175. doi: 10.1007/s10562-007-9030-z

Štengl, V., Henych, J., Slušná, M., and Ecorchard, P. (2014). Ultrasound exfoliation of inorganic analogues of graphene. *Nanoscale Res. Lett.* 9, 167–181. doi: 10.1186/1556-276X-9-167

Sun, X., Dai, J., Guo, Y., Wu, C., Hu, F., Zhao, J., et al. (2014). Semimetallic molybdenum disulfide ultrathin nanosheets as an efficient electrocatalyst for hydrogen evolution. *Nanoscale* 6, 8359–8367. doi: 10.1039/C4NR01894J

Ubani, C. A., Ibrahim, M. A., Teridi, M. A. M., Sopian, K., Ali, J., and Chaudhary, K. T. (2016). Application of graphene in dye and quantum dots sensitized solar cell. *Sol. Energy* 137, 531–550. doi: 10.1016/j.solener.2016.08.055

Wang, H., Feng, H., and Li, J. (2014). Graphene and graphene-like layered transition metal dichalcogenides in energy conversion and storage. *Small* 10, 2165–2181. doi: 10.1002/smll.201303711

Xu, Z., Zhang, G., Cao, Z., Zhao, J., and Li, H. (2010). Effect of N atoms in the backbone of metal phthalocyanine derivatives on their catalytic activity to lithium battery. *J. Mol. Catal. A Chem.* 318, 101–105. doi: 10.1016/j.molcata.2009.11.014

Yan, J., and Saunders, B. R. (2014). Comparison of polymer: fullerene, hybrid polymer. *RSC Adv.* 4, 43286–43314. doi: 10.1039/C4RA07064J

Ye, J., Li, X., Zhao, J., and Mei, X. (2015). A facile way to fabricate high-performance solution-processed n-MoS_2/p-MoS_2 bilayer photodetectors. *Nanoscale Res. Lett.* 10:454. doi: 10.1186/s11671-015-1161-3

Yu, X., and Sivula, K. (2017). Layered 2D semiconducting transition metal dichalcogenides for solar energy conversions. *Curr. Opin. Electrochem.* 2, 97–103. doi: 10.1016/j.coelec.2017.03.007

Yun, W. S., Han, S. W., Hong, S. C., Kim, I. G., and Lee, J. D. (2012). Thickness and strain effects on electronic structures of transition metal dichalcogenides: $2HMX_2$ semiconductors ($M = Mo, W; X = S, Se, Te$). *Phys. Rev.* 85, 1–5. doi: 10.1103/PhysRevB.85.033305

Zhou, Y., and Zhao, Y. (2019). Chemical stability and instability of inorganic halide perovskites. *Energy Environ. Sci.* 12, 1495–1511. doi: 10.1039/C8EE03559H

Zhu, Y., Liu, J., Zhao, J., Li, Y., Qiao, B., Song, C., et al. (2018). Improving the charge carrier transport and suppressing recombination of soluble. *Materials* 11, 759–769. doi: 10.3390/ma11050759

Zou, T., Wang, X., Ju, H., Zhao, L., Guo, T., Wu, W., et al. (2018). Controllable molecular packing motif and overlap type in organic nanomaterials for advanced optical properties. *Crystals* 8, 1–12. doi: 10.3390/cryst8010022

Zubavichus, Y. V., Golub, A. S., Lenenko, N. D., Slovokhotov, Yu. L., Novikov, Yu. N., and Danot, M. (1999). Thermal transformations of nanocomposite material consisting of molybdenum disulfide and nickel hydroxide layers. *Mater. Res. Bull.* 34, 1601–1613. doi: 10.1016/S0025-5408(99)00184-1

Conflict of Interest: The authors declare that the research was conducted in the absence of any commercial or financial relationships that could be construed as a potential conflict of interest.

frontiers in Chemistry

REVIEW
published: 23 December 2020
doi: 10.3389/fchem.2020.617448

A Review of the Antimalarial, Antitrypanosomal, and Antileishmanial Activities of Natural Compounds Isolated From Nigerian Flora

Marzuq A. Ungogo[1,2], **Godwin U. Ebiloma**[3], **Nahandoo Ichoron**[4], **John O. Igoli**[4], **Harry P. de Koning**[2] and **Emmanuel O. Balogun**[5,6]*

[1] Department of Veterinary Pharmacology and Toxicology, Ahmadu Bello University, Zaria, Nigeria, [2] College of Medical, Veterinary and Life Sciences, Institute of Infection, Immunity and Inflammation, University of Glasgow, Glasgow, United Kingdom, [3] School of Health and Life Sciences, Teesside University, Middlesbrough, United Kingdom, [4] Phytochemistry Research Group, Department of Chemistry, University of Agriculture, Makurdi, Nigeria, [5] Department of Biochemistry, Ahmadu Bello University, Zaria, Nigeria, [6] Africa Centre of Excellence for Neglected Tropical Diseases and Forensic Biotechnology (ACENTDFB), Ahmadu Bello University, Zaria, Nigeria

OPEN ACCESS

Edited by:
Simone Brogi,
University of Pisa, Italy

Reviewed by:
Andre Gustavo Tempone,
Adolfo Lutz Institute, Brazil
Oluyomi Adeyemi,
Landmark University, Nigeria
Carmenza Spadafora,
Instituto de Investigaciones Científicas y Servicios de Alta Tecnología, Panama
Stig Milan Thamsborg,
University of Copenhagen, Denmark

***Correspondence:**
Emmanuel O. Balogun
eobalogun@abu.edu.ng

Specialty section:
This article was submitted to Medicinal and Pharmaceutical Chemistry,
a section of the journal Frontiers in Chemistry

Received: 14 October 2020
Accepted: 03 December 2020
Published: 23 December 2020

Citation:
Ungogo MA, Ebiloma GU, Ichoron N, Igoli JO, de Koning HP and Balogun EO (2020) A Review of the Antimalarial, Antitrypanosomal, and Antileishmanial Activities of Natural Compounds Isolated From Nigerian Flora. Front. Chem. 8:617448.
doi: 10.3389/fchem.2020.617448

The West African country Nigeria features highly diverse vegetation and climatic conditions that range from rain forest bordering the Atlantic Ocean in the South to the Desert (Sahara) at the Northern extreme. Based on data from the World Conservation Monitoring Center of the United Nations Environmental Protection, Nigeria, with ∼5,000 documented vascular plants, ranks amongst the top 50 countries in terms of biodiversity. Such a rich biodiversity implies that the country is rich in diverse secondary metabolites—natural products/unique chemicals produced by the plant kingdom to confer selective advantages to them. Like many tropical countries, Nigeria is also endemic to numerous infectious diseases particularly those caused by parasitic pathogens. These phytochemicals have been exploited for the treatment of diseases and as a result, a new branch of chemistry, natural product chemistry, has evolved, to try to reproduce and improve the therapeutic qualities of particular phytochemicals. In this review, we have compiled a compendium of natural products, isolated from Nigerian flora, that have been reported to be effective against certain protozoan parasites with the aim that it will stimulate interests for further investigations, and give impetus to the development of the natural products into registered drugs. In total 93 structurally characterized natural compounds have been identified with various levels of anti-parasite activity mainly from Nigerian plants. The synthesis protocol and molecular target for some of these natural anti-parasite agents have been established. For instance, the anti-plasmodial compound fagaronine (**7**), a benzophenanthridine alkaloid from Fagara zanthoxyloides has been successfully synthesized in the laboratory, and the anti-trypanosomal compound azaanthraquinone (**55**) elicits its effect by inhibiting mitochondrial electron transfer in trypanosomes. This review also discusses the barriers to developing approved drugs from phytochemicals, and the steps that should be taken in order to accelerate the development of new antiparasitics from the highlighted compounds.

Keywords: anti-parasitics, neglected tropical disease (NTD), phytomedicine, Nigeria, drug development

INTRODUCTION

Natural products are broadly defined as chemical entities with pharmacological properties, produced by naturally occurring living organisms such as plants, fungi, bacteria, protists, sponges, including other invertebrates that are present in diverse environments. The prospects of using natural product-based remedies for treating and managing infections can be understood from the perspective of traditional medicines. Historically, natural products have played a key role in fighting infectious diseases across the globe. Archives for such evidence were found in cuneiform engraved on clay tablets from Mesopotamia, which date back to around 2600 BC (Cragg and Newman, 2005).

People living in resource-poor communities in Nigeria and elsewhere continue to depend largely on natural product-derived medicines (particularly those of plant origin) to combat many pathological conditions, notwithstanding the dearth of pharmacological elucidation of their mechanisms of action and of standard clinical trials. This is often due to personal beliefs, economic reasons, or difficulty in accessing pharmaceutical products. In contrast to combinatorial chemistry, natural products provide enormous structural diversity, creating the opportunity to discover novel lead compounds. It is estimated that about 75,000 species of flowering plants are known to exist on earth, out of which only about 10% have been investigated for possible therapeutic value against any condition. Out of this 10%, only 1–5% have been scientifically researched for any bioactivity (Amit Koparde et al., 2019). Thus, countless important natural lead compounds, with a vast range of structures and pharmacological properties, await discovery in the Earth's biodiversity.

Many protozoan diseases are endemic in tropical countries, affecting millions of humans and animals, and causing serious economic losses annually, especially to developing economies. Most of these parasitic diseases attract little attention with regard to the development of new drugs, mainly because of poor profitability prospects. In addition, the development of resistance by these parasites to nearly all currently used chemotherapies, in addition to toxicity issues and the increasing cost of unrelated drugs, has led to an ever-increasing need to explore cheaper, accessible sources of safe new antiprotozoal agents (de Koning, 2017).

To date, a large number of Nigerian medicinal plant extracts has been successfully tested and found to show antiprotozoal activity (Lifongo et al., 2014). Several studies have reported remarkable *in vitro* and *in vivo* activity of extracts and fractions of Nigerian plants against *Plasmodium* spp. (Adebayo and Krettli, 2011), *Trypanosoma* spp. (Abiodun et al., 2012; Nwodo et al., 2015a), and *Leishmania* spp. (Bello et al., 2017). Indeed, promising lead compounds have been identified from some of these plants (Amoa Onguéné et al., 2013; Ntie-Kang et al., 2014; Bekono et al., 2020). However, due to research and resource limitations, the active principles of too many extracts from Nigerian medicinal plants remain unknown, and further studies that would facilitate the translation of the few identified compounds into drug candidates are limited by a lack of funding for such work (Ebiloma et al., 2018b). It should be noted that previous reviews have provided a compilation of evidence of antiprotozoal activity in materials collected from Nigerian flora. Other works have also documented bioactive compounds from plants that grow in Nigeria and the wider African continent, but not necessarily isolated from materials collected in the country or the region (Adebayo and Krettli, 2011; Nwodo et al., 2015a). With detailed analytical chemistry and bioactivity screening of plant materials collected specifically from Nigeria increasing, it has become opportune to document the compounds isolated from these plants, and their utility for development as antiprotozoal drugs. This would provide a guide for a focused and evidence-based approach for advancement and development of natural compounds from Nigeria and hence, from Africa in general.

In this review, we present an overview of some of the most important antimalarial, antitrypanosomal, and/or antileishmanial compounds that have been isolated from medicinal plant materials collected in Nigeria. An extensive internet-based search was carried out on PubMed, Web of Science, Science Direct, and Google Scholar using appropriate combinations of the keywords "antimalarial, antitrypanosomal, antileishmanial, plant, natural product, extract, compound, and Nigeria." The last search was carried out on October 10, 2020 and only compounds with elucidated structures and reported half maximal inhibitory concentration (IC_{50}), half maximal effective concentration (EC_{50}) or minimum inhibitory concentration (MIC) of $\leq 50\,\mu g/mL$ or μM were included. References lists of included and related studies were also screened visually to identify further relevant studies. Beyond evaluating the antiprotozoal utility of these natural drugs, the aim is to identify the current limitations in natural product drug discovery in Nigeria and elsewhere, recommend a way forward, and encourage further studies that would identify the actual translation of the best leads into new antiprotozoal chemotherapies, which are sorely needed.

PLANTS AS A SOURCE OF ANTIPARASITIC DRUGS

The annual global drug market is worth about one trillion USD (Calixto, 2019). A comprehensive analysis of drugs approved by the United States' Food and Drug Administration (FDA) from 1981 to 2010 shows that ∼35% of these drugs were directly or indirectly of natural products origin, including plants (25% of total new pharmaceuticals) (Newman and Cragg, 2012, 2016). Over the last two centuries, the global pharmaceutical industry has significantly profited from the biodiversity of several countries when it comes to identifying new therapeutics against important pathogens, especially the development of new chemotypes for managing protozoal diseases such as malaria and leishmaniasis (Calixto, 2019).

Some of the natural compounds that have been isolated from plants include alkaloids, phenolics, terpenes, saponins, and quinones, and their derivatives (**Table 1**). They are valuable in combating diseases because of their anti-parasitic efficacies and their selective mode of action (Ebiloma et al., 2017). In addition to the direct usage of natural products from plants (phytomedicines or pure drugs), the scaffolds of many of these compounds have been successfully modified to produce pharmacologically more complex or semi-synthetic active molecules. They can also be used as taxonomic indicators for the discovery of new drugs; others can be used as models for designing lead molecules. Antique wisdom is the basis of modern medicine and a significant base of future medicines and therapeutics. Examples of well-established plant-based anti-protozoal drugs currently in use today are quinine and artemisinin, which are used for the treatment of malaria.

For centuries, the bark of *Cinchona* species was used by the natives living in the Amazon area for the treatment of malaria caused by *Plasmodium*. Interestingly, as early as 1820, Pelletier and Caventou successfully isolated quinine, the bioactive principle, from the bark of *Cinchona officinalis* (Dias et al., 2012). Consequently, the curative agent for malaria in those early days was quinine. Subsequently, several synthetic derivatives including chloroquine, mefloquine, amodiaquine, and primaquine were developed. The long history of usage notwithstanding, i.e., first as extract preparations and later as pure compound, malaria chemotherapy is still to an extent dependent on quinine; this is especially true for the most lethal form, cerebral malaria. Interestingly, while resistance to the synthetic derivatives such as chloroquine developed rapidly, resistance to quinine itself is relatively rare (Achan et al., 2011; Okombo et al., 2011).

The remarkable contributions of plants to the discovery of antiprotozoal drugs would not be complete without mentioning the plant *Artemisia annua*. *A. annua* is another plant that was long used for the treatment of fevers, in this case in Chinese folkloric medicine. The successful isolation of the bioactive agent, Artemether [a strong anti-malarial agent that was derived from artemisinin (qinghaosu), a sesquiterpene lactone], from *A. annua* represents one of the most significant discoveries in the fight against diseases caused by a protozoan parasite (Tu, 2011). Since then, several semi-synthetic artemisinin-based derivatives have been approved and registered for use: artesunate, dihydroartemisinin, and artemether (Paddon and Keasling, 2014).

ACTIVE COMPOUNDS FROM NIGERIAN PLANTS

Alkaloids

Alkaloids are a structurally diverse class of secondary metabolites whose key feature is a basic nitrogen (nitrogen in a negative oxidation state) in a carbon ring. They are classified according to their principal C-N skeleton into pyrroles (A1), pyrrolines (A2), pyrrolidines (A3), pyrrolizidines (A4) indoles (A5), pyridines (A6), pyrimidines (A7), piperidines (A8) quinolines (A9), isoquinolines (A10), quinolizidines (A11), tropanes (A12), imidazoles (A13) (**Figure 1**). They can also be classified according to their biological origin. Alkaloids are widely distributed in plants and some animal species. For many years, plant alkaloids have been utilized in the treatment of various health conditions (Bribi, 2018).

An excellent example is the isolation of anti-malarial alkaloids from the fruit rind of *Picralima nitida*. The crude dichloromethane extract displayed *in vitro* antiplasmodial activity with half maximal inhibitory concentration (IC_{50}) values of 1.6–2.4 μg/mL. Moreover, the methanolic extract of the plant's stem bark, root, and fruit rind yielded active alkaloid fractions with IC_{50}s of 0.54–2.16 and 0.79–1.59 μg/mL against *P. falciparum* chloroquine-resistant (W2) and chloroquine-sensitive (D6) clones, respectively (Iwu and Kiayman, 1992). Using pH-zone-refining counter-current chromatography, Okunji et al. (2005) isolated indole alkaloids from the rind of the plant. The purified compounds, alstonine (**1**), akuammigine (**2**), akuammine (**3**), akuammicine (**4**), picraline (**5**), and picratidine (**6**), showed remarkable activity against both *P. falciparum* clones (D6 and W2; IC_{50} 0.01–0.9 μg/mL) (Okunji et al., 2005) (for the structures of compounds **1**–**24** see **Figure 2**).

The crude, semi-purified and purified aqueous extracts of the roots of *Fagara zanthoxyloides*, known as Senegal prickly-ash, displayed highly promising antiplasmodial activity with IC_{50} values of 4.90, 1.00, and 0.13 μg/mL, respectively, using the [^{3}H]-hypoxanthine incorporation assay. Further separation yielded a very potent antiplasmodial benzophenanthridine alkaloid, fagaronine (**7**) with an IC_{50} of 0.018 μg/mL against *P. falciparum* strain 3D7 (Kassim et al., 2005). A short and efficient synthesis for this compound was developed by Rivaud et al. (2012), who also confirmed the compound's activity against chloroquine-sensitive and -resistant *P. falciparum* isolates superior to chloroquine with half maximal effective concentration (EC_{50}) of ∼10 nM *in vitro* and comparable to chloroquine against *P. vinckei in vivo* [median effective dose (ED_{50}) of 6 mg/Kg/day for 4 days]. Moreover, the compound, displayed no toxicity against Vero cells *in vitro* (Rivaud et al., 2012) or by single injection in the mouse at up to 50 mg/Kg (Nakanishi et al., 1999). The methanol extract of *F. zanthoxyloides* also displayed >90% inhibition of *Plasmodium berghei in vivo*, with an estimated EC_{50} of 235 mg/Kg b.w. for the extract while the lethal dose 50 (LD_{50}) was >5,000 mg/Kg b.w. in mice (Enechi et al., 2019), providing independent confirmation of the antimalarial potential of this plant.

A preparation of 80% ethanolic extract of the stem bark of *Nauclea pobeguinii*, containing 5.6% of the beta-carboline alkaloid strictosamide as the presumed active agent, displayed

TABLE 1 | Compounds isolated from Nigerian medicinal plants with antimalarial, antitrypanosomal, and antileishmanial activity.

Compound	Compound class/ subclass	Part of plant studied	Species name	Plant family	Place of collection	Ethnomedicinal use of the plant	Activity of the compound	References
1–6	Indole alkaloid	Fruits	*Picralima nitida*	Apocynaceae	Nnewi	Fever, jaundice, gastrointestinal disorders, and malaria	*Antiplasmodial*	Okunji et al., 2005
7	Benzophenanthridine alkaloid	Root	*Fagara zanthoxyloides*	Rutaceae	Ile-Ife, Osun State	Chewing sticks	*Antiplasmodial*	Kassim et al., 2005
8	Beta carboline Alkaloid	Bark	*Nauclea pobeguinii*	Rubiaceae	Oju LGA Benue State	Fever, jaundice, malaria, diarrhea	*Antitrypanosomal*	Igoli et al., 2011
9 and **10**	Alkaloid	Seed	*Monodora myristica*	Annonaceae	Oju LGA Benue State	Fever, sepsis, stomach-ache, and constipation	*Antitrypanosomal*	Igoli et al., 2011
11–14	Isoquinoline alkaloid	Stembark	*Enantia chlorantha* Oliv.	Annonaceae	Ore, Ondo state	Stomach problems, rickettsia, typhoid fever, jaundice, malaria, and tuberculosis, some	*Antiplasmodial* and *antitrypanosomal*	Imieje et al., 2017
15–24	Steroid alkaloid	Leaves and stembark	*Holarrhena africana* (syn. *Holarrhena floribunda*)	Apocynaceae	Nsukka LGA Enugu State	Convulsion, Fever, malaria, snake venom antidote	*Antitrypanosomal*	Nnadi et al., 2017, 2019
25	Diterpenoid	Leaves	*Hyptis suaveolens*	Lamiaceae	South-Eastern Nigeria	Respiratory tract infections, colds, pain, fever, cramps, and skin diseases	Antiplasmodial	Chukwujekwu et al., 2005
26–28	Diterpenoid	Stembark	*Jatropha multifida*	Euphorbiaceae	Edo State	Hepatitis and leishmaniasis	Antiplasmodial and antileishmanial	Falodun et al., 2014
29–32	Diterpenes/ sesquiterpenes	Rhizomes	*Siphonochilus aethiopicus*	Zingiberaceae	Makurdi, Benue State	Colds, coughs, hysteria, infections, wound dressing, fevers, and pain	Antitrypanosomal	Igoli N. et al., 2011
33–35	Diterpenoid	Leaves	*Polyalthia longifolia*	Annonaceae	Anyigba, Kogi State	In the treatment of trypanosomiasis, leishmaniasis, and malaria	Trypanosomiasis	Ebiloma et al., 2017
36	Diterpenoid	Roots	Jatropha gossypiifolia	Euphorbiaceae	Benin City, Edo State	Leprosy, as an antidote for snakebite and in urinary problems	Antiplasmodial, antileishmanial	Ogbonna et al., 2017
37	Sesquiterpenes	Leaves	*Piliostigma thonningii*	Leguminosae	Abuja	Treatment of ulcers, wounds, heart pain, arthritis, malaria, fever, leprosy, sore throat, diarrhea, toothache, and cough	Antitrypanosomal	Afolayan et al., 2018
38 and **39**	Labdane diterpenes	Leaves	*Piliostigma thonningii*	Leguminosae	Abuja	Treatment of ulcers, wounds, heart pain, arthritis, malaria, fever, leprosy, sore throat, diarrhea, toothache, and cough	Antitrypanosomal and antileishmanial	Afolayan et al., 2018
40	Cassane diterpene	Roots	*Calliandra portoricensis*	Fabaceae	Jos, Plateau State	Treatment of tuberculosis, constipation, and helminthiasis	Antitrypanosomal and antileishmanial	Nvau et al., 2020
41	Terpenoid/ diterpenoid	Leaves	*Eucalyptus maculata*	Myrtaceae	Anyigba, Kogi State	In the treatment of trypanosomiasis, leishmaniasis, and malaria	Antitrypanosomal	Ebiloma et al., 2017
42–44	Triterpenoid	stem bark	*Spathodea campanulata*	Bignoniaciaciae	–	Malaria	Antiplasmodial	Amusan et al., 1996
45 and **46**	Triterpenoid	stem bark	*Khaya grandifoliola*	Meliaceae	–	Malaria and other febrile conditions	Antiplasmodial	Agbedahunsi and Elujoba, 1998
47	Triterpenoid		*Cassia siamea* L.	Fabaceae	Otu, Oyo State	As laxative and in treatment of insomnia, diabetes, and hypertension	Antiplasmodial	Ajaiyeoba et al., 2008
48	Triterpene	Leaves	*Combretum racemosum*	Combretaceae	Ibadan, Oyo State	Parasitic diseases and fever	Antiplasmodial	Oluyemi et al., 2020
49	Tetraterpenoids/ carotenoids	Leaves	*Bridelia ferruginea*	Euphorbiaceae	Eruwa, Oyo State	Purgative and vermifuge	Antitrypanosomal	Afolayan et al., 2019

(Continued)

TABLE 1 | Continued

Compound	Compound class/ subclass	Part of plant studied	Species name	Plant family	Place of collection	Ethnomedicinal use of the plant	Activity of the compound	References
50	Flavonol	Roots	*Spondias mombim*	Anacardiaceae	Oju LGA Benue State	Cough, sore throat, antiseptic soap, and malaria	Antitrypanosomal	Igoli et al., 2011
51	Flavonol	Bark	*Alcornea cordifolia*	Euphorbiaceae	Oju LGA Benue State	Fever, rheumatic pains, urinary tract infections, ringworm, and dysentery	Antitrypanosomal	Igoli et al., 2011
52	Flavonoid	Leaves	*Chromolaena odorata*	*Asteraceae*	Lagos State	Malaria	Antiplasmodial	Ezenyi et al., 2014
53 and **54**	Flavonoid	Leaves	*Vitex simplicifolia*	Verbenaceae	Nsukka LGA, Enugu State	To treat edema, gout, malaria, skin diseases, toothache, and dermatitis	Antitrypanosomal	Nwodo et al., 2015a
55	Chalcone	Leaves	*Cajanus cajan*	Fabaceae	Otu, Oyo State	Laxative, antimalarial	Antiplasmodial	Ajaiyeoba et al., 2013
56	Anthraquinone	Leaves	*Mitracarpus scaber*	Rubiaceae	Zaria, Kaduna State	Headaches, skin and venereal diseases, toothaches, leprosy, amenorrhoea	Antitrypanosomal	Nok, 2002
57	Quinone	Whole plant	*Cassia nigricans*	Caesalpinaceae	Kaduna State	Stomach ulcers	Antiplasmodial	Obodozie et al., 2004
57	Quinone	Stem bark	*Cassia siamea*	Fabaceae	Otu in Oyo State	For insomnia, as laxative and antidiabetic	Antiplasmodial	Ajaiyeoba et al., 2008
58	Anthraquinone	Leaves	*Crateva adansonii*	Capparaceae	Nsukka, Enugu State	Treatment of headaches, ear, and parasitic infections	*Antitrypanosomal*	Igoli et al., 2014
59 and **60**	Isoflavanquinones	Roots	*Abrus precatorius*	Fabaceae	Umuoriehi Umuahia, Abia State	Diabetes, hemoglobinuria, sore throat, rheumatism, skin infections, and jaundice	Antileishmanial	Okoro et al., 2020
61–**65**	Tannins	stem bark	*Terminalia avicennoides* and *Anogeissus leiocarpus*	Combretaceae	Bauchi State	TA: cure dental carries and skin infections AL: diarrhea, dysentery, and malaria,	Antiplasmodial, antitrypanosomal and antileishmanial	Shuaibu et al., 2008a,b,c
66	Coumarin	Stem	*Euphorbia poisonii*	Euphorbiaceae	Oju LGA Benue State	Pain killer, laxative, pesticide, arrow-poison	Antitrypanosomal	Igoli et al., 2011
67	Saponins	Seed	*Dracaena mannii* (DM) and *D. arborea* (DA)	Dracaenaceae	Isi-Enu, Nsukka, Enugu State	DM: Stomach-ache, mental illness gonorrhea, and chest pains DA: epilepsy, measles, smallpox, venereal diseases	Antiplasmodial	Okunji et al., 1996
68–**70**	Glycoside/glucoside	Leaves	Stachytarpheta cayennensis	Verbenaceae	–	Malaria, helminthiasis fever and constipation	Antiplasmodial	Ifeoma Chinwude et al., 2016
71 and **72**	Irodid glucoside	Leaves	*Vitex grandifolia*	Lamiaceae	Ilorin, Kwara State	Colic, umbilical cord infections, toothache, rheumatism, and orchitis	Antileishmaial	Bello et al., 2018
73	Peptide	Leaves	*Crateva adansonii* DC		Nsukka, Enugu State	Treatment of headaches, ear-aches, and parasitic infections	*Antitrypanosomal*	Igoli et al., 2014
74 and **75**	Amine (dipeptides)	Roots	*Zapoteca portoricensis*	Fabaceae	Nsukka, Enugu State	For wound healing, toothache, tonsilitis, diarrhea, and as an anticonvulsant and antispasmodic	*Antitrypanosomal*	Nwodo et al., 2014
76 and **77**	Fatty acids	Leaves	*Carica papaya*	Caricaceae	Abia State	Asthma, rheumatism, fever, diarrhea, boils, and hypertension and as lactogenic	Antiplasmodial	Melariri et al., 2011
78 and **79**	Taccalonolide	Tubers	*Tacca leontopetaloides*	Taccaceae	Benue State	Stomach disorders, gastric ulcers, tooth ache, high blood pressure, hepatitis, enteritis, and sexual dysfunction	*Antitrypanosomal*	Dike et al., 2016
80 and **81**	Pheophorbide	Leaves	*Crateva adansonii* DC	Capparaceae	Nsukka, Enugu State	Treatment of headaches, ear, and parasitic infections.	*Antitrypanosomal*	Igoli et al., 2014
82 and **83**	Pheophytins	Leaves	*Newbouldia laevis*	*Bignoniaceae*	Anyigba, Kogi State	To hasten parturition and placenta delivery	Antitrypanosomal	Ebiloma et al., 2017

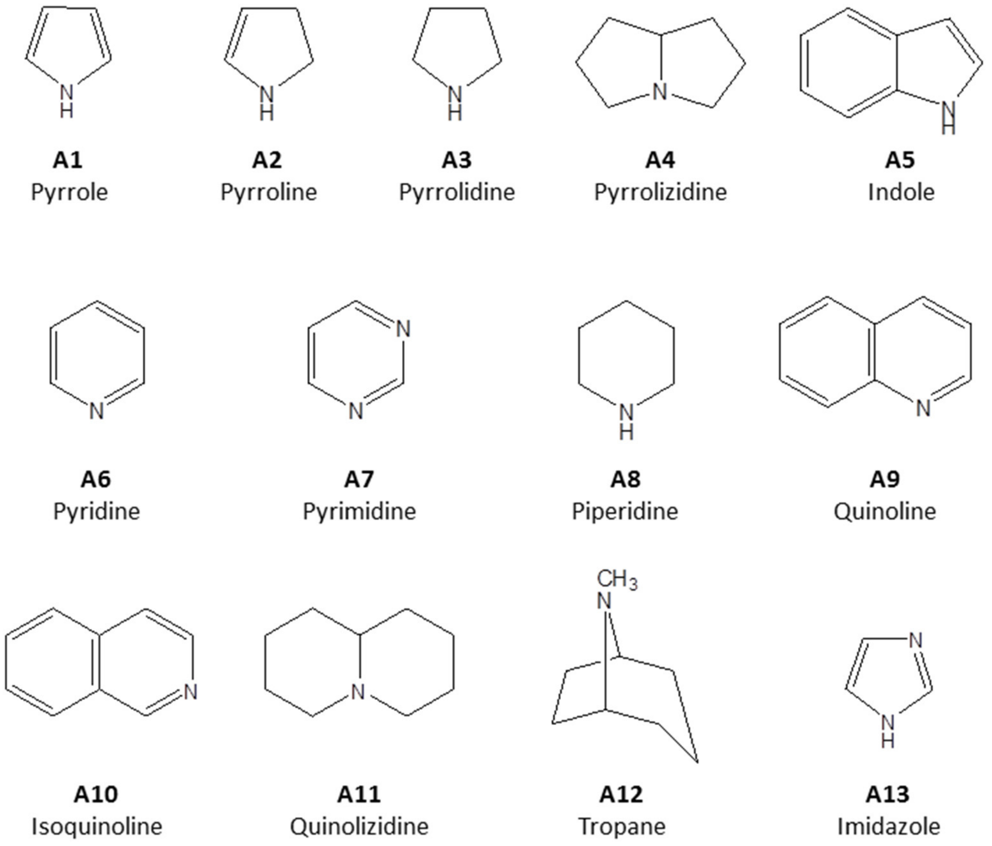

FIGURE 1 | Structure of principal C-N skeleton of alkaloid sub-groups.

highly promising activity against *falciparum* malaria in a Phase IIB clinical trial as a herbal medicine (Mesia et al., 2012). A beta carboline alkaloid, **8**, was isolated from the ethyl acetate extract of the bark of the same plant and showed moderate activity against the causative agent of sleeping sickness, *Trypanosoma brucei*, with a Minimum Inhibitory Concentration (MIC) of 12.5 μg/mL and low cytotoxicity against PNT2A cells with $IC_{50} > 100\ \mu$g/mL (Igoli et al., 2011). Two other alkaloids, compounds **9** and **10**, with similar moderate trypanocidal activity were obtained from the ethyl acetate extract of *Monodora myristica,* showing MICs of 12.5 and 25 μg/mL, respectively, for *T. brucei* (Igoli et al., 2011).

Imieje et al. (2017) screened the crude methanolic extract and different fractions of *Enantia chlorantha* (African Whitewood, family Annonaceae), which is used in Nigerian ethnomedicine for the treatment of wounds, ulcers, and fevers including malaria, for antiprotozoal activity and reported that the extract indeed displayed very high activity against *P. falciparum*, with very good IC_{50} values against chloroquine-sensitive D6 ($<0.37\ \mu$g/mL) and chloroquine-resistant W2 ($<0.32\ \mu$g/mL) clones as well as against *Leishmania donovani* ($IC_{50} <0.8\ \mu$g/mL), but only moderate activity against *T. brucei* (IC_{50} of 15.2 μg/mL). The butanol and ethanol fractions of the extract yielded three closely related isoquinoline alkaloids: jatrorrhizine (**11**), palmatine (**12**), and columbamine (**13**). The steroid β-sitosterol (**14**) was also obtained from the extracts. Compound **11** displayed good but only moderately specific activity against chloroquine-sensitive *P. falciparum* clone D6 (IC_{50} 2.2 μM), but activity against *L. donovani* and *T. brucei* was low (IC_{50}s >29.6 and 18.3 μM, respectively), and IC_{50}s >14.1 and >29.6 to VERO and human acute monocytic leukemia (THP1) cells, respectively. Compounds **12** and **13** showed essentially identical activity as **11** against *P. falciparum* D6 with IC_{50} of 1.90 and 2.16 μM, respectively, showing that the methylation of the isoquinoline hydroxy groups is not essential for activity, whereas **14** displayed only moderate activity (Pf $IC_{50} >11.5$). Compounds **12** and **14** were also tested against *L. donovani* and *T. brucei*, with IC_{50} values $\geq 23.1\ \mu$M (Imieje et al., 2017).

The *in vitro* and *in vivo* antitrypanosomal activity of the aqueous extract of young leaves of *Holarrhena africana* from Nigeria has been reported by multiple authors (Nwodo et al., 2007; Alhaji et al., 2014; Nnadi et al., 2016). Nnadi et al. investigated the antitrypanosomal, antileishmanial and antiplasmodial activity of this plant in more detail, using extracts and fractions from both stem bark and leaves (Nnadi et al., 2016, 2017). The crude extract and alkaloid fraction both displayed potent antitrypanosomal activity. Bioactivity guided fractionation of the active alkaloid fraction led to

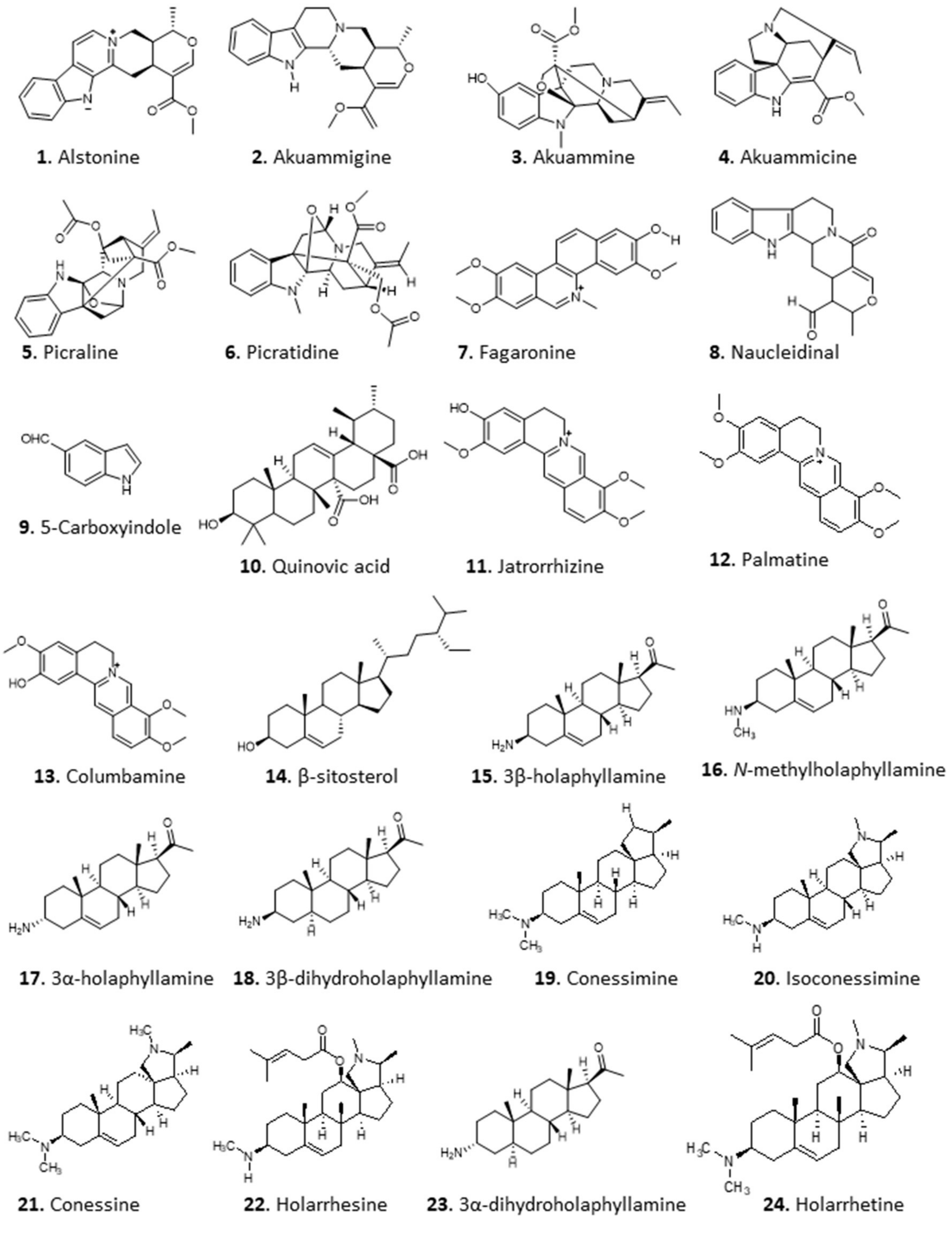

FIGURE 2 | Structure of alkaloids isolated from Nigerian plants with selected antiprotozoal activity.

the isolation of 19 compounds, 17 of which were steroid alkaloids. Remarkable activities (EC_{50} in μM ± absolute deviation) against *T. brucei* rhodesiense were recorded for some aminosteroids from the leaves: 3β-holaphyllamine (0.40 ± 0.28) **15**, N-methylholaphyllamine (0.08 ± 0.01) **16**, 3α-holaphyllamine (0.37 ± 0.16) **17** and 3β-dihydroholaphyllamine (0.67 ± 0.03) **18**. Related compounds from the stembark, Conessimine (0.17 ± 0.08) **19**; isoconessimine (0.17 ± 0.11)

20; conessine (0.42 ± 0.09) **21**; and holarrhesine (0.12 ± 0.08) **22** also showed very high antitrypanosomal activity, with high selectivity to the parasites [selectivity index (SI) >100] compared to mammalian L6 cells (Nnadi et al., 2017). A 3D-Quantitave Structure Activity Relationship (QSAR) study revealed that steric activity around the C-3 amino group tends to increase activity, while steric activity in the vicinity of the amino group of the pyrroline/pyrrolidine rings and the C-17β-acetyl or C-20 methyl groups tended to decrease activity (Nnadi et al., 2018). Following on from this, the active aminosteroids together with **22**, 3α-dihydroholaphyllamine (**23**), and holarrhetine (**24**) were also tested on animal trypanosome species using resazurin-based *in vitro* screening assay in our lab (Nnadi et al., 2019). Interestingly, most of these compounds displayed no cross-resistance with pentamidine, isometamidium, diamidines, and melaminophenyl arsenicals in *T. b. brucei*. The activity of these compounds varies between *T. b. brucei* and *T. congolense*, suggesting possible differences in the mode of action of these compounds in the 2 species as seen with some trypanocides. The compounds with highest activity (IC_{50} ± standard deviation) and selectivity [represented as Selectivity Index (SI)] against *T. congolense* were **20** ($IC_{50} = 0.22 \pm 0.35\,\mu M$; SI = 123.5), **21** ($IC_{50} = 1.65 \pm 0.92\,\mu M$; SI = 37.2), **22** ($IC_{50} = 0.22 \pm 0.13\,\mu M$; SI = 65.9), and **23** ($IC_{50} = 0.045 \pm 0.03\,\mu M$; SI = 2,130) (Nnadi et al., 2019). Further exploration into the mechanism of action revealed that the compounds caused a slow but irreversible trypanocidal effect by targeting the mitochondrion, preventing kinetoplast division (Nnadi et al., 2019).

Terpenoids

Terpenoids are commonly found in plants and are biosynthesized from isoprene units ($CH_2=C(CH_3)\text{-}CH=CH_2$). They are classified based on the number of units in the compound; monoterpenes consist of 2 units, while sesquiterpenes, diterpenes, triterpenes, and tetraterpenes consist of 3, 4, 6, and 8 units, respectively (**Figure 3**). The number of carbon atoms in the compounds are thus 10, 15, 20, 30, and 40 depending on the number of isoprene units. Terpenoids have shown good activity in various assay screens and constitute the active entities in many drugs. Compound **25** (9α, 13α-epi-dioxiabiet-8(14)-en-18-ol) was obtained through a bioassay-guided fractionation of the petroleum ether extract of the leaves of Hyptis suaveolens, a common shrub in the tropics, used traditionally for the treatment of many ailments including fever, colds, and respiratory tract infections (Iwu, 2014). The compound demonstrated high antiplasmodial activity with an IC_{50} of 0.1 µg/mL against chloroquine-sensitive *P. falciparum* clone D10 (Chukwujekwu et al., 2005).

The methanol extract of Jatropha multifidi, known as coral bush, which is in fact used in Nigerian folk medicine for the treatment of parasitic infections as well as cancer (Gill, 1992), yielded 3 closely related macrocyclic lathyrane diterpenoids: 14-deoxy-1β-hydroxy-4(4E)-jatrogrossidentadione **(26)**, the saturated 15-deoxy-1β-hydroxy-4(4E)-jatrogrossidentadione **(27)** and the unsaturated 15-deoxy-1β-hydroxy-4(4E)-jatrogrossidentadione **(28)** (Falodun et al., 2014). The compounds showed particular promise for their antileishmanial activity, with IC_{50} of 11.9, 4.69, and 4.56 µg/mL, respectively, showing that the oxidation state of the oxygen on the cyclopentene ring is likely to be important for high activity. The authors state that traditional healers have used the plant successfully against leishmaniasis. The compounds possessed virtually no activity against chloroquine-sensitive *P. falciparum* D6, with IC_{50}s >7 mg/mL, and poor activity against a panel of bacterial and fungal pathogens, thus confirming specific activity against *Leishmania* species and perhaps other kinetoplastid parasites (Falodun et al., 2014).

The crude hexane extracts of the rhizomes of wild ginger, *Siphonochilus aethiopicus*, showed promising activity against *T. brucei* with an MIC of 6.5 µg/mL and low toxicity against several mammalian cells (MIC of 53.3–114.2 µg/mL). Two active diterpenes, 8(17),12E-labdadiene15,16-dial **(29)**, 15-hydroxy-8(17),12E-labdadiene-16-al **(30)** and two sesquiterpenes, epi-curzerenone **(31)**, furanodienone **(32)** were isolated from the extract (Igoli N. et al., 2011). **29, 31, 32** showed a MIC of 1.55 µg/mL while **30** displayed an MIC of 6.25 µg/mL against *T. brucei*. The compounds appeared to be selective for *T. brucei* as cytotoxicity tests with the mammalian cells showed MICs of 35.9–116 µg/mL, except for **29**, which was toxic to Jurkat and SH-SY5Y cells (MIC 4.1 and 9.0 µg/mL, respectively) (Igoli N. et al., 2011).

The Indian-native ornamental plant *Polyalthia longifolia*, commonly found in Nigeria is an important source of traditional remedies for malaria and fevers (Bankole et al., 2016). The hexane extract of the leaves of *P. longifolia* showed potent activity against *T. b. brucei* in our lab, with EC_{50} ± SEM of 2.4 ± 0.1 µg/mL. Bioactivity-guided fractionation led to the isolation of a diterpenoid identified as clerodane (16-α-hyroxy-cleroda-3-13(-14)-Z-dien-15,16-olide; compound **33**), which displayed an EC_{50} ± SEM of 0.38 ± 0.05 µg/mL against *T. b. brucei*. Other isolated compounds from the fraction were polyalthialdioc acid **(34)** and kolavenic acid **(35)**, which also showed significant antitrypanosomal activity, with EC_{50} ± SEM values of 3.57 ± 0.16 and 12.3 ± 0.5 µg/mL, respectively. Interestingly, all the 3 compounds also showed activity against *T. congolense* and *L. mexicana*, presented no cross-resistance to diamidines and arsenicals, and were not toxic to Human Embryonic Kidney (HEK) cells at up to 200 µg/mL (Ebiloma et al., 2017). Compound **33** has also been previously described as an oral antileishmanial agent with *in vivo* activity (Misra et al., 2010). We further investigated the effect of **33** and reported a multi-target mechanism of action for the compound on *T. brucei*, including severe cell cycle defects, DNA fragmentation, ATP depletion, and a marked depolarisation of the mitochondrial membrane potential (Ebiloma et al., 2018b).

Chromatographic fractionation and separation of fractions of the methanol extract of the root bark of *Jatropha gossypifolia* ("bellyache bush"), a pantropical plant with many ethnopharmacological applications for its various parts (Félix-Silva et al., 2014), yielded a macrocyclic diterpenoid compound, jatrophone **(36)**, with antiprotozoal activity. The compound displayed broad antiparasitic activity, with low EC_{50} values against chloroquine-sensitive *P. falciparum* clone

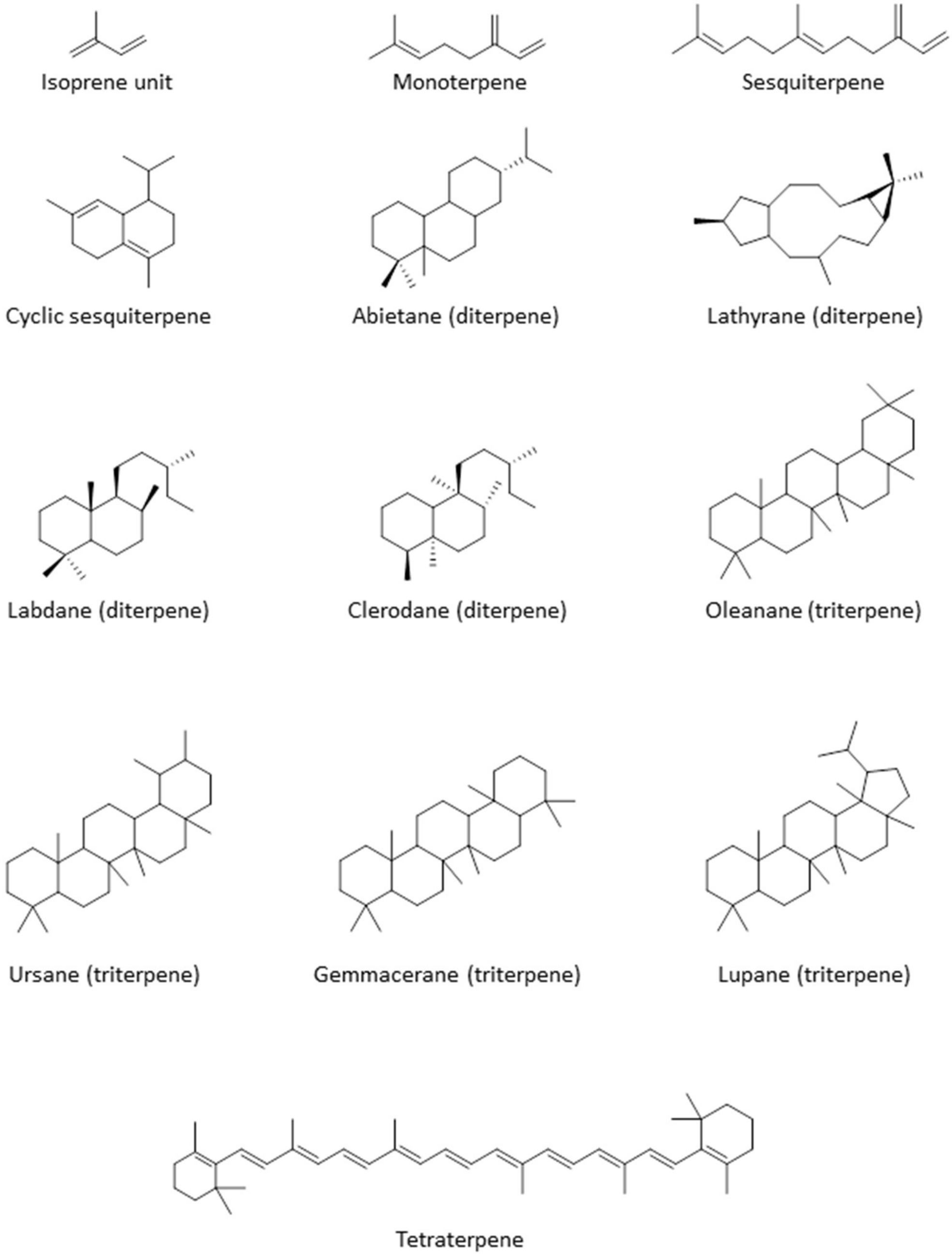

FIGURE 3 | Structure of the basic skeleton of terpene sub-groups.

D6 (0.55 µg/mL), chloroquine-resistant *P. falciparum* clone W2 (<0.52 µg/mL), *L. donovani* (<0.4 µg/mL), and *T. brucei* (<0.4 µg/mL). However, **36** was also found to be similarly active against VERO cells (0.43 µg/mL), and its antiprotozoal effects thus reflect a more general toxicity (Ogbonna et al., 2017).

Several compounds including a bioactive sesquiterpene, 2β-methoxyclovan-9α-ol **(37)**, two active labdane diterpenes, methyl-*ent*-3β-hydroxylabd-8(17)-en-15-oate **(38)** and alepterolic acid **(39)** were obtained from the methanol extract of the leaves of *Piliostigma thonningii*, a plant of the subfamily Caesalpinioideae in the legume family with myriad ethnopharmacological uses. Compounds **37** and **39** were antitrypanosomal with IC_{50}s of 7.89 and 3.42 µM against *T. brucei*, respectively. Compound **38** displayed a broader antikinetoplastid activity with IC_{50} of 3.84 and 7.82 µM in *T. brucei* and *L. donovani*, respectively. The authors suggested that hydroxylation of the sesquiterpenes at C-2 position improves the antileishmanial activity, while hydroxylation at C-3 enhances the antitrypanosomal activity of the labdane diterpenes (Afolayan et al., 2018).

Column chromatography of the ethyl acetate extract of the roots of *Calliandra portericensis* yielded a novel diterpene-substituted chromanyl benzoquinone, bokkosin, **40**. The compound showed potent activity against the kinetoplastid parasites, *T. brucei* (0.69 μg/mL), *T. congolense* (21.6 μg/mL), and *L. mexicana* (5.8 μg/mL). In addition, it exhibited very low prospects of cross-resistance to antitrypanosomal drugs, pentamidine and diminazene, and low toxicity to mammalian cell lines (Nvau et al., 2020). The ethyl acetate extracts of the leaves of *Eucalyptus maculata* also exhibited antitrypanosomal activity (12.3 ± 0.3 μg/mL, EC_{50} ± SEM). An ursane type triterpenoid, 3β,13β-dihydroxy-urs-11-en-28-oic acid (41) isolated from this extract appeared to be the active ingredient, with EC_{50} ± SEM of 1.58 ± 0.03 μg/mL against *T. b. brucei*. Compound 41 showed no cross-resistance to diamidines and arsenicals, and was not toxic to HEK cells at concentrations up to 200 μg/mL (Ebiloma et al., 2017).

Amusan et al. (1996) reported the isolation of antimalarial triterpenoids from the chloroform extract of the stem bark of one of the plants that is tradionally used for the treatment of malaria, *Spathodea campanulata* (Makinde et al., 1987, 1988a). The triterpenoids, 3β-hydroxyurs-12-en-28-oic acid (ursolic acid; **42**) and two of its derivatives, 3β-hydroxyurs-12,19-dien-28-oic acid (tomentosolic acid; **43**) and 3β,20 β-dihydroxyurs-12-en-28-oic (**44**) resulted in a significant ($P < 0.05$) reduction in parasitaemia and enhanced survival of mice infected with *P. berghei.* Notably, the effect of 60 mg/Kg/day of **42** on parasitaemia and survival was comparable to 10 mg/Kg/day chloroquine (Amusan et al., 1996).

The same group reported that aqueous extracts of another Nigerian antimalarial plant, *Khaya grandifoliola* (African mahogany), also displayed activity against *P. berghei* infection in mice (Makinde et al., 1988b), but this extract only suppressed early infections and was ineffective against established infections of the parasite. However, Agbedahunsi et al. re-tested the antimalarial activity of *K. grandifoliola* stem bark extracts using different solvents (Agbedahunsi et al., 1998). Among the extracts tested, the n-hexane crude extract and purified fractions displayed the highest activities, comparable to the reference drug chloroquine diphosphate, with EC_{50} values of 1.4 μg/mL (for a multi-drug resistant clone) or 0.84 μg/mL (for Nigerian *P. falciparum* isolates). Further studies on the active n-hexane fraction yielded a tetranortriterpenoid, methyl-6-acetoxy angolensate (**45**), and a novel compound, grandifolin (**46**) (Agbedahunsi and Elujoba, 1998). Another triterpenoid, lupeol (**47**), isolated from methanol of *Cassia siamea* stem bark extract showed an IC_{50} of 5 μg/mL against *P. falciparum* using a parasite lactate dehydrogenase (pLDH) assay (Ajaiyeoba et al., 2008). Phytochemical investigation of the methanolic leaf extract of *Combretum racemosum* led to the identification of ursane-type triterpenes, with the most active antiplasmodial compound being madecassic acid (**48**) with mean EC_{50} ± SD values of 28 ± 12 and 17 ± 4 μg/mL against chloroquine-sensitive (D10) and chloroquine-resistant (W2) *P. falciparum*, respectively (Oluyemi et al., 2020).

The crude methanolic extract of the leaves of *Bridelia ferruginea* displayed potent activity against *T. brucei* with >90% inhibition and EC_{50} of 8.48 μM. A tetraterpenoid/carotenoid, lutein (49), was isolated from the extract among other compound and showed activity against *T. brucei* (EC_{50} 4.16 μM) and *L. donovani* (EC_{50} 9.3 μM) (Afolayan et al., 2019) (for the structures of compounds **25–49**, see **Figure 4**).

Flavonoids and Chalcones

Flavonoids are secondary metabolites with diverse medicinal properties and are commonly found in fruits, leaves, and flowers of plants. They are phenolics, with structures based on a 15-carbon skeleton made of two benzene rings (A and B) connected by a pyran ring (C) (F1). The saturation (F3) or unsaturation (F2) of the pyran ring, absence of the carbonyl group at C-4 (F4), connection of ring B to ring C at C-3 (F5, F6, F7) and the opening of ring C (F8) is the basis for their classification into flavones, flavanones, flavans, isoflavone, isoflavanones, isoflavans, and chalcones (**Figure 5**). An –OH substituent at C-3 on the flavones skeleton (F2) leads to flavonols, while on flavanone skeleton (F3) leads to flavanonols.

We have reported the isolation of two flavonols, **50** and **51**, from the combined hexane and ethyl acetate extracts of the roots of *Spondias mombim* and the methanolic extract of the bark of *Alcornea cordifolia*, respectively. Compound **50** displayed poor activity against *T. brucei* (EC_{50} 25 μg/mL) whereas **51**, different only by a single hydroxy substituent on the 5′ position, showed quite remarkable activity against this parasite (EC_{50} <0.2 μg/mL). However, **51** also displayed toxicity against PNT2A prostatic cells with an EC_{50} of 1.5 μg/mL and would thus be too toxic for therapeutic use (Igoli et al., 2011). Nonetheless, it might be worth exploring structural variations with the 5′-OH substitution in a SAR study.

The methanol extract of the leaves of the common tropical shrub *Chromolaena odorata*, extracts of which are used to treat malaria in South-Eastern Nigeria, suppressed parasitaemia in mice infected with *P. berghei* by 99.2 and 97.8% at 200 and 400 mg/Kg/day, respectively. The extract yielded a flavonoid identified as 3, 5, 7, 3′-tetrahydroxy-4′-methoxyflavone (**52**), which displayed high antiplasmodial activity, with 81.5% suppression of parasitaemia in mice infected with *P. berghei* at 2.5 mg/Kg/day, even better than the control chloroquine and artemether (Ezenyi et al., 2014). Nwodo et al. (2015b) isolated seven flavonoid derivatives from the leaves of *Vitex simplicifolia* (family Verbenaceae), which is used to treat trypanosomiasis in Nigeria, and evaluated their activity against *T. b. rhodesiense* as well as cytotoxicity in L6 cells. The most active and least toxic of the compounds were 2-(5′-methoxyphenyl)-3,4′,5,7,8-trihydroxychroman-4-one **(53)** with $IC_{50} = 10.2$ μg/mL and SI = 9.8, as well as artemetin **(54)** with $IC_{50} = 4.7$ μg/mL and SI = 9.8 (Nwodo et al., 2015b). This level of selectivity seems insufficient for any clinical development.

The crude methanol extract of the leaves of *Cajanus cajan*, a member of the family Fabaceae used for its antimalarial properties, nevertheless had an IC_{50} value of just 53.5 μg/mL against the multidrug-resistant *P. falciparum* K1 strain *in vitro*;

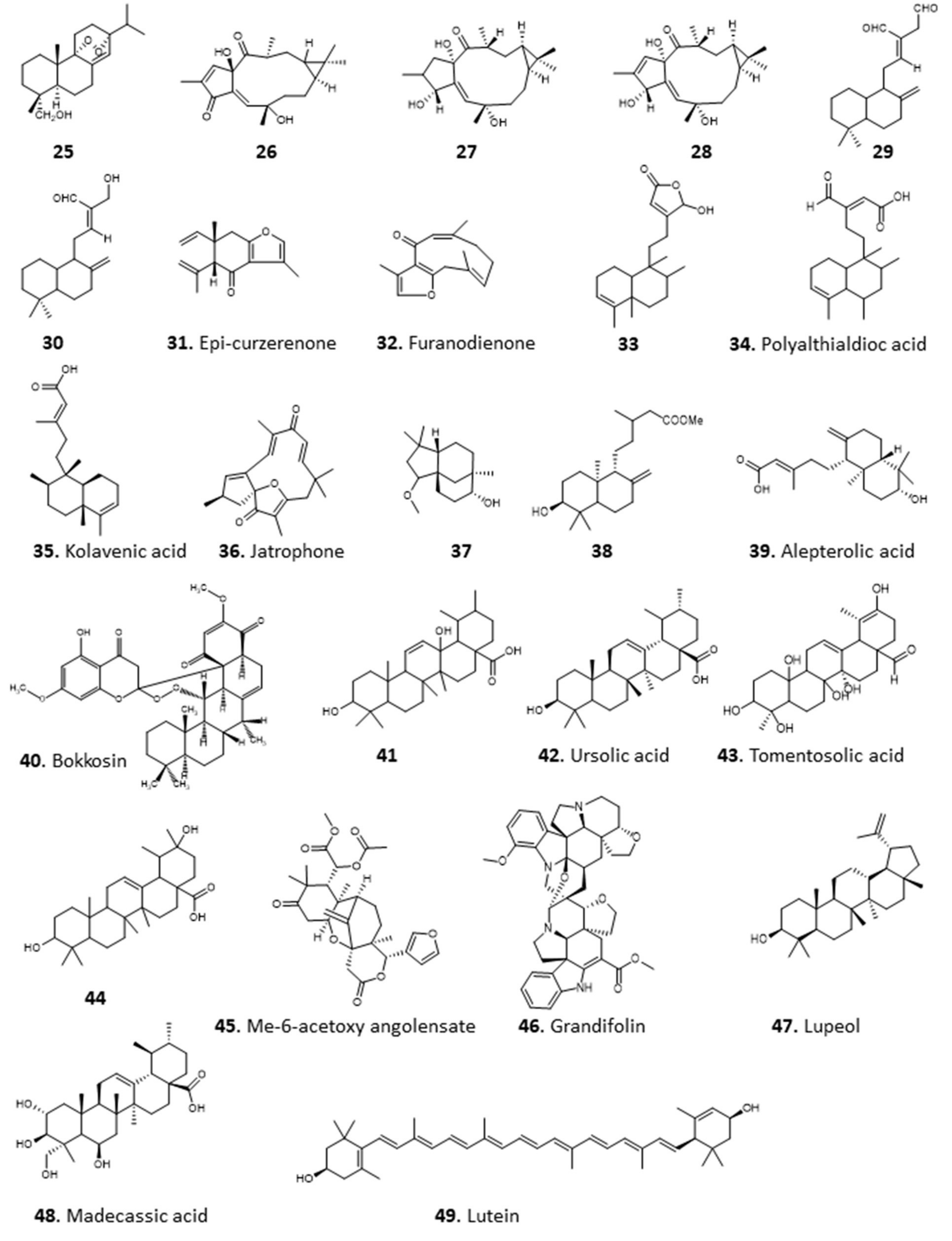

FIGURE 4 | Structure of terpenoids isolated from Nigerian plants with selected antiprotozoal activity.

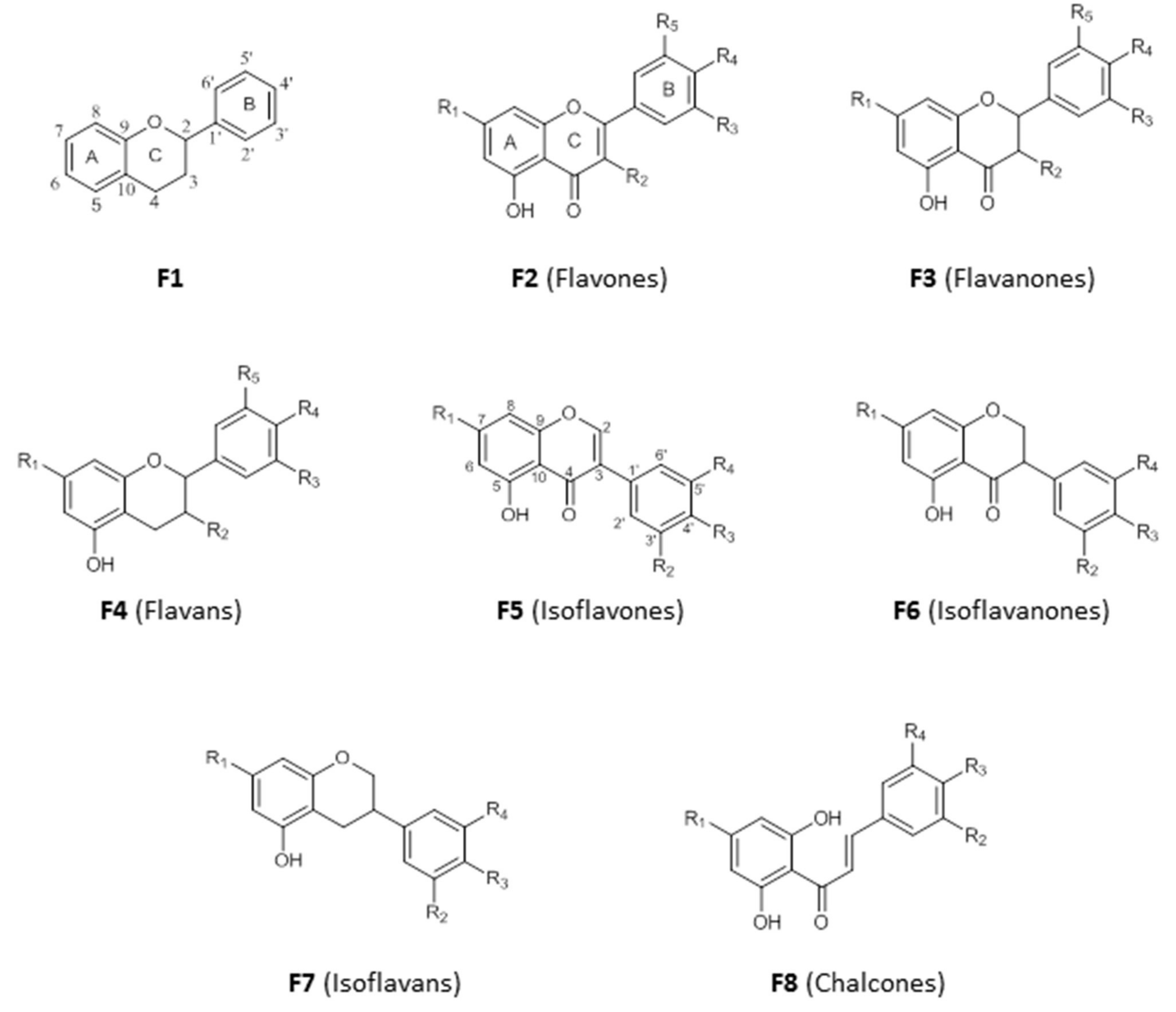

FIGURE 5 | Structure of basic skeleton of flavonoid sub-groups.

however, its ethyl acetate fraction yielded cajachalcone, 2′,6′-dihydroxy-4-methoxy chalcone **(55)** with IC_{50} of 2.0 μg/mL (7.4 μM) (Ajaiyeoba et al., 2013). The relatively simple structures of these flavonoids and chalcones, which lack chiral centers, should enable a systematic exploration of their structure-activity relationships (for the structures of compounds **50–55**, see **Figure 6**).

Quinones

The common feature among quinones is the presence of two carbonyl groups in a six-membered unsaturated ring (carbonyl groups can also be on adjacent rings). They are classified into three main groups: benzoquinones which have two carbonyl groups in a benzene ring (Q1), naphthoquinones, which have two carbonyl groups on one of the rings in naphthalene (Q2) and anthraquinones, which are derivatives of anthracene (Q3) (**Figure 7**). They are found in the leaves, seeds, and woody parts of higher plants, in some fungi and bacteria but rarely in higher animals. Quinones have been reported to have antioxidant, anti-inflammatory, antibiotic, antimicrobial, and anticancer activities (El-Najjar et al., 2011).

Treatment of *Trypanosoma congolense*-infected mice with the crude ethanol extract of the leaves of *Mitracarpus scaber*, a popular medicinal plant with known antifungal and antimicrobial properties (Irobi and Daramola, 1993; Ekpendu et al., 1994), at 50 and 150 mg/Kg/day cleared parasitaemia within 6 and 2 days, respectively, with no relapse for about 2 months. Benz(g)isoquinoline 5,10 dione (Azaanthraquinone; **56**) was isolated from the extract. It completely lysed *T. congolense* cells within 60 min at a concentration of 5 μM,

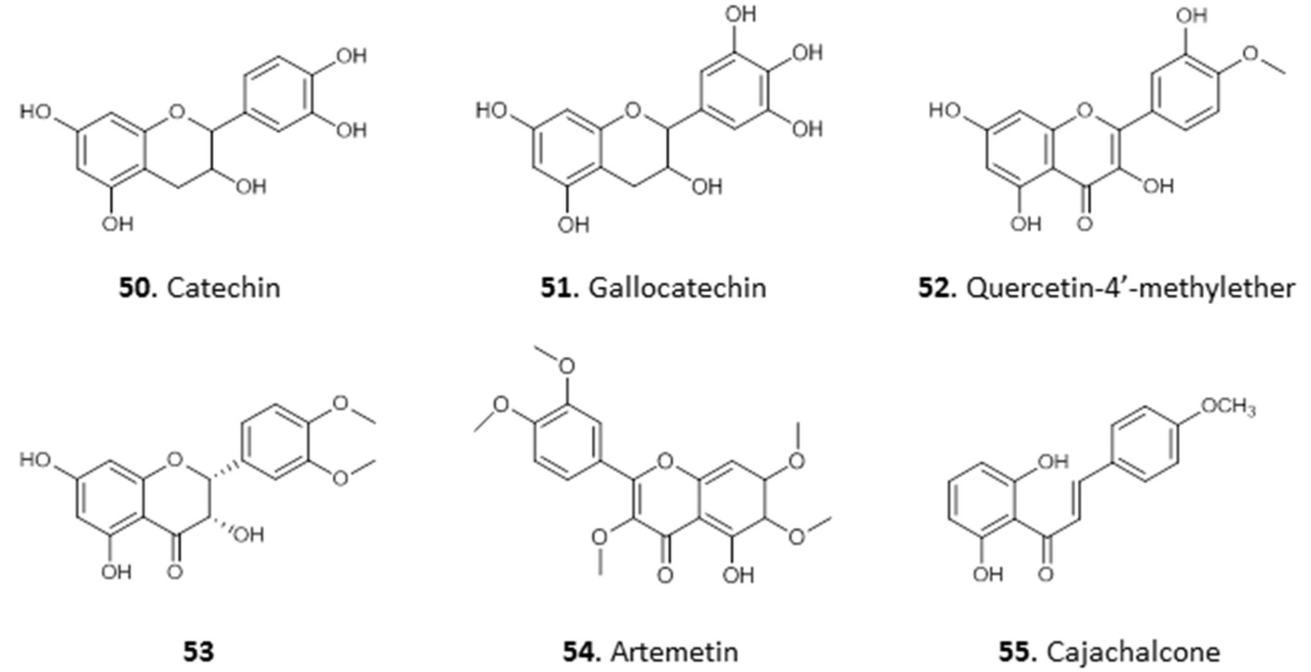

50. Catechin

51. Gallocatechin

52. Quercetin-4′-methylether

53

54. Artemetin

55. Cajachalcone

FIGURE 6 | Structure of flavonoids isolated from Nigerian plants with selected antiprotozoal activity.

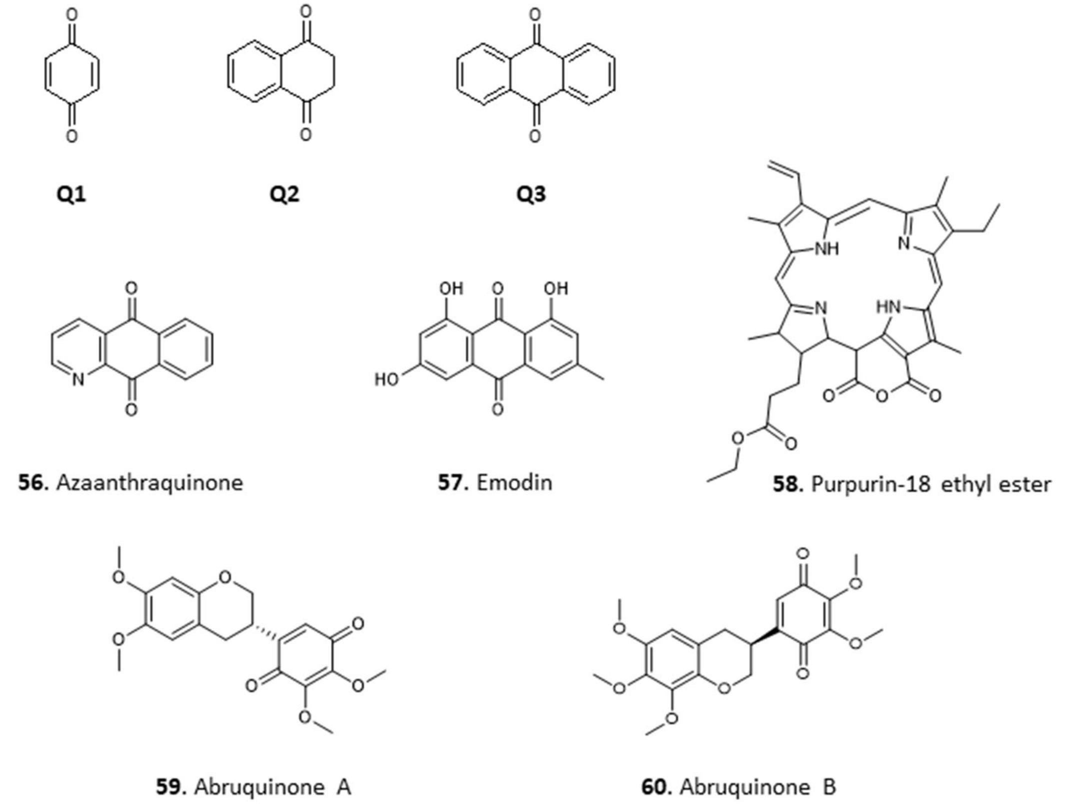

Q1

Q2

Q3

56. Azaanthraquinone

57. Emodin

58. Purpurin-18 ethyl ester

59. Abruquinone A

60. Abruquinone B

FIGURE 7 | Structure of basic skeleton of quinone sub-groups (Q1–Q3) and quinones isolated from Nigerian plants with selected antiprotozoal activity (56–60).

and dose-dependently inhibited their motility and respiration (Nok, 2002). Nok investigated the mechanism of action further and concluded that this *M. scaber* quinone (**56**) interferes with the essential function of coenzyme Q (ubiquinone) in the trypanosomes, which carries electrons for aerobic respiration from mitochondrial glycerol-3-phosphate dehydrogenase to the Trypanosome Alternative Oxidase (TAO) (Ebiloma et al., 2018b). This is a rare example where the mechanism of the antiparasite action of a natural compound is well-understood. Considering that *T. brucei* spp. are even more susceptible to TAO inhibitors than *T. congolense* (Ebiloma et al., 2018a), due to differences in their mitochondrial pathways, it would be worth revisiting the wider trypanocidal activities of **56** (for the structures of compounds **56–60**, see **Figure 7**).

Cassia nigricans is a herbal plant used to treat various fevers in Nigeria. The methanol extract of the whole plant yielded an antiplasmodial compound, emodin **(57)**, an anthraquinone with an IC_{50} of 10.8 μg/mL in chloroquine-resistant *P. falciparum* strain K1 (Obodozie et al., 2004). In another study **57** was isolated from a methanol stem bark extract of another plant from the same genus, *C. siamea,* and confirmed to have strong activity against multidrug-resistant *P. falciparum* K1 strain (IC_{50} of 5 μg/mL) (Ajaiyeoba et al., 2008). Such independent confirmation of the activity is obviously important but unfortunately rare, in part because such data are harder to publish.

The crude hexane and ethyl acetate extracts of the leaves of *Crateva adansonii* showed moderate anti-trypanosomal activity with a MIC of 12.5 μg/mL (Igoli et al., 2012). In a further study, purpurin-18 ethyl ester **(58)**, an anthraquinone derivative, was isolated from the extracts of the leaves of the related species *C. adansonii* and displayed a MIC of 6.25 μM against *T. brucei*. Molecular docking studies of **58** with some trypanosomal proteins revealed glutathione synthetase as its most likely target, followed by sterol-14α-demethylase and riboflavin kinase, with riboflavin kinase showing highest affinity (Igoli et al., 2014), although these models need experimental verification.

The methanol extract of the roots of *Abrus precatorius* was recently reported to possess antileishmanial activity with IC_{50} ± SD of 22.2 ± 0.54 μg/mL. The ethyl acetate fraction of the extract yielded two antileishmanial isoflavanquinones identified as abruquinone A **(59)** and abruquinone B **(60)**, which displayed identical activity against *L. major* (IC_{50} ± SD 6.35 ± 0.005 and 6.32 ± 0.008 μg/mL, respectively) and *L. tropica* (IC_{50} 6.29 ± 0.015 and 6.31 ± 0.005 μg/mL, respectively) (Okoro et al., 2020).

Phenolics

Phenolics represent a diverse class of compounds whose structures contain at least one hydroxyl substituent on an aromatic ring. They include phenyl propanoids, benzoquinones, phenolic acids, acetophenones, phenylacetic acids, hydroxycinnamic acids, phenylpropenes, coumarins and isocoumarins, chromones, naphtoquinones, xanthones, stilbenes, anthraquinones, lignans, neolignans, lignins, and condensed tannins; and have been reported to have various medicinal properties including antioxidant, anticancer, anti-inflammatory, boosting immunity, etc. Phenolics are widely distributed in the plant kingdom.

The antiprotozoal activity of the crude extract fractions and isolated tannins of *Terminalia avicennoides* and *Anogeissus leiocarpus* have been investigated along other Nigerian medicinal plants (Shuaibu et al., 2008a,b,c). Using PicoGreen as flourimetric monitor, the IC_{50} of the compounds against chloroquine-sensitive *P. falciparum* 3D7 was determined and all showed moderate activity: castalagin, **61** (10.57 μg/mL); ellagic acid, **62** (12.14 μg/mL); flavogallonic acid, **63** (8.89 μg/mL); punicalagin, **64** (9.42 μg/mL) and terchebulin, **65** (8.89 μg/mL). None of the compounds showed cross resistance to chloroquine (Shuaibu et al., 2008b). The compounds were also tested against trypanosome species *T. brucei brucei*, *T. b. ambience*, *T. b. rhodesiense*, and *T. evansi* and showed slightly higher activity against *T. b. brucei* with MICs of 22.5, 7.5, and 27.5 μg/mL for **61**, **63**, and **65**, respectively. However, the compounds displayed low antileishmanial activity with **61**, isolated from *Anogeissus leiocarpus*, being the most active with MIC of 55 μg/mL against *L. aethiopica*. Further morphological examination and electron microscopy revealed cell swelling and changes in the ultrastructure of organelles in *L. aethiopica* promastigotes exposed to **61** (Shuaibu et al., 2008a). All the tannins showed an MIC of ≥1,500 μg/mL against Newborn Mouse Heart Fibroblast cells in a cytotoxicity assay, suggesting good antiparasitic selectivity (Shuaibu et al., 2008a). The stem extract of *Euphorbia poisonii* yielded scoparone **66**, a coumarin with strong activity against *T. brucei* (MIC = 1.56 μg/mL) (Igoli et al., 2011) (for the structures of compounds **61–66**, see **Figure 8**).

Glycosides

Glycosides have one or more sugar moieties bonded through the anomeric carbon to a non-sugar group. The glycosidic bond can be carbon (C-glycosides, e.g., mangiferin, **G1**), oxygen (e.g., Luteolin-7-*O*-glucuronide, **G2**), sulfur (in thioglycosides e.g., Sinigrin, **G3**) or nitrogen (in glycosylamines e.g., adenosine, **G4**) (**Figure 9**). The sugar moiety is called the glycone and may contain one or more sugar groups, while the non-sugar group is the aglycone or genin part of the glycoside. According to their glycone moieties, glycosides are grouped into glucosides, fructosides, ribosides, glucuronides (glucuronnoside). Classification can also be based on the orientation of the glycosidic bond, α-glycosides have their glycosidic bond below the plane of the cyclic sugar moiety (glycone) e.g., methyl-α-Dglucopyranoside, **G5**, whereas when the glycosidic bond lies above the plane of the glycone a β-glycoside is formed e.g., methyl-β-D-glucopyranoside, **G6** (**Figure 9**). Classification of glycosides can also be based on their aglycone moieties e.g., steroid (cardiac) glycosides, coumarin glycosides, anthraquinone glycosides, saponins etc. The medicinal properties of glycosides have been exploited extensively for the treatment of heart diseases and as antibiotics, for example streptomycin, kanamycin and neomycin (Kren and Martinkova, 2001).

Okunji et al. isolated a bioactive saponin, identified as Spiroconazole A (**67**), from the methanol extracts of the seed pulp of two "soap tree" species, *Dracaena mannii* and *D.*

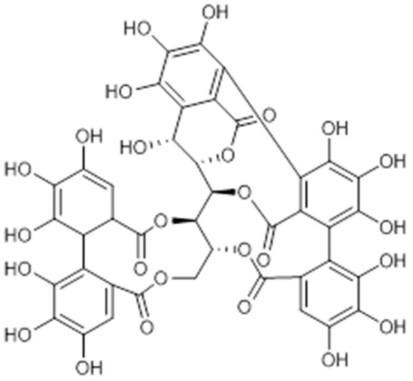

61. Castalgin

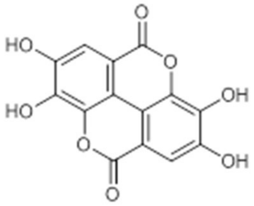

62. Ellagic acid

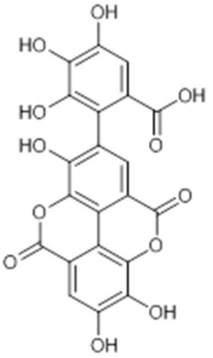

63. Flavogallonic acid dilactone

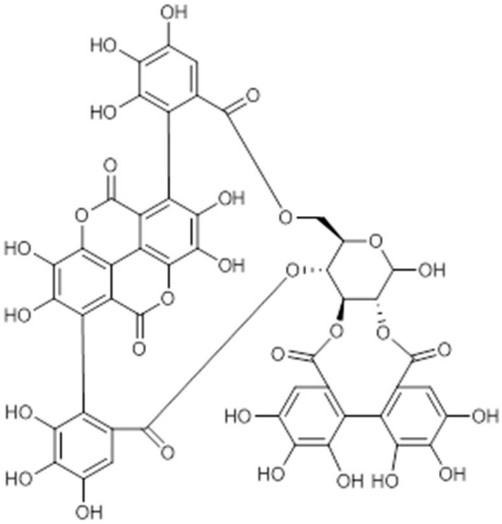

64. Punicalagin

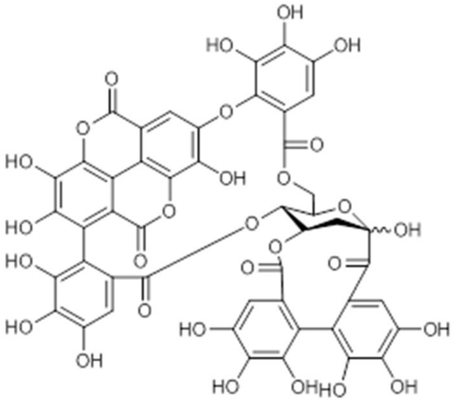

65. Terchebulin

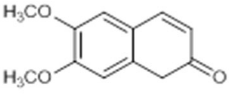

66. Scoparone

FIGURE 8 | Structure of phenolic compounds isolated from Nigerian plants with selected antiprotozoal activity.

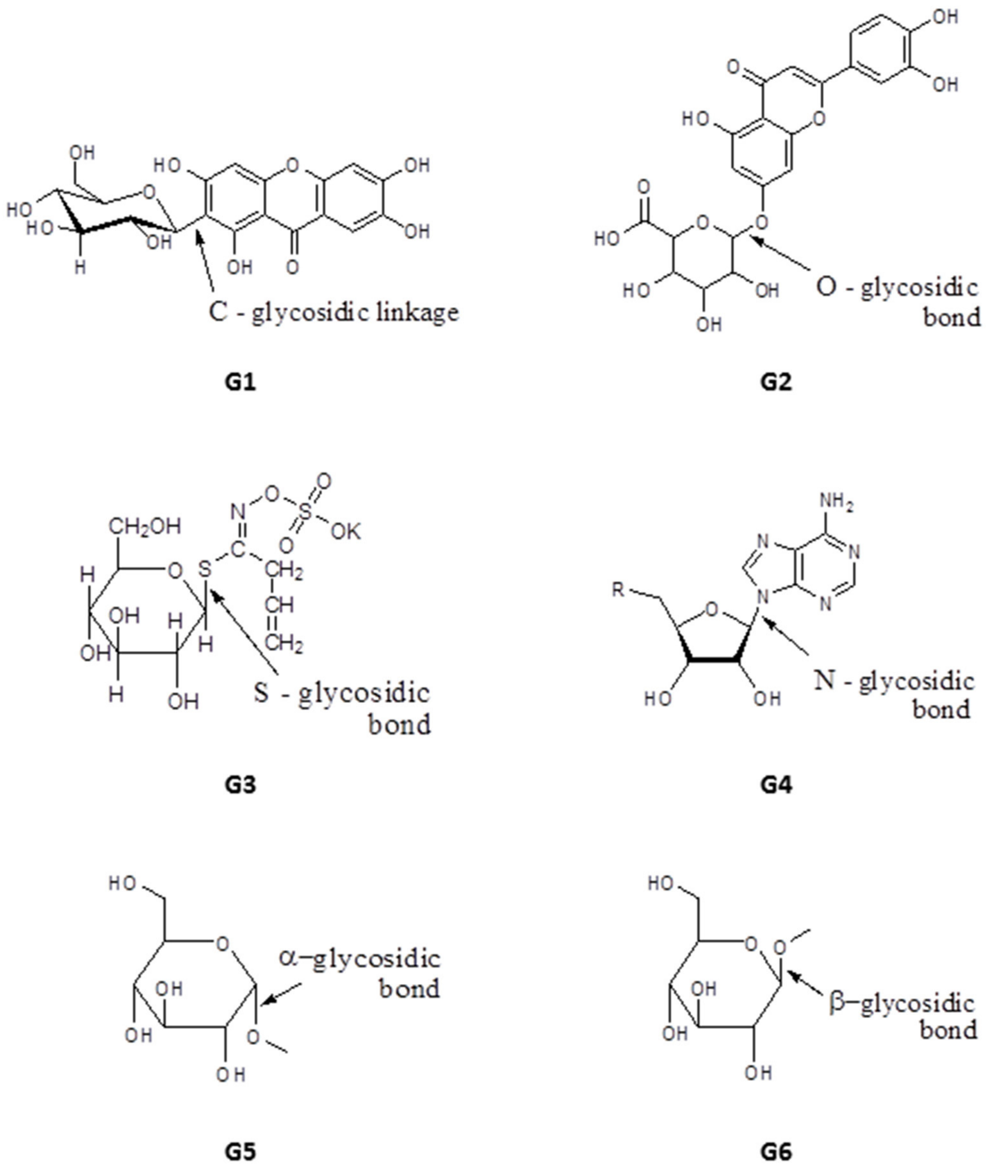

FIGURE 9 | Structure of basic skeleton of glycoside sub-groups showing different glycosidic bonds.

arborea. The compound showed significant antileishmanial and antimalarial activity (Okunji et al., 1996). Three glycosides were obtained from the methanol extract of the leaves of *Stachytarpheta cayennensis*, which is used in Central and West Africa to treat malaria. The compounds were identified as apigenin (**68**), stigmasterol glucoside (**69**) and verbascoside (**70**), and displayed significant ($P < 0.05$) antimalarial activity *in vitro* and *in vivo*, with a dose of 2.5 mg/Kg lowering *P. falciparum* parasitaemia in mice by up to 89% (Ifeoma Chinwude et al., 2016). Two antikinetoplastid irodid glucosides were isolated from the methanol leaf extracts of *Vitex grandifolia.* Agnuside (**71**) showed an IC_{50} of 5.38 and 13.7 µg/mL against *L. donovani* amastigotes in THP1 cells and against *T. brucei*, respectively. However, the other compound, bartsioside (**72**), was essentially inactive, with IC_{50} >25 µg/mL against both parasites, suggesting that the hydroxyl group on C-6 and/or the *p*-hydroxy benzoic acid moiety at C-8 are probably essential for activity (Bello et al., 2018) (for the structures of compounds **67–72**, see **Figure 10**).

Peptides

Peptides are organic polymers made of amino acid monomers in which the alpha amino group (-NH) of one acid is linked to the alpha carboxylic acid group (-CO_2H) of another through an amide bond. Peptides that contain more than 100 amino acid monomers are called proteins. Peptides have been isolated from roots, seeds, flowers, stems, and leaves of plants (Nawrot et al., 2014).

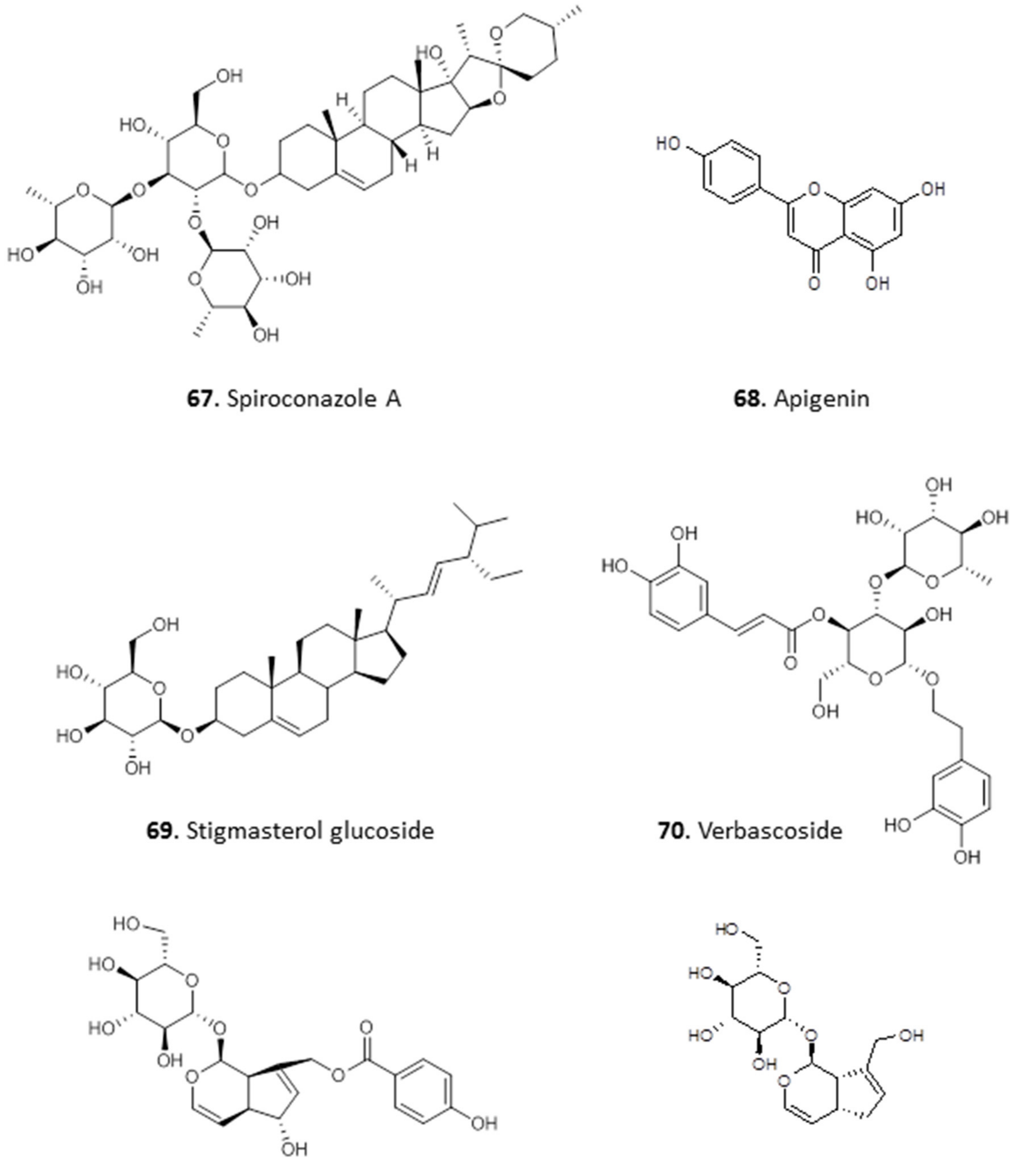

67. Spiroconazole A

68. Apigenin

69. Stigmasterol glucoside

70. Verbascoside

71. Agnuside

72. Bartsioside

FIGURE 10 | Structure of glycosides isolated from Nigerian plants with selected antiprotozoal activity.

One antitrypanosomal peptide from Nigerian plants is aurantiamide acetate (**73**). It was isolated from the leaves of *Crateva adansonii*, and displayed an MIC of 25 μM against *T. brucei.* Further investigation into its possible mechanism of action through docking studies revealed strong binding interactions between **73** and trypanosomal enzymes sterol-14α-demethylase and trypanothione reductase (Igoli et al., 2014). Nwodo et al. (2015a) isolated two dipeptides from the methanol extract of the roots of *Zapoteca portoricensis* elucidated as saropeptide (**74**) and anabellamide (**75**). Compound **74** was selectively active against *T. brucei* with IC_{50} of 3.63 μM, but had only low activity against *Trypanosoma cruzi* ($IC_{50} = 41.6$ μM), which is the causative agent of Chagas disease. On the other hand, **75** displayed moderate activity against both species (*T.*

brucei $IC_{50} = 12.2\,\mu M$; *T. cruzi* $IC_{50} = 16.1\,\mu M$). Although both compounds displayed relatively low toxicity against mammalian L6 cells with IC_{50} values of 92.1 μM and 71.2 μM for **74** and **75**, respectively, this does not seem to leave sufficient selectivity for further development (Nwodo et al., 2014) (for the structures of compounds **73–75**, see **Figure 11**).

Fatty Acid and Steroids

The ethyl acetate and methanol extracts of the leaves of *Carica papaya* exhibited promising antiplasmodial activity with IC_{50} values of 2.6 and 12.8 μg/mL in chloroquine-sensitive *P. falciparum* D10 strain, respectively. Bioassay-guided fractionation of the ethyl acetate extracts yielded two fatty acids, 9,12,15-octadecatrienoic acid (linolenic acid; **76**) and 9,12-octadecadienoic acid (linoleic acid; **77**) with IC_{50} values of 3.58 ± 0.22 and 6.88 ± 0.02 μg/mL in *P. falciparum*. The compounds were not cross-resistant to chloroquine but the level of selectivity for the parasite over Chinese hamster ovarian cells is quite low (SI = 7.43–15.27) and does not invite extensive *in vivo* follow-on (Melariri et al., 2011). In our own investigations of antiprotozoal natural products from Nigeria and beyond, we have reported the isolation of Taccalonolide A (**78**) and its novel derivative, Taccalonolide A 12-propanoate (**79**), from the tubers of *Tacca leontopetaloides*. Both compounds showed activity against *T. brucei*, with EC_{50} ± SEM of 11.4 ± 0.39 and 3.1 ± 0.09 μg/mL. However, we have observed remarkable antitrypanosomal activity in one of the impure fractions (EC_{50} = 0.76 ± 0.03 μg/mL), suggesting a need for further investigation of *T. leontopetaloides* as a source of more potent antiparasitic agents (Dike et al., 2016) (for the structures of compounds **76–79**, see **Figure 12**).

Chlorophyll Metabolites

Extracts of the leaves of *Crateva adansonii* has yielded two pheophorbides, Pyropheophorbide A **(80)** and Ethyl pyropheophorbide A **(81)**. Both **80** and **81** showed potent antitrypanosomal activity with an MIC of 6.5 μM. Both compounds showed strong binding interactions with trypanosomal riboflavin kinase and trypanothione reductase in molecular docking studies (Igoli et al., 2014). The ethyl acetate leaf extracts of *Newbouldia laevis* showed interesting activity against *T. b. brucei* (EC_{50} ± SEM = 4.2 ± 0.7 μg/mL). Two similar antitrypanosomal compounds, pheophytin A **(82)** and pheophytin B **(83)**, with EC_{50} ± SEM values of 25.0 ± 2.8 and 1.58 ± 0.09 μg/mL, respectively, were identified from the extract of *Newbouldia laevis* (Family Bignoniaceae); both compounds were non-toxic to HEK cells (Ebiloma et al., 2017) (for the structures of compounds **80–83**, see **Figure 13**).

COMPOUNDS FROM OTHER NIGERIAN NATURAL SOURCES

Lichen

A depside, 4-(1-hydroxylprop-1-en-1-yl) atranorin-1-carboxylic acid (**84**), was obtained from *Dirinaria picta*, a lichen epiphyte of *Elaeis guineensis* palm trees, collected in Port Harcourt, Rivers State. It showed some antiplasmodial activity with IC_{50} value of 37 μg/mL, and low toxicity to mammalian HeLa cells (IC_{50} = 100 μg/mL) (Afieroho et al., 2018).

Nigerian Red Propolis

We have previously reported on the efficacy of Nigerian red propolis (NRP) in rats experimentally infected with *T. brucei*. Treatment with NRP at 400 and 600 mg/Kg/day resulted in significantly ($P < 0.05$) reduced parasitaemia and improved blood parameters (higher PCV and HBC) and weight gain compared to a DMSO treated control group (Nweze et al., 2017). This prompted further investigation into the active compounds in NRP. The ethanol extract of NRP yielded antitrypanosomal compounds, most of which were flavones and flavonoids (Omar et al., 2016). The MIC against *T. brucei* was determined for three of the compounds: medicarpin, **85** (3.12 μg/mL); pinocembrin, **86** (12.5 μg/mL), and propolin D, **87** (3.12 μg/mL) and EC_{50} values were determined for the remaining compounds. The most active of these were 8-prenylnarigenin (**88**), macarangin (**89**), and vestitol (**90**), with EC_{50} ± SEM of 6.1 ± 0.1, 7.8 ± 0.1, 8.3 ± 0.1 μg/mL, respectively. Other compounds with significant antitrypanosomal activity included calycosin (**91**; EC_{50} ± SEM = 10.0 ± 0.44 μg/mL), 6-prenylnaringenin (**92**; EC_{50} ± SEM = 11.4 ± 0.34 μg/mL), and riverinol (**93**; EC_{50} ± SEM = 16.24 ± 0.24 μg/mL). Interestingly, none of the compounds showed cross-resistance to pentamidine and melarsoprol but **93** was significantly more active against two multi-drug resistant strains (3.6 and 2.5-fold, respectively ($p < 0.001$) (Omar et al., 2016), from which either the TbAT1/P2 (Carter et al., 1999) or the HAPT1/AQP2 drug transporter (Alghamdi et al., 2020) had been deleted (for the structures of compounds **84–93**, see **Figure 14**).

BARRIERS TO NATURAL PRODUCT-BASED RESEARCH AND DRUG DISCOVERY

The challenges facing the development of new natural products-derived drugs discussed in this review are not peculiar to Nigeria alone but to many developing countries with richer natural resources than scientific infrastructure and funding. The identification of a pharmacologically active compound from a medicinal plant in a systematic and efficient manner is not an easy task. However, there is no gainsaying that specialized molecules of plant origin are the spine of our modern-day pharmacopeia, or that traditional herbal remedies continue to be successful in the treatment of many ailments. Notwithstanding this historic significance in drug discovery and development, there has been a steady drop in the number of new natural product-based drugs entering into clinical use in the past 30 years (Wright, 2019). The modern-day pharmaceutical industry has largely shifted from the traditional natural product-based drug discovery strategy to one that could easily be created with a synthetic approach such as combinatorial chemistry combined with high-throughput screening. Consequently, synthetic compounds are currently being favored by the global pharmaceutical industries over the natural product-based compounds as a more tractable alternative

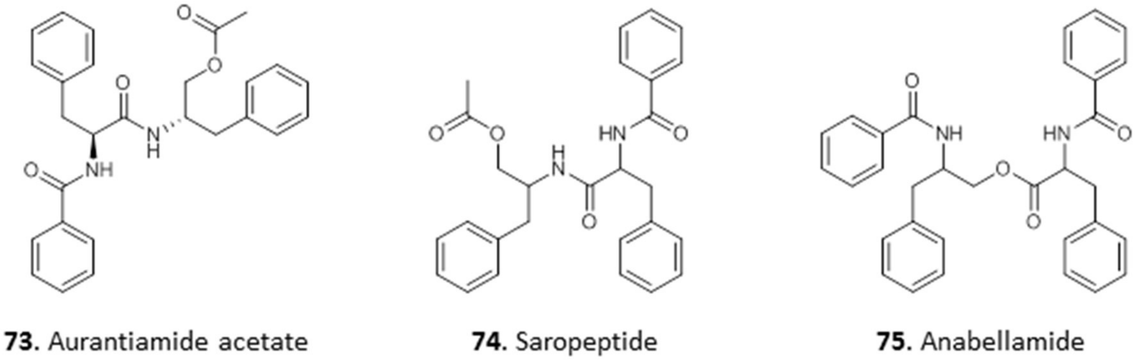

73. Aurantiamide acetate

74. Saropeptide

75. Anabellamide

FIGURE 11 | Structure of peptides isolated from Nigerian plants with selected antiprotozoal activity.

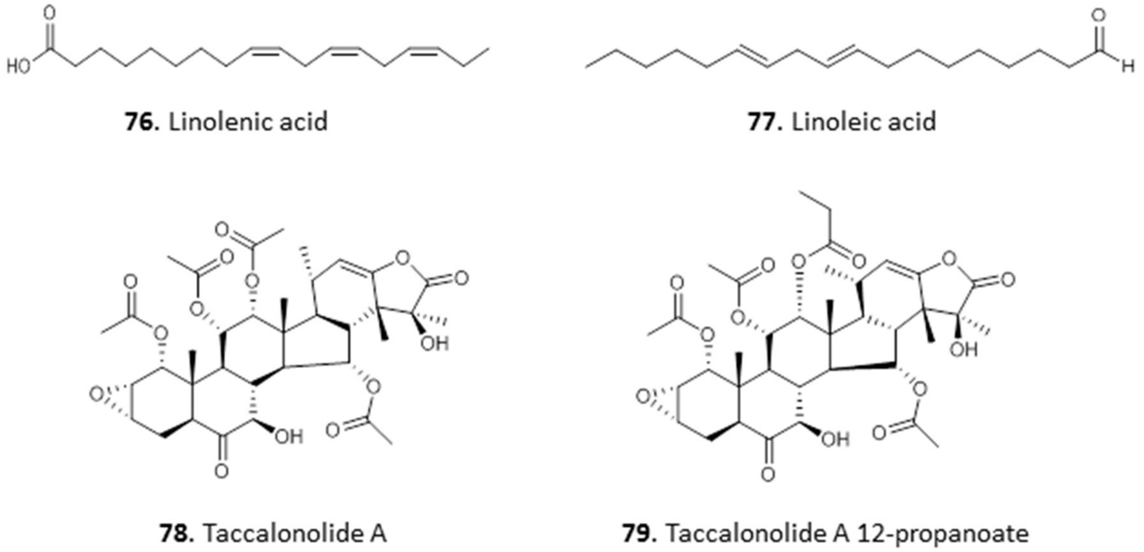

76. Linolenic acid

77. Linoleic acid

78. Taccalonolide A

79. Taccalonolide A 12-propanoate

FIGURE 12 | Structures of fatty acids and steroids isolated from Nigerian plants with selected antiprotozoal activity.

in their use to develop new drugs. This is a consequence of a combination of many factors.

Complexity of Isolation Processes

Perhaps the most challenging impediments to natural product-based drug discovery over the past few decades are the resource intensiveness and the tedious purification protocols involved in the identification of bioactive molecules from the highly complex mixtures that are the initial extracts. When purified, the isolated bioactive compound is often obtained in tiny amounts (usually a few milligrams) that are unlikely to go the full length of the drug discovery process, especially in protocols involving the use of large cultures such as required for metabolomic studies and other assessments of drug action, or for *in vivo* studies. This is compounded by the fact that this tedious process frequently yields subversive compounds with multiple behavior in assays such as covalent bond formation, chelation, membrane perturbation, and redox activity, which are collectively known as Pan Assay Interference compoundS (PAINS) (Baell and Holloway, 2010; Baell, 2016). Prominent natural (plant) products that frequently contain PAINS include catechols, quinones, phenolic manic bases, and hydroxyphenylhydrazones (Baell, 2016). PAINS and PAINS-like, despite a possible nano- or micro-molar potency, lack a distinct biological mechanism, exhibit poor SAR or optimisability, and thus have very low prospects for clinical development (Baell, 2015). Thus, it is important to utilize assay techniques that will screen-out PAINS and to carry out structural studies of complexes of hits-target molecules and structure-activity optimization studies of the hits (Baell and Nissink, 2018; Balogun et al., 2019).

Lack of Precision and Mechanism

In addition to the challenge of the tedious process flow from the screening of medicinal plants to the isolation of new bioactive principle(s) with low yield, the subsequent determination of the exact mechanism of action of the isolated compound requires

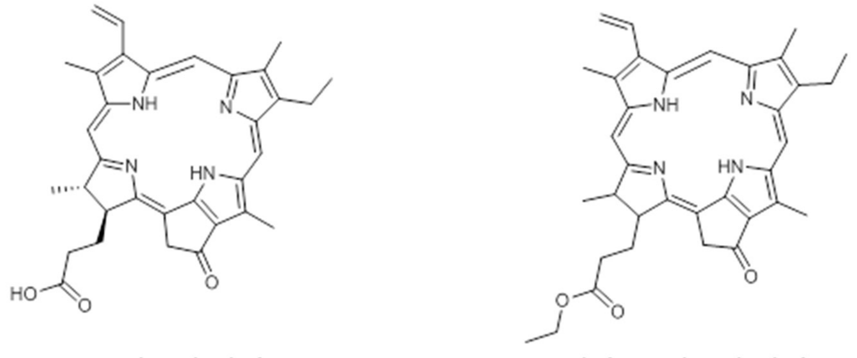

80. Pyropheophorbide A

81. Ethyl pyropheophorbide A

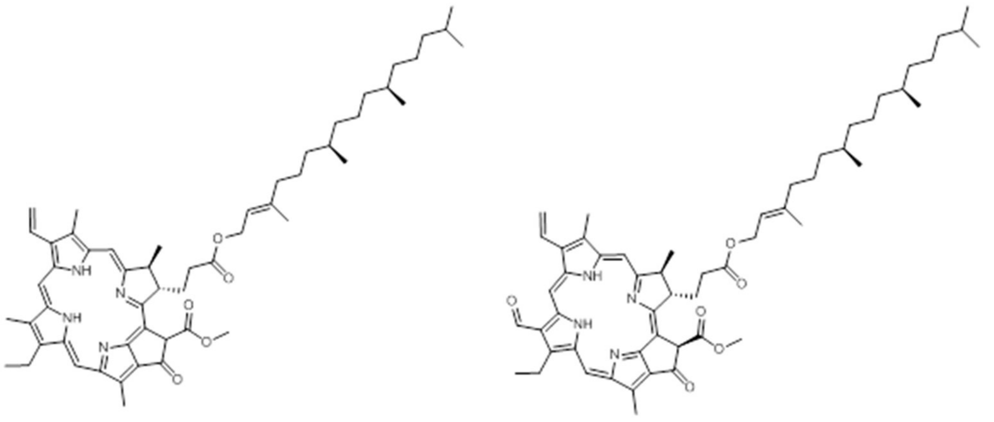

82. Pheophytin A

83. Pheophytin B

FIGURE 13 | Structures of chlorophyll metabolites isolated from Nigerian plants with selected antiprotozoal activity.

expertise, experience, the appropriate research environment (infrastructure and equipment) and substantial amounts of funding. But due to research and resource limitations, finding a robust and viable lead candidate for the drug discovery pipeline has become a challenging scientific task. Hence, the majority of the research efforts aimed at identifying drug leads end up at the level of crude extract testing stage, which is not very informative and fails to give a usable measure of activity as the concentration of the active molecule(s) is unknown. Moreover, the amount of active compound in the extract is likely to be different between preparations.

In addition, the therapeutic effect of natural remedies may be through immuno-modulation rather than a direct antimicrobial activity. Assaying for antimicrobial properties, a compound with immunomodulatory properties will not show bioactivity *in vitro* during the traditional bioassay-guided screening of the complex extract mixture and will be ruled out. This is a serious impediment to determining the exact active principle in a medicinal plant or its extract unless the primary screen is based on an infectious animal model. Furthermore, some natural compounds may exhibit a combined or synergistic effect in their mode of action. Hence, such compounds, when isolated in their pure form, may not appear to have promising activity in the bioassay screening protocol (Druilhe et al., 1988; Williamson, 2001; Wagner, 2011). A prominent example is the case of the presently leading anti-malarial plant, *Artemisia annua*. Herbal teas prepared from the dried leaves of *A. annua* are found to be 6–18 folds more effective at killing the *Plasmodium* parasites than the isolated active anti-malarial agent, artemisinin (Wan et al., 1992; Wright et al., 2010). These possible scenarios can frustrate efforts toward identifying the bioactive compound(s) from some plants/extracts that show initial promise.

Novelty of Isolated Natural Compounds

The majority of compounds isolated from plants will have been previously reported, and such compounds lacking novelty are unlikely to be advanced into drug development and less likely to lead to academic publications. In fact, over 200,000 isolated natural compounds have so far been reported in the scientific literature using the traditional natural product extraction and purification methods (Walsh and Yang, 2017). This means that there is a high probability of identifying known rather than novel molecules using the standard bioassays guided fractionation and

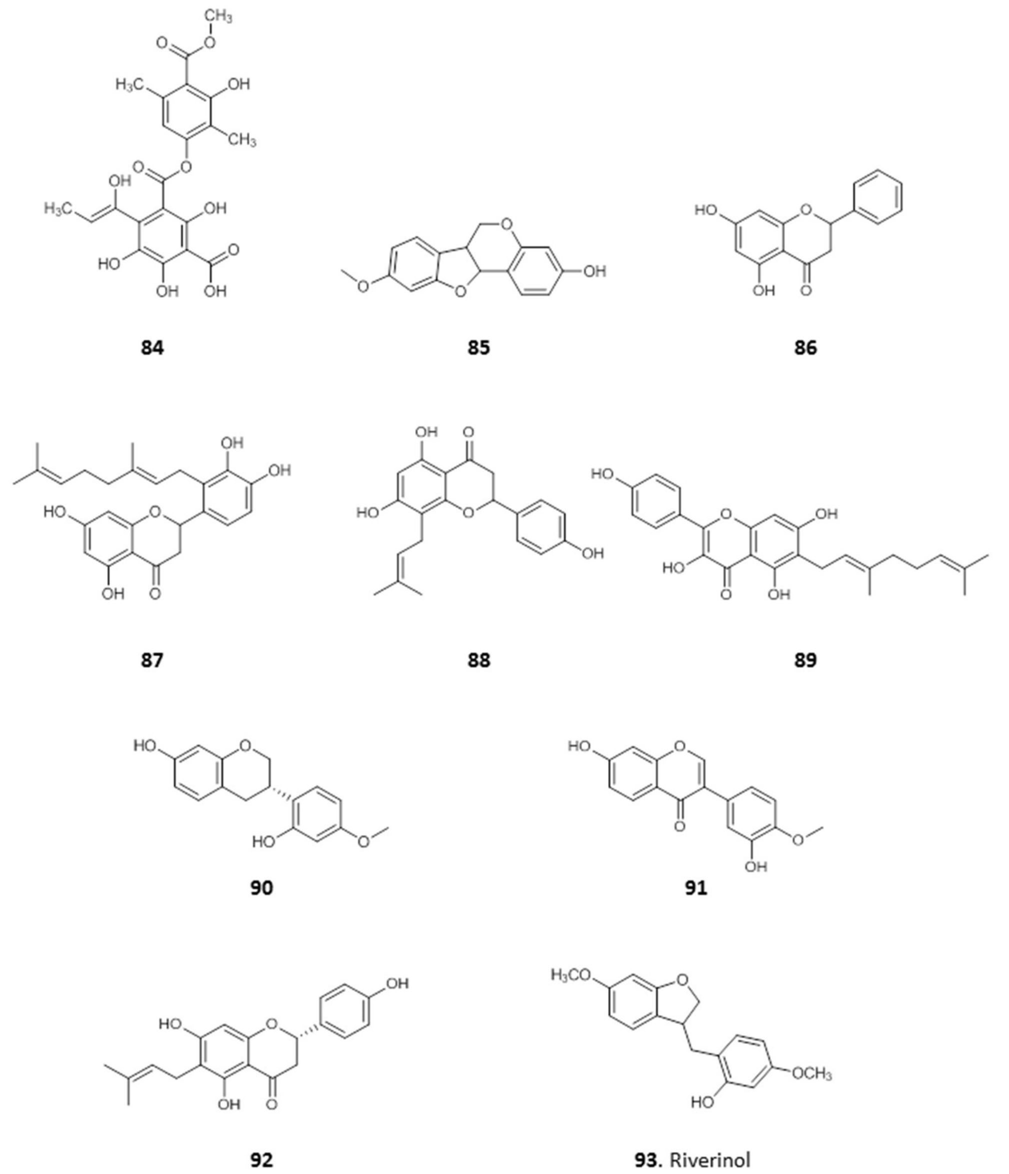

FIGURE 14 | Structures of natural compounds isolated from Nigerian red propolis and lichen with selected antiprotozoal activity.

identification of lead compounds, thus often giving a poor return on investment.

A range of processes known as "dereplication," based on hyphenated techniques are standard procedures that are applied in plant metabolomics to avoid the re-isolation and re-characterization of known compounds by eliminating known entities (Carnevale Neto et al., 2016; Hubert et al., 2017; Kildgaard et al., 2017). However, to systematically extract vital pieces of information from acquired data, chemometric tools are needed for the dereplication process. This is because biological samples such as plant extracts are complex in nature, with a very large concentration range. This notwithstanding, the GC-MS-based technique for identifying non-targeted metabolites is one of the emerging techniques to improve the dereplication method (Carnevale Neto et al., 2016), but the procedures involved can be time-consuming and resource-intensive.

Undesirable Physical Properties

Another fundamental challenge is that in the drug discovery setting, it is predicted that poor absorption becomes probable when there are more than 5 H-bond donors, 5 H-bond acceptors, the molecular weight of the compound is above 500, or the calculated partition coefficient (cLog P) is >5 (Lipinski et al., 1997). This is known as Lipinski's rule of five. Unfortunately, most natural compounds do not obey this rule; hence, in the eye of the pharmaceutical companies, many natural compounds do not have the required drug-like characteristics, based on their structure. This is in addition to the solubility issues associated with some natural compounds; many are not completely soluble in the assay's aqueous environment, which can interfere with the reproducibility of research results. Many of these issues require increased troubleshooting in standardized assays, leading to higher costs and a high rejection rate for otherwise active compounds.

Other undesirable physical properties of natural compounds like colouration make them more difficult to assay using contemporary drug discovery strategies such as the standardized high throughput screening of compound libraries, compared with synthetic compounds. For instance, deep colouration of some plant compounds may interfere with the assay methods involving color change in spectroscopic/colorimetric determinations.

Finally, it is imperative to highlight the huge structural complexities of many natural compounds, making synthesizing them and their derivatives very difficult (Harvey, 2000; Strohl, 2000; Li and Vederas, 2009), and the construction of a large series of related compounds for SAR or pharmacodynamic optimization almost impossible. The combination of these problems diminishes the prospects of using compounds of natural origins for drug discovery.

Accessibility of Plant Materials and Poor Documentation of Herbal Remedies

Another significant challenge is the absence of specific government legislation and international agreements regulating the access to plant resources in the biodiversity-rich flora. Some of the indigenous plants used in folklore are rapidly disappearing due to indiscriminate use, deforestation, and deliberate bush-burning for farming activities and hunting. This makes subsequent access to these important medicinal plants for follow-up studies increasingly difficult, which in turn discourage further natural products research. This is a serious problem particularly in developing countries where the implementation of the Nagoya protocol is yet to be fully implemented. The Nagoya Protocol on Access and Benefit Sharing (ABS) is a build-up on the Convention on Biological Diversity (CBD), which is a key regulatory document for sustainable development aimed at developing national strategies for the conservation and sustainable use of biological diversity in all countries (Convention on Biological Diversity, 2010; Buck and Hamilton, 2011). Contrary to the opinions of critics of ABS who think it will create bottlenecks for scientific research and impedes new discoveries, the implementation of the Nagoya Protocol in Nigeria will prevent the extinction of plants from which useful medicinal products can be discovered. There can also be difficulty in physically gaining access to the natural habitats of these essential medicinal plants. This challenge is due to the absence of accessible roads to the often remote rural areas where the majority of these important medicinal plants are located.

Furthermore, traditional herbal remedies, which are justly regarded as the basis for modern medicine, are based on oral tradition (folklore) and much of that is usually shrouded in secrecy and a reluctance to divulge vital information regarding the preparation or use of the key medicinal plants. To keep the traditional healers in business, the pharmacologically active plants are often used in combination with other plants to prepare the herbal remedies, in order to obfuscate the true source of the medication. Unfortunately, but understandably, permission for the associated extracts/concoctions to be used for scientific research and innovation is frequently denied.

Limited Research Funding

As explained above, the processes involved in the isolation, purification, and chemical characterization of the bioactive agents are expensive and time-consuming. Together with potential worries about continuous access to sufficient quantities of the natural compound, this makes the pharmaceutical industries less interested in investing in such ventures. This lack of investment is further compounded by the problem of reduced funding of academic research institutions, which hinders the provision of modern state-of-the-art facilities including such that enable long-term storage and (high-throughput) screening of natural products-based compound libraries. Scale-up of the production of natural compounds with complex (stereo)-chemistry that elude viable commercial synthesis can be another major hurdle, especially for compounds from relatively rare and/or slow-growing plants, or where very low or variable concentrations of active compounds are found in the primary plant source.

Climate Change

Climate change has also already negatively impacted the natural product-based drug discovery effort. Environmental issues, like desert encroachment due to global warming, have led to the extinction of many valuable land species including key medicinal plants. In addition, there is the disappearance of marine organisms of high medicinal value due to water pollution and temperature increases.

These challenges can be overcome when there is a huge national, multidisciplinary approach to drug discovery efforts, and synergy between academia and pharmaceutical companies. This requires concerted efforts from the appropriate government ministries and parastatals, academia and research institutes, and the pharmaceutical companies. When the lack of resources is factored into this challenge, it is imperative to establish a close partnership between local research institutions and local or foreign pharmaceutical companies.

RECOMMENDATIONS AND FUTURE PERSPECTIVE

In this review we described and listed scores of phytochemicals isolated from Nigerian medicinal plants and, importantly, they have been reported to possess therapeutic capabilities against important Africa-endemic parasitic infectious diseases. The focus of this paper has been on the protozoan infections- malaria, African trypanosomiasis, and leishmaniasis. Apart from malaria, these diseases are popularly termed neglected tropical diseases (NTDs) because they disproportionately affect the economically bottom billion (world's poorest) people; consequently, drug discovery for such diseases is not of interest to the pharmaceutical industry due to projected lack of profitable return on the investments. Since the majority of the people affected by these diseases are Africans, it would be fulfilling, and indeed transformational, to see a few of the novel natural compounds that are highlighted in this review make their ways to the market as drugs of choice for malaria or some of the NTDs. It should be noted that, according to the World Health Organization, Nigeria is the country most afflicted by malaria, shouldering 25% of the global malaria burden (World Health Organization, 2019). In order words, the goal of this review is not only to provide a compendium of antiparasitic natural compounds from Nigerian bioresources, but also to stimulate and channel research focus toward further development of the compounds to marketable drugs. If successful, this will become a leading example of solutions to African problems from Africa, and by Africans. However, at this moment, every single compound listed here is still experimental and in the early stages of drug development. The subsequent paragraphs provide perspectives and steps to be taken toward genuine clinical development of African natural compounds for African diseases.

Advancement of the Compounds Through the Drug Development Pipeline (DDP)

The process of drug development takes 7–15 years of hard work, huge funding, and is comprised of four stages each having multiple steps: (1) the discovery stage, involving successful demonstration of the compound as being potent against the target parasites; (2) the pre-clinical development stage where the compounds are tried in various laboratory animals to understand their safety, pharmacology, *in vivo* potency, and possible mechanism of action; (3) the clinical development stage, which is comprised of five phases of clinical trials; and (4) the approval stage where regulatory bodies evaluate the accumulated data of stages 1–3 and take a decision to approve or reject their use as medicines for specific applications. Certainly, some of the 93 compounds highlighted fulfill the *prima facie* criteria to move from stage 1 to stage 2, and considerations such as compound availability, ease of synthesis, selectivity, solubility, stability etc. would aid in prioritization. It is logical to explore a shortlist further and progress them through the DDP with the overall aim to get new approved medicine(s) for malaria and some NTDs, from the current collection of compounds, although further discovery efforts, coupled to innovative dereplication, remain important. To achieve this, and in order to enhance success within shorter time, it is recommendable that Nigerian scientists form interdisciplinary networks internally, with collaborators within as well as outside the continent, and with pharmaceutical companies and/or international non-profit organizations. One highly encouraging and very recent development is the partnership between the Drugs for Neglected Diseases initiative (DNDi), Institut Pasteur Korea (IPK) and Fundación MEDINA, funded by La Caixa Health Research [Drugs for Neglected Diseases initiative (DNDi), 2020]. This will allow the screening of the large natural compounds library of Fundación MEDINA against *Leishmania* and *T. cruzi* by IPK, using state-of-the art high-throughput imaging technologies. This development shows the added value of large compound libraries held and curated centrally, over the dispersed efforts of many small-scale efforts, when it comes to securing the needed funding and infrastructure. A national or, better, regional repository for medicinal plant species, extracts, and natural compounds should be established in Nigeria as a partner for international funders and consortia. While much excellent work has been done by the individual laboratories, results are not necessarily comparable between them, due to differences in test strains and procedures, among other factors. Nor are compounds produced this way, on a necessarily small scale and often sub-optimally stored, easily available for further experimentation. The proposed facility should be curated by a Society of Herbal Medicine, with State funding.

Exploration of Microbes and Marine Organisms for More Novel Compounds

In addition to length of time needed, the attrition rate in DDP is very high. The number of starting compounds that enters the DDP drastically thins out after each step and stage- from available records only 2.5% of stage-1 compounds make it to stage 2, of which just 2% pass to stage 3, and 5% of the stage-3 candidates may eventually end up getting approved to be in the market (Kola and Landis, 2004; Tonkens, 2005). The implication is that only 1 out of 250 candidate compounds that enters stage 2 may become an approved medicine. With limited funding for even stage 2 studies, critical selection of what enters this stage is essential to decrease the attrition rate. Bearing in mind the aforementioned, it is advisable to continue natural compound discovery and screening against target pathogens, in a coordinated fashion, in order to expand this collection of compounds. Since most of the compounds at hand thus far are from plants, we are recommending that we expand our efforts to less-explored sources of medicinal natural products such as the microbial and marine organisms. Nigeria, and Africa at large, is blessed with diverse ecosystems that are habitats to myriad aquatic and non-aquatic macro- and micro-organisms. While the antibiotic penicillin is a leading example of drugs from microorganisms, the analgesic drug, Ziconotide was the first approved medicine from marine source. After these, numerous drugs from microbial and marine sources have been successfully brought to market (Molinski et al., 2009; Lobanovska and Pilla, 2017).

Formulate a Virtual Library of the Compounds

The recent advances in the fields of medicinal chemistry, and computer and information technology have resulted in a synergy that birthed an emerging field known as computational medicinal chemistry, which basically entails *in silico* approaches for the curation, design, development, testing and synthesis of pharmacologically active compounds. *In silico* curation is simply the act of keeping a collection of information in computers and making it accessible to interested people remotely, this is simply a database or virtual library. This can be organized relatively easily and even after the establishment of a national repository as described above, would retain its relevance if actively curated and updated by the research community. Numerous relevant virtual libraries/databases are available containing information on parasites—e.g., for genomes PlasmoDB (https://plasmodb.org/plasmo/app), TriTrypDB (https://tritrypdb.org/tritrypdb/app); metabolism (http://vm-trypanocyc.toulouse.inra.fr/; Shameer et al., 2015) and small molecules, e.g., ChEMBL (https://www.ebi.ac.uk/chembl/), PubChem (https://pubchem.ncbi.nlm.nih.gov/), and the recently curated TrypInDB (http://trypindb.biomedinformri.com/; Vijayakumar et al., 2020). Likewise, we propose the formulation of a virtual library/database to contain the 93 highlighted antiparasitic natural products of Nigerian origin, as well as information on all tested but inactive natural compounds in order to minimize needless replication, and continue to expand the library as new pharmacologically active compounds are being discovered. This database should further be expanded in collaboration, first to include natural compounds reported from other African nations, and potentially from other continents. As the database will be freely accessible, it will promote collaborations with scientists within and outside the continent and accelerate the process of drug discovery. As it grows, it should be explored whether this database could be linked to other resources such as TrypInDB or CHEMBL in order to promote its visibility.

Setting Up Synthesis Programs for the Various Compounds

Except for compounds **84–93**, which were isolated from Nigerian propolis, the remaining compounds (**1–83**) enumerated were isolated from plants (**Table 1**) and as expected, the final yields are very low. Environmental concerns and low yield are major hurdles for drug development efforts using natural products from plants because large amounts of compounds are usually required, particularly at stages 2 and 3. Moreover, even after approval of a final drug, it would be hard to envisage a good business model built on a product whose supply is reliant on its isolation from plants in very small quantities—especially since the cost per treatment for NTDs must necessarily be low. Thus, in many cases the crux of a profitable and sustainable drug development plan for plant products may be to be able to establish a process for its large-scale production independent of the native plant. Above, we have already highlighted the ease of synthesis as one of the shortlisting criteria for progressing natural compounds down the DDP, and efforts should be initiated to establish economically viable synthesis routes for the selected candidates. To the best of our knowledge, so far only compound **7** (fagaronine) has an established chemical synthesis procedure (Rivaud et al., 2012) and funding of natural compounds synthesis research should be part of the national scientific strategy of Nigeria.

Most of the natural compounds are structurally and stereochemically complex, making their chemical synthesis routes difficult, and often non-feasible in terms of cost/yield. For such compounds, the alternative to chemical synthesis will be synthetic biology. The use of the synthetic biology approach requires: (1) identification of the biosynthesis pathways and the genes encoding the enzymes for every step in the biosynthesis of the secondary metabolite (natural compound) in the native organism, (2) heterologous assemblage of the pathway in a suitable microorganism, which is achieved by cloning and transformation of all the genes into the surrogate microorganism, (3) establishment of a fermentation technology for the large-scale culture and production of the product, and (4) a standardized large-scale purification method for the produced secondary metabolite. Recently, the antimalarial terpenoid artemisinin, which is natively produced by the plant *Artemisia annua*, has been partially produced in yeast and *Escherichia coli* through synthetic biology, yielding quantities as high as 25 g/L of culture (Tsuruta et al., 2009; Paddon et al., 2013). Another interesting example of synthetic biology is the complete biosynthesis of noscapine in *Saccharomyces cerevisiae*. Noscapine is a potential anticancer drug that is natively derived from the opium poppy plant, *Papaver somniferum*. Engineering *S. cerevisiae* by introducing 10-gene clusters from opium poppy, which encodes 30 enzymes in the biosynthetic pathway of noscapine resulted in the heterologous production of the compound with a yield 2.2 mg/L (Li et al., 2018).

CONCLUSION

Over the years, the bioactivity of extracts from Nigerian flora has been established, thus validating the widespread use of herbal medicine in that part of the world. Bioactivity-driven fractionation efforts have now identified candidate drug leads in some of these plants, including potential antiprotozoal agents. However, the number of pure compounds isolated and investigated is still low, despite the thousands of preliminary studies showing promising activity of plant extracts. Furthermore, the translation of *in vitro* anti-protozoal activity of the already identified phytochemicals into *in vivo* preclinical studies has also been slow. While the challenges affecting the development of these natural compounds are numerous and complex, they can be surmounted by concerted collaborative and multi-disciplinary efforts, especially when underpinned by a national strategy and the establishment of a natural compounds repository to enable it. This will facilitate competitive bids for international funding, enable synergy between academia and pharmaceutical companies and not-for-profit organizations, and would bridge many gaps in scientific infrastructure. Thus, while investment in research in developing countries like Nigeria is indispensable, coordination within the country is essential for the development of international collaborations. Nigeria has the raw materials and resources as well as the drive and the talent in their scientific community, now is the time to translate these into valuable pharmaceutics that benefit its population.

AUTHOR CONTRIBUTIONS

MU, JI, and GE conceptualized the project. MU, GE, HK, NI, and EB contributed to the development and writing of the manuscript. HK, JI, and EB contributed in validating, reviewing, and supervising the project. All authors contributed to the article and approved the submitted version.

FUNDING

MU was in receipt of a PhD studentship from the Petroleum Technology Development Fund of Nigeria. EB was a Fulbright Fellow and also supported by an Africa Center of Excellence for Development (ACE Impacts) project through funding to the Africa Center of Excellence for Neglected Tropical Disease and Forensic Biotechnology (ACENTDFB), Ahmadu Bello University, Nigeria.

REFERENCES

Abiodun, O. O., Gbotosho, G. O., Ajaiyeoba, E. O., Brun, R., and Oduola, A. M. (2012). Antitrypanosomal activity of some medicinal plants from Nigerian ethnomedicine. *Parasitol. Res.* 110, 521–526. doi: 10.1007/s00436-011-2516-z

Achan, J., Talisuna, A. O., Erhart, A., Yeka, A., Tibenderana, J. K., Baliraine, F. N., et al. (2011). Quinine, an old anti-malarial drug in a modern world: role in the treatment of malaria. *Malar. J.* 10:144. doi: 10.1186/1475-2875-10-144

Adebayo, J. O., and Krettli, A. U. (2011). Potential antimalarials from Nigerian plants: a review. *J. Ethnopharmacol.* 133, 289–302. doi: 10.1016/j.jep.2010.11.024

Afieroho, O. E., Noundou, X. S., Krause, R. W., Isaacs, M., Olley, L., Hoppe, H. C., et al. (2018). An antiplasmodial depside from a nigerian lichen dirinaria picta, epiphytic on the oil palm elaeis guineense. *Rev. Boliv. Química* 35. Available online at: http://www.redalyc.org/articulo.oa?id=426355610005

Afolayan, M., Srivedavyasasri, R., Asekun, O. T., Familoni, O. B., Orishadipe, A., Zulfiqar, F., et al. (2018). Phytochemical study of *Piliostigma thonningii*, a medicinal plant grown in Nigeria. *Med. Chem. Res.* 27, 2325–2330. doi: 10.1007/s00044-018-2238-1

Afolayan, M., Srivedavyasasri, R., Asekun, O. T., Familoni, O. B., and Ross, S. A. (2019). Chemical and biological studies on *Bridelia ferruginea* grown in Nigeria. *Nat. Prod. Res.* 33, 287–291. doi: 10.1080/14786419.2018.1440225

Agbedahunsi, J., and Elujoba, A. (1998). Grandifolin from khaya gradifoliola stem bark. *Niger. J. Nat. Prod. Med.* 2, 34–36. doi: 10.4314/njnpm.v2i1.11779

Agbedahunsi, J. M., Elujoba, A. A., Makinde, J. M., and Oduda, A. M. J. (1998). Antimalarial activity of *Khaya grandifoliola* stem-bark. *Pharm. Biol.* 36, 8–12. doi: 10.1076/phbi.36.1.8.4613

Ajaiyeoba, E. O., Ashidi, J. S., Okpako, L. C., Houghton, P. J., and Wright, C. W. (2008). Antiplasmodial compounds from *Cassia siamea* stem bark extract. *Phyther. Res.* 22, 254–255. doi: 10.1002/ptr.2254

Ajaiyeoba, E. O., Ogbole, O. O., Abiodun, O. O., Ashidi, J. S., Houghton, P. J., and Wright, C. W. (2013). Cajachalcone: an antimalarial compound from cajanus cajan leaf extract. *J. Parasitol. Res.* 2013:703781. doi: 10.1155/2013/703781

Alghamdi, A. H., Munday, J. C., Campagnaro, G. D., Gurvic, D., Svensson, F., Okpara, C. E., et al. (2020). Positively selected modifications in the pore of TBAQP2 allow pentamidine to enter *trypanosoma brucei*. *Elife* 9:e56416. doi: 10.7554/ELIFE.56416

Alhaji, U. I., Samuel, N. U., Aminu, M., Chidi, A. V., Umar, Z. U., Umar, U. A., et al. (2014). *In vitro* antitrypanosomal activity, antioxidant property and phytochemical constituents of aqueous extracts of nine Nigerian medicinal plants. *Asian Pacific J. Trop. Dis.* 4, 348–355. doi: 10.1016/S2222-1808(14)60586-7

Amit Koparde, A., Chandrashekar Doijad, R., and Shripal Magdum, C. (2019). "Natural products in drug discovery," in *Pharmacognosy - Medicinal Plants*, eds S. Perveen and A. Al-Taweel (IntechOpen). doi: 10.5772/intechopen.82860

Amoa Onguéné, P., Ntie-Kang, F., Lifongo, L., Ndom, J., Sippl, W., and Mbaze, L. (2013). The potential of anti-malarial compounds derived from African medicinal plants, part I: a pharmacological evaluation of alkaloids and terpenoids. *Malar. J.* 12:449. doi: 10.1186/1475-2875-12-449

Amusan, O. O. G., Adesogan, E. K., and Makinde, J. M. (1996). Antimalarial active principles of *Spathodea campanulata* stem bark. *Phyther. Res.* 10, 692–693. doi: 10.1002/(SICI)1099-1573(199612)10:8<692::AID-PTR928>3.0.CO;2-O

Baell, J. B. (2015). Screening-based translation of public research encounters painful problems. *ACS Med. Chem. Lett.* 6, 229–234. doi: 10.1021/acsmedchemlett.5b00032

Baell, J. B. (2016). Feeling nature's PAINS: natural products, natural product drugs, and Pan Assay Interference Compounds (PAINS). *J. Nat. Prod.* 79, 616–628. doi: 10.1021/acs.jnatprod.5b00947

Baell, J. B., and Holloway, G. A. (2010). New substructure filters for removal of Pan Assay Interference Compounds (PAINS) from screening libraries and for their exclusion in bioassays. *J. Med. Chem.* 53, 2719–2740. doi: 10.1021/jm901137j

Baell, J. B., and Nissink, J. W. M. (2018). Seven year itch: Pan-Assay Interference Compounds (PAINS) in 2017—utility and limitations. *ACS Chem. Biol.* 13, 36–44. doi: 10.1021/acschembio.7b00903

Balogun, E. O., Inaoka, D. K., Shiba, T., Tsuge, C., May, B., Sato, T., et al. (2019). Discovery of trypanocidal coumarins with dual inhibition of both the glycerol kinase and alternative oxidase of *Trypanosoma brucei brucei*. *FASEB J.* 33, 13002–13013. doi: 10.1096/fj.201901342R

Bankole, A. E., Adekunle, A. A., Sowemimo, A. A., Umebese, C. E., Abiodun, O., and Gbotosho, G. O. (2016). Phytochemical screening and *in vivo* antimalarial activity of extracts from three medicinal plants used in malaria treatment in Nigeria. *Parasitol. Res.* 115, 299–305. doi: 10.1007/s00436-015-4747-x

Bekono, B. D., Ntie-Kang, F., Onguéné, P. A., Lifongo, L. L., Sippl, W., Fester, K., et al. (2020). The potential of anti-malarial compounds derived from African medicinal plants: a review of pharmacological evaluations from 2013 to 2019. *Malar. J.* 19:183. doi: 10.1186/s12936-020-03231-7

Bello, O., Ogbesejana, A., and Osibemhe, M. (2018). Iridoid glucosides from *Vitex grandifolia* displayed anti-inflammatory and antileishmania effects and structure activity relationship. *J. Appl. Sci. Environ. Manag.* 22:373. doi: 10.4314/jasem.v22i3.14

Bello, O. M., Zaki, A. A., Khan, S. I., Fasinu, P. S., Ali, Z., Khan, I. A., et al. (2017). Assessment of selected medicinal plants indigenous to West Africa for antiprotozoal activity. *South African J. Bot.* 113, 200–211. doi: 10.1016/j.sajb.2017.08.002

Bribi, N. (2018). Pharmacological activity of alkaloids: a review. *Asian J. Bot.* 1, 1–6. doi: 10.1016/S2221-1691(12)60116-6

Buck, M., and Hamilton, C. (2011). The nagoya protocol on access to genetic resources and the fair and equitable sharing of benefits arising from their utilization to the convention on biological diversity. *Rev. Eur. Community Int. Environ. Law* 20, 47–61. doi: 10.1111/j.1467-9388.2011.00703.x

Calixto, J. B. (2019). The role of natural products in modern drug discovery. *An. Acad. Bras. Cienc.* 91(Suppl. 3):e20190105. doi: 10.1590/0001-3765201920190105

Carnevale Neto, F., Pilon, A. C., Selegato, D. M., Freire, R. T., Gu, H., Raftery, D., et al. (2016). Dereplication of natural products using GC-TOF mass spectrometry: improved metabolite identification by spectral deconvolution ratio analysis. *Front. Mol. Biosci.* 3:59. doi: 10.3389/fmolb.2016.00059

Carter, N. S., Barrett, M. P., and De Koning, H. P. (1999). A drug resistance determinant in *Trypanosoma brucei*. *Trends Microbiol.* 7, 469–471. doi: 10.1016/S0966-842X(99)01643-1

Chukwujekwu, J. C., Smith, P., Coombes, P. H., Mulholland, D. A., and van Staden, J. (2005). Antiplasmodial diterpenoid from the leaves of *Hyptis suaveolens*. *J. Ethnopharmacol.* 102, 295–297. doi: 10.1016/j.jep.2005.08.018

Convention on Biological Diversity (2010). *About The Nagoya Protocol on Access and Benefit Sharing*. Available online at: https://www.cbd.int/abs/about/ (accessed November 21, 2020).

Cragg, G. M., and Newman, D. J. (2005). Biodiversity: a continuing source of novel drug leads. *Pure Appl. Chem.* 77, 7–24. doi: 10.1351/pac200577010007

de Koning, H. P. (2017). Drug resistance in protozoan parasites. *Emerg. Top. Life Sci.* 1, 627–632. doi: 10.1042/etls20170113

Dias, D. A., Urban, S., and Roessner, U. (2012). A historical overview of natural products in drug discovery. *Metabolites* 2, 303–336. doi: 10.3390/metabo2020303

Dike, V. T., Vihiior, B., Bosha, J. A., Yin, T. M., Ebiloma, G. U., de Koning, H. P., et al. (2016). Antitrypanosomal activity of a novel taccalonolide from the tubers of tacca leontopetaloides. *Phytochem. Anal.* 27, 217–221. doi: 10.1002/pca.2619

Drugs for Neglected Diseases initiative (DNDi) (2020). *Fundación MEDINA, DNDi, and Institut Pasteur Korea Announce New Funding from "la Caixa" Health Research for Research Partnership to Discover New Natural Products against Leishmaniasis and Chagas Disease*. Available online at: https://dndi.org/press-releases/2020/fundacion-medina-dndi-institut-pasteur-korea-announce-new-funding-from-la-caixa-health-research-to-discover-new-natural-products-against-leishmaniasis-chagas-disease/ (accessed October 11, 2020).

Druilhe, P., Brandicourt, O., Chongsuphajaisiddhi, T., and Berthe, J. (1988). Activity of a combination of three cinchona bark alkaloids against *Plasmodium falciparum in vitro*. *Antimicrob. Agents Chemother*. 32, 250–254. doi: 10.1128/AAC.32.2.250

Ebiloma, G. U., Ayuga, T. D., Balogun, E. O., Gil, L. A., Donachie, A., Kaiser, M., et al. (2018a). Inhibition of trypanosome alternative oxidase without its N-terminal mitochondrial targeting signal (ΔMTS-TAO) by cationic and non-cationic 4-hydroxybenzoate and 4-alkoxybenzaldehyde derivatives active against *T. brucei* and *T. congolense*. *Eur. J. Med. Chem*. 150, 385–402. doi: 10.1016/j.ejmech.2018.02.075

Ebiloma, G. U., Igoli, J. O., Katsoulis, E., Donachie, A. M., Eze, A., Gray, A. I., et al. (2017). Bioassay-guided isolation of active principles from Nigerian medicinal plants identifies new trypanocides with low toxicity and no cross-resistance to diamidines and arsenicals. *J. Ethnopharmacol*. 202, 256–264. doi: 10.1016/j.jep.2017.03.028

Ebiloma, G. U., Katsoulis, E., Igoli, J. O., Gray, A. I., and De Koning, H. P. (2018b). Multi-target mode of action of a Clerodane-type diterpenoid from *Polyalthia longifolia* targeting African trypanosomes. *Sci. Rep*. 8:4613. doi: 10.1038/s41598-018-22908-3

Ekpendu, T. O., Akah, P. A., Adesomoju, A. A., and Okogun, J. I. (1994). Antiinflammatory and antimicrobial activities of mitracarpus scaber extracts. *Pharm. Biol*. 32, 191–196. doi: 10.3109/13880209409082992

El-Najjar, N., Gali-Muhtasib, H., Ketola, R. A., Vuorela, P., Urtti, A., and Vuorela, H. (2011). The chemical and biological activities of quinones: overview and implications in analytical detection. *Phytochem. Rev*. 10, 353–370. doi: 10.1007/s11101-011-9209-1

Enechi, O. C., Amah, C. C., Okagu, I. U., Ononiwu, C. P., Azidiegwu, V. C., Ugwuoke, E. O., et al. (2019). Methanol extracts of *Fagara zanthoxyloides* leaves possess antimalarial effects and normalizes haematological and biochemical status of Plasmodium berghei-passaged mice. *Pharm. Biol*. 57, 577–585. doi: 10.1080/13880209.2019.1656753

Ezenyi, I. C., Salawu, O. A., Kulkarni, R., and Emeje, M. (2014). Antiplasmodial activity-aided isolation and identification of quercetin-4'-methyl ether in *Chromolaena odorata* leaf fraction with high activity against chloroquine-resistant *Plasmodium falciparum*. *Parasitol. Res*. 113, 4415–4422. doi: 10.1007/s00436-014-4119-y

Falodun, A., Imieje, V., Erharuyi, O., Joy, A., Langer, P., Jacob, M., et al. (2014). Isolation of antileishmanial, antimalarial and antimicrobial metabolites from *Jatropha multifida*. *Asian Pac. J. Trop. Biomed*. 4, 374–378. doi: 10.12980/APJTB.4.2014C1312

Félix-Silva, J., Giordani, R. B., Silva-Jr., A. A., Da, Zucolotto, S. M., and Fernandes-Pedrosa, M. D. F. (2014). *Jatropha gossypiifolia L. (Euphorbiaceae)*: a review of traditional uses, phytochemistry, pharmacology, and toxicology of this medicinal plant. Evidence-based complement. *Altern. Med*. 2014, 1–32. doi: 10.1155/2014/369204

Gill, L. S. (1992). *Ethnomedical Uses of Plants in Nigeria*. Nigeria: University of Benin Press.

Harvey, A. (2000). Strategies for discovering drugs from previously unexplored natural products. *Drug Discov. Today* 5, 294–300. doi: 10.1016/S1359-6446(00)01511-7

Hubert, J., Nuzillard, J.-M., and Renault, J.-H. (2017). Dereplication strategies in natural product research: How many tools and methodologies behind the same concept? *Phytochem. Rev*. 16, 55–95. doi: 10.1007/s11101-015-9448-7

Ifeoma Chinwude, E., Peter Achunike, A., and Charles Ogbonnaya, O. (2016). Antiplasmodial Activity and some active compounds from *Stachytarpheta cayennensis Vahl. (Verbenaceae)* leaf fractions. *Anti Infective Agents* 14, 132–138. doi: 10.2174/2211352514666160725130125

Igoli, J. O., Grey, A. I., Clements, C. J., and Mouad, H. A. (2011). "Anti-trypanosomal activity and cytotoxicity of some compounds and extracts from nigerian medicinal plants," in *Phytochemicals - Bioactivities and Impact on Health* (London: IntechOpen), 375–388. doi: 10.5772/26203

Igoli, N., Clements, C., Singla, R., Igoli, J., Uche, N., and Gray, A. (2014). Antitrypanosomal activity & docking studies of components of *Crateva adansonii* DC leaves: novel multifunctional scaffolds. *Curr. Top. Med. Chem*. 14, 981–990. doi: 10.2174/1568026614666140324120006

Igoli, N., Obanu, Z., Gray, A., and Clements, C. (2011). Bioactive diterpenes and sesquiterpenes from the rhizomes of wild ginger (*Siphonochilus aethiopicus* (Schweinf) B.L Burtt). *Afr. J. Tradit. Complement. Altern. Med*. 9, 88–93. doi: 10.4314/ajtcam.v9i1.13

Igoli, N. P., Gray, A. I., Clements, C. J., Igoli, J. O., Nzekwe, U., and Singla, R. K. (2012). Scientific investigation of antitrypanosomal activity of *Crateva adansonii* DC leaves extracts. *Indo Glob. J*. 2, 226–229. http://www.iglobaljournal.com/wp-content/uploads/2012/11/1.-Ngozichukwuka-Peace-Igoli-et-al-2012.pdf

Imieje, V., Falodun, A., Zaki, A., Ali, Z., Imieje, V., Khan, I., et al. (2017). Antiprotozoal and cytotoxicity studies of fractions and compounds from enantia chlorantha. *Trop. J. Nat. Prod. Res*. 1, 89–94. doi: 10.26538/tjnpr/v1i2.8

Irobi, O. N., and Daramola, S. O. (1993). Antifungal activities of crude extracts of *Mitracarpus villosus* (*Rubiaceae*). *J. Ethnopharmacol*. 40, 137–140. doi: 10.1016/0378-8741(93)90059-E

Iwu, M. M. (2014). *Handbook of African Medicinal Plants, 2nd Edn*. Boca Raton, FL: CRC Press.

Iwu, M. M., and Kiayman, D. L. (1992). Evaluation of the *in vitro* antimalarial activity of *Picralima nitida* extracts. *J. Ethnopharmacol*. 36, 133–135. doi: 10.1016/0378-8741(92)90012-G

Kassim, O. O., Loyevsky, M., Elliott, B., Geall, A., Amonoo, H., and Gordeuk, V. R. (2005). Effects of root extracts of *Fagara zanthoxyloides* on the *in vitro* growth and stage distribution of *Plasmodium falciparum*. *Antimicrob. Agents Chemother*. 49, 264–268. doi: 10.1128/AAC.49.1.264-268.2005

Kildgaard, S., Subko, K., Phillips, E., Goidts, V., de la Cruz, M., Díaz, C., et al. (2017). A dereplication and bioguided discovery approach to reveal new compounds from a marine-derived fungus *Stilbella fimetaria*. *Mar. Drugs* 15:253. doi: 10.3390/md15080253

Kola, I., and Landis, J. (2004). Can the pharmaceutical industry reduce attrition rates? *Nat. Rev. Drug Discov*. 3, 711–716. doi: 10.1038/nrd1470

Kren, V., and Martinkova, L. (2001). Glycosides in medicine: "the role of glycosidic residue in biological activity". *Curr. Med. Chem*. 8, 1303–1328. doi: 10.2174/0929867013372193

Li, J. W. H., and Vederas, J. C. (2009). Drug discovery and natural products: end of an era or an endless frontier? *Science* 325, 161–165. doi: 10.1126/science.1168243

Li, Y., Li, S., Thodey, K., Trenchard, I., Cravens, A., and Smolke, C. D. (2018). Complete biosynthesis of noscapine and halogenated alkaloids in yeast. *Proc. Natl. Acad. Sci. U.S.A*. 115, E3922–E3931. doi: 10.1073/pnas.1721469115

Lifongo, L. L., Simoben, C. V., Ntie-Kang, F., Babiaka, S. B., and Judson, P. N. (2014). A bioactivity versus ethnobotanical survey of medicinal plants from Nigeria, West Africa. *Nat. Products Bioprospect*. 4, 1–19. doi: 10.1007/s13659-014-0005-7

Lipinski, C. A., Lombardo, F., Dominy, B. W., and Feeney, P. J. (1997). Experimental and computational approaches to estimate solubility and permeability in drug discovery and development settings. *Adv. Drug Deliv. Rev*. 23, 3–25. doi: 10.1016/S0169-409X(96)00423-1

Lobanovska, M., and Pilla, G. (2017). Penicillin's discovery and antibiotic resistance: lessons for the future? *Yale J. Biol. Med*. 90, 135–145.

Makinde, J. M., Adesogan, E. K., and Amusan, O. O. G. (1987). The schizontocidal activity of *Spathodea campanulata* leaf extract on *Plasmodium berghei* berghei in mice. *Phyther. Res*. 1, 65–68. doi: 10.1002/ptr.2650010205

Makinde, J. M., Amusan, O. O. G., and Adesogan, E. K. (1988a). The antimalarial activity of *Spathodea campanulata* stem bark extract on *Plasmodium berghei* berghei in mice. *Planta Med*. 54, 122–125. doi: 10.1055/s-2006-962367

Makinde, J. M., Awe, S. O., and Agbedahunsi, J. M. (1988b). Effect of *Khaya grandifoliola* extract on *Plasmodium berghei* berghei in mice. *Phyther. Res*. 2, 30–32. doi: 10.1002/ptr.2650020104

Melariri, P., Campbell, W., Etusim, P., and Smith, P. (2011). Antiplasmodial properties and bioassay-guided fractionation of ethyl acetate extracts from *Carica papaya* leaves. *J. Parasitol. Res*. 2011:104954. doi: 10.1155/2011/104954

Mesia, K., Tona, L., Mampunza, M., Ntamabyaliro, N., Muanda, T., Muyembe, T., et al. (2012). Antimalarial efficacy of a quantified extract of *Nauclea Pobeguinii* stem bark in human adult volunteers with diagnosed uncomplicated falciparum malaria. Part 2: a clinical phase IIB trial. *Planta Med*. 78, 853–860. doi: 10.1055/s-0031-1298488

Misra, P., Sashidhara, K. V., Singh, S. P., Kumar, A., Gupta, R., Chaudhaery, S. S., et al. (2010). 16α-hydroxycleroda-3,13 (14)Z-dien-15,16-olide from *Polyalthia longifolia*: a safe and orally active antileishmanial agent. *Br. J. Pharmacol*. 159, 1143–1150. doi: 10.1111/j.1476-5381.2009.00609.x

Molinski, T. F., Dalisay, D. S., Lievens, S. L., and Saludes, J. P. (2009). Drug development from marine natural products. *Nat. Rev. Drug Discov*. 8, 69–85. doi: 10.1038/nrd2487

Nakanishi, T., Suzuki, M., Saimoto, A., and Kabasawa, T. (1999). Structural considerations of NK109, an antitumor benzo[c]phenanthridine alkaloid. *J. Nat. Prod*. 62, 864–867. doi: 10.1021/np990005d

Nawrot, R., Barylski, J., Nowicki, G., Broniarczyk, J., Buchwald, W., and Gozdzicka-Józefiak, A. (2014). Plant antimicrobial peptides. *Folia Microbiol*. 59, 181–196. doi: 10.1007/s12223-013-0280-4

Newman, D. J., and Cragg, G. M. (2012). Natural products as sources of new drugs over the 30 years from 1981 to 2010. *J. Nat. Prod*. 75, 311–335. doi: 10.1021/np200906s

Newman, D. J., and Cragg, G. M. (2016). Natural products as sources of new drugs from 1981 to 2014. *J. Nat. Prod*. 79, 629–661. doi: 10.1021/acs.jnatprod.5b01055

Nnadi, C., Althaus, J., Nwodo, N., and Schmidt, T. (2018). A 3D-QSAR study on the antitrypanosomal and cytotoxic activities of steroid alkaloids by comparative molecular field analysis. *Molecules* 23:1113. doi: 10.3390/molecules23051113

Nnadi, C., Ebiloma, G., Black, J., Nwodo, N., Lemgruber, L., Schmidt, T., et al. (2019). Potent antitrypanosomal activities of 3-aminosteroids against African trypanosomes: investigation of cellular effects and of cross-resistance with existing drugs. *Molecules* 24:268. doi: 10.3390/molecules24020268

Nnadi, C., Nwodo Ngozi, J., Brun, R., Kaiser, M., and Schmidt, T. (2016). Antitrypanosomal alkaloids from *Holarrhena africana*. *Planta Med*. 81, S1–S381. doi: 10.1055/s-0036-1596866

Nnadi, C. O., Nwodo, N. J., Kaiser, M., Brun, R., and Schmidt, T. J. (2017). Steroid alkaloids from *Holarrhena africana* with strong activity against *Trypanosoma Brucei* rhodesiense. *Molecules* 22:1129. doi: 10.3390/molecules22071129

Nok, A. J. (2002). Azaanthraquinone inhibits respiration and *in vitro* growth of long slender bloodstream forms of *Trypanosoma congolense*. *Cell Biochem. Funct*. 20, 205–212. doi: 10.1002/cbf.948

Ntie-Kang, F., Onguéné, P., Lifongo, L. L., Ndom, J., Sippl, W., and Mbaze, L. (2014). The potential of anti-malarial compounds derived from African medicinal plants, part II: a pharmacological evaluation of non-alkaloids and non-terpenoids. *Malar. J*. 13:81. doi: 10.1186/1475-2875-13-81

Nvau, J. B., Alenezi, S., Ungogo, M. A., Alfayez, I. A. M., Natto, M. J., Igoli, J. O., et al. (2020). Antiparasitic and cytotoxic activity of bokkosin, a novel diterpene-substituted chromanyl benzoquinone from *Calliandra portoricensis*. *Front. Chem*. 8:574103. doi: 10.3389/fchem.2020.574103

Nweze, N. E., Okoro, H. O., Al Robaian, M., Omar, R. M. K., Tor-Anyiin, T. A., Watson, D. G., et al. (2017). Effects of nigerian red propolis in rats infected with *Trypanosoma brucei brucei*. *Comp. Clin. Path*. 26, 1129–1133. doi: 10.1007/s00580-017-2497-0

Nwodo, N., Ibezim, A., Ntie-Kang, F., Adikwu, M., and Mbah, C. (2015a). Anti-trypanosomal activity of Nigerian plants and their constituents. *Molecules* 20, 7750–7771. doi: 10.3390/molecules20057750

Nwodo, N., Okoye, F., Lai, D., Debbab, A., Kaiser, M., Brun, R., et al. (2015b). Evaluation of the *in vitro* trypanocidal activity of methylated flavonoid constituents of *Vitex simplicifolia* leaves. *BMC Complement. Altern. Med*. 15:82. doi: 10.1186/s12906-015-0562-2

Nwodo, N. J., Brun, R., and Osadebe, P. O. (2007). *In vitro* and *in vivo* evaluation of the antitrypanosomal activity of fractions of *Holarrhena africana*. *J. Ethnopharmacol*. 113, 556–559. doi: 10.1016/j.jep.2007.07.018

Nwodo, N. J., Okoye, F. B. C., Lai, D., Debbab, A., Brun, R., and Proksch, P. (2014). Two trypanocidal dipeptides from the roots of *Zapoteca portoricensis* (*fabaceae*). *Molecules* 19, 5470–5477. doi: 10.3390/molecules19055470

Obodozie, O. O., Okpako, L. C., Tarfa, F. D., Orisadipe, A. T., Okogun, J. I., Inyang, U. S., et al. (2004). Antiplasmodial principles from *Cassia nigricans*. *Pharm. Biol*. 42, 626–628. doi: 10.1080/13880200490902545

Ogbonna, J. C., Igbe, I., Erharuyi, O., Imieje, V. O., and Falodun, A. (2017). Biological activities of a macrocyclic diterpenoid isolated from the roots of *Jatropha gossypiifolia*. *J. African Assoc. Physiol. Sci*. 5, 111–120. https://www.ajol.info/index.php/jaaps/article/view/164946

Okombo, J., Ohuma, E., Picot, S., and Nzila, A. (2011). Update on genetic markers of quinine resistance in *Plasmodium falciparum*. *Mol. Biochem. Parasitol*. 177, 77–82. doi: 10.1016/j.molbiopara.2011.01.012

Okoro, E. E., Ahmad, M. S., Osoniyi, O. R., and Onajobi, F. D. (2020). Antifungal and antileishmanial activities of fractions and isolated isoflavanquinones from the roots of *Abrus precatorius*. *Comp. Clin. Path*. 29, 391–396. doi: 10.1007/s00580-019-03073-z

Okunji, C. O., Iwu, M. M., Ito, Y., and Smith, P. L. (2005). Preparative separation of indole alkaloids from the rind of *Picralima nitida* (Stapf) T. Durand & H. Durand by pH-zone-refining countercurrent chromatography. *J. Liq. Chromatogr. Relat. Technol*. 28, 775–783. doi: 10.1081/JLC-200048915

Okunji, C. O., Iwu, M. M., Jackson, J. E., and Tally, J. D. (1996). "Biological activity of saponins from two dracaena species," in *Advances in Experimental Medicine and Biology*, (Boston, MA: Springer), 415–428. doi: 10.1007/978-1-4899-1367-8_33

Oluyemi, W. M., Samuel, B. B., Kaehlig, H., Zehl, M., Parapini, S., D'Alessandro, S., et al. (2020). Antiplasmodial activity of triterpenes isolated from the methanolic leaf extract of *Combretum racemosum P. Beauv. J. Ethnopharmacol*. 247:112203. doi: 10.1016/j.jep.2019.112203

Omar, R. M. K., Igoli, J., Gray, A. I., Ebiloma, G. U., Clements, C., Fearnley, J., et al. (2016). Chemical characterisation of Nigerian red propolis and its biological activity against *Trypanosoma Brucei*. *Phytochem. Anal*. 27, 107–115. doi: 10.1002/pca.2605

Paddon, C. J., and Keasling, J. D. (2014). Semi-synthetic artemisinin: a model for the use of synthetic biology in pharmaceutical development. *Nat. Rev. Microbiol*. 12, 355–367. doi: 10.1038/nrmicro3240

Paddon, C. J., Westfall, P. J., Pitera, D. J., Benjamin, K., Fisher, K., McPhee, D., et al. (2013). High-level semi-synthetic production of the potent antimalarial artemisinin. *Nature* 496, 528–532. doi: 10.1038/nature12051

Rivaud, M., Mendoza, A., Sauvain, M., Valentin, A., and Jullian, V. (2012). Short synthesis and antimalarial activity of fagaronine. *Bioorg. Med. Chem*. 20, 4856–4861. doi: 10.1016/j.bmc.2012.05.061

Shameer, S., Logan-Klumpler, F. J., Vinson, F., Cottret, L., Merlet, B., Achcar, F., et al. (2015). TrypanoCyc: a community-led biochemical pathways database for *Trypanosoma brucei*. *Nuc. Acids Res*. 43, D637–D644. doi: 10.1093/nar/gku944

Shuaibu, M. N., Pandey, K., Wuyep, P. A., Yanagi, T., Hirayama, K., Ichinose, A., et al. (2008a). Castalagin from *Anogeissus leiocarpus* mediates the killing of leishmania *in vitro*. *Parasitol. Res*. 103, 1333–1338. doi: 10.1007/s00436-008-1137-7

Shuaibu, M. N., Wuyep, P. A., Yanagi, T., Hirayama, K., Tanaka, T., and Kouno, I. (2008b). The use of microfluorometric method for activity-guided isolation of antiplasmodial compound from plant extracts. *Parasitol. Res*. 102, 1119–1127. doi: 10.1007/s00436-008-0879-6

Shuaibu, M. N., Wuyep, P. T. A., Yanagi, T., Hirayama, K., Ichinose, A., Tanaka, T., et al. (2008c). Trypanocidal activity of extracts and compounds from the stem bark of *Anogeissus leiocarpus* and *Terminalia avicennoides*. *Parasitol. Res*. 102, 697–703. doi: 10.1007/s00436-007-0815-1

Strohl, W. R. (2000). The role of natural products in a modern drug discovery program. *Drug Discov. Today* 5, 39–41. doi: 10.1016/S1359-6446(99)01443-9

Tonkens, R. (2005). An overview of the drug development process. *Physician Exec*. 31, 48–52.

Tsuruta, H., Paddon, C. J., Eng, D., Lenihan, J. R., Horning, T., Anthony, L. C., et al. (2009). High-level production of amorpha-4,11-diene, a precursor of the antimalarial agent artemisinin, in *Escherichia coli*. *PLoS ONE* 4:e4489. doi: 10.1371/journal.pone.0004489

Tu, Y. (2011). The discovery of artemisinin (*qinghaosu*) and gifts from Chinese medicine. *Nat. Med*. 17, 1217–1220. doi: 10.1038/nm.2471

Vijayakumar, S., Ranjan, R., Kumar, R., and Das, P. (2020). TrypInDB: a searchable online resource of small molecule inhibitors against *Trypanosoma* sp. *Parasitol. Int*. 78:102131. doi: 10.1016/j.parint.2020.102131

Wagner, H. (2011). Synergy research: approaching a new generation of phytopharmaceuticals. *Fitoterapia* 82, 34–37. doi: 10.1016/j.fitote.2010.11.016

Walsh, C. T., and Yang, T. (2017). *Natural Product Biosynthesis: Chemical Logic and Enzymatic Machinery*. London: Royal Society of Chemistry.

Wan, Y. D., Zang, Q. Z., and Wang, J. S. (1992). Studies on the antimalarial action of gelatin capsule of *Artemisia annua*. *Chinese J. Parasitol. Parasit. Dis.* 10, 290–294.

Williamson, E. (2001). Synergy and other interactions in phytomedicines. *Phytomedicine* 8, 401–409. doi: 10.1078/0944-7113-00060

World Health Organization (2019). *World Malaria Report 2019*. Available online at: https://www.who.int/publications/i/item/9789241565721; https://www.who.int/news-room/fact-sheets/detail/malaria

Wright, C. W., Linley, P. A., Brun, R., Wittlin, S., and Hsu, E. (2010). Ancient Chinese methods are remarkably effective for the preparation of artemisinin-rich extracts of Qing Hao with potent antimalarial activity. *Molecules* 15, 804–812. doi: 10.3390/molecules15020804

Wright, G. D. (2019). Unlocking the potential of natural products in drug discovery. *Microb. Biotechnol.* 12, 55–57. doi: 10.1111/1751-7915.13351

Conflict of Interest: The authors declare that the research was conducted in the absence of any commercial or financial relationships that could be construed as a potential conflict of interest.

frontiers in Chemistry

ORIGINAL RESEARCH
published: 11 March 2021
doi: 10.3389/fchem.2021.628316

Photodynamic Antimicrobial Action of Asymmetrical Porphyrins Functionalized Silver-Detonation Nanodiamonds Nanoplatforms for the Suppression of *Staphylococcus aureus* Planktonic Cells and Biofilms

Yolande I. Openda[1], Bokolombe P. Ngoy[1,2] and Tebello Nyokong[1]*

[1]Institute for Nanotechnology Innovation, Department of Chemistry, Rhodes University, Makhanda, South Africa, [2]Département de Chimie, Université de Kinshasa, Kinshasa, Democratic Republic of the Congo

Edited by:
Simone Brogi,
Department of Pharmacy, University of Pisa, Italy

Reviewed by:
Shigetoshi Okazaki,
Hamamatsu University School of Medicine, Japan

****Correspondence:***
Bokolombe P. Ngoy
bokolombe@gmail.com

Specialty section:
This article was submitted to Medicinal and Pharmaceutical Chemistry,
a section of the journal Frontiers in Chemistry

Received: *11 November 2020*
Accepted: *03 February 2021*
Published: *11 March 2021*

Citation:
Openda YI, Ngoy BP and Nyokong T (2021) Photodynamic Antimicrobial Action of Asymmetrical Porphyrins Functionalized Silver-Detonation Nanodiamonds Nanoplatforms for the Suppression of Staphylococcus aureus *Planktonic Cells and Biofilms.*
Front. Chem. 9:628316.
doi: 10.3389/fchem.2021.628316

New asymmetrical porphyrin derivatives containing a *p*-hydroxyphenyl moiety and *p*-acetylphenyl moieties along with their functionalized silver-detonation nanodiamonds nanohybrids were characterized and their photophysicochemical properties were established. The study provides evidence that the metalated porphyrin derivatives were red-shifted in absorption wavelength and possessed high singlet oxygen quantum yield comparative to the unmetalated core, thus making them suitable agents for photodynamic antimicrobial chemotherapy. As a result of conjugation to detonation nanodiamonds and silver nanoparticles, these compounds proved to be more effective as they exhibited stronger antibacterial and anti-biofilm activities on the multi-drug resistant *S. aureus* strain due to synergetic effect, compared to Ps alone. This suggests that the newly prepared nanohybrids could be used as a potential antimicrobial agent in the treatment of biofilms caused by *S. aureus* strain.

Keywords: asymmetrical porphyrins, detonation nanodiamonds, silver nanoparticles, staphylococcal biofilms, photodynamic antimicrobial therapy

INTRODUCTION

Microbial biofilms are the main cause of up to 80% of all human bacterial infections (Hu et al., 2018). These biofilms can be described as a community of microbial cells that are firmly embedded into an extracellular polymeric matrix that attaches to a living or non-living surfaces (Hu et al., 2020). Commonly, due to the altered physiological and metabolic conditions of cells living in a biofilm, these infectious pathogens can tolerate 10–1,000 times higher dosage of antibiotics than their planktonic forms (free floating bacteria cells) (Donlan, 2002; Mirzahosseinipour et al., 2020). This makes it more difficult to eradicate bacterial biofilm cells as they develop more resistance to the available antibiotic treatments via various mechanisms (Wang et al., 2019). In addition, eradicating *S. aureus* is challenging not only because of the emergence of antibiotic resistances (such as Methicillin and Vancomycin) but also due to their high ability to form biofilms (Mamone et al., 2016). This results in increased need for the development and the establishment of novel alternative approaches for the suppression of infectious biofilms without causing development of resistance.

Amongst the proposed technics, photodynamic antimicrobial chemotherapy (PACT), known as a physicochemical treatment (Xu et al., 2016), has shown promising results for the management of relevant localized bacterial infections such as chronic wound infections and dental biofilms (Al-Mutairi et al., 2018). This new antimicrobial approach is considered as a favorable alternative to antibiotic therapy because unlike conventional antibiotics, PACT uses a broad spectrum of actions with efficient inactivation of resistant microorganisms and show low mutagenicity (Tim, 2015). This mode of treatment targets various site in bacterial cell, and presents limited damage to the host tissue, but most importantly, no resistance occurs following several treatments (Liu et al., 2015; Ghorbani et al., 2018).

The photodynamic antimicrobial chemotherapy protocol consists on the use of dyes also known as photosensitisers (PS) and light. The principle is based on the localization of the photosensitizer inside the cell especially in the mitochondria (Mahalingam et al., 2018) or on the bacteria wall and not in the neighboring tissue (Schastak et al., 2010). These chromophores are subsequently exposed to low doses of visible light of specific wavelength in the presence of molecular oxygen (Amos-Tautua et al., 2019), generating harmful species, such as reactive nitrogen species (RNS) and reactive oxygen species (ROS) especially singlet oxygen ($^1O_2$), which are toxic and capable of killing target cells (Baltazar et al., 2015). Characteristics including type, concentration, nature and spectral properties of a PS are crucial in the efficacy of PACT (Afrasiabi et al., 2020). Photosensitizers investigated for PACT include phthalocyanines, and porphyrins (Zhang et al., 2019).

Porphyrins (Ps) are among the most widely used PACT photosensitizers for planktonic cells and biofilms inactivation (Mamone et al., 2016). Porphyrins have received great attention as photosensitisers because of their effective singlet oxygen generation ability (Managa et al., 2019). In order to enhance their application in biomedicine, various nano-carriers have been designed in order to enhance their physicochemical properties and reduce aggregation issue. Examples of some of these nano-carriers are carbon nanomaterials such as detonation nanodiamonds (DNDs) and silver nanoparticles (Ag NPs). DNDs have core-shell structural design with diamond inner core (sp^3 carbon atoms) and graphitic outer shell (sp^2 carbon atoms) with hanging bonds ended with functional groups, which include carboxylic acid groups, anhydride, hydroxyl groups and epoxide groups. Due to the presence of carboxylic groups, DNDs suspensions are stable in water and have the capability of complexing with water soluble drugs which is an advantage over other carbon nanomaterials (Chauhan et al., 2020).

Therefore, to the best of our knowledge we report for the first time on the synthesis of new asymmetrical ester containing free base, zinc (II), gallium (III), and indium (III) porphyrins as well as their novel nanoplatforms obtained via covalent linking of the porphyrins to DNDs and colloidal Ag NPs to enhance PACT activities of the Ps by synergetic effect in this work. Asymmetrical porphyrins are employed since asymmetry is known to result in high singlet oxygen quantum yield in porphyrins (Oliveira et al., 2009). In addition, AgNPs and DNDS used in this work are also known for their antimicrobial potency (Szunerits et al., 2016; Grün et al., 2018). A metal free porphyrin have been linked to Ag NPs (Ag-S bond), for antimicrobial studies (Elashnikov et al., 2019). In this work we employ porphyrins containing heavy metals (Zn, In, Ga), which will improve PACT activity. Porphyrins have also been linked to DNDs, but not for PACT (Picollo et al., 2019), and they are applied for PACT for the first time in this work.

EXPERIMENTAL SECTION

Materials

4-Hydroxybenzaldehyde, methyl 4-formylbenzoate, pyrrole, Zinc tetraphenyl-porphyrin (ZnTPP), anhydrous zinc acetate, anhydrous indium (III) chloride, gallium (III) chloride and *N*,*N*'-dicyclohexylcarbodiimide (DCC) and *N*-hydroxysuccinimide (NHS), tryptic soy broth, crystal violet and 9,10 dimethylanthracene (DMA) were purchased from Sigma-Aldrich.

The synthesis of silver nanoparticles was done following a procedure described in literature (Agnihotri et al., 2014). Detonation nanodiamonds (DNDs) were obtained from the Nanocarbon Research Institute Ltd.

Dimethylformamide (DMF), dimethylsulfoxide (DMSO) and all other reagents were obtained from commercial suppliers and were of analytical grade purity and used without further purification. For sample purification, silica gel 60 (0.04–0.063 mm) was used for column chromatography.

The antibacterial experiments were carried out using *Staphylococcus aureus* obtained from Davies Diagnostics, South Africa. The nutrient agar and nutrient broth used to evaluate the bacteria growth and to feed the biofilms were purchased from Merk (Pty) Ltd. South Africa. Phosphate buffer saline (10 mM PBS, pH 7.4) was prepared using appropriate amounts of Na_2HPO_4 and NaOH using highly purified H_2O from ELGA, Veolia water PURELAB, Flex system (Marlow, United Kingdom).

Equipment

^{1}H NMR measurements were performed in a Bruker® AVANCE 600 MHz NMR spectrometer using deuterated DMSO as a solvent. Mass spectra were recorded on Brucker AutoFLEX III Smartbeam TOF/TOF Mass spectrometer using a positive ion mode using alpha-cyano-4-hydroxycinnamic acid as a MALDI matrix. Infrared spectroscopy was carried on using a Bruker Alpha IR (100 FT-IR) spectrophotometer with universal attenuated total reflectance (ATR), whereas a Shimadzu UV-2250 spectrophotometer was used to record all the ground state absorption spectra and the singlet oxygen quencher degradation.

A Varian Eclipse spectro-fluorimeter was employed to measure the fluorescence excitation including emission in solution, and the triplet lifetimes were determined using a laser flash photolysis system consisting of an LP980 spectrometer with a PMT-LP detector and an ICCD camera (Andor DH320T-25F03) and they were determined by exponential fitting of the kinetic curve using Origin Pro 8 software.

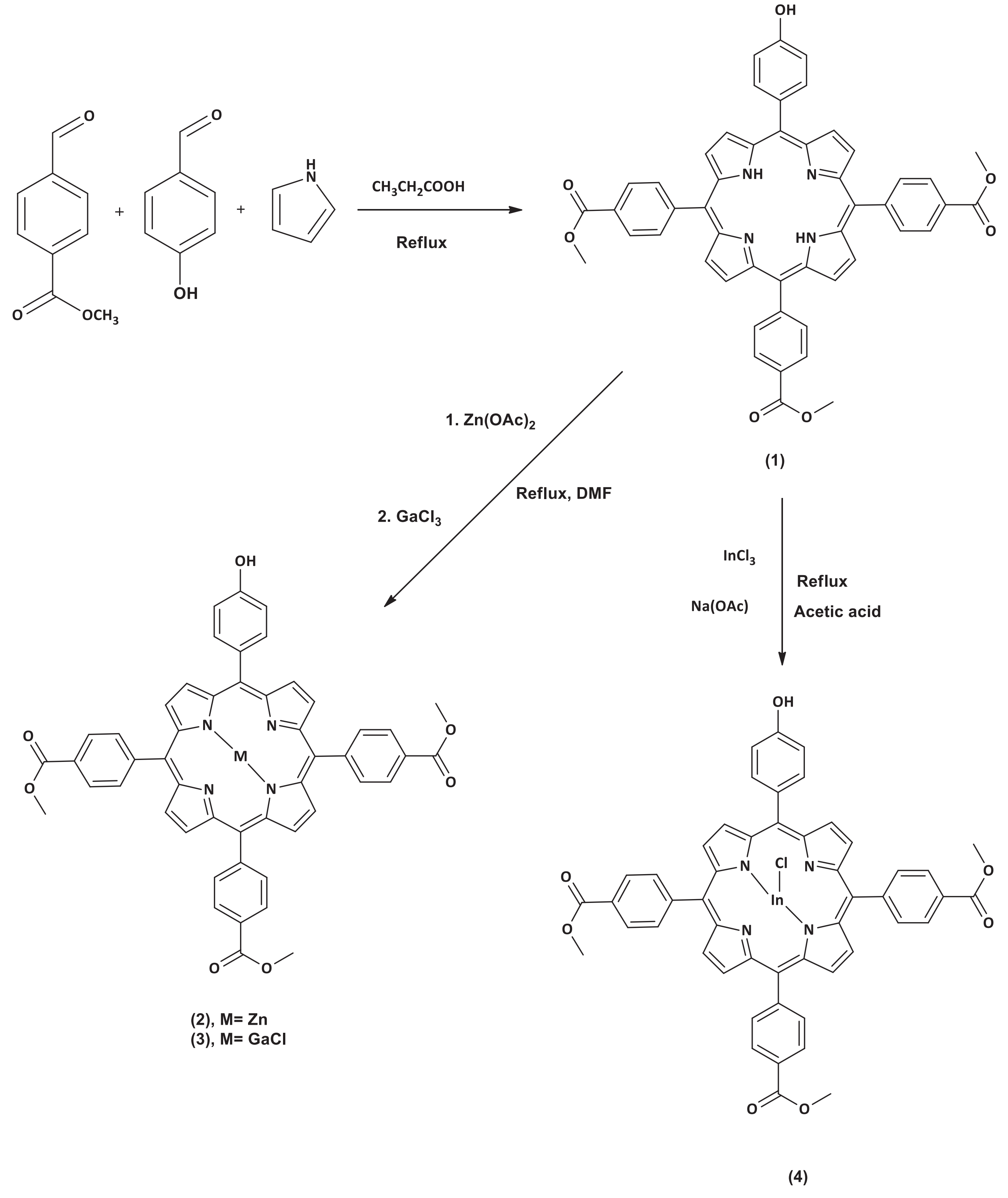

SCHEME 1 | The synthesis of asymmetrical porphyrins **1**, **2**, **3** and **4** in DMSO.

To determine the singlet oxygen production of the compounds, photo-irradiations were done using a Spectra-Physics Quanta Ray Indi-40–10 (118 mJ @ 355 nm, 7 ns, 10 Hz) Nd:YAG laser to pump a Spectra-Physics primoScan OPO (405–2,855 nm, 39 mJ @ 430 nm). The irradiation wavelength was determined to be the crossover wavelength between the respective samples and the ZnTPP used as standard.

The size and morphologies of the synthesized compounds were assessed by transmission electron microscopy (TEM) using a Zeiss Libra model 120 operated at 100 kV and an INCA PENTA FET coupled to the VAGA TESCAM using 20 kV accelerating voltage. Thermogravimetric analysis (TGA) was carried out using a Perkin Elmer TGA 800 instrument.

Merck Eppendorf centrifuge 5,810 was used for precipitates extraction, and HERMLE Z233M-2 centrifuge was used for the harvesting of the bacteria cells. PRO VSM-3 Labplus Vortex mixer was used for the homogenization of the bacteria suspension. A thermostatic Oven was used for incubation processes. The Optical density of the bacteria was determined using the LEDETECT 96, a scanner from Interscience for Microbiology Scan® 500 was used to evaluate the colony forming units CFU/ml of the bacteria and for the biofilms quantification. To quantify the biofilms, crystal violet was used as staining agent. The absorbance of the 96-well plates were read at an excitation wavelength of 590 nm using a Synergy 2 multimode microplates reader (BioTek1). Irradiation for PACT studies was conducted using LED shinning at 415 nm.

Synthesis

All the reactions were carried out under argon atmosphere. A modified procedure for asymmetrical porphyrins synthesis (Zięba et al., 2012) was applied in this work to prepare complex **1** (**Scheme 1**). Afterward, compound **1** was used as starting material to synthesize the metalated complexes **2**, **3**, and **4** (**Scheme 1**) through a metalation reaction which was achieved by inserting different metals, zinc (II), gallium (III) and indium (III), into the porphyrin core. The reaction completion was monitored using UV-Vis spectrometry to check the absence of two of the four Q-bands exhibited previously in the spectrum of complex **1**. The MALDI-TOF MS data and ^{1}H NMR data were found to be in full agreement with the proposed structures.

5-(4-Hydroxyphenyl)-tris-10, 15, 20-(4-acetylphenyl)-porphyrin (1)

In a three necked flask equipped with two dropping funnels and a condenser, propionic acid (100 mL) was refluxed at 140°C for 30 min. Then a mixture of 4-hydroxybenzaldehyde (0.5 g, 4.09 mmol), methyl 4-formylbenzoate (2 g, 12.18 mmol) in propionic acid and a pyrrole (1.34 ml, 19.31 mmol) in 6 ml *n*-toluene were simultaneously added dropwise in the three necked flask for a period of 15 min and this was left to stir at refluxing temperature for 2 h. Afterward, the temperature was cooled to 50–60°C and methanol (30 ml) was added and left to stir for another 30 min. The resulting solution was filtered under vacuum and the obtained crude product was washed with methanol and then dried for 30 min in the oven at 60°C. The desired pure compound was obtained as a purple solid after silica gel column chromatography using dichloromethane as an eluent.

Yield: 362 mg (11%). FT-IR: ν, cm^{-1} 3.394 (O-H stretch), 2.999 (Alph. C-H stretch), 2.916 (Ar. C-H stretch), 1.716 (ester C=O stretch), 1.602 (C=N and C=C stretches), 1.432 (C-H bend), 1.270 (ester C-O stretch), 1.104 (C-N stretch), and 959 (=C-H bend). ^{1}H NMR (600 MHz, DMSO-d_6): δ_H, ppm 10.01 (*s*, 1H, -OH), 8.93 (*d*, *J* = 8 Hz, 2H, Ar-H), 8.81 (*d*, *J* = 8 Hz, 6H, Ar-H), 8.38 (*d*, *J* = 8 Hz, 6H, Ar-H), 8.34 (*d*, *J* = 8 Hz, 6H, pyrrole-H), 8.00 (*d*, *J* = 8 Hz, 2H, Ar-H), 7.21 (*d*, *J* = 8 Hz, 2H, pyrrole-H), 4.04 (*s*, 9H, -OCH$_3$), and 2.54 (*s*, 2H, -NH$_2$). MALDI TOF-MS, calc. 804.26, found 804.42 [M]$^+$.

Zinc 5-(4-Hydroxyphenyl)-tris-10, 15, 20-(4-acetylphenyl)-porphyrin (2)

Complex **1** (0.1 g, 0.12 mmol) was added into a refluxing DMF. The reaction mixture was left to stir while heating until complete dissolution of the starting material. Then, anhydrous zinc acetate (0.078 g, 0.44 mmol) was added and the mixture was continuously heated at 100°C until completion which was monitored using a UV/Vis spectrophotometry. At the completion, the reaction was left to cool at room temperature followed by the addition of ethanol/water mixture (50 ml, 1:1 v/v) to precipitate out the zinc porphyrin (**2**) which was filtered off, washed with Millipore water and dried in vacuo.

Yield: 93.1 mg (90%). FT-IR: ν, cm^{-1} 3.395 (O-H stretch), 3.003 (Alph. C-H stretch), 2.918 (Ar. C-H stretch), 1.714 (ester C=O stretch), 1.656 (C=N and C=C stretches), 1.434–1.409 (C-H bend), 1.314–1.276 (ester C-O stretch), 1.106 (C-N stretch) and 950 (=C-H bend). ^{1}H NMR (600 MHz, DMSO-d_6): δ_H, ppm 10.09 (*s*, 1H, -OH), 9.12 (*d*, *J* = 8 Hz, 2H, Ar-H), 9.04 (*d*, *J* = 8 Hz, 4H, pyrrole-H), 8.95 (*d*, *J* = 8 Hz, 2H, Ar-H), 8.45 (*d*, *J* = 8 Hz, 6H, Ar-H), 8.38 (*d*, *J* = 8 Hz, 6H, Ar-H), 8.01 (*d*, *J* = 8 Hz, 2H, pyrrole-H), 7.20 (*d*, *J* = 8 Hz, 2H, pyrrole-H), and 4.01 (*s*, 9H, -OCH$_3$). MALDI TOF-MS, calc. 866.17, found 866.61 [M]$^+$.

Chloro Gallium 5-(4-Hydroxyphenyl)-tris-10, 15, 20-(4-acetylphenyl)-porphyrin (3)

Complex **3** was prepared using a similar procedure as described for complex **2**, except complex **1** (0.1 g, 0.12 mmol) and gallium chloride (0.076 g, 0.44 mmol) were used.

Yield: 105 mg (97%). FT-IR: ν, cm^{-1} 3.374 (O-H stretch), 2.996 (Alph. C-H stretch), 2.776 (Ar. C-H stretch), 1.718 (ester C=O stretch), 1.604 (C=N and C=C stretches), 1.466–1.434 (C-H bend), 1.345–1.274 (ester C-O stretch), 1.107 (C-N stretch) and 952 (=C-H bend). ^{1}H NMR (600 MHz, DMSO-d_6): δ_H, ppm 10.11 (*s*, 1H, -OH), 9.14 (*d*, *J* = 8 Hz, 2H, Ar-H), 9.04 (*d*, *J* = 8 Hz, 4H, pyrrole-H), 8.95 (*d*, *J* = 8 Hz, 2H, Ar-H), 8.44 (*d*, *J* = 8 Hz, 6H, Ar-H), 8.38 (*d*, *J* = 8 Hz, 6H, Ar-H), 8.01 (*d*, *J* = 8 Hz, 2H, pyrrole-H), 7.25 (*d*, *J* = 8 Hz, 2H, pyrrole-H), and 4.06 (*s*, 9H, -OCH$_3$). MALDI TOF-MS, calc. 906.14, found 906.49 [M]$^+$ and 871.48 [M-Cl]$^+$.

Chloro Indium 5-(4-Hydroxyphenyl)-tris-10, 15, 20-(4-acetylphenyl)-porphyrin (4)

Complex **1** (0.1 g, 0.12 mmol) was dissolved in glacial acetic acid (20 ml) and the mixture stirred and refluxed at 100°C. Indium

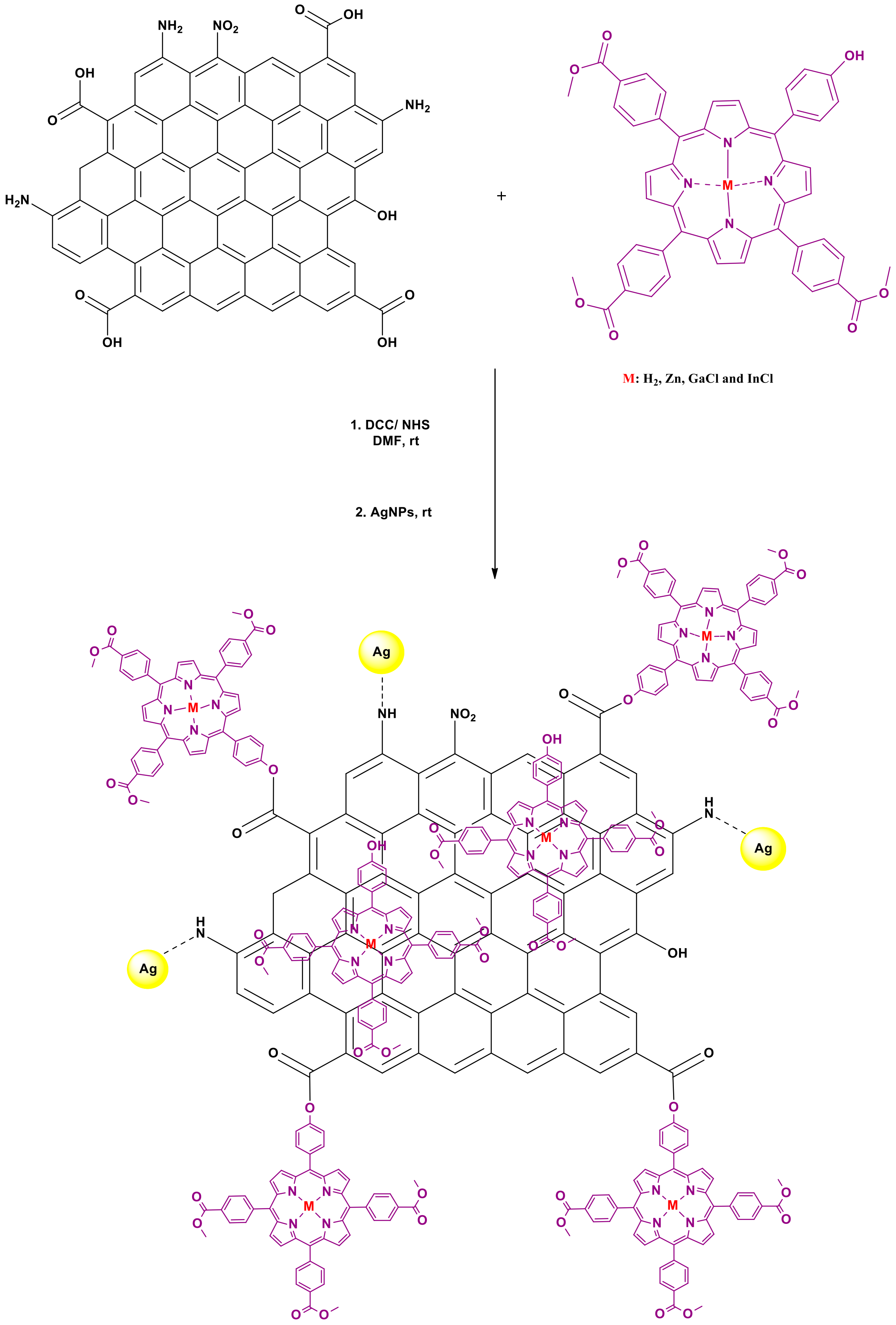

SCHEME 2 | The synthesis of Ps-DNDs@Ag nanohybrids from DNDs, Ps and AgNPs.

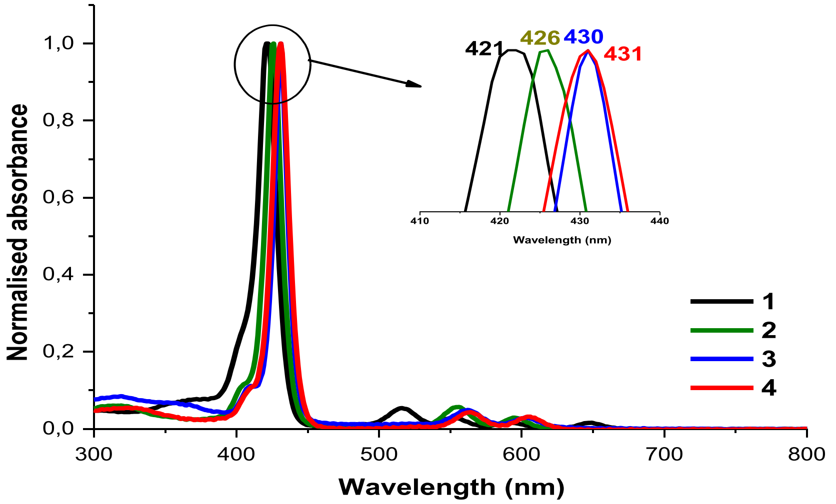

FIGURE 1 | The normalized absorption spectra of asymmetrical porphyrins **1**, **2**, **3** and **4** in DMSO. Arrow shows expansion of the B bands.

Chloride (0.138 g, 0.62 mmol) and sodium acetate (0.356 g, 4.4 mmol) were then added to the reaction mixture and left to reflux for 18 h. Afterward, the reaction mixture was cooled to room temperature then poured in cold water to obtain complex 4 as a green-purple precipitate, which was filtered off, severally washed with water and dried in vacuo.

Yield: 77 mg (67%). FT-IR: ν, cm^{-1} 3.384 (O-H stretch), 3.085 (Alph. C-H stretch), 2.951 (Ar. C-H stretch), 1.717 (ester C=O stretch), 1.603 (C=N and C=C stretches), 1.529–1.434 (C-H bend), 1.350–1.274 (ester C-O stretch), 1.105 (C-N stretch) and 966 (=C-H bend). ^{1}H NMR (600 MHz, DMSO-*d*$_6$): δ_H, ppm 10.11 (*s*, 1H, -OH), 9.14 (*d*, *J* = 8 Hz, 2H, Ar-H), 9.04 (*d*, *J* = 8 Hz, 4H, pyrrole-H), 8.95 (*d*, *J* = 8 Hz, 2H, Ar-H), 8.45 (*d*, *J* = 8 Hz, 6H, Ar-H), 8.39 (*d*, *J* = 8 Hz, 6H, Ar-H), 8.01 (*d*, *J* = 8 Hz, 2H, pyrrole-H), 7.26 (*d*, *J* = 8 Hz, 2H, pyrrole-H), and 4.07 (*s*, 9H, -OCH$_3$). MALDI TOF-MS, calc. 952.12, found 953.41 [M+H]$^+$ and 918.38 [M-Cl+H] $^+$.

Nanoconjugation of Porphyrin Complexes to DNDs and Ag NPs

Firstly, an ester covalent bond between Ps and DNDs was formed according to a previously reported method (Matshitse et al., 2019), taking advantage of the OH group on the Ps and the COOH from DNDs to result in Ps-DNDs nanohybrids (Scheme 2). Briefly, DNDs (10 mg) were dissolved in 3 ml dry DMF and DCC (0.010 g, 0.049 mmol) was added separately to activate COOH groups on DNDs with continuous stirring for 48 h. Thereafter, respective Ps (10 mg each) and NHS (0.008 g, 0.07 mmol) as well as the bare AgNPs (5 mg) were subsequently added to the respective vessels and were allowed to react while stirring at room temperature for another 72 h. It is important to note that physical interactions will take place between AgNPs and nitrogen atoms on DNDs through Ag-nitrogen affinity.

The mixtures were repeatedly centrifuged at 3,500 rpm for 5 min in ethanol to remove the unreacted starting materials and the obtained precipitates were air dried in the fume hood. The formed nanoconjugates are represented as **1**-DNDs@Ag, **2**-DNDs@Ag, **3**-DNDs@Ag and **4**-DNDs@Ag.

PACT Studies

Antibacterial Assays on Planktonic Cells

The antibacterial effect of the newly prepared Ps and the nanoconjugates was tested on the Gram positive bacteria S*taphylococcus aureus* ATCC 25923. The later was prepared according to protocols described in literature with slight modifications (Openda et al., 2020a). Briefly, an aliquot of *S. aureus* was aseptically added into 5 mL of newly prepared agar broth and the suspension was allowed to incubate at 37°C while shaking until a mid-logarithmic phase (OD 0.6–0.8 at 620 nm) was observed. Thereafter, the bacterial suspension was centrifuged (4000 RPM for 10 min) and washed three times with PBS. The resulting *S. aureus* pallet was resuspended in 100 ml of PBS to make a dilution factor of 10^{-2} bacterial suspension stock. Afterwards, serial dilutions of 10^{-3}, 10^{-4}, 10^{-5}, 10^{-6}, and 10^{-7} were prepared for the bacteria optimization. For this, 100 µL from each dilution were aseptically inoculated on agar plates in triplicates, followed by 18 h incubation at 37°C. Then a CFU counting was performed

TABLE 1 | Photophysicochemical data of synthesized complexes in DMSO.

Complex^a	λ_{abs} (nm)	λ_{em} (nm)	Φ_F	τ_T (µs)	Φ_Δ
1	426	657,719	0.074	283	0.27
2	430	615,664	0.069	232	0.43
3	431	610,662	0.033	201	0.48
4	422	607,652	0.021	182	0.54
1-DNDs@Ag (13)	429	657,721	0.048	185	0.33
2-DNDs@Ag (20)	431	610,655	0.036	180	0.51
3-DNDs@Ag (24)	431	606,658	0.015	176	0.58
4-DNDs@Ag (31)	426	605,655	0.021	140	0.59

^{a}*TEM sizes (nm) in brackets. DNDs = 2.4 nm, Ag NPs = 7.0 nm.*

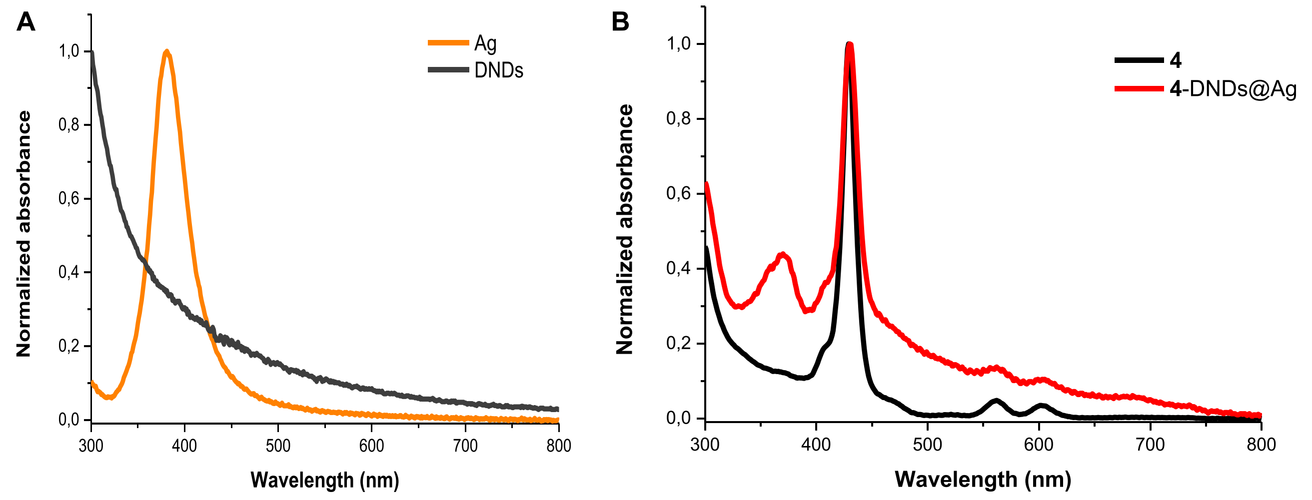

FIGURE 2 | Electronic absorption spectra of **(A)** DNDs and Ag NPs and **(B)** **4** and **4**-DNDs@Ag in DMSO (as an example).

and the dilution factor of 10^{-6}, corresponding to a count with 3.02×10^{10} CFU/mL), was practically the best to be used for this study. The concentration of 10^{-6} was chosen as working concentration since the plates contained an average of 377 colonies.

PACT was carried on following a slightly modified procedure (Makola et al., 2020). For this, 1% DMSO/PBS was used to dissolve all the samples. 2.5, 5, 10, 20, and 40 μg/mL were prepared to optimize the Ps concentration and the optimal concentration for Ps was found to be 10 μg/ml. Light emitting diode M415L4 (LED) was used as a light source at a constant irradiance of $15.6\ \mu W/mm^2$ at 415 nm excitation wavelength for 2 h with 30 min intervals.

Biofilm Formation and Photodynamic Assays

The single-species biofilm of *S. aureus* was formed with slight modifications (Openda et al., 2020b) as follows: Newly prepared inocula of the bacterial species at 10^8 CFU/mL was diluted to 10^9 CFU/mL using tryptic soy broth. 200 μl of the suspension were seeded in 96 well plates and put to incubate statically and anaerobically at 37°C for 5 days, while regularly removing unbound cells after every 18 h by gently washing with PBS and refilling the wells with 200 μL fresh tryptic soy broth to stimulate biofilm formation.

At the end of the incubation period, the biofilm-coated wells were carefully washed twice with PBS and left to air dry for 30 min.

For PACT assays, 100 μL of each sample were added into the 96-well plates containing biofilms with different concentrations of 25, 50, and 100 μg/mL). The suspensions were after that allowed to incubate for 30 min in the dark at 37°C, before irradiating at 415 nm excitation wavelength for 30 min with a LED. After irradiation, on one hand, to quantify the biofilms survival, 200 μl of 1% aqueous crystal violet (CV) solution was added into the 96-well plate to stain the cells for 30 min. Afterwards, the excess CV was washed off thrice with PBS and the wells were refilled with PBS for the cell survival counting.

On the other hand, the suspensions were diluted 1,000 times in PBS, and 100 μL of each sample were aseptically inoculated on agar plates then incubated for 18 h at 37°C to determine the number of CFU/mL. The same was also done for the samples kept in dark and all tests were performed in triplicate and the wells with bacterial films in 1% DMSO/PBS served as a positive control.

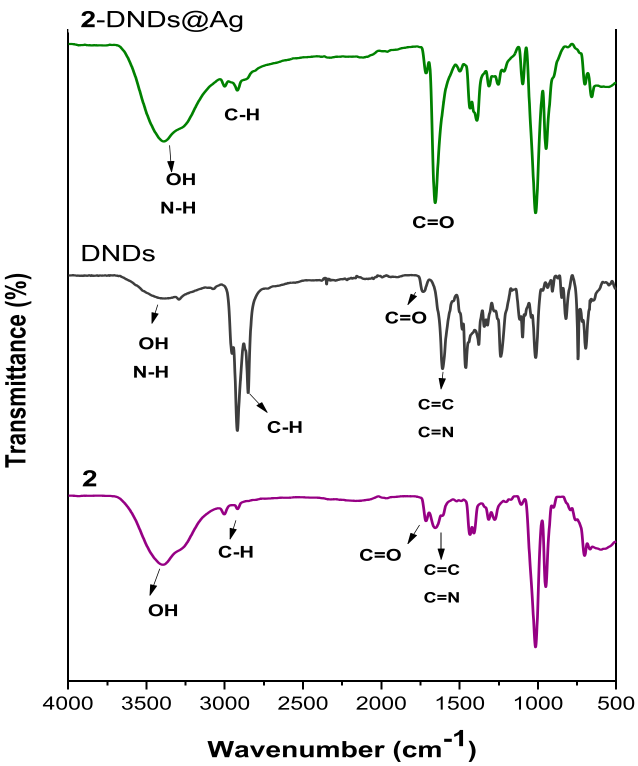

FIGURE 3 | The FT-IR spectra of **2**, DNDs, **2**-DNDs@Ag (used as an example).

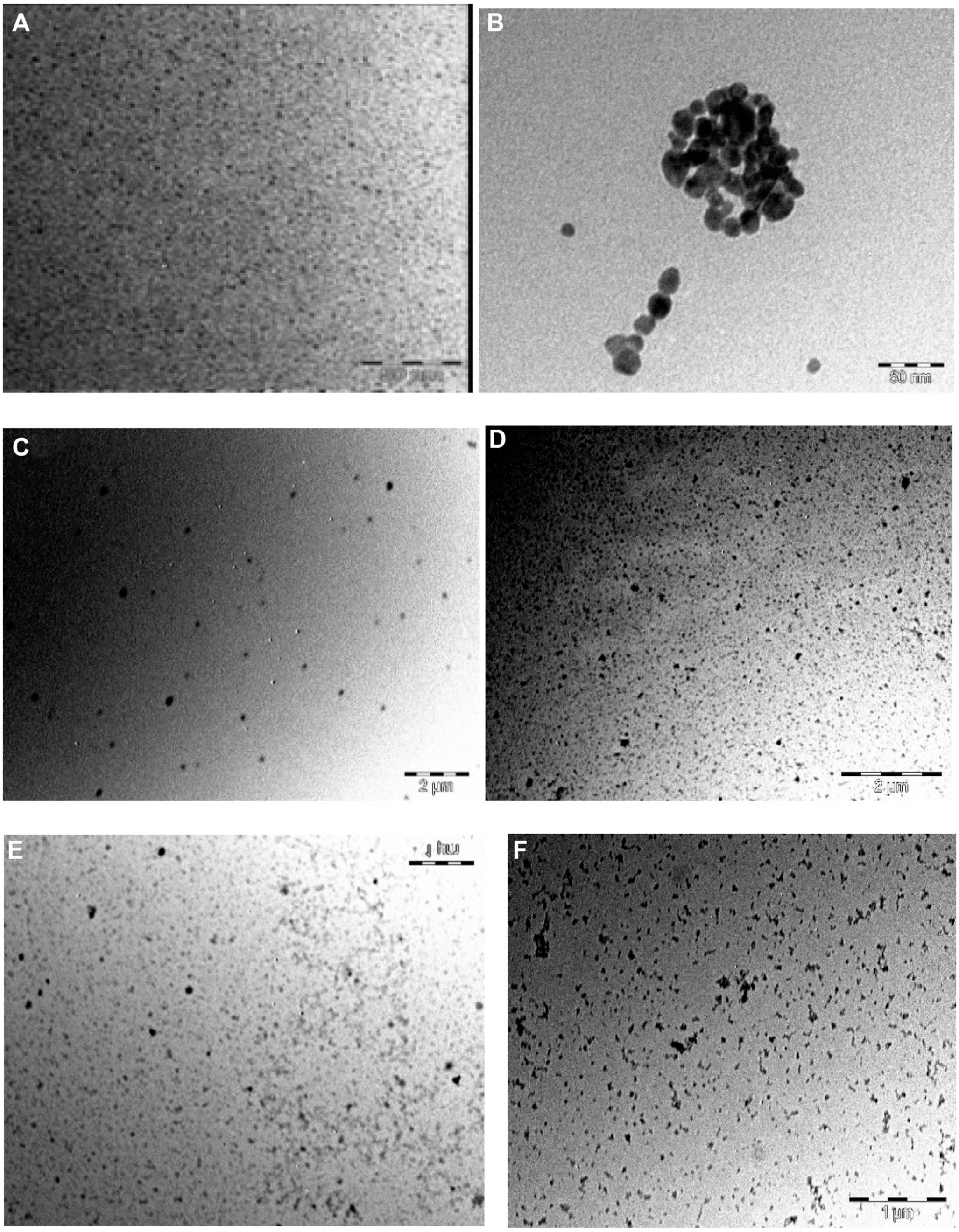

FIGURE 4 | TEM images of **(A)** DNDs, **(B)** Ag NPs, **(C)** **1**-DNDs@Ag, **(D)** **2**-DNDs@Ag, **(E)** **3**-DNDs@Ag and **(F)** **4**-DNDs@Ag (showing the size and morphology).

Statistical Analysis

Three independent ($n = 3$) experiments were done in triplicates. Triplicate measurements were made to ensure accuracy and the results were compared by using a 3-way factorial ANOVA. The data were presented as means ± standard deviation (SD) of $\log_{10}$ CFU values for the planktonic cells or means ± standard deviation (SD) of cell survival for the biofilms. A p-value of 0.05 was considered statistically significant.

RESULTS AND DISCUSSION

Synthesis and Characterization

In this study, we synthesized the unsymmetrical derivatives Ps **2**, **3** and **4** by introducing Zn, GaCl and InCl into the core of the free base Ps **1** (**Scheme 1**), respectively. Afterwards nanohybrids were acquired by linking the Ps to the DNDs via ester bonds, then nitrogen atoms on the DNDs and Ag NPs were linked via physical

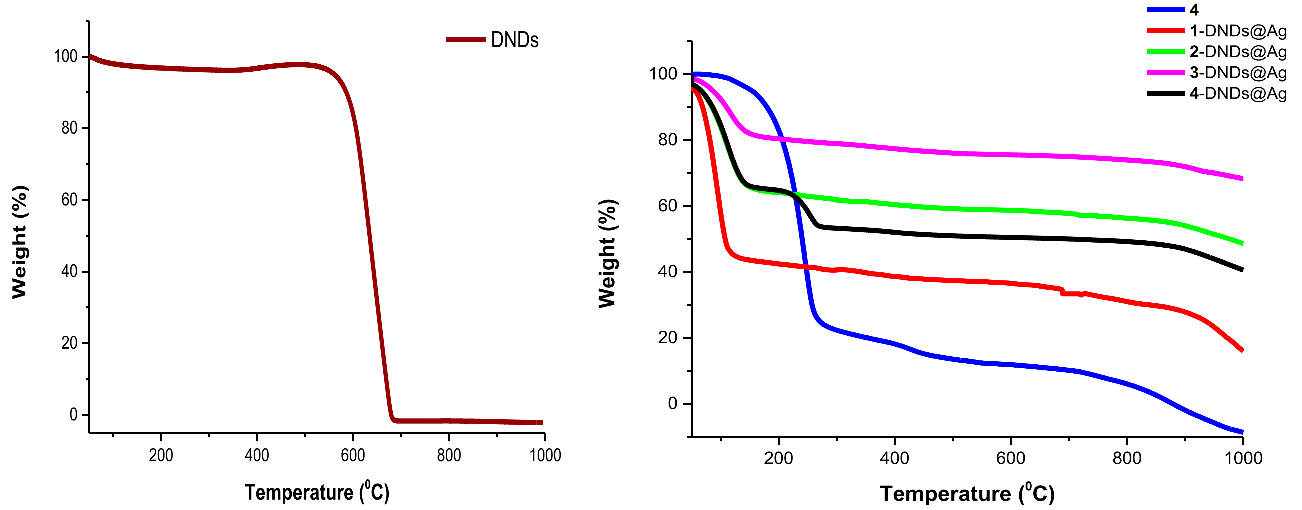

FIGURE 5 | TGA thermograms of DNDs, complex **4** and the nanoconjugates showing thermal stability after conjugation.

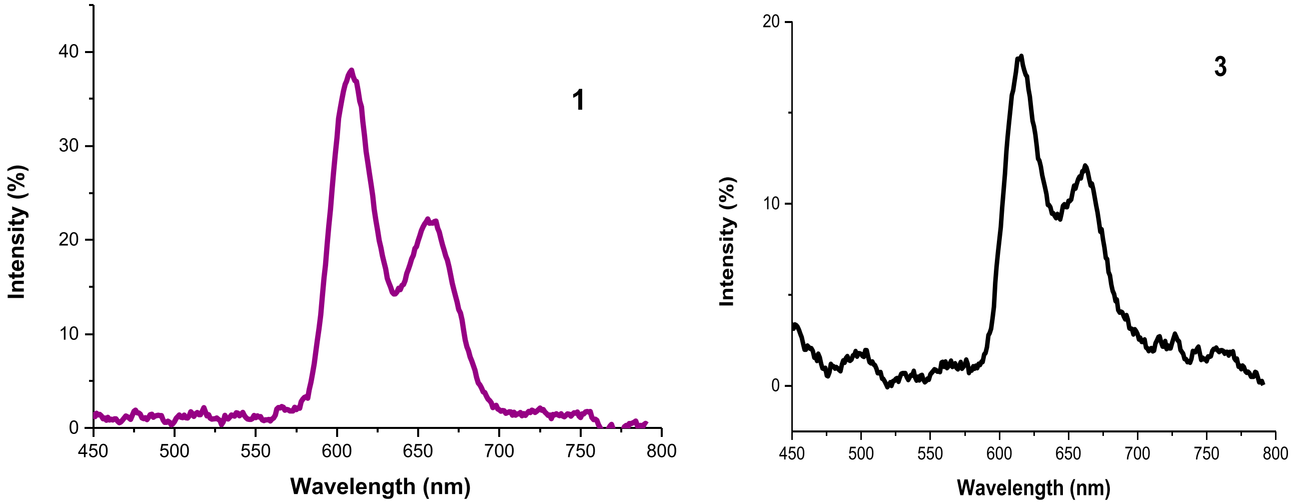

FIGURE 6 | The emission spectra of **1** and **3** in DMSO.

interactions (**Scheme 2**), to get more enhanced photoantimicrobial results due the synergetic effects. The compounds were characterized by NMR, IR, UV-Vis, MALDI-TOF MS, TEM, and TGA (see **Supplementary Figures S1–S6** in the SI for MS and NMR) and the acquired data were consistent with the predicted structures.

UV-Vis Spectroscopy

As explained by Gouterman's four orbital model, porphyrins optical spectra usually contain a very intense Soret or B-band rising around 400 nm and multiple Q bands observed between 500 and 600 nm (Gouterman 1978; Huang et al., 2015). **Figure 1** shows typical absorbance spectra of porphyrins. The B-band of **1** appears at 421 nm (**Table 1**) with four Q-bands in DMSO. Following the insertion of respective metals in compound **1**, the B-bands of complexes **2**, **3** and **4** appeared red-shifted at 426, 430, and 431 nm, respectively (**Table 1**), as the four Q-bands collapsed into two. The observed spectral red-shifts of the Soret bands results from the heavy metal effect which could cause a degree of perturbation and electron delocalisation within the porphyrin macrocycle (Uttamlal and Holmes-Smith, 2008). Indium derivatives showed the largest shifts due to the non-planar effect of the In (III) ion and its bigger atomic radius compared to Zn (II) and Ga (III) ions (Gürel et al., 2015).

In **Figure 2A**, DNDs showed a broad feature with no absorption peak in the visible region, however the Ag NPs showed a surface plasmon resonance (SPR) band at 380 nm. In the conjugates spectra, the increased absorption in the region

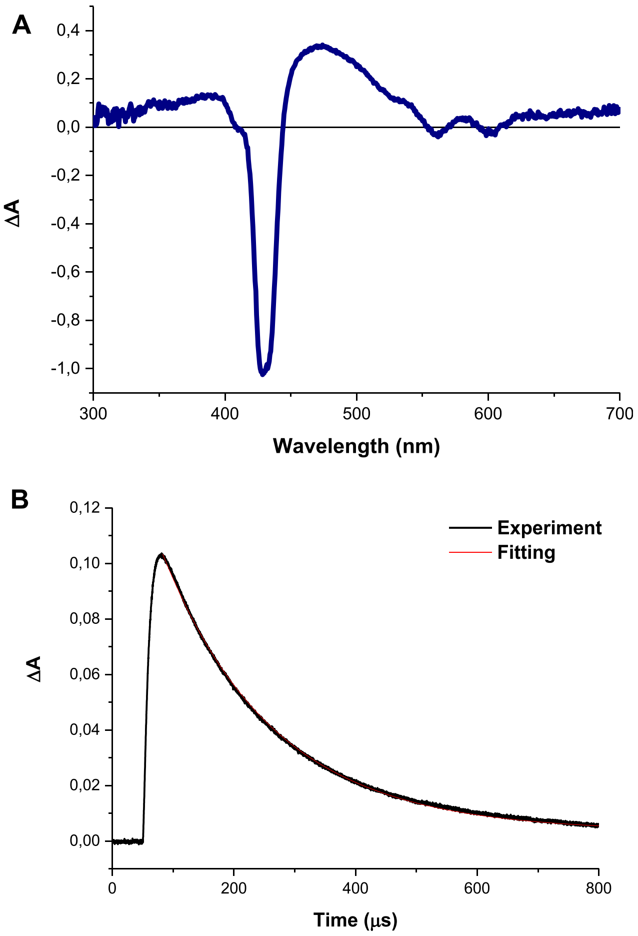

FIGURE 7 | (A) Absorption spectra obtained with LFP at 1 μs after excitation and **(B)** transient decay curve (using complex 4 as an example) observed at 425 nm in DMSO.

below 410 nm indicates the absorbance of the SPR band of Ag NPs which has absorption wavelength almost close to the Soret band of the porphyrins but also the presence of DNDs (**Figure 2B** and **Supplementary Figures S7,S8**). The slight spectral red-shifts in the Soret and Q-bands maxima for Ps in 1-DNDs@Ag (422 nm), 2-DNDs@Ag (429 nm), 3-DNDs@Ag (431 nm), and 4-DNDs@ Ag (431 nm) following conjugation (**Scheme 1**) are brought by J aggregation. These slight red shifts were also seen in the tetrasulfonated zinc Pc-graphene complex and were related to a J type aggregation (Zhang and Xi, 2011). However, in the nanoconjugates UV-Vis spectra, the enhancement of absorbance observed especially in the region below 450 nm indicate the presence of the nanoparticles, **Supplementary Figures S7,S8** used as examples.

The mass loading of the Ps onto the nanohybrids was calculated using UV-Vis absorption technic This method consist of comparing the Q band absorbance intensities of the nanohybrids to that of the respective Ps alone. Thus, equal masses (mg) for Ps alone and their respective conjugates were separately weighed and dissolved in the same volume of solvent. The respective masses were 893, 854, 802, and 747 μg (Ps)/mg DNDs@Ag for **1**-DNDs@Ag, **2**-DNDs@Ag, **3**-DNDs@Ag and **4**-DNDs@Ag, respectively. The observed higher loadings are most likely due to the presence of both π-π interactions and the ester bond. **1**-DNDs@Ag showed the highest loading due to the absence of central metal whose size can limit strong interactions between the molecule and the DNDs surface.

FT-IR Spectra Analysis

The formation of the ester linkage between the porphyrins and the DNDs was confirmed by FT-IR spectra (**Figure 3** and **Supplementary Figure S9**). The spectral analysis of Ps alone indicates the presence of characteristic vibration peaks at about 3,395–3,374 cm^{-1} and 1716 cm^{-1} for O-H and ester-C=O stretches, respectively. These characteristic peaks of the Ps alone cannot be distinguished because they overlap with the characteristic peaks of the nanoconjugates.

Hence the successful crafting of Ps to the DNDS can be confirmed by the evident increase in the intensity of OH and C=O groups as well as their shifts to higher frequencies in the spectra of the conjugates, suggesting a high predominance of these groups in the as prepared nanohybrids since they contain both the Ps and the DNDs that also possess -OH and carboxylic C=O groups. Shifts in FT-IR bands confirm molecular interactions.

Transmission Electron Microscopy (TEM)

As noticed, the acquired images in **Figure 4** show that the DNDs and the silver NPs were spherical with an average size of 2.4 nm and 7 nm, respectively. The size increased as a result of aggregation caused by conjugation to complexes. The size became ~ 13, 20, 24, and 31 nm for **1**-DNDs@Ag, **2**-DNDs@Ag, **3**-DNDs@Ag and **4**-DNDs@Ag, respectively, **Table 1**.

Thermogravimetric Analysis (TGA)

TGA analysis was carried out to ascertain the thermal stability of DNDs before and after linkage to Ps and capping with silver nanoparticles. To determine the thermal stability of these compounds, the weight loss was estimated as a function of temperature. To do so, the experiments were recorded at atmospheric pressure under nitrogen flow at a temperature from 50 up to 1000°C with a heating rate of 10°C/min.

The results prove that DNDs started to decompose around 560°C showing a weight loss of 95.03%. This agrees with literature data confirming that nanodiamonds graphitization begins nearby 600°C (Efremov et al., 2018). In comparison to the nanohybrids, at 560°C, the weight loss was of 35%, 58%, 75%, and 70% for **1**-DNDs@Ag, **2**-DNDs@Ag, **3**-DNDs@Ag, and **4**-DNDs@Ag, respectively. **Figure 5** (used as an example) illustrates that upon functionalizing the DNDs with complex **4** (as an example) and the Ag NPs, decreased weight loss was observed compared to the DNDs alone 95%, thus indicating improvement in thermal stability of DNDs. Similar trends were also observed for DNDs functionalised with silicon phthalocyanines (Matshitse and Nyokong, 2020) and for single walled carbon nanotubes (SWCNTs) following their functionalization to zinc

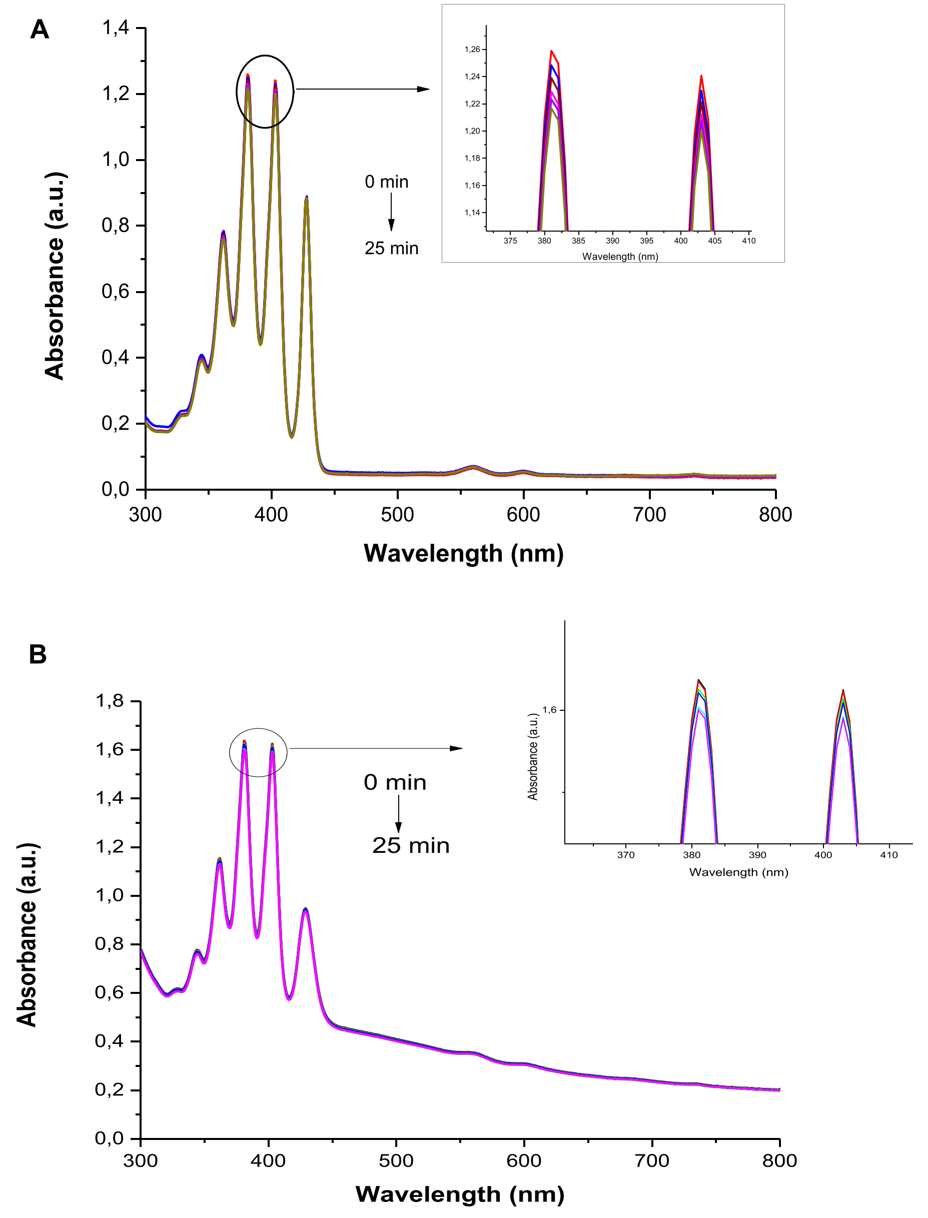

FIGURE 8 | Photobleaching of DMA in DMSO in the presence of **(A) 3** and **(B) 3**-DNDs@Ag as examples.

monocarboxyphenoxy phthalocyanine spermine (Ogbodu et al., 2015).

Complete weight loss (100%) of the DNDs was observed around 679°C and at this temperature the conjugates lost weight was 37%, 59%, 76%, and 51% for **1**-DNDs@Ag, **2**-DNDs@Ag, **3**-DNDs@Ag, and **4**-DNDs@Ag, respectively as shown in **Figure 5**.

Photophysicochemical Properties

Photophysicochemical parameters such as fluorescence quantum yield (Φ_F), triplet lifetime (τ_T) and singlet oxygen quantum yield (Φ_Δ) were investigated using comparative methods as described in literature with equations shown in the supporting information. ZnTPP was used as a standard in DMSO with $\Phi_F = 0.030$ and $\Phi_\Delta = 0.53$ (Makola et al., 2020) as obtained in DMF.

Emission Spectra and Fluorescence Quantum Yield (Φ_F)

All the experiments were run in DMSO and the absorbance of the photosensitizers at the excitation wavelength was 0.05. The emission spectra showed two characteristic bands of porphyrins (Uttamlal and Holmes-Smith, 2008; Topkaya et al., 2017) as seen in **Figure 6** (as an example), **Table 1** and in **Supplementary Figure S10**. The decrease in fluorescence intensities for the metalated Ps and the nanoconjugates could be supported by the heavy central metal effects (Nyokong, 2007)

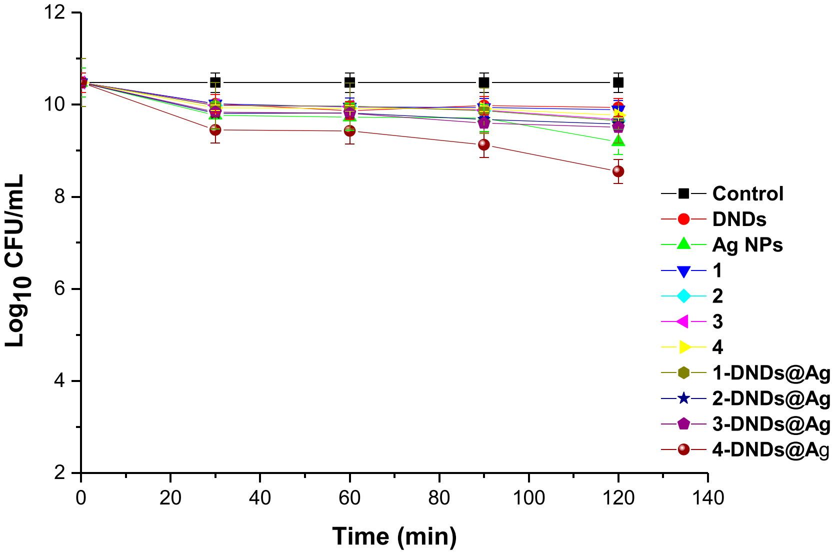

FIGURE 9 | Dark studies of the synthesized compounds on *S. aureus* planktonic cells (irradiation at 415 nm). Concentration = 10 μg/mL. Data represent the mean ± SD (standard deviation).

and the presence of electron donating groups on the DNDs favor intersystem crossing process to the triplet state over fluorescence process (De Souza et al., 2016). Additionally, the high aggregation observed in the nanoconjugates contribute to transform electronic excitation energy to vibrational energy, thus resulting in less fluorescent compounds (Muthukumar et al., 2016). Also, Ag NPs have been reported to quench fluorescence (Rapulenyane et al., 2013). Hence, lower Φ_F values listed in **Table 1** were obtained for metalated Ps-DNDs@Ag for the reason above mentioned. A similar trend has previously been observed for phthalocyanines-like complexes (Openda et al., 2020b).

Transient Spectroscopy

Nanosecond laser flash photolysis of compound **4** gave a transient absorption spectrum with a strong maximum around 432 nm shown in **Figure 7A** with a decay lifetime curve in degassed DMSO solution (**Figure 7B**). The transient absorption spectra and the decay lifetime were attributed to the triplet state of the studied compounds. Triplet state absorption spectra and lifetimes for some selected porphyrins were reported to be in the range of 430–470 nm and microsecond respectively (Barbosa Neto et al., 2013).

The triplet lifetime (τ_T) can be defined as the time that the excited molecules spend in the triplet state before returning to the

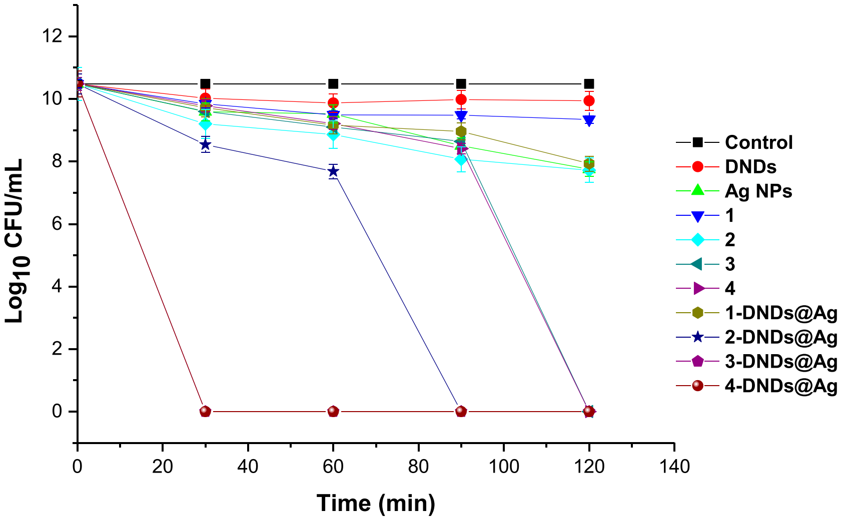

FIGURE 10 | Photoinhibition studies of the synthesized compounds on *S. aureus* planktonic cells (irradiation at 415 nm). Concentration = 10 μg/mL. Data represent the mean ± SD (standard deviation).

TABLE 2 | Log reduction values for 10 µg/mL of samples in 1% DMSO/PBS after irradiation on *S. aureus*.

Complex	Log reduction	Time of irradiation (min)
DNDs	0.54 ± 0.002	120
Ag NPs	2.73 ± 0.003	120
1	1.13 ± 0.003	120
2	2.75 ± 0.005	120
3	10.48 ± 0.004	120
4	10.48 ± 0.003	120
1-DNDs@Ag	2.54 ± 0.003	120
2-DNDs@Ag	10.48 ± 0.003	90
3-DNDs@Ag	10.48 ± 0.003	30
4-DNDs@Ag	10.48 ± 0.003	30

ground state and the energy transfer efficiency to molecular oxygen. In the present study, the samples were dissolved in DMSO then saturated with argon gas. The synthesis of the Ps-DNDs@Ag resulted in decreased τ_T values, as shown in **Table 1**, compared to Ps alone.

The triplet lifetime values (an example of the triplet decay curve is shown in **Figure 7**) were in the range of 140–283˚µs (**Table 1**). As expected, the triplet lifetimes of the Ps decreased after conjugation to the nanoparticles.

Singlet Oxygen Quantum Yield (Φ_Δ)

Singlet oxygen quantum yields is the main parameter used to evaluate the ability of a photosensitizer to destroy bacteria cells. This reactive oxygen species is formed via an energy transfer process between the excited triplet state of the photosensitizer and the ground state molecular oxygen *via* the so called type II reaction (Çakır et al., 2016).

The Φ_Δ values were determined by monitoring the photobleaching of DMA in DMSO with irradiation at 424 nm, cross-over wavelength with the ZnTPP standard. DMSO

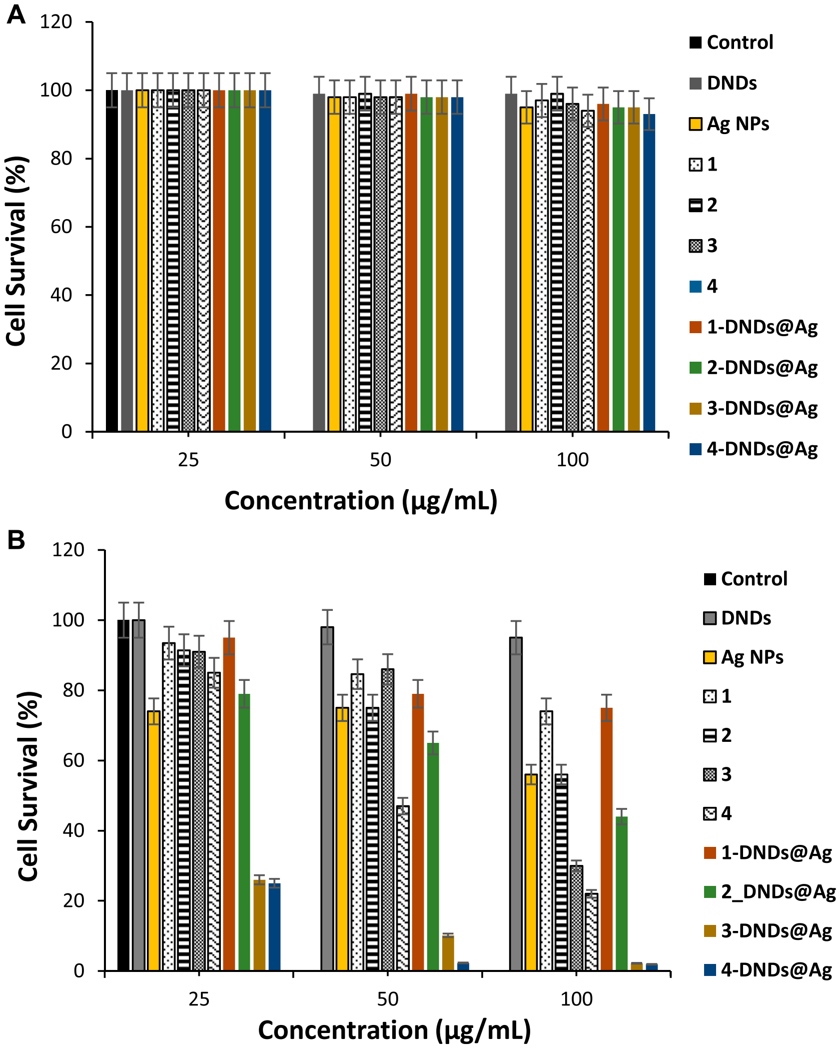

FIGURE 11 | (A) Dark toxicity studies and, **(B)** Photoinhibition studies of the synthesized compounds on *S. aureus* biofilms cells (30 min irradiation at 415 nm). Data represent the mean ± SD (standard deviation).

TABLE 3 | Cell survival values of samples in 1% DMSO/PBS after 30 min irradiation on *S. aureus* biofilms.

Complex	Cell survival (%)		
	25 μg/mL	50 μg/mL	100 μg/mL
DNDs	100.00	99.00	98.00
Ag NPs	100.00	98.00	95.00
1	93.46	74.50	74.00
2	91.40	75.56	56.78
3	91.98	86.90	30.84
4	95.00	47.20	22.00
1-DNDs@Ag	95.00	79.09	75.60
2-DNDs@Ag	79.00	75.54	44.00
3-DNDs@Ag	26.00	10.15	2.20
4-DNDs@Ag	25.23	2.30	1.92

solutions of photosensitizer (1.5 x 10^{-5} M) and DMA (2 x 10^{-5} M) were prepared in the dark under ambient conditions. The irradiation was done at the crossover wavelength with ZnTPP using a laser. **Figure 8** (**3**-DNDs@Ag used as an example) and **Supplementary Figure S11** confirm the stability of the Ps as no change in the absorption of B bands of the porphyrins was identified. The Φ_Δ data are supplied in **Table 1** and were determined to be 0.27, 0.43, 0.48 and 0.54 for 1, 2, 3, and 4, respectively, whereas were obtained for 0.33, 0.51, 0.58, and 0.59 for **1**-DNDs@Ag, **2**-DNDs@Ag, **3**-DNDs@Ag, and **4**-DNDs@Ag, respectively.

The higher Φ_Δ values were obtained for complexes containing diamagnetic metals, known to have high singlet oxygen quantum yields and long triplet lifetimes which are important for the photoinactivation process (Oluwole et al., 2016). The Φ_Δ values were slightly increased for the nanoconjugates when compared to the complexes alone, due to the effect of the nanoparticles, with the reason mentioned above about the presence of electron donating groups on the DNDs as well as the Ag NPs that stimulate the intersystem crossing process to the excited triplet state from where the singlet oxygen is generated. In addition, the presence of a reactive carbonyl group in a molecule is reported to augment singlet oxygen quantum yields because of the n-π^x transition are favored by oxygen atom (Wang et al., 2016). The capacity of studied compounds to generate such high singlet oxygen quantum yield makes them good candidates for PACT studies.

Photodynamic Antimicrobial Studies

For a material to be considered as suitable for PACT applications, it should be able to produce singlet oxygen, and that is the case for the newly synthesized materials in the present work. The bacteria strain of interest is *S. aureus* since it is notorious for high resistance to the commonly used antimicrobial treatments (Chambers and DeLeo, 2009). For the efficient PACT activity on planktonic cells and biofilms of *S. aureus*, in the current work, we developed functionalized DNDs with newly synthesized Ps and Ag NPs that could be able to efficiently bind to the cell-wall, thus to facilitate the penetration of the drug and ability to act within the cell since the generation of singlet oxygen is done within the cell (Tokubo et al., 2018).

In vitro Antibacterial Activity on Planktonic Cells

The control solutions were prepared with 1% DMSO/PBS without the photosensitizers. And these controls showed no antibacterial effect neither after dark or light treatments as seen in **Figures 9**,**10**.

A concentration of 10 μg/mL in 1% DMSO/PBS was prepared for all the samples for comparison reason. Afterwards, the photosensitizers were subjected to dark toxicity and irradiation processes. In this case, no dark toxicity was observed for the samples as **Figure 9** exhibited no significant change in $\log_{10}$ (CFU, colony forming units) values except for **4**-DNDs@Ag which had a value of 1.93 $\log_{10}$ reduction.

For the irradiation processes, as displayed in **Figure 10** and data in **Table 2**, the conjugates of gallium and indium effectively killed the bacteria strains in a short period of time of 30 min with a log reduction of 10.48 ± 0.003 as their complexes counterparts showed full activity at 120 min. These results were expected most likely due to reactive oxygen species such as singlet oxygen and radicals produced by the Ps-DNSs@Ag conjugates. The trend was also confirmed by the high values of singlet oxygen quantum yield which is almost the same for **3**-DNDs@Ag and **4**-DNDs@Ag, **Table 1**.

The zinc conjugate completely inhibited the bacteria at 90 min of irradiation giving a log reduction of 10.48 ± 0.003 yet the zinc porphyrin alone killed gave a log reduction of 2.75 ± 0.005 after 120 min irradiation. For the core, inhibition with log reduction of 1.13 ± 0.003 and 2.54 ± 0.003 were obtained after 120 min for 1 and **1**-DNDs@Ag, respectively. The efficient killing mostly observed for the metalated compounds is expected as the compounds present stronger affinity to the cell-wall thus resulting in complete cell membrane destruction and enhanced drug-cell uptake for efficient photo-antibacterial abilities since they are producing the singlet oxygen in a close proximity of the cell. Also the synergetic effect from the antibacterial activities of Ag NPs which has shown good activity of 2.73 ± 0.003 $\log_{10}$ reduction, has contributed to the results.

The log reductions for complexes alone were lower compared to corresponding conjugate derivatives even at a high irradiation time of 120 min, thus showing the importance of the conjugation to nanoparticles, **Table 2**.

Since PACT process relies on singlet oxygen production by the photosensitizer, the data presented in this work are in perfect agreement with singlet oxygen generated by the compounds. These values also confirm the importance of conjugation of photosensitizers to carbon nanomaterials and AgNPs that have also been reported to possess intrinsic antibacterial properties. The synthesized nanoconjugates showed better PACT activities corresponding to high singlet oxygen quantum yields.

In vitro Biofilms Eradication

To determine the therapeutic efficacy of the new photosensitizers we carried on studies using three different concentrations of 25, 50, and 100 μg/mL of each of the synthesized compounds for the photo-antibiofilm activity after 30 min of irradiation at 415 nm.

The treatment doses were increased for biofilms compare to planktonic cells studies owing to the lower sensitivity of biofilms toward antimicrobial treatment compared to their planktonic cells counterparts. This is can be explained by the composition of the extracellular polymeric matrixes of biofilms that stops the penetration of drugs within the biofilms (Donnelly et al., 2007; Deng et al., 2019).

The quantification of biofilms formation by crystal violet assays showed that *S. aureus* is a strong biofilm producer. **Figure 11A** illustrates that all the compounds did not show dark toxicity activities on the bacteria at all concentrations.

As listed in **Table 3**, for *S. aureus* biofilms, **3**-DNDs@Ag and **4**-DNDs@Ag showed lowest values of 2.20% and 1.92%, photoinhibition of biofilm cells at 100 μg/mL, respectively. While at 50 μg/mL they gave 10.15% and 2.30%, respectively.

As displayed in **Figure 11B**, only the indium and gallium derivatives were able to statistically give significant reductions in biofilm at 100 μg/ml upon 30 min of irradiation. The complexes alone exhibited no major reductions in biofilms in comparison to the respective untreated control groups. The great decrease in cell viability and the successful eradication of the *S. aureus* biofilm species under 30 min light exposition observed specially for the gallium and indium nanoconjugates could be due to the synergistic effect brought by the DNDs, Ag NPs and the Ps alone.

To the best of our knowledge, this work reports for the first time on the photo-eradication of *S. aureus* biofilms using as photosensitizers agents the nanoplatforms containing asymmetrical porphyrins, detonation nanodiamonds and silver nanoparticles. The basic mode of action of the new compounds studied might include inhibition of cell metabolism and growth, damage to the cytoplasmic membrane and increase in cell permeability due the charges found on the moieties (Ribeiro et al., 2013; Rosseti et al., 2014). All of the obtained data further confirm that the newly prepared nanohybrides could be used as potential photoantibacterial agents against *S. aureus* planktonic cells and biofilms at low concentrations of the complexes with small light doses.

CONCLUSION

Novel asymmetrical ester substituted porphyrins and their DNDs and Ag NPs functionalized derivatives are reported for the first time in this work. The prepared compounds proved to be able to generate singlet oxygen and have high potential in the eradication of not only the bacterial planktonic cells of S. aureus, but they also possessed good activities against their difficultly treated bacterial biofilms. In the current study, we also reports on the characterization and photophysicochemical parameters of all the as-prepared compounds. The indium and gallium derivatives were found to have better properties as well as the Ps-DNDs@Ag. In most cases, high singlet oxygen quantum yields were obtained. The photo-antimicrobial activities the complexes/conjugates using PACT with irradiation at 415 nm were also determined on *S. aureus* planktonic and biofilms cells. The obtained data in PACT were all in agreement with the reported photophysicochemical results. The *in vitro* results indicate that at lower concentration the synthesized photosensitisers have a great prospective in biofilms ablation.

DATA AVAILABILITY STATEMENT

The original contributions presented in the study are included in the article/**Supplementary Material**, further inquiries can be directed to the corresponding author.

AUTHOR CONTRIBUTIONS

YO made considerable contributions to synthesize the metalated porphyrins **2**, **3** and **4**, design, acquisition, analysis, interpretation of data and participated in drafting the manuscript. TN made considerable contributions to provide the resources, conceptualize and supervised the research. BN made considerable contributions to design, synthesize the free base porphyrin 1, participated in the writing of the manuscript and was the corresponding author in preparing the manuscript. All authors gave final approval of the submitted manuscript.

FUNDING

This work was supported by the Department of Science and Technology (DST) Innovation and National Research Foundation (NRF), South Africa through DST/NRF South African Research Chairs Initiative for Professor of Medicinal Chemistry and Nanotechnology (UID 62620), Rhodes University, the Organization for Women in Science for the Developing World (OWSD) and Swedish International Development Cooperation Agency (Sida).

SUPPLEMENTARY MATERIAL

The Supplementary Material for this article can be found online at: https://www.frontiersin.org/articles/10.3389/fchem.2021.628316/full#supplementary-material.

REFERENCES

Afrasiabi, S., Pourhajibagher, M., Chiniforush, N., Aminian, M., and Bahador, A. (2020). Anti-biofilm and anti-metabolic effects of antimicrobial photodynamic therapy using chlorophyllin-phycocyanin mixture against Streptococcus mutans in experimental biofilm caries model on enamel slabs. *Photodiagnosis Photodyn Ther.* 29, 101620. doi:10.1016/j.pdpdt.2019.101620

Agnihotri, S., Mukherji, S., and Mukherji, S. (2014). Size-controlled silver nanoparticles synthesized over the range 5–100 nm using the same protocol and their antibacterial efficacy. *RSC Adv.* 4, 3974–3983. doi:10.1039/C3RA44507K

Al-Mutairi, R., Tovmasyan, A., Batinic-Haberle, I., and Benov, L. (2018). Sublethal photodynamic treatment does not lead to development of resistance. *Front. Microbiol.* 9, 1699. doi:10.3389/fmicb.2018.01699

Amos-Tautua, B. M., Songca, S. P., and Oluwafemi, O. S. (2019). Application of porphyrins in antibacterial photodynamic therapy. *Molecules* 24, 2456. doi:10.3390/molecules24132456

Baltazar, L. M., Ray, A., Santos, D. A., Cisalpino, P. S., Friedman, A. J., and Nosanchuk, J. D. (2015). Antimicrobial photodynamic therapy: an effective alternative approach to control fungal infections. *Front. Microbiol.* 6, 202. doi:10.3389/fmicb.2015.00202

Barbosa Neto, N. M., Correa, D. S., De Boni, L., Parra, G. G., Misoguti, L., Mendonça, C. R., et al. (2013). Excited states absorption spectra of porphyrins-solvent effects. *Chem. Phys. Lett.* 587, 118–123. doi:10.1016/j.cplett.2013.09.066

Çakır, V., Goksel, M., Durmus, M., and Biyiklioglu, Z. (2016). Synthesis and photophysicochemical properties of novel water soluble phthalocyanines. *Dyes Pigm.* 125, 414–425. doi:10.1016/j.dyepig.2015.10.035

Chambers, H. F., and DeLeo, F. R. (2009). Waves of resistance: Staphylococcus aureus in the antibiotic era. *Nat. Rev. Microbiol.* 7 (9), 629–641. doi:10.1038/nrmicro2200

Chauhan, S., Jain, N., and Nagaich, U. (2020). Nanodiamonds with powerful ability for drug delivery and biomedical applications: recent updates on *in vivo* study and patents. *J. Pharm. Anal.* 10, 1–12. doi:10.1016/10.1016/j.jpha.2019.09.003

De Souza, T. G. B., Vivas, M. G., Mendonça, C. R., Plunkett, S., Filatov, M. A., Senge, M. O., et al. (2016). Studying the intersystem crossing rate and triplet quantum yield of meso-substituted porphyrins by means of pulse train fluorescence technique. *J. Porphyr. Phthalocyanines* 20, 282–291. doi:10.1142/S1088424616500048

Deng, Q., Sun, P., Zhang, L., Liu, Z., Wang, H., Ren, J., et al. (2019). Porphyrin MOF dots-based, function-adaptive nanoplatform for enhanced penetration and photodynamic eradication of bacterial biofilms. *Adv. Funct. Mater.* 29, 1903018. doi:10.1002/adfm.201903018

Donlan, R. M. (2002). Biofilms: microbial life on surfaces. *Emerg. Infect. Dis.* 8, 881–890. doi:10.3201/eid0809.020063

Donnelly, R. F., McCarron, P. A., Tunney, M. M., and Woolfson, A. D. (2007). Potential of photodynamic therapy in treatment of fungal infections of the mouth. Design and characterisation of a mucoadhesive patch containing toluidine blue O. *J. Photochem. Photobiol. B, Biol.* 86, 59–69. doi:10.1016/j.jphotobiol.2006.07.011

Efremov, V. P., Zakatilova, E. I., Maklashova, I. V., and Shevchenk, N. V. (2018). Thermal stability of detonation-produced micro and nanodiamonds. *J. Phys. Conf. Ser.* 946, 012107. doi:10.1088/1742-6596/946/1/012107

Elashnikov, R., Radocha, M., Panov, I., Rimpelova, S., Ulbrich, P., Michalcova, A., et al. (2019). Porphyrin-silver nanoparticles hybrids: synthesis, characterization and antibacterial activity. *Mater. Sci. Eng. C. Mater. Biol. Appl.* 102, 192–199. doi:10.1016/j.msec.2019.04.029

Ghorbani, J., Rahban, D., Aghamiri, S., Teymouri, A., and Bahador, A. (2018). Photosensitizers in antibacterial photodynamic therapy: an overview. *Laser Ther.* 27 (4), 293–302. doi:10.5978/islsm.27_18-RA-01

Gouterman, M. (1978). *The porphyrins, Part A. Physical Chemistry*. 1st Edn., Editor D. Dolphin (Cambridge, MA: Academic Press), 3.

Grün, A. Y., App, C. B., Breidenbach, A., Meier, J., Metreveli, G., Schaumann, G. E., et al. (2018). Effects of low dose silver nanoparticle treatment on the structure and community composition of bacterial freshwater biofilms. *PLoS ONE* 13 (6), e0199132-18. doi:10.1371/journal10.1371/journal.pone.0199132

Gürel, E., Pişkin, M., Altun, S., Odabaş, Z., and Durmuş, M. (2015). Synthesis, characterization and investigation of the photophysical and photochemical properties of highly soluble novel metal-free, zinc (II), and indium (III) phthalocyanines substituted with 2, 3, 6-trimethylphenoxy moieties. *Dalton Trans.* 44, 6202–6211. doi:10.1039/c5dt00304k

Hu, D., Deng, Y., Jia, F., Jin, Q., and Ji, J. (2020). Surface charge switchable supramolecular nanocarriers for nitric oxide synergistic photodynamic eradication of biofilms. *ACS Nano* 14, 347–359. doi:10.1021/acsnano.9b05493

Hu, X., Huang, Y. Y., Wang, Y., Wang, X., and Hamblin, M. R. (2018). Antimicrobial photodynamic therapy to control clinically relevant biofilm infections. *Front. Microbiol.* 9, 1299. doi:10.3389/fmicb.2018.01299

Huang, H., Song, W., Rieffel, J., and Lovell, J. F. (2015). Emerging applications of porphyrins in photomedicine. *Front. Phys.* 3, 23. doi:10.3389/fphy.2015.00023

Liu, Y., Qin, R., Zaat, S. A. J., Breukink, E., and Heger, M. (2015). Antibacterial photodynamic therapy: overview of a promising approach to fight antibiotic-resistant bacterial infections. *J. Clin. Transl. Res.* 1, 140–167.

Mahalingam, S. M., Ordaz, J. D., and Low, P. S. (2018). Targeting of a photosensitizer to the mitochondrion enhances the potency of photodynamic therapy. *ACS Omega* 3, 6066–6074. doi:10.1021/acsomega.8b00692

Makola, C. L., Managa, M., and Nyokong, T. (2020). Enhancement of photodynamic antimicrobialtherapy through the use of cationic indium porphyrin conjugated to Ag/CuFe$_2$O$_4$ nanoparticles. *Photodiagnosis Photodyn. Ther.* 30, 101736. doi:10.1016/j.pdpdt.2020.101736

Mamone, L., Ferreyra, D. D., Gándara, L., Di Venosa, G., Vallecorsa, P., Sáenz, D., et al. (2016). Photodynamic inactivation of planktonic and biofilm growing bacteria mediated by a meso-substituted porphyrin bearing four basic amino groups. *J. Photochem. Photobiol. B.* 161, 222–229. doi:10.1016/j.jphotobiol.2016.05.026

Managa, M., Ngoy, P. B., and Nyokong, T. (2019). Photophysical properties and photodynamic therapy activity of a meso-tetra (4-carboxyphenyl) porphyrintetramethyl ester-graphene quantum dot conjugate. *New J. Chem.* 43, 4518–4524. doi:10.1039/C8NJ06175K

Matshitse, R., Khene, S., and Nyokong, T. (2019). Photophysical and nonlinear optical characteristics of pyridyl substituted phthalocyanine-Detonation nanodiamonds conjugated systems in solution. *Diam. Relat. Mater.* 94, 218–232. doi:10.1016/j.diamond.2019.03.013

Matshitse, R., and Nyokong, T. (2020). Substituent effect on the photophysical and nonlinear optical characteristics of Si phthalocyanine-Detonated nanodiamond conjugated systems in solution. *Inorganica Chim. Acta* 504, 119447. doi:10.1016/j.ica.2020.119447

Mirzahosseinipour, M., Khorsandi, K., Hosseinzadeh, R., Ghazaeian, M., and Shahidi, F. K. (2020). Antimicrobial photodynamic and wound healing activity of curcumin encapsulated in silica nanoparticles. *Photodiagnosis Photodyn Ther.* 29, 101639. doi:10.1016/j10.1016/j.pdpdt.2019.101639

Muthukumar, P., Kim, H. S., Ku, K. S., Park, J. H., and Son, Y. A. (2016). Synthesis characterization and aggregation and fluorescence properties of novel highly soluble zinc phthalocyanines bearing tetrakis-4-(3-(piperidin-1-yl)phenoxy) with tetra and dodecachloro substituents. *Fibers Polym.* 17, 553–559. doi:10.1007/s12221-016-5812-5

Nyokong, T. (2007). Effects of substituents on the photochemical and photophysical properties of main group metal phthalocyanines. *Coord. Chem. Rev.* 251 (13), 1707–1722. doi:10.1016/j.ccr.2006.11.011

Ogbodu, R. O., Limson, J. L., Prinsloo, E., and Nyokong, T. (2015). Photophysical properties and photodynamic therapy effect of zinc phthalocyanine-spermine-single walled carbon nanotube conjugate on MCF-7 breast cancer cell line. *Synth. Met.* 204, 122–132. doi:10.1016/j.synthmet.2015.03.011

Oliveira, A. S., Licsandru, D., Boscencu, R., Socoteanu, R., Nacea, V., and Ferreira, L. F. V. (2009). A singlet oxygen photogeneration and luminescence study of unsymmetrically substituted mesoporphyrinic compounds. *Int. J. Photoenergy* 2009, 413915. doi:10.1155/2009/413915

Oluwole, D. O., Prinsloo, E., and Nyokong, T. (2016). Photophysicochemical properties of nanoconjugates of zinc (II) 2(3)-mono-2-(4-oxy)phenoxy)acetic acid phthalocyanine with cysteamine capped silver and silver-gold nanoparticles. *Polyhedron* 119, 434–444. doi:10.1016/j.poly.2016.09.034

Openda, Y. I., Sen, P., Managa, M., and Nyokong, T. (2020a). Acetophenone substituted phthalocyanines and their graphene quantum dots conjugates as photosensitizers for photodynamic antimicrobial chemotherapy against Staphylococcus aureus. *Photodiagnosis Photodyn Ther.* 29, 101607. doi:10.1016/j10.1016/j.pdpdt.2019.101607

Openda, Y. I., Matshitse, R., and Nyokong, T. (2020b). A search for enhanced photodynamic activity against Staphylococcus aureus planktonic cells and biofilms: the evaluation of phthalocyanine-Detonation nanodiamonds-Ag nanoconjugates. *Photochem. Photobiol. Sci. RSC.* 19, 75. doi:10.1039/D0PP00075B

Picollo, F., Mino, L., Battiato, A., Tchernij, S. D., Forneris, J., Martina, K., et al. (2019). Synthesis and characterization of porphyrin functionalized nanodiamonds. *Diam. Relat. Mater.* 91, 22–28. doi:10.1016/j.diamond.2018.11.001

Rapulenyane, N., Antunes, E., and Nyokong, T. (2013). A study of the photophysicochemical and antimicrobial properties of two zinc phthalocyanine-silver nanoparticle conjugates. *New J. Chem.* 37, 1216–1223. doi:10.1039/C3NJ41107A

Ribeiro, A. P., Andrade, M. C., Silva, J. d., Primo, F. L., Tedesco, A. C., Tedesco, A. C., et al. (2013). Photodynamic inactivation of planktonic cultures and biofilms of *Candida albicans* mediated by aluminum-chloride-phthalocyanine entrapped in nanoemulsions. *Photochem. Photobiol.* 89, 111–119. doi:10.1111/j.1751-1097.2012.01198.x

Rosseti, I. B., Chagas, L. R., and Costa, M. S. (2014). Photodynamic antimicrobial chemotherapy (PACT) inhibits biofilm formation by Candida albicans, increasing both ROS production and membrane permeability. *Lasers Med. Sci.* 29, 1059–1064. doi:10.1007/s10103-013-1473-4

Schastak, S., Ziganshyna, S., Gitter, B., Wiedemann, P., and Claudepierre, T. (2010). Efficient photodynamic therapy against gram-positive and gram-negative bacteria using THPTS, a cationic photosensitizer excited by infrared wavelength. *PLoS One* 5 (7), e11674. doi:10.1371/journal.pone.0011674

Szunerits, S., Barras, A., and BoukherroubInt, R. (2016). Antibacterial applications of nanodiamonds. *Int. J. Environ. Res. Public Health* 13, 413. doi:10.3390/ijerph13040413

Tim, M. (2015). Strategies to optimize photosensitizers for photodynamic inactivation of bacteria. *J. Photochem. Photobiol. B.* 150, 2–10. doi:10.1016/j.jphotobiol.2015.05.010

Tokubo, L. M., Rosalen, P. L., de Cássia Orlandi Sardi, J., Freires, I. A., Fujimaki, M., Umeda, J. E., et al. (2018). Antimicrobial effect of photodynamic therapy using erythrosine/methylene blue combination on Streptococcus mutans biofilm. *Photodiagnosis Photodyn Ther.* 23, 94–98. doi:10.1016/j.pdpdt.2018.05.004

Topkaya, D., Ng, S. Y., Bretonniere, Y., Lafont, D., Chung, L. Y., Lee, H. B., et al. (2017). Design, synthesis and phototoxicity studies of novel iodated amphiphilic porphyrins. *Photodiagnosis Photodyn. Ther.* 17, A61. doi:10.1016/j.pdpdt.2017.01.137

Uttamlal, M., and Holmes-Smith, A. S. (2008). The excitation wavelength dependent fluorescence of porphyrins. *Chem. Phys. Lett.* 454, 223–228. doi:10.1016/j.cplett.2008.02.012

Wang, H., Jiang, S., Chen, S., Li, D., Zhang, X., Shao, W., et al. (2016). Enhanced singlet oxygen generation in oxidized graphitic carbon nitride for organic synthesis. *Adv. Mater. Weinheim* 28, 6940–6945. doi:10.1002/adma.201601413

Wang, W., Cheng, X., Liao, J., Lin, Z., Chen, L., Liu, D., et al. (2019). Synergistic photothermal and photodynamic therapy for effective implant-related bacterial infection elimination and biofilm disruption using Cu9S8 nanoparticles. *ACS Biomater. Sci. Eng.* 5, 6243–6253. doi:10.1021/acsbiomaterials.9b01280

Xu, Z., Gao, Y., Meng, S., Yang, B., Pang, L., Wang, C., et al. (2016). Mechanism and *in vivo* evaluation: photodynamic antibacterial chemotherapy of lysine-porphyrin conjugate. *Front. Microbiol.* 7, 242. doi:10.3389/fmicb.2016.00242

Zhang, R., Li, Y., Zhou, M., Wang, C., Feng, C., Miao, W., et al. (2019). Photodynamic chitosan nano-assembly as a potent alternative candidate for combating antibiotic-resistant bacteria. *ACS Appl. Mater. Interfaces.* 11, 26711–26721. doi:10.1021/acsami.9b09020

Zhang, X. F., and Xi, Q. (2011). A graphene sheet as an efficient electron acceptor and conductor for photoinduced charge separation. *Carbon* 49, 3842–3850. doi:10.1016/j.carbon.2011.05.019

Zięba, G., Rojkiewicz, M., Kozik, V., Jarzembek, K., Jarczyk, A., Sochanik, A., et al. (2012). The synthesis of new potential photosensitizers. 1. Mono-carboxylic acid derivatives of tetraphenylporphyrin. *Monatsh. Chem.* 143, 153–159. doi:10.1007/s00706-011-0586-3

Conflict of Interest: The authors declare that the research was conducted in the absence of any commercial or financial relationships that could be construed as a potential conflict of interest.

frontiers in Chemistry

ORIGINAL RESEARCH
published: 17 March 2021
doi: 10.3389/fchem.2021.576913

Preparation and Characterization of Sodium Alginate-Based Oxidized Multi-Walled Carbon Nanotubes Hydrogel Nanocomposite and its Adsorption Behaviour for Methylene Blue Dye

Edwin Makhado* and Mpitloane Joseph Hato*

Nanotechnology Research Lab, Department of Chemistry, School of Physical and Mineral Sciences, University of Limpopo, Polokwane, South Africa

Herein, a sodium alginate/poly (acrylic acid)/oxidized-multi-walled carbon nanotubes hydrogel nanocomposite (SA/p(AAc)/*o*-MWCNTs HNC) was synthesized by *in situ* free-radical polymerization method. The synthesized SA/p(AAc)/*o*-MWCNTs HNC was used to remove methylene blue (MB) from aqueous solution. The synthesized HNC was confirmed by employing various characterization techniques. The SA/p(AAc)/*o*-MWCNTs HNC exhibited a maximum swelling capacity of 2265.4% at pH 8.0. The influence of vital parameters in the sorption process including the initial pH, adsorption dose, contact time and concentration were systematically examined on a batch mode. Subsequently, adsorption kinetics as well as isotherm models were applied to assess the nature and mechanism of the adsorption process. Adsorption kinetics were best described by pseudo-second-order model, while the Langmuir isotherm model governed the adsorption isotherm. The SA/p(AAc)/o-MWCNTs HNC exhibited a maximum adsorption capacity of 1596.0 mg/g at 25°C. This adsorbent showed excellent MB uptake and good regeneration ability.

Keywords: sodium alginate, multi-walled carbon nanotubes, hydrogel nanocomposite, adsorption process, methylene blue 2

Edited by:
Shivani Mishra,
University of South Africa, South Africa

Reviewed by:
Raghvendra Ashok Bohara,
National University of Ireland Galway, Ireland
Shangru Zhai,
Dalian Polytechnic University, China

****Correspondence:***
Edwin Makhado
edwinmakhado@yahoo.com
Mpitloane Joseph Hato
mpitloane.hato@ul.ac.za

Specialty section:
This article was submitted to Nanoscience, a section of the journal Frontiers in Chemistry

Received: *27 June 2020*
Accepted: *02 February 2021*
Published: *17 March 2021*

Citation:
Makhado E and Hato MJ (2021) Preparation and Characterization of Sodium Alginate-Based Oxidized Multi-Walled Carbon Nanotubes Hydrogel Nanocomposite and its Adsorption Behaviour for Methylene Blue Dye. Front. Chem. 9:576913. doi: 10.3389/fchem.2021.576913

INTRODUCTION

Rapid industrialization has resulted in a substantial increase of dye-containing industrial effluents. The discharge of dyes into water streams give rise to negative effects on human health and the environment. Several studies reported that the exposure and indigestion of dyes can cause several health problems such as eye burn, cancer, skin irritation, nausea and dermatitis to name a few (Ngah et al., 2011; Thakur et al., 2016; Hui et al., 2018). Dyes accumulate in water due to their complex structures, which inhibit penetration of sunlight, sequentially delay photosynthesis from taking place. Consequently, it is of great importance to remove toxic dyes from wastewater. The sorption process is considered as a promising option for remediation of water mainly due to several advantages such as ease design and operation, and low cost. In this regard, various materials have been employed as adsorbents which include agricultural waste (i.e. rice husk, sawdust and bagasse) (Juang et al., 2002; Oh and Park, 2002; Malik, 2003), clay minerals such as montmorillonite, zeolites (Armağan et al., 2004; Taleb et al., 2012), chitosan and chitin (Wu et al., 2001; Crini, 2006), as well as carbon-based materials (activated carbons, multi-walled nanotubes and graphene oxide) (Ma et al., 2012; Manitha et al., 2017; Mahmoodi et al., 2018). However, the use of aforementioned materials is restricted by their partial adsorption capacity, poor reusability, production of a large amount of sludge, high operational cost and non-biodegradability (Crini and Badot, 2008; Adegoke and Bello, 2015).

The development of highly efficient, potentially sustainable and inexpensive materials for adsorption of aquatic pollutants from water is exceedingly challenging and warranted for treatment of water pollutions. Among a wide spectrum of adsorbents used for adsorption of pollutants from wastewater, hydrogels proved to be a promising adsorbents. Hydrogels represent a class of three-dimensional (3D) material consisting of cross-linked hydrophilic polymer chains, which are able to absorb and hold a large volume of liquids (Makhado et al., 2019a). Hydrogels have gained popularity among researchers due to their well-known structural features such as rapid swelling behaviour, elasticity and biocompatibility. These distinctive properties pave a way for hydrogels as potential candidates to be used in various fields including agriculture, wound dressing, drug delivery, diapers, beauty care products and wastewater treatment (Ahmed, 2015; Makhado et al., 2019b). In particular, hydrogels have spurred great interest as potential materials for adsorption of synthetic dyes and metal ions from wastewater (Pandey et al., 2020). This is due to physiochemical properties such as tunable structure, high porosity, swelling ability, fast sorption rate, and recovery capacities and reusability (El-Hag Ali et al., 2003; Shi et al., 2013). However, the applicability of hydrogels has been overshadowed due to their weak mechanical strength and partial adsorption capacity.

Given these challenges, the ongoing interest in the field of water remediation has incited the preparation of hydrogel nanocomposite with distinctive nanostructured materials. Nanomaterials including clays (Hosseinzadeh et al., 2011; Liu et al., 2018; Malatji et al., 2020), titanium dioxide (Mittal and Ray, 2016), silica (Makhado et al., 2019c), carbon-based materials (Madima et al., 2020), graphene oxide (Chen et al., 2016; Makhado et al., 2018a; Hu et al., 2020) and multi-walled carbon nanotubes (Hosseinzadeh et al., 2018) have been introduced into the hydrogel networks to synthesize hydrogel nanocomposites for wastewater remediation. Furthermore, the incorporation of these inorganic components within the polymeric hydrogel matrices can enhance the performance of a hydrogel material. In recent years, multi-walled carbon nanotubes (MWCNTs) have attracted a great deal of attention due to their unique hollow tubular structure, optical properties, excellent electrical and thermomechanical properties (Ren et al., 2011; Ma et al., 2012). However, the absence of polar functional groups on the surface of MWCNTs restricts their application in the adsorption process. Therefore, pre-treatment of MWCNTs is an ideal approach to impart polar functional groups on the surface of MWCNTs (Ma et al., 2012). Several researchers incorporated pre-treated MWCNTs in the polymer matrices and applied the prepared adsorbent for adsorption of dyes. For example, Chatterjee et al. (2010) synthesized chitosan-based MWCNTs hydrogel beads and the resultant composite was used for the removal of Congo red (CR) (Chatterjee et al., 2010). In another study, superabsorbent hydrogel nanocomposite was synthesized via graft co-polymerization of acrylamide and itaconic acid in the presence of MWCNTs by Mohammadinezhad et al. (2018). The authors reported that the addition of MWCNTs within the hydrogel networks improved mechanical properties, thermal stability and adsorption capacity toward inorganic pollutant (Mohammadinezhad et al., 2018). In another study, Makhado et al. (2018b) prepared XG/o-MWCNTs hydrogel nanocomposite and used it as an adsorbent for sequestration of methylene blue (MB) dye from aqueous medium. In their work, they reported that hydrogel nanocomposite outcompeted the hydrogel. For example, XG/o-MWCNTs hydrogel nanocomposite showed improved adsorption ability, recovery capacities and reusability, wettability and comparatively high thermal stability as compared to a bare hydrogel (Makhado et al., 2018b). It transpires from aforementioned discussions that an incorporation of the pre-treated MWCNTs in the hydrogel matrix results in the formation of hydrogel nanocomposite with improved thermal stability, adsorption capacity, as well as wettability. In our recent study, we have reported on the fabrication of sodium alginate poly(acrylic acid) (SA-poly(AA)) hydrogel and sodium alginate poly(acrylic acid)/zinc oxide (SA-poly(AA)/ZnO) hydrogel nanocomposite (HNC) via an *in situ* free-radical polymerization for the sequestration of toxic MB dye from aqueous solution (Makhado et al., 2020). In this study, we have reported that the adsorption capacity (1529.6 mg/g) for SA-poly(AA)/ZnO HNC was higher than that of the SA-poly(AA) of 1129.0 mg/g at pH 6.0 within 40 min. Interestingly, the HNC exhibited outstanding reusability with relatively better adsorption efficiencies as compared to SA-poly(AA) hydrogel. Based on the literature, we hypothesize that the incorporation of an *o*-MWCNTs in the hydrogel matrix will enhance the thermal stability, thermomechanical properties, swelling and adsorption capacity.

Herein, we report on the preparation of SA/p(AAc)/*o*-MWCNTs HNC as a potential adsorbent for adsorption of MB from aqueous solution. To elucidate the influence of *o*-MWCNTs on the formation of SA/p(AAc)/*o*-MWCNTs HNC, the structure and morphology, physicochemical characteristics (gel strength and swelling ability), thermal properties and adsorption behaviour were investigated using thermogravimetric analysis (TGA), dynamic mechanical analysis (DMA), high resolution transmission electron microscopy (HR-TEM), scanning electron microscopy (SEM), Fourier transform infrared (FTIR), Raman and X-ray diffraction (XRD). The adsorption kinetics as well as adsorption isotherm models were investigated to understand the sorption process.

EXPERIMENTAL

Materials

The biopolymer, sodium alginate (SA) having a formula weight of 176.10 g/mg and molecular formula $C_6H_8O_6$, acrylic acid (AAc, 99 %), *N*,*N′*-methylene bis-acrylamide (MBA, 99%), ammonium persulfate (APS) (≥98%; 248614), and MWCNTs were procured from Sigma-Aldrich (South Africa). Acetone, sodium hydroxide (NaOH), nitric acid (HNO_3, 65%), hydrochloric acid (HCl) and MB were supplied by Merck (South Africa). All chemicals used in this study were of analytical grade and used without any further purification. Deionized (DI) water was used throughout the experiment. Typically, 1.0 g of MB powder was dissolved in 1000 ml volumetric flask in DI water, stock solutions were further prepared by diluting the as-prepared stock solution from batch experiments.

Materials Synthesis

Preparation of *o*-MWCNTs

Oxidation of MWCNTs was prepared according to our previously reported protocol (Makhado et al., 2018b). In brief, 0.5 g MWCNTs were weighed and added into 200 mL HNO_3. The reaction mixture was placed in the ultrasonicator for about 10 min followed by refluxing for 12 h at 80°C under continuous stirring. The reaction mixture was allowed to cool down, then the prepared *o*-MWCNTs were washed repeatedly with DI water through filtering system. The *o*-MWCNTs were washed up until the filtrate solution reached pH 7.0, and then the obtained *o*-MWCNTs were dried in an oven.

Synthesis of SA/p(AAc)/*o*-MWCNTs HNC

Typically, 10 mg of SA was weighed and dissolved in 10 ml of DI water. To this mixture, appropriate amounts of APS, AAc and MBA were dissolved and added under stirring maintaining the overall volume of 30 ml. An optimum amount of *o*-MWCNTs was sonicated with 6 ml of DI water for about 5 min; this solution was then poured into 100 mL beaker reaction mixture containing SA, APS, AAc, and MBA under continuous stirring. The total volume of the reaction mixture was maintained at 30 ml. The reaction was heated at 70°C for 3 h in an oven. The product was cut to small pieces then washed with acetone followed by DI water to remove the reactant. SA/p(AAc)/*o*-MWCNTs HNC was dried in an oven at 60°C for about 24 h, subsequently milled to a fine powder.

Materials Characterization

Spectrum II spectrometer (Perkin-Elmer) Fourier transform infrared (FTIR) was employed to record the spectra in the wavenumber ranging between 400–4,500 cm^{-1} and resolution of 4 cm^{-1}. The X-ray diffraction (XRD) patterns of the samples were collected with a PAnalytical Xpert Pro spectrometer employing Ni filtered CuKα radiation (λ = 0.1514 nm). The thermal stability was performed using a simultaneous thermal analyzer (STA) 6,000 manufactured by Perkin-Elmer (Boston, MA). The STA was connected to a PolyScience digital temperature controller under N_2 gas purged at a flow rate of 20 ml/min. The prepared samples ranging from 1–4 mg were heated from 30–600°C at a constant heating rate of 10°C/min. The data was collected and analyzed using Pyris software®. The morphology and the elemental analysis of the prepared materials were investigated using the scanning electron microscopy (SEM) (JSM7500F, JEOL). The internal morphology of the samples was studied using high resolution-transmission electron microscopy (HR-TEM, JOEL JEM 2100, Tokyo, Japan). A dynamic mechanical analysis (DMA) was used on a single-cantilever bending mode by DMA 8000 (Perkin-Elmer) to study the mechanical stability of the synthesized hydrogels. The frequency dependence of the loss modulus and storage modulus were performed at a fixed temperature (30°C). The strain amplitude was set at 0.05%, and the ramp rate was 5°C/min in the frequency range of 0.01–100 Hz. Ultraviolet-visible spectrophotometer (UV-vis) was utilized to analyze the MB dye concentration after adsorption. The Raman spectra were recorded on a Horiba Jobin-Yvon LabRam HR 2000 confocal Raman microscope with a wavelength of 514 nm.

Swelling Studies

To study the hydrogel swelling ratio, 100 mg of the samples were immersed in about 80 ml of DI water at 25°C for 48 h. Thereafter, the swollen samples were removed from DI water and the excess water on the surface of the samples was wiped gently, re-weighed to determine the swelling ratio of the samples. The swelling capacity (SC) of the samples was calculated using **Eq. 1**.

$$SC = \frac{W_s - W_d}{W_d}, \tag{1}$$

where W_d and W_s represent the weight of the initial dry sample and the weight of the swollen hydrogel sample, respectively.

Adsorption Studies

The sorption behavior of MB dye onto SA/p(AAc)/*o*-MWCNTs HNC was investigated on a batch mode. The adsorption studies were carried out in 30 ml of MB dye solution using 10 mg of adsorbents and agitated in a temperature-controlled shaker set at 160 rpm for a particular period. The dye-containing solutions were withdrawn and filtered with 0.45 μ PVDF syringe filters after adsorption. The influence of initial pH on the adsorption of MB was studied and the effect of pH on the adsorption capacity were ranged from 2.0 to 9.0. The influence of adsorbent dose on the adsorption capacity was varied for 10–50 mg. For adsorption kinetics studies, the contact time was altered from 10 to 60 min. For adsorption isotherm experiments, the MB dye concentrations were varied from 530 to 1,350 mg/L. The influence of contact time and equilibrium concentration was evaluated at three different temperatures 25, 35, and 45°C. After adsorption process, the aliquots were filtered and the concentration was measured using the UV-vis spectrophotometer (Cary 300) at λ_{max} of 662 nm for MB dye. The adsorption percentage and adsorption capacity (q_e) were determined using **Eqs 2,3**, respectively.

$$\text{Adsorption}\,(\%) = \left(\frac{C_o - C_e}{C_o}\right) \times 100, \tag{2}$$

$$q_e\left(\frac{\text{mg}}{\text{g}}\right) = q_t = \left(\frac{C_o - C_e}{m}\right)V, \tag{3}$$

where q_t (mg/g) represents the amount of MB adsorbed per unit mass of the adsorbent at a certain time (t). C_e (mg/L) is the equilibrium concentration f MB, m (g) is the mass of the adsorbent, and V (L) is the volume of the MB dye solution.

Sorption Kinetics

To evaluate the underlying mechanism and to govern the rate constant of the sorption process the pseudo-first-order (**Eq. 4**) (Lagergren, 1898) and the pseudo-second-order (**Eq. 5**) (Ho, and McKay, 1998) were applied. Their linear forms of the former and the later equations are provided in **Eqs 4**,**5**, respectively;

$$\log\left(q_e - q_t\right) = \log\left(q_e\right) - \frac{k_1}{2.030}t, \tag{4}$$

$$\frac{t}{q_t} = \frac{1}{k' q_e^2} + \left(\frac{1}{q_e}\right)t, \tag{5}$$

where, q_e (mg/g) is the amount of MB adsorbed at equilibrium, q_t (mg/g) is the amount of MB adsorbed at any time t and equilibrium, $k'_1(\text{min}^{-1})$, k'_2 (g mg^{-1} min^{-1}) are pseudo-first-order and pseudo-second-order rate constants, respectively. For pseudo-first-order model, the straight-line plot of $\log(q_e - q_t)$ against t gives $\log(q_e)$ and intercept equal to $k'_1/2.303$. Thus, the amount of solute sorbed per gram of sorbent at equilibrium (q_e) and k'_1 can be evaluated from the slope and the intercept.

Adsorption Isotherm Studies

The Langmuir Isotherm Model

The Langmuir isotherm model is based on the monolayer adsorption of adsorbate and assumed that the adsorption takes place at the specific homogeneous adsorbent surface (Langmuir, 1918), and this is presented in **Eq. 6**;

$$q_e = \frac{q_m b C_e}{1 + bC_e}. \tag{6}$$

The Langmuir equation can be rearranged to a linear form for the convenience of plotting and determination of its constant (K_L) as provided **Eq. 7**;

$$\frac{C_e}{q_e} = \frac{1}{q_m b} + \frac{1}{q_m}C_e, \tag{7}$$

where q_m is the monolayer adsorption capacity per unit of adsorbent (mg/g), q_e is the adsorption capacity at equilibrium (mg/g), and b relates the heat of adsorption (L/mg). C_e is the concentration of MB solution at equilibrium (mg/l). The values of q_m and K_L can be determined from the linear plot of C_e/q_e against C_e. The essential features of the Langmuir isotherm can be employed to predict the affinity between the sorbate and the sorbent using the dimensionless equilibrium constant (R_L) (Makhado et al., 2017b). which can be expressed in **Eq. 8**:

$$R_L = \frac{1}{1 + K_L C_o}, \tag{8}$$

where R_L value reveals the shape and feasibility of the sorption isotherm. This parameter indicates favourable sorption if $0 < R_L < 1$, unfavorable ($R_L > 1$), linear ($R_L = 1$), and irreversible if $R_L = 0$.

Freundlich Isotherm Model

The Freundlich isotherm model is valid for the multilayer adsorption of adsorbate at the heterogeneous adsorbent surface (Freundlich, 1906). Furthermore, the adsorption capacity depends upon the concentration of adsorbate. The Freundlich isotherm is generally expressed by the following empirical **Eq. 9**:

$$q_e = K_F\, C_e^{\frac{1}{n}}. \tag{9}$$

The linear expression takes the following form given in **Eq. 10**:

$$\log q_e = \log K_f + \left(\frac{1}{n}\right)\log C_e, \tag{10}$$

where K_F is the Freundlich equilibrium constant ($\text{mg/g(L/mg)}^{1/n}$), C_e is the equilibrium concentration (mg/l), and the parameter 1/n is the adsorption heterogeneity constant (varies with the nature of the adsorbent/adsorbate system) and q_e is the amount of adsorbate adsorbed per unit adsorbent at equilibrium (mg/g). Both K_F and 1/n are evaluated from the intercept and the slope respectively, of the linear plot of log q_e against $\log C_e$.

Temkin Isotherm Model

The Temkin isotherm model takes into consideration the adsorbate-adsorbent interaction (Temkin, 1941). This model also suggests that the heat of adsorption decreases linearly with the increase in adsorption quantity. The model is provided by **Eqs 11–13** as follows:

$$q_e = \frac{RT}{b_T}\ln A_T + \frac{RT}{b_T}\ln C_e, \tag{11}$$

$$b = \frac{RT}{b_T}, \tag{12}$$

$$q_e = \beta \ln A_T + \beta \ln C_e, \tag{13}$$

where b_T is Temkin isotherm constant, A_T is the Temkin isotherm equilibrium binding constant (L/g), β is constant related to the heat of adsorption (J/mol), R is the universal gas constant (8.314 J/mol/K) and T is the temperature at (273.15 K).

Determination of Point of Zero Charge

The point of zero charge (pH_{pzc}) is simply the pH at which the adsorbent surface has a net charge of zero. pH_{pzc} is obtained from the difference between the initial and the final pH (ΔpH). To determine the pH_{pzc}, measured amounts of the hydrogel and the hydrogel nanocomposite were immersed in aqueous solutions of pH ranging between 2.0–10.0 and agitated in a shaker (170 rpm, ambient temperature) for 48 h. The solution pH was recorded and the pH_{pzc} was calculated using **Eq. 14**:

$$\Delta pH = pH_{final} - pH_{initial}. \tag{14}$$

Statistical Analysis

The root-mean-squared error (RMSE) was measured to assess how well the adsorption kinetics and isotherm model performed. The RMSE is calculated using the following Equation:

$$\mathrm{RMSE} = \sqrt{\sum_{i=1}^{N} \frac{\left(q_{\exp} - q_{\mathrm{mod}}\right)^2}{n}} \tag{15}$$

where $q_{\exp}$ is the equilibrium capacity, q_{mod} denotes the model predictions of equilibrium capacity and n is the number of experimental data points (Sun et al., 2010; Despotovic et al., 2016; Matome et al., 2020).

Desorption and Regeneration Studies

Reusability of samples was studied through repeated adsorption-desorption experiments. The MB-loaded adsorbents were recovered and recycled by rinsing with 0.1 M HCl solution and agitated at 170 rpm for 3 h, then neutralized with 0.1 M NaOH solution followed by DI water. The absorbent were dried at 50°C, pulverized, and reused in the next cycle of the adsorption. The dye adsorption/desorption cycles were repeated six times and calculated as given in **Eq. 16**.

$$\text{Desorption percentage}\,(\%) = \frac{\text{Concentration desorbed }(\mathrm{mg/l})}{\text{Concentration adsorbed }(\mathrm{mg/l})} \times 100. \tag{16}$$

RESULTS AND DISCUSSIONS

FTIR, Structural and TGA Studies

The FTIR spectra of SA, *o*-MWCNTs, SA/p(AAc) hydrogel and SA/p(AAc)/*o*-MWCNTs HNC are shown in **Figure 1A**. It is noticeable that *o*-MWCNTs displayed a broad characteristic peak at 3,666 $\mathrm{cm^{-1}}$ to 3,015 $\mathrm{cm^{-1}}$, corresponding to the–OH groups. The sharp peaks at 2,922 $\mathrm{cm^{-1}}$ and 2,841 $\mathrm{cm^{-1}}$, attributed to the asymmetric stretching and symmetric vibrations of CH_2 group (Dyke and Tour, 2004). The characteristic bands corresponding to C-O and–COO groups at 1,035 $\mathrm{cm^{-1}}$ and 1608 $\mathrm{cm^{-1}}$, respectively. The spectrum of SA revealed a wide band between 3,100 and 3,620 $\mathrm{cm^{-1}}$ related to the stretching vibration of the hydroxyl groups present in the SA polymer chain. The peak at 2,922 $\mathrm{cm^{-1}}$ was assigned to the –CH, which stretching vibrations of the CH_2 (Makhado et al., 2017a; Makhado et al., 2017b). Two absorption peaks at about 1,608 and 1,407 $\mathrm{cm^{-1}}$ were ascribed to the COO^- groups and the C-C bending vibration, respectively. The band at 1,034 $\mathrm{cm^{-1}}$ emanated from the C-O-C stretching frequencies (Hu et al., 2018; Wattie et al., 2018). The characteristic peak at 802 $\mathrm{cm^{-1}}$ relates to the Na-O of the SA (Thakur et al., 2016; Olad et al., 2018). After graft co-polymerization of AAc onto SA, an increase in the peak intensity of SA was observed at 802 $\mathrm{cm^{-1}}$ which was attributed to the β-glycosidic linkage between the guluronic units and a very broad absorption peak appeared at 3,660–2,500 $\mathrm{cm^{-1}}$ due to carboxylic acid OH stretch. Furthermore, the shift in the position of the characteristic peaks of SA shifted from 1,680 to 1,700 $\mathrm{cm^{-1}}$ which is possibly due to the strong interaction with AAc and the stretching of the C-O-C bond shifted from 1,023 to 1,121 $\mathrm{cm^{-1}}$ which confirms the SA/p(AAc) hydrogel formation (Thakur et al., 2016). In the spectrum of SA/p(AAc)/*o*-MWCNTs HNC, the characteristic peaks emanating from SA/p(AAc) hydrogel were all observed with a reduction in the intensity after the formation of hydrogel nanocomposite, these results suggest that the internal hydrogen bonding occurred between the *o*-MWCNTs and SA/p(AAc) hydrogel.

The XRD patterns of pure MWCNTs and *o*-MWCNTs are illustrated in **Supplementary Figure S1B**. Both samples showed three diffraction peaks at $2\theta = 25.8^\circ$ relating to the (002) plane of the graphitic carbon (JCPDS-ICDD No. 751621), $2\theta = 43.1^\circ$ corresponding to the (001) and $2\theta = 53.3^\circ$ belonging to the (004) reflections of the carbon atoms. The diffraction patterns of samples exhibited the same trend without any shift in the 2θ peak positions, which indicate that the microstructure of MWCNTs was not destroyed during oxidizing. Moreover, the intensity of diffraction peaks of the *o*-MWCNTs spectrum was slightly higher than that of pure MWCNTs, confirming that pure MWCNTs were oxidized (**Supplementary Figure S1B**). These observations were in good agreement with the results obtained from Raman studies (**Supplementary Figure S1A**). XRD spectra of pure SA, SA/p(AAc) hydrogel and SA/p(AAc)/*o*-MWCNTs HNC are displayed in **Figure 1B**. In the case of pure SA, 2θ diffraction peaks at 13.8°, 21.5°, and 39.1° can be attributable to the reflection of (110) plane from polyguluronate unit, (200) plane from polymannuronate and the latter from amorphous halo, respectively. After graft copolymerization of AAc onto SA backbone, the peaks emanating from SA emerged and formed a broad diffraction peak at $2\theta = 18.9^\circ$, without any clear diffraction peaks confirming the amorphous nature of SA/p(AAc) hydrogel. The disappearance of two diffraction peaks suggested successful grafting of AAc onto SA backbone. Several studies showed that grafting of AAc onto biopolymer results in the interference of the backbone diffraction peaks (Thakur et al., 2016; Verma et al., 2020). Subsequent SA/p(AAc)/*o*-MWCNTs HNC formation, the appearance of a wide broad peak with higher intensity was observed at $2\theta = 18.9^\circ$ and a diffraction peak at $2\theta = 43.2^\circ$ corresponding to (100) reflection, which may be due to a short-range order in *o*-MWCNTs layers. The XRD results are in good agreement with the FTIR results, confirming the formation of SA/p(AAc) hydrogel as well as SA/p(AAc)/*o*-MWCNTs HNC.

The TGA of *o*-MWCNTs, SA, SA/p(AAc) hydrogel and SA/p(AAc)/*o*-MWCNTs HNC is shown in **Figure 1C**. The thermal characteristics of the *o*-MWCNTs showed high stability over the studied range 25–600°C. It was observed that SA exhibits two degradation steps. In the first step, weight loss of about 10% occurred between 50 and 180°C which may be attributed to dehydration of SA and volatilization of water. The major weight loss of around 40% occurred over the range 250–300°C, which was mainly due to the SA backbone decomposition. The thermal characteristics of SA/p(AAc) hydrogel and SA/p(AAc)/

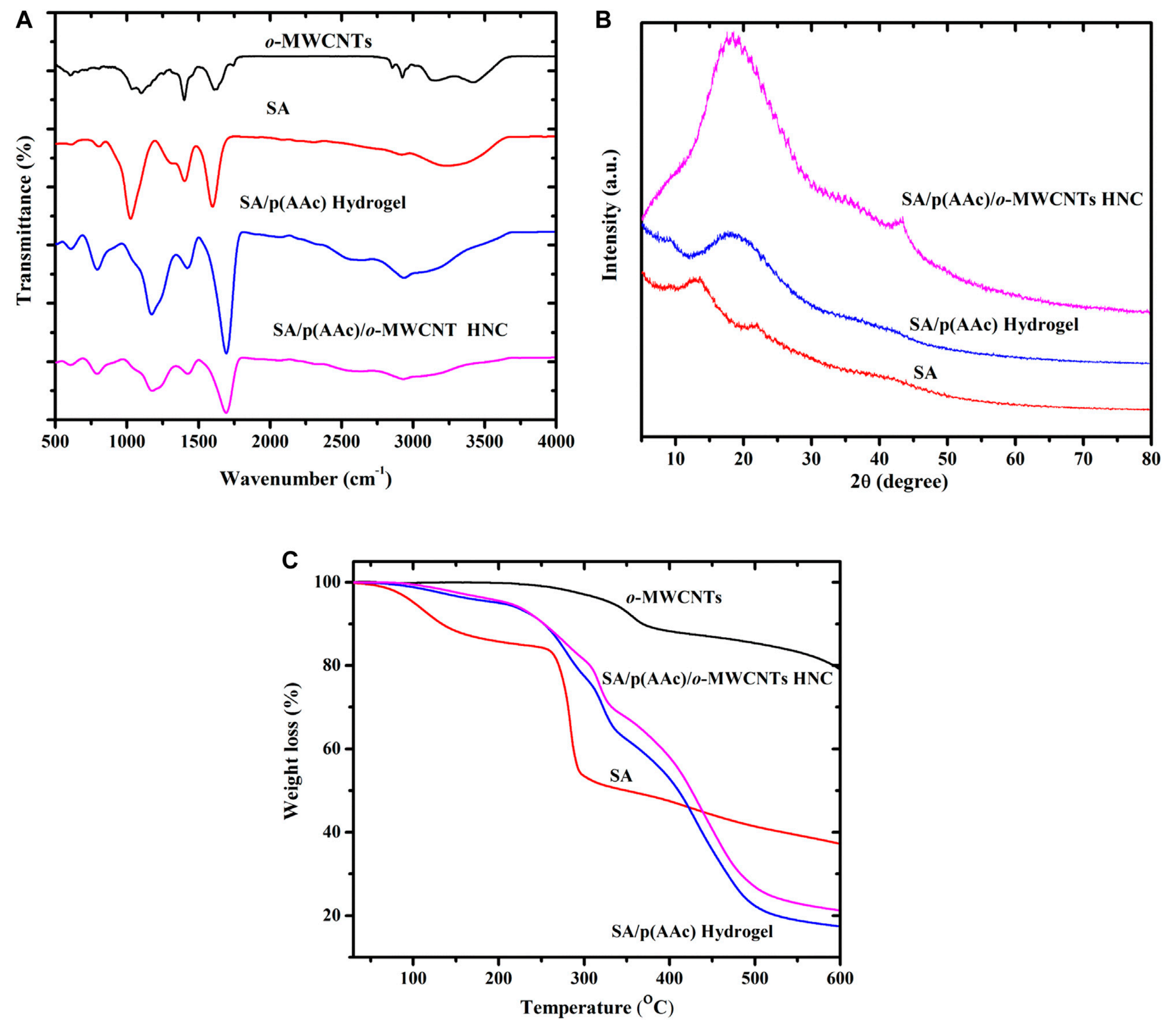

FIGURE 1 | (A) FTIR, **(B)** XRD spectra and **(C)** TGA thermograms of *o*-MWCNTs, SA, SA/p(AAc) hydrogel and SA/p(AAc)/*o*-MWCNTs HNC.

o-MWCNTs HNC demonstrated similar degradation profiles with curves disintegrated in three steps. The first degradation of 5% occurred in the temperature range of 90–210°C due to the loss of water residual. In the temperature region of 250–350°C, there was a second decomposition stage of about 20% due to degradation of SA and residue carbide form (Soares et al., 2004). In the third degradation profile, about 50% weight reduction occurred in the temperature range of 330–500°C due to the breaking of its carboxyl from acrylic acid groups and degradation of the residual copolymer. Overall, the correlation analysis demonstrated that SA/p(AAc)/*o*-MWCNTs HNC had improved thermal stability as compared to SA/p(AAc) hydrogel. The presence of *o*-MWCNTs in the hydrogel matrix enhanced the thermal property of the hydrogel.

Morphological Characteristics

Structural morphologies of SA, SA/p(AAc) hydrogel and SA/p(AAc)/*o*-MWCNTs HNC was subjected to SEM analysis. **Figures 2A,B** depicts low and high magnification of SA. Fragment-like loose surface was observed for the pure SA, which is indicative of semi-crystalline and amorphous structure. After the formation of the three-dimensional polymer network, the surface morphology presented a relatively continuous coarse surface which is a consequence of the presence of AA (**Figures 2C,D**). **Figures 2E,F** illustrated the low and high magnification of SA/p(AAc)/*o*-MWCNTs HNC. It was observed that subsequent hydrogel nanocomposite formation, the surface morphology of became utterly different from the continuous coarse surface to rough, irregular and porous structure. The rough, irregular and porous structure results from

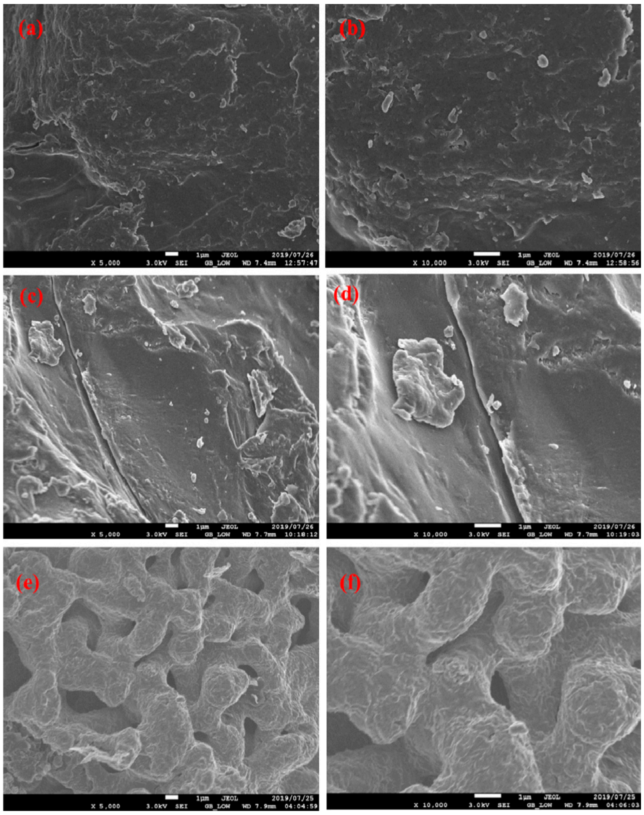

FIGURE 2 | SEM images of **(A, B)** SA **(C, D)** SA/p(AAc) hydrogel **(E, F)** SA/p(AAc)/o-MWCNTs HNC.

interactions between *o*-MWCNTs and polymeric hydrogel matrices.

To get information on the homogeneity of *o*-MWCNTs on the SA/p(AAc) hydrogel matrix, TEM analysis was performed and the results are shown in **Figures 3A,B**. From the micrographs, it is seen that *o*-MWCNTs were mostly uniformly dispersed on the SA/p(AAc) hydrogel matrix to form SA/p(AAc)/*o*-MWCNTs HNC. The *o*-MWCNTs were compatible with the polymeric matrices due to availability of hydrophilic functional groups, which promote strong H bonding interactions.

Mechanical Properties

The viscoelastic property of polymeric hydrogel is an important factor which affects their applications. The storage modulus, G' (elastic response) and loss modulus, G'' (viscous behavior) of the SA/p(AAc) hydrogel and SA/p(AAc)/*o*-MWCNTs HNC were measured as a function of frequency using DMA. **Figure 4A** shows the G' of SA/p(AAc) hydrogel and its nanocomposite in the 0.01–100 Hz frequency range and similar trends were noticed. It can be seen that both SA/p(AAc) hydrogel and SA/p(AAc)/*o*-MWCNTs HNC exhibited elastic character at low frequencies. The SA/p(AAc)/*o*-MWCNTs HNC revealed lower elastic response than SA/p(AAc) hydrogel. This result suggests that the incorporation of *o*-MWCNTs in the polymeric hydrogel matrices weakened the degree of cross-linking density and caused the decrease in G'. **Figure 4B** displays the viscous behavior of SA/p(AAc) hydrogel and SA/p(AAc)/*o*-MWCNTs HNC as a function of frequency. The G'' of SA/p(AAc) hydrogel was slightly higher than that of SA/p(AAc)/*o*-MWCNTs HNC in the frequency range of 0.01–30 Hz, cross over was noticed at 30 Hz. As the frequency of the system was increased above the characteristic frequency of the segments, the dissipative component increased. It can be observed from **Figures 4A,B** that the storage modulus was greater than the loss modulus throughout the studied frequency range, which was indicative of elastic character.

Swelling Studies

The water uptake of SA/p(AAc) hydrogel and SA/p(AAc)/*o*-MWCNTs HNC was investigated in the pH range 3.0–9.0 (**Figure 4C**). The swelling studies results demonstrated that both adsorbents had pH-dependent behavior. Moreover, both adsorbents showed similar trends for the water uptake throughout the studied pH range. In acidic conditions, both adsorbents displayed the lowest swelling degree. It was observed that the increase in the solution pH increased the swelling capacity of SA/p(AAc) hydrogel and SA/p(AAc)/*o*-MWCNTs HNC. The maximum swelling percentage of 1,669.7 and 2,268.4% was observed at pH 8.0 for SA/p(AAc)

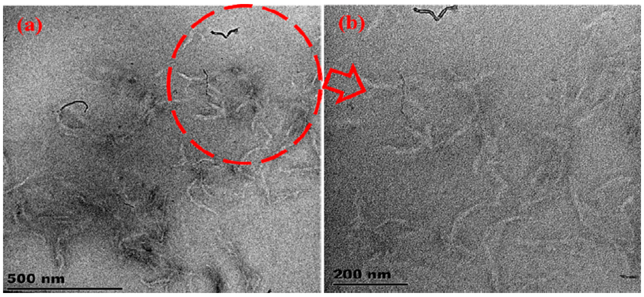

FIGURE 3 | TEM images of **(A)** and **(B)** SA/p(AAc)/*o*-MWCNTs HNC.

hydrogel and SA/p(AAc)/*o*-MWCNTs HNC, respectively. In the alkaline pH, the network structure of both adsorbents exhibited extensive swelling in the aqueous medium due to the presence of hydrophilic groups, i.e., -COOH, which renders a negative charge density that participates in the electrostatic interactions with the water molecules. The *o*-MWCNTs incorporated hydrogel nanocomposite exhibited greater swelling capacities than the SA/p(AAc) hydrogel. The increment in the swelling degree of SA/p(AAc)/*o*-MWCNTs HNC can be ascribed to the addition of hydrophilic *o*-MWCNTs in the hydrophilic polymeric matrices (Makhado et al., 2018b). The swelling degree of SA/p(AAc)/*o*-MWCNTs HNC was comparatively high, which is owing to the low gel strength. It is well proven that the improvement in the gel strength is inversely proportional to the swelling degree (Thakur et al., 2016). Therefore, the swelling studies results support the mechanical studies results.

Effect of Ionic Strength on the Swelling Capacity

The influence of salts (0.1 M of NaCl and $CaCl_2$) on the swelling capacity of SA/p(AAc) hydrogel and SA/p(AAc)/*o*-MWCNTs HNC was investigated and the results are shown in **Figure 4D**. It was observed that both adsorbents exhibited high swelling capacity in the absence of salts. The maximum swelling capacity of 136.0 and 150.1 g/g for SA/p(AAc) hydrogel and SA/p(AAc)/*o*-MWCNTs HNC was recorded for the solution of NaCl, respectively. In the solution of $CaCl_2$, the highest water uptake was found to be 124.8 and 149.7 g/g for SA/p(AAc) hydrogel and SA/p(AAc)/*o*-MWCNTs HNC. These observations demonstrate that salts reduced the water molecule adsorption efficiency of both adsorbents. These reductions may be attributed to the competition between water molecules and the surface of the adsorbent. The pH value at the point of zero charges (pHpzc) on the SA/p(AAc) hydrogel surface was found to be 2.2 and the surface become negatively charged with increasing pH values. On the other hand, SA/p(AAc)/*o*-MWCNTs HNC demonstrated negatively charged surface in the studied pH range and the negative charge on the surface of SA/p(AAc)/*o*-MWCNTs HNC increased with increasing pH values (**Figure 4E**). These results may be explained by dissociation of the hydroxyl groups that imparts the negative charge to the MWCNTs surface. The negatively charged surface promote the adsorption of positively charged adsorbate such as MB. A similar behaviour was reported in the literature (Makhado et al., 2018b).

Adsorption Studies

Various factors influencing the adsorption process such as solution pH, adsorption dose, contact time and initial dye concentration in the solution must be optimized for application in real-world situations.

Effect of Initial Solution pH on the Adsorption of MB Dye

The influence of solution pH plays a significant role in the adsorption process. The solution pH governs the interaction between the ions present in the reaction system and the adsorbent surface. **Figure 5A** showed that the adsorption capacity increased with the increasing solution pH and subsequently the equilibrium was reached at pH 6.0. FTIR results confirmed that SA/p(AAc)/*o*-MWCNTs HNC has carboxylic groups which could be attributed to the high MB affinity at pH above 5.0. In an acidic medium, the carboxylic groups on the SA/p(AAc)/*o*-MWCNTs HNC surface were protonated limiting MB uptake due to columbic repulsion. With an increase in the solution pH, electrostatic interaction between negatively charged SA/p(AAc)/*o*-MWCNTs HNC surface and cationic MB dye molecules enhanced the adsorption capacity. In a basic medium, the high adsorption capacity was obtained due to ionization of carboxylic groups at higher pH, favoring intermolecular interaction between adsorbate and adsorbent. Therefore, the optimum solution pH used for the adsorption of MB in this study was 6.0. Similar observations were noticed with SA/p(AAc) hydrogel.

Effect of Adsorbent Dose on the Adsorption of MB Dye

It is conspicuous in **Figure 5B** that the adsorption capacity was decreased with the increasing the amount of SA/p(AAc) hydrogel and SA/p(AAc)/*o*-MWCNTs HNC in the adsorption process. The adsorption capacity of SA/p(AAc)/*o*-MWCNTs HNC

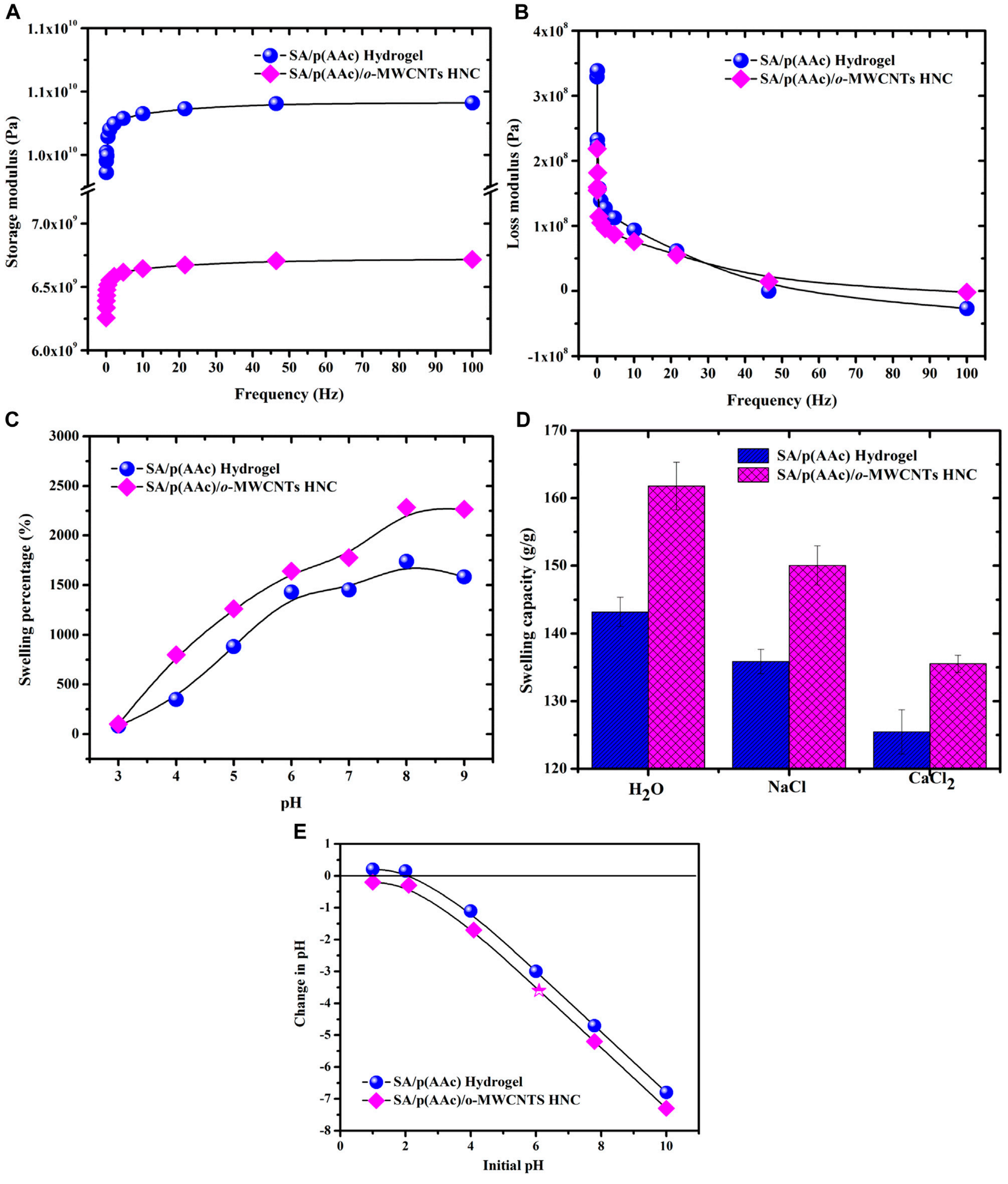

FIGURE 4 | DMA of SA/p(AAc) hydrogel and SA/p(AAc)/*o*-MWCNTs HNC; **(A)** storage modulus, **(B)** loss modulus, **(C)** effect of pH on the swelling percentage, **(D)** effect of salts on the swelling capacity and **(E)** pH_{PZC}.

decreased from 1,540 to 1,350 mg/g as the adsorbent dose was increased from 0.33 to 1.67 g/l at a fixed solution pH, contact time and equilibrium concentration. The high adsorption capacity was achieved at low adsorbent dose due to complete occupation of the active sites. At high adsorbent loading, the adsorption capacity decreased due to less occupation of adsorption active sites and

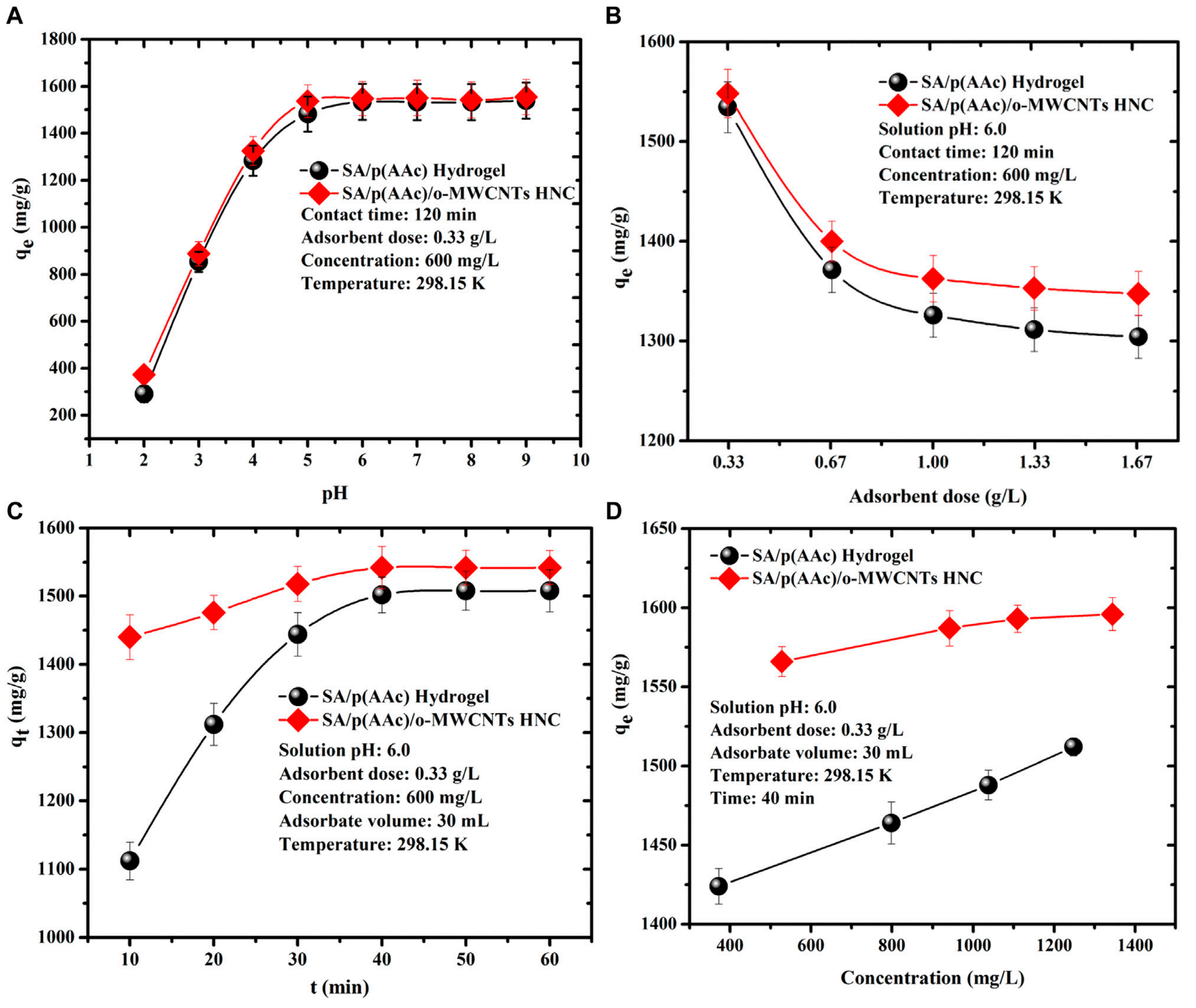

FIGURE 5 | Effect of **(A)** initial pH, **(B)** adsorbent dose, **(C)** contact time, and **(D)** equilibrium concentration on the adsorption capacity of MB dye.

agglomeration of the particles in the reaction mixture. SA/p(AAc)/*o*-MWCNTs HNC showed a high adsorption capacity as compared to the neat SA/p(AAc) hydrogel throughout the studied range.

Effect of Contact Time and Adsorption Kinetics

The influence of contact time on the adsorption capacity of MB by SA/p(AAc) hydrogel and SA/p(AAc)/*o*-MWCNTs HNC was evaluated in the range of 10–50 min at solution pH of 6.0, 0.33 g/l adsorbent dose and 600 mg/l at three different temperatures. As depicted in **Figure 5C**, the adsorption capacity of MB was rapid and then, attained equilibrium within 40 min. The adsorption kinetic models were applied to investigate the adsorption mechanism of adsorbent and adsorbate. To better understand the adsorption process, the experimental data in **Supplementary Figure S2C** were evaluated using two common kinetic models namely pseudo-first-order and pseudo-second-order. As shown in **Figures 6A,B** and **Table 1**, the pseudo-second-order displays the correlation coefficient (R^2) of 0.999, which is higher than that of the pseudo-first-order model. Moreover, the calculated RMSE values favored the pseudo-second-order model as a probable kinetic model. These results and kinetic theory, suggest that MB adsorption onto SA/p(AAc)/*o*-MWCNTs HNC was governed by chemisorption and physicochemical interactions (Makhado et al., 2019b).

The effect of the of initial concentration MB dye on the adsorption capacity of the SA/p(AAc)/*o*-MWCNTs HNC was evaluated in the range 530–1,350 mg/L of under optimum conditions (pH 6.0, 50 min contact time and a dose of 0.33 g/

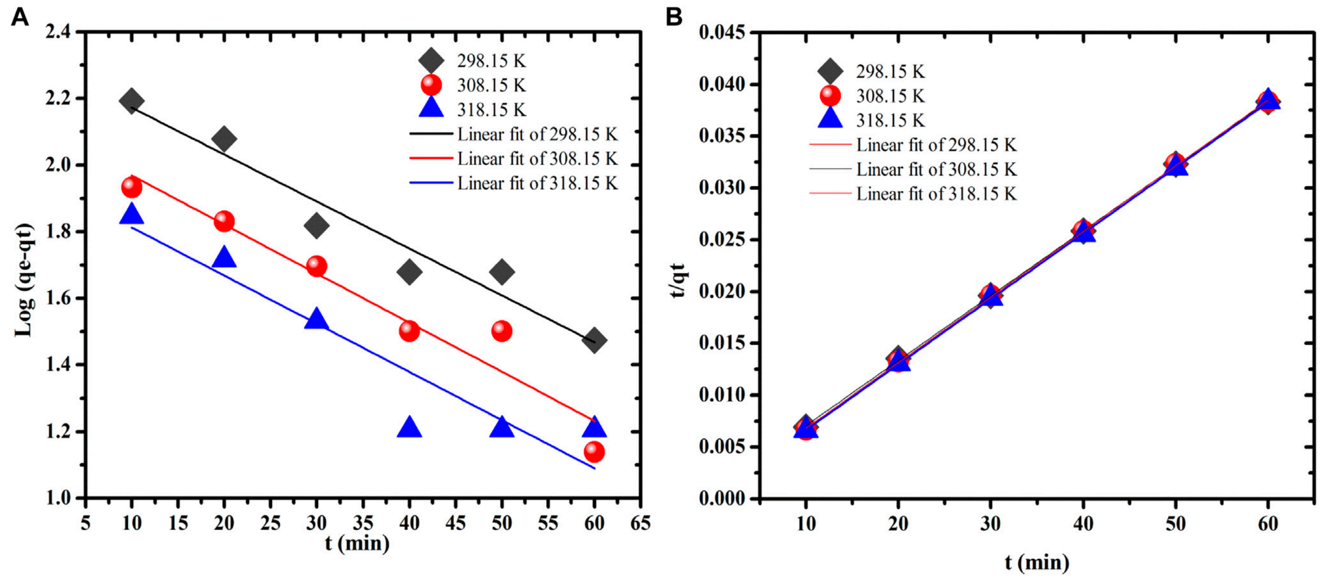

FIGURE 6 | Adsorption kinetic plots for MB dye onto SA/p(AAc)/*o*-MWCNTs HNC **(A)** pseudo-first-order and **(B)** pseudo-second-order model.

L) at three different temperatures, and the results are presented in **Supplementary Figure S2D**. It was observed that the adsorption capacity of SA/p(AAc)/*o*-MWCNTs HNC increased with increasing temperature, which implied that the adsorption process was endothermic in nature. The increase in adsorption capacity with increasing initial concentration demonstrated that the mass gradient functions as the driving force for the adsorption process. Furthermore, an increase in the concentration of MB dye solution at fixed SA/p(AAc)/*o*-MWCNTs HNC amount raised the mass transfer process.

To understand the relationship between the initial MB concentration and SA/p(AAc)/*o*-MWCNTs HNC the experimental adsorption data were fitted directly to three isotherm models namely Langmuir, Freundlich and Temkin models **Figures 7A–C**, respectively. The related isotherm parameters were calculated and tabulated in **Table 2**. The best-fitting adsorption isotherm model was selected based on the correlation coefficient value. The Langmuir isotherm model was the best fit for describing the adsorption process, which assumes that the adsorption process was monolayer coverage and the adsorption site on the SA/p(AAc)/*o*-MWCNTs HNC surface was homogeneous. The maximum adsorption capacities determined by Langmuir isotherm were found to be 1,596.0, 1,673.9, and 1,838.9 mg/g at 298.15, 308.15, and 318.15 K, respectively. The applicability of the Langmuir isotherm model was supported by the values of R_L, which were less than 1 for the sorption of MB dye. Moreover, the RMSE values for Langmuir isotherm were found to be least among other studied other isotherm models, confirming that the Langmuir isotherm model is an excellent one. A brief list of the reported adsorbents, used for the removal of MB from aqueous solution as well as the obtained maximum adsorption capacity, including the prepared adsorbents in this study, is presented in **Table 3** (Mittal et al., 2015; Sun et al., 2015; Mittal and Ray, 2016; Dai et al., 2017; Mahdavinia et al., 2017; Makhado et al., 2018a; Makhado et al., 2018b; Hassan et al., 2019; Ribeiro et al., 2019; Makhado et al., 2020). These results suggest that the SA/p(AAc)/*o*-MWCNTs HNC may be applied for the adsorption of MB from the aqueous phase. Moreover, SA/p(AAc)/*o*-MWCNTs HNC exhibited improved adsorption capacity as compared to unmodified hydrogel as shown in **Figure 5D**. SA/p(AAc)/*o*-MWCNTs HNC showed better maximum adsorption capacity than the one reported for SA/p(AAc) hydrogel (Makhado et al., 2020).

TABLE 1 | Adsorption kinetic model parameters for MB removal by SA/p(AAc)/*o*-MWCNTs HNC at three different temperatures. Influence of initial MB concentration and adsorption isotherm studies.

Kinetic models	Parameters	298.15 (K)	308.15 (K)	318.15 (K)
Pseudo-first-order	K'_1 (min^{-1})	0.0141	0.0147	0.0145
	R^2	0.9389	0.9192	0.8555
	RMSE	0.1067	0.0145	0.0107
Pseudo-second-order	$q_{e\ (cal.)}$ (mg/g)	1595.8	1579.8	1581.8
	K'_2 (g mg^{-1} min^{-1})	0.0008	0.0005	0.0004
	R^2	0.9998	0.9998	0.9999
	RMSE	0.00006	0.00005	0.00002

Adsorption Thermodynamics

The spontaneity of the MB dye adsorption using the prepared SA/p(AAc)/*o*-MWCNTs HNC at a temperature ranging from 298.15 to 318.15 K was evaluated to obtain thermodynamic parameters. Thermodynamics parameters such as enthalpy change (ΔH°), entropy change (ΔS°), and Gibbs free change (ΔG°) were

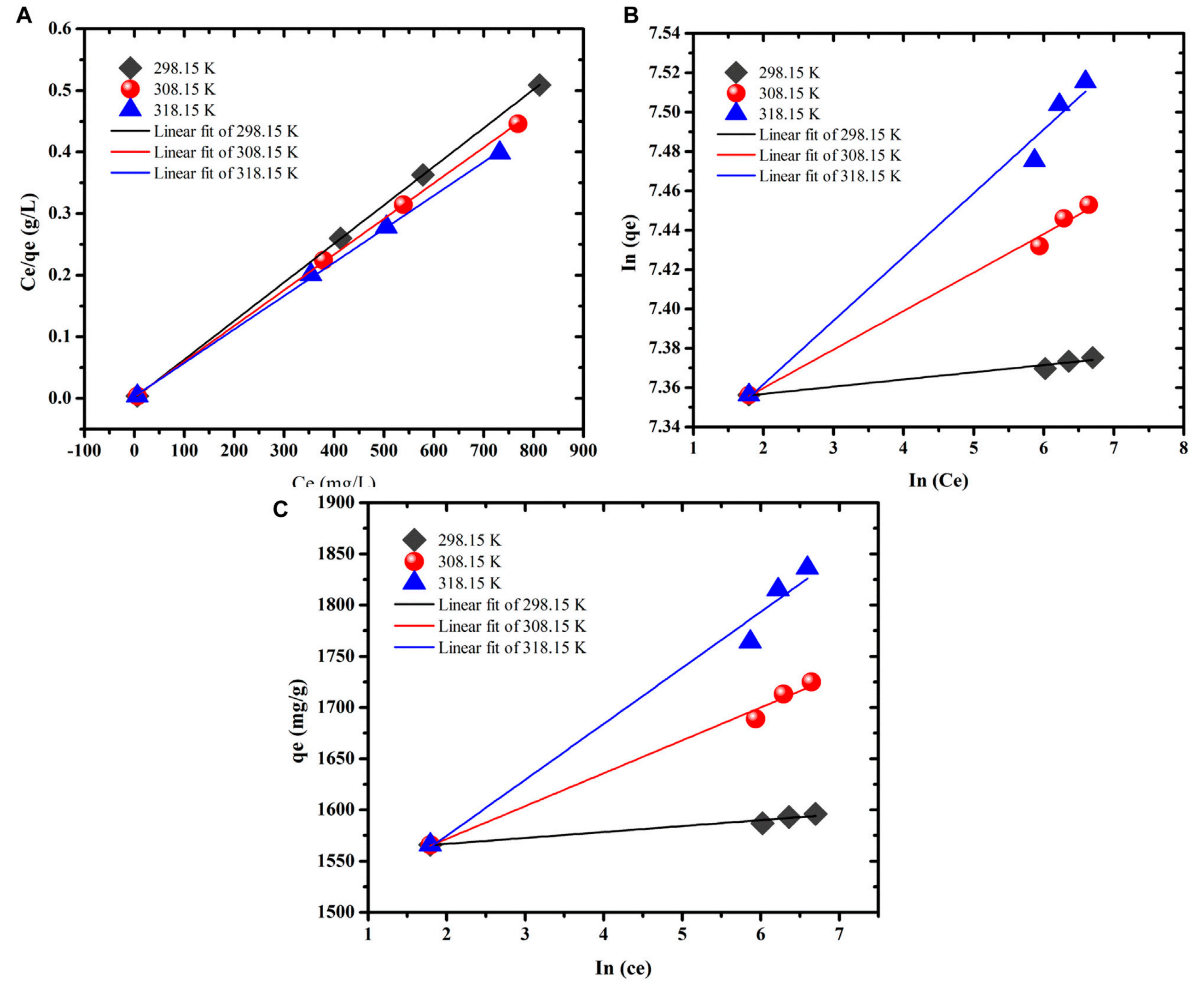

FIGURE 7 | Adsorption isotherm models for MB dye onto SA/p(AAc)/*o*-MWCNTs HNC **(A)** Langmuir, **(B)** Freundlich, and **(C)** Temkin model.

investigated via Vant Hoff' equation, which is expressed as shown in **Eqs 16,17**:

$$\Delta G^{\circ} = \Delta H^{\circ} - T\Delta S^{\circ}, \qquad (16)$$

$$\ln\left(\frac{q_e}{C_e}\right) = \frac{\Delta H^{\circ}}{RT} - \frac{\Delta S^{\circ}}{R}, \qquad (17)$$

where R is a universal gas constant (8.314 J/mol K), T is the temperature (K) and (qe/ce) is equilibrium constant. The values of ΔH° and ΔS° were calculated from the slope and intercept of the linear plot between In (q_e/c_e) and 1/T shown in **Figure 8A**, the values of ΔG° were obtained from **Eq. 16** and all thermodynamic parameters are summarized in **Supplementary Table S1**. The positive value of ΔS° and ΔH° indicated that the adsorption process was disordering and randomness at the solid-liquid interface on the adsorbent. Improved sorption efficiency, as well as the endothermic process, was validated by the positive value of ΔH°. The negative ΔG° values showed the spontaneous nature of the sorption process (Dogan et al., 2009). Moreover, the decrease in values of ΔG° with increasing temperature suggests that the sorption is favorable at high temperatures.

Regeneration Studies

The desorption of MB dye molecules adsorbed on the surface of SA/p(AAc)/*o*-MWCNTs HNC was conducted using HCl solution. The applicability of the hydrogel nanocomposite was investigated in six adsorption-desorption cycles and the results are shown in **Figure 8B**. The obtained results showed that the SA/p(AAc)/*o*-MWCNTs HNC maintained high adsorption percentage even after the sixth successive cycles under the same conditions. In conclusion, SA/p(AAc)/*o*-MWCNTs HNC can be used repeatedly for adsorption of MB dye without a significant decrease in MB dye affinity. This

TABLE 2 | Langmuir, Freundlich, and Temkin isotherm models for the MB adsorption.

Isotherm models	Isotherm constants	298.15 K	308.15 K	318.15 K
Langmuir	q_m(mg/g)	1596.0	1673.9	1838.9
	b	1.1176	0.3079	0.1673
	R_L	0.0017–0.0008	0.0061–0.0024	0.0112–0.0044
	R^2	0.999	0.999	0.999
	RMSE	0.0022	0.0008	0.0013
Freundlich	1/n	0.004	0.020	0.032
	K_F	1555.4	1511.1	1475.8
	R^2	0.961	0.988	0.982
	RMSE	3.678	0.0003	0.0007
Temkin	b_T (kJ·mol^{-1})	427.4	79.83	48.41
	β (J·mol^{-1})	5.799	32.09	54.64
	R^2	0.960	0.989	0.982
	RMSE	0.188	0.528	1.313

TABLE 3 | Comparison of the MB adsorption capacity of adsorbent with other reported adsorbents.

Adsorbents	Q_{max} (mg/g)	References
PVP/PCMC/GO/bentonite hydrogel	172.1	Dai et al. (2017)
Magnetic PVA/laponite RD hydrogel nanocomposite	251.0	Mahdavinia et al. (2017)
Chitosan/silica/ZnO nanocomposite	293.3	Hassan et al. (2019)
Xylan/poly(acrylic acid) magnetic hydrogel nanocomposite	438.6	Sun et al. (2015)
XG-cl-pAA/o-MWCNTs hydrogel nanocomposite	521.0	Makhado et al. (2018b)
XG-cl-pAA/rGO hydrogel nanocomposite	793.6	Makhado et al. (2018a)
AGMOF@AA superabsorbent hybrid	1,097.4	Ribeiro et al. (2019)
SA-poly(AA)/ZnO HNC	1,129.0	Makhado et al. (2020)
TiO_2NP-containing Gg-cl-PAAm composite hydrogel	1,305.5	Mittal and Ray (2016)
GK-cl-(PAA-co-AAM)/SiO_2 hydrogel nanocomposite	1,408.7	Mittal et al. (2015)
SA-poly(AA)/ZnO HNC	1,529.6	Makhado et al. (2020)
SA/p(AAc)/*o*-MWCNTs HNC	1,596.0	Present work

adsorbent holds great potential for remediation of MB wastewater.

Adsorption Mechanisms

Figure 8C shows the plausible mechanism for the adsorption of MB dye onto SA/p(AAc)/*o*-MWCNTs HNC. Both hydrogel and filler (*o*-MWCNTs) consist of carboxyl groups on the surface. Therefore, the formation of the SA/p(AAc)/*o*-MWCNTs HNC was achieved via strong hydrogen bond between hydrogel and *o*-MWCNTs. The adsorption studies (effect of solution pH) showed that high adsorption of MB onto the SA/p(AAc)/*o*-MWCNTs HNC surface was achieved at pH range 5–9. This result suggests strong electrostatic attraction between the adsorbent and the MB dye molecules. Abundant of carboxyl groups on the surface of SA/p(AAc)/*o*-MWCNTs HNC dissociated into carboxylate anions, which influenced attraction of positively charged MB dye molecules. The π-π stacking interaction between MB onto *o*-MWCNTs may also be responsible for the high sorption capacity of SA/p(AAc)/*o*-MWCNTs HNC.

CONCLUSION

In this work, the synthesis of SA/p(AAc)/*o*-MWCNTs HNC was successfully achieved via graft co-polymerization process. Different analytical techniques confirmed the presence of *o*-MWCNTs within the hydrogel network. The right degree of o-MWCNTs distribution in the polymeric hydrogel matrix was evident from TEM and SEM analysis. Moreover, the FTIR analysis showed the reduction in the absorption intensity of SA/p(AAc) hydrogel after the incorporation of *o*-MWCNTs confirming that the internal hydrogen bonding occurred among the carboxyl groups. The prepared SA/p(AAc)/*o*-MWCNTs HNC was applied as an adsorbent material for the removal of MB from aqueous solution via batch mode. The adsorption of MB onto adsorbent was influenced by several parameters including initial pH, adsorbent dose, contact time as well as equilibrium concentration. The adsorption kinetics and isotherm model revealed that the sorption process was best described by pseudo-second-order and the Langmuir models, respectively. Under optimal condition, the maximum adsorption capacity of SA/p(AAc)/*o*-MWCNTs HNC for MB dye was found to be 1,596.0 mg/g at 25°C obtained from the Langmuir isotherm model. The regeneration experiments demonstrated that the prepared adsorbent could be applied repeatedly for several cycles without significant reduction in the adsorption capacity. The adsorption studies showed that the electrostatic interaction was the main driving force for the sorption process. The SA/p(AAc)/*o*-MWCNTs HNC prepared in this

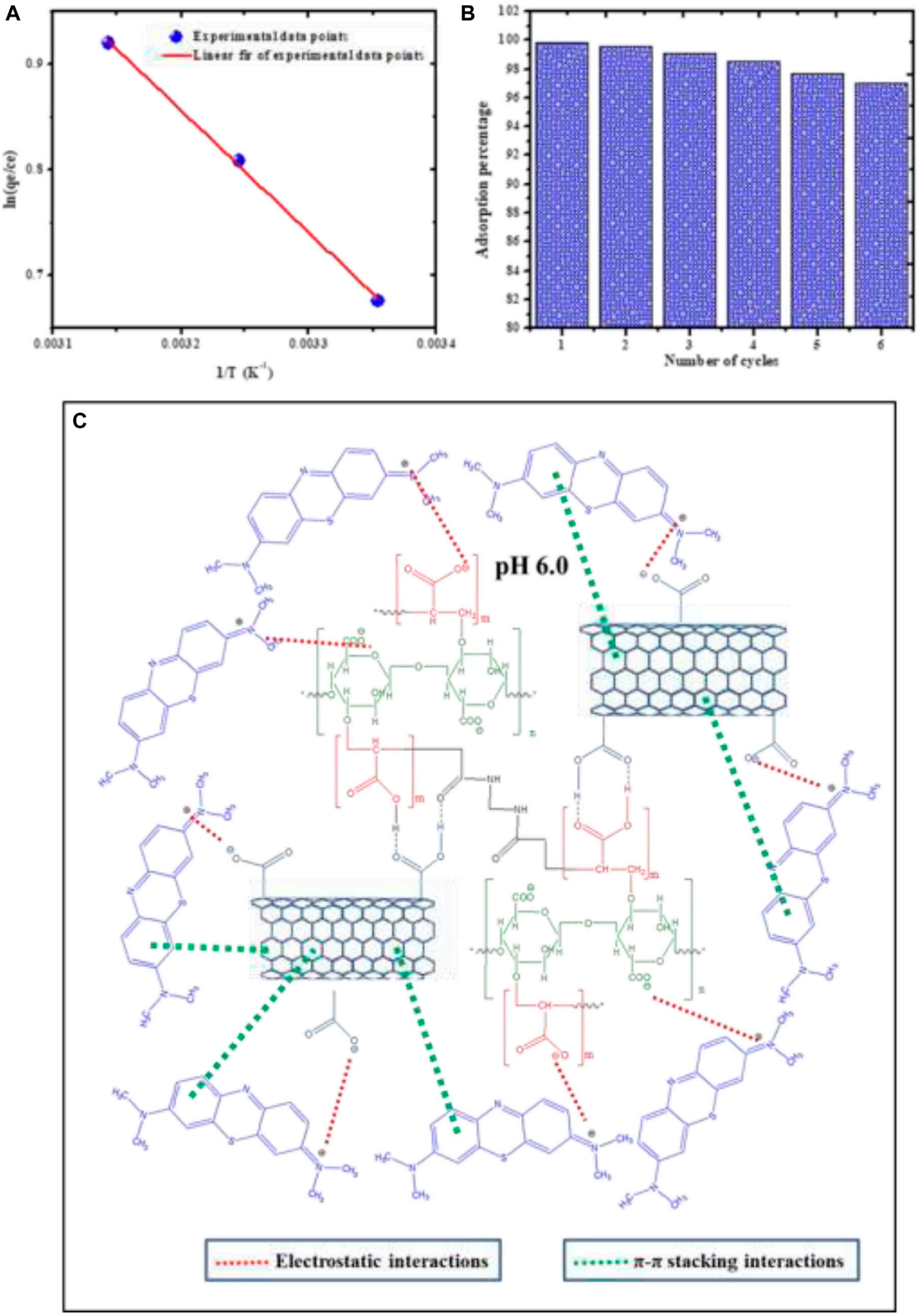

FIGURE 8 | (A) ln (q_e/c_e) vs. 1/T, **(B)** The regeneration of adsorbent for six-cycles adsorption/desorption of MB dye, and **(C)** Plausible mechanism for SA/p(AAc)/*o*-MWCNTs HNC and MB dye interaction.

study holds great potential for implementation in wastewater treatment.

DATA AVAILABILITY STATEMENT

The raw data supporting the conclusions of this article will be made available by the authors, without undue reservation.

AUTHOR CONTRIBUTIONS

EM investigated the methodology, validation, data curation, conceptualization, software, formal analysis, funding acquisition, and writing of the original draft. MH contributed in conceptualization, visualization, resources, supervision, funding acquisition, formal analysis, review and editing of the manuscript. All authors contributed to the article and approved the submitted version.

ACKNOWLEDGMENTS

The authors greatly acknowledge the financial aid from the National Research Foundation (NRF) under the Thuthuka program (UID 117727), NRF Grant Nos. 116679, and the University of Limpopo, South Africa.

SUPPLEMENTARY MATERIAL

The Supplementary Material for this article can be found online at: https://www.frontiersin.org/articles/10.3389/fchem.2021.576913/full#supplementary-material.

REFERENCES

Adegoke, K. A., and Bello, O. S. (2015). Dye sequestration using agricultural wastes as adsorbents. *Water Resour. Ind.* 12, 8–24. doi:10.1016/j.wri.2015.09.002

Ahmed, E. M. (2015). Hydrogel: preparation, characterization, and applications: a review. *J. Adv. Res.* 6, 105–121. doi:10.1016/j.jare.2013.07.006

Armağan, B., Turan, M., and Sȩlik, M. (2004). Equilibrium studies on the adsorption of reactive azo dyes into zeolite. *Desalination* 170, 33–39. doi:10.1016/j.desal.2004.02.091

Chatterjee, S., Lee, M. W., and Woo, S. H. (2010). Adsorption of Congo red by chitosan hydrogel beads impregnated with carbon nanotubes. *Bioresource Technol.* 101, 1800–1806. doi:10.1016/j.biortech.2009.10.051

Chen, X., Zhou, S., Zhang, L., You, T., and Xu, F. (2016). Adsorption of heavy metals by graphene oxide/cellulose hydrogel prepared from NaOH/urea aqueous solution. *Materials* 9, 582. doi:10.3390/ma9070582

Crini, G., and Badot, P.-M. (2008). Application of chitosan, a natural aminopolysaccharide, for dye removal from aqueous solutions by adsorption processes using batch studies: a review of recent literature. *Prog. Polym. Sci.* 33, 399–447. doi:10.1016/j.progpolymsci.2007.11.001

Crini, G. (2006). Non-conventional low-cost adsorbents for dye removal: a review. *Bioresource Technol.* 97, 1061–1085. doi:10.1016/j.biortech.2005.05.001

Dai, H., Huang, Y., and Huang, H. (2017). Eco-friendly polyvinyl alcohol/carboxymethyl cellulose hydrogels reinforced with graphene oxide and bentonite for enhanced adsorption of methylene blue. *Carbohydr. Polym.* 185, 1–11.

Despotovic, M., Nedic, V., Despotovic, D., and Cvetanovic, S. (2016). Evaluation of empirical models for predicting monthly mean horizontal diffuse solar radiation. *Renew. Sust. Energ. Reviews* 56, 246–260. doi:10.1016/j.rser.2015.11.058

Dogan, M., Karaoglu, M. H., and Alkan, M. (2009). Adsorption kinetics of maxilon yellow 4GL and maxilon red GRL dyes on kaolinite. *J. Hazard. Mater.* 165, 1142–1151. doi:10.1016/j.jhazmat.2008.10.101

Dyke, C. A., and Tour, J. M. (2004). Covalent functionalization of single-walled carbon nanotubes for materials applications. *J. Phys. Chem. A* 108, 11151–11159. doi:10.1021/jp046274g

El-Hag Ali, A., Shawky, H. A., Abd El Rehim, H. A., and Hegazy, E. A. (2003). Synthesis and characterization of PVP/AAc copolymer hydrogel and its applications in the removal of heavy metals from aqueous solution. *Eur. Polym. J.* 39, 2337–2344. doi:10.1016/s0014-3057(03)00150-2

Freundlich, H. M. F. (1906). Uber die adsorption in losungen. *Z. Phys. Chem.* 57, 385–470.

Hassan, H., Salama, A., El-ziaty, A. K., and El-Sakhawy, M. (2019). New chitosan/silica/zinc oxide nanocomposite as adsorbent for dye removal. *Int. J. Biol. Macromol.* 131, 520–526. doi:10.1016/j.ijbiomac.2019.03.087

Ho, Y. S., and McKay, G. (1998). Sorption of dye from aqueous solution by peat. *Chem. Eng. J.* 70, 115–124. doi:10.1016/s0923-0467(98)00076-1

Hosseinzadeh, H., Pashaei, S., Hosseinzadeh, S., Khodaparast, Z., Ramin, S., and Saadat, Y. (2018). Preparation of novel multi-walled carbon nanotubes nanocomposite adsorbent via RAFT technique for the adsorption of toxic copper ions. *Sci. Total Environ.* 640-641, 303–314. doi:10.1016/j.scitotenv.2018.05.326

Hosseinzadeh, H., Sadeghzadeh, M., and Babazadeh, M. (2011). Preparation and properties of carrageenan-g-poly(acrylic acid)/bentonite superabsorbent composite. *Jbnb* 02, 311–317. doi:10.4236/jbnb.2011.23038

Hu, T., Liu, Q., Gao, T., Dong, K., Wei, G., and Yao, J. (2018). Facile preparation of tannic acid-poly(vinyl alcohol)/sodium alginate hydrogel beads for methylene blue removal from simulated solution. *ACS Omega* 3, 7523–7531. doi:10.1021/acsomega.8b00577

Hu, Z., Zhang, X., Li, J., and Zhu, Y. (2020). Comparative study on the regeneration of Fe_3O_4@graphene oxide composites. *Front. Chem.* 8, 150. doi:10.3389/fchem.2020.00150

Hui, M., Shengyan, P., Yaqi, H., Rongxin, Z., Anatoly, Z., and Wei, C. (2018). A highly efficient magnetic chitosan “fluid” adsorbent with a high capacity and fast adsorption kinetics for dyeing wastewater purification. *Chem. Eng. J.* 345, 556–565. doi:10.1016/j.cej.2018.03.115

Juang, R.-S., Wu, F.-C., and Tseng, R.-L. (2002). Characterization and use of activated carbons prepared from bagasses for liquid-phase adsorption. *Colloids Surf, A Physicochem Eng. Asp.* 201, 191–199. doi:10.1016/s0927-7757(01)01004-4

Lagergren, S. (1898). About the theory of so called adsorption of soluble substances. *Ksver Veterskapsakad Handl* 24, 1–6.

Langmuir, I. (1918). The adsorption of gases on plane surfaces of glass, mica and platinum. *J. Am. Chem. Soc.* 40, 1361–1403. doi:10.1021/ja02242a004

Liu, C., Omer, A. M., and Ouyang, X.-k. (2018). Adsorptive removal of cationic methylene blue dye using carboxymethyl cellulose/k-carrageenan/activated montmorillonite composite beads: isotherm and kinetic studies. *Int. J. Biol. Macromol.* 106, 823–833. doi:10.1016/j.ijbiomac.2017.08.084

Ma, J., Yu, F., Zhou, L., Jin, L., Yang, M., and Luan, J., (2012). Enhanced adsorptive removal of methyl orange and methylene blue from aqueous solution by alkali-activated multiwalled carbon nanotubes. *ACS Appl. Mater. Interfaces* 4, 5749–5760. doi:10.1021/am301053m

Madima, N., Mishra, S. B., Inamuddin, I., and Mishra, A. K. (2020). Carbon-based nanomaterials for remediation of organic and inorganic pollutants from wastewater. A review. *Environ. Chem. Lett.* 18, 1169–1191. doi:10.1007/s10311-020-01001-0

Mahdavinia, G. R., Soleymani, M., Sabzi, M., Azimi, H., and Atlasi, Z. (2017). Novel magnetic polyvinyl alcohol/laponite RD nanocomposite hydrogels for efficient removal of methylene blue. *J. Environ. Chem. Eng.* 5, 2617–2630. doi:10.1016/j.jece.2017.05.017

Mahmoodi, N. M., Taghizadeh, M., Taghizadeh, A., and aghizadeh, A. (2018). Mesoporous activated carbons of low-cost agricultural bio-wastes with high adsorption capacity: preparation and artificial neural network modeling of dye removal from single and multicomponent (binary and ternary) systems. *J. Mol. Liq.* 269, 217–228. doi:10.1016/j.molliq.2018.07.108

Makhado, E., Pandey, S., Kang, M., and Fosso-Kanke, E. (2019a). Microwave assisted synthesis of xanthan gum-cl-Dimethyl acrylamide hydrogel based silica hydrogel as adsorbent for cadmium (II) removal. *Int'l Conference on Science, Eng. Technol. and Waste Manag. (Setwm-19)* 1, 1–6. doi:10.1016/j.ijbiomac.2018.07.104

Makhado, E., Pandey, S., Modibane, K. D., Kang, M., and Hato, M. J. (2020). Sequestration of methylene blue dye using sodium alginate poly(acrylic acid) @ZnO hydrogel nanocomposite: kinetic, Isotherm, and Thermodynamic Investigations. *Int. J. Biol. Macromol.* 162, 60–73. doi:10.1016/j.ijbiomac.2020.06.143

Makhado, E., Pandey, S., Nomngongo, P. N., and Ramontja, J. (2017a). Fast microwave-assisted green synthesis of xanthan gum grafted acrylic acid for enhanced methylene blue dye removal from aqueous solution. *Carbohydr. Polym.* 176, 315–326. doi:10.1016/j.carbpol.2017.08.093

Makhado, E., Pandey, S., Nomngongo, P. N., and Ramontja, J. (2019b). *New horizons in wastewaters management: emerging monitoring and remediation, hydrogel nanocomposites: innovations in nanotechnology for water treatment*. Hauppauge, NY: Nova Science Publishers, 87–113.

Makhado, E., Pandey, S., Nomngongo, P. N., and Ramontja, J. (2018a). Preparation and characterization of xanthan gum-cl-poly(acrylic acid)/o-MWCNTs hydrogel nanocomposite as highly effective re-usable adsorbent for removal of methylene blue from aqueous solutions. *J. Colloid Interface Sci.* 513, 700–714. doi:10.1016/j.jcis.2017.11.060

Makhado, E., Pandey, S., Nomngongo, P. N., and Ramontja, J. (2017b). Xanthan gum-cl-poly (acrylic acid)/reduced graphene oxide hydrogel nanocomposite as adsorbent for dye removal. *Int'l Conference on Adv. in Science, Eng. Technol. and Waste Manag. (Asetwm-171)*, 159–164. doi:10.17758/EARES

Makhado, E., Pandey, S., and Ramontja, J. (2018b). Microwave assisted synthesis of xanthan gum-cl-poly (acrylic acid) based-reduced graphene oxide hydrogel composite for adsorption of methylene blue and methyl violet from aqueous solution. *Int. J. Biol. Macromol.* 119, 255–269. doi:10.1016/j.ijbiomac.2018.07.104

Makhado, E., Pandey, S., and Ramontja, J. (2019c). Microwave-assisted green synthesis of xanthan gum grafted diethylamino ethyl methacrylate: an efficient adsorption of hexavalent chromium. *Carbohydr. Polym.* 222, 114989–114999. doi:10.1016/j.carbpol.2019.114989

Malatji, N., Makhado, E., Ramohlola, K. E., Modibane, K. D., Maponya, T. C., and Monama, G. R. (2020). Synthesis and characterization of magnetic clay-based carboxymethyl cellulose-acrylic acid hydrogel nanocomposite for methylene blue dye removal from aqueous solution. *Environ. Sci. Pollut. Res.* 27, 44089–44105. doi:10.1007/s11356-020-10166-8

Malik, P. K. (2003). Use of activated carbons prepared from sawdust and rice-husk for adsorption of acid dyes: a case study of acid yellow 36. *Dyes and Pigm.* 56, 239–249. doi:10.1016/s0143-7208(02)00159-6

Matome, S. M., Makhado, E., Katata-Seru, L. M., Maponya, T. C., Modibane, K. D., Hato, M. J., et al. (2020). Green synthesis of polypyrrole/nanoscale zero valent iron nanocomposite and use as an adsorbent for hexavalent chromium from aqueous solution. *South Afr. J. Chem. Eng.* 34, 1–10.

Minitha, C. R., Lalitha, M., Jeyachandran, Y. L., Senthilkumar, L., and Kumar, R. T. (2017). Adsorption behaviour of reduced graphene oxide towards cationic and anionic dyes: Co-action of electrostatic and π–π interactions. *Mater. Chem. Phys.* 194, 243–252. doi:10.1016/j.matchemphys.2017.03.048

Mittal, H., Maity, A., and Ray, S. S. (2015). Synthesis of co-polymer-grafted gum karaya and silica hybrid organic-inorganic hydrogel nanocomposite for the highly effective removal of methylene blue. *Chem. Eng. J.* 279, 166–179. doi:10.1016/j.cej.2015.05.002

Mittal, H., and Ray, S. S. (2016). A study on the adsorption of methylene blue onto gum ghatti/TiO_2 nanoparticles-based hydrogel nanocomposite. *Int. J. Biol. Macromol.* 88, 66–80. doi:10.1016/j.ijbiomac.2016.03.032

Mohammadinezhad, A., Marandi, G. B., Farsadrooh, M., and Javadian, H. (2018). Synthesis of poly(acrylamide-co-itaconic acid)/MWCNTs superabsorbent hydrogel nanocomposite by ultrasound-assisted technique: swelling behavior and Pb (II) adsorption capacity. *Ultrason. Sonochem.* 49, 1–12. doi:10.1016/j.ultsonch.2017.12.028

Ngah, W. S. W., Teong, L. C., and Hanafiah, M. A. K. M. (2011). Adsorption of dyes and heavy metal ions by chitosan composites: a review. *Carbohydr. Polym.* 83, 1446–1456. doi:10.1016/j.carbpol.2010.11.004

Oh, G. H., and Park, C. R. (2002). Preparation and characteristics of rice-straw-based porous carbons with high adsorption capacity. *Fuel* 81, 327–336. doi:10.1016/s0016-2361(01)00171-5

Olad, A., Pourkhiyabi, M., Gharekhani, H., and Doustdar, F. (2018). Semi-IPN superabsorbent nanocomposite based on sodium alginate and montmorillonite: reaction parameters and swelling characteristics. *Carbohydr. Polym.* 190, 295–306. doi:10.1016/j.carbpol.2018.02.088

Pandey, S., Do, J. Y., Kim, J., and Kang, M. (2020). Fast and highly efficient removal of dye from aqueous solution using natural locust bean gum based hydrogels as adsorbent. *Int. J. Biol. Macromol.* 143, 60–75. doi:10.1016/j.ijbiomac.2019.12.002

Ren, X., Chen, C., Nagatsu, M., and Wang, X. (2011). Carbon nanotubes as adsorbents in environmental pollution management: a review. *Chem. Eng. J.* 170, 395–410. doi:10.1016/j.cej.2010.08.045

Ribeiro, S. C., de Lima, H. H. C., Kupfer, V. L., da Silva, C. T. P., Veregue, F. R., and Radovanovic, E. (2019). Synthesis of a superabsorbent hybrid hydrogel with excellent mechanical properties: water transport and methylene blue absorption profiles. *J. Mol. Liq.* 294, 111553. doi:10.1016/j.molliq.2019.111553

Shi, Y., Xue, Z., Wang, X., Wang, L., and Wang, A. (2013). Removal of methylene blue from aqueous solution by sorption on lignocellulose-g-poly(acrylic acid)/montmorillonite three-dimensional cross-linked polymeric network hydrogels. *Polym. Bull.* 70, 1163–1179. doi:10.1007/s00289-012-0898-4

Sun, D., Zhang, X., Wu, Y., and Liu, X. (2010). Adsorption of anionic dyes from aqueous solution on fly ash. *J. Hazard. Mater.* 181, 335–342. doi:10.1016/j.jhazmat.2010.05.015

Sun, X.-F., Liu, B., Jing, Z., and Wang, H. (2015). Preparation and adsorption property of xylan/poly(acrylic acid) magnetic nanocomposite hydrogel adsorbent. *Carbohydr. Polym.* 118, 16–23. doi:10.1016/j.carbpol.2014.11.013

Taleb, M. F. A., Hegazy, D. E., and Ismail, S. A. (2012). Radiation synthesis, characterization and dye adsorption of alginate–organophilic montmorillonite nanocomposite. *Carbohydr. Polym.* 87, 2263–2269. doi:10.1016/j.carbpol.2011.10.058

Temkin, M. I. (1941). Adsorption equilibrium and process kinetics on nonhomogenous surface with interaction between adsorbed molecules. *Zhurnal Fizicheskoi Khimii* 15, 296–332.

Thakur, S., Pandey, S., and Arotiba, O. A. (2016). Development of a sodium alginate-based organic/inorganic superabsorbent composite hydrogel for adsorption of methylene blue. *Carbohydr. Polym.* 153, 34–46. doi:10.1016/j.carbpol.2016.06.104

Verma, A., Thakur, S., Mamba, G., Prateek, P., Gupta, R. K., and Thakur, P. (2020). Graphite modified sodium alginate hydrogel composite for efficient removal of malachite green dye. *Int. J. Biol. Macromol.* 148, 1130–1139. doi:10.1016/j.ijbiomac.2020.01.142

Wang, J. P., Santos, J. E., Chierice, G. O., and Cavalheiro, E. T. G. (2004). Thermal behavior of alginic acid and its sodium salt. *Eclet. Quím.* 29, 57–64. doi:10.1590/s0100-46702004000200009

Wattie, B., Dumont, M.-J., and Lefsrud, M. (2018). Synthesis and properties of feather keratin-based superabsorbent hydrogels. *Waste Biomass Valor.* 9, 391–400. doi:10.1007/s12649-016-9773-0

Wu, F.-C., Tseng, R.-L., and Juang, R.-S. (2001). Kinetic modeling of liquid-phase adsorption of reactive dyes and metal ions on chitosan. *Water Research* 35, 613–618. doi:10.1016/s0043-1354(00)00307-9

Conflict of Interest: The authors declare that the research was conducted in the absence of any commercial or financial relationships that could be construed as a potential conflict of interest.

frontiers in Chemistry

REVIEW
published: 07 April 2021
doi: 10.3389/fchem.2021.635344

Photodynamic Antimicrobial Chemotherapy: Advancements in Porphyrin-Based Photosensitize Development

James Oyim[1,2], *Calvin A. Omolo*[1,3] *and Edith K. Amuhaya*[1]*

[1]*School of Pharmacy and Health Sciences, United States International University-Africa, Nairobi, Kenya,* [2]*Department of Chemistry, University of Nairobi, Nairobi, Kenya,* [3]*Discipline of Pharmaceutical Sciences, College of Health Sciences, University of KwaZulu-Natal, Durban, South Africa*

The reduction of available drugs with effectiveness against microbes is worsening with the current global crisis of antimicrobial resistance. This calls for innovative strategies for combating antimicrobial resistance. Photodynamic Antimicrobial Chemotherapy (PACT) is a relatively new method that utilizes the combined action of light, oxygen, and a photosensitizer to bring about the destruction of microorganisms. This technique has been found to be effective against a wide spectrum of microorganisms, including bacteria, viruses, and fungi. Of greater interest is their ability to destroy resistant strains of microorganisms and in effect help in combating the emergence of antimicrobial resistance. This manuscript reviews porphyrins and porphyrin-type photosensitizers that have been studied in the recent past with a focus on their structure-activity relationship.

Keywords: photodynamic antimicrobial chemotherapy, photosensitizers, antimicrobial resistance, porphyrins, microorganisms

Edited by:
Tebello Nyokong,
Rhodes University, South Africa

Reviewed by:
Lukasz Sobotta,
Poznan University of Medical Sciences, Poland
Reama Chinedu George,
Obafemi Awolowo University, Nigeria

****Correspondence:***
Edith K. Amuhaya
eamuhaya@usiu.ac.ke

Specialty section:
This article was submitted to Organic Chemistry, a section of the journal Frontiers in Chemistry

Received: *30 November 2020*
Accepted: *15 February 2021*
Published: *07 April 2021*

Citation:
Oyim J, Omolo CA and Amuhaya EK (2021) Photodynamic Antimicrobial Chemotherapy: Advancements in Porphyrin-Based Photosensitize Development. Front. Chem. 9:635344. doi: 10.3389/fchem.2021.635344

INTRODUCTION

Infectious diseases continue to be one of the greatest healthcare challenges worldwide. The burden associated with these diseases remains high with the predominant diseases being tuberculosis, HIV/AIDS, acute lower respiratory tract infections, diarrheal diseases, urinary tract infections, skin and soft tissue infections, infective endocarditis, and sepsis among others (Laxminarayan et al., 2020; Nicholson, 2020). The emergence of antimicrobial resistance (AMR) has further exacerbated the situation. A recent review by O'Neal forecasted that over 10 million deaths will be attributed to AMR by the year 2050 (O'Neill, 2014). Of these infectious diseases, bacterial infections play a significant role, with a high number of deaths worldwide associated with them. Since the launch of antibiotics more than 70 years ago, with the introduction of penicillin, antibiotics have contributed significantly to the decrease in morbidity and mortality rates associated with bacterial infections (Frieri et al., 2017). However, the increasingly rampant antibacterial resistance threatens to send us back to the pre-antibiotic era. Consequently, the WHO has recognized 'the fight against antimicrobial resistance' as a global priority that urgently requires newer treatment strategies (WHO, 2018; WHO, 2020).

One of the common denominators to AMR has been the use of conventional antimicrobial agents. These conventional agents have various limitations such as insufficient bacterial concentrations at the site of infections, exposure of healthy tissues and normal flora to the drug, poor adherence to prescribed regimens that require frequent administration, and various undesirable adverse events that have led to the development of bacterial resistance, consequently limiting the success of the treatment

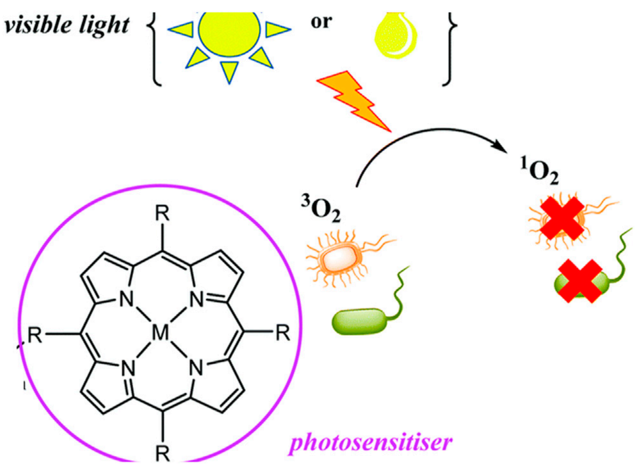

FIGURE 1 | Production of ROS by porphyrins and application in PACT. The illustration shows a generation of singlet oxygen upon irradiation by light which leads to microorganism destruction. Adapted with permission from Spagnul et al. (2017).

regimens (Omolo et al., 2018). The widespread misuse of antibiotics has also resulted in the growing problem of antimicrobial resistance in community and hospital settings (Rice, 2012). Moreover, most antimicrobial classes of antibiotics such as the β-lactams, glycopeptides, and fluoroquinolones have reportedly already developed resistance (Rice, 2012). Furthermore, most of the antimicrobial agents newly introduced to the market are modifications of the existing antimicrobial agents, and they thus lack a new mechanism of action (Theuretzbacher et al., 2020). Therefore, there is a need for a paradigm shift by introducing new agents that have novel mechanisms of action to fight AMR. This review summarizes the available research evidence on the use of porphyrin photosensitizers and their application in Photodynamic Antimicrobial Chemotherapy to eliminate disease-causing microbes. Additionally, the review will focus on structural modifications that have been made on porphyrins and delivery technologies that have been incorporated to further enhance their antimicrobial properties.

PHOTODYNAMIC ANTIMICROBIAL CHEMOTHERAPY

Photodynamic Antimicrobial Chemotherapy (PACT) is a promising strategy to eliminate pathogenic bacteria. Its mechanism of action occurs via the cytotoxic reactive oxygen species (ROS), which are generated by the photosensitive moieties after light irradiation. Upon absorption of light, the photosensitizer is excited to a higher excited singlet state. This is immediately followed by intersystem crossing of the excited photosensitizer to the excited triplet state. The electrons are then quenched by molecular oxygen to generate the toxic ROS, which is responsible for killing the microorganism. (Mai et al., 2017), (Coitiño et al., 2014). The ability of PACT to act on a wide range of bacteria, i.e., gram-negative and gram-positive, antibiotic-sensitive, and multi-resistant strains, presents a tremendous advantage that has made the technique gain a lot of research attention as an alternative strategy to combat antimicrobial resistance (Zeina et al., 2001; Sobotta et al., 2019). To date, various photosensitizers such as phenothiazines, acridines, phthalocyanines chlorins, and porphyrins have been studied for use as PACT photosensitizers (Skwor et al., 2016).

Porphyrins in PACT

Porphyrins and other tetrapyrrole molecules such as phthalocyanines and chlorins possess many desirable properties for use as photosensitizers in PACT. Key among these is their ability to absorb strongly in the UV-Vis near the IR region of the electromagnetic spectrum and their ability to generate a considerable triplet quantum yield, which makes them remarkable generators of ROS (Biscaglia and Gobbo, 2018; Nam et al., 2000) as shown in **Figure 1**. As a result, porphyrins have been found to have remarkable potential as antimicrobial agents (Vzorov et al., 2002).

Finetuning Porphyrin-Based Photosensitizers Properties for PACT

Porphyrins have a very flexible structure that can be modified in different ways to improve their photophysical and biological properties. This can be achieved through the insertion of different metals in the porphyrin's core or by selectively changing the peripheral substituents attached to the porphyrin skeleton at the meso, β-positions, or the porphyrin core (Beirão et al., 2014; Prasanth et al., 2014; Zoltan et al., 2015). Moreover, porphyrins have been reported to have very low bioavailability, a property that is attributed to their poor water solubility due to their hydrophobicity. Therefore, modifying their structures by adding polar substituents or by conjugating them with hydrophilic moieties such as amino acids, peptides, and proteins can lead to improved water solubility, which is an important property for their application in PACT (**Figures 2–4**).

As illustrated in **Table 1**, free porphyrins show potential for PACT application. Using various techniques that involve either complexation or covalent conjugations, various biomaterials have been employed in the modification of the physico-chemical and pharmacological properties of the attached porphyrin. For example, metals such as titanium dioxide (TiO_2) have been complexed with meso-tetrakis (p-sulfonatophenyl) porphyrin, and the resulting complexes showed improved photostability, fluorescence, and self-assembly into nanoparticles (Sułek et al., 2019). Another approach has involved the conjugation with amino acids, which added hydrophilicity and overall positive charge of the system. Conjugation with antimicrobial peptides (AMPs) and cell-penetrating peptides (CPPs) has also been reported. The use of AMPs and CPPs has led to an extended spectrum of activity, photostability, antimicrobial properties in the presence or absence of light, and the ability of the system to penetrate the cells and targeted organs (Dosselli et al., 2010). Other biomaterials also commonly used for fine-tuning the porphyrins are fatty acids. As shown in **Table 1**, fatty acids such as oleic acid and palmitic acid have been used to make superior porphyrin-based PACT systems. Such systems have exhibited better membrane penetration ability, enhanced microbial activity, reduction in aggregation of porphyrins, and high single oxygen production (Babu et al., 2019; Babu et al., 2020b). These

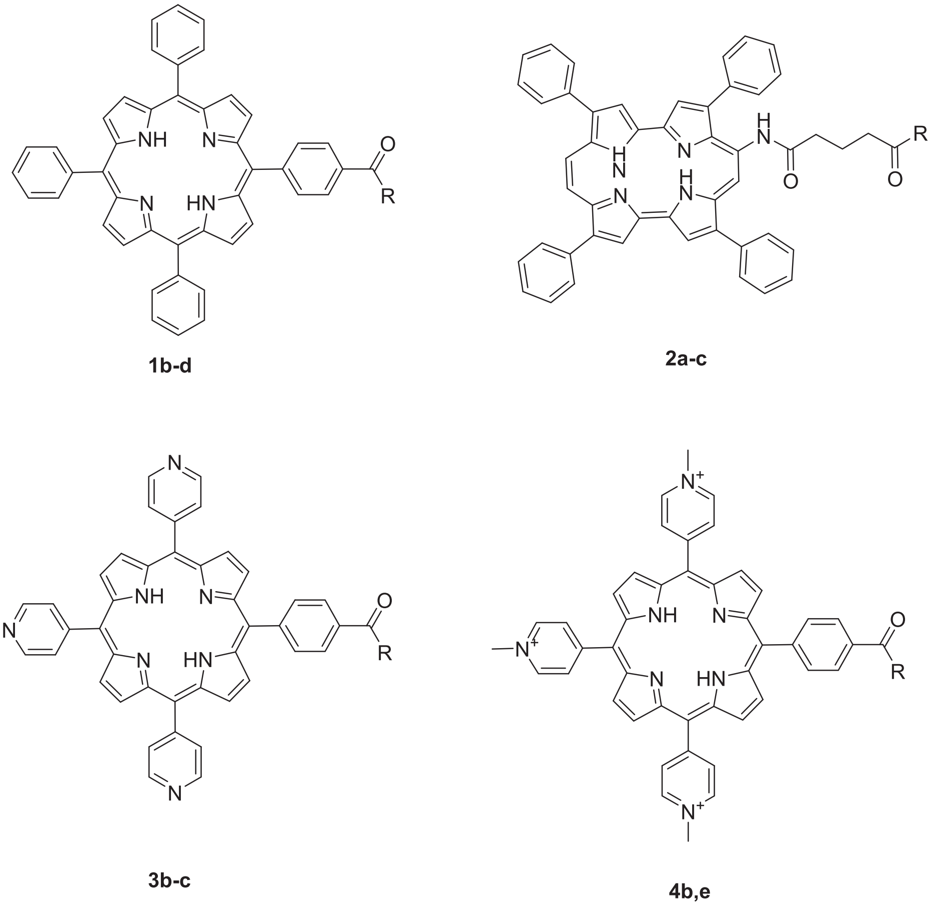

1b-d

2a-c

3b-c

4b,e

a. R= -OCH3 **b. R= -OH**

c. R= -Gly-Asn-Asn-Arg-Pro-Val-Tyr-Ile-Pro-Gln-Pro-Arg-Pro-Pro-His-Pro-His-Pro-Arg-Leu-OH

d. R= -Gly-Pro-Arg-Pro-Pro-His-Pro-Arg-Leu-OH

e. R= - Gly-Asn-Asn-Arg-Pro-Val-Tyr-Ile-Pro-Gln-Pro-Arg-Pro-Pro-His(N+CH3)-Pro-Arg-Leu-OH

FIGURE 2 | Conjugates obtained from the conjugation of porphyrins with antimicrobial peptides. There was enhanced PACT activity when the conjugates were used. By the use of the amide linkage, different peptides with different amino acid sequences and lengths were couped to the free porphyrins. The hydrophilicity offered by peptides together with the hydrophobicity of the peptides resulted in a conjugate that was amphophilic. The amphiphilicity results in better solubility of the free porphyrins Reproduced with permission from Dosselli et al. (2013).

modifications and the observed improvements are summarized in **Table 1**.

ADVANCEMENT OF PORPHYRIN-BASED PHOTOSENSITIZERS FOR TARGETED ANTIMICROBIAL PHOTODYNAMIC THERAPY

Recent advancements in synthetic chemistry and material science have resulted in the development of programable systems that respond to physiological changes due to diseases. PACT has followed a similar trend with the fabrication of systems that are stimuli-responsive to target bacteria. This section will focus on the advancement of porphyrin-based PACT systems for targeting bacteria and bacterial infection sites.

Porphyrin-Based Photosensitizer Nanosystems

The conjugation of porphyrins to nanoparticles has been explored. The conjugates have been found to exhibit enhanced antimicrobial properties and this is attributed to their biocompatibility and synergistic properties for PACT (Shabangu et al., 2020). By taking advantage of the small size of the porphyrins and porphyrin-nanoparticle conjugates, the photosensitizers can attach to the bacterial cell wall through a self-assembly process, resulting in

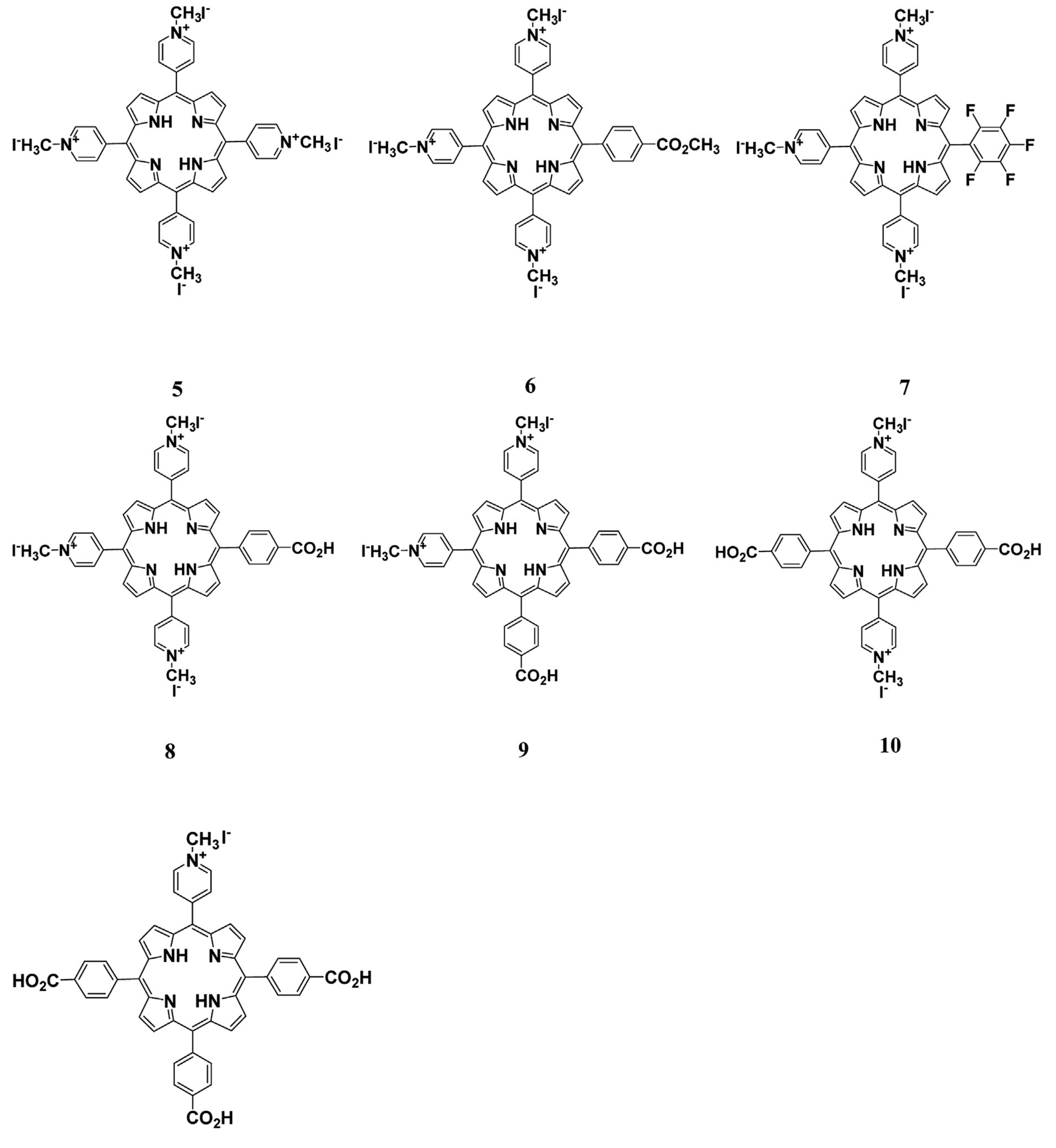

5 6 7 8 9 10 11

FIGURE 3 | Cationic porphyrin derivatives employed for photoinactivation of bacteria. Quaternization of the porphyrins resulted in systems with high positive charge density. Highly cationic systems were found to have enhanced antimicrobial activity. The positive charge was found to enhance the binding of the system to negatively charged bacteria leading to bacteria destruction. Reproduced with permission from Alves et al. (2009).

cell death. In some cases, however, these conjugations have led to unexpected interactions such as reduced uptake by the cells and reduced antimicrobial activity. (Wei et al., 2015; Kashef et al., 2017). The following sections will discuss various porphyrin-based nanoformulations.

Self-Assembled Porphyrin-Based Photosensitizers

Formulation of self-assembling photosensitizers has recently become a focus of interest in the field of photodynamic therapy with the synthesis of self-assembled porphyrin-based photosensitizers (SAPPs). SAPPs are synthesized by

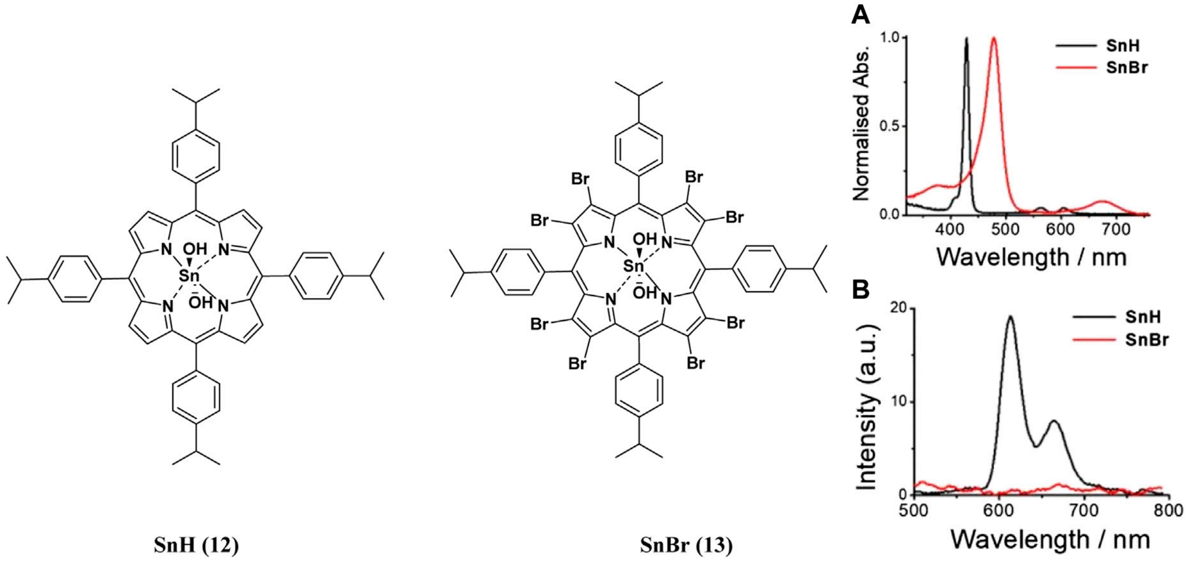

FIGURE 4 | (A) UV-Vis absorption **(B)** and emission spectra of porphyrins 12 and 13. These indicate the redshift in wavelength of absorption and quenching of the fluorescence upon bromination of the porphyrin. Reproduced with permission from porphyrin. Reproduced with permission from (Babu et al., 2020a).

conjugating hydrophobic porphyrins to hydrophilic or amphiphilic biomaterials such as polymers via covalent or supramolecular conjugations. These conjugations result in self-assembled nanostructures such as micelles (Spiller et al., 1998), polymersomes (Lanzilotto et al., 2018), honeycombs (Wang et al., 2014), nanofibers (Wang Q. et al., 2018), and metal-organic frameworks (MOFs) (Zhu et al., 2020). Electron spin-resonance spectroscopy (ESR) studies have shown that self-assembled porphyrins generate high oxygen singlets that are extremely effective for Photodynamic Therapy (Wang D. et al., 2018). Using supramolecular chemistry, Özkan and co-workers synthesized SAPPs from cucurbit (Wang Q. et al., 2018) uril and porphyrin to form a multifunctional system. The system was found to efficiently eliminate broad-spectrum bacteria via a light-trigger. To further potentiate the antibacterial activity, the system could be loaded effectively with drug molecules. As illustrated in **Figure 5,** the system was synthesized by conjugation of cucurbit (Omolo et al., 2018) uril shell, which acted as host for loaded drugs, to a free-base porphyrin core via suitable linkers (Kumar et al., 2019; Özkan et al., 2019). While the resulting system exhibited no dark activity towards *E. coli* (gram-negative bacteria), it showed relatively high cytotoxicity on *B. subtilis* (gram-positive bacteria). However, upon exposure to light, the self-assembled system had 100% bacteria elimination for both *E. coli* and *B. subtilis*. Similar SAPPs have been reported, with the systems showing improved PACT activities compared to the free porphyrins (Liu et al., 2013; Li et al., 2018; Khan et al., 2019).

Dendrimer Based Porphyrin Photosensitizers

Given that porphyrins are hydrophobic and have large π conjugation domains, they usually exhibit aggregation which ultimately affects their photo functionalities. This disadvantage can be overcome by Dendrimer porphyrins (DPs) (Gerhardt et al., 2003). DPs have unique photo functional properties including large absorption surface area, increased fluorescence emission, and enhanced photosensitizing properties (Wirotius et al., 2013). DPs remain soluble in aqueous media as a result of the large number of anionic functional groups on their periphery, which arise from the dendrimer conjugations **(Figure 6).** Moreover, they have wedges that effectively prevent aggregation. Studies have shown that DPs have about 10–100-fold higher photosensitizing effects when compared to bare protoporphyrin systems (Zhang et al., 2003). Penon and co-workers constructed a DP superstructure by coating the surface of the iron nanoparticles with two modified protoporphyrin molecules. From the study, it was found that DP with tris(hydroxymethyl)aminomethane (TRIS) modified protoporphyrin had two-fold singlet oxygen production ability when compared to the hydrophobic porphyrin system. It was concluded that hydrophilic systems were better for photodynamic therapy than hydrophobic ones (Penon et al., 2016). In another study, Staegemann and co-workers synthesized a high molecular dendritic mannose-functionalized hyperbranched polyglycerol and loaded it to a zinc porphyrin. The hydrophobic zinc (II) porphyrin photosensitizer was solubilized when it was loaded in the mannose- polyglycerol system. Further studies showed that an increased number of mannose molecules resulted in increased solubility of the zinc porphyrin, which led to better photosensitivity and consequently enhanced antibacterial activity (Staegemann et al., 2017). The increased photosensitivity and improved antimicrobial activity has been attributed to properties such as multivalence, an increased surface area to volume ratio, and an increased solubility that dendrimers have (Omolo et al., 2018).

Liposomes Based Porphyrin Photosensitizers

Liposomes are excellent vehicles for intracellular delivery as they easily fuse with biological membranes (Omolo et al., 2019). Ferro

TABLE 1 | Porphyrin fine tuning and the resulting conjugate properties.

Type of porphyrins	Material used in modification	Effect of modification	References
5,10,15,20-tetrakis-(4-sulfonatophenyl)porphyrin (TPPS); 5,10,15,20-tetrakis(2,6-difluoro-3-sulfophenyl)porphyrin (F2POH), and 5,10,15,20-tetrakis(2,6-difluoro-3-sulfophenyl)porphyrin Zn(II) (ZnF2POH)	titanium dioxide (qTiO$_2$)	Stability of the resulting nanoparticles Increase in the fluorescence when compared to free Porphyrins Increased levels of ROS generation after impregnation of qTiO2 Multiple mechanisms of ROS generation Exhibited antimicrobial activity at a very low concentration Broad-spectrum of activity	Sułek et al. (2019)
5-(4-nitrophenyl)-10,15,20-tripyridylporphyrin	Filter paper (cellulose) and cyanuric chloride as the linking agent	A strong photobactericidal effect against *S. aureus* and *E. coli.*	Mbakidi et al. (2013)
5,10,15,20-Tetrakis(4-N-methylpyridyl)-21H,23H-porphyrin.	Polymyxin B	Synergistic effect of Polymyxin B and PACT Increased uptake by Fibroblasts thus increasing wound healing. Expanded spectrum of activity of Polymyxin B to gram-positive bacteria after conjugation.	Le Guern et al. (2017)
Nitrotetraphenylporphyrin	amino acids, l-lysine, l-histidine, and l-arginine,	Amino acid conjugation resulted in water solubility Increased photostabilities Increasing conjugation with lysine increased production of singlet oxygen species Better photoinactivation abilities of bacteria when compared to the free Porphyrins Conjugates were resistant to degradation in serum within 24 h. Good biocompatibility	Meng et al. (2015)
2-hydroxypyridine axial ligated indium 5,10,15,20-tetrakis-(4-phenylmethylthio) porphyrin (3) and quaternized 2-hydroxypyridine axial ligated indium 5,10,15,20-tetrakis-(4-phenylmethylthio) porphyrin	oleyamine and oleic acid (OLA)	8 log reduction in bacteria 100% bacteria elimination after 25 min irradiation	Collen Makola et al. (2021)
tetrakis(N-methylpyridyl)porphyrin (TMPyP)	Lysine Analogue of Polymyxin B	4 log reduction compared to the untreated control) Photobactericidal activity against Gram-positive as well as Gram-negative bacteria	Le Guern et al. (2018)
Tetrakis(4-carboxyphenyl) porphyrin (TCPP)	DNA	High ROS generation efficiency and photostability Improved killing efficiency of gram-positive *S. aureus* bacteria	Kumari et al. (2017)
5(4′-carboxyphenyl)-10,15,20-triphenylporphyrin (cTPP)	cationic antimicrobial peptide, apidaecin Ib	Increased water solubility Broad spectrum of activity Improved antibacterial activity when compared to the free porphyrin	Dosselli et al. 2010
tricationic porphyrin [(5,10,15-tris(1-methylpyridinium-4-yl)-20-(pentafluorophenyl) porphyrin triiodide, Tri-Py+-Me-PF] Sn(IV) porphyrins	1-palmitoyl-2-oleoyl-sn-glycero-3-phosphatidylethanolamine pyridyloxyl trans-axial ligand	Improved antimicrobial effects and hence broad-spectrum coverage against drug-resistant strains of bacteria	Alves et al. (2013)
		Reduction in the aggregation of the porphyrins High singlet oxygen production High killing efficacy against *Staphylococcus aureus*	Babu et al. (2019), Babu et al. (2020b)

and co-workers explored the positive traits of liposomes for intracellular delivery of two photosensitizing agents, hematoporphyrin and chlorophyll, for the elimination of Methicillin-resistant *Staphylococcus aureus* (MRSA) (Ferro et al., 2006). From the study, when loaded with hematoporphyrin, the liposome led to improved endocellular absorption of the photosensitizer compared to when the cells were incubated with the free porphyrin. The hematoporphyrin-loaded liposome also displayed improved binding and more efficient photoinactivation of MRSA. Interestingly, hematoporphyrin did not affect the three-dimensional organization of the liposome during the photoinactivation of MRSA. On the other hand, chlorophyll markedly destroyed the structure of the lipid vesicle with no visible phototoxicity to MRSA. The same research group synthesized a positively charged *meso*-substituted porphyrin, (5-[4-(1-dodecanoylpyridinium)]-10,15,20-triphenyl-porphyrin) and delivered it *via* cationic liposomes for the elimination of MRSA. The free porphyrin had an unusually large fluorescence quantum yield (0.95), which led to the limited generation of singlet oxygen

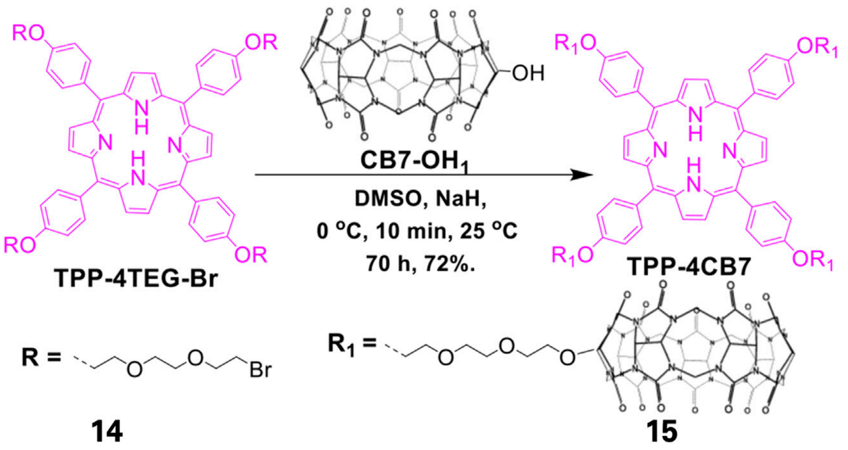

FIGURE 5 | Synthesis of Cucurbit[7]uril-linked Porphyrin-based complex. The free TPP porphyrin was first conjugated to hydrophilic polyethylene glycol after which the resulting conjugate was complexed with that of Cucurbit[7]uril. This reaction resulted in a self-assembling amphiphilic system. Adapted with permission from Özkan et al. (2019).

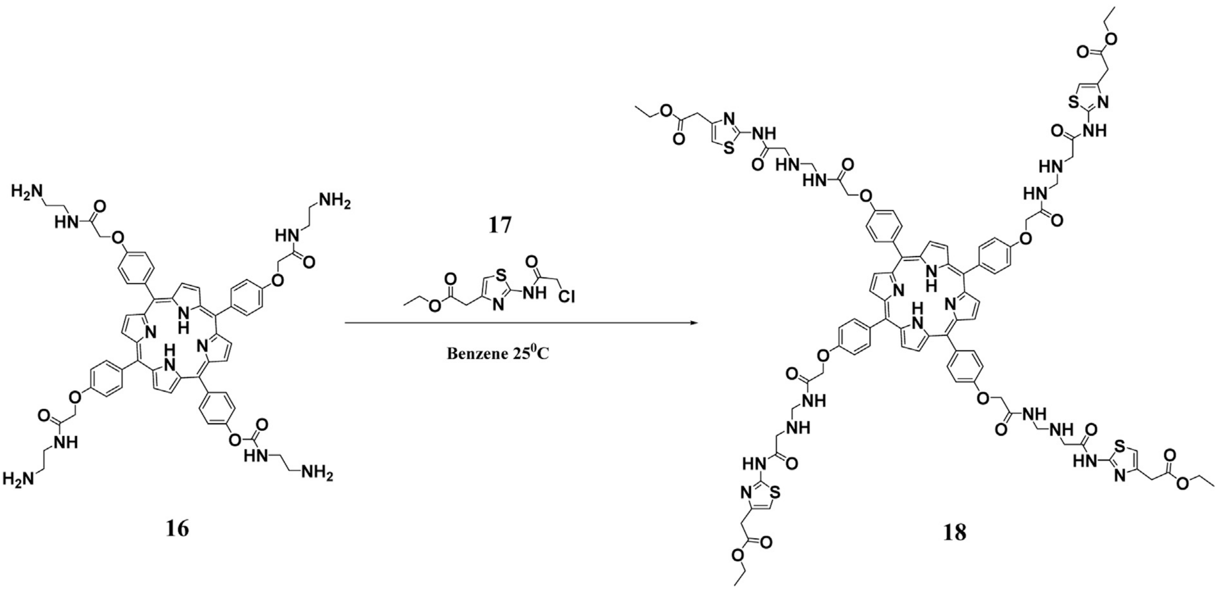

FIGURE 6 | Synthesis of hydrophilic DPs. This scheme shows the reaction of a polyamidoamine (PAMAM) functionalized porphyrin with ethyl 2-(2-chloroacetamido)-4-thiazoleacetate to obtain the hydrophylic DP. Reproduced with permission from Hernández Ramírez et al. (2020).

(Ferro et al., 2007). The porphyrin displayed a relatively low photosensitizing activity against MRSA when dissolved in an aqueous solution or when incorporated into neutral liposomes. However, when the porphyrin was loaded to a cationic liposome, the phototoxicity effects against the bacteria increased remarkably. The increased effect upon loading the synthesized porphyrin in the cationic delivery system was attributed to the increased positive charge density (Hassan et al., 2020) that destroyed the bacterial wall, thereby enhancing the permeability of the photosensitizer. A similar study was reported by Bombelli and co-workers (Bombelli et al., 2008). Moreover, high cationic charge density often has non-selective toxicity even to human cells (Fischer et al., 2003). Despite the good antimicrobial results, the study did not perform any cytotoxicity studies, and the application of the system on biotic systems will therefore be questionable.

Other Nano Based Porphyrin Photosensitizers

PACT has drawn the interest of nanotechnology as the efficacy of the treatment can be greatly augmented using nanoparticles. Nano-based porphyrin photosensitizers can be morphed into

TABLE 2 | Different nanosystems for delivery of photosensitizers.

Porphyrin used	Biomaterials	Nanocarrier	Irradaiation conditions	Bacteria tested on	Activity	Significant findings	References
4-(15-(4-(2-carboxyethyl)phenyl) porphyrin-5-yl)-1-methylpyridin-1-ium Iodide	Gelatin	phototheranostic polymeric nanoparticle	Green LED (0.5W, 520–560 nm) for about 3 h	*Escherichia coli, Serratia marcescens, Pseudomonas putida, Bacillus subtilis, Candida viswanathii*	5 and 6 log antimicrobial activity translating to about 99.999% elimination	Excellent hydrophilicity, biocompatibility, and stability, High $^1O_2$ quantum yield (44%), High fluorescence quantum yield (69%) Elimination of up 99.9999% of the gram-negative and positive bacteria and fungus.	Kirar et al. (2019)
Hematoporphyrin (HP) and Chlorophyll a (Chlorin)	Cationic lipids	Liposomes	White light from a Teclas Lamp, 100 mW/cm^2 For 30 min	MRSA	>5 log inhibition of MRSA by chlorin alone in 10 min. There was, however, a reduction in activity when the delivery systems were applied For HP, the delivery system greatly enhanced the inhibition activity	Endocellular concentration of photosensitizer Elimination of MRSA	Ferro et al. (2006)
zinc meso-tetra (4-pyridyl) porphyrin (ZnTPyP)	Zinc *meso*-tetra (4-pyridyl) porphyrin	Cubic nanoparticles	Solar simulator for 120 min	*E. coli*	50% was eliminated after 30 min. By 120 min, all the *E. Coli* was completely eliminated	Synthesized porphyrin self-assembled into cubic nanoparticles High singlet oxygen quantum yields Fairly stable for a long time in dark at ambient conditions. Attractive property for storage and transportation. Effective elimination of bacteria	Wang D. et al. (2018)
Sinoporphyrin sodium (DVDMS)	PLGA	Nanohybrids	Different visible laser doses	*Staphylococcus aureus* and multidrug-resistant (MDR) *S. Aureus*	4-log (99.9918%) inactivation of MRSA and 5-log (99.9995%) inactivation of *S. aureus*	Eliminated *Staphylococcus aureus* and multidrug-resistant (MDR) *S. Aureus* Accelerated wound healing in a burn infection model. Increased several regenerative factors. Fluorescence imaging achieved	Mai et al. (2020)
Tetrakis(4-carboxyphenyl) porphyrin	Bimetallic PCN-224(Zr/Ti)	Metal–Organic Framework	Visible light (200 mW cm^{-2}) for 3 min	*S. aureus, S. epidermidis, E. coli, A. baumannii,* MRSA, MRSE, MDR *E. coli and* MDR *A. baumannii*	96.4% MDR E. coli, 96.8% MRSA, and 96.2% MRSE were eliminated	Elimination of multidrug-resistant bacteria High singlet oxygen quantum yields Accelerated wound healing	Chen et al. (2020)

various nanosystems. One of the applications of the nanosystems is the improvement in the delivery of a photosensitizer to the bacteria and fluorescence inactivation kinetics. Nanosystems such as polymeric nanoparticles have been loaded with porphyrins to enhance the delivery to microorganisms and improve PACT activity. The polymeric nanosystems in focus have been on systems coined from biocompatible and biodegradable polymers such as from polylactic glycolic acid (PLGA) (Mai et al., 2020), poly(ε-caprolactone) (PCL) (Liu et al., 2017; Kubát et al., 2019; Chen et al., 2020; Contreras et al., 2020), gelatin (Kirar et al., 2019), and cyclodextrins (Ferro et al., 2009; Castriciano et al., 2017; Khurana et al., 2019; Zagami et al., 2020). Several reports of many nanosystems for PACT have been reported with great success as shown in **Table 2.**

Table 2 summarizes the improvements in the physicochemical and pharmacological properties of PACT systems when porphyrins are incorporated in nanocarriers. Different porphyrins have been incorporated in various nanosystems, such as liposomes, cubosomes, nanohybrids, and metal organic frameworks (MOF), to form multifunctional systems. For example, the combination of the porphyrins with biomaterials has resulted in systems that can be employed for theranostic purposes and PACT (Kirar et al., 2019). The porphyrin-based nanoformulations have also been reported to have controlled release and distribution properties for the singlet oxygen species and enhanced absorption in targeted cells and organs.

Multifunctional Porphyrin Based Systems

The advancement of synthetic chemistry and material science has resulted in the development of various multifunctional porphyrin-based systems. These include systems such as theranostic, wound-healing, and antimicrobial systems that have been reported in literature. Mai and co-workers reported a multifunctional porphyrin loaded nanosystem that was employed in the treatment of burn infections, stimulation of wound healing, elimination of a wide spectrum of bacterial via PACT, and bioimaging **(Figure 7)** The system was composed of the porphyrin photosensitizer, sinoporphyrin sodium (DVDMS), and poly(lactic-co-glycolic acid) (PLGA) was encapsulated with basic fibroblast growth factor (bFGF) and formed nanospheres. The nanospheres were implanted in a carboxymethyl chitosan (CMCS)–sodium alginate hybrid hydrogel. The system was evaluated for antibacterial properties against multidrug resistance bacteria (MDR), rheological properties, fluorescence imaging, and biocompatibility. The results indicated that the system had a 99.99% elimination of *S. aureus* and MDR *S. aureus* in mice models. Moreover, the nanosystem exhibited enhanced wound healing and regulation of regenerative and proinflammatory factors (**Figure 8**) (Mai et al., 2020). Another multifunctional porphyrin system was reported by Dai and co-workers. Their system was a thermosensitive and photosensitive micelle that was formulated from a star polymer, poly(ε-caprolactone)-block-Poly(*N*-isopropylacrylamide), which had a porphyrin-core (Dai et al., 2014). The system showed potential for multifunctionality and application. However, further characterization of the system is needed. Other multi-functional porphyrin-based systems, with antimicrobial and cancer therapy applications, have been reported in the literature (Belali et al., 2017; Cao-Milán et al., 2020; Li et al., 2020).

IN VIVO APPLICATIONS OF PACT BASED ON PORPHYRINS

In vivo studies are paramount to evaluate the translational ability of the formulated system to human trials. PACT systems have been gaining momentum as a treatment. The possible evaluation of clinical applications of PACT has included treatment of wound infections, body cavity infections (such as the mouth, nasal sinuses, and ear), and surface infections of the skin and cornea. This section will evaluate the various application of PACT systems in animal models.

PACT in Treatment of Wounds and Acceleration of Wound Healing

The effects of PACT on the treatment of skin infections have mostly been demonstrated in *in vitro* studies. What is still lacking is a complete *in vivo* evaluation of the feasibility of PACT in treating skin and soft-tissue infections. Many researchers have in recent times discouraged the over-reliance on *in vitro* studies results in PACT because of the variations of outcomes encountered when carrying out the complementary *in vivo* studies. This means that conducting *in vivo* follow-up studies, right after an *in vitro* study, is key in establishing the overall efficacy of PACT.

In vivo studies were carried out by Fila and co-workers where they utilized four photosensitizers in a murine model with chronic wounds that were infected with *Pseudomonas aeruginosa* and MRSA. While comparing the *in vivo* results with their past *in vitro* findings, they observed that there was a considerable reduction of the effectiveness of the therapy *in vivo*. The photosensitizers, 5,10,15,20-tetrakis(1-methyl pyridinium-4-yl) porphyrin (TMPyP), Rose Bengal, [Ru(2,2′ -bipyridine)2(2-(2′,2″:5″,2‴-terthiophene)-imidazo[4,5-f][1,10] phenanthroline)]2+ (TLD-1411), and methylene blue demonstrated good antimicrobial efficacy in 1–50 μM planktonic solutions; however, in *in-vivo,* there was a 24–48 h growth delay for MRSA and an extended growth inhibition of *P. aeruginosa* by the TLD-1411-assisted photodynamic therapy. In the *in vitro* studies, a 6 $\log_{10}$ reduction was attained even with the least concentration of 1 mM. However, in the *in vivo* tests, none of the photosensitizers achieved sterilization that was even equivalent to 3 $\log_{10}$ reduction based on bioluminescence radiance measurement (Fila et al., 2016).

Nonetheless, completely different observations have been made in other studies with better outcomes emerging during *in vivo* studies. For instance, Xu and co-workers (2016) studied the wound healing effect of PACT on mixed bacterial infections in rats using the lysin conjugate of 5,10,15,20-tetrakis(1-methyl pyridinium-4-yl)porphyrin tetra-iodide. Their studies demonstrated that the porphyrin was highly potent both *in vitro* and *in vivo*. It was also observed that the applied dose of light was a key factor for the success of PACT. In this study, a light dose of 50 J/cm^2 was established as the most suitable (Xu et al., 2016). A similar study done by Yuan and co-workers (Yuan et al., 2017) found that the cationic lysine-porphyrin conjugate (**12**) accelerated wound healing, while the cytotoxicity test conducted in mice showed that the porphyrin was not toxic.

The effectiveness of PACT in treating infected wounds has also been recently studied by Zhao and co-workers using a protoporphyrin IX–ethylenediamine derivative **(13)** against *Pseudomonas aeruginosa* in an *in vivo* model of *P. aeruginosa*-infected wounds. Their study

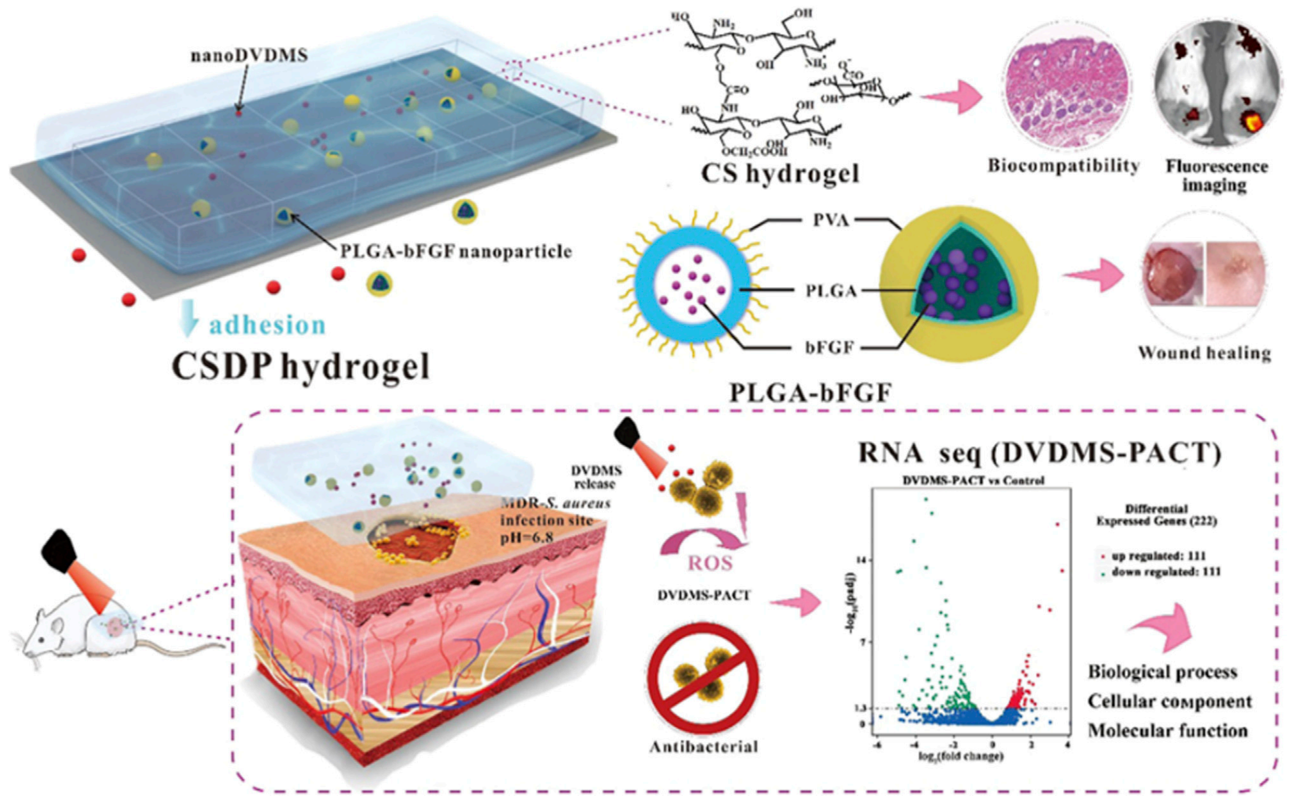

FIGURE 7 | Schematic representation of the multifunctionalities of the hydrogel; with improved bioavailability, there's improved reduction in bacteria and improved wound healing. Adapted with permission from Mai et al. (2020).

showed a significant reduction of the number of *P. aeruginosa* colonies. Additionally, the histological analysis demonstrated a very high wound healing rate (98%) after 14 days of therapy (**Figure 9**). According to the findings, 100 μM concentration of the porphyrin resulted in a 4.2 $\log_{10}$ reduction of *P. aeruginosa* colony units, which translated to about 10% more activity compared to the control group (Zhao et al., 2020).

PACT in Treatment of Body Cavity Infections

In vivo studies on the effects of PACT in oral fungal infections commonly caused by *C. albicans* were studied by Mima and co-workers. The group used Photogene (hematoporphyrin derivative) and two light sources—blue (455 nm) and red (630 nm)—to carry out their studies. From their results, there was a significant reduction in *C. albicans* obtained from the tongues of mice. The results from the histological evaluation showed that the local mucosa was not adversely affected by PACT (Mima et al., 2010). In a study by de Santi and co-workers (2018), PACT was also found to be effective against yeast cells that cause vaginal candidiasis. Utilizing protoporphyrin IX, among other photosensitizers, there was a significantly reduced *C. albicans* population, which was accompanied by prevention of further re-infection for about 1 week (de Santi et al., 2018). The results of these studies show alternative treatment of fungal infections by PACT is not only feasible but also safe.

Researchers have in the recent past explored various treatment methods including the effectiveness of PACT in the treatment of periodontitis (Moreira et al., 2015; Stájer et al., 2020). For instance, Prasanth and co-workers synthesized pyridinium-substituted porphyrin derivative **14** and *meso*-imidazolium-substituted porphyrin derivative **15** and studied their activity. The derivatives not only showed complete penetration into biofilms but also displayed better efficacy against the oral pathogens associated with periodontitis such as *F. nucleatum*, *E. faecalis*, and *A. actinomycetemcomitans* (Prasanth et al., 2014).

With most studies focusing on *in vitro* evaluation, an *in vivo* study was successfully carried out by Sigusch and co-workers using the beagle dog model. From this study, they observed that photodynamic therapy using chlorine e6 and 662 nm laser light source resulted in significant suppression of *P. gingivalis* and there was an overall reduction of the periodontal signs of redness and bleeding on probing (Sigusch et al., 2005). To experiment on human models, a full-mouth PACT in *F.nucleatum*-infected patients was carried out. The study established that the adjuvant application PACT method was effective in reducing periodontal inflammatory symptoms and treatment of *F. nucleatum* (Sigusch et al., 2010).

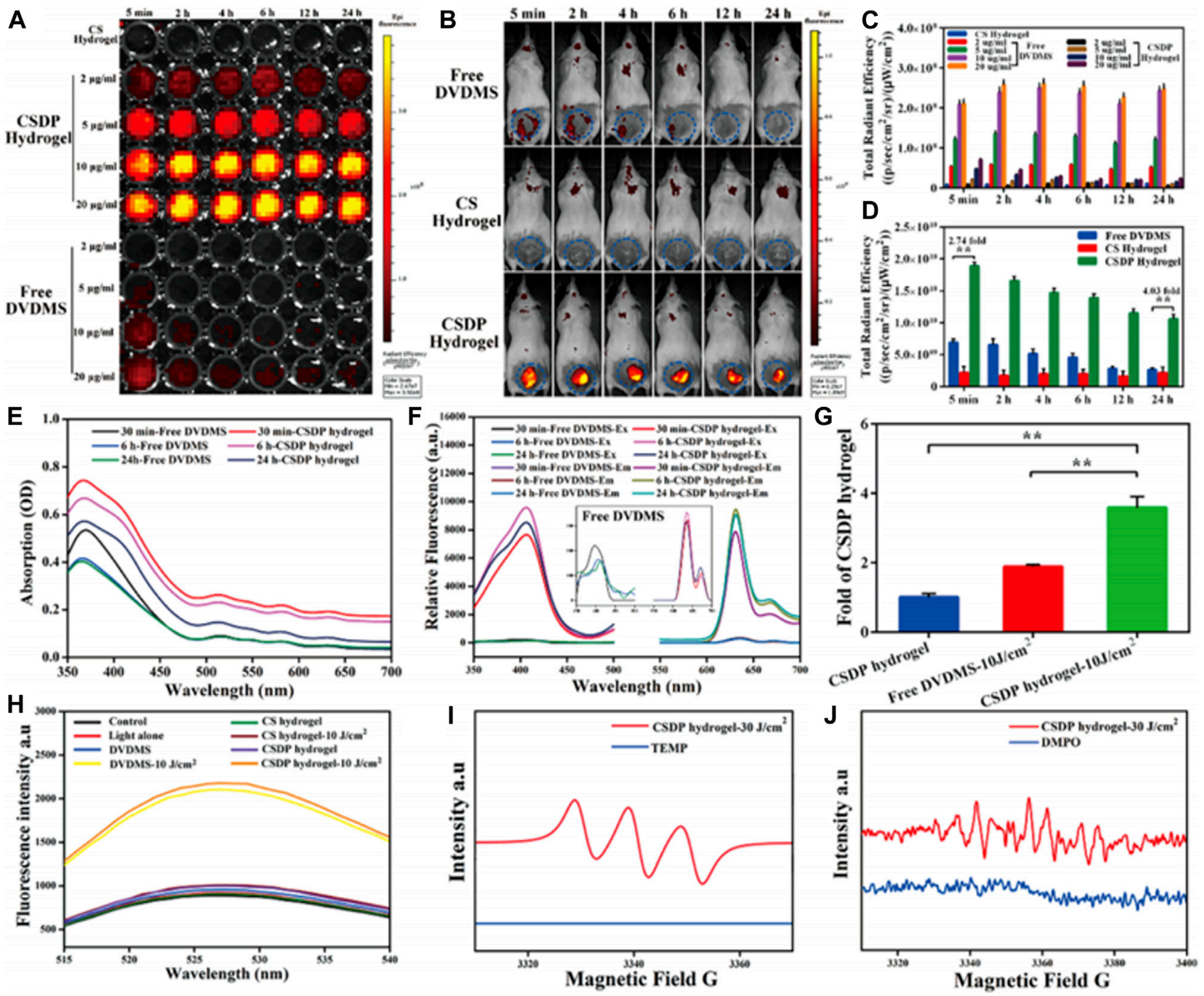

FIGURE 8 | Fluorescence imaging of the hydrogel via 96 well-plates **(A)** and *in vivo* mice models **(B)**. The figures showed the emittance of fluorescence from the hydrogel loaded with an imaging agent and PACT. The *in vitro* results were reproduced in tests done in animals through the mice model showing the translational potential of the system. **(C,D)** quantitative analysis of the fluorescence imaging *in vitro* and *in vivo*, respectively. Absorbance **(E)** and fluorescence spectra **(F)** of nanosysten, hydrogel loaded with the nanospheres. **(G)** Singlet oxygen yields of hydrogel, free nanospheres, and hydrogel-loaded nanospheres as determined *via* a fluorescence spectrophotometer. **(H)** SOSG spectra of different groups. **(I,J)** Detection of free radicals via ESR spectra and single oxygen species generation from the hydrogel in the dark and light irradiation, respectively. From the results, the hydrogel formulation was determined to be superior to the free systems. Reproduced with permission from Mai et al. (2020).

FUTURE PERSPECTIVES

As we have described in this review, porphyrins and their use in PACT continue to draw a lot of attention, with novel porphyrins and porphyrin conjugates being continuously synthesized. Indeed, the possibilities are unlimited. With the development of many different porphyrin synthetic routes coupled with their flexibility for modifications and conjugations to different moieties, more superior porphyrins can be designed and synthesized as the search for more efficient antibacterial agents for use in PACT are developed.

Much more still needs to be done in the application of PACT in dermatological and control of infectious diseases, especially in the management of acne and skin infections in general. Given the wide range of bacteria, it has been noted that the potential application of PACT in the treatment of infectious diseases is still lagging even with the positive acceptance of photodynamic therapy in treatment for other diseases such as psoriasis and skin cancers. There is, therefore, a need for researchers to further explore this application.

While the application of the PACT systems has been extensively evaluated for topical/local approach for animal model evaluations, more studies on systemic application still need to be done to fully evaluate their *in vivo* stability and therapeutic modality. It is important to fully understand their mechanisms of action and fine-tune them appropriately to improve their sensitivity and

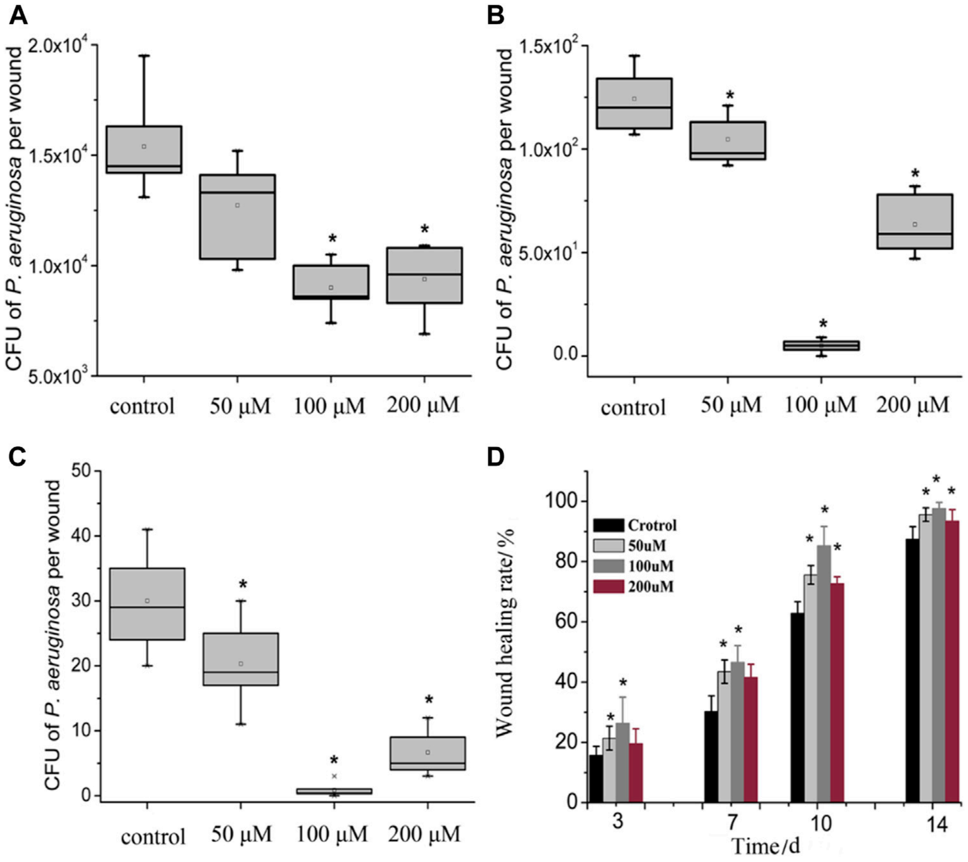

FIGURE 9 | Box plot of the viability of bacteria in wounded tissue in. Wound healing rate in the PACT chemotherapy groups when compared control groups on evaluated at different days. **(A–C)** showed there was a dose-dependent reduction of the CFU recovered from the wounds in various treatment groups when compared to the control. Treatment groups receiving 100 µM showed the best antimicrobial activity. **(D)** showed that the healing percentage correlated to the reduction of CFUs illustrated in **(A–C)**. A reduction in CFU recovered was accompanied by an increase in wound healing percentage. Reproduced with permission from Zhao et al. (2020).

selectivity. Notably, most studies discussed in this mini-review lacked toxicity data, and there is a need, therefore, for future studies to carry out toxicity studies (either short term or long term). This is very important because toxicity profile evaluation will go along way to bringing confidence in PACT systems before submitting the final products to regulatory endorsements.

Despite the gaps, the reported studies in this review indicate that there is a possibility of adding PACT systems to the current therapeutic arsenals for combating microbial resistance, especially where the conventional antimicrobials have failed. We believe that as the field of PACT continues to grow, the development of even more robust photosensitizers is more likely, based on the improved understanding of the specific action mechanisms and disease targeting ability of the developed systems. Such changes will lead to an increased role of PACT in the management of microbial infections.

AUTHOR CONTRIBUTIONS

JO, CO, and EA conceptualized the idea and contributed to the writing of the article.

REFERENCES

Alves, E., Costa, L., Carvalho, C. M., Tomé, J. P., Faustino, M. A., Neves, M. G., et al. (2009). Charge effect on the photoinactivation of Gram-negative and gram-positive bacteria by cationic meso-substituted porphyrins. *BMC Microbiol.* 9 (1), 70. doi:10.1186/1471-2180-9-70

Alves, E., Santos, N., Melo, T., Maciel, E., Dória, M. L., Faustino, M. A. F., et al. (2013). Photodynamic oxidation of *Escherichia coli* membrane phospholipids: new insights based on lipidomics. *Rapid Commun. Mass Spectrom.* 27 (23), 2717–2728. doi:10.1002/rcm.6739

Babu, B., Amuhaya, E., Oluwole, D., Prinsloo, E., Mack, J., and Nyokong, T. (2019). Preparation of NIR absorbing axial substituted tin(iv) porphyrins and their photocytotoxic properties. *MedChemComm* 10 (1), 41–48. doi:10.1039/c8md00373d

Babu, B., Mack, J., and Nyokong, T. (2020a). An octabrominated Sn(iv) tetraisopropylporphyrin as a photosensitizer dye for singlet oxygen biomedical applications. *Dalton Trans.* 49 (28), 9568–9573. doi:10.1039/d0dt01915a

Babu, B., Soy, R. C., Mack, J., and Nyokong, T. (2020b). Non-aggregated lipophilic water-soluble tin porphyrins as photosensitizers for photodynamic therapy and photodynamic antimicrobial chemotherapy. *New J. Chem.* 44 (26), 11006–11012. doi:10.1039/d0nj01564d

Beirão, S., Fernandes, S., Coelho, J., Faustino, M. A. F., Tomé, J. P. C., Neves, M. G. P. M. S., et al. (2014). Photodynamic inactivation of bacterial and yeast biofilms with a cationic porphyrin. *Photochem. Photobiol.* 90 (6), 1387–1396. doi:10.1111/php.12331

Belali, S., Karimi, A. R., and Hadizadeh, M. (2017). Novel nanostructured smart, photodynamic hydrogels based on poly(N-isopropylacrylamide) bearing porphyrin units in their crosslink chains: a potential sensitizer system in cancer therapy. *Polymer* 109, 93–105. doi:10.1016/j.polymer.2016.12.041

Biscaglia, F., and Gobbo, M. (2018). Porphyrin–peptide conjugates in biomedical applications. *J. Pept. Sci.* 110 (5), e24038. doi:10.1002/pep2.24038

Bombelli, C., Bordi, F., Ferro, S., Giansanti, L., Jori, G., Mancini, G., et al. (2008). New cationic liposomes as vehicles of m-tetrahydroxyphenylchlorin in photodynamic therapy of infectious diseases. *Mol. Pharm.* 5 (4), 672–679. doi:10.1021/mp800037d

Cao-Milán, R., Gopalakrishnan, S., He, L. D., Huang, R., Wang, L. S., Castellanos, L., et al. (2020). Thermally gated bio-orthogonal nanozymes with supramolecularly confined porphyrin catalysts for antimicrobial uses. *Chem* 6, 1113–1124. doi:10.1016/j.chempr.2020.01.015

Castriciano, M. A., Zagami, R., Casaletto, M. P., Martel, B., Trapani, M., Romeo, A., et al. (2017). Poly(carboxylic acid)-cyclodextrin/anionic porphyrin finished fabrics as photosensitizer releasers for antimicrobial photodynamic therapy. *Biomacromolecules* 18 (4), 1134–1144. doi:10.1021/acs.biomac.6b01752

Chen, M., Long, Z., Dong, R., Wang, L., Zhang, J., Li, S., et al. (2020). Titanium incorporation into Zr-porphyrinic metal-organic frameworks with enhanced antibacterial activity against multidrug-resistant pathogens. *Small* 16 (7), 1906240. doi:10.1002/smll.201906240

Coitiño, E. L. M., Mella, A., and Cárdenas-Jirón, G. I. (2014). Theoretical assessment of the photosensitization mechanisms of porphyrin-ruthenium(II) complexes for the formation of reactive oxygen species. *J. Photochem. Photobiol. A* 294, 68–74. doi:10.1016/j.jphotochem.2014.08.003

Collen Makola, L., Nyokong, T., and Amuhaya, E. K. (2021). Impact of axial ligation on photophysical and photodynamic antimicrobial properties of indium (III) methylsulfanylphenyl porphyrin complexes linked to silver-capped copper ferrite magnetic nanoparticles. *Polyhedron* 193, 114882. doi:10.1016/j.poly.2020.114882

Contreras, A., Raxworthy, M. J., Wood, S., and Tronci, G. (2020). Hydrolytic degradability, cell tolerance and on-demand antibacterial effect of electrospun photodynamically active fibres. *Pharmaceutics* 12 (8), 711. doi:10.3390/pharmaceutics12080711

Dai, X.-H., Jin, H., Yuan, S. S., Pan, J. M., Wang, X. H., Yan, Y. S., et al. (2014). Synthesis and characterization of thermosensitive, star-shaped poly(ε-caprolactone)-block-Poly(N-isopropylacrylamide) with porphyrin-core for photodynamic therapy. *J. Polym. Res.* 21 (6), 412. doi:10.1007/s10965-014-0412-9

de Santi, M. E. S. O., Prates, R. A., França, C. M., Lopes, R. G., Sousa, A. S., Ferreira, L. R., et al. (2018). Antimicrobial photodynamic therapy as a new approach for the treatment of vulvovaginal candidiasis: preliminary results. *Lasers Med. Sci.* 33 (9), 1925–1931. doi:10.1007/s10103-018-2557-y

Dosselli, R., Gobbo, M., Bolognini, E., Campestrini, S., and Reddi, E. (2010). Porphyrin-apidaecin conjugate as a new broad spectrum antibacterial agent. *ACS Med. Chem. Lett.* 1 (1), 35–38. doi:10.1021/ml900021y

Dosselli, R., Tampieri, C., Ruiz-González, R., De Munari, S., Ragàs, X., Sánchez-García, D., et al. (2013). Synthesis, characterization, and photoinduced antibacterial activity of porphyrin-type photosensitizers conjugated to the antimicrobial peptide apidaecin 1b. *J. Med. Chem.* 56 (3), 1052–1063. doi:10.1021/jm301509n

Ferro, S., Jori, G., Sortino, S., Stancanelli, R., Nikolov, P., Tognon, G., et al. (2009). Inclusion of 5-[4-(1-dodecanoylpyridinium)]-10,15,20-triphenylporphine in supramolecular aggregates of cationic amphiphilic cyclodextrins: physicochemical characterization of the complexes and strengthening of the antimicrobial photosensitizing activity. *Biomacromolecules* 10 (9), 2592–2600. doi:10.1021/bm900533r

Ferro, S., Ricchelli, F., Mancini, G., Tognon, G., and Jori, G. (2006). Inactivation of methicillin-resistant *Staphylococcus aureus* (MRSA) by liposome-delivered photosensitising agents. *J. Photochem. Photobiol. B, Biol.* 83 (2), 98–104. doi:10.1016/j.jphotobiol.2005.12.008

Ferro, S., Ricchelli, F., Monti, D., Mancini, G., and Jori, G. (2007). Efficient photoinactivation of methicillin-resistant *Staphylococcus aureus* by a novel porphyrin incorporated into a poly-cationic liposome. *Int. J. Biochem. Cell Biol.* 39 (5), 1026–1034. doi:10.1016/j.biocel.2007.02.001

Fila, G., Kasimova, K., Arenas, Y., Nakonieczna, J., Grinholc, M., Bielawski, K. P., et al. (2016). Murine model imitating chronic wound infections for evaluation of antimicrobial photodynamic therapy efficacy. *Front. Microbiol.* 7, 1258. doi:10.3389/fmicb.2016.01258

Fischer, D., Li, Y., Ahlemeyer, B., Krieglstein, J., and Kissel, T. (2003). *In vitro* cytotoxicity testing of polycations: influence of polymer structure on cell viability and hemolysis. *Biomaterials* 24 (7), 1121–1131. doi:10.1016/s0142-9612(02)00445-3

Frieri, M., Kumar, K., and Boutin, A. (2017). Antibiotic resistance. *J. Infect. Public Health* 10 (4), 369–378. doi:10.1016/j.jiph.2016.08.007

Gerhardt, S. A., Lewis, J. W., Kliger, D. S., Zhang, J. Z., and Simonis, U. (2003). Effect of micelles on oxygen-quenching processes of triplet-state para-substituted tetraphenylporphyrin photosensitizers. *J. Phys. Chem. A.* 107 (15), 2763–2767. doi:10.1021/jp0270912

Hassan, D., Omolo, C. A., Fasiku, V. O., Elrashedy, A. A., Mocktar, C., Nkambule, B., et al. (2020). Formulation of pH-responsive quatsomes from quaternary bicephalic surfactants and cholesterol for enhanced delivery of vancomycin against methicillin resistant *Staphylococcus aureus*. *Pharmaceutics* 12 (11), 1093. doi:10.3390/pharmaceutics12111093

Hernández Ramírez, R. E., Lijanova, I. V., Likhanova, N. V., Olivares Xometl, O., Hernández Herrera, A., Federico Chávez Alcalá, J., et al. (2020). Synthesis of PAMAM dendrimers with porphyrin core and functionalized periphery as templates of metal composite materials and their toxicity evaluation. *Arab. J. Chem.* 13 (1), 27–36. doi:10.1016/j.arabjc.2017.01.013

Kashef, N., Huang, Y.-Y., and Hamblin, M. (2017). Advances in antimicrobial photodynamic inactivation at the nanoscale. *Nanophotonics* 6 (5), 853–879. doi:10.1515/nanoph-2016-0189

Khan, R., Özkan, M., Khaligh, A., and Tuncel, D. (2019). Water-dispersible glycosylated poly(2,5'-thienylene)porphyrin-based nanoparticles for antibacterial photodynamic therapy. *Photochem. Photobiol. Sci.* 18 (5), 1147–1155. doi:10.1039/c8pp00470f

Khurana, R., Kakatkar, A. S., Chatterjee, S., Barooah, N., Kunwar, A., Bhasikuttan, A. C., et al. (2019). Supramolecular nanorods of (N-Methylpyridyl) porphyrin with captisol: effective photosensitizer for anti-bacterial and anti-tumor activities. *Front. Chem.* 7, 452. doi:10.3389/fchem.2019.00452

Kirar, S., Thakur, N. S., Laha, J. K., and Banerjee, U. C. (2019). Porphyrin functionalized gelatin nanoparticle-based biodegradable phototheranostics: potential tools for antimicrobial photodynamic therapy. *ACS Appl. Bio Mater.* 2 (10), 4202–4212. doi:10.1021/acsabm.9b00493

Kubát, P., Henke, P., Raya, R. K., Štěpánek, M., and Mosinger, J. (2019). Polystyrene and poly(ethylene glycol)-b-Poly(ε-caprolactone) nanoparticles with porphyrins: structure, size, and photooxidation properties. *Langmuir* 36 (1), 302–310. doi:10.1021/acs.langmuir.9b03468

Kumari, R., Khan, M. I., Bhowmick, S., Sinha, K. K., Das, N., and Das, P. (2017). Self-assembly of DNA-porphyrin hybrid molecules for the creation of antimicrobial nanonetwork. *J. Photochem. Photobiol. B* 172, 28–35. doi:10.1016/j.jphotobiol.2017.05.010

Kumar, Y., Patil, B., Khaligh, A., Hadi, S. E., Uyar, T., and Tuncel, D. (2019). Novel supramolecular photocatalyst based on conjugation of cucurbit[7]uril to non-metallated porphyrin for electrophotocatalytic hydrogen generation from water splitting. *ChemCatChem* 11 (13), 2994–2999. doi:10.1002/cctc.201900144

Lanzilotto, A., Kyropoulou, M., Constable, E. C., Housecroft, C. E., Meier, W. P., and Palivan, C. G. (2018). Porphyrin-polymer nanocompartments: singlet oxygen generation and antimicrobial activity. *J. Biol. Inorg. Chem.* 23 (1), 109–122. doi:10.1007/s00775-017-1514-8

Laxminarayan, R., Van Boeckel, T., Frost, I., Kariuki, S., Khan, E. A., Limmathurotsakul, D., et al. (2020). The lancet infectious diseases commission on antimicrobial resistance: 6 years later. *Lancet Infect. Dis.* 20 (4), e51–e60. doi:10.1016/S1473-3099(20)30003-7

Le Guern, F., Ouk, T. S., Ouk, C., Vanderesse, R., Champavier, Y., Pinault, E., et al. (2018). Lysine analogue of polymyxin B as a significant opportunity for photodynamic antimicrobial chemotherapy. *ACS Med. Chem. Lett.* 9 (1), 11–16. doi:10.1021/acsmedchemlett.7b00360

Le Guern, F., Sol, V., Ouk, C., Arnoux, P., Frochot, C., and Ouk, T. S. (2017). Enhanced photobactericidal and targeting properties of a cationic porphyrin following the attachment of polymyxin B. *Bioconjug. Chem.* 28 (9), 2493–2506. doi:10.1021/acs.bioconjchem.7b00516

Li, C., Lin, F., Sun, W., Wu, F. G., Yang, H., Lv, R., et al. (2018). Self-assembled rose bengal-exopolysaccharide nanoparticles for improved photodynamic inactivation of bacteria by enhancing singlet oxygen generation directly in the solution. *ACS Appl. Mater. Interfaces* 10 (19), 16715–16722. doi:10.1021/acsami.8b01545

Li, D., Fang, Y., and Zhang, X. (2020). Bacterial detection and elimination using a dual-functional porphyrin-based porous organic polymer with peroxidase-like and high near-infrared-light-enhanced antibacterial activity. *ACS Appl. Mater. Interfaces* 12 (8), 8989–8999. doi:10.1021/acsami.9b20102

Liu, K., Liu, Y., Yao, Y., Yuan, H., Wang, S., Wang, Z., et al. (2013). Supramolecular photosensitizers with enhanced antibacterial efficiency. *Angew Chem. Int. Ed. Engl.* 52 (32), 8285–8289. doi:10.1002/anie.201303387

Liu, M., Wang, L., Zheng, X., and Xie, Z. (2017). Zirconium-based nanoscale metal-organic framework/poly(ε-caprolactone) mixed-matrix membranes as effective antimicrobials. *ACS Appl. Mater. Interfaces* 9 (47), 41512–41520. doi:10.1021/acsami.7b15826

Mai, B., Gao, Y., Li, M., Wang, X., Zhang, K., Liu, Q., et al. (2017). Photodynamic antimicrobial chemotherapy for *Staphylococcus aureus* and multidrug-resistant bacterial burn infection *in vitro* and *in vivo*. *Int. J. Nanomed.* 12, 5915–5931. doi:10.2147/IJN.S138185

Mai, B., Jia, M., Liu, S., Sheng, Z., Li, M., Gao, Y., et al. (2020). Smart hydrogel-based DVDMS/bFGF nanohybrids for antibacterial phototherapy with multiple damaging sites and accelerated wound healing. *ACS Appl. Mater. Interfaces* 12 (9), 10156–10169. doi:10.1021/acsami.0c00298

Mbakidi, J. P., Herke, K., Alvès, S., Chaleix, V., Granet, R., Krausz, P., et al. (2013). Synthesis and photobiocidal properties of cationic porphyrin-grafted paper. *Carbohydr. Polym.* 91 (1), 333–338. doi:10.1016/j.carbpol.2012.08.013

Meng, S., Xu, Z., Hong, G., Zhao, L., Zhao, Z., Guo, J., et al. (2015). Synthesis, characterization and *in vitro* photodynamic antimicrobial activity of basic amino acid-porphyrin conjugates. *Eur. J. Med. Chem.* 92, 35–48. doi:10.1016/j.ejmech.2014.12.029

Mima, E. G., Pavarina, A. C., Dovigo, L. N., Vergani, C. E., Costa, C. A., Kurachi, C., et al. (2010). Susceptibility of *Candida albicans* to photodynamic therapy in a murine model of oral candidosis. *Oral Surg. Oral Med. Oral Pathol. Oral Radiol. Endod.* 109 (3), 392–401. doi:10.1016/j.tripleo.2009.10.006

Moreira, A. L., Novaes, A. B., Grisi, M. F., Taba, M., Souza, S. L., Palioto, D. B., et al. (2015). Antimicrobial photodynamic therapy as an adjunct to non-surgical treatment of aggressive periodontitis: a split-mouth randomized controlled trial. *J. Periodontol.* 86 (3), 376–386. doi:10.1902/jop.2014.140392

Nam, W., Lim, M. H., Oh, S.-Y., Lee, J. H., Lee, H. J., Woo, S. K., et al. (2000). Remarkable anionic axial ligand effects of iron (III) porphyrin complexes on the catalytic oxygenations of hydrocarbons by H_2O_2 and the formation of oxoiron(IV) porphyrin intermediates by m-chloroperoxybenzoic acid. *Angew Chem. Int. Ed.* 39 (20), 3646–3649. doi:10.1002/1521-3773(20001016)39:20<3646::aid-anie3646>3.0.co;2-q

Nicholson, F. (2020). "Infectious diseases: the role of the healthcare professional," in *Clinical forensic medicine*, Editor M. M. Stark (Berlin, Germany: Springer), 343–392.

Omolo, C. A., Kalhapure, R. S., Agrawal, N., Jadhav, M., Rambharose, S., Mocktar, C., et al. (2018). A hybrid of mPEG-b-PCL and G1-PEA dendrimer for enhancing delivery of antibiotics. *J. Control Release* 290, 112–128. doi:10.1016/j.jconrel.2018.10.005

Omolo, C. A., Megrab, N. A., Kalhapure, R. S., Agrawal, N., Jadhav, M., Mocktar, C., et al. (2019). Liposomes with pH responsive 'on and off' switches for targeted and intracellular delivery of antibiotics. *J. Liposome Res.* 31, 1–19. doi:10.1080/08982104.2019.1686517

Özkan, M., Kumar, Y., Keser, Y., Hadi, S. E., and Tuncel, D. (2019). Cucurbit[7]uril-Anchored porphyrin-based multifunctional molecular platform for photodynamic antimicrobial and cancer therapy. *ACS Appl. Bio Mater.* 2 (11), 4693–4697. doi:10.1021/acsabm.9b00763

O'Neill, J. (2014). "Antimicrobial resistance: tackling a crisis for the health and wealth of nations, in *Review on antimicrobial resistance*. London, United Kingdom.

Penon, O., Marín, M. J., Amabilino, D. B., Russell, D. A., and Pérez-García, L. (2016). Iron oxide nanoparticles functionalized with novel hydrophobic and hydrophilic porphyrins as potential agents for photodynamic therapy. *J. Colloid Interface Sci.* 462, 154–165. doi:10.1016/j.jcis.2015.09.060

Prasanth, C. S., Karunakaran, S. C., Paul, A. K., Kussovski, V., Mantareva, V., Ramaiah, D., et al. (2014). Antimicrobial photodynamic efficiency of novel cationic porphyrins towards periodontal gram-positive and gram-negative pathogenic bacteria. *Photochem. Photobiol.* 90 (3), 628–640. doi:10.1111/php.12198

Rice, L. B. (2012). Mechanisms of resistance and clinical relevance of resistance to β-lactams, glycopeptides, and fluoroquinolones. *Mayo Clin. Proc.* 87, 198. doi:10.1016/j.mayocp.2011.12.003

Shabangu, S. M., Babu, B., Soy, R. C., Oyim, J., Amuhaya, E., and Nyokong, T. (2020). Susceptibility of *Staphylococcus aureus* to porphyrin-silver nanoparticle mediated photodynamic antimicrobial chemotherapy. *J. Lumin.* 222, 117158. doi:10.1016/j.jlumin.2020.117158

Sigusch, B. W., Engelbrecht, M., Völpel, A., Holletschke, A., Pfister, W., and Schütze, J. (2010). Full-mouth antimicrobial photodynamic therapy in *Fusobacterium nucleatum*-infected periodontitis patients. *J. Periodontol.* 81 (7), 975–981. doi:10.1902/jop.2010.090246

Sigusch, B. W., Pfitzner, A., Albrecht, V., and Glockmann, E. (2005). Efficacy of photodynamic therapy on inflammatory signs and two selected periodontopathogenic species in a beagle dog model. *J. Periodontol.* 76 (7), 1100–1105. doi:10.1902/jop.2005.76.7.1100

Skwor, T. A., Klemm, S., Zhang, H., Schardt, B., Blaszczyk, S., and Bork, M. A. (2016). Photodynamic inactivation of methicillin-resistant *Staphylococcus aureus* and *Escherichia coli*: a metalloporphyrin comparison. *J. Photochem. Photobiol. B, Biol.* 165, 51–57. doi:10.1016/j.jphotobiol.2016.10.016

Sobotta, L., Skupin-Mrugalska, P., Piskorz, J., and Mielcarek, J. (2019). Porphyrinoid photosensitizers mediated photodynamic inactivation against bacteria. *Eur. J. Med. Chem.* 175, 72–106. doi:10.1016/j.ejmech.2019.04.057

Spagnul, C., Turner, L. C., Giuntini, F., Greenman, J., and Boyle, R. W. (2017). Synthesis and bactericidal properties of porphyrins immobilized in a polyacrylamide support: influence of metal complexation on photoactivity. *J. Mater. Chem. B* 5 (9), 1834–1845. doi:10.1039/c6tb03198f

Spiller, W., Kliesch, H., Wöhrle, D., Hackbarth, S., Röder, B., and Schnurpfeil, G. (1998). Singlet oxygen quantum yields of different photosensitizers in polar solvents and micellar solutions. *J. Porphyr. Phthalocyanines* 02 (02), 145–158. doi:10.1002/(sici)1099-1409(199803/04)2:2<145::aid-jpp60>3.0.co;2-2

Staegemann, M. H., Gitter, B., Dernedde, J., Kuehne, C., Haag, R., and Wiehe, A. (2017). Mannose-functionalized hyperbranched polyglycerol loaded with zinc porphyrin: investigation of the multivalency effect in antibacterial photodynamic therapy. *Chem. Eur. J.* 23 (16), 3918–3930. doi:10.1002/chem.201605236

Stájer, A., Kajári, S., Gajdács, M., Musah-Eroje, A., and Baráth, Z. (2020). Utility of photodynamic therapy in dentistry: current concepts. *Dent. J.* 8 (2), 43. doi:10.3390/dj8020043

Sułek, A., Pucelik, B., Kobielusz, M., Łabuz, P., Dubin, G., and Dąbrowski, J. M. (2019). Surface modification of nanocrystalline TiO_2 materials with sulfonated porphyrins for visible light antimicrobial therapy. *Catalysts* 9 (10), 821. doi:10.3390/catal9100821

Theuretzbacher, U., Outterson, K., Engel, A., and Karlén, A. (2020). The global preclinical antibacterial pipeline. *Nat. Rev. Microbiol.* 18 (5), 275–285. doi:10.1038/s41579-019-0288-0

Vzorov, A. N., Dixon, D. W., Trommel, J. S., Marzilli, L. G., and Compans, R. W. (2002). Inactivation of human immunodeficiency virus type 1 by porphyrins. *Antimicrob. Agents Chemother.* 46 (12), 3917–3925. doi:10.1128/aac.46.12.3917-3925.2002

Wang, D., Niu, L., Qiao, Z. Y., Cheng, D. B., Wang, J., Zhong, Y., et al. (2018). Synthesis of self-assembled porphyrin nanoparticle photosensitizers. *ACS Nano.* 12 (4), 3796–3803. doi:10.1021/acsnano.8b01010

Wang, Q., Chen, W., Zhang, Q., Ghiladi, R. A., and Wei, Q. (2018). Preparation of photodynamic P(MMA-co-MAA) composite nanofibers doped with MMT: a facile method for increasing antimicrobial efficiency. *Appl. Surf. Sci.* 457, 247–255. doi:10.1016/j.apsusc.2018.06.041

Wang, Y., Liu, Y., Li, G., and Hao, J. (2014). Porphyrin-based honeycomb films and their antibacterial activity. *Langmuir* 30 (22), 6419–6426. doi:10.1021/la501244s

Wei, L., Lu, J., Xu, H., Patel, A., Chen, Z. S., and Chen, G. (2015). Silver nanoparticles: synthesis, properties, and therapeutic applications. *Drug Discov. Today* 20 (5), 595–601. doi:10.1016/j.drudis.2014.11.014

WHO (2018). *WHO Report on Surveillance of Antibiotic Consumption: 2016–2018 Early implementation*. Geneva, Switzerland: World health oganisation.

WHO (2020). Antimicrobial resistance. Available at: https://www.who.int/news-room/fact-sheets/detail/antimicrobial-resistance (Accessed October 13, 2020).

Wirotius, A.-L., Ibarboure, E., Scarpantonio, L., Schappacher, M., McClenaghan, N. D., and Deffieux, A. (2013). Hydrosoluble dendritic poly(ethylene oxide)s with zinc tetraphenylporphyrin branching points as photosensitizers. *Polym. Chem.* 4 (6), 1903–1912. doi:10.1039/c2py20936e

Xu, Z., Gao, Y., Meng, S., Yang, B., Pang, L., Wang, C., et al. (2016). Mechanism and in vivo Evaluation: photodynamic antibacterial chemotherapy of lysine-porphyrin conjugate. *Front. Microbiol.* 7, 242. doi:10.3389/fmicb.2016.00242

Yuan, Y., Liu, Z. Q., Jin, H., Sun, S., Liu, T. J., Wang, X., et al. (2017). Photodynamic antimicrobial chemotherapy with the novel amino acid-porphyrin conjugate 4I: *in vitro* and *in vivo* studies. *PLoS One* 12 (5), e0176529. doi:10.1371/journal.pone.0176529

Zagami, R., Franco, D., Pipkin, J. D., Antle, V., De Plano, L., Patanè, S., et al. (2020). Sulfobutylether-β-cyclodextrin/5,10,15,20-tetrakis(1-methylpyridinium-4-yl) porphine nanoassemblies with sustained antimicrobial phototherapeutic action. *Int. J. Pharm.* 585, 119487. doi:10.1016/j.ijpharm.2020.119487

Zeina, B., Greenman, J., Purcell, W. M., and Das, B. (2001). Killing of cutaneous microbial species by photodynamic therapy. *Br. J. Dermatol.* 144 (2), 274–278. doi:10.1046/j.1365-2133.2001.04013.x

Zhang, G. D., Harada, A., Nishiyama, N., Jiang, D. L., Koyama, H., Aida, T., et al. (2003). Polyion complex micelles entrapping cationic dendrimer porphyrin: effective photosensitizer for photodynamic therapy of cancer. *J. Control Release* 93 (2), 141–150. doi:10.1016/j.jconrel.2003.05.002

Zhao, Z. J., Xu, Z. P., Ma, Y. Y., Ma, J. D., and Hong, G. (2020). Photodynamic antimicrobial chemotherapy in mice with *Pseudomonas aeruginosa*-infected wounds. *PLoS One* 15 (9), e0237851. doi:10.1371/journal.pone.0237851

Zhu, Y., Chen, J., and Kaskel, S. (2020). Porphyrin-based metal-organic Frameworks for biomedical applications. *Angew. Chem. Int. Ed.* 60, 5010–5035. doi:10.1002/anie.201909880

Zoltan, T., Vargas, F., López, V., Chávez, V., Rivas, C., and Ramírez, Á. H. (2015). Influence of charge and metal coordination of meso-substituted porphyrins on bacterial photoinactivation. *Spectrochim. Acta A Mol. Biomol. Spectrosc.* 135, 747–756. doi:10.1016/j.saa.2014.07.053

Conflict of Interest: The authors declare that the research was conducted in the absence of any commercial or financial relationships that could be construed as a potential conflict of interest.

frontiers in Chemistry

REVIEW
published: 15 April 2021
doi: 10.3389/fchem.2021.634630

Perovskite Oxide–Based Materials for Photocatalytic and Photoelectrocatalytic Treatment of Water

Oluchi V. Nkwachukwu[1] *and Omotayo A. Arotiba*[1,2]*

[1]Department of Chemical Sciences, University of Johannesburg, Johannesburg, South Africa, [2]Centre for Nanomaterials Science Research, University of Johannesburg, Johannesburg, South Africa

Meeting the global challenge of water availability necessitates diversification from traditional water treatment methods to other complementary methods, such as photocatalysis and photoelectrocatalysis (PEC), for a more robust solution. Materials play very important roles in the development of these newer methods. Thus, the quest and applications of a myriad of materials are ongoing areas of water research. Perovskite and perovskite-related materials, which have been largely explored in the energy sectors, are potential materials in water treatment technologies. In this review, attention is paid to the recent progress in the application of perovskite materials in photocatalytic and photoelectrocatalytic degradation of organic pollutants in water. Water treatment applications of lanthanum, ferrite, titanate, and tantalum (and others)-based perovskites are discussed. The chemical nature and different synthetic routes of perovskites or perovskite composites are presented as fundamental to applications.

Keywords: perovskites, water treatment, photocatalysis, photoelectrocatalysis, degradation

Edited by:
Aziz Amine,
University of Hassan II Casablanca,
Morocco

Reviewed by:
Vincenzo Vaiano,
University of Salerno, Italy
Jia Hong Pan,
North China Electric Power University,
China

****Correspondence:***
Omotayo A. Arotiba
oarotiba@uj.ac.za

Specialty section:
This article was submitted to
Catalysis and Photocatalysis,
a section of the journal
Frontiers in Chemistry

Received: *28 November 2020*
Accepted: *19 February 2021*
Published: *15 April 2021*

Citation:
Nkwachukwu OV and Arotiba OA
(2021) Perovskite Oxide–Based
Materials for Photocatalytic and
Photoelectrocatalytic Treatment
of Water.
Front. Chem. 9:634630.
doi: 10.3389/fchem.2021.634630

INTRODUCTION

A perovskite by definition is a material with the same crystal structure as $CaTiO_3$, $BaTiO_3$, $CaSiO_3$, or $SrTiO_3$. Perovskite mineral was discovered in the Ural Mountains, Russia, in 1839. A German mineralogist and crystallographer named Gustav Rose received the samples from Alexander Kämmerer—a Russian mineralogist. Rose did a lot of work on the determination of the properties of perovskite, and taking that into account, he named this mineral after Lev Perovski, who was a Russian politician and mineralogist (Park et al., 2016; Katz, 2020; Etgar, 2016). Typically, perovskites are binary metal oxides with a general formula ABO_3, where A cation can be lanthanide, alkaline, or alkaline earth cation, and B cation is a metallic element with 3-, 4-, or 5-day configuration (Arandiyan et al., 2018). Perovskite and perovskite-related materials have emerged as an important new class of materials due to their fascinating physicochemical properties such as thermal stability, electron mobility, and redox behavior (Zhu et al., 2015; Arandiyan et al., 2018), and their versatile applications in catalysis, water splitting, solar cells, optical devices, and superconductors (Khalesi et al., 2008a; Khalesi et al., 2008b).

An ideal perovskite structure has an ABO_3 stoichiometry and a cubic crystal structure (**Figure 1**). The cubic cell is composed of a three-dimensional framework of corner-sharing BO_6 octahedra. The B-site cation is a transition metal element (Kubacka et al., 2012). The A-site cation occupies the 12 coordinate position formed by the BO_6 network and often consists of an alkaline earth metal element

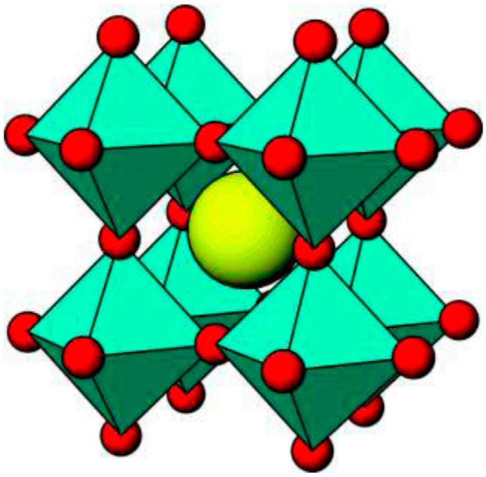

FIGURE 1 | Ideal cubic perovskite structure for ABO3 (cyan, BO_6 units; yellow, A atoms; Kubacka et al. (2012).

or a rare earth element. With comparison to the ideal cubic perovskite ABO_3, perovskite-related structures arise from the loss of one or more of the symmetry operator in the cubic structure and exhibit lattice distortion to varying degrees, thereby resulting in a nonideal structure of the crystal phases such as orthogonal, rhombohedral, tetragonal, monoclinic, and triclinic phases. Although primitive cubic is the idealized structure, the differences in radii between both cations can in fact distort the structure. This normally involves tilting of the BO_6 units (octahedral tilting; Kong et al., 2019). This distortion is created in the crystalline structure as perovskites adopt a wide range of different composition by partially substituting either A or B cation of the same or different valences, resulting in a general formula A1-xAx'B1-yB'yO3±δ, where "+" denotes oxygen excess and "−" denotes oxygen deficiency. It is important to note that both A and B or either offers great flexibility with regard to tailoring and tuning of the physicochemical properties (Zhang et al., 1990; Zhu et al., 2015; Torregrosa-Rivero et al., 2017; Arandiyan et al., 2018). For example, Gade et al. (2018) studied the photocatalytic efficiency in $ALaTi_2O_6$, where A is Na, Ag, or Cu. This new class of material efficiently and effectively mineralized the Congo red dye, 4-chlorophenol, and 4-4′-bis (2 sulfostyryl) biphenyl used as model pollutants (Gade et al., 2018). The stability of the perovskite is summarized by the Goldschmidt tolerance factor, $t = (rA + rO)/\ \sqrt{2}\ (rB + rO)$, where rA, r_B, and r_O are the, respective, radii of A, B, and oxygen ions. For the perovskite structure, the Goldschmidt tolerance factor lies between 0.76 and 1.13 (Zhu A. et al., 2014; Acharya et al., 2015; Kumar et al., 2019).

The diverse composition of emerging pollutants in water suggests that no single method of water treatment can be termed universal. This necessitates the exploration of newer water treatment methods and the tailoring of these methods to certain segments of wastewater. In response to this water treatment challenge, advanced oxidation processes (AOPs) have been developed as an effective technology to remove persistent organic pollutants from wastewater. AOPs are based on *in situ* generation of radicals that nonselectively react with most organics and are able to degrade highly recalcitrant compounds (Brillas and Martínez-Huitle, 2015; Garcia-Segura and Brillas, 2017; Peleyeju and Arotiba, 2018; Umukoro et al., 2018). This review is in addition to the existing body of knowledge around AOPs for water treatment. It is however distinct as it focuses on the application of perovskites in advanced oxidation processes related to water treatment. The so-called first-generation photocatalysts such as TiO_2, SnO, and ZnO have the limitations of wide bandgap and thus only UV responsive. The second-generation photocatalysts (WO_3, Fe_2O_3, and Cu_2O) have the challenge of low quantum yield due to their rapid electron–hole recombination and poor stability (Kong et al., 2019). Perovskite and perovskite-related materials are considered as third-generation photocatalysts which form a stable structure and solid solution with several ranges of metal ions to achieve the appropriate band engineering for photoelectrocatalytic applications (Yang et al., 2009; Kong et al., 2019). Emphasis will be on photocatalysis and electrochemically advanced oxidation systems such as electrocatalysis and photoelectrocatalysis, with perovskites as the semiconductor. Prior to the discussions of the applications of the perovskites in water treatment, brief accounts on synthesis and types of this interesting material are provided.

GENERAL SYNTHESIS METHODS FOR PEROVSKITES

Perovskites are usually formed at elevated temperature because from their composition, perovskite oxides are compounds consisting of two or more simple oxides having high melting points (Arandiyan et al., 2018). The approach to synthesize perovskite oxide must be selected according to the specific application, specific demands of activity, and selectivity as these depend on the arrangement of atoms within its surface (Lim et al., 2019). For example, the solid-state synthesis method is commonly used to prepare perovskite in the pure form due to the availability of impurity-free precursors, and they find application in electronics. The downside of the solid-state synthesis approach is that it requires annealing at high temperature for a long time and frequent intermediary grindings which results in poor homogeneity as well as difficulty in controlling the particle size. Thus, problem arises when perovskites from solid-state methods are subjected to surface-related studies.

Since this review focuses on photocatalysis and photoelectrocatalysis, the methods discussed are those related to improved porosity, to achieve high surface area, *etc.* Efforts have been made by researchers in synthesizing perovskites at low temperatures with improved porosity (Labhasetwar et al., 2015). To overcome the homogeneity drawback of solid-state methods and to achieve nanocrystalline phase, reproducibility, and pure powder, several groups have focused on wet chemistry methods such as citrate sol–gel method, precipitation method, electrospinning technique, ultrasonic method, hydrothermal method, and microwave-assisted synthesis methods. Wet chemistry methods are characterized by their simplicity, reduced sintering time, mass production, high level of repeatability, lower temperature (than solid-state reaction), better flexibility in thin film–forming superior homogeneity, improved control of stoichiometry, purity, particle size, and a low industrialization implementation cost (Assirey, 2019). One of the challenges faced in the development of perovskite catalyst is obtaining the right structure and maintaining high surface area because of high calcination temperature employed sometimes during synthesis (Akinlolu et al., 2019). Hence, the choice of method of preparation is a top priority.

Hydrothermal Method

The hydrothermal method is a useful technique for synthesizing perovskites. This method depends on solubility of minerals in hot water under high pressure, and many syntheses of perovskites for catalytic purpose have been carried out with various advancements using this method. The hydrothermal method is useful in perovskite synthesis as the particle size and shape can be affected by controlling the reaction temperature, pH, time, and concentration of reactants. Biasotto et al. (2011) hydrothermally synthesized bismuth ferrite (BFO) nanoparticles at a low temperature of 180°C within 1 h. In comparison with solid-state reaction process, the authors recorded submicron crystallites of BFO with enhanced homogeneity. Met and group (Kostyukhin et al., 2019) synthesized $LaFeO_3$ *via* a hydrothermal microwave-assisted synthesis at a relatively low temperature of 240°C and pressure of 60 bar. In the procedure, the precursors were mixed in deionized water with the addition of KOH gradually while stirring. The presence of microwave as the heating source assisted in an enhanced crystallization rate of nanoparticles. Gao et al. (2015) synthesized $BiFeO_3$ using nitrates of bismuth and iron *via* a hydrothermal method. KOH was added as a mineralizer to assist in the coprecipitation of Bi^{3+} and Fe^{3+}. The XRD result shows that a single-phase cube-like $BiFeO_3$ was successfully synthesized. Also, the effects of reaction time, KOH concentration, and organic dispersant on the $BiFeO_3$ particle morphology size were investigated. The prepared photocatalyst showed excellent photodegradation of methyl orange dye (MO) under visible light (>420 nm).

Additionally, hydrothermal technique has also been adopted for the preparation of doped perovskites as well as perovskite-based heterojunctions. For instance, Baeissa, 2016 synthesized gold-doped $NaNbO_3$ through a hydrothermal method for photocatalytic degradation of malachite green dye. The morphology of sodium niobate was studied by changing the hydrothermal temperature from 100 to 250°C. The XRD results reveal that all samples prepared at different temperature were of the perovskite structure. The hydrothermal temperature played an important role in the structure and surface area of the obtained sodium niobate as the temperatures at 100, 150, 200, and 250°C led to photocatalysts with surface area of 7, 9, 13, and 16 m^2/g, respectively. Wen et al. (2017) synthesized a novel $SrTiO_3/BiOI$ heterostructure photocatalyst through hydrothermal and facile chemical bath methods with the aid of ethylene glycol. The XRD pattern of $SrTiO_3$ depicts a characteristic tetragonal structure with a cubic $SrTiO_3$ perovskite structure, and the morphology of $SrTiO_3$ possesses nanosheets of irregular edges. It was also noticed that the $SrTiO_3$ nanosheets fasten on the surface of BiOI nanoplates, forming a $SrTiO_3/BiOI$. Photocatalytic activity, photoluminescence, and electrochemical impedance spectroscopy analysis confirmed higher photo-induced charge separation efficiency possessed in $SrTiO_3/BiOI$ composites, which they attributed to an intimate contact between $SrTiO_3$ and BiOI.

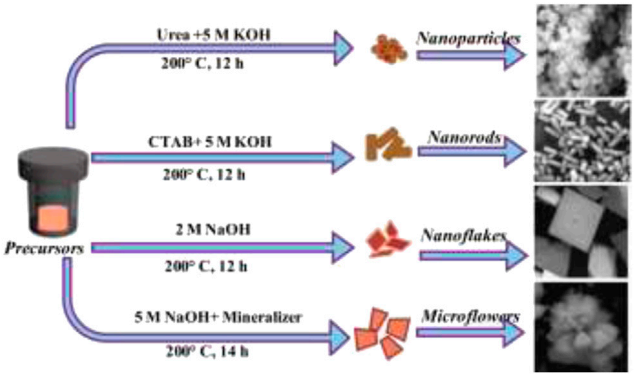

FIGURE 2 | Schematic illustration for tuning the morphology BFO nanostructures with different experimental conditions by the hydrothermal process (Remya et al., 2020).

These reports show that hydrothermal synthesis is ideal for the preparation of pristine perovskites as well as composites containing perovskites. However, the efficiency of the hydrothermal method is dependent on various modifications of experimental conditions such as temperature and solvents used in dissolution of precursor reagents. Remya and group (Remya et al., 2020) synthesized $BiFeO_3$ *via* hydrothermal methods with different experimental conditions for the fine-tuning of the final product (**Figure 2**).

Citrate Sol–Gel Method

The citrate sol–gel method is usually used to prepare nanosized materials. Although its application is limited due to stability of its precursor system, it is difficult to control the chemical composition of complex oxides. The sol–gel procedure in aqueous medium uses inorganic salts and a chelating agent of carboxylic acid such as citric acid as a precursor. This technique has widely been used in making thin films with low temperature. Chu et al. (2018) reported a B site–deficient perovskite prepared *via* the classic sol–gel calcination method. In these methods, the nitrates of the metal ions were dissolved in deionized water, citric acid, and ethylene glycol to form a homogeneous solution at a certain pH, calcination temperature, and time. The XRD pattern showed that pure perovskite was successfully formed. SEM images revealed that most of the nanoparticles are non-agglomerated due to low calcination temperature. The prepared photocatalyst displayed a good photocatalytic property.

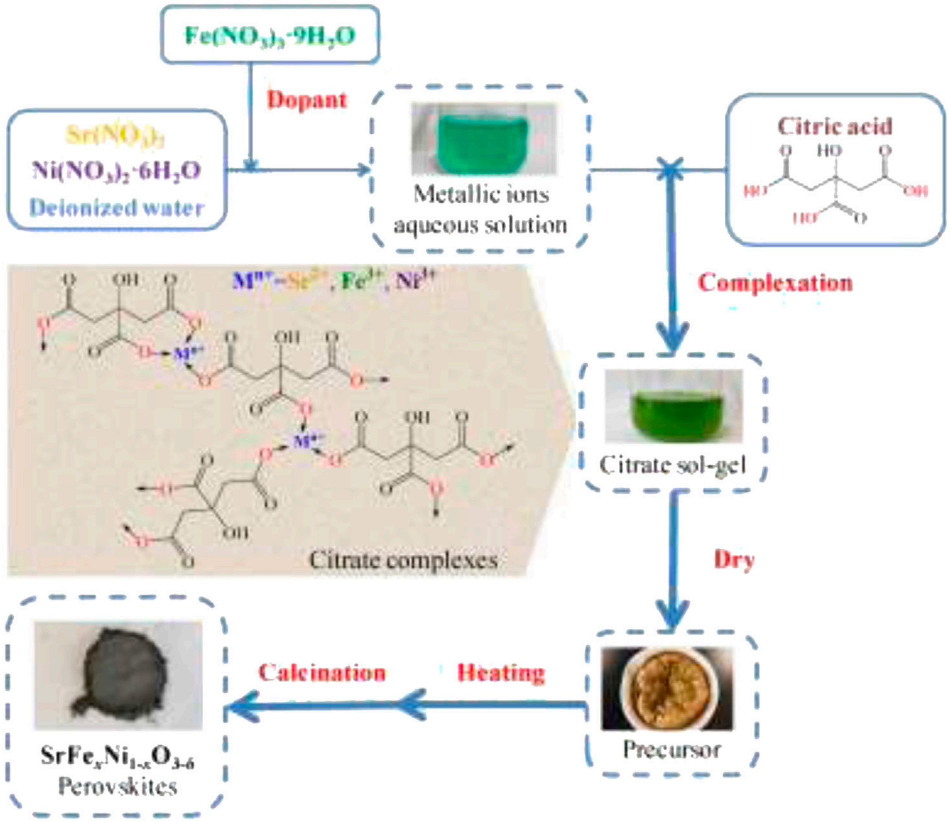

FIGURE 3 | Schematic diagram of the fabrication process of the SrFe$_x$Ni$_{1-x}$O$_{3-\delta}$ perovskites (Zhang Y. et al., 2019).

In another report, LaMg$_x$Fe$_{x-1}$O$_{3-\delta}$ perovskite prepared *via* sol–gel route showed a formation of well-crystallized perovskite. LaMgFe$_3$ and LaMgFe$_4$ photocatalysts presented a particle size of around 100–150 nm with a well-defined size. The photocatalytic efficiency of LaMgFe$_4$ was higher than that of other prepared catalysts owing to its smaller particle size distribution and higher surface area (Teresita et al., 2016). Zhang Y. et al. (2019) prepared SrFe$_x$Ni$_{1x}$O$_{3-\delta}$ (x = 0, 0.1, 0.2, 0.3, 0.4, and 0.5) *via* the citrate sol–gel method (**Figure 3**). They recorded their optimum catalyst with good electrocatalytic performance for water treatment was prepared at a reaction time of 120 min, a calcination temperature of 700°C, and Fe-doping content of x = 0.3.

Coprecipitation Method

Coprecipitation occurs as a result of different cations in solution precipitating simultaneously, and this method encourages homogeneity of products. Coprecipitation plays a critical role in controlling the temperature, concentration, pH, and solution homogeneity. Haron et al. (2017) prepared a nanostructured perovskite oxide such as LaMO$_3$ (M = Al, Co, or Fe) by the coprecipitation method. They observed a formation of single-phase nanocrystalline with high purity, larger surface areas, and porosity.

Djoudi reported a study on LaAl$_{1-x}$Ni$_x$O$_{3-\delta}$ prepared *via* the coprecipitation method using NaOH. They observed an increase in peak shift as the concentration of doping material increases, and crystallinity of all samples varies as the calcination temperature was adjusted. Therefore, the pure perovskite phase sample was calcined at 700°C for 6 h with no impurity. The morphology of the sample showed partial agglomeration, and interestingly, the material exhibited great electroactivity properties, which indicates a good electrocatalyst for oxygen reduction and evolution (Djoudi and Omari, 2015).

PEROVSKITE OXIDE–BASED MATERIALS IN PHOTOCATALYSIS AND PHOTOELECTROCATALYSIS

Perovskite Materials in Photocatalysis

In recent years, advanced oxidation processes (AOPs) have emerged to be efficient and effective methods for the treatment of wastewaters. They are utilized for the removal of organic pollutants during water treatment due to the generation and use of hydroxyl radicals as oxidizing species, which initiate other reactions for the degradation and possibly mineralization of organic pollutants. Among the AOPs, photocatalysis has attracted attention as a promising technique for solving environmental problems. Photocatalysis is a process that occurs when a semiconductor absorbs a photon of energy greater than its bandgap (the region between the electron-fill valance band and the empty conduction band of a semiconductor), and an electron is excited to the conduction band, thereby creating a hole in the valence band. The generation of the electrons could lead to oxidation and reduction reactions on the surface of the semiconductor (Umukoro et al., 2016). Semiconductors such as TiO_2, SnO, and ZnO are widely used as a catalyst in photocatalytic reactions. TiO_2 has been widely applied in photocatalysis owing to its stability, low toxicity, low cost, and high oxidation efficiency. However, its rapid recombination of photogenerated electron–hole pairs and low absorption of visible light are shortcomings that necessitate the need for other materials that have narrower bandgap and wider range of wavelength of light absorption in the visible range, and high solar energy. A suitable photocatalyst should have the following characteristics: i) it should have a bandgap ≥1.2 eV to provide energetic electrons and a bandgap ≤3.0 eV to allow effective absorption of overlap with the solar spectrum; ii) its photogenerated charge carriers should be easily available for use with the electrolyte, and it should be resistant to photocorrosion (Ge et al., 2016; Kumar A. et al., 2020). Other beneficial factors include low cost, facile preparation method, and amenability to bandgap tuning. Perovskites fit into these characterizes to a large extent. The shortcomings of recombination and photocorrosion can be minimized by perovskite composites such as in doping and/or heterojunction formation. **Table 1** shows some recent perovskites that found their application on photocatalysis for water treatment. The different classes of perovskites used in PC are discussed in the following sections.

Lanthanum-Based Perovskites in Photocatalysis

Lanthanum-based perovskites have raised interest as a result of their intriguing properties such as oxygen mobility, ionic conductivity, and excellent magnetic properties. For example, $LaFeO_3$ had been proposed to be a significant material in photocatalytic areas because it exhibited several attention due to its properties such as narrow bandgap (E_g = 1.86–2.36 eV), more stability, and also environmental friendliness (Yahya et al., 2019). Thus, various synthesis approaches such as using template reagent and doping with other metals have been used to improve surface areas and enhance the charge transfer and light captivation through local surface plasmon resonance to improve its catalytic performance. For instance, Wang and group (Zhang W. et al., 2019) synthesized porous lanthanum–titanium $La_2Ti_2O_7$ using CTAB as a template reagent through the sol–gel method toward the degradation of azophloxine dye. The authors observed that the presence of CTAB influenced the specific surface area and the crystallinity of the $La_2Ti_2O_7$. The maximum number of hydroxyl radical was generated on the $La_2Ti_2O_7$ sample obtained with 4 g of CTAB, which degraded about 100% of the dye after 180 min from UV-Vis absorption analysis. The photocatalytic degradation efficiencies for the first and the fifth cycles are 100 and 91%, respectively. The authors attributed this slight decline to the loss of fine $La_2Ti_2O_7$ powder when taking solution samples for examination. This observation is consistent with one of the major challenges of photocatalysis–catalyst recovery. Also, in order to improve the photocatalytic performance of lanthanum-based perovskites, multiple complex or layered perovskite oxides containing lanthanum have been used. For example, Verduzco et al. (2018) synthesized a layered perovskite oxide $Sr_{2.7\text{-}x}Ca_xLn_{0.3}Fe_2O_{7\text{-}\delta}$ (Ln = Nd and La) by a conventional solid–state reaction for degradation of methylene blue (MB) dye under solar and UV irradiation.

Varying the stoichiometry or doping of perovskite with a cation of different valence states can change the electronic structure, which dictates the electrical and optical properties (Zhang et al., 2010). The photocatalytic properties of $Sr_{3.2\text{-}x}Ca_xLa_{0.8}Fe_{1.5}Co_{1.5}O_{10\text{-}\delta}$ (Oliva et al., 2017) were studied by monitoring the degradation of methylene blue (MB) dye. This Ca-doped layered perovskite belonging to Ruddlesden–Popper (R-P) family exhibited increase in absorbance due to the creation of defects such as atomic dislocation induced by the replacement of Sr by Ca. It is worthy to note that the formation of these defects such as oxygen vacancies or trapping centers is suitable for photocatalysis because these oxygen vacancies diminish the rate of electron–hole recombination (Wu et al., 2016). As reported by Oliva et al. (2017), higher photocatalytic degradation was observed as the Ca content increased. The layered perovskites (SCLFCO sample) with $x = 0.8$ produced a total degradation of MB (100%) after 150 min at a pH = 6.0, whereas the undoped sample with $x = 0$ showed only a maximum degradation of 27% after 300 min. The authors attributed this to the lower bandgap, the low level of agglomeration, and particle size. The authors also explained that the chemical reaction for the degradation was due to the presence of Cl^- ion in MB molecule that balanced the charge with methyl group attached to a positive N^+. So the presence of Ca^{2+} ion on the surface of the doped SCLFCO attracted Cl^- in the MB, thereby creating an unbalanced charge which facilitated the breaking of chemical bonds of the methyl groups attached to the chain of the MB molecule. Yang's group (Guan et al., 2020) immobilized $LaFeO_3$ and Au nanoparticles on the Cu_2O surface as a ternary composite photocatalyst for rhodamine B degradation. The composite demonstrated a far more photocatalytic degradation performance than bare $LaFeO_3$ and Cu_2O. This avenue assists in facilitating the spatial separation of photo-induced electron hole. In another study, Ag nanoparticle was used to decorate $LaTiO_3$ for the degradation of pesticide in water. The authors (Shawky et al., 2020) observed an improvement in the surface texture as observed from the morphological analysis. The composite demonstrated an enhancement in light absorption and reduced recombination rate as compared to the pure $LaTiO_3$; as a result, complete degradation of atrazine pollutant within 40 min of irradiation was observed. Numerous reports have shown that incorporation or decoration of lanthanum-based perovskites with other metals or semiconductors results in

TABLE 1 | Recent perovskites in photocatalysis for water treatment.

Perovskite	Co-catalyst	Light source	Method	Pollutant	Pollutant conc	Catalyst conc	Time	% Removal	References
$BiFeO_3$	N-rGO	Hg arc lamp	—	Rhodamine B	100 mg/L	10 mg/L	3 h	98.7	Dixit et al. (2020)
$LaTiO_3$	Ag	300 W Xe	Hydrothermal	Atrazine	—	1.2 g/L	40 min	100	Shawky et al. (2020)
$SrTiO_3$	rGO	450 W Xe	Hydrothermal	Rhodamine B	0.04 mg	0.01 g	—	94.5	Rosy and Kalpana (2018)
$LaMnO_3$	Ca	25 mW cm-2	Hydrothermal	Methylene blue	7 ppm	0.07 g/L	360 min	73	Arabi et al. (2018)
$CaSnO_3$	rGO	UV	Microwave irradiation	Methylene blue	100 mg/L	0.1 g	150 min	92	Venkatesh et al. (2020b)
La_2MnTiO_6	—	400 W	Sol gel	AB 113	50 mg/L	30 mg/L	120 min	72	Shirazi et al. (2020)
$SmFeO_3$	CuO	300 W	Sol gel calcination	Rhodamine B phenol	20 mg/L 20 mg/L	0.15 g	120 min	93 85	Behzadifard et al. (2018)
$BiFeO_3$	BiOI	—	Hydrothermal	—	60 ppm	0.12 g/L	136 min	—	Bahmani et al. (2020)
$SrTiO_3$	Ag/Ag_3PO_4	500 W Xe	Hydrothermal	Tetracycline	10 mg	0.2 g/L	15 min	72	Yu et al. (2020)
$SrTiO_3$	La, Fe	150 W	Ball milling	Methyl orange	5 ppm	0.6 g/L	150 min	96	Abdi et al. (2020)
$SrTiO_3$	La, Cr	300 W Xe	Sol gel hydrothermal	Tetracycline	20 mg/L	50 mg	90 min	83	Jiang et al. (2019)
$LaNiO_3$	TiO_2	300 W Xe	Sol gel	Methyl orange ciprofloxacin	10 mg/L 10 mg/L	100 mg 50 mg	150 min 210 min	100 54	Chen C. et al. (2020)
$BiBaFeO_3$	Na, K	250 W Xe	Sol gel	Methylene blue	10 mg/L	15 mg	120 min	65	Haruna et al. (2020)
$CaTiO_3$	2D/1Dg-C3N4	Sunlight	Hydrothermal	Crystal violet malachite	10 mg/L 10 mg/L	20 mg/L	180 min 90 min	99.76 95.02	Chen X. et al. (2020)
$LaCoO_3$	Mn, N	32 W	Pechini-type sol gel	Malachite green	10 mg/L	40 mg/L	5.5 h	80	Nakhostin Panahi et al. (2020)
$LaCoO_3$	Ag	—	Hydrothermal	Methylene blue	N/A	N/A	10 min	99	Jayapandi et al. (2018)
(NaBi) TiO_2–BaTiO	Ag, N-Ni	300 W	Solid state	Rhodamine B	10 mg/L	1 g/L	80 min	92.4	Xiao et al. (2020)
$CsPbBr_3$	QD	300 W	Precipitation	Tetracycline methyl orange	10 mg/L	100 mg	30 min	76 70	Qian et al. (2020)
$SrZrO_3$	Sb_2O_3	450 W	Solid state	Tetracycline	10 ppm	0.2	180 min	70	Huerta-Flores et al. (2018)
$[BaNiNbO_3]$	$[KNbO_3]$	UV	Solid state	Methylene blue	20 mg/L	150 mg	120 min	55	Zhang et al. (2020)
$CaTiO_3$	$Bi_{12}O_{17}Cl_2$	300 W Xe	Hydrothermal	Tetracycline	0.02 mol/L	50 mg	30 min	90.7	Jiang et al. (2020)
$LaFeO_3$	CA	100 W	Gel combustion	Azo dye RB5	30 mg/L	0.1 g	80 min	100	Yahya et al. (2019)
$La_2Ti_2O_7$	CTAB	20 W	Sol gel	Azophloxine	40 mg/L	600 mg	180 min	—	Zhang et al. (2019)
$AgLaTi_2O6$	Na, Cu	25 W	Sol gel	Congo red IWW	10–4, 50 ml	50 mg	60 min 240 min	24	Gade et al. (2018)
$LaMnO_3$	—	Solar	Citrate sol gel	Methyl orange	6.5 ppm	N/A	60 min	100	Rekavandi et al. (2019)
$CaTi0_5$	G	11 W UV	Solvothermal	Methyl orange	1 × 10–4 M, 50 ml	10 mg	36 h	N/A	Dong et al. (2020)
$KTaO_3$	N	150 W	Solvothermal	Methylene blue	1 × 10-5 M	20 mg	360 min	Complete degradation	Rao et al. (2018)
$MgTiO_3$	$MgFe_2O_4$	UV	Sol gel	Acid black	500 ppm	0.1 g	30 min	67.9	Kiani et al. (2019)
$CaTiO_3$	Li, Ce	UV	Sol gel	Methyl orange	14 ppm	26 mg	150 min	90	Mužina et al. (2020)
$BiFeO_3$	LNR	Sunlight	Sol gel	Methyl orange	10 ppm	0.15 g	3 h	98.9	Ridzuan et al. (2020)
$SrSnO_3$	ZrO_2	UV	Pechini method	Azo dye	10 mg/L	60 mg	10 h	98	Honorio et al. (2020)
$La_2Ti_2O_7$	HTAB	UV	Sol gel	Olfloxacin	40 mg/L	30 mg	30 min	58.6	Han et al. (2020)
$BiFeO_3$	—	100 W	Chemical route	Methylene blue	10 mg/L	20 mg	N/A	N/A	Verma et al. (2020)
$LaFeO_3$	Au, Cu_2O	200 W Xe	Sol gel	Rhodamine	5 mg/L	1 g/L	180 min	88.4	Guan et al. (2020)
$BiFeO_3$	La	500 W	Sol gel	Methylene blue	15 mg/L	1 g/L	2.20 h	78.8	Kumar A. et al. (2020)
$LaMnO_3$	CTAB	—	Hydrothermal	Methylene violet	15 ppm	5 mg	315 min	95	Priyatharshni et al. (2020)

pronounced enhancement in the photocatalysis (Arabi et al., 2018; Yahya et al., 2019; Chen C. et al., 2020; Nakhostin Panahi et al., 2020).

Non–Lanthanum-Based Perovskites

The applications of other non–lanthanum-based perovskites in photocatalysis have been reported. The following sections discuss ferrite-based, titanate-based, tantalum, and other types of perovskites for photocatalysis.

Ferrite-Based Perovskite in Photocatalysis

Iron-based perovskites have the general formula $AFeO_3$, where A is a metal ion like Ca, Sr, Ba, Bi, La, Gd, Ga, or Y (Tang et al., 2011; Dhanasekaran and Gupta, 2012; Ramadan et al., 2013). Iron-based compounds could also adopt the $FeAO_3$ structure, where A could be Ti (Gross-Sorokin et al., 2006; AlSalka et al., 2019). In this case, physical properties such as magnetism and/or ferroelectricity, which can be beneficial for the photocatalytic activity, are added to the material. Magnetism and/or ferroelectricity facilitate in extracting the photocatalyst from solution by an external magnet and also assist in the separation of the photogenerated charges.

Ferrite-based perovskites have proven to be promising materials for photocatalytic and photoelectrocatalytic applications in the field of environmental remediation. The interest and advantage of ferrite oxide could be attributed to its excellent properties such as narrow bandgap, nontoxicity, abundance of constituent element, low cost, and excellent electrical and catalytic properties (Liu et al., 2016). Ferrite-based perovskites attract attention due to their exceptional magnetic and electronic properties. They have intrinsic electric dipole moment due to a distortion in their crystal structures, which promotes separation of photogenerated charges during the photoexcitation process (Chen et al., 2017; AlSalka et al., 2019).

Most of the iron-based perovskites exhibit bandgaps within the visible region of the solar spectrum. For instance, bismuth iron oxide $BiFeO_3$ (BFO), a multi-ferroic member of the iron-based perovskites, is a typical case where simultaneously and spontaneously antiferromagnetic (TN = 643 K) and ferroelectric (TC~1123 K) order coexist well above room temperature (Sosnowska et al., 1992; Sati et al., 2015). $BiFeO_3$ (BFO) with a rhombohedral distorted perovskite is a promising visible light responsive photocatalyst for organic pollutants degradation due to the suitable narrow bandgap (2.2–2.8 eV), excellent chemical stability, as well as intrinsic electric polarization (Ramadan et al., 2013). Charge-transfer (CT) transitions and spectroscopic measurements of the dielectric function of $BiFeO_3$ single crystal (Pisarev et al., 2009) showed a defect-free intrinsic bandgap of ~3.0 eV superimposed on a weak absorption band at 2.5 eV. This result signified the effect of defects and oxygen vacancies on the bandgap, and the shifting of the optical properties into the visible region. Electronic structure investigations have established the strongly hybridized nature of the valence band (Neaton et al., 2005; Clark and Robertson, 2007). However, some researchers reported that the photocatalytic activity of BFO was not impressive (Wang S. et al., 2016; Dixit et al., 2020), and they reported some drawbacks from BFO such as poor carrier mobility and rapid recombination of photogenerated electron–hole pairs. Based on these challenges, several strategies have been in place to improve its photocatalytic activity such as metal ion doping (Wang L. et al., 2016), heterostructure construction (Wang et al., 2017), structural control (Meng et al., 2016), and cocatalyst loadings (Behzadifard et al., 2018).

It has been recognized that metal ion doping assists in producing electron–hole trapping site which would probably accelerate the separation and transfer of the excited electron–hole pairs during the photocatalytic reaction (Wang S. et al., 2016; Dixit et al., 2020). Doping can also introduce surface defects such as oxygen vacancies by charge compensation arising between the dopant and the parent cation (Wang L. et al., 2016; Wang S. et al., 2016). Wang (Wang et al., 2017) studied the effects of oxygen vacancies induced by zirconium doping in bismuth ferrite for catalysis. The morphology features investigated by SEM and TEM showed the Zr-doped BFO with a smaller particle size of 50–150 nm significantly reduced aggregation as compared to the pristine BFO. The incorporation of Zr into BFO was confirmed by XPS. They reported that the optical absorption of the Zr-doped samples slightly shifted toward the shorter wavelength as opposed to the pristine BFO which has a strong absorption both in UV and visible light regions. A better photocatalytic performance in degradation of methyl orange (MO) using 2% Zr–BFO sample compared to the pure BFO and other Zr percentage loading samples was reported (Wang et al., 2017). Meng et al. (2016) studied the effect of the influence of lanthanum doping on photocatalytic properties of $BiFeO_3$ for phenol degradation. The catalyst was prepared by a one-step facile sol–gel method using citric acid as the chelating agent. The gel was calcined at 500°C for 2 h and then at 600°C for 1 h in a muffle furnace. From the XRD result, the $BiFeO_3$ structured was formed with the rhombohedral phase along with $Bi_{25}FeO_{40}$ impurity. As the wt% loading of La doping increases, the characteristic peak of the impurity disappeared. The result inferred that appropriate amount of La^{3+} doping can suppress the generation of impurity. SEM result also showed that 15 wt% La-doped $BiFeO_3$ assisted to decrease the catalyst particle size. The bandgap of the samples was studied using the Kubelka-Munk (K-M) formula. The authors suggested that La doping narrowed the bandgap.

Several studies have been done on ferrite-based perovskites, and majorities of them are in combination with other metals, nanomaterials, and other semiconductors with a purpose of extending light absorption range, retarding the electron hole recombination, and boosting the electron mobility toward efficient charge separation to achieve an excellent photocatalytic degradation of pollutants in water (Behzadifard et al., 2018; Malathi et al., 2018; Yahya et al., 2019; Bahmani et al., 2020; Dixit et al., 2020; Diyan et al., 2020; Haruna et al., 2020; Kumar P. et al., 2020).

Titanate-Based Perovskites in Photocatalysis

Titanate-based perovskite ($MTiO_3$) as a material has been explored in several applications. According to Alammar et al. (2015), they are promising materials for photocatalytic processes because of their excellent resistance to photocorrosion and high thermal stability. Ternary titanate-based perovskites such as $CaTiO_3$, $BaTiO_3$, and $SrTio_3$ are wide bandgap titanate perovskite semiconductors with interesting electronic, optical, and magnetic properties (Alammar et al., 2015).

The preparation of titanate-based perovskite *via* the solid-state method often contains agglomerated particles of different sizes, morphologies, and impurities. Therefore, other methods where size, shape, and purity can be improved are favored. Titanate-based perovskites have offered applications in the area of photocatalytic hydrogen production and hydrocarbon reforming (Hbaieb et al., 2017). According to Zhang et al. (2007), the perovskite structure consisting of oxygen octahedral, such as TiO_6, seems to play an important role for active photocatalysts, and the band edge positions, width of the conduction band, bandgap, and migration of photogenerated charge carriers as well as the photocatalytic activities are closely related to the distortion and the connectivity of the MO_6 (M = Ti^{4+}, Nb^{5+}, and Ta^{5+}) octahedra in perovskite titanates, niobates, and tantalates.

Titanate-based perovskites are reported to be photoactive materials, but their performance is impeded sometimes because of their wide bandgaps. However, titanate-based perovskites (such as $SrTiO_3$ perovskite) exhibit good photostability and are thus applied in H_2 production, solar cells, *etc*. Alammar et al. (2015) investigated the application of $MTiO_3$ (M = Ca, Sr, and Ba) on the degradation of methylene blue using UV light. They reported that nitrogen-doped $SrTiO_3$ showed good photocatalytic properties under visible light irradiation due to the formation of new states in the bandgap, allowing absorption of visible light. Huang S.-T.et al. (2014) studied the photocatalytic activity of $SrTiO_3$ (STO) synthesized by the autoclave hydrothermal method under the alkaline concentration and time. In photodegradation of the model pollutant-crystal violet (CV) dye, STO prepared with 3 M NaOH for 72 h at 130°C showed best photocatalytic performance with UV light. In tailoring the optical and photocatalytic properties of $SrTiO_3$, Lu et al. (2017) successfully incorporated bismuth ferrite into it, forming a structure $Sr_{1-x}Bi_xTi_{1-x}Fe_xO_3$. The synergetic effect resulted in more substantial visible light absorption, narrow bandgap, and enhanced photocatalytic performance. This study shows the possibility of tuning the bandgap of titanate-based perovskites into the visible light region. Lakhera et al. (2018) synthesized a visible light–responsive titanate-based perovskite by preparing a composite of TiO_2 and $NiTiO_3$ for photocatalytic degradation and hydrogen production activity. The photocatalytic activity of the nanocomposite was investigated by the photodegradation of rhodamine B dyes and tetracycline. With different calcination temperatures, the samples behaved differently. The optimized sample NT@750C nanocomposite displayed the highest degradation activity for RhB with about 75% total degradation within 2 h and nearly 58% degradation of tetracycline in 2 h with visible light. The total organic carbon (TOC) removal for both pollutants was lower than the respective decolorization rate, which is an indication of intermediate formation. The reusability test results for RhB dye showed that the photocatalyst can be reused for up to three cycles consecutively without major lost in the photocatalytic activity. In another study, Kiani et al. (2019) reported that a facile method was used to prepare magnesium titanate with magnesium ferrite nanocomposite as a support to improve the photocatalytic activity in degrading azo dyes. As a result of the heterostructure formed, the holes migrated to the valence band of $MgFe_2O_4$, while the electrons in the conduction band (CB) of $MgFe_2O_4$ migrated to the CB of $MgTiO_3$, enabling an efficient charge separation and low recombination rate, hence allowing room for more charges to participate in redox reaction. Therefore, the photodegradation efficiency of the nanocomposite $MgTiO_3$–$MgFe_2O_4$ increased about 30% relative to $MgTiO_3$. Combination power of microstructure and heterojunction techniques in a quest to remould the inherent wide bandgap and enhance its visible light absorption capacity and photocatalytic performance cannot be down played. A multi-shelled cube structure of the $CaTiO_3$–$Bi_{12}O_{17}Cl_2$ heterostructure was synthesized by Jiang et al. (2020) for degradation of tetracycline in water. They observed a greater percentage of tetracycline degradation within a short period with the multi-shelled hollow cube $CaTiO_3$–$Bi_{12}O_{17}Cl_2$ heterostructure. They attributed the achievement to the larger surface area exhibited by the composite which led to more active sites than those participated in the redox reaction. There was a reduction of bandgap from 3.51 to 2.61 eV, thereby enhancing the absorption and utilization of visible light irradiation. The photochemical properties of the prepared samples which include photocurrent response, electrochemical impedance spectroscopy (EIS), photoluminescence spectra (PL), and linear sweep voltammetry (LSV) showed that the heterostructured photocatalyst exhibited an excellent photostability, preferable electron–hole pair separation and longer lifetime, less charge migration resistance, and highest electric current densities.

Several researchers have reported titanate-based perovskite with heterostructure and co-doping. A majority of them have demonstrated an excellent photocatalytic performance as compared to their bare samples, and this is due to reduced bandgaps and efficient migration of charge pairs, hence reduced recombination rate which produces great catalytic activity within the redox reaction (Rosy and Kalpana, 2018; Jiang et al., 2019; Abdi et al., 2020; Chen X. et al., 2020; Dong et al., 2020; Han et al., 2020; Mužina et al., 2020; Tomar et al., 2020; Xiao et al., 2020; Yao et al., 2020; Yu et al., 2020). For instance, Abdi recorded 96% photodegradation of methyl orange within 150 min with Fe–La–doped $SrTiO_3$ nanoparticle as compared to 5% from bare $SrTiO_3$ (Abdi et al., 2020). In addition, these heterostructures contribute in generating more h^+ and superoxide O_2, which are crucial oxidizing species involved in the catalytic system.

Tantalum and Other Perovskite-Based Materials in Photocatalysis

Tantalum-based perovskites ($MTaO_3$) have received attention as a new class of material. They have been explored greatly in the area of water splitting. Kudo and Kato have carried out several studies on tantalum-related materials (Kato and Kudo, 1998; Kato and Kudo, 2001; Kudo et al., 2000). Tantalum-based perovskites ($MTaO_3$) have also found applications in photocatalysis. Li and Zang (2011) prepared La-doped $NaTaO_3$ *via* the hydrothermal method for the degradation of salfranine T dye under UV irradiation. The $NaTaO_3$: La nanocube structure showed higher photocatalytic activity than the undoped. Usually narrow bandgap indicates convenient excitation from the valence band to the conductor band. Therefore, the authors attributed the higher catalytic activity observed on the doped material to the narrow bandgap it exhibited.

In the quest to improve the photocatalytic activity in perovskite, anion doping has been found attractive in improving the photocatalytic activity under visible light. Liu et al. (2011) synthesized N-doped $NaTaO_{3-x}\ N_x$ *via* the one-step hydrothermal method for the degradation of methyl orange. Doping with nonmetals has been shown to increase the catalytic activity of material as it narrows the bandgap and creates oxygen vacancies. The photocatalytic decolorization efficiency of N-doped $NaTaO_3$ was enhanced more than that of undoped because the interstitial nitrogen moved to the local state below the conduction band, and therefore excitation to the CB from the local state was convenient as a result of the "add on shoulder" on the N-doped $NaTaO_3$. They recorded complete decolorization within 14 h irradiation of sunlight at pH 4 and COD removal percentage of 95.21% under the same conditions.

N-doped potassium tantalate perovskite has also been used for the photocatalytic degradation of dye (Rao et al., 2018). The authors recorded reduction of bandgap and also extension of absorption of light from the UV region to the visible region which accelerates the photocatalytic activity. Modak and Ghosh (2014) successfully synthesized N (p-type) and F (n-type) doping in $NaTaO_3$ under visible light. Co-doping with N and F resulted in the formation of charge compensation and the isoelectronic system on $NaTaO_3$. There was a reduction in bandgaps and visible light active material as a result of doping with N and F, which improved the photocatalytic activity. Apart from doping, the formation of heterojunction has also been reported for visible light photocatalytic applications. WO_3-wrapped $NaTaO_3$ prepared through a facile hydrothermal method was used to degrade tetracycline (Qu et al., 2015). An optimum percentage of 60.88% was recorded by the sample $NaTaO_3/WO_3$ which the authors attributed to an effective separation of the photogenerated electron–hole as well as the expansion of the absorption edge to the visible region due to the heterojunction structure.

Some other types of perovskites that have found applications on photocatalysis are discussed below. Huerta-Flores et al. (2018) synthesized the $SrZrO_3$–Sb_2O_3 heterostructure for photocatalytic degradation of pharmaceutical compound. The heterostructure was successfully constructed using the impregnation method and was confirmed by XRD and SEM analyses. Results showed that they exhibited a weaker photoluminescence PL activity than Sb_2O_3 and $SrZrO_3$, which is an indication that there was adequate charge separation and mobility in the interface of $SrZrO_3$–Sb_2O_3, hence a minimized recombination rate. The open circuit potential (OCP) was used to evaluate the stability of the samples. The heterostructure exhibited good photostability because the presence of $SrZrO_3$ inhibited the oxidation of Sb_2O_3. The higher amount of electron accumulated in the conduction band in the heterostructure was evident because the change in the OCP negative value from dark to light was higher. It was also recorded that Sb_2O_3 induced a rapid electron transfer to the solution, which was effective in avoiding the charge carrier recombination, thereby increasing the use of electron–hole pairs in the redox reaction. Results from the Nyquist plot showed a smaller arc radius for Sb_2O_3 and $SrZrO_3$–Sb_2O_3 than the large semi-circle from $SrZrO_3$ material. The decrease in the arc radius indicates a faster interfacial charge transfer. The authors summarized that as a result of diminished electron–hole recombination in the $SrZrO_3$–Sb_2O_3 heterostructure, there was an increased availability of electron–hole separation which led to enhanced photodegradation of tetracycline.

Alkaline earth perovskite stannates such as $ZnSnO_3$, $CaSnO_3$, $SrSnO_3$, and $BaSnO_3$ have been widely used as photocatalysts. These materials have been found to be interesting for a number of potential applications in industry, such as components of dielectric ceramics; multifunctional signal sensors to detect temperature, humidity, and gas; as negative electrode active materials for long-life energy storage applications, and in the fabrication of ceramic boundary-layer capacitors (Zhang et al., 2006; Zhang et al., 2007; Fang et al., 2009). $SrSnO_3$ has been explored and also proven to be an effective photocatalyst owing to its powerful oxidation and reduction capabilities. However, it is associated with large bandgap and a high recombination rate of photogenerated electron–hole pairs. Therefore, the applications of its heterostructured composites have attracted attention in recent years. For instance, Venkatesh et al. (2020a) synthesized a heterostructure rGO–$SrSnO_3$ nanocomposite *via* hydrothermal methods. The authors recorded 97% methylene blue degradation and 80.66% for pure $SrSnO_3$. The optical property showed that a wide absorption band was identified at 220–270 nm for pure and rGO–$SrSnO_3$ composite, respectively. They recorded a reduced bandgap after incorporating rGO from 4.2 to 3.75 eV. Reduced graphene oxide has been an excellent electron acceptor with quick electron transport kinetics, and by that, the support of $SrSnO_3$ with rGO assisted in transferring the photo-induced electron to participate in the reaction, thereby leading to enhanced photocatalytic performance. Zhang et al. (2020) synthesized $[KNbO_3]_{0.9}$-$[BaNi_{0.5}Nb_{0.5}O_{3-\delta}]$ perovskite *via* a solid phase reaction method for methylene blue degradation. KBNNO perovskite has a bandgap of 1.39 eV, which is much smaller than that of the parent perovskite KNO. Incorporation of Ni^{2+} and K^+ encourages oxygen vacancies and charge compensation, respectively. The photocatalytic degradation efficiency of KBNNO was 55% in 120 min. They concluded that the catalyst loading and dye concentration played a crucial role in the photocatalytic efficiency. Due to the octahedral tilting in the crystalline network of SnO_6, this distortion plays an important role in the migration of photogenerated charge carriers in $SrSnO_3$, $CaSnO_3$, and $BaSnO_3$ for photocatalytic degradation of pollutants (Honorio et al., 2020). Honorio et al. (2020) synthesized $SrSnO_3$ with ZrO_2 as a supporting semiconductor for photocatalytic degradation of a textile azo dye pollutant. Honorio discovered from SEM analysis that $SrSnO_3$ was uniformly dispersed on ZrO_2 which infers higher activity as a result of $SrSnO_3$ active phase even in a smaller amount. Therefore, they recorded 63 and 98% degradation at time 2 and 10 h, respectively. But, the doping

TABLE 2 | Recent perovskites in photoelectrocatalysis for water treatment.

Perovskite	Cocatalyst	Light source	Method	Pollutant	Substrate	Pollutant conc	Catalyst conc	Time, min	% Removal	Ref
$BiFeO_3$	Sm, Pd	300 W, Xe lamp	Conventional sol-gel	Methyl orange, phenol	FTO	5 mg/L	0.3 g	120	8750.1	Wang L. et al. (2016)
$SrTiO_3$	TiO_2	300 W, Xe lamp	Hydrothermal/ anodization	Methylene blue	Ti	N/A	N/A	20	99.93	Huang J.-R. et al. (2014)
$BiFeO_3$	TiO_2-NT	500 W, Xe lamp	Citric sol-gel/ultrasonic immersion	Rhodamine	Ti	20 mg/L	N/A	150	100	Zhu A. et al. (2014)
$LaFeO_3$	$SrTiO_2$	420 nm LED	Ultrasonic spray pyrolysis	NO	FTO	400 ppb	0.1 g	N/A	40	Zhang et al. (2017)

of $SrSnO_3$ with ZrO_2 did not significantly affect their bandgaps. They attributed this to be the presence of Sn(ll) having lower binding energy may have occupied the inter-band states below the conduction band of Sn(IV). Some studies have been carried out on Tin-based perovskites for photocatalysis which have yielded excellent catalytic performance (Wang et al., 2009; Junploy et al., 2013; Wang et al., 2014).

Photoelectrocatalysis

Photocatalysis has been widely utilized, and it is an important route for the degradation of organic waste. Its efficiency strongly relies on the catalyst. This technique has prominent advantages, including low cost and no secondary pollution. However, it has some drawbacks such as electron–hole pair recombination and catalyst recovery. Electrochemical oxidation localizes the semiconductor in the form of an electrode or substrate. Thus, the degradation of the organic pollutants occurs at the electrode surface or close to the electrode surface (hydroxyl radical in the bulk solution). This approach solves the catalyst recovery problem in photocatalysis. This electrochemical approach, however, requires high voltage and is prone to oxygen evolution, and the process is limited by mass transfer (Malpass et al., 2010; Sirés et al., 2014; Brillas and Martínez-Huitle, 2015; Kusmierek and Chrzescijanska, 2015; Umukoro et al., 2017; Wang et al., 2018). The quest for improved techniques led to the emergence of photoelectrochemical oxidation or photoelectrocatalytic (PEC) processes. PEC is an electrolytic system containing a semiconductor-based anode that is simultaneously subjected to light illumination and a constant bias potential to the anode (E_{anod}), a constant cell potential (E_{cell}), or a constant anodic current density (j_{anod}). This process promotes the extraction of photo-induced e^{-CB} by the external electrical circuit, thereby yielding an efficient separation of the $e^{-CB/h+}$ $_{VB}$ pairs (Daghrir et al., 2012; Georgieva et al., 2012; Sirés and Brillas, 2012; Bessegato et al., 2015; Meng et al., 2015). The prevention of charge recombination promotes the photocatalytic efficiency of the anode and thus the acceleration of organic oxidation. The excitation of the anodic semiconductor and prolonged separation increases the lifetime of the hole so as to have more opportunities to either directly oxidize the organic pollutants adsorbed on the photoanode surface or indirectly react with absorbed water to form more hydroxyl radicals. Another advantage of PEC is the ease of recovery of photocatalyst after usage and possibility of multiple cycles of treatment. A myriad of semiconductor materials such as TiO_2, ZnO, WO_3, and $BiVO_4$ have been used as photoanodes in PEC. Another class of semiconductor used in PEC is perovskites. As seen in photocatalysis, their recent trend is to use visible light as the photoexcitation source for the anode.

Perovskite in Photoelectrocatalysis for Water Treatment

Perovskites have been extensively used in photocatalysis. In the area of photoelectrocatalysis (PEC), however, most applications of perovskites are in the energy sectors such as water splitting (Ni et al., 2007; Bin Adnan et al., 2018; Phoon et al., 2018) and solar cells (Muñoz-Gil et al., 2018; Fan et al., 2020). The application of perovskite in PEC for water treatment is still at its infancy. This review seeks to capture the recent application of perovskites in PEC and thus provide a valuable resource for materials, perovskites, and environmental research communities. Reports on PEC for water treatment are shown in **Table 2** and reviewed in the following paragraphs. The chemistry of catalyst (perovskites) improvement strategies is similar to that of those explained earlier. Owing to the need to fabricate an anode (usually by depositing the semiconductor), different synthesis and electrode preparation methods peculiar to PEC are expected.

The first task in the application of perovskites in photoelectrocatalytic removal of organic pollutants in water is to understand the electrochemical and photoelectrochemical behaviors of the perovskites. To get such information, the perovskites have to be fabricated into an electrode. One of the common substrates for the deposition of perovskites for PEC application is the fluorine-doped tin oxide glass (FTO). For example, Fermin and coworkers studied the photoelectrochemical properties of $LaFeO_3$ nanoparticles by pasting an adhesive film of $LaFeO_3$ (along with other diluents) on a FTO coated glass (Celorrio et al., 2014). Although this work was not on water treatment, valuable data such as photocurrent responses obtained from this work are necessary characterizations that inform the potential applicability of the perovskites for PEC water treatments. With the use of a similar electrode preparation strategy, Zhang carried out a robust study on the photoelectrochemical behavior of heterostructured perovskite of the $LaFeO_3$–$SrTiO_3$ composite on FTO glass for NO removal (Zhang et al., 2017). The electrode was characterized along with the control electrodes of pristine $LaFeO_3$ (LFO) and

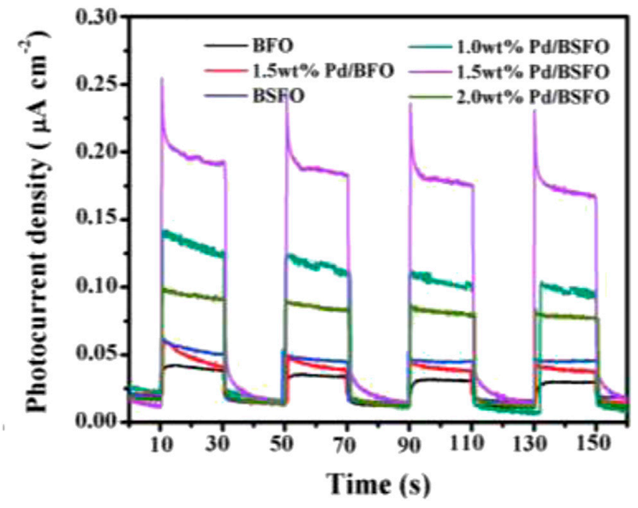

FIGURE 4 | Photocurrent action spectra of the prepared photocatalyst samples (Wang S. et al., 2016).

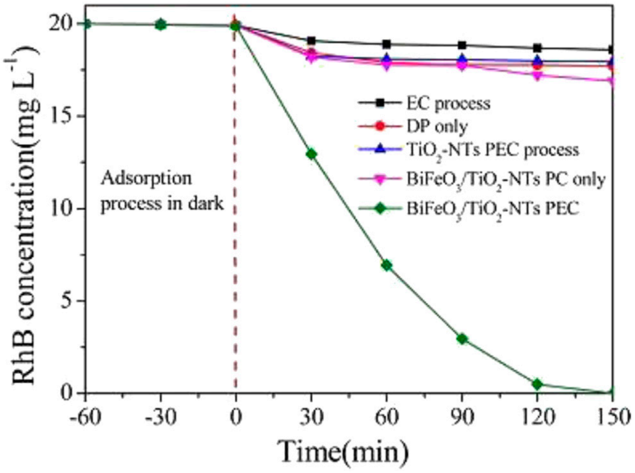

FIGURE 5 | RhB concentration varying with time through different degradation processes. PC, photocatalytic process; EC, electrochemical oxidation. Note: label "b" is from the original author reproduced with permission (Zhu J. et al. (2014).

$SrTiO_3$ (STO). While all the photoanodes showed good photoelectric responses, the composite (LFO–STO) showed very pronounced response, indicating that heterojunction greatly promotes the separation of photo-induced electron–hole pairs and leads to the improved catalytic reaction rate. The authors concluded that the improved catalytic activity is due to the broad visible light harvest, enlarged surface area, and a suppressed surface charge recombination that emanated from the perfectly matched $LaFeO_3$ and $SrTiO_3$ interface and facile charge transfer. Wang S. et al. (2016) also carried out photoelectrochemical studies to investigate the effect of a Pd cocatalyst and samarium doping in bismuth ferrite (BFO). Accordingly, the authors recorded a higher photocurrent response in Pd/BSFO (BSFO = Sm-doped BFO) samples than in BFO, Pd/BFO, and BSFO. They concluded that photocatalytic analysis and electrochemical analysis such as photocurrent response as shown in **Figure 4** demonstrated that the combination of Pd loading and Sm doping could significantly promote the separation of photogenerated electron–hole pairs in the Pd/BSFO sample, thereby improving the photocatalytic activities.

As demonstrated by Arotiba and coworkers, such a photocurrent response from a photoanode can give a measure of how effective the electrode will be when used for PEC degradation (Umukoro et al., 2018; Orimolade et al., 2019; Orimolade et al., 2020; Orimolade and Arotiba, 2020).

One of the earliest work where a perovskite based photoanode was prepared and used for the PEC degradation of an organic pollutant is the work of (Zhu A. et al., 2014). The authors prepared TiO_2 nanotubes (TiO_2-NT) by anodic oxidation of titanium sheet and then deposited the $BiFeO_3$ nanoparticles from its precursor on the TiO_2-NTs via an ultrasonic-immersion strategy to form the $BiFeO_3$/TiO_2-NTs photoanode. The electrodes were extensively characterized by UV–vis diffuse-reflectance spectra, surface photovoltage, photoluminescence, electrochemical impedance spectroscopy etc. As shown in **Figure 5** with the applied bias potential of 0.6 V, the photoanode displayed a pronounced efficiency as compared to photocatalysis and electrochemical analysis. This is in agreement with the electrochemical impedance that the photoanode $BiFeO_3$/TiO_2-Nts possessed a faster charge transfer across the electrode surface to the Ti substrate. These results point to a marked improvement in the photo-electrochemical properties of the $BiFeO_3$/TiO_2-NTs over TiO_2-NTs. These improvements were attributed to ease of charge transfer between the two materials, the ferroelectric properties of $BiFeO_3$ and the enhancement of charge separation. The $BiFeO_3$/TiO_2-NTs was used in the degradation of rhodamine B dye. A degradation of nearly 100% was achieved at the $BiFeO_3$/TiO_2-NTs photoanode after 150 min. This was significantly higher than when other techniques such as electrochemical oxidation, direct photolysis and photocatalysis process were employed. The schemes suggested by the authors for the electrode, bandgap alignment and schematic pathways are presented in **Figure 6**. From the diagram, the formation of heterostructure assisted in the formation of appropriate Fermi level, the application of bias potential channelled the electrons generated from the conduction band of $BiFeO_3$ to the conduction band of TiO_2-NTs. The separated, photogenerated electrons reacted with the surface chemisorbed O_2 to generate the strong oxidative species O^{2-}, which combines with H^+ from solution to form H_2O_2. Finally, accumulated electrons in the counter electrode can react with H_2O_2 to generate OH. This effective charge separation attributes to an excellent oxidation and reduction of the pollutants.

The positive coupling effect of combining TiO_2 and other semiconductors is considered as an efficacious approach to promote TiO_2 reactive properties. This enables the photogenerated charge carriers to migrate to the heterostructured interface to retard recombination.

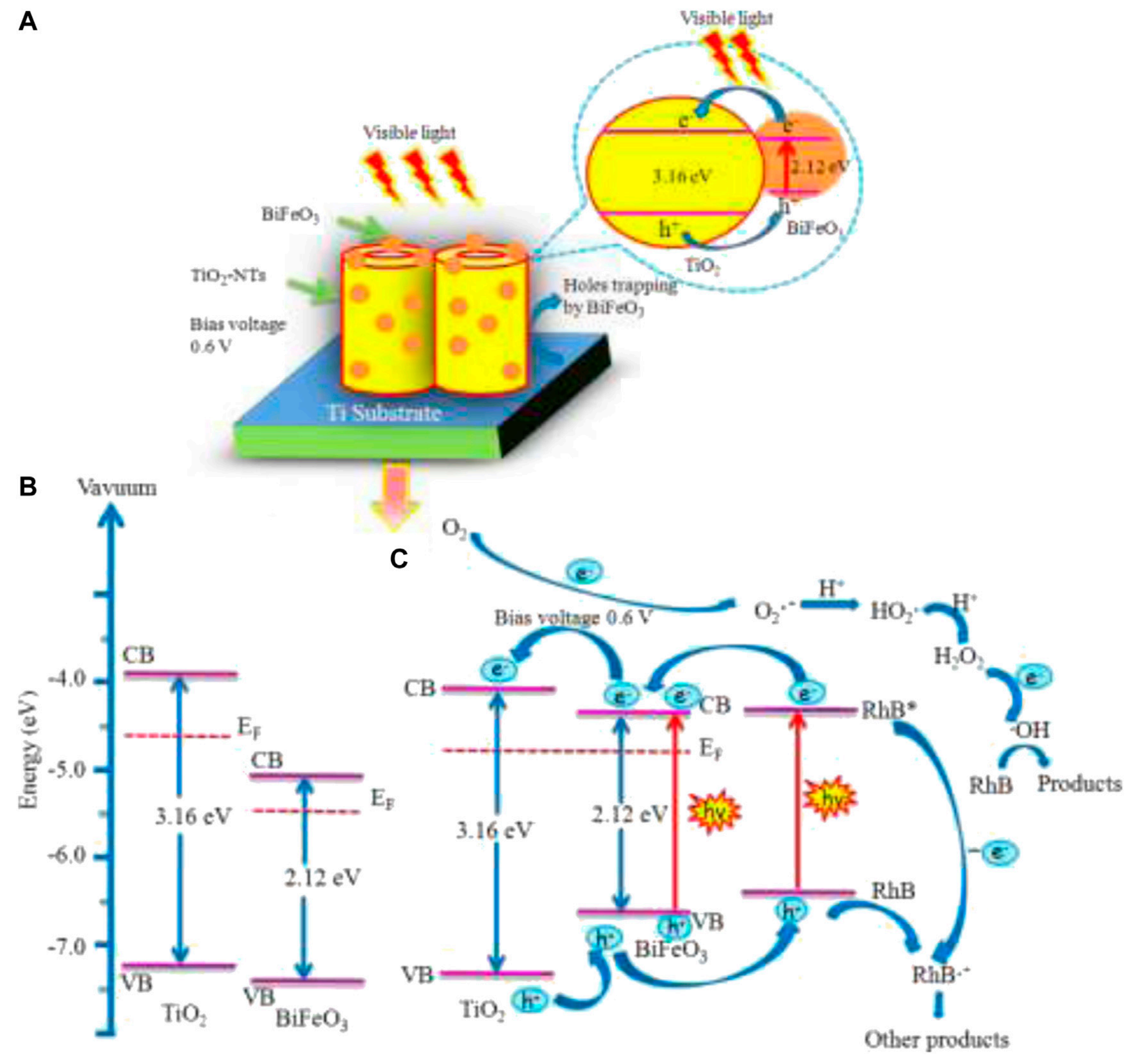

FIGURE 6 | (A) Cartoon diagram of the photogenerated electron generation, separation, and transfer path in $BiFeO_3/TiO_2$-NTs upon visible-light excitation. **(B)** Conduction band, valence band, and Fermi-level positions of independent n-type TiO_2 and n-type $BiFeO_3$. **(C)** Schematic pathways of PEC degradation of RhB over $BiFeO_3/TiO_2$-NTs under a bias of 0.6 V applied onto the composite electrode (Zhu A. et al., 2014).

Huang J.-R.et al. (2014) constructed a heterostructured nanotube with $TiO_2/SrTiO_3$ for PEC degradation of methylene blue (MB) dye. The photocurrent response among all the prepared catalyst TSr3 (TNT in $Sr(OH)_2$, 30 min hydrothermal time) showed the highest peak current, and it is twice as large as TNT2 (TiO_2 nanotube on Ti substrate). Their photocurrent response is such that when light is turned off, they returned instantly to zero; hence, the author concluded that the heterostructure composites under UV light can significantly promote the photogenerated electron/hole separation. The PEC degradation peak value was in good agreement with the rate constant K with the optimal sample TSr3. The MB percentage degradation and rate constant were 99.93% and 0.38492 E^{-4} min^{-1}, respectively. The authors attributed the result to be as a result of the positive cooperation of the high-reactive TiO_2 {001} facet with $TiO_2/SrTiO_3$ heterostructured interface which strongly inhibited the photogenerated electron/hole recombination.

Effect of pH, Initial Concentration, and Catalyst Loadings of Perovskites in Photocatalysis and Photoelectrocatalysis

Effect of pH

The pH of a solution influences the surface charge and protonation of the functional groups in a catalyst. It also promotes the efficiency and the performance of the process. Haruna et al. (2020) studied the pH of the solution for the degradation of 10 mg/L methylene blue using $Bi_{0.85-x}M_xBa_{0.15}FeO_3$ (M = Na, K and x = 0, 0.1) at pH 3, pH 7, and pH 11. The observed improved photodegradation at pH 7 and pH

11 of doped and undoped catalyst was attributed to the interaction of the highly negative oxide species and the anion which influenced the surface charge of the photocatalyst. Another study shows the degradation of tetracycline at pH 3, pH 5.60, and pH 10 using tungsten-doped $BaTiO_3$. The authors recorded the degradation rate of 90 and 80% for pH 10 and pH 5.60, respectively, after 3 h irradiation and 43% at pH 3. They concluded that increasing OH ions on catalyst surface promoted more OH^- radicals which participated in the redox reactions (Demircivi and Simsek, 2019). Depending on the nature of the pollutant and the photocatalyst, the degradation efficiency varies with pH of the solution, hence the need to detect the optimum conditions that are favorable at any given time. Simsek et al. (2020) studied the effect of pH in photocatalysis and photo-Fenton for the degradation of caffeine using $LaFeO_3$. They observed that the photocatalyst performed optimally at natural pH 6.5 compared with pH 3 and pH 10. According to Yao, the effect of pH and degradation of pollutant varies, and it is controversial (Haruna et al., 2020; Yao et al., 2004).

Effect of Initial Concentration of Pollutants

The increase in pollutant concentration could decrease the penetration of light into the solution for photocatalytic activity, thereby causing turbidity and opaqueness. Yahya et al. (2018) investigated the effect of initial concentration of humic acid using $LaFeO_3$. They observed the photocatalytic removal in the order of 98, 90, 85, and 86% for 10, 20, 30, and 40 g/L, respectively. It shows that at lowest initial concentration of humic acid, the photocatalytic activity was at its best. Therefore, they concluded that at a high pollutant dosage, the penetration of light needed to travel to the active site to activate the photodegradation was blocked, resulting in few active sites and poor photocatalytic activity. Also, a similar result was obtained by Pelin, where the degradation of tetracycline solution with an initial concentration of 5, 20, and 40 mg/L showed a degradation rate of 93, 80, and 47%, respectively (Demircivi and Simsek, 2019). Increase in turbidity, which can be due to high initial pollutant concentration is expected to reduce the efficiency of photoelectrocatalytic degradation of pollutants with perovskite-based photoanodes. This is because of insufficient light reaching the photoanode owing to poor penetration or scattering just as it is observed in photocatalysis. The issue of turbidity is not restricted to the pollutant concentration alone. Thus, for practicality, the process of simple filtration or sedimentation to remove suspended solids may precede PEC to improve the delivery of light onto the electrode or the catalyst.

Effect of Catalyst Loadings

Usually, at lower catalyst dosage, there are few active sites available for photodegradation, and at higher catalyst loadings, there are agglomeration, high turbidity, and scattering effects which lower the degradation efficiency in photocatalysis (Yahya et al., 2018; Yahya et al., 2020). Behzadifard et al. (2018) investigated the effect of CuO (10 wt%) $SmFeO_3$ composites for degradation of 10 mg/L rhodamine dye. They reported that the degradation rate of rhodamine increased with increasing catalyst loading from 0.05 to 0.15 g; however, at 0.20 g, the performance dropped, which they attributed to agglomeration and decrease in light penetration. It is therefore crucial to obtain the optimum value of catalyst loadings for cost-effectiveness and better photocatalytic performance.

BANDGAP POSITIONS AND CHARGE TRANSFER MECHANISM OF PEROVSKITE OXIDES IN PHOTOCATALYSIS AND PHOTOELECTROCATALYSIS

Bandgap calculation, tuning, and alignment are important in the characterization and in the prediction of the photocatalytic and photoelectrocatalytic efficiency of perovskite oxides (and other semiconductors) in water treatment. There are several ways of calculating band edge positions such as electronegativity-based calculation, density functional theory (DFT), the Mott–Schottky plot, dependence of photovoltage on pH, and photocurrent-potential measurement (Zhang and Jaroniec, 2018). Some band edge potentials of selected perovskite oxides discussed in this review are shown in **Figure 7**. Mukherjee et al. (2018) highlighted the effect of bandgap on photocatalytic improvement by the preparation of a composite of BFO and reduced graphene oxide (RGO). The conduction band (CB) and valence band (VB) edge potentials suggest band bending which arises in the equilibration of the Fermi level with the increase in the space region of the composite. The increase in the space region of the BFO–RGO composite resulted in the negative shift in the band edge potential, which facilitated the charge carrier concentration and consequently increased the chances of faster electron transfer, suppressed recombination, and better photoelectrocatalytic degradation (see **Figure 8**). In another report, Wang S. et al. (2016) explored the effect of rare earth (Sm) doping and noble (Pd) cocatalyst doping in $BiFeO_3$. The flat band potential measurement was calculated using the Mott–Schokkty plot. Doping of bismuth ferrite with foreign atoms in their A, B, or O sites of the ABO_3 lattice has been proven to be an effective route to improving its photocatalytic properties (Mukherjee et al., 2018). From the band diagram in **Figure 9**, as reported by Wang L. et al. (2016), the hole could react with H_2O on the surface to generate OH for oxidation reaction because the VB potential of 1.5 wt% Pd–BSFO composite (+2.35 eV) is positive enough when compared to $-OH/{}^{\cdot}OH$ (+2.27 V vs NHE) as opposed to the CB potential of 1.5 wt% Pd–BSFO (+0.27 eV) which is less negative than the potential E^o $(O_2/O_2^{\cdot})$ (−0.046 V vs NHE). Doping with rare earth metal served as an electron trapping specie to separate the photogenerated electron–hole from recombination, thereby promoting efficient charge carrier separation and consequently encouraging excellent

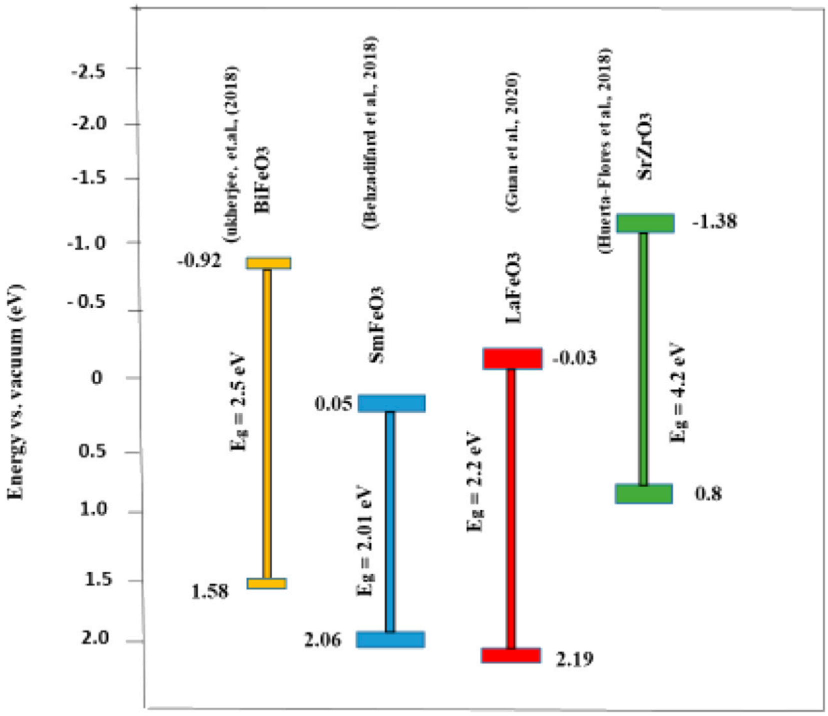

FIGURE 7 | Band positions of some perovskite oxide–based materials in photocatalytic and photoelectrocatalytic treatment of water.

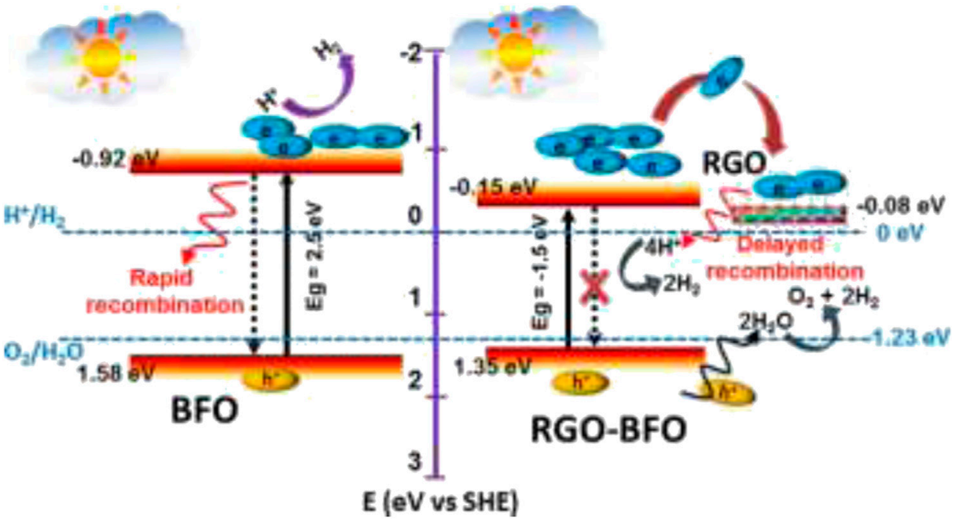

FIGURE 8 | Schematic representation of the proposed mechanism of photocatalysis of BFO and RGO–BFO reproduced with permission (Mukherjee et al. (2018)).

photocatalytic activity. Behzadifard et al. (2018) studied the photocatalytic degradation of rhodamine and phenol. The band edge potentials were calculated using electronegativity methods. From the calculations, the VB and CB potentials for CuO were 1.97 and 0.65 eV and those of $SmFeO_3$ were 2.06 and 0.05 eV, respectively. Owing to the low negative CB potential value of $SmFeO_3$, adsorbed oxygen cannot be converted to $–O_2$. On the other hand, the CB potential of CuO is more positive than $SmFeO_3$; hence, electrons can migrate to the CB of CuO. In other words, CuO is acting as electro acceptor and is able to trap the electrons. Also, the CB potential of CuO (0.65 eV) is positive enough and closer to the potential for O_2/H_2O_2 (+0.695 eV), and the electrons are able to react with adsorbed oxygen to produce H_2O_2 and

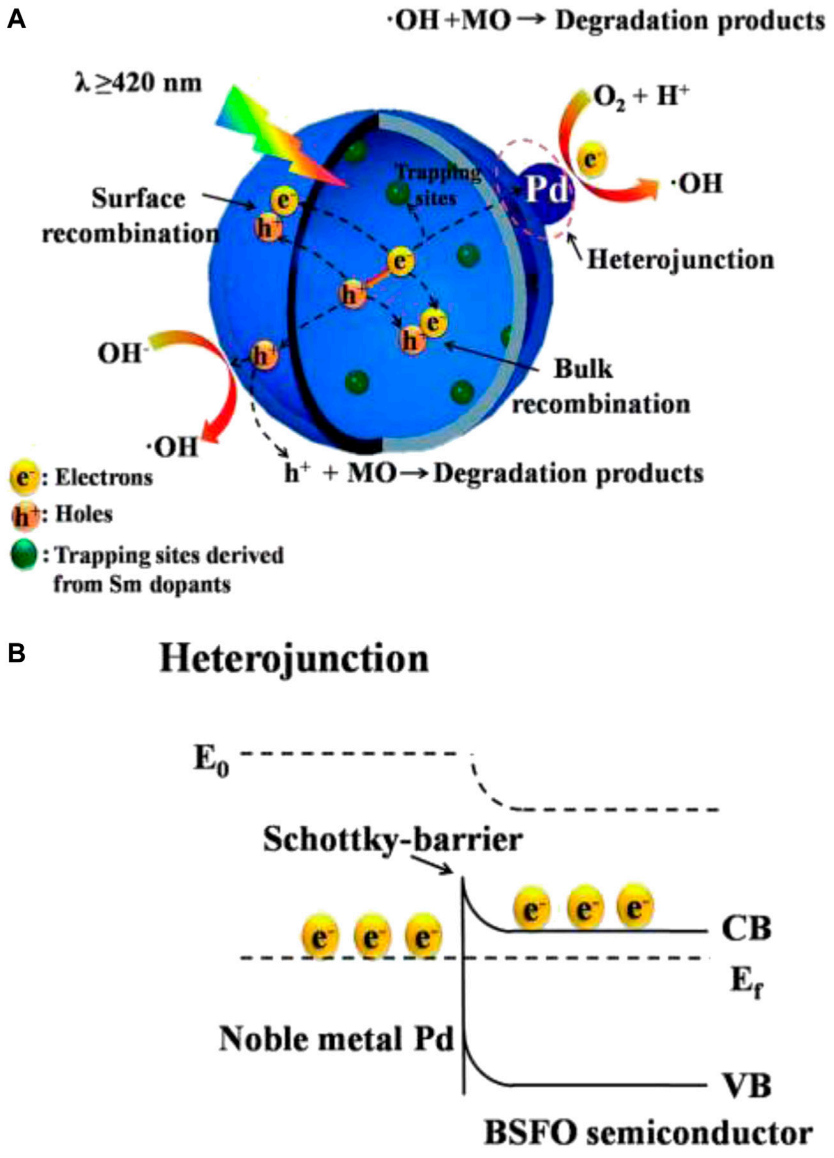

FIGURE 9 | (A) Schematic diagram for the proposed visible light photocatalytic mechanism of Pd/BSFO samples and **(B)** schematic illustration of Schottky barrier formed at the interface between Pd and BSFO (reproduced with permission (Wang S. et al., (2016).

subsequently $^{\cdot}$OH. The holes generated were transferred from the VB of $SmFeO_3$ to CuO because the VB potential of $SmFeO_3$ (+2.06) was not high enough to oxidize the adsorbed –OH ($-OH/{}^{\cdot}OH$ = +2.38 eV) and H_2O ($H_2O/{}^{\cdot}OH$ = +2.72 eV) to OH; hence, holes in $SmFeO_3$ could have directly oxidized the organics had it enough potentials. The formation of the heterojunction promoted the charge separation and suppressed the recombination of charge carriers.

The mechanism of reaction was summarized in **Eqs. 1–4** (Behzadifard et al., 2018; Zhang and Jaroniec, 2018).

$$CuO/SmFeO_3 + hv\ (\text{visible light}) \rightarrow e^{-}CB\ (CuO\ \text{and}\ SmFeO_3)$$
$$+ h\ + VB\,(\,CuO\ \text{and}\ SmFeO_3), \qquad (1)$$

$$2e^{-}CB\ (CuO)\ +\ 2H +\ +\ O_2\ H_2O_2, \qquad (2)$$

$$H_2O_2 + e^{-} \rightarrow {}^{-}OH + OH, \qquad (3)$$

$$\text{Pollutant}\ +\ OH/h^{+} \rightarrow \text{Intermediates} \rightarrow \text{degradation products.} \qquad (4)$$

CONCLUSION AND RECOMMENDATION

In this review, we discussed the recent progress in the field of photocatalysis and photoelectrocatalysis based on perovskite and perovskite-related materials. Recently, research has geared toward photocatalytic materials that are capable of absorbing light in the visible region. Perovskite and perovskite-related materials such as $BiFeO_3$, $LaMnO_3$, and $LaFeO_3$, which are mostly visible–light active materials, are gaining attention as suitable anodic material for photoelectrocatalysis in degradation of organic pollutant due to their fascinating properties. Few photoelectrocatalysis degradation reports discussed here show that synergy of photocatalysis and electrolysis promotes better degradation performance. Reports have also shown that immobilizing catalyst onto substrate and application of bias potential aid in catalyst recovery, reduce electron–hole recombination, and increase charge resistance. In particular, the formation of perovskites as photoanodes through novel nanostructure engineering, surface modification with exotic element doping or cocatalyst loading, and innovative system design based on heterojunction configuration are excellent strategies for improving light harvest, charge separation, as well as surface reaction kinetics as compared to the single perovskites, for example, $BiFeO_3$ doped with Sm and Pd (Wang S. et al., 2016). Agreeably, great progress has been made over the years; however, for ultimate realization of the inherent potential in perovskite, more work needs to be done in discovering new perovskites for photoelectrocatalysis. Furthermore, in order to maximize the degradation efficiencies in vast composition of organic pollutants, other advanced oxidation processes such as sono-photoelectrocatalysis and photo-Fenton process can be incorporated with perovskite material for complete mineralization of the recalcitrant pollutants.

Therefore, for the advancement of perovskite-based material for photoelectrocatalysis treatment of water, continuous research into a better crystal structure for stability as well as performance improvement is essential. Perovskites with long-term stability and exceptional optical and electrochemical properties are essential for sustainability.

AUTHOR CONTRIBUTIONS

ON: conceptualization, writing—original draft. OA: conceptualization, writing—review and editing, supervision, funding acquisition, and resources.

ACKNOWLEDGMENTS

The authors wish to acknowledge the National Research Foundation of South Africa (CPRR Grant number 118546) and the Center for Nanomaterials Science Research, the University of Johannesburg for financial supports.

REFERENCES

Abdi, M., Mahdikhah, V., and Sheibani, S. (2020). Visible light photocatalytic performance of La-Fe co-doped SrTiO3 perovskite powder. *Opt. Mater.* 102, 109803. doi:10.1016/j.optmat.2020.109803

Acharya, S., Martha, S., Sahoo, P. C., and Parida, K. (2015). Glimpses of the modification of perovskite with graphene-analogous materials in photocatalytic applications. *Inorg. Chem. Front.* 2, 807–823. doi:10.1039/c5qi00124b

Akinlolu, K., Omolara, B., Kehinde, O., and Shailendra, T. (2019). Synthesis and characterization of A site doped lanthanum based perovskite catalyst for the oxidation of soot. *IOP Conf. Ser.: Mater. Sci. Eng.* 509, 012062. doi:10.1088/1757-899X/509/1/012062

Alammar, T., Hamm, I., Wark, M., and Mudring, A.-V. (2015). Low-temperature route to metal titanate perovskite nanoparticles for photocatalytic applications. *Appl. Catal. B: Environ.* 178, 20–28. doi:10.1016/j.apcatb.2014.11.010

AlSalka, Y., Granone, L. I., Ramadan, W., Hakki, A., Dillert, R., and Bahnemann, D. W. (2019). Iron-based photocatalytic and photoelectrocatalytic nano-structures: facts, perspectives, and expectations. *Appl. Catal. B: Environ.* 244, 1065–1095. doi:10.1016/j.apcatb.2018.12.014

Arabi, A., Fazli, M., and Ehsani, M. H. (2018). Synthesis and characterization of calcium-doped lanthanum manganite nanowires as a photocatalyst for degradation of methylene blue solution under visible light irradiation. *Bull. Mater. Sci.* 41, 1–8. doi:10.1007/s12034-018-1590-6

Arandiyan, H., Wang, Y., Sun, H., Rezaei, M., and Dai, H. (2018). Ordered meso- and macroporous perovskite oxide catalysts for emerging applications. *Chem. Commun. (Camb)* 54, 6484–6502. doi:10.1039/c8cc01239c

Assirey, E. A. R. (2019). Perovskite synthesis, properties and their related biochemical and industrial application. *Saudi Pharm. J.* 27, 817–829. doi:10.1016/j.jsps.2019.05.003

Baeissa, E. S. (2016). Photocatalytic degradation of malachite green dye using Au/NaNbO3 nanoparticles. *J. Alloys Compd.* 672, 564–570. doi:10.1016/j.jallcom.2016.02.024

Bahmani, M., Mowla, D., Esmaeilzadeh, F., and Ghaedi, M. (2020). BiFeO3-BiOI impregnation to UiO-66(Zr/Ti) as a promising candidate visible-light-driven photocatalyst for boosting urea photodecomposition in a continuous flow-loop thin-film slurry flat-plate photoreactor. *J. Solid State. Chem.* 286, 121304. doi:10.1016/j.jssc.2020.121304

Behzadifard, Z., Shariatinia, Z., and Jourshabani, M. (2018). Novel visible light driven CuO/SmFeO3 nanocomposite photocatalysts with enhanced photocatalytic activities for degradation of organic pollutants. *J. Mol. Liquids* 262, 533–548. doi:10.1016/j.molliq.2018.04.126

Bessegato, G. G., Guaraldo, T. T., de Brito, J. F., Brugnera, M. F., and Zanoni, M. V. B. (2015). Achievements and trends in photoelectrocatalysis: from environmental to energy applications. *Electrocatalysis* 6, 415–441. doi:10.1007/s12678-015-0259-9

Biasotto, G., Simões, A. Z., Foschini, C. R., Zaghete, M. A., Varela, J. A., and Longo, E. (2011). Microwave-hydrothermal synthesis of perovskite bismuth ferrite nanoparticles. *Mater. Res. Bull.* 46, 2543–2547. doi:10.1016/j.materresbull.2011.08.010

Bin Adnan, M. A., Arifin, K., Minggu, L. J., and Kassim, M. B. (2018). Titanate-based perovskites for photochemical and photoelectrochemical water splitting applications: a review. *Int. J. Hydrogen Energ.* 43, 23209–23220. doi:10.1016/j.ijhydene.2018.10.173

Brillas, E., and Martínez-Huitle, C. A. (2015). Decontamination of wastewaters containing synthetic organic dyes by electrochemical methods. An updated review. *Appl. Catal. B: Environ.* 166-167, 603–643. doi:10.1016/j.apcatb.2014.11.016

Celorrio, V., Bradley, K., Weber, O. J., Hall, S. R., and Fermín, D. J. (2014). Photoelectrochemical properties of LaFeO3Nanoparticles. *ChemElectroChem* 1, 1667–1671. doi:10.1002/celc.201402192

Chen, C.Zhou, J., Geng, J., Bao, R., Wang, Z., Xia, J., et al. (2020). Perovskite LaNiO3/TiO2 step-scheme heterojunction with enhanced photocatalytic activity. *Appl. Surf. Sci.* 503, 144287. doi:10.1016/j.apsusc.2019.144287

Chen, X.He, X., Yang, X., Wu, Z., and Li, Y. (2020). Construction of novel 2D/1D g-C3N4/CaTiO3 heterojunction with face-to-face contact for boosting photodegradation of triphenylmethane dyes under simulated sunlight. *J. Taiwan Inst. Chem. Eng.* 107, 98–109. doi:10.1016/j.jtice.2019.12.002

Chen, Y.-W., Kuo, J.-L., and Chew, K.-H. (2017). Polar ordering and structural distortion in electronic domain-wall properties of BiFeO3. *J. Appl. Phys.* 122, 075103. doi:10.1063/1.4998456

Chu, Y., Tan, X., Shen, Z., Liu, P., Han, N., Kang, J., et al. (2018). Efficient removal of organic and bacterial pollutants by Ag-La0.8Ca0.2Fe0.94O3-δ perovskite via catalytic peroxymonosulfate activation. *J. Hazard. Mater.* 356, 53–60. doi:10.1016/j.jhazmat.2018.05.044

Clark, S. J., and Robertson, J. (2007). Band gap and Schottky barrier heights of multiferroic BiFeO3. *Appl. Phys. Lett.* 90, 132903. doi:10.1063/1.2716868

Daghrir, R., Drogui, P., and Robert, D. (2012). Photoelectrocatalytic technologies for environmental applications. *J. Photochem. Photobiol. A: Chem.* 238, 41–52. doi:10.1016/j.jphotochem.2012.04.009

Demircivi, P., and Simsek, E. B. (2019). Visible-light-enhanced photoactivity of perovskite-type W-doped BaTiO3 photocatalyst for photodegradation of tetracycline. *J. Alloys Compd.* 774, 795–802. doi:10.1016/j.jallcom.2018.09.354

Dhanasekaran, P., and Gupta, N. M. (2012). Factors affecting the production of H2 by water splitting over a novel visible-light-driven photocatalyst GaFeO3. *Int. J. Hydrogen Energ.* 37, 4897–4907. doi:10.1016/j.ijhydene.2011.12.068

Dixit, T. K., Sharma, S., and Sinha, A. S. K. (2020). Development of heterojunction in N-rGO supported bismuth ferrite photocatalyst for degradation of Rhodamine B. *Inorg. Chem. Commun.* 117, 107945. doi:10.1016/j.inoche.2020.107945

Djoudi, L., and Omari, M. (2015). Synthesis and characterization of perovskite oxides LaAl1−x Ni x O3−δ (0 ≤ x ≤ 0.6) via Co-precipitation method. *J. Inorg. Organomet. Polym.* 25, 796–803. doi:10.1007/s10904-014-0162-5

Dong, W., Liu, H., Bao, Q., and Gu, X. (2020). Facile synthesis of metastable CaTi2O5 nanostructure and its photocatalytic properties. *Opt. Mater.* 105, 109921. doi:10.1016/j.optmat.2020.109921

Etgar, L. (2016). *Hole Conductor Free Perovskite-based Solar Cells*, Switzerland: Springer

Fan, W., Sun, Z., Bai, Y., Wu, K., Zhou, J., and Cheng, Y. (2020). *In situ* growth of nanoparticles in A-site deficient ferrite perovskite as an advanced electrode for symmetrical solid oxide fuel cells. *J. Power Sourc.* 456, 228000. doi:10.1016/j.jpowsour.2020.228000

Fang, C., Geng, B., Liu, J., and Zhan, F. (2009). D-fructose molecule template route to ultra-thin ZnSnO3 nanowire architectures and their application as efficient photocatalyst. *Chem. Commun. (Camb)*, 2350–2352. doi:10.1039/b821459j

Fuentes, M. K., Kumar, A., Das, T., Kumar, V., Singh, S., Rai, V. S., et al. (2020). BiFeO3 perovskite as an efficient photocatalyst synthesised by soft chemical route. *Mater. Technol.* 105, 1–9. doi:10.1080/10667857.2020.1782061

Gade, R., Ahemed, J., Yanapu, K. L., Abate, S. Y., Tao, Y.-T., and Pola, S. (2018). Photodegradation of organic dyes and industrial wastewater in the presence of layer-type perovskite materials under visible light irradiation. *J. Environ. Chem. Eng.* 6, 4504–4513. doi:10.1016/j.jece.2018.06.057

Gao, T., Chen, Z., Niu, F., Zhou, D., Huang, Q., Zhu, Y., et al. (2015). Shape-controlled preparation of bismuth ferrite by hydrothermal method and their visible-light degradation properties. *J. Alloys Compd.* 648, 564–570. doi:10.1016/j.jallcom.2015.07.059

Garcia-Segura, S., and Brillas, E. (2017). Applied photoelectrocatalysis on the degradation of organic pollutants in wastewaters. *J. Photochem. Photobiol. C: Photochem. Rev.* 31, 1–35. doi:10.1016/j.jphotochemrev.2017.01.005

Ge, M. Z., Cao, C. Y., Huang, J. Y., Li, S. H., Zhang, S. N., Deng, S., et al. (2016). Synthesis, modification, and photo/photoelectrocatalytic degradation applications of TiO2 nanotube arrays: a review. *Nanotechnology Rev.* 5 (1), 75–112. doi:10.1515/ntrev-2015-0049

Georgieva, J., Valova, E., Armyanov, S., Philippidis, N., Poulios, I., and Sotiropoulos, S. (2012). Bi-component semiconductor oxide photoanodes for the photoelectrocatalytic oxidation of organic solutes and vapours: a short review with emphasis to TiO2-WO3 photoanodes. *J. Hazard. Mater.* 211-212, 30–46. doi:10.1016/j.jhazmat.2011.11.069

Gross-Sorokin, M. Y., Roast, S. D., and Brighty, G. C. (2006). Assessment of feminization of male fish in English rivers by the environment agency of England and Wales. *Environ. Health Perspect.* 114 Suppl 1, 147–151. doi:10.1289/ehp.8068

Guan, S., Li, R., Sun, X., Xian, T., and Yang, H. (2020). Construction of novel ternary Au/LaFeO3/Cu2O composite photocatalysts for RhB degradation via photo-Fenton catalysis. *Mater. Technol.* 00, 1–13. doi:10.1080/10667857.2020.1782062

Han, M., Ma, Z., Zhang, W., and Wang, H. (2020). The influences of hexadecyl trimethyl ammonium bromide on lanthanum titanate photocatalyst for ofloxacin degradation. *J. Sol-gel Sci. Technol.* 96, 480. doi:10.1007/s10971-020-05341-9

Haron, W., Wisitsoraat, A., and Wongnawa, S. (2017). Nanostructured perovskite oxides - LaMO3 (M=Al, Co, Fe) prepared by co-precipitation method and their ethanol-sensing characteristics. *Ceramics Int.* 43, 5032–5040. doi:10.1016/j.ceramint.2017.01.013

Haruna, A., Abdulkadir, I., and Idris, S. O. (2020). Synthesis, characterization and photocatalytic properties of Bi0.85−XMXBa0.15FeO3 (M = Na and K, X = 0, 0.1) perovskite-like nanoparticles using the sol-gel method. *J. King Saud Univ. - Sci.* 32, 896–903. doi:10.1016/j.jksus.2019.05.005

Hbaieb, K., Rashid, K. K. A., and Kooli, F. (2017). Hydrogen production by autothermal reforming of dodecane over strontium titanate based perovskite catalysts. *Int. J. Hydrogen Energ.* 42, 5114–5124. doi:10.1016/j.ijhydene.2016.11.127

Honorio, L. M. C., Oliveira, A. L. M. d., Silva Filho, E. C. d., Osajima, J. A., Hakki, A., Macphee, D. E., et al. (2020). Supporting the photocatalysts on ZrO2: an effective way to enhance the photocatalytic activity of SrSnO3. *Appl. Surf. Sci.* 528, 146991. doi:10.1016/j.apsusc.2020.146991

Huang, J.-R.Tan, X., Yu, T., Zhao, L., and Hu, W.-L. (2014). Enhanced photoelectrocatalytic and photoelectrochemical properties by high-reactive TiO 2/SrTiO 3 hetero-structured nanotubes with dominant {001} facet of anatase TiO 2. *Electrochimica Acta* 146, 278–287. doi:10.1016/j.electacta.2014.09.043

Huang, S.-T.Lee, W. W., Chang, J.-L., Huang, W.-S., Chou, S.-Y., and Chen, C.-C. (2014). Hydrothermal synthesis of SrTiO3 nanocubes: characterization, photocatalytic activities, and degradation pathway. *J. Taiwan Inst. Chem. Eng.* 45, 1927–1936. doi:10.1016/j.jtice.2014.02.003

Huerta-Flores, A. M., Torres-Martínez, L. M., Moctezuma, E., and Carrera-Crespo, J. E. (2018). Novel SrZrO3-Sb2O3 heterostructure with enhanced photocatalytic activity: band engineering and charge transference mechanism. *J. Photochem. Photobiol. A: Chem.* 356, 166–176. doi:10.1016/j.jphotochem.2017.12.049

Jayapandi, S., Lakshmi, D., Premkumar, S., Packiyaraj, P., and Anitha, K. (2018). Augmented photocatalytic and electrochemical activities of Ag tailored LaCoO3 perovskite semiconductor. *Mater. Lett.* 218, 205–208. doi:10.1016/j.matlet.2018.02.015

Jiang, E., Yang, L., Song, N., Zhang, X., Liu, C., and Dong, H. (2020). Multi-shelled hollow cube CaTiO3 decorated with Bi12O17Cl2 towards enhancing photocatalytic performance under the visible light. *J. Colloid Interf. Sci.* 576, 21–33. doi:10.1016/j.jcis.2020.05.019

Jiang, J., Jia, Y., Wang, Y., Chong, R., Xu, L., and Liu, X. (2019). Insight into efficient photocatalytic elimination of tetracycline over SrTiO3(La,Cr) under visible-light irradiation: the relationship of doping and performance. *Appl. Surf. Sci.* 486, 93–101. doi:10.1016/j.apsusc.2019.04.261

Junploy, P., Thongtem, S., and Thongtem, T. (2013). Photoabsorption and photocatalysis of SrSnO3 produced by a cyclic microwave radiation. *Superlattices and Microstructures* 57, 1–10. doi:10.1016/j.spmi.2013.01.008

Kato, H., and Kudo, A. (1998). New tantalate photocatalysts for water decomposition into H2 and O2. *Chem. Phys. Lett.* 295, 487–492. doi:10.1016/S0009-2614(98)01001-X

Kato, H., and Kudo, A. (2001). Water splitting into H2 and O2 on alkali tantalate photocatalysts ATaO3(A = Li, Na, and K). *J. Phys. Chem. B* 105, 4285–4292. doi:10.1021/jp004386b

Katz, E. A. (2020). Perovskite: name puzzle and German-Russian odyssey of discovery. *Helvetica Chim. Acta* 103, e200006. doi:10.1002/hlca.2020000610.1002/hlca.202000061

Khalesi, A., Arandiyan, H. R., and Parvari, M. (2008b). Effects of lanthanum substitution by strontium and calcium in La-Ni-Al perovskite oxides in Dry reforming of methane. *Chin. J. Catal.* 29, 960–968. doi:10.1016/S1872-2067(08)60079-0

Khalesi, A., Arandiyan, H. R., and Parvari, M. (2008a). Production of syngas by CO2Reforming on MxLa1−xNi0.3Al0.7O3−d(M = Li, Na, K) catalysts. *Ind. Eng. Chem. Res.* 47, 5892–5898. doi:10.1021/ie800111e

Kiani, A., Nabiyouni, G., Masoumi, S., and Ghanbari, D. (2019). A novel magnetic MgFe2O4-MgTiO3 perovskite nanocomposite: rapid photo-degradation of toxic dyes under visible irradiation. *Composites B: Eng.* 175, 107080. doi:10.1016/j.compositesb.2019.107080

Kong, J., Yang, T., Rui, Z., and Ji, H. (2019). Perovskite-based photocatalysts for organic contaminants removal: current status and future perspectives. *Catal. Today* 327, 47–63. doi:10.1016/j.cattod.2018.06.045

Kostyukhin, E. M., Kustov, A. L., and Kustov, L. M. (2019). One-step hydrothermal microwave-assisted synthesis of LaFeO3 nanoparticles. *Ceramics Int.* 45, 14384–14388. doi:10.1016/j.ceramint.2019.04.155

Kubacka, A., Fernández-García, M., and Colón, G. (2012). Advanced nanoarchitectures for solar photocatalytic applications. *Chem. Rev.* 112, 1555–1614. doi:10.1021/cr100454n

Kudo, A., Kato, H., and Nakagawa, S. (2000). Water splitting into H2and O2on new Sr2M2O7(M = Nb and Ta) photocatalysts with layered perovskite structures: factors affecting the photocatalytic activity. *J. Phys. Chem. B* 104, 571–575. doi:10.1021/jp9919056

Kumar, A.Kumar, A., and Krishnan, V. (2020). Perovskite oxide based materials for energy and environment-oriented photocatalysis. *ACS Catal.* 10 (17), 10253–10315. doi:10.1021/acscatal.0c02947

Kumar, A., Kumar, S., and Krishnan, V. (2019). "Synthesis and characterization of A site doped lanthanum based perovskite catalyst for the oxidation of soot," in *Nanophotocatalysis and environmental applications*. Cham: Springer, 139–165.

Kumar, P.Chand, P., and Singh, V. (2020). La3+ substituted BiFeO3-a proficient nano ferrite photo-catalyst under the application of visible light. *Chem. Phys. Lett.* 754, 137715. doi:10.1016/j.cplett.2020.137715

Kusmierek, E., and Chrzescijanska, E. (2015). Application of TiO2-RuO2/Ti electrodes modified with WO3 in electro- and photoelectrochemical oxidation of Acid Orange 7 dye. *J. Photochem. Photobiol. A: Chem.* 302, 59–68. doi:10.1016/j.jphotochem.2015.01.009

Labhasetwar, N., Saravanan, G., Kumar Megarajan, S., Manwar, N., Khobragade, R., Doggali, P., et al. (2015). Perovskite-type catalytic materials for environmental applications. *Sci. Technol. Adv. Mater.* 16, 036002. doi:10.1088/1468-6996/16/3/036002

Lakhera, S. K., Hafeez, H. Y., Veluswamy, P., Ganesh, V., Khan, A., Ikeda, H., et al. (2018). Enhanced photocatalytic degradation and hydrogen production activity of *in situ* grown TiO2 coupled NiTiO3 nanocomposites. *Appl. Surf. Sci.* 449, 790–798. doi:10.1016/j.apsusc.2018.02.136

Yang, Y., Chen, Q., Yin, Z., and Li, J. (2009). Study on the photocatalytic activity of K2La2Ti3O10 doped with vanadium (V). *J. Alloys Compd.* 488, 364–369. doi:10.1016/j.jallcom.2009.08.136

Li, X., and Zang, J. (2011). Hydrothermal synthesis and characterization of Lanthanum-doped NaTaO3 with high photocatalytic activity. *Catal. Commun.* 12, 1380–1383. doi:10.1016/j.catcom.2011.05.004

Liu, D. R., Jiang, Y. S., and Gao, G. M. (2011). Photocatalytic degradation of an azo dye using N-doped NaTaO3 synthesized by one-step hydrothermal process. *Chemosphere* 83, 1546–1552. doi:10.1016/j.chemosphere.2011.01.033

Liu, J., He, F., Chen, L., Qin, X., Zhao, N., Huang, Y., et al. (2016). Novel hexagonal-YFeO 3/α-Fe 2 O 3 heterojunction composite nanowires with enhanced visible light photocatalytic activity. *Mater. Lett.* 165, 263–266. doi:10.1016/j.matlet.2015.12.008

Lu, L., Lv, M., Wang, D., Liu, G., and Xu, X. (2017). Efficient photocatalytic hydrogen production over solid solutions Sr1-xBixTi1-xFexO3 (0 ≤ x ≤ 0.5). *Appl. Catal. B: Environ.* 200, 412–419. doi:10.1016/j.apcatb.2016.07.035

Malathi, A., Arunachalam, P., Kirankumar, V. S., Madhavan, J., and Al-Mayouf, A. M. (2018). An efficient visible light driven bismuth ferrite incorporated bismuth oxyiodide (BiFeO3/BiOI) composite photocatalytic material for degradation of pollutants. *Opt. Mater.* 84, 227–235. doi:10.1016/j.optmat.2018.06.067

Malpass, G. R., Miwa, D. W., Machado, S. A., and Motheo, A. J. (2010). SnO(2)-based materials for pesticide degradation. *J. Hazard. Mater.* 180, 145–151. doi:10.1016/j.jhazmat.2010.04.006

Meng, W., Hu, R., Yang, J., Du, Y., Li, J., and Wang, H. (2016). Influence of lanthanum-doping on photocatalytic properties of BiFeO 3 for phenol degradation. *Chin. J. Catal.* 37, 1283–1292. doi:10.1016/S1872-2067(16)62449-X

Meng, X., Zhang, Z., and Li, X. (2015). Synergetic photoelectrocatalytic reactors for environmental remediation: a review. *J. Photochem. Photobiol. C: Photochem. Rev.* 24, 83–101. doi:10.1016/j.jphotochemrev.2015.07.003

Modak, B., and Ghosh, S. K. (2014). Improvement of photocatalytic activity of NaTaO 3 under visible light by N and F doping. *Chem. Phys. Lett.* 613, 54–58. doi:10.1016/j.cplett.2014.08.054

Mužina, K., Tkalčević, M., Brleković, F., Munda, I. K., Šipušić, J., and Kurajica, S. (2020). Sol-gel synthesis and characterization of lithium and cerium codoped perovskite. 9, 17–24. doi:10.32732/jma.2020.9.1.17

Mukherjee, A., Chakrabarty, S., Kumari, N., Su, W. N., and Basu, S. (2018). Visible-light-mediated electrocatalytic activity in reduced graphene oxide-supported bismuth ferrite. *Acs Omega* 3 (6), 5946–5957. doi:10.1021/acsomega.8b00708

Muñoz-Gil, D., Urones-Garrote, E., Pérez-Coll, D., Amador, U., and García-Martín, S. (2018). Crystal structure and compositional effects on the electrical and electrochemical properties of GdBaCo2−xMnxO5+δ (0 ≤ x ≤ 2) oxides for use as air electrodes in solid oxide fuel cells. *J. Mater. Chem. A.* 6, 5452–5460. doi:10.1039/c7ta10923g

Nakhostin Panahi, P., Rasoulifard, M. H., and Babaei, S. (2020). Photocatalytic activity of cation (Mn) and anion (N) substitution in LaCoO3 nanoperovskite under visible light. *Rare Met.* 39, 139–146. doi:10.1007/s12598-019-01329-9

Neaton, J. B., Ederer, C., Waghmare, U. V., Spaldin, N. A., and Rabe, K. M. (2005). First-principles study of spontaneous polarization in multiferroicBiFeO3. *Phys. Rev. B* 71, 1–9. doi:10.1103/PhysRevB.71.014113

Ni, M., Leung, M. K. H., Leung, D. Y. C., and Sumathy, K. (2007). A review and recent developments in photocatalytic water-splitting using TiO2 for hydrogen production. *Renew. Sustain. Energ. Rev.* 11, 401–425. doi:10.1016/j.rser.2005.01.009

Oliva, J., Garcia, C. R., Verduzco, E., Martinez, A. I., Manthiram, A., and Padmasree, K. P. (2017). Enhancing the photocatalytic activity of the perovskite-based intergrowth oxide Sr3.2La0.8Fe1.5Co1.5O10-δ with Ca substitution. *Ceramics Int.* 43, 14074–14081. doi:10.1016/j.ceramint.2017.07.143

Orimolade, B. O., and Arotiba, O. A. (2020). Towards visible light driven photoelectrocatalysis for water treatment: application of a FTO/BiVO4/Ag2S heterojunction anode for the removal of emerging pharmaceutical pollutants. *Sci. Rep.* 10, 1–13. doi:10.1038/s41598-020-62425-w

Orimolade, B. O., Koiki, B. A., Peleyeju, G. M., and Arotiba, O. A. (2019). Visible light driven photoelectrocatalysis on a FTO/BiVO4/BiOI anode for water treatment involving emerging pharmaceutical pollutants. *Electrochimica Acta* 307, 285–292. doi:10.1016/j.electacta.2019.03.217

Orimolade, B. O., Zwane, B. N., Koiki, B. A., Tshwenya, L., Peleyeju, G. M., Mabuba, N., et al. (2020). Solar photoelectrocatalytic degradation of ciprofloxacin at a FTO/BiVO4/MnO2 anode: kinetics, intermediate products and degradation pathway studies. *J. Environ. Chem. Eng.* 8, 103607. doi:10.1016/j.jece.2019.103607

Park, N. G., Grätzel, M., and Miyasaka, T. (2016). Organic-inorganic halide perovskite photovoltaics: from fundamentals to device architectures. Springer International Publishing. doi:10.1007/978-3-319-35114-8

Peleyeju, M. G., and Arotiba, O. A. (2018). Recent trend in visible-light photoelectrocatalytic systems for degradation of organic contaminants in water/wastewater. *Environ. Sci. Water Res. Technol.* 4, 1389–1411. doi:10.1039/c8ew00276b

Phoon, B. L., Lai, C. W., Pan, G.-T., Yang, T. C.-K., and Juan, J. C. (2018). One-pot hydrothermal synthesis of strontium titanate nanoparticles photoelectrode using electrophoretic deposition for enhancing photoelectrochemical water splitting. *Ceramics Int.* 44, 9923–9933. doi:10.1016/j.ceramint.2018.03.017

Pisarev, R. V., Moskvin, A. S., Kalashnikova, A. M., and Rasing, T. (2009). Charge transfer transitions in multiferroicBiFeO3and related ferrite insulators. *Phys. Rev. B* 79. doi:10.1103/PhysRevB.79.235128

Priyatharshni, S., Rajesh Kumar, S., Viswanathan, C., and Ponpandian, N. (2020). Morphologically tuned LaMnO3 as an efficient nanocatalyst for the removal of organic dye from aqueous solution under sunlight. *J. Environ. Chem. Eng.* 8, 104146. doi:10.1016/j.jece.2020.104146

Qian, X., Chen, Z., Yang, X., Zhao, W., Liu, C., Sun, T., et al. (2020). Perovskite cesium lead bromide quantum dots: a new efficient photocatalyst for degrading antibiotic residues in organic system. *J. Clean. Prod.* 249, 119335. doi:10.1016/j.jclepro.2019.119335

Qu, L., Lang, J., Wang, S., Chai, Z., Su, Y., and Wang, X. (2016). Nanospherical composite of WO3 wrapped NaTaO3: improved photodegradation of tetracycline under visible light irradiation. *Appl. Surf. Sci.* 388, 412–419. doi:10.1016/j.apsusc.2015.12.095

Ramadan, W., Shaikh, P. A., Ebrahim, S., Ramadan, A., Hannoyer, B., Jouen, S., et al. (2013). Highly efficient photocatalysis by BiFeO3/α(γ)-Fe2O3 ferromagnetic nano p/n junctions formed by dopant-induced phase separation. *J. Nanopart Res.* 15 (8), 1–10. doi:10.1007/s11051-013-1848-2

Rao, M. P., Nandhini, V. P., Wu, J. J., Syed, A., Ameen, F., and Anandan, S. (2018). Synthesis of N-doped potassium tantalate perovskite material for environmental applications. *J. Solid State. Chem.* 258, 647–655. doi:10.1016/j.jssc.2017.11.031

Rekavandi, N., Malekzadeh, A., and Ghiasi, E. (2019). Methyl orange degradation using nano-LaMnO 3 as a green catalyst under the mild conditions. *Nanochem Res.* 4, 1–10. doi:10.22036/ncr.2019.01.001

Remya, K. P., Prabhu, D., Joseyphus, R. J., Bose, A. C., Viswanathan, C., and Ponpandian, N. (2020). Tailoring the morphology and size of perovskite BiFeO3 nanostructures for enhanced magnetic and electrical properties. *Mater. Des.* 192, 108694. doi:10.1016/j.matdes.2020.108694

Ridzuan, N. D. M., Kaus, N. H. M., Lazim, M. A. S. M., Kobayashi, T., Adnan, R., Othman, M. Z., et al. (2020). Photocatalytic heterostructures-based BiFeO3 embedded liquid natural rubber (LNR) for highly removal of cationic dye under direct sunlight. *J. Environ. Chem. Eng.* 8 (5), 104152. doi:10.1016/j.jece.2020.104152

Rosy, A., and Kalpana, G. (2018). Reduced graphene oxide/strontium titanate heterostructured nanocomposite as sunlight driven photocatalyst for degradation of organic dye pollutants. *Curr. Appl. Phys.* 18, 1026–1033. doi:10.1016/j.cap.2018.05.019

Sati, P. C., Kumar, M., Chhoker, S., and Jewariya, M. (2015). Influence of Eu substitution on structural, magnetic, optical and dielectric properties of BiFeO3 multiferroic ceramics. *Ceramics Int.* 41, 2389–2398. doi:10.1016/j.ceramint.2014.10.053

Lim, P. F., Leong, K. H., Sim, L. C., Saravanan, P., and Abd Aziz, A. (2019). Perovskite Oxide–Based Photocatalysts for Excellent Visible Light–Driven Photocatalysis and Energy Conversion. in *Plant Nanobionics*, Cham: Springer, 35–54.

Shawky, A., Mohamed, R. M., Mkhalid, I. A., Youssef, M. A., and Awwad, N. S. (2020). Visible light-responsive Ag/LaTiO3 nanowire photocatalysts for efficient elimination of atrazine herbicide in water. *J. Mol. Liquids* 299, 112163. doi:10.1016/j.molliq.2019.112163

Shirazi, P., Rahbar, M., Behpour, M., Ashrafi, M., and Behpour, M. (2020). La2MnTiO6 double perovskite nanostructures as highly efficient visible light photocatalysts. *New J. Chem.* 44, 231–238. doi:10.1039/c9nj04932k

Simsek, E. B., Tuna, Ö., and Balta, Z. (2019). Construction of stable perovskite-type LaFeO3 particles on polymeric resin with boosted photocatalytic Fenton-like decaffeination under solar irradiation. *Sep. Purif. Technol.* 237, 116384. doi:10.1016/j.seppur.2019.116384

Sirés, I., Brillas, E., Oturan, M. A., Rodrigo, M. A., and Panizza, M. (2014). Electrochemical advanced oxidation processes: today and tomorrow. A review. *Environ. Sci. Pollut. Res.* 21, 8336–8367. doi:10.1007/s11356-014-2783-1

Sirés, I., and Brillas, E. (2012). Remediation of water pollution caused by pharmaceutical residues based on electrochemical separation and degradation technologies: a review. *Environ. Int.* 40, 212–229. doi:10.1016/j.envint.2011.07.012

Sosnowska, I., Loewenhaupt, M., David, W. I. F., and Ibberson, R. M. (1992). Investigation of the unusual magnetic spiral arrangement in BiFeO3. *Physica B: Condensed Matter* 180-181, 117–118. doi:10.1016/0921-4526(92)90678-L

Tang, P., Chen, H., Cao, F., and Pan, G. (2011). Magnetically recoverable and visible-light-driven nanocrystalline YFeO3 photocatalysts. *Catal. Sci. Technol.* 1, 1145–1148. doi:10.1039/c1cy00199j

Teresita, V. M., Manikandan, A., Josephine, B. A., Sujatha, S., and Antony, S. A. (2016). Electromagnetic properties and humidity-sensing studies of magnetically recoverable LaMg x Fe1−x O 3−δ perovskites nano-photocatalysts by sol-gel route. *J. Supercond. Nov. Magn.* 29, 1691–1701. doi:10.1007/s10948-016-3465-7

Tomar, R., Prajapati, R., Verma, S., and Rana, N. (2021). Enhanced photoluminescence and efficient photocatalytic activity of Sn doped barium titanate. *Mater. Today Proc.* 34, 608–611. doi:10.1016/j.matpr.2020.01.543

Torregrosa-Rivero, V., Albaladejo-Fuentes, V., Sánchez-Adsuar, M.-S., and Illán-Gómez, M.-J. (2017). Copper doped BaMnO3 perovskite catalysts for NO oxidation and NO2-assisted diesel soot removal. *RSC Adv.* 7, 35228–35238. doi:10.1039/c7ra04980c

Umukoro, E. H., Peleyeju, M. G., Idris, A. O., Ngila, J. C., Mabuba, N., Rhyman, L., et al. (2018). Photoelectrocatalytic application of palladium decorated zinc oxide-expanded graphite electrode for the removal of 4-nitrophenol: experimental and computational studies. *RSC Adv.* 8, 10255–10266. doi:10.1039/c8ra00180d

Umukoro, E. H., Peleyeju, M. G., Ngila, J. C., and Arotiba, O. A. (2016). Photocatalytic degradation of acid blue 74 in water using Ag-Ag 2 O-Zno nanostuctures anchored on graphene oxide. *Solid State. Sci.* 51, 66–73. doi:10.1016/j.solidstatesciences.2015.11.015

Umukoro, E. H., Peleyeju, M. G., Ngila, J. C., and Arotiba, O. A. (2017). Towards wastewater treatment: photo-assisted electrochemical degradation of 2-nitrophenol and orange II dye at a tungsten trioxide-exfoliated graphite composite electrode. *Chem. Eng. J.* 317, 290–301. doi:10.1016/j.cej.2017.02.084

Venkatesh, G., Geerthana, M., Prabhu, S., Ramesh, R., and Prabu, K. M. (2020a). Enhanced photocatalytic activity of reduced graphene oxide/SrSnO3 nanocomposite for aqueous organic pollutant degradation. *Optik* 206, 164055. doi:10.1016/j.ijleo.2019.164055

Venkatesh, G., Prabhu, S., Geerthana, M., Baskaran, P., Ramesh, R., and Prabu, K. M. (2020b). Facile synthesis of rGO/CaSnO3 nanocomposite as an efficient photocatalyst for the degradation of organic dye. *Optik* 212, 164716. doi:10.1016/j.ijleo.2020.164716

Verduzco, L. E., Garcia-Diaz, R., Oliva, J., Martinez, A. I., Gomez-Solis, C., Garcia, C. R., et al. (2018). Enhanced photocatalytic activity of layered perovskite oxides Sr2.7-xCaxLn0.3Fe2O7-δ for MB degradation. *Ceramics Int.* 44, 17079–17086. doi:10.1016/j.ceramint.2018.06.155

Wang, F., Chen, D., Zhang, N., Wang, S., Qin, L., Sun, X., et al. (2017). Oxygen vacancies induced by zirconium doping in bismuth ferrite nanoparticles for enhanced photocatalytic performance. *J. Colloid Interf. Sci.* 508, 237–247. doi:10.1016/j.jcis.2017.08.056

Wang, L., Xia, L., Wu, Y., and Tian, Y. (2016). Zr-doped β-in2S3 ultrathin nanoflakes as photoanodes: enhanced visible-light-driven photoelectrochemical water splitting. *ACS Sustain. Chem. Eng.* 4, 2606–2614. doi:10.1021/acssuschemeng.6b00090

Wang, Q., Zhou, S., Xiao, S., Wei, F., Zhao, X., Qu, J. e., et al. (2018). Novel perovskite-based composites, La$_{1-x}$NdxFeO$_3$@activated carbon, as efficient catalysts for the degradation of organic pollutants by heterogeneous electro-Fenton reactions. *RSC Adv.* 8, 14775–14786. doi:10.1039/c8ra00244d

Wang, S., Chen, D., Niu, F., Zhang, N., Qin, L., and Huang, Y. (2016). Pd cocatalyst on Sm-doped BiFeO3 nanoparticles: synergetic effect of a Pd cocatalyst and samarium doping on photocatalysis. *RSC Adv.* 6, 34574–34587. doi:10.1039/c6ra01140c

Wang, W., Bi, J., Wu, L., Li, Z., and Fu, X. (2009). Hydrothermal synthesis and catalytic performances of a new photocatalyst CaSnO3 with microcube morphology. *Scripta Materialia* 60, 186–189. doi:10.1016/j.scriptamat.2008.10.001

Wang, W., Liang, S., Ding, K., Bi, J., Yu, J. C., Wong, P. K., et al. (2014). Microwave hydrothermal synthesis of MSnO3 (M2+ = Ca2+, Sr2+, Ba2+): effect of M2+ on crystal structure and photocatalytic properties. *J. Mater. Sci.* 49, 1893–1902. doi:10.1007/s10853-013-7880-x

Wu, J.-g., Fang, T., Cai, R., Li, S.-y., Wang, Y., Zhao, C.-e., et al. (2016). Fabrication of an Ag/Fe2O3/ZnO ternary composite with enhanced photocatalytic performance. *RSC Adv.* 6, 4145–4150. doi:10.1039/c5ra20403h

Wu, X.-J., Niu, C.-G., Zhang, L., Liang, C., and Zeng, G.-M. (2017). An in depth mechanism insight of the degradation of multiple refractory pollutants via a novel SrTiO3/BiOI heterojunction photocatalysts. *J. Catal.* 356, 283–299. doi:10.1016/j.jcat.2017.10.022

Wei, H., Luo, C., Huangfu, G., and Guo, Y. (2020). Boosting the photocatalytic ability of bandgap engineered (Na0.5Bi0.5)TiO3-BaTiO3 by N-Ni codoping. *J. Phys. Chem. C* 124, 11810–11818. doi:10.1021/acs.jpcc.0c02542

Yahya, N., Nasir, A. M., Daub, N. A., Aziz, F., Aizat, A., Jaafar, J., et al. (2020). Visible light-driven perovskite-based photocatalyst for wastewater treatment. In *Handbook of Smart Photocatalytic Materials*, Amsterdam, Netherlands: . Elsevier, 265-302.

Yahya, N., Aziz, F., Enriquez, M. A. O. A., Aizat, A., Lau, W. J., Yusof, N., et al. (2018). Preparation and characterization of Lafeo3 using dual-complexing agents for photodegradation of humic acid. *Environ. Eco. Sci. (EES)* 2 (2), 30-34. doi:10.26480/ees.02.2018.30.34

Yahya, N., Aziz, F., Jamaludin, A., Aizat, A., Mutalib, M. A., Jaafar, J., et al. (2019). Effects of the citric acid addition on the morphology, surface area, and photocatalytic activity of LaFeO3 nanoparticles prepared by glucose-based gel combustion methods. *Ind. Eng. Chem. Res.* 58, 609–617. doi:10.1021/acs.iecr.8b04263

Yao, W. F., Xu, X. H., Wang, H., Zhou, J. T., Yang, X. N., Zhang, Y., et al. (2004). Photocatalytic property of perovskite bismuth titanate. *Appl. Catal. B. Environ.* 52, 109–116. doi:10.1016/j.apcatb.2004.04.002

Yao, L., Chen, Z., Li, J., and Shi, C. (2020). Creation of oxygen vacancies to activate lanthanum-doped bismuth titanate nanosheets for efficient synchronous photocatalytic removal of Cr(VI) and methyl orange. *J. Mol. Liquids* 314, 113613. doi:10.1016/j.molliq.2020.113613

Yu, X., Wang, J., Fu, X., Meng, H., Zhu, Y., and Zhang, Y. (2020). Construction of Z-scheme SrTiO3/Ag/Ag3PO4 photocatalyst with oxygen vacancies for highly efficient degradation activity towards tetracycline. *Separat. Purif. Technol.* 241, 116718. doi:10.1016/j.seppur.2020.116718

Zhang, D., Lv, S., and Luo, Z. (2020). A study on the photocatalytic degradation performance of a [KNbO3]0.9-[BaNi0.5Nb0.5O3−δ]0.1 perovskite. *RSC Adv.* 10, 1275–1280. doi:10.1039/c9ra07310h

Zhang, H., Chen, G., Li, Y., and Teng, Y. (2010). Electronic structure and photocatalytic properties of copper-doped CaTiO3. *Int. J. Hydrogen Energ.* 35, 2713–2716. doi:10.1016/j.ijhydene.2009.04.050

Zhang, H., Shimizu, Y., Teraoka, Y., Miura, N., and Yamazoe, N. (1990). Oxygen sorption and catalytic properties of La1$minus;xSrxCo1$minus;yFeyO3 Perovskite-type oxides. *J. Catal.* 121, 432–440. doi:10.1016/0021-9517(90)90251-E

Zhang, L., and Jaroniec, M. (2018). Toward designing semiconductor-semiconductor heterojunctions for photocatalytic applications. *Appl. Surf. Sci.* 430, 2–17. doi:10.1016/j.apsusc.2017.07.192

Zhang, Q., Huang, Y., Peng, S., Zhang, Y., Shen, Z., Cao, J.-j., et al. (2017). Perovskite LaFeO3-SrTiO3 composite for synergistically enhanced NO removal under visible light excitation. *Appl. Catal. B: Environ.* 204, 346–357. doi:10.1016/j.apcatb.2016.11.052

Zhang, W., Li, H., Ma, Z., Li, H., and Wang, H. (2019). Photocatalytic degradation of azophloxine on porous La2Ti2O7 prepared by sol-gel method. *Solid State. Sci.* 87, 58–63. doi:10.1016/j.solidstatesciences.2018.11.004

Zhang, W., Tang, J., and Ye, J. (2007). Structural, photocatalytic, and photophysical properties of perovskite MSnO3 (M = Ca, Sr, and Ba) photocatalysts. *J. Mater. Res.* 22, 1859–1871. doi:10.1557/jmr.2007.0259

Zhang, W. F., Tang, J., and Ye, J. (2006). Photoluminescence and photocatalytic properties of SrSnO3 perovskite. *Chem. Phys. Lett.* 418, 174–178. doi:10.1016/j.cplett.2005.10.122

Zhang, Y., Jin, Z., Chen, L., and Wang, J. (2019). SrFexNi1−xO3−δ perovskites coated on Ti anodes and their electrocatalytic properties for cleaning nitrogenous wastewater. *Materials* 12, 511. doi:10.3390/ma12030511

Zhu, A., Zhao, Q., Li, X., and Shi, Y. (2014). BiFeO3/TiO2 nanotube arrays composite electrode: construction, characterization, and enhanced photoelectrochemical properties. *ACS Appl. Mater. Inter.* 6, 671–679. doi:10.1021/am404774z

Zhu, H., Zhang, P., and Dai, S. (2015). Recent Advances of lanthanum-based perovskite oxides for catalysis. *ACS Catal.* 5, 6370–6385. doi:10.1021/acscatal.5b01667

Zhu, J., Li, H., Zhong, L., Xiao, P., Xu, X., Yang, X., et al. (2014). Perovskite oxides: preparation, characterizations, and applications in heterogeneous catalysis. *ACS Catal.* 4, 2917–2940. doi:10.1021/cs500606g

Conflict of Interest: The authors declare that the research was conducted in the absence of any commercial or financial relationships that could be construed as a potential conflict of interest.

frontiers
in Chemistry

ORIGINAL RESEARCH
published: 21 April 2021
doi: 10.3389/fchem.2021.624741

Two New Antiprotozoal Diterpenes From the Roots of *Acacia nilotica*

John V. Anyam[1*†], **Priscilla E. Daikwo**[1†], **Marzuq A. Ungogo**[2,3†], **Nwakaego E. Nweze**[4†], **Ngozichukwuka P. Igoli**[5†], **Alexander I. Gray**[6], **Harry P. De Koning**[2†] **and John O. Igoli**[1†]

[1]Phytochemistry Research Group, Department of Chemistry, University of Agriculture, Makurdi, Nigeria, [2]Institute of Infection, Immunity and Inflammation, College of Medical, Veterinary and Life Sciences, University of Glasgow, Glasgow, United Kingdom, [3]Department of Veterinary Pharmacology and Toxicology, Ahmadu Bello University, Zaria, Nigeria, [4]Department of Veterinary Medicine, Faculty of Veterinary Medicine, University of Nigeria, Nsukka, Nigeria, [5]Centre for Food Technology and Research, Benue State University, Makurdi, Nigeria, [6]Strathclyde Institute of Pharmacy and Biomedical Science, University of Strathclyde, Glasgow, United Kingdom

Edited by:
Eno E. Ebenso,
North-West University, South Africa

Reviewed by:
Paul-Henri Ducrot,
INRA UMR1318 Institut Jean Pierre Bourgin, France
Mohamed Saleh Abdelfattah,
Helwan University, Egypt

***Correspondence:**
John V. Anyam
johnversh@gmail.com

†ORCID:
John V. Anyam
orcid.org/0000-0002-6678-5707
Priscilla Idakwo
orcid.org/0000-0003-0076-0061
Marzuq A. Ungogo
orcid.org/0000-0003-4918-1423
Nwakaego E. Nweze
orcid.org/0000-0002-1735-2622
Ngozichukwuka P. Igoli
orcid.org/0000-0001-9986-7453
Harry De-Koning
orcid.org/0000-0002-9963-1827
John O. Igoli
orcid.org/0000-0002-8013-2702

Specialty section:
This article was submitted to Organic Chemistry, a section of the journal Frontiers in Chemistry

Received: *04 November 2020*
Accepted: *29 January 2021*
Published: *21 April 2021*

Citation:
Anyam JV, Daikwo PE, Ungogo MA, Nweze NE, Igoli NP, Gray AI, De Koning HP and Igoli JO (2021) Two New Antiprotozoal Diterpenes From the Roots of Acacia nilotica. *Front. Chem. 9:624741. doi: 10.3389/fchem.2021.624741*

The powdered roots of the medicinal plant *Acacia nilotica* were extracted with hexane and ethyl acetate, and the extracts were subjected to column chromatography for the isolation of potentially bioactive compounds and their screening against kinetoplastid pathogens. NMR and HREI mass spectrometric analyses identified two new diterpenes, characterized as 16, 19-dihydroxycassa-12-en-15-one (Sandynone, **1**) and (5S, 7R, 8R, 9R, 10S, 13Z, 17S)-7,8:7,17:16,17-triepoxy-7,8-seco-cassa-13-ene (niloticane B, **2**). The previously reported (5S,7R,8R,9R,10S) -(-)-7,8-seco-7, 8-oxacassa-13,15-diene-7,17-diol (**3**), (5S,7R,8R,9R,10S) -(-)-7,8-seco-7, 8-oxacassa-13,15-dien-7-ol-17-al (**4**), and (5S,7R,8R,9R,10S) -(-)-7,8-seco-7, 8-oxacassa-13,15-dien-7-ol (**5**) a, mixture of stigmasterol (**6a**) and sitosterol (**6b**), and lupeol (**7**) were also isolated. Several column fractions displayed significant activity against a panel of *Trypanosoma* and *Leishmania* spp., and from the most active fraction, compound **4** was isolated with high purity. The compound displayed high activity, particularly against *T. brucei*, *T. evansi*, and *L. mexicana* (0.88–11.7 μM) but only a modest effect against human embryonic kidney cells and no cross-resistance with the commonly used melaminophenyl arsenical and diamidine classes of trypanocides. The effect of compound **4** against *L. mexicana* promastigotes was irreversible after a 5-h exposure, leading to the sterilization of the culture between 24 and 48 h.

Keywords: Nigeria, spectroscopy, *Acacia nilotica*, diterpenes, seco-oxocassanes, trypanosomiasis, *Leishmania*

INTRODUCTION

Parasitic kinetoplastid diseases, including trypanosomiasis and leishmaniasis, threaten millions of people in resource-poor countries around the world. *Trypanosoma* spp. and *Leishmania* spp., belonging to the family Trypanosomatida and the order Kinetoplastida, are among the most important agents of neglected tropical diseases (Butler, 2007; Vieira de Morais et al., 2015). These diseases occur mostly in the tropics where the humidity and high environmental temperatures favor both vector and parasite growth and attract insufficient resources (Patz et al., 2000).

African trypanosomiasis is endemic in 36 sub-Saharan African countries, including Nigeria, where there are tsetse flies that transmit the disease. While the number of new human African trypanosomiasis (HAT, or sleeping sickness) infections has significantly decreased in recent years, with only 977 cases recorded in 2018 (WHO, 2019b), African animal trypanosomiasis (AAT) still remains a major constraint to the use of livestock in the region (Geerts et al., 2001). About 50 million heads of cattle are exposed to AAT, and 35 million doses of trypanocides are used annually (Mattioli et al., 2004) in prevention and treatment. The direct and indirect losses of AAT are put at about US$ 4.5 billion (Geerts et al., 2001). Beyond Africa, surra and dourine, caused by *T. evansi* and *T. equiperdum*, respectively, affect millions of high-value animals in Asia, Europe, Australia, and South America (Brun et al., 1998; Desquesnes et al., 2013).

Leishmaniasis generally affects the poorest of the poor and is associated with malnutrition, population displacement, poor housing, a weak immune system, and a lack of financial resources (WHO, 2019a). The disease manifests as visceral, cutaneous, and mucocutaneous infections. It is endemic in 98 countries, predominantly in Latin America, South and Central Asia, and parts of Africa (Alvar et al., 2012) where approximately 350 million people are at risk of contracting the infection. An estimated 700,000 to 1 million new cases and some 26,000 to 65,000 deaths occur annually (WHO, 2019a).

Nigerian medicinal plants are a rich source of natural compounds with potent antiprotozoal activity (Ungogo et al., 2020). *Acacia nilotica* Linn. (Mimosaceae) is a common medicinal plant found in subtropical and tropical Africa from Nigeria to Egypt and South Africa and other parts of the world (Chowdhury et al., 1983; Van Wyk et al., 1997 Roozbeh and Darvish, 2016). The plant is a small- to medium-size tree (Boulos, 2000), 7–13 m tall, with a stem diameter of 20–30 cm. The bark is dark brown to black. It has bright yellow flowers with bipinnate leaves. The plant is attractive to a wide range of pests, diseases, and wild animals (Sheik, 1989). There are several ethnobotanical uses of the plant, including treatment of abdominal pain, diarrhea, dysentery, and genital and urinary tract infections, and as an expectorant (Boulos, 1983). It possesses antimicrobial, antiplasmodial, antihypertensive, and antioxidant activities (Ali et al., 2012). Niloticane, a cassane diterpene (Eldeen et al., 2010), and umbelliferone, a coumarin (Singh et al., 2010), have been isolated from the plant, as well as some flavonoids and phenolic compounds (Saleem, 2011). Other *Acacia* species have yielded seco-oxacassanes and unusual diterpenoids such as schaffnerine, isolated from *Acacia schaffneri* (Manríquez-Torres et al., 2011; Manríquez-Torres et al., 2013). In the present study, we have carried out further phytochemical studies on *Acacia nilotica* and hereby report the isolation and characterization of two novel diterpenes from the roots.

Most of the drugs available for the treatment of trypanosomiasis and leishmaniasis are outdated and associated with toxic side effects, prolonged duration of treatment, and resistance (Anene et al., 2001; WHO, 2010; De Koning, 2020). Therefore, there is an urgent need for new drugs for the treatment of trypanosomiasis and leishmaniasis, and the active ingredients of traditionally used medicinal plants are a prime source of unrelated, new compounds. Hence, the compounds and mixtures obtained from *A. nilotica* were also investigated for antitrypanosomal and antileishmanial activities as well as for toxicity against human cell lines *in vitro*. Activity-guided fractionation yielded one pure compound with activity against several *Trypanosoma* species and against *Leishmania mexicana* below 0.5 µg/ml. The effect on *Leishmania mexicana* promastigotes was irreversible within 5 h and fatal after 24 h.

MATERIALS AND METHODS

General Experimental Procedures

Column chromatography was carried out using silica gel 60 (0.040–0.063 mm) (230–400 mesh ASTM). Thin-layer chromatography (TLC) was performed on precoated aluminum sheets coated with silica gel F250 (Merck, Germany). Nuclear magnetic resonance (NMR) experiments were carried out on a Bruker AVIII (500 MHz) spectrophotometer using $CDCl_3$ as the solvent and TMS as the internal standard. Mass spectral data were acquired on a JEOL MStation JMS-700 mass spectrometer.

Plant Material

Roots of *Acacia nilotica* were collected from trees growing on the campus of the University of Agriculture, Makurdi. The plant was authenticated at the Department of Forestry and Wildlife of the university and a voucher specimen deposited at their herbarium.

Isolation of Compounds

Dried roots of the plant were ground to powder (250 g) and extracted with hexane and ethyl acetate. The extracts were combined (based on similarity on TLC) and subjected to column chromatography using silica gel in a glass column. The column was packed wet in a hexane: ethyl acetate (95:5) mixture and eluted with ethyl acetate in hexane gradient starting with 5% ethyl acetate in hexane and increasing the amount of ethyl acetate by 5% until 100% ethyl acetate collecting 10-ml vials to obtain 186 fractions. The fractions were examined by TLC, and similar ones were combined and allowed to dry in a fume hood to obtain a mixture of compounds **1** and **3** (fractions 76–79), mixture of compounds **2** and **5** (fractions 18–19), compound **4** (fractions 64–67), a mixture of compounds **6a** and **6b** (fractions 59–60), and compound **7** (fractions 25–28) as white crystalline solids. The compounds were analyzed by NMR (1D and 2D) spectroscopy and mass spectrometry.

Determination of Antiprotozoal and Cytotoxic Activity

Parasites, Mammalian Cells, and Culture Conditions

Two strains of *Trypanosoma brucei brucei* bloodstream form (BSF) were used in this study: 1) wild-type (WT) *T. b. brucei* strain Lister 427 (De Koning et al., 2000) and 2) a multidrug resistant strain, B48, which was derived from a TbAT1-KO strain (Matovu et al., 2003) after increasing *in vitro* exposure to pentamidine and lacks both the TbAT1/P2 transporter and the high-affinity pentamidine transporter (HAPT1) (Bridges et al., 2007). The two *T. b. brucei* strains and drug-sensitive (WT) strains of *T. evansi* and *T. equiperdum* were used throughout as

TABLE 1 | ^1H NMR data for compounds **1** (at 500 MHz) and **2** (at 400 MHz) in $CDCl_3$.

	Compound 1			Compound 2		Literature report (compd 2)[a]
Position	**^1H (δ in ppm; mult, *J* in Hz)**	**^{13}C (mult)**	**^1H (δ in ppm; mult, *J* in Hz)**	**^{13}C (mult)**	**^1H (δ in ppm)**	**^{13}C**
1	0.97, 1.62	38.9 (CH_2)	0.98, 1.97	40.9 (CH_2)	0.94, 1.94	40.7
2	0.82 (m)	18.0 (CH)	1.44, 1.51	18.9 (CH_2)	1.40, 1.47	18.7
3	1.41, 1.30	35.4 (CH_2)	1.16, 1.42	41.8 (CH_2)	1.14, 1.43	41.6
4	—	37.7 (C)	—	34.5 (C)	—	34.3
5	1.22	48.4 (CH)	1.23 (br d)	47.8 (CH)	1.28	47.6
6	1.57 (m)	21.3 (CH_2)	1.83, 1.61	31.6 (CH_2)	1.65, 1.87	31.4
7	1.67 (m)	30.5 (CH_2)	5.21 (dd, 10.4,5.2)	95.1 (CH)	5.26	94.9
8	1.51	34.9 (CH)	4.47 (d, 8.9)	67.4 (CH)	4.52	67.2
9	1.38 (d, 3.7)	43.9 (CH)	1.23 (d, 4.0)	56.6 (CH)	1.21	56.4
10	—	36.7 (C)	—	39.2 (C)	—	39.0
11	2.23 (d,4.3), 2.08	26.1 (CH_2)	1.74, 1.21 (d, 4.0)	21.4 (CH_2)	1.76, 1.30	21.2
12	6.74 (t, 4.0)	141.0 (CH)	1.78 (m), 2.04 (d, 2.1)	32.0 (CH_2)	2.09, 1.83	31.8
13	—	142.0 (C)	—	135.9 (C)	—	135.8
14	2.70 (q, 6.2)	31.4 (CH)	—	129.9 (C)	—	129.6
15	—	198.0 (C)	2.31 (d, 7.1), 1.64 (d. 5.3)	30.4 (CH_2)	2.37, 1.30	30.2
16	4.44 (d, 17.6), 4.56 (d, 17.6)	64.4 (CH_2)	3.84 (td, 11.4, 3.8), 3.69 (dd, 11.0, 5.7)	56.4 (CH_2)	3.66, 3.82	56.2
17	0.86 (d, 6.2)	15.1 (CH_3)	5.72 (br s)	88.6 (CH)	5.70	88.4
18	3.12, 3.42	72.1 (CH_2)	0.89 (s)	33.2 (CH_3)	0.87	33.0
19	0.80	18.0 (CH_3)	0.87 (s)	22.5 (CH_3)	0.85	22.3
20	0.88	22.5 (CH_3)	0.90 (s)	15.7 (CH_3)	0.88	15.5

[a] *Manríquez-Torres et al. (2013).*

bloodstream trypomastigotes and cultured in standard Hirumi's modified Iscove's medium 9 (HMI9), supplemented with 10% heat-inactivated fetal bovine serum (FBS), 14 μL/L β-mercaptoethanol, and 3.0 g/L sodium hydrogen carbonate (pH 7.4). The parasites were cultured in vented flasks at 37°C in 5% CO_2 atmosphere and were passaged every 3 days (Rodenko et al., 2015). The bloodstream forms of *T. congolense* savannah-type strain IL3000 and *T. congolense* strain 6C3 [diminazene-resistant (Alenezi et al., 2020)] were cultured, as described by Coustou et al. (2010). *Leishmania mexicana* promastigotes (MNYC/BZ/62/M379 strain) were grown in hemoflagellate modified minimal essential medium (HOMEM) (Gibco®, Life technologies, Ghent, Belgium) (pH 7.4) supplemented with 10% heat-inactivated FBS at 27°C.

Human embryonic kidney (HEK) cells were cultured in Dulbecco's modified Eagle's medium (DMEM; Sigma D-5671) supplemented with 10% heat-inactivated FBS, 10 ml/L penicillin/streptomycin (Gibco 15140-122), and 10 ml/L of 200 mM glutamine (Gibco 25030-024). The cells were maintained at 37°C in 5% CO_2 atmosphere.

Test Compounds/Fractions

All compounds and mixtures were dissolved in DMSO at 10 mg/ml, and the stock solutions were stored at −20°C.

In vitro Drug Sensitivity Assay Using Resazurin (alamarBlue) in Bloodstream Forms of *T. b. brucei*, *T. equiperdum*, *T. evansi*, and *T. Congolense*

The susceptibilities of bloodstream formtrypanosomes to the compounds and mixtures were determined using resazurin (alamarBlue)-based assay, as described previously (Nvau et al., 2020). In brief, serial double dilutions of the test compounds were prepared in cell-specific medium in 96-well plates (200 μg/ml top concentration: 23 dilutions over 2 rows, last well drug-free control). This is followed by the addition of 100 μL of parasite suspension in the appropriate medium, to each well of the 96-well plate, adjusted to the desired cell density. For *T. brucei* s427, *T. brucei* B48, and *T. equiperdum*, a seeding density of 2×10^4 cells/well was used, whereas cell densities of 4×10^4 and 5×10^4 were used for *T. evansi* and the *T. congolense* strains (IL3000 and 6C3), respectively. Trypanosome cultures with the test drugs were incubated for 48 h, followed by the addition of 20 μL of filter-sterilized 125 μg/ml resazurin sodium salt in phosphate-buffered saline (PBS). This was followed by a further 24 h of incubation. Standard drugs including diminazene aceturate and suramin were used as positive control as appropriate for the species. Fluorescence was measured in 96-well plates with a FLUOstar Optima (BMG Labtech, Durham, NC, United States) at wavelengths of 544 nm for excitation and 590 nm for emission. EC_{50} values were calculated by nonlinear regression using an equation for a sigmoidal dose–response curve with variable slope (GraphPad 7.0, GraphPad Software Inc., San Diego, CA, United States).

Drug Sensitivity Using alamarBlue in *L. mexicana* Promastigotes

Drug sensitivity assay in *L. mexicana* was carried out using a similar method as described above. However, a seeding density of

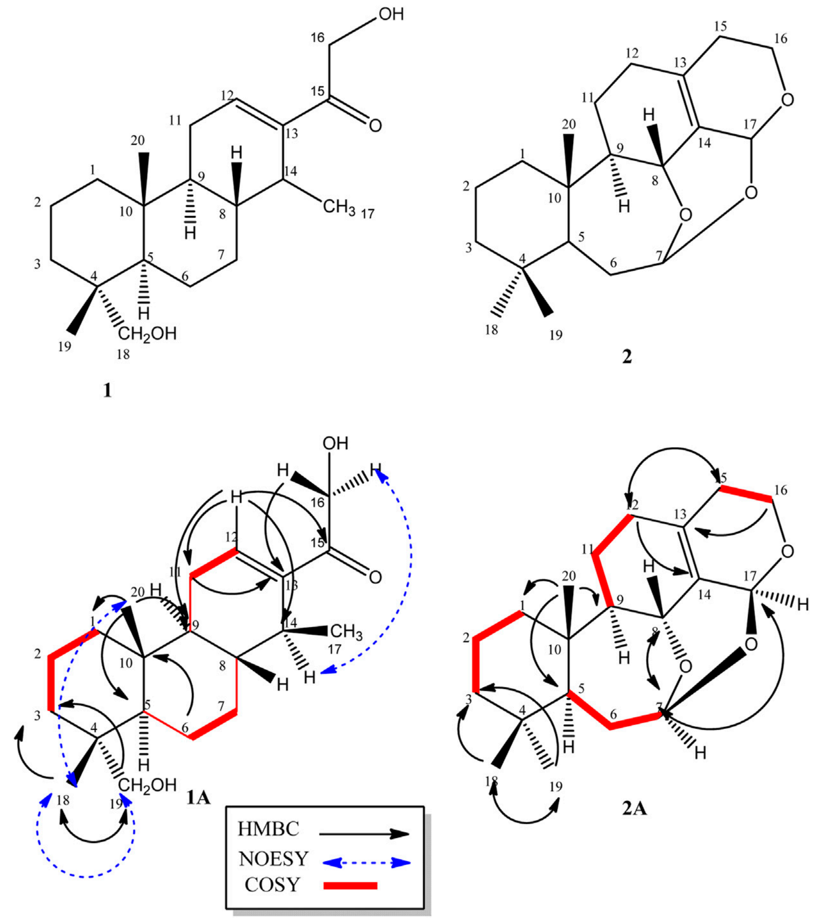

FIGURE 1 | Structure of compounds **1** and 2, including their selected COSY and HMBC correlations (1A and 1B).

2×10^5 cells/well was used for this species. The plate containing the cells and drug dilutions was incubated for a period of 72 h at 27°C, followed by the addition of 20 μL 125 μg/ml resazurin and a further 48 h of incubation. Pentamidine was used as a control drug. Fluorescence was measured as above.

Assessment of Cytotoxicity of Test Compounds on Human Embryonic Kidney (HEK) 293T Cells

HEK cells were harvested at 80–85% confluence using 0.25% Trypsin–EDTA solution (Sigma T-4049). The cells were washed by centrifugation at 1200 rpm for 10 min and reconstituted in fresh medium at 3×10^5 cells/ml. Then, 100 μL of the cell suspension was distributed to each well of a 96-well plate and incubated for 24 h to allow the cells to adhere to the bottom of the wells. Doubling serial dilutions of the test compounds and control drug were prepared in a separate 96-well plate, across 1 row (11 dilutions plus no-drug control). And then, 100 μL of each dilution was transferred to respective wells of the plate containing the cells, and the plate was incubated for another 30 h. This was followed by the addition of 10 μL 125 μg/ml resazurin sodium salt to each well, and a further incubation was done for 24 h. The plates were read and EC_{50} determined as above. The selectivity index (SI) was also calculated for each compound/mixture as the ratio of the EC_{50} in HEK cells to the EC_{50} in a parasite species.

Determination of the Effect of HEAN 19b on *L. mexicana* Growth

L. mexicana cultures were set at 10^6 cells/ml in a 24-well plate with or without varying concentrations of HEAN-19b and pentamidine. Depending on intended duration of exposure, cells were centrifuged at 5 h and 48 h and resuspended in either fresh medium or medium containing the drug. Cells were counted manually using a hemocytometer, and a growth curve was plotted using cell density at each time recorded.

RESULTS AND DISCUSSION

Structure Elucidation

Compound **1**, a white crystalline solid, was obtained as the minor component of combined fractions 76-79. The molecular formula $C_{20}H_{32}O_3$ was derived from its high resolution mass spectrum (Supplementary Material 1), which yielded an $[M\text{-}H]^-$ ion at *m/*

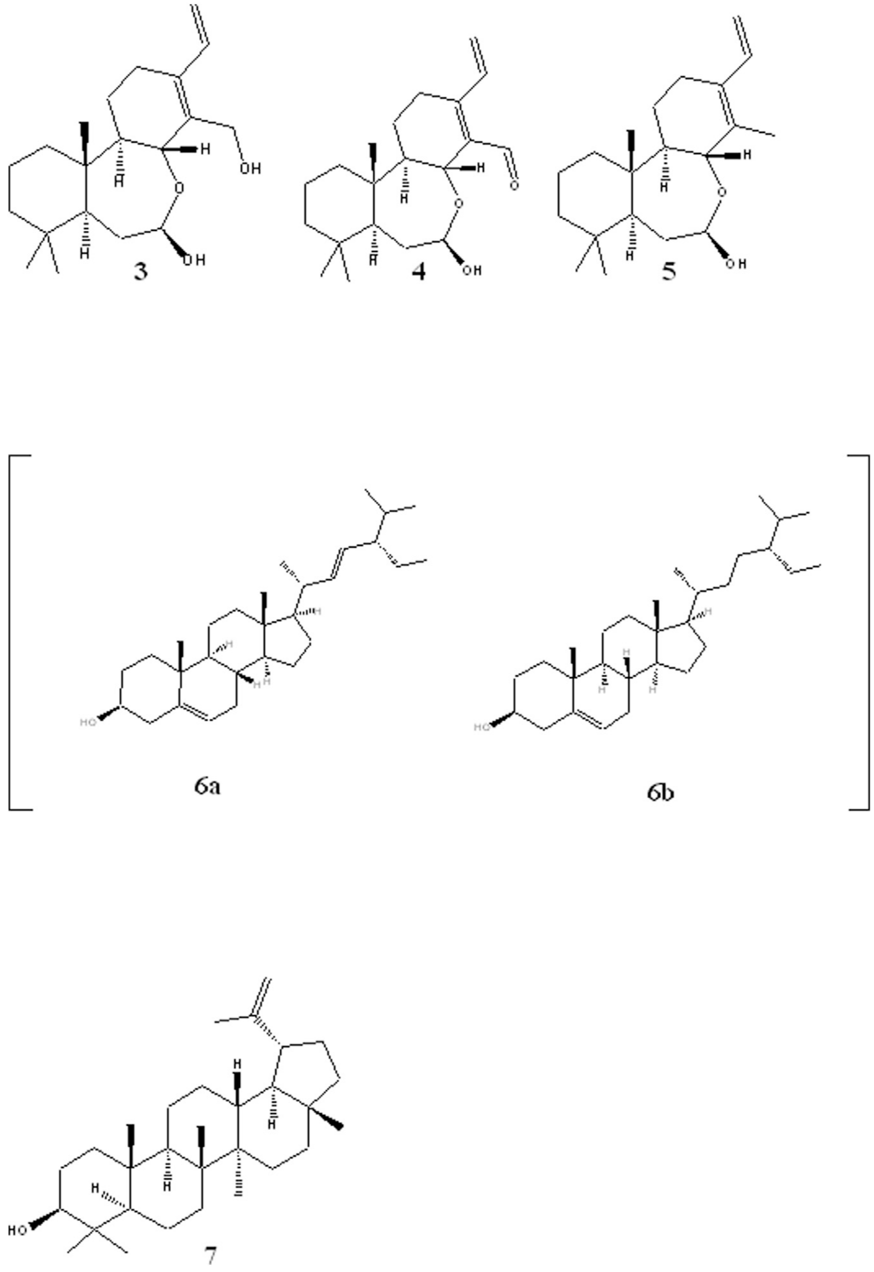

FIGURE 2 | Structures of other isolated compounds: oxacassadienes (**3**, **4** and **5**); stigmasterol **6a** and β-sitosterol **6b** and lupeol **7**.

z = 319.2229 (calculated 319.2273 for $C_{20}H_{31}O_3$). Its proton spectrum (Supplementary Material 2 and **Table 1**) showed an olefinic proton at δ_H 6.74 ppm (1H, t, J = 4.0 Hz, H-12) and two sets of oxymethylene protons at 4.44 (1H, d, J = 17.6 Hz, H-16), 4.56 (1H, d, J = 17.6 Hz, H-16), 3.12 (1H, d, J = 10.8 Hz, H-19), and 3.42 (1H, d, J = 10.8 Hz, H-19). It also displayed signals for three methyl protons made up of a methyl doublet at 0.86 (3H, d, J = 6.2 Hz, H-17) and two singlets at 0.80 (3H, s, H-18) and 0.88 (3H, s, H-20). The rest of the signals were for three methine (including a quartet at 2.70 (1H, q, J = 6.2 Hz, H-14) and six pairs of methylene protons. Its ^{13}C spectrum (Supplementary Material 3) gave signals for 20 carbon atoms including one ketone carbonyl at δ_C 198.0 and two hydroxyl bearing carbons at 72.1 and 64.4 ppm. There were also two olefinic carbons, one proton bearing at 141.0 and the other a quaternary at 142.0. The rest of the signals were for three methyls, six methylenes, four methines, and two quaternary carbons. Using correlations in its 2D NMR spectra (Supplementary Material 4–6), the structure (**Figure 1**) was deduced as follows: correlations from the olefinic proton at 6.74 ppm to the carbonyl carbon at 198.0 (C-15) indicated it was

TABLE 2 | EC_{50} of two mixtures and compound **4** against *Trypanosoma* and *Leishmania* species (n = 3).

Compound/mixture	*T. brucei* s427	*T. congolense* IL3000 WT	*T. equiperdum*	*T. evansi*	*L. mexicana*
PAN-76 compounds 1 and 3 (µg/ml)	10.1 ± 1.0	44.1 ± 3.2	7.2 ± 0.6	4.3 ± 0.1	34.1 ± 11.2
HEAN-18 compounds 2 and 5 (µg/ml)	25.9 ± 2.6	194.8 ± 98.9	17.2 ± 2.6	ND	51.9 ± 3.8
HEAN 1 crude extract containing compound 4 (µg/ml)	5.7 ± 0.1	35.8 ± 4.3	7.3 ± 1.7	5.4 ± 0.1	10.1 ± 0.6
HEAN 19b compound 4 (µg/ml)	0.45 ± 0.02 (1.41 µM)	3.72 ± 0.54 (11.7 µM)	1.39 ± 0.27 (4.36 µM)	0.33 ± 0.05 (1.04 µM)	0.28 ± 0.05 (0.88 µM)
Diminazene (µM)	0.0878 ± 0.0355	0.228 ± 0.0446	0.0382 ± 0.0050	0.0438 ± 0.0005	ND
Suramin (µM)	0.0189 ± 0.0004	8.74 ± 1.634	0.021 ± 0.006	ND	ND
Pentamidine (µM)	ND	ND	ND	ND	0.786 ± 0.022

ND, not done.

TABLE 3 | Cross-resistance of two mixtures and compound 4 with existing drugs.

Compound/mixture	*T. brucei* B48		*T. congolense* 6C3	
	RF	*p* value	RF	*p* value
PAN-76 compounds 1 and 3	1.05	0.83	0.94	0.63
HEAN -18 compounds 2 and 5	1.2	0.10	1.23	0.77
HEAN 1 crude extract	1.05	0.83	0.94	0.76
HEAN 19b compound 4	1.38	0.27	1.12	0.69
Diminazene	5.70	0.19	6.96	0.014
Suramin	0.62	0.50	0.87	0.74

RF, resistance factor, being the ratio of the EC50 values of the resistant and control strains. p *value was obtained using unpaired Student's test between the EC50 values of the resistant line and control, obtained in parallel* (n *= 3).*

three bonds away from it. Other correlations from the olefinic proton are to C-9 and C-14 and to this was attached the proton quartet; hence, the methyl doublet C-17 must be attached at C-14. This was confirmed by correlations from H-14 to C-12, C-15, and C-17. Others were ^{2}J long-range correlations from H-16 to C-15 and H-18 to C-19, thus confirming by HMBC and HSQC, H-16, C-16 and H-19, C-19 to be -CH_2OH (hydroxymethylene groups). The absence of germinal methyl groups usually at C-4, further confirmed C-19 to be a hydroxymethylene carbon and C-18 a methyl carbon. Therefore, correlations from H-19 and H-18 were used to identify C-3, C-4, and C-5 and from H-5 to identify C-1, C-7, C-10, and C-20 and confirm C-9. The compound was identified as 16, 19-dihydroxycassa-12-en-15-one and given the trivial name Sandynone **1**, and its chemical shifts compared very well with similar compounds (Mendoza et al., 2003). The relative stereochemistry was determined using its NOESY (Supplementary Material 7) and is shown in **Figure 1**.

Compound **2** was also isolated as a white crystalline solid. The molecular formula was established based on its $[M]^+$ ion in its HR-EIMS spectrum (Supplementary Material 12) at m/z = 318.2195 (calculated 318.2195 for $C_{20}H_{30}O_3$). The ^{1}H NMR spectrum (Supplementary Material 13 and **Table 1**) showed two acetal protons at δ_H 5.70 (br s, H-17) and 5.26 (dd, J = 10.4, 5.2 Hz, H-7), a methine geminal to oxygen at δH 4.52 (br d, J = 8.0 Hz, H-8), and two methylene protons H-16 geminal to oxygen at δ_H 3.77 (dt, J = 11.4, 3.9 H-16 β) and 3.61 (ddd, J = 11.4, 6.6, 1.2, H-16α) coupled with the H-15 methylene protons at δ_H 2.31 and 1.64 ppm. There were three methyl groups observed at δ_H 0.83 (Me-20), 0.80 (Me-19), and 0.83 (Me-18). In the ^{13}C DEPT-135 spectrum (Supplementary Material 14), 20 signals were observed including two quaternary olefinic carbons at δ_C 135.9 (C-13) and 129.9 (C-14), two acetal carbons at δ_C 95.1 (C-7) and 88.6 (C-17), one oxymethylene carbon at 56.4 (C-16), and an oxymethine carbon at 67.4 (C-8). The rest of the signals were for two methine (C-5, C-9), seven methylene, three methyl, and two quaternary carbons. The structure was confirmed using its 2D NMR spectra (Supplementary Material 15–16) as follows: long-range correlations from the acetal proton H-7 identified carbon C-5, C-8, and C-17, while from the second acetal proton H-17, carbons C-7, C-8, C-13, C-14, and C-16. Similarly, long-range correlations from H-18 and H-19 indicated they were germinal and identified C-3, C-4, and C-5, and H-20 also confirmed C-5 as well identifying C-1, C-9, and C-10. The HSQC spectrum confirmed the proton bearing carbons in the compound and their attached protons, while the COSY spectrum confirmed neighbouring protons.

Compared to the macrocyclic dimer isolated from *Acacia schaffneri* (Manríquez-Torres, et al., 2013), their chemical shifts were identical (**Table 1**); however, the exact mass obtained was for a monomer with the acetal link between C-7 and C-17. There was no mass higher than the molecular ion in its HR-EIMS spectrum and no mass fragment which could suggest the compound being dimeric. Hence the presence of a dimer or the compound existing as a dimeric molecule could not be confirmed, and the compound was therefore identified as the seco-oxacassane, (5S, 7R, 8R, 9R, 10S, 13Z, 17S)-7,8:7,17:16,17-triepoxy-7,8-seco-cassa-13-ene (niloticane B, **2**) and confirmed by literature reports (Manríquez-Torres, et al., 2013).

The rest of the compounds (**Figure 2**) were identified based on their NMR spectra and comparison with literature reports. Compound **3** was identified as (5S,7R,8R,9R,10S) -(-)-7,8-*seco*-7, 8-oxacassa-13,15-diene-7,17-diol, compound **4** as 5S,7R,8R,9R,10S) -(-)-7,8-*seco*-7, 8-oxacassa-13,15-dien-7-ol-17-al and compound **5** as (5S,7R,8R,9R,10S) -(-)-7,8-seco-7, 8-oxacassa-13,15-dien-7-ol (Manríquez-Torres et al., 2011). While compounds **6a** and **6b** were identified as a mixture of sitosterol and stigmasterol and compound **7** as lupeol.

Antiprotozoal and Cytotoxic Activity of Fractions and Isolated Compounds

Two compound mixtures and a pure compound were tested for activity against bloodstream forms of four species of

TABLE 4 | Toxicity of mixtures and compound 4 to HEK cells.

Compound/mixture	**EC_{50} for HEK cells (n = 4)**	**Selectivity index (SI)**				
		SI *T. brucei* s427	**SI *T. congolense* IL3000**	**SI *T. equiperdum***	**SI *T. evansi***	**SI *L. mexicana***
PAN-76 compound 1 and 3 (µg/ml)	56.8 ± 2.7	5.65	1.29	7.92	13.3	1.67
HEAN-1 crude (µg/ml)	75.5 ± 6.6	13.6	2.11	10.4	13.9	7.45
HEAN -19b compound 4 (µg/ml)	9.39 ± 1.37 (29.5 µM)	21.1	2.53	6.75	28.1	33.8
PAO (µM)	2.8 ± 0.08	—	—	—	—	—

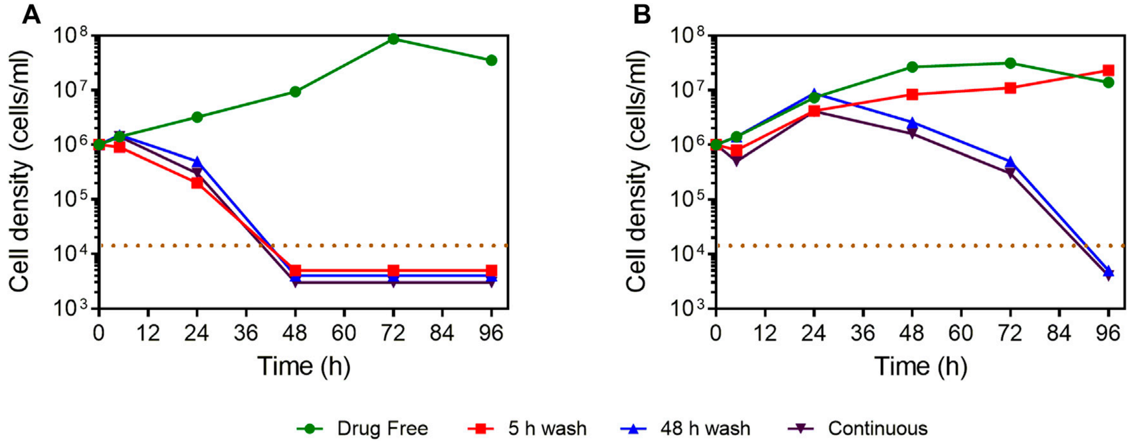

FIGURE 3 | Manual cell count of *L. mexicana* cultures grown in the presence or absence of compound **4** and pentamidine at 5 × EC_{50}, with or without wash after 5 or 48 h of incubation. **(A)** Compound **4**. **(B)** Pentamidine. The dotted brown line indicates the detection limit, being 10^4 cells/ml. For convenience, where no cells were observed in the counting chamber, the values of 5,000, 4,000, or 3,000 cells/ml were entered to facilitate a graphical representation.

Trypanosoma and *L. mexicana* promastigotes using resazurin-based drug sensitivity assay. This assay is cheap and allows for efficient and reproducible screening of compounds for activity against cultured cells and is therefore commonly employed in parasitology (Räz et al., 1997; Gould et al., 2008). In addition, the compound and mixtures were investigated for toxicity in HEK cells and for cross-resistance to the commonly used melaminophenyl arsenical and diamidine classes of trypanocides (Bridges et al., 2007; Giordani et al., 2019). PAN-76, a mixture of compounds **1** (80%) and **3** (20%), showed promising antitrypanosomal activity with lowest EC_{50} of 4.27 ± 0.06 µg/ml against *T. evansi* (**Table 2**). Another mixture, HEAN-18, containing compounds **2** (70%) and **5** (30%), had only modest to poor activity against all the *Trypanosoma* and *Leishmania* species assayed. However, crude extract HEAN-1 displayed good activity against all the kinetoplastid species, except *T. congolense* ($EC_{50} \leq 10$ µg/ml), and was thus selected for further purification, yielding compound **4**. This compound showed very potent antiprotozoal activity with EC_{50} as low as 0.45 ± 0.02 µg/ml, 0.33 ± 0.05 µg/ml, and 0.28 ± 0.05 µg/ml against *T. b. brucei*, T. *evansi*, and *L. mexicana*, respectively.

However, all of the mixtures and, to a lesser extent, compound **4**, exhibited only moderate to low activity against *T. congolense* IL3000, suggesting poor prospects for development as agents in the treatment of AAT, where the infecting species is usually not known, although applications outside the African tsetse belt (*T. evansi* and *T. equiperdum*) look more promising. It is a very common occurrence for drugs and test compounds to vary in activity between *T. congolense* and the species in the *T. brucei* group of species, making drug development for AAT even more challenging as drug candidates need to be active against three different species, that is, *T. b. brucei*, *T. congolense*, and *T. vivax*. In addition, while PAN-76 and HEAN-18, containing various amounts of compounds **1**, **2**, **3**, and **5**, demonstrated at best modest antileishmanial activity, whereas the purified compound **4** displayed an EC_{50} of 0.28 ± 0.05 µg/ml (**Table 2**).

Due to the enormous challenge drug resistance poses to the control of trypanosomiasis and leishmaniasis (De Koning, 2017), it is important that test compounds are tested for the prospect of cross-resistance to existing drugs. Neither of the three mixtures nor compound **4** was cross-resistant to diminazene and pentamidine as there were no significant differences ($p > 0.05$) between EC_{50} in the *T. brucei* WT and multidrug-resistant B48 strain, and between the *T. congolense* WT and the diminazene-resistant 6C3 strain (**Table 3**). This also means that for the *brucei* group species, there is no cross-resistance with melaminophenyl arsenical compounds such as melarsoprol and cymelarsan, which, like pentamidine, rely on the P2 and HAPT1 transporters for their trypanocidal activities (Bridges et al., 2007; Munday et al., 2015). In all cases for the mixtures and compound 4, the resistance factor (RF), which is the ratio of the EC_{50} in a drug-resistant strain over the EC_{50} of the WT control, was ≤1.4.

The PAN-76 and HEAN-1 mixtures and compound **4** were tested against HEK cells to determine whether their toxicity is selective to the parasites, or general. While the mixtures showed highest selectivity to *T. evansi* (**Table 4**), compound 4 is selective to *T. brucei, T. evansi*, and *L. mexicana* (SI = 21.2 – 33.8). Although compound **4** in purified form is more toxic to HEK cells than the crude fraction from which it was isolated, it remains low at ~30 μM. Thus, compound **4** shows some promise as an antiprotozoal compound, especially against *Leishmania* spp. and will need to be further investigated.

The selective antiparasitic activity of compound **4** prompted the investigation of its effect on growth of *L. mexicana* promastigotes *in vitro*. At a concentration of 5 × EC_{50}, the compound irreversibly inhibited the growth of *L. mexicana* even after a short exposure of 5 h (**Figure 3**). In addition, the compound showed faster onset of action and killing than the control drug, pentamidine.

CONCLUDING REMARKS

Due to the unprofitable market for kinetoplastid agents, new developments are unlikely to emerge through the regular discovery process of the pharmaceutical industry, especially for veterinary applications. Alternative local solutions are potentially available in the form of medicinal plants, a practice that is ongoing but requires scientific validation in order to delineate which extracts or isolated compounds from which plants work reliably against which pathogens. Here, we find that crude extracts of *Acacia nilotica* yielded two new diterpenes that had limited anti-kinetoplastid activity and one oxacassadiene, compound **4**, isolated from a fraction of the extract which displayed promising activity against several *Trypanosoma* species and *Leishmania mexicana*. Production of this compound from the widely available plant should now be scaled up for tests with further *Leishmania* species, intracellular amastigotes, and *in vivo* studies with relevant disease models.

DATA AVAILABILITY STATEMENT

The datasets presented in this study can be found in online repositories. The names of the repository/repositories and accession number(s) can be found below: Figshare DOI: 10.6084/m9.figshare.13547816.

AUTHOR CONTRIBUTIONS

All authors listed have made a substantial, direct, and intellectual contribution to the work and approved it for publication.

FUNDING

MAU was in receipt of a Ph.D. studentship from the Petroleum Technology Development Fund of Nigeria (Grant number: 18/UK/PHD/042).

SUPPLEMENTARY MATERIAL

The Supplementary Material for this article can be found online at: https://www.frontiersin.org/articles/10.3389/fchem.2021.624741/full#supplementary-material.

REFERENCES

Alenezi, S. S., Natto, M. J., Igoli, J. O., Gray, A. I., Fearnley, J., Fearnley, H., et al. (2020). Novel flavanones with anti-trypanosomal activity isolated from Zambian and *Tanzanian propolis* samples. *Int. J. Parasitol. Drugs Drug Resist.* 14, 201–207. doi:10.1016/j.ijpddr.2020.10.011

Ali, A., Akhtar, N., Khan, B. A., Khan, M. S., Rasul, A., Zaman, S. U., et al. (2012). *Acacia nilotica*: a plant of multi-purpose medicinal uses. *J. Med. Plants Res.* 6, 1492–1496. doi:10.5897/JMPR11.1275

Alvar, J., Velez, I. D., Bern, C., Herrero, M., Desjeux, P., Cano, J., et al. (2012). Leishmaniasis worldwide and global estimates of its incidence. *PLoS One* 7 (5), e35671. doi:10.1371/journal.pone.0035671

Anene, B. M., Onah, D. N., and Nawa, Y. (2001). Drug resistance in pathogenic African trypanosomes: what hopes for the future? *Vet. Parasitol.* 96, 83–100. doi:10.1016/s0304-4017(00)00427-1

Boulos, L. (1983). *Medicinal plants of North Africa*. Algonac, MI, United States: Reference Publications, Inc

Boulos, L. (2000). *Flora of Egypt*. Cairo: Al Hadara publishing, Vol. 2, 229–242.

Bridges, D. J., Gould, M. K., Nerima, B., Mäser, P., Burchmore, R. J. S., and de Koning, H. P. (2007). Loss of the high-affinity pentamidine transporter is responsible for high levels of cross-resistance between arsenical and diamidine drugs in African trypanosomes. *Mol. Pharmacol.* 71, 1098–1108. doi:10.1124/mol.106.031351

Brun, R., Hecker, H., and Lun, Z.-R. (1998). *Trypanosoma evansi* and *T. equiperdum*: distribution, biology, treatment and phylogenetic relationship (a review). *Vet. Parasitol.* 79, 95–107. doi:10.1016/s0304-4017(98)00146-0

Butler, D. (2007). Lost in translation. *Nature* 449 (7159), 158–159. doi:10.1038/449158a

Chowdhury, A. R., Banerji, R., Misra, G., and Nigam, S. K. (1983). Chemical composition of Acacia seeds. Carbon Cycling in Northern Peatlands. *J. Am. Oil Chem.' Soc.* 60, 1893–1894.

Coustou, V., Guegan, F., Plazolles, N., and Baltz, T. (2010). Complete *in vitro* life cycle of *Trypanosoma congolense*: development of genetic tools. *PLoS Negl. Trop. Dis.* 4, e618. doi:10.1371/journal.pntd.0000618

De Koning, H. P., MacLeod, A., Barrett, M. P., Cover, B., and Jarvis, S. M. (2000). Further evidence for a link between melarsoprol resistance and P2 transporter function in African trypanosomes. *Mol. Biochem. Parasitol.* 106, 181–185. doi:10.1016/s0166-6851(99)00206-6

De Koning, H. P. (2017). Drug resistance in protozoan parasites. *Emerg. Top. Life Sci.* 1, 627–632. doi:10.1042/etls20170113

De Koning, H. P. (2020). The drugs of sleeping sickness: their mechanisms of action and resistance, and a brief history. *Trop. Med. Infect. Dis.* 5 (1), 14. doi:10.3390/tropicalmed5010014

Desquesnes, M., Dargantes, A., Lai, D. H., Lun, Z. R., Holzmuller, P., and Jittapalapong, S. (2013). *Trypanosoma evansi* and surra: a review and perspectives on transmission, epidemiology and control, impact, and zoonotic aspects. *Biomed. Res. Int.* 2013, 321237. doi:10.1155/2013/321237

Eldeen, I. M. S., Van Heerden, F. R., and Van Staden, J. (2010). *In vitro* biological activities of niloticane, a new bioactive cassane diterpene from the bark of *Acacia nilotica* subsp. *kraussiana*. *J. Ethnopharmacol.* 128, 555–560. doi:10.1016/j.jep.2010.01.057

Geerts, S., Holmes, P. H., Eisler, M. C., and Diall, O. (2001). African bovine trypanosomiasis: the problem of drug resistance. *Trends in parasitol.* 17(1), 25–28. doi:10.1016/S1471-4922(00)01827-4

Giordani, F., Khalaf, A. I., Gillingwater, K., Munday, J. C., de Koning, H. P., Suckling, C. J., et al. (2019). Novel minor groove binders cure animal African Trypanosomiasis in an *in vivo* mouse model. *J. Med. Chem.* 62 (6), 3021–3035. doi:10.1021/acs.jmedchem.8b01847

Gould, M. K., Vu, X. L., Seebeck, T., and De Koning, H. P. (2008). Propidium iodide-based methods for monitoring drug action in the kinetoplastidae: comparison with the Alamar blue assay. *Anal. Biochem.* 382, 87–93. doi:10.1016/j.ab.2008.07.036

Manríquez-Torres, J. J., Torres-Valencia, J. M., Gomez-Hurtado, M. A., Motilva, V., Garcia-Mauri~no, S., Avila, J., et al. (2011). Absolute configuration of 7,8-seco-7,8-Oxacassane diterpenoids from *Acacia schaffneri*. *J. Nat. Prod.* 74, 1946–1951. doi:10.1021/np200445y

Manríquez-Torres, J. J., Torres-Valencia, J. M., Velázquez-Jiménez, R., Valdez-Calderón, A., Alvarado-Rodríguez, J. G., Cerda-García-Rojas, C. M., et al. (2013). A macrocyclic dimeric diterpene with a C2 symmetry axis. *Org. Lett.* 15 (18), 4658–4661. doi:10.1021/ol401890v

Matovu, E., Stewart, M. L., Geiser, F., Brun, R., Mäser, P., Wallace, L. J. M., et al. (2003). Mechanisms of arsenical and diamidine uptake and resistance in *Trypanosoma brucei*. *Eukaryot. Cell* 2, 1003–1008. doi:10.1128/ec.2.5.1003-1008.2003

Mattioli, R. C., Feldmann, G., Hendricks, G., Wint, W., Jannin, J., and Slingenbergh, J. (2004). Tsetse and trpanosomiasis intervention policies supporting sustainable animal agricultural development. *Food Agric. Environ.* 2 (2), 310–314.

Mendoza, D. T., Ureña González, L. D., Ortega-Barría, E., Capson, T. L., and Rios, L. C. (2003). Five new cassane diterpenes from *Myrospermum frutescens* with activity against Trypanosomacruzi. *J. Nat. Prod.* 66, 928–932. doi:10.1021/np030010o

Munday, J. C., Settimo, L., and De Koning, H. P. (2015). Transport proteins determine drug sensitivity and resistance in a protozoan parasite, *Trypanosoma brucei*. *Front. Pharmacol.* 6, 32. doi:10.3389/fphar.2015.00032

Nvau, J. B., Alenezi, S., Ungogo, M. A., Alfayez, I. A. M., Natto, M. J., Gray, A. I., et al. (2020). Antiparasitic and cytotoxic activity of bokkosin, A novel diterpene-substituted Chromanyl Benzoquinone from *Calliandra portoricensis*. *Front. Chem.* 8, 574103. doi:10.3389/fchem.2020.574103

Patz, J. A., Graczyk, T. K., Geller, N., and Vittor, A. Y. (2000). Effects of environmental change on emerging parasitic diseases. *Int. J. Parasitol.* 30 (12–13), 1395–1405. doi:10.1016/s0020-7519(00)00141-7

Räz, B., Iten, M., Grether-Bühler, Y., Kaminsky, R., and Brun, R. (1997). The Alamar blue assay to determine drug sensitivity of African trypanosomes (*T. b. rhodesiense* and *T. b. gambiense*) *in vitro*. *Acta Trop.* 68 (2), 139–147. doi:10.1016/s0001-706x(97)00079-x

Rodenko, B., Wanner, M. J., Alkhaldi, A. A. M., Ebiloma, G. U., Barnes, R. L., Kaiser, M., et al. (2015). Targeting the parasite's DNA with methyltriazenyl purine analogs is a safe, selective, and efficacious antitrypanosomal strategy. *Antimicrob. Agents Chemother.* 59, 6708–6716. doi:10.1128/aac.00596-15

Roozbeh, N., and Darvish, L. (2016). *Acacia nilotica*: new plant for help in pelvic organ prolapse. *J. Menopausal Med.* 22 (3), 129–130. doi:10.6118/jmm.2016.22.3.129

Saleem, N. (2011). An ethno-pharmacological study of Egyptian Bedouin women's knowledge of medicinal plants. PhD thesis. Glasgow (United Kingdom): University of Strathclyde Glasgow.

Singh, R., Singh, B., Singh, S., Kumar, N., Kumar, S., and Arora, S. (2010). Umbelliferone–An antioxidant isolated from Acacia nilotica (L.) Willd. ex. Del. *Food Chem.* 120, 825–830. doi:10.1016/j.foodchem.2009.11.022

Sheik, M. I. (1989). *Acacia nilotica (L.) Willd. ex Del. Its production, Management and Utilization. Pakistan. Regional wood energy development programme in Asia* (No. 20). GCP/RAS/111/NET Field document.

Ungogo, M. A., Ebiloma, G. U., Ichoron, N., Igoli, J. O., de Koning, H. P., and Balogun, E. O. (2020). A review of the antimalarial, antitrypanosomal, and antileishmanial activities of natural compounds isolated from Nigerian flora. *Front. Chem.* 8, 617448. doi:10.3389/fchem.2020.617448

Van Wyk, B-E., Van Oudtshoom, B., and Gericke, N. (1997). *Medicinal plants of southern Africa*. Pretoria, South Africa: Briza Publications.

Vieira de Morais, C. G., Castro Lima, A. K., Terra, R., Freire dos Santos, R., Da-Silva, S. A. G., and Dutra, P. M. L. (2015). The dialogue of the host-parasite relationship: *Leishmanis spps* and *Trypanosoma cruzi* infections. *BioMed Res. Int.* 2015, 324915. doi:10.1155/2015/324915

World Health Organization (2010). Control of the leishmaniases. *World Health Organ. Tech. Rep. Ser.* xii–xiii, 1-186.

WHO (2019a). Leishmaniasis. Available at: who.int/leishmaniasis/disease/clinical_forms_leishmaniases/en/ (Accessed February 17, 2020).

WHO (2019b). Trypanosomiasis, human African (sleeping sickness). Available at: https://www.who.int/news-room/fact-sheets/detail/trypanosomiasis-human-african-%28sleeping-sickness%29 (Accessed February 17, 2020).

Conflict of Interest: The authors declare that the research was conducted in the absence of any commercial or financial relationships that could be construed as a potential conflict of interest.

frontiers in Chemistry

ORIGINAL RESEARCH
published: 07 May 2021
doi: 10.3389/fchem.2021.621057

Electrochemical Impedance Spectroscopy Microsensor Based on Molecularly Imprinted Chitosan Film Grafted on a 4-Aminophenylacetic Acid (CMA) Modified Gold Electrode, for the Sensitive Detection of Glyphosate

Fares Zouaoui[1,2], Saliha Bourouina-Bacha[2], Mustapha Bourouina[2,3]*, Albert Alcacer[4], Joan Bausells[4], Nicole Jaffrezic-Renault[1]*, Nadia Zine[1] and Abdelhamid Errachid[1]

[1] Institut des Sciences Analytiques, Université de Lyon, Villeurbanne, France, [2] Département de Génie des Procédés, Faculté de Technologie, Université de Bejaia, Bejaia, Algeria, [3] Departement de Chimie, Faculté des Sciences Exactes, Université de Bejaia, Bejaia, Algeria, [4] Institute of Microelectronics of Barcelona IMB-CNM-CSIC, Autonomous University of Barcelona, Barcelona, Spain

Edited by:
Aziz Amine,
University of Hassan II
Casablanca, Morocco

Reviewed by:
Hui Xu,
Ludong University, China
Abdellatif Ait Lahcen,
King Abdullah University of Science and Technology, Saudi Arabia

***Correspondence:**
Nicole Jaffrezic-Renault
nicole.jaffrezic@univ-lyon1.fr
Mustapha Bourouina
bouryas@yahoo.fr

Specialty section:
This article was submitted to Analytical Chemistry, a section of the journal Frontiers in Chemistry

Received: 24 October 2020
Accepted: 06 April 2021
Published: 07 May 2021

Citation:
Zouaoui F, Bourouina-Bacha S, Bourouina M, Alcacer A, Bausells J, Jaffrezic-Renault N, Zine N and Errachid A (2021) Electrochemical Impedance Spectroscopy Microsensor Based on Molecularly Imprinted Chitosan Film Grafted on a 4-Aminophenylacetic Acid (CMA) Modified Gold Electrode, for the Sensitive Detection of Glyphosate. Front. Chem. 9:621057. doi: 10.3389/fchem.2021.621057

A novel electrochemical impedance spectroscopy (EIS) microsensor was implemented for the dosage of traces of glyphosate, in real and synthetic water samples. Molecularly imprinted chitosan was covalently immobilized on the surface of the microelectrode previously modified with 4-aminophenylacetic acid (CMA). The characterization of the resulting microelectrodes was carried out by using cyclic voltammetry measurement (CV), scanning electron microscopy (SEM), and electrochemical impedance spectrometry (EIS). EIS responses of the CS-MIPs/CMA/Au microsensor toward GLY was well-proportional to the concentration in the range from 0.31×10^{-9} to 50×10^{-6} mg/mL indicating a good correlation. The detection limit of GLY was 1 fg/mL (S/N = 3). Moreover, this microsensor showed good reproducibility and repeatability, high selectivity, and can be used for the detection of GLY in river water.

Keywords: microsensor, CMA, MIP, chitosan, Gly, EIS

INTRODUCTION

Glyphosate is an herbicide used to destroy what are commonly known as weeds. From the 1970s, the production and use of glyphosate increased steadily around the world. So far, despite the risks involved, this herbicide continues to be widely used (Cuhra et al., 2013). Glyphosate works by interrupting the synthesis of aromatic amino acids essential for the functioning of plants (Lopes et al., 2018). Recently, there has been growing concern about the impact of glyphosate on living things and the environment (Johansson et al., 2018; Seide et al., 2018). Among the many effects of this herbicide are toxicity, changes in the activity of antioxidant enzymes, endocrine disruption, damage to lipids, histological damage, etc. (Lopes et al., 2018; Ren et al., 2018; Lorenz et al., 2019). Glyphosate can be found as a contaminant in soil, plants and food products. GLY has a high solubility in water and its intensive use leads to contamination of surface and ground water (Ruiz de Arcaute et al., 2018). A certain number of approaches have been adopted for the detection of glyphosate in various media such as chromatography, photometry, mass spectrometry, etc. (Clegg et al., 1999). However, these techniques are long, difficult to implement, expensive, and often require qualified personnel. Moreover, their application is limited to the laboratory scale.

The challenge for analytical chemistry is to develop alternative analytical methods with an emphasis on simplicity, efficiency and cost. Molecularly imprinted polymers (MIPs) seem to be a very good alternative for designing analysis tools because of its many properties such as selectivity, robustness, physical and chemical resistance, inertia and ease of synthesis and Low cost (Haupt and Mosbach, 2000, Qiao et al., 2006). MIPs can selectively recognize a molecule or even a family of analogous molecules. Molecular printing consists of creating cavities, which are complementary from the structural and functional point of view of the target molecules within a functional polymer. The synthesis of MIPs is the interaction of the functional monomer with template molecules through covalent, semi-covalent, and non-covalent interactions (Yan and Row, 2006); which leads to the formation of the pre-polymerization complex. After the addition of a crosslinking monomer, a polymer network is formed around the functional monomer/template complex by copolymerization between the functional monomers and the crosslinking monomer, thus allowing the formation of a more resistant and more stable matrix (Wulff et al., 1983). As a last step, cavities complementary to the target molecules with regard to their size and the presence of specific functional groups are obtained after the extraction of the template from the polymer. The porous matrices obtained can be used to specifically recomplex the target molecules present in various media. The selectivity of MIPs is conditioned by the functional monomer involved in the synthesis of molecular printing. The monomer is chosen according to its physicochemical properties and its ability to interact with the template (Pichon and Haupt, 2006).

The many properties of chitosan (CS) allow it to be a very good choice for use in the synthesis of MIPs. It is in particular biocompatible, biodegradable, non-toxic and has good antimicrobial and antioxidant activities (Younes and Rinaudo, 2015). In addition, this material has various physical and chemical characteristics. It is considered to be the second most abundant natural biopolymer after cellulose. Chitosan is a natural cationic polysaccharide (in dilute acid medium) extracted from chitin having as reactive functional groups a primary and secondary hydroxyl group and a primary amino group (Pa and Yu, 2001).

The strong functionality of chitosan through its hydroxyl and primary amine functions gives it a considerable opportunity of chemical modification (Aranaz et al., 2010). These modifications were intended in order to enhance the characteristics and internal morphology of the CS or to give it new properties (Wang et al., 2016). Many studies have looked at the modification of chitosan (Martins et al., 2004; Pereira et al., 2013). Chitosan is biofunctionalized according to a very common technique resulting in the formation of a bond of the primary amine of chitosan with a carboxylic acid (Chung et al., 2002). Nucleophilic reactions on electrophilic carbons such as aldehydes, ketones and carboxylic acids are thus made possible by the non-binding nucleophilic doublet possessed by the primary amine. The use of chitosan in the MIP matrix is increasingly widespread and the number of published works reporting the extent of research in this area is constantly expanding (Karrat et al., 2020; Zouaoui et al., 2020a). Chitosan combined with the MIP technique have been reported for the preparation of the electrochemical sensors for different target molecules including pharmaceutical compounds (Lin et al., 2015; Song et al., 2019), protein (Fatoni et al., 2014; Xia et al., 2016), sweet (Li et al., 2014), phenolic compounds (Deng et al., 2013; Li et al., 2013; Chakroun Galai et al., 2020; Salvo-Comino et al., 2020), organic compounds (Chen et al., 2011), ions (Wu et al., 2020), and pesticides (Zouaoui et al., 2020a).

Several sensors are being developed by electrodeposition of molecularly imprinted chitosan. The application of a negative potential during the electrodeposition of chitosan causes release of hydrogen gas. H_2 remains trapped in the membrane of the CS which makes it inhomogeneous and affects its sensitivity. The covalent grafting of chitosan allows eliminating these effects and achieving a more stable response (Zouaoui et al., 2020a).

In this work, covalent modifications of the surfaces of gold microelectrodes were explored by the use of a 4-aminophenylacetic acid, more commonly called CMA, to ensure the covalent immobilization of molecularly imprinted chitosan in order to develop microsensors, distinguished to detect traces of glyphosate in water.

The process used to deposit CMA resides in the formation of a diazonium salt cation which makes it possible to form a covalent bond between the acid and the gold surface. The diazonium cation is an unstable species, easily hydrolyzable at room temperature and very reactive (Chira et al., 2017).

The diazonium ion can be prepared by a standard diazotisation procedure, by treatment of aromatic amines with nitrites NO_2^- in the presence of hydrochloric acid (HCl). After this treatment, the $-NH_2$ group of the aniline derivative was converted to a $-N_2^+$ group leads to the formation of an aryl diazonium. The electrochemical reduction of the diazonium cation on a metal cathode by an electron transfer from the surface of the electrode to the diazonium salt generates an intermediate aryl radical after the release of N_2. The aryl radical attaches to the conductive surface by formation of a covalent bond between the carbon of the aromatic cycle and the metallic element (Corgier et al., 2005).

The carboxylic function of the acid is then available as an accessible surface of the electrode for grafting chitosan. CS is functionalized by the CMA via the formation of an amide bond. The pair 1-ethyl-3- (3-dimethylaminopropyl) carbodiimide and N-hydroxysuccinimide (EDC/NHS) makes possible the preceding amide bond, thanks to its carboxylic acid function. It consists of the formation of an ester intermediate between NHS and the carboxylic function. The intermediate thus formed reacts more easily with the primary amine of chitosan which improves the reaction kinetics. Better adhesion of the chitosan will thus make it possible to obtain a homogeneous functionalized chitosan membrane on the surface of the sensor (Corgier et al., 2005).

MATERIALS AND METHODS

Reagents

Chitosan (CS, degree of deacetylation 80.0–95%), acetic acid (purity 99.7%), methanol (purity 99.9%), 1-ethyl-3-(3-dimethylaminopropyl)carbodiimide (EDC), 4-aminophenylacetic acid (CMA), sodium nitrite ($NaNO_2$), hydrochloric acid (37%, HCl), Pure ethanol (99.8%), Sulfuric acid (purity 95%), sodium hydroxide (NaOH) and glyphosate were obtained from Sigma Aldrich, France. N-hydroxysuccinimide (NHS) was purchased from Acros Organics, France. All interferents: gluphosinate-ammonium (GLU), chlorpyrifos (CHL), and phosmet (PHO) were supplied by Sigma Aldrich, France. The experimental runs were performed at room temperature with analytical grade reagents.

Apparatus

The data of electrochemistry were obtained through a multichannel potentiostat analyzer (Biologic-EC-Lab VMP3). The tests were performed with a transducer supplied by the National Center for Microelectronics (CNM), CSIC, Barcelona. It's made up of a plate of four bare gold working microelectrodes (WE) (s = 0.64 mm^2), one counter microelectrode (CE) (s = 0.13 mm^2), and two Ag/AgCl reference microelectrodes (RE) (s = 1.37 mm^2) (see transducer in **Figure 1**). The use of the four working microelectrodes allowed us to go faster in the experimental part. With the multichannel potentiostat it was possible to prepare four microsensors at the same time and to use them simultaneously either for detection, interference studies, regeneration, and analysis of the real sample. With the responses of the four microsensors we made the error bars.

A pH- meter: Mettler Toledo FE20/EL20 was used for the measure of solution pH. A FEI Quanta FEG 250 SEM (University of Lyon 1), France, was used to obtain the Scanning Electron Microscopy (SEM) images.

CS-MIPs/CMA/Au Sensor Fabrication

Diazonium Grafting Onto Gold Microelectrodes

Preparation of Diazonium Salt (CMA)

3 mM CMA solution was prepared with 20 mM of HCl (20 mM) and 20 mM of $NaNO_2$ (20 mM) in an aqueous solution (**Figure 1** step. 1). Then, the mixture was stored at 4 °C until the appearance of a pinkish hue (about 5 min) (El Alami El Hassani et al., 2019).

Electrodeposition of CMA

The Au microelectrodes were washed beforehand for 10 min with ethanol and deionized water under ultrasound. The final step is their exposure for 30 min to UV/ozone. 5 cyclic voltammetry (CV) scans between −1.2 and 0.0 V at a scanning rate of 50 mV/s were carried out for the electrodeposition of the CMA solution (**Figure 1** step. 2). A cathodic peak is observed; the decrease in maximum intensity with each successive sweep (**Figure 2**) is probably due to the obstruction of the working electrode surface. After electrodeposition, the microelectrodes undergo rinsing with deionized water and drying under a stream of nitrogen.

Activation of the Carboxylic Function

Solution of 400 mM of 1-ethyl-3- (3 dimethylaminopropyl) carbodiimide (EDC) and 100 mM of N-Hydroxysuccinimide

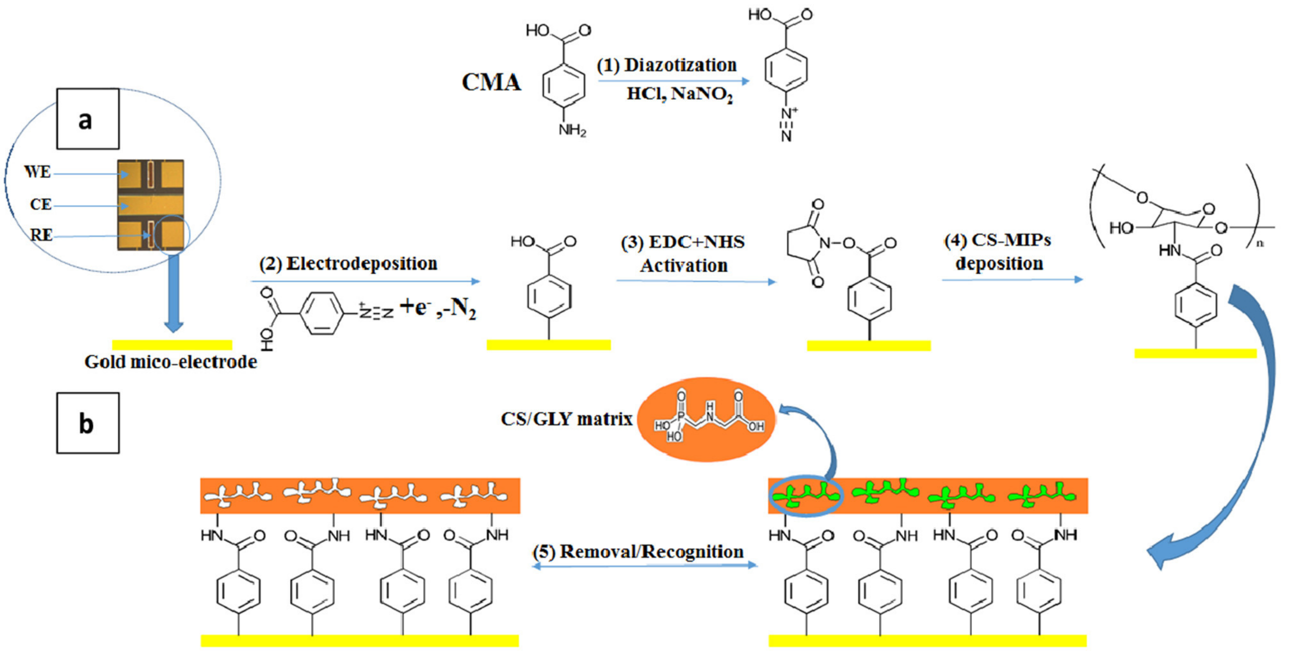

FIGURE 1 | (A) Transducer holding an array of four bare-gold working microelectrodes (WE) s = 0.64 mm^2, one counter microelectrode (CE) s = 0.13 mm^2, and two Ag/AgCl reference microelectrodes (RE) s = 1.37 mm^2. **(B)** Preparation of CS-MIPs/CMA/Au and its recognition for GLY.

(NHS) was prepared in absolute ethanol. The microelectrodes functionalized by the CMA were incubated in this solution for 1 h to activate the carboxylic function (**Figure 1** step. 3). Then, the devices were carefully rinsed with pure ethanol and dried using nitrogen (El Alami El Hassani et al., 2019).

Grafting of CS on Activated CMA

Preparation of GLY/CS Mixture

To prepare the CS solution, 1 g of CS powder was dissolved in a volume of 100 mL of acetic acid 0.1 M and ultrasonicated for 6 h at room temperature. 1 mg/mL of GLY was prepared in CS solution and stirring of the suspension for 2 h is followed by an adjustment of the pH to 5 with a solution of ammonia hydroxide. Chitosan used has a medium molecular weight (≈250 kDa). The monomer/template ratio is 1/1, that means that in the mixture consists of one glyphosate molecule for each glycosamine monomer. The molecular weight of chitosan being 250 kDa which correspond to 1,470 glycosamine monomers per polymer chain, the mixture contains one molecule of glyphosate for one glycosamine monomer.

CS-MIPs Deposition

GLY/CS mixture was deposited by drop-casting on the functionalized microelectrodes surface for 24 h. The deposition was followed by incubation during 1 h of the GLY-CS/CMA/Au in 0.5 M H_2SO_4 as the cross-linker to remove residues of chitosan. Chitosan is soluble in all mineral acids except sulfuric acid. In this case, sulfuric acid is used as a crosslinking agent during the formation of the biopolymer. The deposited CS film remains stable; moreover the reproducibility results confirm this (see section About the Sensor Regeneration and Reproducibility). During the crosslinking, ionic bonds are formed between the sulfate ions of sulfuric acid and the ammonium ions of chitosan. The mechanism of crosslinking of chitosan with sulfuric acid is presented in **Supplementary Figure 1**.

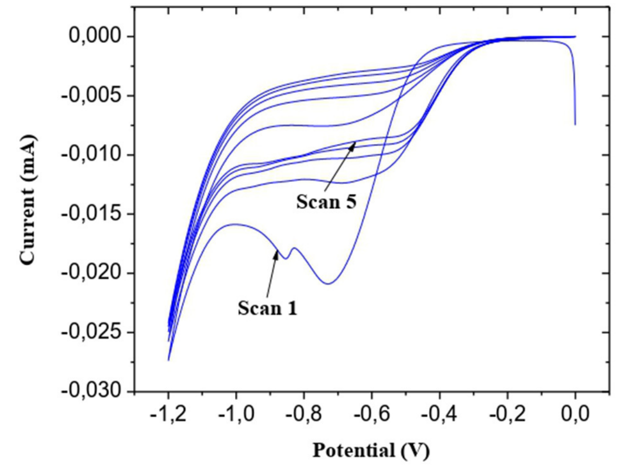

FIGURE 2 | Cyclic voltammogram of electrodeposition of CMA on the microelectrode surface.

To eliminate the molecule template, a second incubation of about 30 min was made in acetic acid/methanol solution (1:1, v/v). The incubation time of 30 min is considered to be an optimal time for maximum extraction of GLY from the CS film. Because for an incubation time >30 min, EIS plot and CV voltammogram can be superimposed on those for an extraction time of 30 min. Knowing that initially the GLY (anionic) is adsorbed on active sites of chitosan (cationic biopolymer) by electrostatic interaction at pH = 5, it is desorbed in AcAC/methanol (1:1; v:v) solution at pH <4.5 for the most part. While the chitosan remains adherent and fixed by covalent bonds to the surface of the functionalized microelectrode.

So, a microsensor constructed with CS molecularly imprinted film modified with CMA was applied for a specific recognition of GLY. The process is shown in **Figure 1** (step. 4 and 5).

The steps in making the unprinted polymer sensor (CS-NIP/CMA/Au) are identical to those for the CS-MIP/CMA/Au microelectrodes, except that GLY was absent from the entire process. Storage at ambient temperature of the sensors was carried out for further applications.

Experimental Conditions

A multichannel potentiosat (Biologic-EC-Lab VMP3) was used for the characterization by the techniques of cyclic voltammetry (CV) and electrochemical impedance spectroscopy (EIS) of all the modifications made to the working microelectrodes. All the measurements were performed in 5 mM ferro-ferricyanide ($[Fe(CN)_6]^{3-/4-}$) and phosphate buffer saline solution (PBS). For the cyclic voltammetric measurements, the potential was scanned between 0 and 0.45 V at a scan rate of 80 mV/s. EIS data are obtained for an initial potential of 0.2 V and a frequency range varying from 300 mHz to 100 kHz. For detection step, after an immersion in aqueous GLY solutions of concentrations varying between 0.31×10^{-9} and 50×10^{-6} mg/mL for a period of 30 min, CS-MIPs/CMA/Au electrodes were characterized by EIS.

RESULTS AND DISCUSSION

Characterization of the Surface Modifications

Electrochemical impedance spectroscopy (EIS) has emerged as an alternative to conventional analysis techniques to study the modified surfaces. EIS provides information on the kinetics of molecular phenomena at the interface, as well as on the coverage rates and the effectiveness of surface modifications (Proud and Müller, 1993). By modeling the electrochemical response by equivalent electrical circuits, it is possible to relate the physical and chemical properties of the electrode material to the data from the EIS curves (Janata, 2002).

The equivalent circuit shown in **Figure 3C** was used to fit the Nyquist plots a, b, c, and d of **Figure 3A**, and the equivalent circuit shown in **Figure 5B** was used to fit the Nyquist plots e of **Figure 3A**.

From the examination of **Figure 3A**, a, it emerges that the sensor has a high charge transfer rate for $[Fe(CN)6]^{3-/4-}$ (R_{ct} = 783 Ohm). An obvious increase of the charge transfer resistance value was observed with the electrodeposition of CMA on the

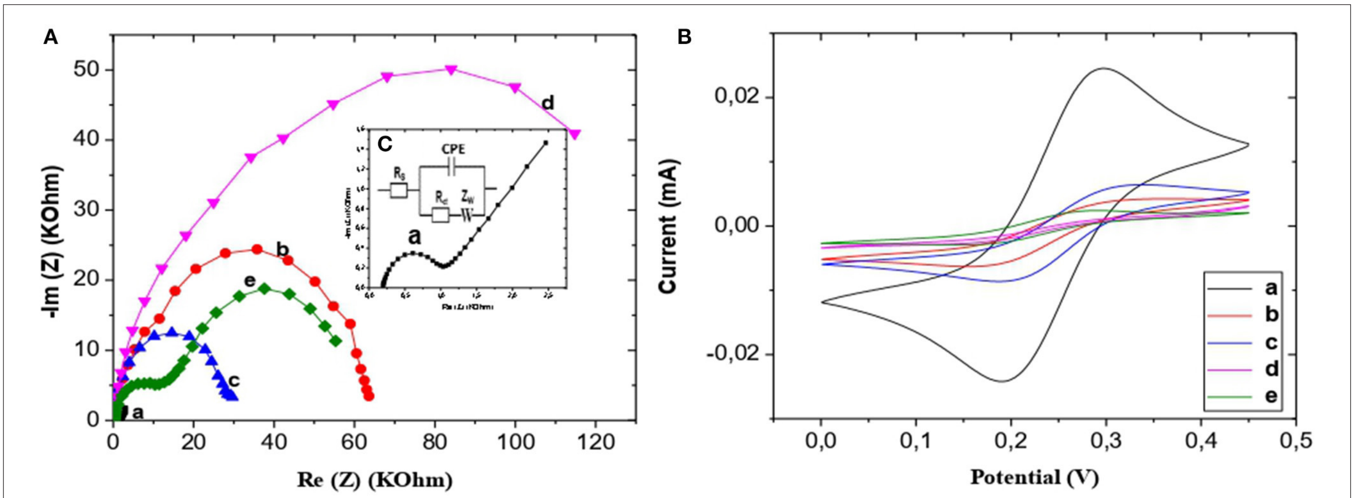

FIGURE 3 | (A) EIS of bare Au (a), CS-NIPs/CMA/Au (b), CMA/Au (c),CS-MIPs/CMA/Au before extraction of template (d), CS-MIPs/CMA/Au after extraction of template (e), in 5 mM $[Fe(CN)_6]^{3-/4-}$ and PBS, initial potential E = 0.2 V. Highest Freq = 100 khz, Lowest Freq = 300 mHz. **(B)** VC of bare Au (a), CS-NIPs/CMA/Au (b),CMA/Au (c),CS-MIPs/CMA/Au before extraction of template (d), CS-MIPs/CMA/Au after extraction of template (e), in 5 mM $[Fe(CN)_6]^{3-/4-}$ and PBS, from 0 to 0.45 V at a scan rate of 80 mV/s. **(C)** Randles' circuit, where R_s is the electrolyte resistance, CPE is the constant phase elements, R_{ct} is the charge transfer resistance and Z_w is the Warburg impedance.

gold microelectrode surface (R_{ct} = 26,269 Ohm) (**Figure 3A**, c). Impedance becomes higher value after the chemical deposition of chitosan (R_{ct} = 95,452 Ohm) (**Figure 3A**, d).

From the comparison of the diagrams obtained with the NIP film (**Figure 3A**, b), the MIP film (**Figure 3A**, d) has a larger Re (Z), and therefore, a greater thickness than that of the NIP film. Indeed, the NIP, the chitosan chains are positioned in a flat manner on the CMA. Logically, the thickness of the NIP membrane equals the width of the glucosamine in the chitosan.

For the MIP, the presence of glyphosate gives a film with curvatures which modifies the morphology of the film, in particular its thickness in comparison with the NIP film. If the film is thicker, its resistance to electron transfer is higher. Also, it is possible that the presence of glyphosate in the MIP film makes it more resistive in comparison with the NIP film (see diagram of the **Supplementary Figure 2**).

The removal of the pesticide template from the MIPs was lead to significant decrease in impedance (**Figure 3A**, e) and the formation of two well-defined loops has been observed (for the first semicircle R_2 = 11,775 Ohm, for the second semicircle R_3 = 53,728 Ohm). Moreover, charge transfer resistance of NIPs (R_{ct} = 59,890 Ohm) is higher than MIPs film after removing template, due to the presence of imprinted cavities on MIPs layer, which favors the electron transfer.

This result is also proved by the cyclic voltammetry (CV) curves obtained in a ferro-ferricyanide solution (E varying from 0 to 0.45 V and scan rate of 80 mV/s). Like the results of the EIS, those of the CV (**Figure 3B**) correspond to the same characteristics of the electrodes. It can be seen from the CV (**Figure 3B**), after electrodeposition of CMA (**Figure 3B**, c) the decrease of intensity current of redox peaks was recorded compared with bare gold surface (**Figure 3B**, a). Then, redox peaks is lower after deposition of the CS which is a non-conductor polymer (**Figure 3B**, d). It was observed that redox peaks of NIPs film (**Figure 3B**, b) are higher than MIPs film which is thicker. Due to extraction of template from the MIPs matrix (**Figure 3B**, e), it was observed a significant increase in redox peak, this peak is bigger comparing to NIPs which is related to the presence of imprinted hole promoting the charge transfer.

Surface Features

The surface morphologies investigations of CMA/Au, CS-MIPs/CMA/Au and CS-NIP/CMA/Au (**Figure 4**) were carried out by scanning electron microscopy (SEM). It can be seen from the completely different morphologies of the surfaces of the bare electrodes (**Figure 4a**) and that of the modified with CMA (**Figure 4b**), that the operation of depositing the CMA film was well-accomplished. After the chemical deposition of the chitosan onto CMA layer, another morphology modification has appeared on the surface of the microelectrode which confirms the deposition of the CS (**Figure 4c**). Therefore, SEM does not allow seeing the difference between the morphology of MIPs (**Figure 4b**) and NIPs films (**Figure 4c**); because the diameters of the cavities on the chitosan layer have the same order of magnitude with the GLY molecules; in the order of a few nanometers.

Electrochemical Responses of MIPs to Glyphosate

From the EIS graphs in **Figure 5A**, we can see a very remarkable variation in response amplitudes with increasing GLY concentration, which is an indicator of the relationship between the latter and the impedance of the GLY sensor.

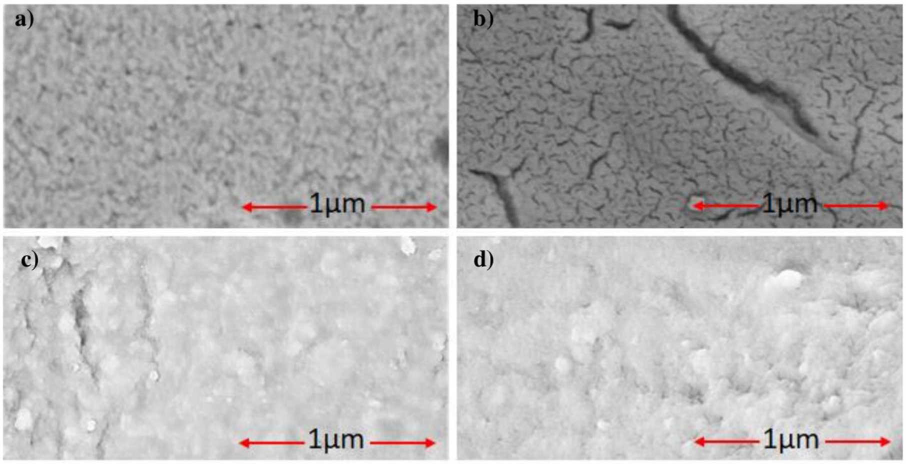

FIGURE 4 | SEM images. **(a)** Bare gold, **(b)** CMA/Au, **(c)** CS-MIPs/CMA/Au, **(d)** CS-NIPs/CMA/Au.

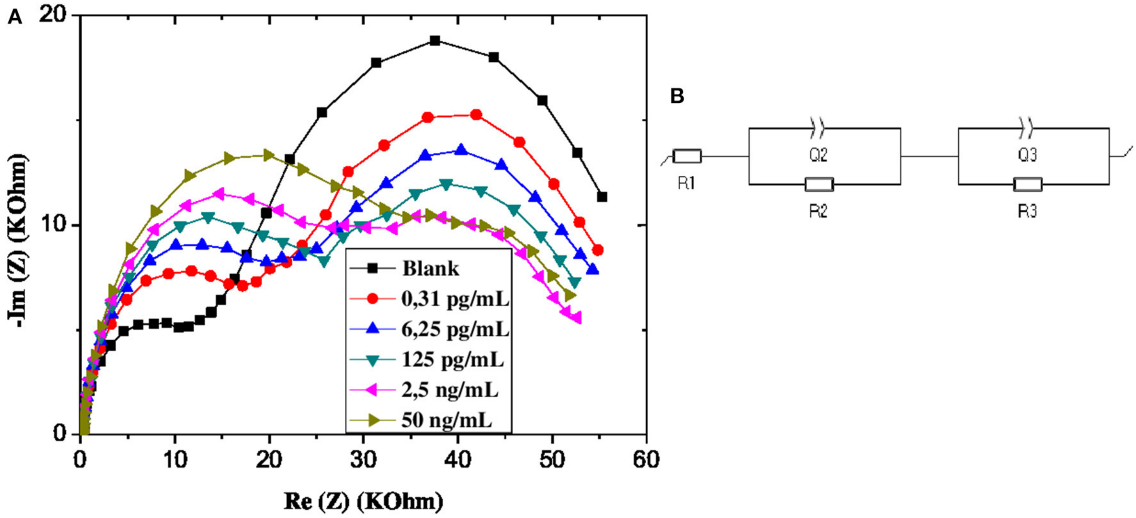

FIGURE 5 | (A) EIS of CS-MIPs/CMA/Au in 5 mM $[Fe(CN)6]^{3-/4-}$ and PBS. Before pre-concentration and after incubation in different concentrations of GLY. **(B)** Schematic of equivalent electrical circuit.

TABLE 1 | Estimated values of the parameters fitted by equivalent electrical circuit model $R_1 + Q_2/R_2 + Q_3/R_3$.

$[GLY].10^9$ mg/mL	R_1 (Ohm)	R_2 (Ohm)	Q_2. 10^7 ($F.s^{n-1}$)	n_2	R_3 (Ohm)	Q_3. 10^6 ($F.s^{n-1}$)	n_3	X^2
Blank	147.0	11,775	3.09	0.86	53,728	8.84	0.74	0.042
0.31	142.4	14,633	2.49	0.88	45,421	8.52	0.72	0.013
6.25	135.1	19,369	2.22	0.88	40,029	7.72	0.73	0.014
125	134.8	21,937	2.16	0.88	34,817	7.21	0.73	0.013
2,500	132.6	23,910	2.03	0.87	30,561	6.45	0.73	0.013
50, 000	131.6	28,397	2.83	0.87	28,673	5.73	0.77	0.011

The EIS data were fitted by equivalent electrical circuit model (EEC). The optimal fit was done using ($R_1 + Q_2/R_2 + Q_3/R_3$) EEC, which consists of three components associated in series (**Figure 5B**). The first component R_1 expresses the electrolyte resistance. The parallel elements Q_2 and R_2, which are related to the first Nyquist semi-circle, correspond respectively to the constant phase element (CPE) and the charge transfer resistance. For to the second Nyquist semi-circle, the parallel elements Q_3 and $R_{3,}$ correspond respectively to CPE and charge transfer resistance. This electrical circuit was reported to characterize porous structures. CPE_1 and CPE_2 are interpreted as the non-ideal capacitances which are caused by the surface geometry, roughness, and porosity. The relation between these constant phase elements Q and the impedance Z is given by: $Z_{CPE} = 1/Q(j\omega)^n$; where j is the imaginary number, ω is the angular frequency and n is correction factor ($0 < n < 1$). If the value n tends to 0, CPE becomes less capacitive (Ebdelli et al., 2011; Gaied et al., 2014; Aymen et al., 2015). The selection of the equivalent circuit was dependent upon the fitting of the Nyquist plot to produce the smallest error, expressed as the standard deviation (X^2).

The estimated values of the parameters after adjusting the model of the equivalent circuit with the impedance spectra are given in **Table 1**. The results reported by the fitting reveals that n_2 and n_3 are <1, which confirmed the roughness and the heterogeneity of the microelectrode surface. As these values are invariant with the increase in the applied potential, the stability of the electrode surface is confirmed.

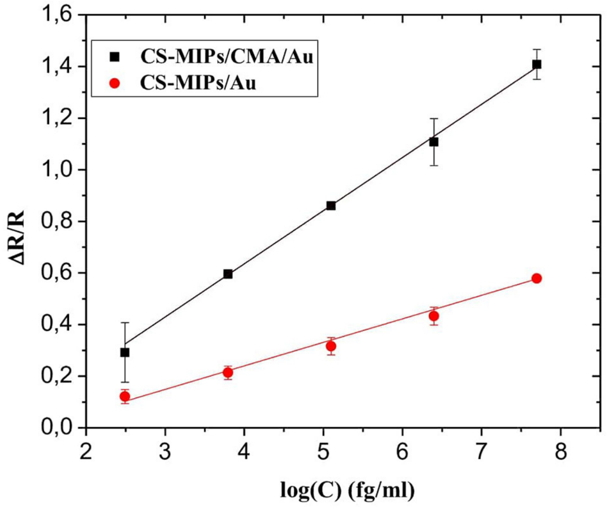

FIGURE 6 | Sensitivity of CS-MIPs/CMA/Au (ΔR/R = 0.206 log [GLY] – 0.188, $R^2 = 0.999$) and CS-MIPs/Au (ΔR/R = 0.087 log [GLY] +0.673; $R^2 = 0.991$).

At high frequencies, the Nyquist plot shows a first semi-circle, while the second is observed at lower frequencies. This element is comprised of contributions from three different processes which are electron transfer process, diffusion control and adsorption of ionic species (Terbouche et al., 2016; Tanujit and Asokan, 2019).

The diminution of R_3 charge transfer resistance is probably related to the adsorption of $[Fe(CN)_6]^{3-/4-}$ on the CMA microelectrode, or may be attributed to the electrostatic interaction between this negative ions and membranes modified surface. This decrease is due to the accumulation of ions on the surface, which increases the active surface area of the electrode. These behaviors are allowed by the morphology and surface porosity of the CS-MIPs/CMA/Au electrodes.

On another side, the resistance R_2 increases due to re-occupancy of the complementary sites which are located on the membrane of the biopolymer. These complexations make the surface of the electrode more resistant to charge transfer.

If R_2 and R are the load transfer resistances of the sensor corresponding respectively to a given and zero concentration of GLY, the ratio $|R–R_2|/R_2 = \Delta R/R$, therefore makes it possible to measure the relative variation of the charge transfer resistance of the electrode. Therefore, ΔR/R is related to the evolution of the GLY content of the solution. The exploitation of the data of the EIS diagrams made it possible to find a linear relation between this parameter and the logarithm of the concentration of GLY. The linear range is from 0.31×10^{-9} up to 50×10^{-6} mg/mL as shown in **Figure 6**. The calibration equation is given below (with a coefficient of determination = 0.998):

$$\Delta R/R = 0.206 \log[GLY] - 0.188,$$

This new sensor has a detection limit (LOD) of 10^{-12} mg/mL. The estimation of the LOD is carried out thanks to the commonly used equation: 3S/m (Shrivastava and Gupta, 2011), S and m are respectively the residual standard deviation and the slope of the calibration line. The high sensitivity of these MIP/Au/CMA sensors allows them to be used successfully for the detection of very low concentrations of GLY. Indeed, the LOD obtained is $1/10^8$ times lower compared to the EQS value of pesticides equal to 0.1 µg/mL.

TABLE 2 | A comparison of analytical parameters of the proposed electrode with other MIP electrochemical sensors.

Electrode	Technique	Linear range mg/mL	Limit of detection mg/mL	Sensitivity	References
Ppy-MIP/ $HAuCl_4$-PB/ITO	DPV	400×10^{-6}–$1,200 \times 10^{-6}$	92×10^{-6}	/	Xu et al., 2017
Ppy-MIP/Au	DPV	5×10^{-6}–800×10^{-6}	$0,27 \times 10^{-6}$	12,8	Zhang et al., 2017
Ppy-MIP/Au	SWV	$1,7 \times 10^{-11}$–$1,7 \times 10^{-2}$	$1,7 \times 10^{-10}$	/	Mazouz et al., 2017
CS-MIP/Au	EIS	$0,31 \times 10^{-9}$–50×10^{-6}	10^{-12}	0,087	Zouaoui et al., 2020b
CS-MIP/CMA/Au	EIS	$0,31 \times 10^{-9}$–50×10^{-6}	10^{-12}	0,206	This work

Ppy-MIP/$HAuCl_4$-PB/ITO, Molecularly imprinted Polypyrrole/Composite of urchin-like gold nanoparticles and Prussian Blue/Indium-Tin Oxide glass; Ppy-MIP/Au, Molecularly imprinted Polypyrrole/Gold electrode; CS-MIP/Au, Molecularly imprinted Chitosan/Gold microelectrode; DPV, Differential Pulse Voltammetry; SWV, Square Wave Voltammetry.

The analytical performance of the CS-MIPs/CMA/Au sensor was compared to other MIPs electrochemical sensors used for GLY detection reported in the literature (**Table 2**). To the best of our knowledge, this sensor had the best analytical characteristics than most previously reported sensors.

CMA Effect on Sensor Sensitivity

The sensitivity of the sensor based on CS-MIPs modified with CMA (CS-MIPs/CMA/Au) was compared with the sensitivity of the sensor based only on chitosan membrane (CS-MIPs/Au) (Zouaoui et al., 2020b). As shown in **Figure 6**, the sensitivity of CS-MIPs/CMA/Au is 2.37 times higher than CS-MIPs/Au. For applications in the sensor field, the electrodeposition of chitosan (CS-MIPs/Au) on a conductive surface by pH gradient causes the degassing of H_2. These molecules are blocked inside the membrane, which makes it non-homogeneous. "The grafting of chitosan onto the diazonium salt by the formation of strong interactions probably leads to more homogeneous membranes and to the resolution of interface problems."

Interference

The selective sensing of the designed microsensor of the GLY was tested using interfering pesticides; this includes phosmet (PHO), gluphosinate-ammonium (GLU), and chlorpyrifos (CHL). EIS analyzes are performed using the same experimental process as that for GLY detection. The detection tests of PHO, GLU, and CHL were performed in the same concentration range between 0.31×10^{-9} and 50×10^{-6} mg/mL (**Figure 7**). For the different interferences, the response of CS-MIPs/CMA/Au sensor were lower compared with GLY detection indicating that the microsensor displays the best selectivity to GLY.

Non-imprinted microsensor (CS-NIPs/CMA/Au) was used to study the effectiveness of the imprinting in the presence of GLY. As seen in **Figure 7**, ΔR/R of the CS-MIPs/CMA/Au were stronger compared with ΔR/R of the CS-NIPs/CMA/Au indicating that the proposed sensor had excellent specificity, because the fixation of GLY molecule by the CS-NIPs/CMA/Au microsensor is very low which confirms the success and efficiency of the GLY's impression.

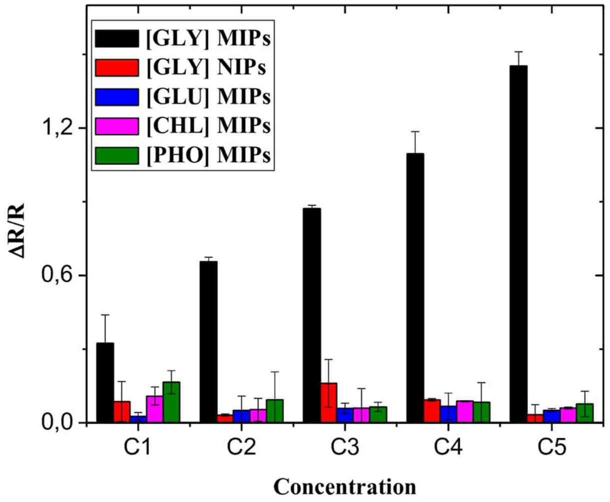

FIGURE 7 | Selectivity of CS-MIPs/CMA/Au microsensor (black) response of CS-MIPs/CMA/Au to GLY, (red) response of CS-NIPs/CMA/Au to GLY, (blue) response of CS-MIPs/CMA/Au to GLU, (pink) response of CS-MIPs/CMA/Au to CHL, and (green) response of CS-MIPs/CMA/Au to PHO.

About the Sensor Regeneration and Reproducibility

Three working microelectrodes, prepared according to the same method, are used to study the reproducibility of the CS-MIPs/CMA/Au microsensor. Acceptable reproducibility is obtained with a relative standard deviation of 1.46%.

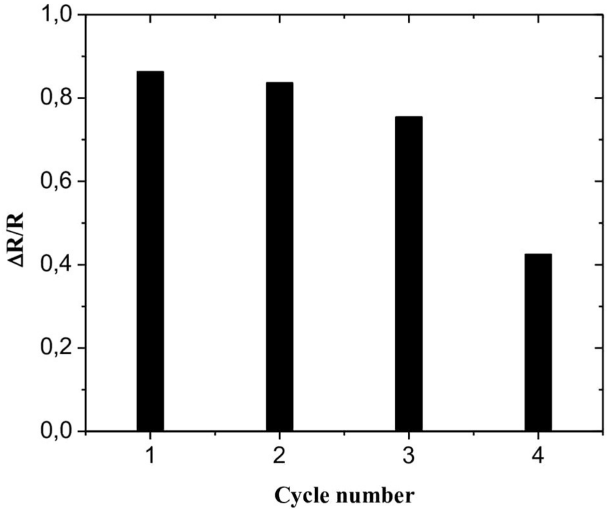

FIGURE 8 | Regeneration of the CS-MIPs/CMA/Au microsensor.

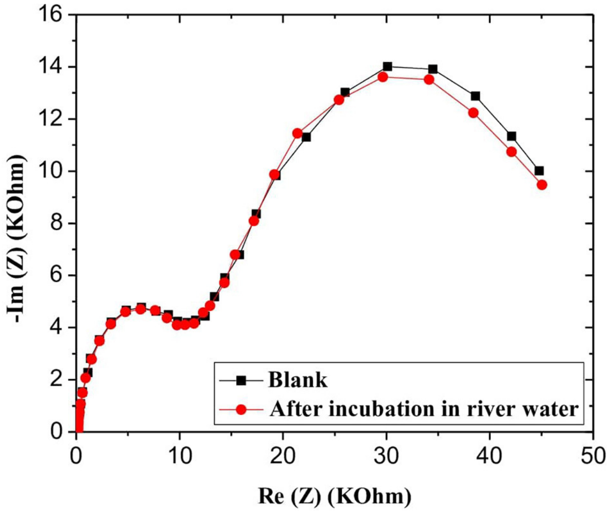

FIGURE 9 | EIS of CS-MIPs/CMA/Au before and after incubation in Rhone river water.

To study the regeneration of the CS-MIPs/CMA/Au microsensor, EIS repetitive measurements were carried out using the same imprinted microsensor which was re-immersed in solutions containing 125 pg/mL of GLY. After each measurement, the CS-MIPs/CMA/Au microsensor was incubated for 5 min in CH_3COOH/ CH_3OH solution (1:1, v/v) to eliminate attached GLY molecules. As shown in **Figure 8**, the results of second and the third repeat measurements showed weak relative variation of ΔR/R compared with the first cycle (3.08 and 12.75%, respectively). For the fourth repeat, the variation was more significant (50.75%), indicating that the sensor can only be regenerated twice.

REAL SAMPLE ANALYSIS

In order to assess the robustness and the applicability of the developed microsensor in a real environment, water samples retrieved from the Rhone River in Lyon, France, were analyzed. CS-MIPs/CMA/Au microsensor was incubated in river water samples for 30 min, and then EIS experiments were carried out for different GLY concentrations. The EIS diagrams were plotted to deduce electron transfer resistance of the sensor surface. Respective Nyquist plots before and after the sample analysis are almost superimposed, probably indicating the absence of GLY in the analyzed sample (**Figure 9**).

To confirm the above observation, the GLY was quantified using the standard additions method. A remarkable variation of impedance spectra was observed with a gradual increase of GLY concentration in the river water sample in the interval of 0.31 $\times 10^{-9}$-50 $\times 10^{-6}$ mg/mL (**Figure 10A**). A linear relationship between GLY concentration and the relative transfer resistance has been registered with good correlation coefficient equals to 0.997 (**Figure 10B**). The form of regression equation y = ax (ΔR/R = 0.20log[GLY]) is an indication of the absence of GLY in the river water considered. In addition, the sensitivity of this designed microsensor in the real and buffer samples were very close, which indicated that the CS-MIPs/CMA/Au exhibited high reliability.

CONCLUSION

This work is a new investigation around the design of a sensitive and selective sensor for the detection of traces of GLY in synthetic and real water samples. It is based on the grafting of the MIP molecularly imprinted CS chitosan onto an Au microelectrode modified with 4-aminophenylacetic acid CMA. Thanks to EIS investigations, the quantification of GLY was carried out to in a linear concentration range between 0.31 $\times 10^{-9}$ and 50 $\times 10^{-6}$ mg/mL and a limit of detection of 10^{-12} mg/mL.

The sensitivity of CS-MIPs/CMA/Au is higher compared with CS-MIPs/Au which arouses the interest to use this diazonium salt. The developed electrochemical microsensor has very good selectivity for GLY in comparison to three interferent compounds. The printing efficiency was confirmed using non-imprinted microsensor. In addition, the high reliability of this biosensor allows it to be used precisely to detect low traces of GLY in both synthetic and real water samples. The ease of implementation, the simplicity and the miniaturization of this sensor guide research for the development of economical, precise, and rapid tools for environmental analysis.

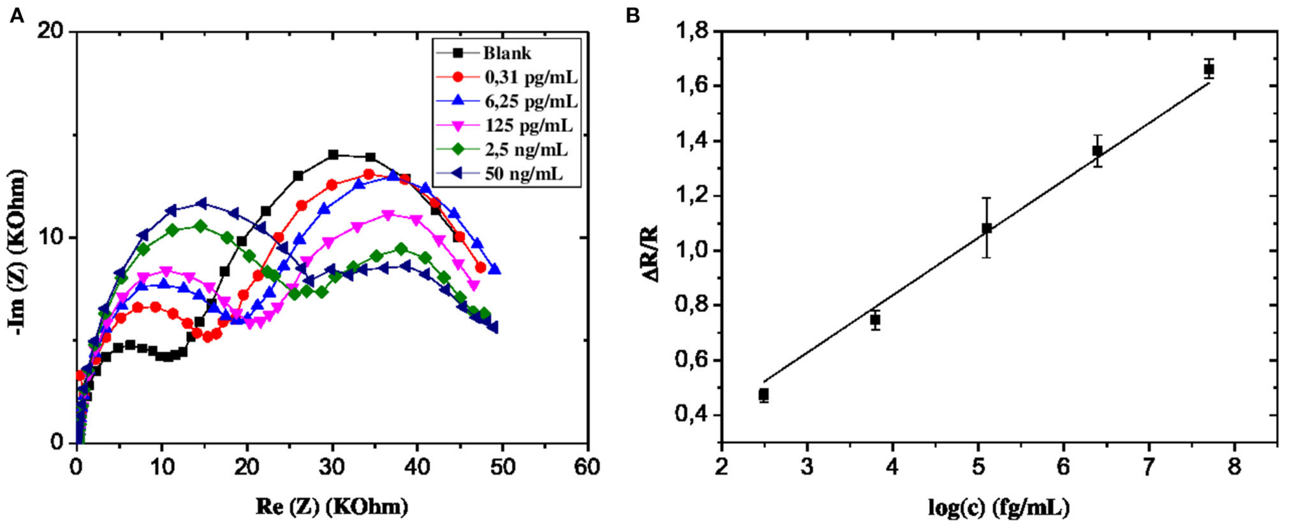

FIGURE 10 | (A) EIS of CS-MIPs/CMA/Au in 5 mM $[Fe(CN)_6]^{3-/4-}$ and PBS Before pre-concentration and after incubation in river water with different concentrations of GLY. **(B)** detection of GLY in Rhone river water using standard addition method with the following concentrations (0.031 pg/mL, 6.25 pg/ml, 125 pg/ml, 2.5 ng/ml, and 50 ng/ml) (ΔR/R = 0.20 log [GLY]; $R^2 = 0.997$).

DATA AVAILABILITY STATEMENT

The raw data supporting the conclusions of this article will be made available by the authors, without undue reservation.

AUTHOR CONTRIBUTIONS

FZ carried out the experimental work under the supervision of NJ-R and AE, and wrote the article. JB and AA contributed to the design of the sensors. NJ-R supervised and contributed writing and editing. MB and SB-B revised and corrected the document. All authors have read and accepted the published version of the manuscript.

FUNDING

The authors acknowledge the financial support of CAMPUS FRANCE program under grant agreement PROFAS B+ and PHC PROCOPE #40544QH and the EU H2020 research and innovation program entitled Kardia Tool grant agreement #768686.

SUPPLEMENTARY MATERIAL

The Supplementary Material for this article can be found online at: https://www.frontiersin.org/articles/10.3389/fchem.2021.621057/full#supplementary-material

REFERENCES

Aranaz, I., Harris, R., and Heras, A. (2010). Chitosan amphiphilic derivatives. Chemistry and applications. *Curr. Organ. Chem*. 14, 308–330. doi: 10.2174/138527210790231919

Aymen, F., Kraiem, H., Lassaad, S. (2015). “Electrical motor parameters estimator improved by a computational algorithm,” in *Handbook of Research on Advanced Intelligent Control Engineering and Automation*. doi: 10.4018/978-1-4666-7248-2.ch021

Chakroun Galai, H., Namour, P., Bonhomme, A., Bessueille, F., Besbes Hentati, S., and Jaffrezic-Renault, N. (2020). Elaboration of an Imprinted Polymer Film Based on Chitosan Electrodeposition for the Voltammetric Detection of BPA. *J. Electrochem. Soc.* 167:027507. doi: 10.1149/1945-7111/ab6283

Chen, J.-P.,Yang, P.-C., Ma, Y.-H., Wu, T. (2011). Characterization of chitosan magnetic nanoparticles for in situ delivery of tissue plasminogen activator. *Carbohydr. Polym.* 84, 364–372. doi: 10.1016/j.carbpol.2010.11.052

Chira, A., Bucur, B., and Radu, G.-L. (2017). Electrodeposited organic layers formed from aryl diazonium salts for inhibition of copper corrosion. *Mater* 10, 235–248. doi: 10.3390/ma10030235

Chung, T. W., Yang, J., Akaike, T., Cho, K. Y., Nah, J. W., Kim, S. I., et al. (2002). Preparation of alginate/galactosylated chitosan scaffold for hepatocyte attachment. *Biomaterials* 23, 2827–2834. doi: 10.1016/S0142-9612(01)00399-4

Clegg, B. S., Stephenson, G. R., and Hall, J. C. (1999). Development of an enzyme-linked immunosorbent assay for the detection of glyphosate. *J. Agric. Food Chem.* 47, 5031–5037. doi: 10.1021/jf990064x

Corgier, B. P., Marquette, C. A., and Blum, L. J. (2005). Diazonium–protein adducts for graphite electrode microarrays modification: direct and addressed electrochemical immobilization. *JACS* 127, 18328–18332. doi: 10.1021/ja056946w

Cuhra, M., Traavik, T., and Bøhn, T. (2013). Clone- and age-dependent toxicity of a glyphosate commercial formulation and its active ingredient in Daphnia magna. *Ecotoxicology* 22, 251–262. doi: 10.1007/s10646-012-1021-1

Deng, P., Xu, Z., Li, J., and Kuang, Y. (2013). Acetylene black paste electrode modified with a molecularly imprinted chitosan film for the detection of bisphenol A. *Microchim Acta* 180, 861–869. doi: 10.1007/s00604-013-1001-z

Ebdelli, R., Rouis, A., Mlika, R., Bonnamour, I., Jaffrezic-Renault, N., Ben Ouada, H., et al. (2011). Electrochemical impedance detection of Hg2+, Ni2+ and Eu3+ ions by a new azo-calix[4]arene membrane. *J. Electroanal. Chem.* 661, 31–38. doi: 10.1016/j.jelechem.2011.07.007

El Alami El Hassani, N., Baraket, A., Boudjaoui, S., Taveira Tenório Neto, E., Bausells, J., El Bari, N., et al. (2019). Development and application of a novel electrochemical immunosensor for tetracycline screening in honey using a fully integrated electrochemical Bio-MEMS. *Biosens. Bioelectron.* 130, 330–337. doi: 10.1016/j.bios.2018.09.052

Fatoni, A., Numnuam, A., Kanatharana, P., Limbut, W., and Thavarungkul, P. (2014). A novel molecularly imprinted chitosan–acrylamide, graphene, ferrocene composite cryogel biosensor used to detect microalbumin. *Analyst* 139, 6160–6167. doi: 10.1039/C4AN01000K

Gaied, A., Jaballah, N., Teka, S., and Mejdoub, M. (2014). A water-insoluble Î²-cyclodextrin derivative for hydroquinone sensor applications. *J. Applicable Chem*. 3, 1655–1664. doi: 10.13140/RG.2.1.1272.0726

Haupt, K., and Mosbach, K. (2000). Molecularly imprinted polymers and their use in biomimetic sensors. *Chem. Rev*. 100, 2495–2504. doi: 10.1021/cr990099w

Janata, J. (2002). Electrochemical sensors and their impedances: a tutorial. *Crit. Rev. Anal. Chem.* 32, 109–120. doi: 10.1080/10408340290765470

Johansson, H. K. L., Schwartz, C. L., Nielsen, L. N., Boberg, J., Vinggaard, A. M., Bahl, M. I., et al. (2018). Exposure to a glyphosate-based herbicide formulation, but not glyphosate alone, has only minor effects on adult rat testis. *Reprod. Toxicol.* 82, 25–31. doi: 10.1016/j.reprotox.2018.09.008

Karrat, A., Lamaoui, A., Amine, A., Palacios-Santander, J. M., and Cubillana-Aguilera, L. (2020). Applications of chitosan in molecularly and ion imprinted polymers. *Chem. Afr.* 3, 513–533. doi: 10.1007/s42250-020-00177-w

Li, H. X., Yao, W., Wu, Q., and Xia, W. S. (2014). Glucose molecularly imprinted electrochemical sensor based on chitosan and nickel oxide electrode. *Adv. Mater. Res.* 1052, 215–219. doi: 10.4028/www.scientific.net/AMR.1052.215

Li, S., Du, D., Huang, J., Tu, H., Yang, Y., and Zhang, A. (2013). One-step electrodeposition of a molecularly imprinting chitosan/phenyltrimethoxysilane/AuNPs hybrid film and its application in the selective determination of p-nitrophenol. *Analyst* 138:2761. doi: 10.1039/c3an36497f

Lin, L., Lian, H.-T., Sun, X.-Y., Yu, Y.-M., and Liu, B. (2015). An L-dopa electrochemical sensor based on a graphene doped molecularly imprinted chitosan film. *Anal. Methods* 7, 1387–1394. doi: 10.1039/C4AY02524E

Lopes, F. M., Sandrini, J. Z., and Souza, M. M. (2018). Toxicity induced by glyphosate and glyphosate-based herbicides in the zebrafish hepatocyte cell line (ZF-L). *Ecotoxicol. Environ. Saf.* 162, 201–207. doi: 10.1016/j.ecoenv.2018.07.005

Lorenz, V., Milesi, M. M., Schimpf, M. G., Luque, E. H., and Varayoud, J. (2019). Epigenetic disruption of estrogen receptor alpha is induced by a glyphosate-based herbicide in the preimplantation uterus of rats. *Mol. Cell. Endocrinol.* 480, 133–141. doi: 10.1016/j.mce.2018.10.022

Martins, A. O., da Silva, E. L., Carasek, E., Gonçalves, N. S., Laranjeira, M. C. M., and de Fávere, V. T. (2004). Chelating resin from functionalization of chitosan with complexing agent 8-hydroxyquinoline: application for metal ions on line preconcentration system. *Anal. Chim. Acta* 521, 157–162. doi: 10.1016/j.aca.2004.06.033

Mazouz, Z., Rahali, S., Fourati, N., Zerrouki, C., Aloui, N., Seydou, M., et al. (2017). Highly selective polypyrrole mip-based gravimetric and electrochemical sensors for picomolar detection of glyphosate. *Sensors* 17:2586. doi: 10.3390/s17112586

Pa, J., and Yu, T. L. (2001). Light scattering study of chitosan in acetic acid aqueous solutions. *Macromol. Chem. Phys.* 202, 985–991. doi: 10.1002/1521-3935(20010401)202:7<985::AID-MACP985>3.0.CO;2-2

Pereira, F. S., da Silva Agostini, D. L., Job, A. E., and González, E. R. P. (2013). Thermal studies of chitin–chitosan derivatives. *J. Therm. Anal. Calorim.* 114, 321–327. doi: 10.1007/s10973-012-2835-z

Pichon, V., and Haupt, K. (2006). Affinity separations on molecularly imprinted polymers with special emphasis on solid-phase extraction. *J. Liq. Chromatogr. Related Technol.* 29, 989–1023. doi: 10.1080/10826070600574739

Proud, W. G., and Müller, C. (1993). The electrodeposition of nickel on vitreous carbon: impedance studies. *Electrochim. Acta* 38, 405–413. doi: 10.1016/0013-4686(93)85158-U

Qiao, F., Sun, H., Yan, H., and Row, K. H. (2006). Molecularly imprinted polymers for solid phase extraction. *Chromatographia* 64, 625–634. doi: 10.1365/s10337-006-0097-2

Ren, X., Li, R., Liu, J., Huang, K., Wu, S., Li, Y., et al. (2018). Effects of glyphosate on the ovarian function of pregnant mice, the secretion of hormones and the sex ratio of their fetuses. *Environ. Pollut.* 243, 833–841. doi: 10.1016/j.envpol.2018.09.049

Ruiz de Arcaute, C., Soloneski, S., and Larramendy, M. L. (2018). Opposite effects of mixtures of commercial formulations of glyphosate with auxinic herbicides on the ten spotted live-bearer fish Cnesterodon decemmaculatus (Pisces, Poeciliidae). *Environ. Pollut.* 240, 858–866. doi: 10.1016/j.envpol.2018.05.036

Salvo-Comino, C., Rassas, I., Minot, S., Bessueille, F., Rodriguez-Mendez, M. L., Errachid, A., et al. (2020). Voltammetric sensor based on electrodeposited molecularly imprinted chitosan film on BDD electrodes for catechol detection in buffer and in wine samples. *Mater. Sci. Eng. C* 110:110667. doi: 10.3390/ma13030688

Seide, V. E., Bernardes, R. C., Pereira, E. J. G., and Lima, M. A. P. (2018). Glyphosate is lethal and Cry toxins alter the development of the stingless bee Melipona quadrifasciata. *Environ. Pollut.* 243, 1854–1860. doi: 10.1016/j.envpol.2018.10.020

Shrivastava, A., and Gupta, V. (2011). Methods for the determination of limit of detection and limit of quantitation of the analytical methods. *Chron. Young Sci.* 2:21. doi: 10.4103/2229-5186.79345

Song, Y., Han, J., Xu, L., Miao, L., Peng, C., and Wang, L. (2019). A dopamine-imprinted chitosan film/porous ZnO NPs@carbon nanospheres/macroporous carbon for electrochemical sensing dopamine. *Sens. Actuat. B* 298:126949. doi: 10.1016/j.snb.2019.126949

Tanujit, B., and Asokan, S. (2019). Electrochemical Impedance spectroscopy study of AgI-Ag2O-MoO3 glasses: understanding the diffusion, relaxation, fragility and power law behavior. *Philos. Magazine* 101, 400–419. doi: 10.1080/14786435.2020.1841914

Terbouche, A., Lameche, S., Ait-Ramdane-Terbouche, C., Guerniche, D., Lerari, D., and Bachari, K. (2016). A new electrochemical sensor based on carbon paste electrode/Ru(III) complex for determination of nitrite: electrochemical impedance and cyclic voltammetry measurements. *Measurement* 92, 524–533. doi: 10.1016/j.measurement.2016.06.034

Wang, J., Wang, L., Yu, H., Zain-ul-Abdin, S., Chen, Y., Chen, Q., et al. (2016). Recent progress on synthesis, property and application of modified chitosan: an overview. *Int. J. Biol. Macromol.* 88, 333–344. doi: 10.1016/j.ijbiomac.2016.04.002

Wu, S., Li, K., Dai, X., Zhang, Z., Ding, F., and Li, S. (2020). An ultrasensitive electrochemical platform based on imprinted chitosan/gold nanoparticles/graphene nanocomposite for sensing cadmium (II) ions. *Microchem. J.* 155:104710. doi: 10.1016/j.microc.2020.104710

Wulff, G., Kemmerer, R.,Vietmeier, J., and Poll, H. G. (1983). Chirality of vinyl polymers. The preparation of chiral cavities in synthetic polymers. *Nouveau J. Chim.* 6, 681–687.

Xia, J., Cao, X., Wang, Z., Yang, M., Zhang, F., Lu, B., et al. (2016). Molecularly imprinted electrochemical biosensor based on chitosan/ionic liquid–graphene composites modified electrode for determination of bovine serum albumin. *Sens. Actuat. B* 225, 305–311. doi: 10.1016/j.snb.2015.11.060

Xu, J., Zhang, Y., Wu, K., Zhang, L., Ge, S., and Yu, J. (2017). A molecularly imprinted polypyrrole for ultrasensitive voltammetric determination of glyphosate. *Microchim. Acta* 184, 1959–1967. doi: 10.1007/s00604-017-2200-9

Yan, H., and Row, K. (2006). Characteristic and synthetic approach of molecularly imprinted polymer. *Int. J. Mol. Sci.* 7, 155–178. doi: 10.3390/i7050155

Younes, I., and Rinaudo, M. (2015). Chitin and chitosan preparation from marine sources. structure, properties and applications. *Mar. Drugs* 13, 1133–1174. doi: 10.3390/md13031133

Zhang, C., She, Y., Li, T., Zhao, F., Jin, M., Guo, Y., et al. (2017). A highly selective electrochemical sensor based on molecularly imprinted polypyrrole-modified gold electrode for the determination of glyphosate in cucumber and tap water. *Anal. Bioanal. Chem.* 409, 7133–7144. doi: 10.1007/s00216-017-0671-5

Zouaoui, F., Bourouina-Bacha, S., Bourouina, M., Abroa-Nemeir, I., Ben Halima, H., Gallardo-Gonzalez, J., et al. (2020b). Electrochemical impedance spectroscopy determination of glyphosate using a molecularly imprinted chitosan. *Sens. Actuat. B.* 309:127753. doi: 10.1016/j.snb.2020.127753

Zouaoui, F., Bourouina-Bacha, S., Bourouina, M., Jaffrezic-Renault, N., Zine, N., and Errachid, A. (2020a). Electrochemical sensors based on molecularly imprinted chitosan: a review. *TrAC B* 30:115982. doi: 10.1016/j.trac.2020.115982

Conflict of Interest: The authors declare that the research was conducted in the absence of any commercial or financial relationships that could be construed as a potential conflict of interest.

frontiers in Chemistry

ORIGINAL RESEARCH
published: 02 June 2021
doi: 10.3389/fchem.2021.587142

Oriented Antibody Covalent Immobilization for Label-Free Impedimetric Detection of C-Reactive Protein *via* Direct and Sandwich Immunoassays

Abiola Adesina[1] *and Philani Mashazi*[1,2]*

[1]*Department of Chemistry, Rhodes University, Makhanda, South Africa,* [2]*Institute for Nanotechnology Innovation, Rhodes University, Makhanda, South Africa*

OPEN ACCESS

Edited by:
Ashok Mulchandani,
University of California, Riverside,
United States

Reviewed by:
Lingxin Chen,
Yantai Institute of Coastal Zone Research (CAS), China
Chaker Tlili,
Chongqing Institute of Green and Intelligent Technology (CAS), China

***Correspondence:**
Philani Mashazi
p.mashazi@ru.ac.za

Specialty section:
This article was submitted to Analytical Chemistry, a section of the journal Frontiers in Chemistry

Received: *24 July 2020*
Accepted: *07 May 2021*
Published: *02 June 2021*

Citation:
Adesina A and Mashazi P (2021) Oriented Antibody Covalent Immobilization for Label-Free Impedimetric Detection of C-Reactive Protein via *Direct and Sandwich Immunoassays.*
Front. Chem. 9:587142.
doi: 10.3389/fchem.2021.587142

The detection and monitoring of biological markers as disease indicators in a simple manner is a subject of international interest. In this work, we report two simple and sensitive label-free impedimetric immunoassays for the detection of C-reactive protein (CRP). The gold electrode modified with boronic acid–terminated self-assembled monolayers afforded oriented immobilization of capture glycosylated antibody (antihuman CRP monoclonal antibody, mAb). This antibody-modified surface was able to capture human CRP protein, and the impedance signal showed linear dependence with CRP concentration. We confirmed the immobilization of anti-CRP mAb using surface sensitive X-ray photoelectron spectroscopy (XPS) and electrochemical impedance. The oriented covalent immobilization of mAb was achieved using glycosylated Fc (fragment, crystallizable) region specific to boronic acid. The direct immunoassay exhibited a linear curve for concentration range up to 100 ng $\mathrm{ml^{-1}}$. The limit of detection (LoD) of 2.9 ng $\mathrm{ml^{-1}}$, limit of quantification (LoQ) of 9.66 ng $\mathrm{ml^{-1}}$, and sensitivity of 0.585 kΩ $\mathrm{ng^{-1}}$ ml $\mathrm{cm^{-2}}$ were obtained. The sandwich immunoassay was carried out by capturing polyclonal anti-CRP antibody (pAb) onto the CRP antigen immunoreaction. The impedance signal after pAb capture also showed linear dependence with CRP antigen concentration and acted as a CRP antigen detection signal amplifier. The detection of the CRP antigen using sandwich pAb immunoassay improved LoD to 1.2 ng $\mathrm{ml^{-1}}$, LoQ to 3.97 ng $\mathrm{ml^{-1}}$, and enhanced the sensitivity to 0.885 kΩ $\mathrm{ng^{-1}}$ ml $\mathrm{cm^{-2}}$. The real sample analysis, using newborn calf serum, showed excellent selectivity and % recovery for the human CRP ranging from 91.2 to 96.5%. The method was reproducible to 4.5% for direct immunoassay and 2.3% for sandwich immunoassay.

Keywords: C-reactive protein, immunosensor, oriented antibody, impedance immunoassay, boronate ester

INTRODUCTION

C- reactive protein (CRP) is a pentraxin family of protein secreted in the liver in response to interleukin 6 (IL-6). The concentration of CRP increases about 1,000 fold in response to injury, inflammation, and tissue damage (Quershi et al., 2009; Qureshi et al., 2012; Boonkaew et al., 2019). CRP is therefore a well-known biomarker for inflammation and tissue damage (Libby et al., 2002). CRP has been identified as the most specific biomarker for inflammation that can independently predict the risk of myocardial infarction (Pepys and Hirschfield, 2003; Hansson, 2005; Casas et al., 2008). The American Heart Association (AHA) and the Center for Disease Control and Prevention (CDC) reported (Verma and Yeh, 2003; Hu et al., 2006; Yang et al., 2009; Chinnadayyala et al., 2019) that individuals with CRP concentrations of less than $1.0\,\mu g\,ml^{-1}$ ($1.0\,ng\,\mu l^{-1}$) are at low risk of cardiovascular disease, while those that have CRP concentrations between 1.0 and $3.0\,\mu g\,ml^{-1}$ (1.0 and $3.0\,ng\,\mu l^{-1}$) are at moderate risk of cardiovascular disease. Individuals with more than $3.0\,\mu g\,ml^{-1}$ ($>3.0\,ng\,\mu l^{-1}$) CRP concentrations are at high risk of cardiovascular disease. Therefore, monitoring the concentration of CRP in the body and quantifying the amounts may help reduce and predict the risk of cardiovascular disease (CVD) (Sonuç Karaboğa and Sezgintürk, 2018). In the clinical laboratories, enzyme-linked immunosorbent assay (ELISA), turbidimetry, and nephelometry are the major methods used for quantifying the concentration of CRP in human samples (Dominici et al., 2004; Clarke et al., 2005; Parra et al., 2005; Vilian et al., 2019). Although ELISA is a sensitive technique, it is time-consuming and expensive and requires bulky equipment and highly skilled personnel for performing the analysis and result interpretation (Ding et al., 2013). These requirements make ELISA technique not suitable for diagnosis, especially in low-resource settings. An alternative method that offers improved clinical diagnosis of CVD and offers quantitative analysis in a cheap, easy, and fast manner is desirable. The use of electrochemical immunoassays is the promising method that can overcome the ELISA drawbacks, and the detection signal output can be digitized.

Electrochemical immunoassays have received a lot of attention in the field of clinical diagnosis, owing to their higher analytical efficiency as well as the unique advantages of high sensitivity, fast response, portability, low cost, simple instrumentation, and ease of miniaturization (Yu and Wang, 2010; Zhang et al., 2011; Dong et al., 2019; Rong et al., 2019). The electrochemical impedance spectroscopy (EIS) is a powerful technique to investigating a wide variety of electrochemical systems. It is an effective tool for sensing the formation of antibody–antigen affinity reactions occurring on the electrode surface by probing the interfacial properties (Vogt et al., 2016). EIS-based immunosensors are nondestructive and require no labeling of the antibody for signal generation (Repo et al., 2002; Chowdhury et al., 2017). Electrochemical methods are based on the interaction between the antibody and the antigen or aptamer and protein interactions (Wang et al., 2017; Kowalczyk et al., 2018). The results are direct in that the affinity interactions between the antibody and antigen can be directly detected using the changes in charge transfer resistance (R_{CT}) (Rodriguez et al., 2005; Bogomolova et al., 2009). The effective immobilization of biomolecules is a major factor in the fabrication of electrochemical impedimetric immunosensors. The sensitivity of an electrochemical impedimetric immunosensor toward the antigen can be enhanced by increasing the loading and the orientation of the capture antibodies. The immobilized capture antibodies must be oriented to allow for the optimum binding of the antigen, that is, with the antigen binding site away from the solid support (Makaraviciute and Ramanaviciene, 2013; Vashist and Luong, 2018). Antibody immobilization *via* adsorption results in various random orientations such as head-on, end-on, and side-on. Head-on antibody orientation results in the Fab (antigen-binding fragment) region attached and blocking the antigen binding. The end-on antibody orientation is *via* the Fc region attachment with antigen binding exposed, and side-on results in the Fc and Fab regions attached leaving at least one Fab antibody arm exposed for antigen binding. A method that seeks to control the orientation and exposes the antigen binding sites is of paramount importance. There are several methods for oriented immobilization of antibodies and these are streptavidin–biotin, C-terminus Fc targeting with amine surfaces, and boronic ester–glycoprotein reaction. Boronic acid and Fc glycoprotein reaction has attracted our research attention due to the high reactivity and can afford maximum antigen binding with both antigen sites exposed.

In this work, we investigate a method of immobilizing monoclonal anti-CRP antibody (mAb) onto the gold electrode surface modified *via* self-assembled monolayer (SAM) of 4-mercaptobenzoic acid (MBA), Au-MBA SAM. 4-aminophenylboronic acid (APBA) was attached *via* amide coupling onto Au-MBA SAM, to yield Au-MBA-APBA SAM. The use of Au-MBA-APBA SAM is to our knowledge for the first time reported for the immobilization of anti-CRP monoclonal antibody (anti-CRP mAb) using boronate ester. The surface analysis using electrochemical cyclic voltammetry, impedance spectroscopy, and X-ray photoelectron spectroscopy was used to confirm the fabrication of gold electrode and the attachment of anti-CRP mAb and blocking nonspecific binding sites with glucose to yield Au-MBA-APBA-mAb/glucose immunosensor. The fabricated impedimetric immunosensor was evaluated for the detection of human CRP antigen in direct and sandwich immunoassays.

EXPERIMENT

Materials and Reagents

Monoclonal mouse antihuman CRP (MCA5880G, mAb capture antibody), polyclonal goat antihuman CRP (1707-0189G, pAb detection antibody), and native human CRP (1707-2029) were purchased from AbD Serotech. Potassium ferricyanide ($K_3Fe(CN)_6$), potassium ferrocyanide ($K_4Fe(CN)_6$), potassium chloride (KCl), 4-mercaptobenzoic acid (MBA), 4-aminophenylboronic acid (APBA), N-hydroxysuccinimide (NHS), 1-ethyl-3 (3-dimethyl aminopropyl)-carbodiimide (EDC), glucose (blocking reagent), and newborn calf serum

(NCS) were purchased from Sigma-Aldrich. Phosphate buffered saline (PBS, 10 mM) solutions of pH 8.0 and 7.4 were prepared using 10 mM KH_2PO_4:K_2HPO_4 and 0.15 M NaCl; the pH adjustments were conducted using 0.10 M of either HCl or NaOH. All chemicals were of analytical grade. Ultrapure water with a resistivity of 18.2 MΩ cm (at 25°C) was obtained from Milli-Q water purification system and used throughout the experiment.

Equipment

The electrochemical analysis was carried out using the instrument specifications reported in the Electronic Support Information (ESI). The X-ray photoelectron spectroscopy surface analysis setup reported (Nxele et al., 2015) was followed in this work; the data analysis and fitting of the high resolution spectra interpretation were accomplished using the National Institute of Standards and Technology (NIST) database (Naumkin et al., 2012). The XPS high resolution peak fitting of various components binding energy values were corrected using carbonaceous (C 1s) set at 284.9 eV.

Fabrication of the Immunosensor

The clean gold surface was modified using self-assembly monolayer (SAM) method by immersing in an absolute ethanol solution containing 4-mercaptobenzoic (MBA, 5.0 mM) for 24 h. The modified gold surface was represented as Au-MBA SAM. The Au-MBA SAM electrode was removed from the thiol solution and rinsed with water and ethanol to remove the physically adsorbed MBA molecules. The terminal -COOH group of the MBA SAM reacted with the amino functional group of 4-aminophenylboronic acid (APBA) using amide coupling reaction. The carboxylic acid of the Au-MBA SAM was activated in 0.40 M of EDC and 0.10 M of NHS in 10 mM PBS pH 7.4 solution for 2 h. The electrode was further rinsed with water and dried with argon gas. The NHS-/EDC-activated electrode was then immersed in pH 7.4 PBS solution containing 25 mM 4-aminophenylboronic solution. After 6 h, the resulting phenylboronic acid electrode, represented as Au-MBA-APBA SAM, was rinsed with water and ethanol to remove unreacted 4-aminophenylboronic acid. The Au-MBA-ABPA SAM was further dried in continuous flow of argon atmosphere. The capture mouse antihuman CRP monoclonal antibody (mAb) was immobilized onto the Au-MBA-APBA SAM to give the Au-MBA-APBA-mAb. The Au-MBA-APBA SAM was immersed into the 10 µl mouse antihuman CRP at pH 7.4 solution (30 µg ml^{-1}) at 4°C for 24 h. The antibody-modified gold electrode was washed with PBS (pH 7.4) to remove the unbound antibodies. The unreacted boronic acid sites were blocked by reacting with glucose solution (30 µg ml^{-1} in pH 7.4 PBS) at room temperature for 2 h to give Au-MBA-APBA-mAb/glucose and was stored at 4°C before use.

Assay Procedure for Detection of Native Human CRP Using Au-MBA-APBA-mAb/Glucose

To assess the analytical performance of the Au-MBA-APBA-mAb/glucose immunosensor, 20 µL solution of CRP antigen with different concentrations ranging from 10 to 400 ng ml^{-1} in PBS (pH 7.4) was applied to the electrode surface. The Au-MBA-APBA-mAb/glucose electrode was incubated for 1 h at room temperature in the various CRP antigen concentrations. Functionalized electrode was reused several times, and the fresh Au-MBA-APBA-mAb/glucose surfaces were obtained by exposing the electrode to 0.1 M HCl solution. The cyclic voltammogram and the impedance were measured and found to be the same as that of a freshly prepared Au-MBA-APBA-mAb/glucose. All measurements were performed in triplicates. The analysis and fitting of the impedance data (Nyquist plot representation) was accomplished using the Randles–Sevcik equivalent circuit. The topology of the circuit contained a solution resistance (R_S) which was connected in series to a parallel combination of charge transfer resistance (R_{CT}) and capacitance (double layer, C_{DL} or constant phase element, CPE) with Warburg impedance (Zw) in the series to the R_{CT}. The fitted data was accepted if the %error was less than 5%.

The change in total charge transfer resistance (ΔR_{CT}) for each concentration was calculated using **Eq. 1**:

$$\Delta R_{CT} = R_{CT\left(Ab-Ag\right)} - R_{CT(Ab)} \tag{1}$$

where $R_{CT(Ab)}$ is the charge transfer resistance of the Au-MBA-APBA-mAb/glucose before the CRP antigen immunoreaction and $R_{CT(Ab\text{-}Ag)}$ is the value of the Au-MBA-APBA-mAb/glucose after an immunoreaction with the CRP antigen. Also for sandwich immunoassay, the $R_{CT(Ab\text{-}Ag)}$ represented the charge transfer after CRP antigen and polyclonal antibody immunoreaction.

RESULTS AND DISCUSSION

Fabrication of Anti-CRP Immunosensor

The fabrication of the CRP-sensing gold surface was modified following the step-by-step procedure shown in **Scheme 1** and as described in the experimental section above. The method followed was chosen to allow for oriented immobilization of the monoclonal mouse antihuman CRP antibody (mAb) *via* site-specific glycosylated (glycans) and boronic acid reaction. The unreacted boronic acid reactive surfaces from the Au-MBA-APBA-mAb were blocked with glucose. After glucose reaction, the immunosensor was represented as Au-MBA-ABPA-mAb/glucose. The step-by-step modification of gold surfaces was followed using electrochemistry and X-ray photoelectron spectroscopy (XPS).

Electrochemical Characterization of the Immunosensor Fabrication

Cyclic voltammetry (CV) and electrochemical impedance spectroscopy (EIS) were used to confirm the step-by-step fabrication of the Au-MBA-APBA-mAb/glucose immunosensor. The inhibition of electron transfer properties of the bare gold surface upon modification in the presence of redox probe, $[Fe(CN)_6]^{3-/4-}$, was use as a measure of surface functionalization. **Figure 1** shows (A) CV and (B) EIS of (i) bare

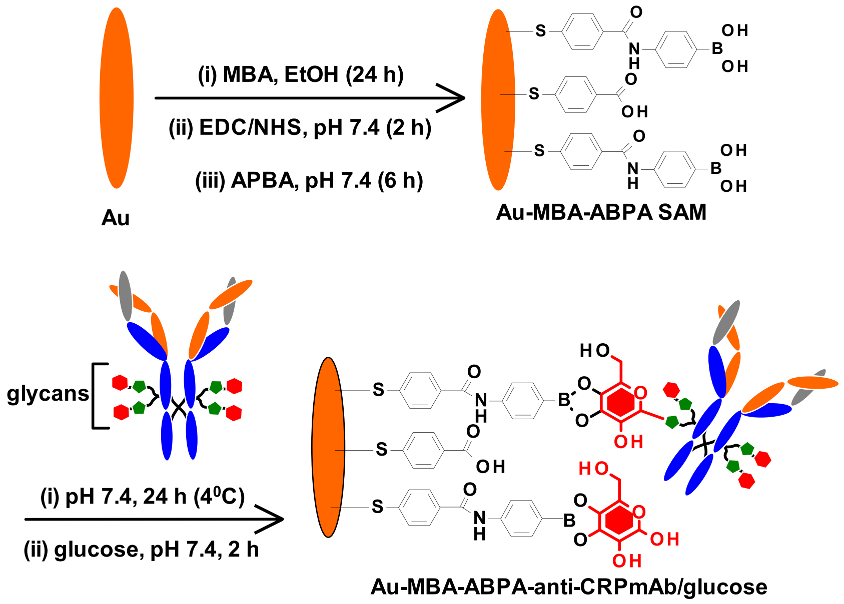

SCHEME 1 | Step-by-step modification of gold surface to form MBA-APBA SAM and the immobilization of monoclonal antihuman CRP antibody.

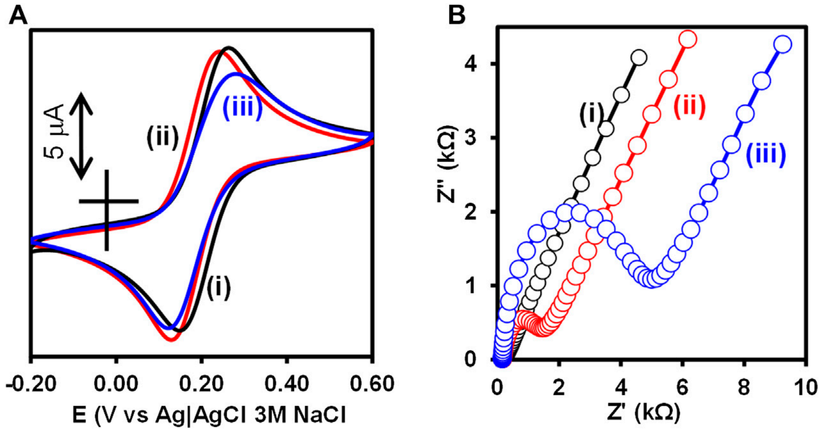

FIGURE 1 | (A) Cyclic voltammograms and **(B)** Nyquist plot of (i) bare Au, (ii) Au-MBA-APBA SAM, and (iii) Au-MBA-APBA-mAb/glucose in (1:1) 2 mM $K_3Fe(CN)_6$: $K_4Fe(CN)_6$ solution containing 0.10 M KCl.

Au, (ii) Au-MBA-APBA SAM, and (iii) Au-MBA-APBA-mAb/glucose in (1:1) 2 mM $K_3Fe(CN)_6$:$K_4Fe(CN)_6$ solution containing 0.1 M KCl. The cyclic voltammogram of the bare electrode, in **Figure 1Ai**, exhibited a reversible redox couple due to $[Fe(CN)_6]^{3-/4-}$ with peak-to-peak separation (ΔE) of 0.115 V. For Au-MBA SAM in **Supplementary Figure S1Aii**, an increase in ΔE from 0.115 to 0.167 V was observed due to electrostatic repulsion between the negatively charged carboxyl group and negatively charged $[Fe(CN)_6]^{-3/-4}$. The redox couple was not completely blocked as the Au-MBA SAM was still permeable to solution ions. A decrease in ΔE from 0.167 to 0.113 V was observed when amide coupling between Au-MBA SAM and 4-aminophenylboronic acid occurred, Au-MBA-APBA SAM in **Figure 1Aii**. The decrease in the peak-to-peak separation at the Au-MBA-APBA SAM was due to the coupling of 4-aminophenylboronic acid and neutralization of the COO^- functional group of Au-MBA SAM. The deprotonation of COO^- at Au-MBA SAM is due to the high pH conditions (pH 7.4) of the redox probing species solution, $[Fe(CN)_6]^{3-/4-}$, and the pKa of 5.8 for the carboxylic acid functional group of Au-MBA SAM. Upon amide coupling of the phenylboronic acid, the neutral monolayer resulted due to the fact that the pKa of the boronic acid (OH) functional group is 8.83. At the Au-MBA-APBA-mAb/glucose, in **Figure 1Aiii**, a slight decrease in current density was observed and due to the blocking behaviour and insulating properties of the mAb and glucose. In addition an increase in ΔE from 0.113 to 0.188 V was observed. The fabrication of Au-MBA-APBA-mAb/glucose resulted in a decrease in peak current density and an increase in ΔE in cyclic voltammogram. This confirms the successful

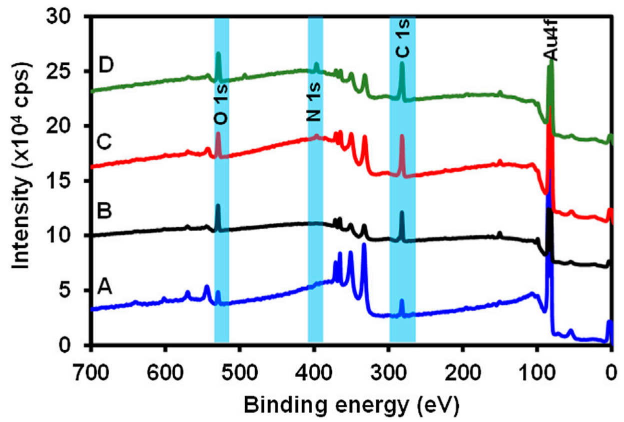

FIGURE 2 | The survey spectra of **(A)** bare Au, **(B)** Au-MBA SAM, **(C)** Au-MBA-APBA SAM, and **(D)** Au-MBA-APBA-mAb/glucose.

immobilization of the mAb and the blocking of nonspecific binding sites by glucose.

The electrochemical impedance spectroscopy was used to monitor and further confirm the immobilization of monoclonal anti-CRP antibody as this is a more sensitive technique than the cyclic voltammetry. The bare gold electrode exhibited a small semicircle at high frequency region with a charge transfer resistance (R_{CT}) value of 60.1 Ω, in **Figure 1Bi**. An increase in R_{CT} (3.10 kΩ) was obtained after the formation of the MBA SAM on the Au-electrode (Au-MBA SAM), in the ESI **Supplementary Figure S1Aii**. The increase in R_{CT} was an indication of the electrostatic repulsion between the negatively charged carboxyl (COO^-) groups of the Au-MBA SAM and the negatively charged $[Fe(CN)_6]^{3-/4-}$ ions. This reduces the ability of the $[Fe(CN)_6]^{3-/4-}$ ions to reach the underlying gold electrode surface and has been reported before (Moreno-Guzmán et al., 2012). Upon further modification with aminophenylboronic acid (Au-MBA-APBA SAM), in **Figure 1Bii**, a drastic decrease in R_{CT} from 3.10 to 1.10 kΩ was observed. This could be attributed to the neutralization of the negative charge carboxylic group upon reaction with the amino group of 4-aminophenylboronic acid. Upon the immobilization of mAb and blocking the nonspecific binding site with glucose, Au-MBA-APBA-mAb/glucose modified electrode, in **Figure 1Biii**, the R_{CT} increased from 1.10 to 4.09 kΩ due to the insulating properties of the immobilized monoclonal antibody and the glucose. This results in slow rate of electron transfer properties of the gold electrode and increase in the charge transfer resistance. The optimum concentration of glucose (30 μg ml^{-1}) for the blocking was used and did not have an effect on the capture of the biomarker (human CRP protein). Table S1 shows the summary of the CV and EIS parameters. The EIS and CV results confirm the successful modification of the electrode surface. Additional characterization of the gold electrode surface modification was carried out using surface sensitive and quantitative capabilities of the X-ray photoelectron spectroscopy (XPS).

XPS Characterization of the Immunosensor Fabrication

XPS is a highly sensitive, versatile, and quantitative surface characterization technique that gives insight into the type of bonding and interactions that exist on a surface (Korin et al., 2017). The elemental and the atomic composition can be evaluated using the XPS survey spectra, thus giving this technique the quantitative analytical capability (Etorki et al., 2012). To ascertain the successful fabrication of the immunosensor, different modification stages of the immunosensor design were characterized using XPS. **Figure 2** shows the survey spectrum of (**A**) bare Au, (**B**) 4-mercaptobenzoic acid modified surface (Au-MBA SAM), (**C**) 4-aminophenylboronic acid modified (Au-MBA-APBA SAM), and (**D**) anti-CRP antibody modified electrode (Au-MBA-APBA-mAb/glucose). The survey spectra of the bare Au revealed the presence of major peaks due to gold (Au 4f, Au 4p, and Au 4d) and other elements such as chromium (Cr), silver (Ag), oxygen (O1s), and carbon (C1s) peaks. The presence of carbon and oxygen peaks could be due to the washing of the bare Au surface using ethanol and air before measurement. The presence of silver and chromium peak is attributed to the surface coating of the gold-coated quartz crystal to obtain a smooth gold thin layer with the Cr underlayer and conducting silver. The atomic percentage (at %) of carbon and oxygen were found to be 45.2 and 12.2%, respectively, for the bare electrode (**Figure 2A**). Upon formation of the self-assembled monolayer of MBA (**Figure 2B**), a significant increase in both for carbon (from 45.2 to 60.4%) and oxygen (from 12.2 to 18.9%) was observed. The observed increase in both carbon and oxygen for the MBA SAM accounts for the successful formation of the self-assembled monolayer. Furthermore, the silver composition percent decreased from 5.67 to 1.67%. This is attributed to addition of the SAM layer on the electrode surface thereby causing a reduction of the silver concentration. The covalent immobilization of 4-aminophenylboronic acid onto Au-MBA SAM (**Figure 2C**, Au-MBA-ABPA SAM) resulted in the appearance of nitrogen (N 1s). The N 1s peak is attributed to amide (-CONH-) moiety that formed during the amide coupling of the 4-aminophenylboronic acid to the EDC-/NHS-activated COOH-terminated surface of the Au-MBA SAM. The presence of boron (B 1s) element was also seen at the APBA-modified electrode which is an indication of the successful modification of the electrode with APBA. A significant increase in the intensity of the N 1s peak was observed upon boronate ester formation of the Au-MBA-ABPA SAM with the Fc saccharides of the anti-CRP monoclonal antibody to yield an Au-MBA-ABPA-mAb surface (**Figure 2D**). The boronate ester reactions allow for the oriented immobilization of the antibody exposing the antigen-binding site. The increase in N 1s intensity at Au-MBA-ABPA-mAb is attributed to the immobilization of the antibody containing numerous peptide bonds.

Figure 3 shows the high-resolution C 1s (**A**) Au-MBA SAM, (**B**) Au-MBA-APBA SAM, and (**C**) Au-MBA-APBA-mAb/glucose and O 1s (**A’**) Au-MBA SAM, (**B’**) Au-MBA-APBA SAM, and (**C’**) Au-MBA-APBA-mAb/glucose. The deconvoluted C 1s high-resolution

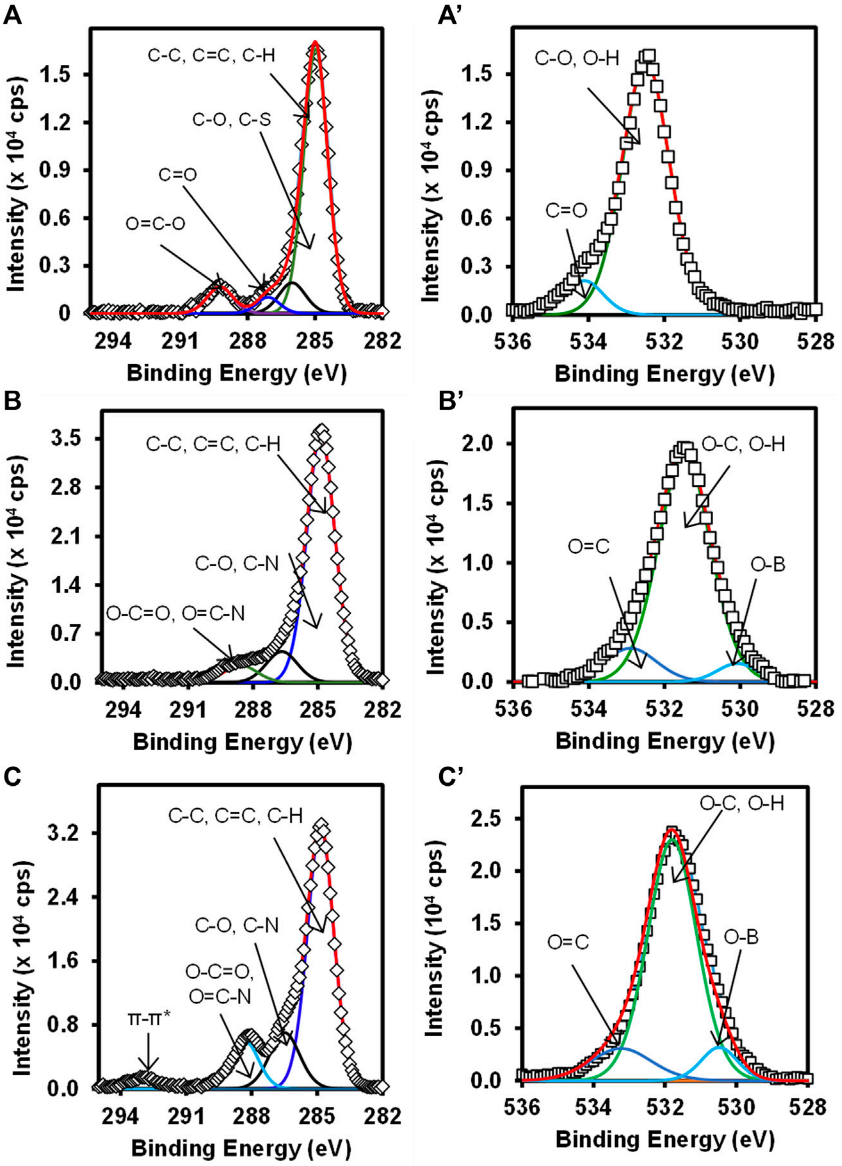

FIGURE 3 | High-resolution spectra of C 1s **(A)** Au-MBA SAM, **(B)** Au-MBA-APBA SAM, and **(C)** Au-MBA-APBA-mAb/glucose and O 1s **(A')** Au-MBA SAM, **(B')** Au-MBA-APBA SAM, and **(C')** Au-MBA-APBA-mAb/glucose.

spectra gave the chemical environment of carbon present on the surface and according to the material used for the modification. For Au-MBA-SAM (**Figure 3A**), four components were observed at 284.9, 286.0, 287.1, and 289.1 eV. The components observed at 284.9 eV was assigned to C-C, C=C, and C-H (Gruian et al., 2012; Maya Girón et al., 2016). The component at 286.0 eV was assigned to C-O and C-S from Au-MBA SAM. The component at 287.1 eV was assigned C=O. The component at 289.1 eV is due to O-C=O (Barriet et al., 2007; Fabre and Hauquier, 2017; Liu et al., 2016). The C 1s high resolution of the Au-MBA-APBA SAM surface (**Figure 3B**) shows three components at 284.9, 287.5, and 288.5 eV, and their assignments are similar to the Au-MBA SAM except the component at 288.5 eV is assigned N-C=O (amide bond) (Song and Yoon, 2009). The C 1s spectrum of Au-MBA-APBA-mAb/glucose surface was deconvoluted and four components were synthesized (**Figure 3C**) at 284.9, 287.0, 288.6, and 293.2 eV. The component at 284.9 eV is assigned as the above. The component at 287.0 eV corresponds to C-O, C-S, and C-N carbons of the protein backbone (Iucci et al., 2004). The third component at 288.6 eV is assigned to the carboxyl (O-C=O) and peptide carbon (N-C=O) (Lebugle et al., 1996) due to various amide bonds on the backbone of the antibody. The last component seen at 293.2 eV is the shake-up which is associated with carbon in the aromatic ring (Dave et al., 2015). The high-resolution O 1s for (**A'**) Au-MBA-SAM, (**B'**) Au-MBA-APBA SAM, and (**C'**) Au-MBA-APBA-mAb/glucose surfaces is also presented in **Figure 3**.

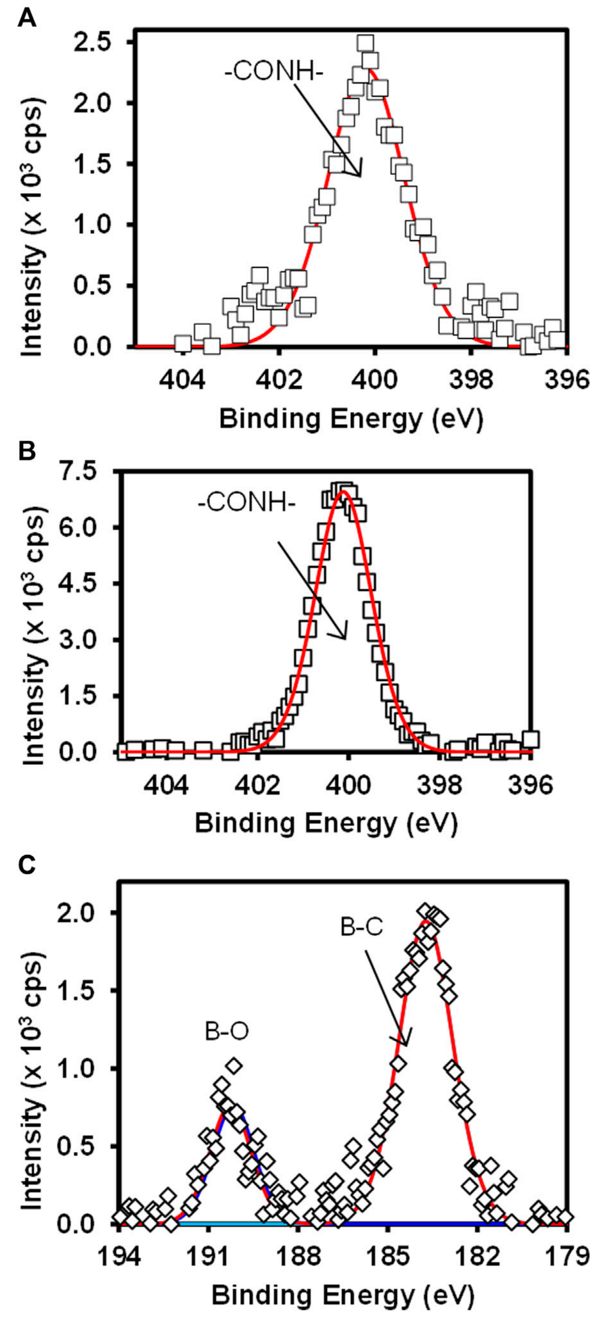

FIGURE 4 | High-resolution spectra of N 1s for **(A)** Au-MBA-APBA SAM and **(B)** Au-MBA-APBA-mAb/glucose and **(C)** the high-resolution spectrum of B 1s of Au-MBA-APBA SAM.

The deconvolution of the O 1s Au-MBA-SAM in **Figure 3A'** was fitted into two components. The component at 532.5 eV is assigned to the O-C and O-H of the mercaptobenzoic acid (Au-MBA SAM). The second component at 534.4 eV is due to the carbonyl oxygen (C=O) of the carboxyl group (Caprioli et al., 2013). The deconvolution of the O 1s spectrum in **Figures 3B',C'** for Au-MBA-APBA SAM and Au-MBA-APBA-mAb/glucose both fitted into three components. The components were observed at binding energies at 530.2, 531.6, and 532.7 eV for Au-MBA-APBA SAM corresponding to O-B, (O-C, O-H), and O=C, respectively. For the Au-MBA-ABPA-mAb/glucose, the binding energies were at 530.6, 531.6, and 533.1 eV corresponding to O-B, (O-C, O-H) and O=C, respectively, from the MBA-ABPA-mAb/glucose. The binding energy at 531.6 eV can be assigned to O-C and O-H (Whelan et al., 2004). The component centered at approximately 530.2 eV or 530.6 eV is assigned to B-O bond due to boron atom (Kim et al., 2017), and components at approximately 532.7 and 533.1 eV are attributed to the carbonyl oxygen (C=O) present in COOH and amide (HNCO) functional group (Kang et al., 2017). The presence of the observed carbon and oxygen species with their chemical environments confirmed the immobilization of the MBA, MBA-ABPA, and MBA-ABPA-mAb/glucose. There was also an increase in the intensity after each immobilization signifying the attachment of the various materials.

Figure 4 shows the high-resolution N 1s for (**A**) Au-MBA-APBA SAM and (**B**) Au-MBA-APBA-mAb/glucose surfaces and (**C**) the boron (B 1s) for Au-MBA-ABPA SAM. The high resolution of N 1s for Au-MBA-APBA SAM and Au-MBA-APBA-mAb/glucose in **Figures 4A,B** shows single component at 400.2 and 400.3 eV, respectively, attributed to the amide (CONH) bond (Costello et al., 2012; Eissa and Zourob, 2017). It was interesting to observe a remarkable increase in N 1s intensity from 2.5×10^3 cps to 7.5×10^3 cps after the immobilization of mAb/glucose on the Au-MBA-APBA SAM. This confirmed that blocking by glucose did not result in the displacement of mAb. Two major and distinct components were observed from the high-resolution spectrum of B 1s in **Figure 4C** and were centered at 183.9 and 190.5 eV. These components are indicative of the presence of boron element with two chemical environments. The component at 183.9 eV was assigned to B-C bond, while the other component at 190.5 eV was assigned to B-O bond (Yang et al., 2016). The presence of boron and nitrogen peaks on the Au-MBA-APBA SAM confirms the successful amide coupling of APBA onto an Au-MBA SAM. However, the disappearance of boron element was observed with the Au-MBA-APBA-mAb/glucose electrode and due to the bulky mAb and glucose boronate ester formation. This observation could further be attributed to the macro size of the mAb which confirms the successful immobilization of the antibody onto the MBA-APBA SAM functionalized gold surface. The quantitative analysis results are summarized in **Supplementary Table S2** (ESI).

Detection of Human CRP Antigen

The Au-MBA-APBA-mAb/glucose immunosensor was used to detect CRP antigen at different concentrations ranging from 10 to 400 ng ml^{-1} using direct and sandwich immunoassay formats. The total ΔR_{CT} values obtained with their relative standard deviation (% RSD) for the direct and sandwich assays at different CRP antigen concentrations are shown in **Table S3** (ESI). **Figure 5** shows the Nyquist plots (**A**) and (**B**) with their corresponding linear graphs of ΔR_{CT} against CRP antigen concentrations (**A'**) and (**B'**) for the (**A**) direct and (**B**)

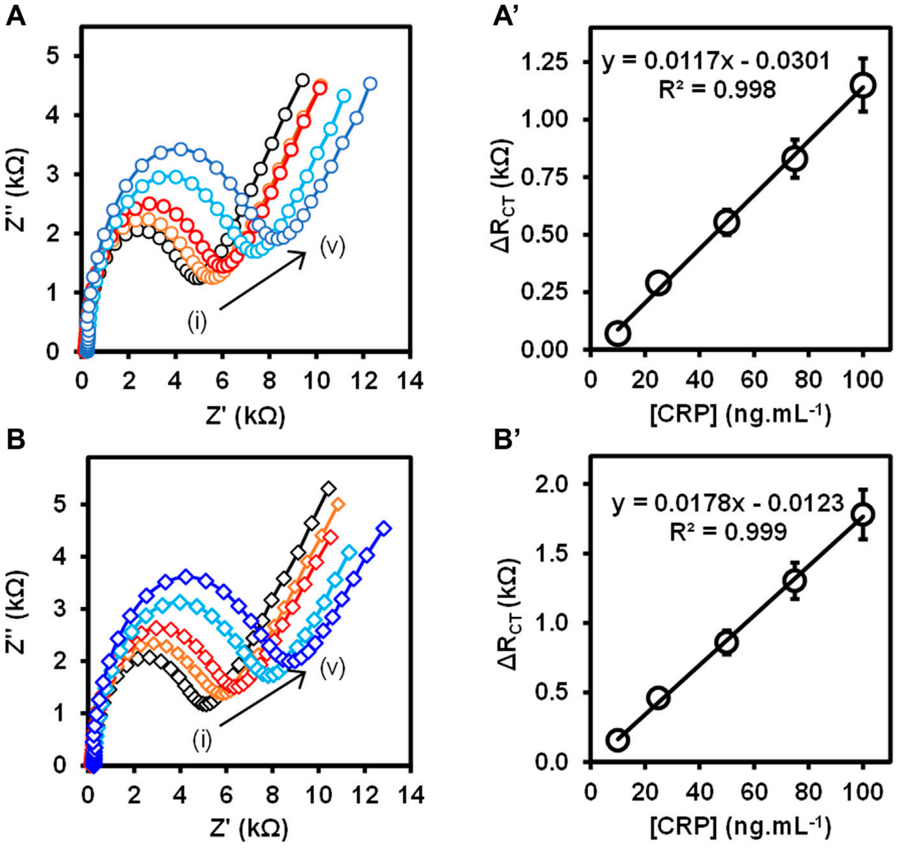

FIGURE 5 | (A,B) Nyquist plots and **(A',B')** the corresponding calibration curves at varied CRP antigen concentrations (i) 10 ng ml^{-1}, (ii) 25 ng ml^{-1}, (iii) 50 ng ml^{-1}, (iv) 75 ng ml^{-1}, and (v) 100 ng ml^{-1} for the **(A)** direct and **(B)** sandwich immunoassays. (n = 3, SD ≤ 9.0%).

sandwich immunoassays. For the direct immunoassay, the anti-CRP mAb/glucose immunosensor was exposed to the CRP antigen, and the impedance spectroscopy was measured. The increase in the charge transfer resistance (R_{CT}) was observed with increasing CRP antigen concentrations. The change in total charge transfer resistance (ΔR_{CT}) for each CRP antigen concentration was calculated using **Eq. 1**. ΔR_{CT} increased linearly with increasing antigen concentration from 10 to 100 ng ml^{-1} and the linear regression equation was ΔR_{CT} = 0.0117 [CRP antigen] −0.0301 and $R^2 = 0.998$ ($n = 3$), shown in **Figure 5A'**. However, at higher antigen concentration, a decrease in the R_{CT} value was observed between 200 and 400 ng ml^{-1} in **Supplementary Figure S2**, ESI. This is attributed to excess amount of CRP antigen competing for the same binding site, thus leading to partial binding. Upon rinsing the partially bound CRP antigen washes off. This phenomenon has been observed before (Songjaroen et al., 2016) for immunosensors based on antigen–antibody affinity detection. The high concentration of CRP antigen results in the reduction of the binding efficiency between the immobilized anti-CRP monoclonal antibody and CRP antigen. The sandwich assay using polyclonal anti-CRP antibody (pAb) that recognizes different epitopes on the captured CRP antigen was used for the signal amplification. The sandwich immunoassay involved two steps: 1) the capture of CRP antigen followed by rinsing and 2) exposing the captured CRP antigen to pAb. After rinsing, the impedance spectroscopy was recorded and R_{CT} was obtained after fitting the Nyquist plot using the Randles–Sevcik equivalent circuit.

Figure 5B shows the Nyquist plots for the detection of different concentrations of CRP antigen (10–100 ng ml^{-1}) for the sandwich immunoassay. The pAb was kept constant at 5.0 µg ml^{-1}. The increase in the semicircle (R_{CT}) was observed with increasing concentration of CRP antigen confirming that the binding occurred between the surface bound mAb antibody and CRP antigen and lastly the pAb, resulting in the mAb/CRP/pAb immunoreaction. The calibration curve is shown in **Figure 5B'** for the change in total charge transfer resistance according to **Eq. 1**, given above. The linear regression equation was ΔR_{CT} = 0.0178 [CRP antigen] −0.0123 with $R^2 = 0.999$ ($n = 3$) was obtained for the sandwich immunoassay. The sensitivity of the direct immunoassay was 0.585 kΩ ng^{-1} ml cm^{-2} and increased for the sandwich immunoassay to 0.885 kΩ ng^{-1} ml cm^{-2}. The increase in the sensitivity for the sandwich assay was attributed to the enhancement in the signal generated by the pAb as observed in **Figure 5B'**. The key analytical parameters for evaluating the developed method and the performance are the limit of detection (LoD) and limit of quantification (LoQ). The LoD and the LoQ were calculated using the IUPAC method of 3 × SD/m and 10 × SD/m, respectively, where m is the slope of the calibration curve and SD is

TABLE 1 | Analytical parameters for the electrochemical immunosensor for CRP antigen detection compared with reported methods.

Detection method	Assay linear range (ng ml^{-1})	Sens. (kΩ.ng^{-1}. mL.cm^{-2})	R^2	LoD (ng ml^{-1})	LoQ (ng ml^{-1})	Ref
Impedance spectroscopy	10–100^a 10–100^b	0.585^a 0.885^b	0.998^a 0.999^b	2.90^a 1.20^b	9.66^a 3.97^b	This work
Electrochemistry	50–5,000	—	—	11.0	—	Gupta et al. (2014)
Electrochemistry	8.5–9,120	—	—	3.50	—	Rajesh et al. (2010)
Electrochemistry	1.56–400	—	—	0.46	—	Lv et al. (2017)
Electrochemistry	0–100	—	—	2.2	—	Fakanya and Tothill. (2014)
Electrochemistry	0.5–200	—	—	1.2	—	Zhou et al. (2010)
Electrochemistry	0.2–80	—	—	0.040	—	Zhang et al. (2016)

^{a}*is the measurement using the direct immunoassay.*
^{b}*is the measurement using sandwich immunoassays.*

the standard deviation of the blank measurements without the presence of the CRP antigen. The LoD and LoQ for the direct immunoassay were calculated to be 2.90 and 9.66 ng ml^{-1}, respectively, and for the sandwich immunoassay, the LoD was 1.20 and LoQ was 3.97 ng ml^{-1}. The lower LoD and LoQ for the sandwich immunoassay were attributed to the high sensitivity and the signal amplification. The immunosensor is highly sensitive and shows lower LoDs and LoQs than the method used for the detection of CRP antigen and summarized in **Table 1**. The developed immunoassay for the detection of CRP is comparable in terms of the LoDs and linear concentration range to the various methods reported in **Table 1**. The enhanced detection and better analytical properties of the designed immunosensor is further attributed to the oriented immobilization of the capture monoclonal anti-CRP antibody (mAb). This method of immobilizing mAb *via* Fc-specific region using boronate ester allows for the CRP antigen site to be exposed to the analyte (CRP antigen). Lower LoDs 1.20 ng ml^{-1} and 2.90 ng ml^{-1} and LoQs 3.97 ng ml^{-1} and 9.66 ng ml^{-1} for sandwich and direct immunoassays are, respectively, reported for the detection of human CRP antigen. The LoDs were lower than those reported in literature (Rajesh et al., 2010; Gupta et al., 2014) and higher than the values reported by Lv et al. (2017). The better LoDs reported by Lv et al. (2017) used the quantum dots for fluorescence detection. However, the immunosensor yielded a very narrow range for the detection of human CRP, that is, 10–100 ng ml^{-1}. This range falls outside the clinically relevant range for the human CRP which is 1.0–3.0 ng μl^{-1}. The previously reported methods have a wider concentration range. The other parameter determined in this work was the sensitivity which was 0.585 kΩ ng^{-1} ml cm^{-2} for the direct immunoassay and 0.885 kΩ ng^{-1} ml cm^{-2} for the sandwich immunoassay. The reason for the observed narrow concentration range is that the capture mAb immobilized onto gold electrode surface reached saturation at human CRP concentrations of 100 ng ml^{-1} for both the direct and sandwich immunoassays. The study, however, paves a way of fabricating stable antibody thin films and their use in the detection of biologically relevant biomarkers.

Specificity and Reproducibility of the Fabricated Immunosensor

To assess the specificity of the immunosensor, a control experiment was carried out with the direct interaction of the anti-CRP mAb–modified gold electrode with the polyclonal anti-CRP antibody (pAb). R_{CT} for the anti-CRP mAb was found to be 5.46 kΩ, and after exposure to pAb, the R_{CT} value of 5.48 kΩ showed no change in R_{CT}. This confirmed that an increase in the total change in charge transfer resistance (ΔR_{CT}) between anti-CRP antibody (mAb) and the CRP antigen in **Figure 5** is due to the formation of an immunocomplex. Without the CRP antigen, there was no change in R_{CT} values 5.46 and 5.48 kΩ. The reproducibility of the immunosensor was investigated since it is a crucial factor to be considered in real-life applications. For reproducibility studies, three different immunosensors were prepared independently at the same and varied experimental conditions. The immunosensors were evaluated against the same CRP antigen concentration. The relative standard deviation (% RSD) for the immunosensor was found to be 4.47% for the direct immunoassay and 2.31% for the sandwich immunoassay tested for 50 ng ml^{-1} CRP antigen concentration. This confirmed that the method of designing the CRP antigen sensing was reproducible with about 2.31 and 4.47% variation.

Real Sample Analysis

The accuracy of the proposed immunosensor toward the detection of CRP antigen was investigated in serum sample through a recovery experiment. The recovery test was carried out in 10% newborn calf serum in PBS (pH 7.4). Two different CRP antigen concentrations (25 and 50 ng ml^{-1}) were used for the recovery experiment. The percentage obtained from the recovery test was between 91.18 and 96.47%. The amount recovered was very close to 100%. This shows that the immunosensor can be applied in clinical applications for the analysis of CRP antigen. The use of the newborn calf serum was to mimic the real samples. Human serum would have been ideal and is planned for future investigation. **Table 2** shows the summarized information for both the direct and sandwich immunoassays.

TABLE 2 | Spike and recovery results obtained from the fabricated CRP immunosensor in serum samples.

Sample number	Spiked (ng ml^{-1})	Found (ng ml^{-1})	Recovery (%)
1	25 (direct)	27.30	95.87
2	25 (sandwich)	26.50	96.47
3	50 (direct)	49.90	94.94
4	50 (sandwich)	49.00	91.18

CONCLUSION

This work demonstrated the fabrication of electrochemical impedimetric immunosensor for the detection of C-reactive protein antigen. The electrochemical and X-ray photoelectron spectroscopy characterization methods were used to confirm the formation of the self-assembled monolayer of 4-mercaptobenzoic acid, coupling of 4-aminophenylboronic acid *via* amide bond and immobilization of anti-human CRP monoclonal antibody onto gold electrode surface. The increase in intensity of C 1s, O 1s, and N 1s confirmed the immobilization and coupling (*via* amide and boronate ester) of various materials studied. An excellent sensitivity of the immunosensor was obtained to be $0.585\,\mathrm{k\Omega\,ng^{-1}\,ml\,cm^{-2}}$ for the direct immunoassay. An even better sensitivity was obtained for the sandwich immunoassay to be $0.885\,\mathrm{k\Omega\,ng^{-1}\,ml\,cm^{-2}}$ and almost double that of the direct immunoassay. The excellent sensitivity was ascribed to the oriented immobilization *via* boronate ester targeting an Fc region of the capture anti-CRP monoclonal antibody. The analytical parameters for the immunosensors for the direct immunoassay were calculated to be $2.90\,\mathrm{ng\,ml^{-1}}$ for LoD and $9.66\,\mathrm{ng\,ml^{-1}}$ for LoQ. For the sandwich immunoassay, the enhanced analytical parameters were $1.20\,\mathrm{ng\,ml^{-1}}$ for the LoD and $3.97\,\mathrm{ng\,ml^{-1}}$ for the LoQ. The immunosensor showed good reproducibility with % RSD of 4.47% for the direct immunoassay and 2.31% for the sandwich immunoassay. The immunosensor shows promising results toward the label-free detection of C-reactive protein. The newborn calf serum analysis showed good % recovery of the actual amounts injected in the sample. The % recovery ranged from 91.18 to 96.47%. Human plasma or blood samples are subject of our continued research for the detection of human CRP antigen as an important biomarker.

DATA AVAILABILITY STATEMENT

The original contributions presented in the study are included in the article/**Supplementary Material**; further inquiries can be directed to the corresponding author.

AUTHOR CONTRIBUTIONS

AA: Experimental design and analysis, draft manuscript, data collation, result interpretation, experimental design and analysis, PM: Postgraduate supervision, idea generation, manuscript drafting and finalization, result interpretation, experimental design and analysis, and project funding and resources.

FUNDING

Research reported in this publication was supported by the South African Medical Research Council under a Self-Initiated Research Grant (MRC-SIR); National Research Foundation through Thuthuka Post-PhD Programme (NRF-TTK UID-842230, Rated Incentive funding (UID 96001); and Rhodes University Research Council and Researcher Development Grant (RDG P5/17/2015). AA thanks Adekunle Ajasin University (Nigeria) for a sabbatical staff assistantship.

SUPPLEMENTARY MATERIAL

The Supplementary Material for this article can be found online at: https://www.frontiersin.org/articles/10.3389/fchem.2021.587142/full#supplementary-material

REFERENCES

Barriet, D., Yam, C. M., Shmakova, O. E., Jamison, A. C., and Lee, T. R. (2007). 4-mercaptophenylboronic Acid SAMs on Gold: Comparison with SAMs Derived from Thiophenol, 4-mercaptophenol, and 4-mercaptobenzoic Acid. *Langmuir* 23, 8866–8875. doi:10.1021/la7007733

Bogomolova, A., Komarova, E., Reber, K., Gerasimov, T., Yavuz, O., Bhatt, S., et al. (2009). Challenges of Electrochemical Impedance Spectroscopy in Protein Biosensing. *Anal. Chem.* 81, 3944–3949. doi:10.1021/ac9002358

Boonkaew, S., Chaiyo, S., Jampasa, S., Rengpipat, S., Siangproh, W., and Chailapakul, O. (2019). An Origami Paper-Based Electrochemical Immunoassay for the C-Reactive Protein Using a Screen-Printed Carbon Electrode Modified with Graphene and Gold Nanoparticles. *Microchim. Acta* 186 (1–10), 153. doi:10.1007/s00604-019-3245-8

Caprioli, F., Martinelli, A., Di Castro, V., and Decker, F. (2013). Effect of Various Terminal Groups on Long-Term Protective Properties of Aromatic SAMs on Copper in Acidic Environment. *J. Electroanalytical Chem.* 693, 86–94. doi:10.1016/j.jelechem.2013.01.025

Casas, J. P., Shah, T., Hingorani, A. D., Danesh, J., and Pepys, M. B. (2008). C-reactive Protein and Coronary Heart Disease: A Critical Review. *J. Intern. Med.* 264, 295–314. doi:10.1111/j.1365-2796.2008.02015.x

Chinnadayyala, S. R., Park, J., Kim, Y. H., Choi, S. H., Lee, S.-M., Cho, W. W., et al. (2019). Electrochemical Detection of C-Reactive Protein in Human Serum Based on Self-Assembled Monolayer-Modified Interdigitated Wave-Shaped Electrode. *Sensors* 19, 5560–5615. doi:10.3390/s19245560

Chowdhury, A., Singh, P., Bera, T. K., Ghoshal, D., and Chakraborty, B. (2017). Electrical Impedance Spectroscopic Study of Mandarin orange during Ripening. *Food Measure* 11, 1654–1664. doi:10.1007/s11694-017-9545-y

Clarke, J. L., Anderson, J. L., Carlquist, J. F., Roberts, R. F., Horne, B. D., Bair, T. L., et al. (2005). Comparison of Differing C-Reactive Protein Assay Methods and Their Impact on Cardiovascular Risk Assessment. *Am. J. Cardiol.* 95, 155–158. doi:10.1016/j.amjcard.2004.08.087

Costello, C. M., Kreft, J.-U., Thomas, C. M., Hammes, D. M., Bao, P., Evans, S. D., et al. (2012). Exploiting Additive and Subtractive Patterning for Spatially Controlled and Robust Bacterial Co-cultures. *Soft Matter* 8, 9147–9155. doi:10.1039/c2sm26111a

Dave, K., Park, K. H., and Dhayal, M. (2015). Characteristics of Ultrasonication Assisted Assembly of Gold Nanoparticles in Hydrazine Reduced Graphene Oxide. *RSC Adv.* 5, 107348–107354. doi:10.1039/c5ra23018g

Ding, P., Liu, R., Liu, S., Mao, X., Hu, R., and Li, G. (2013). Reusable Gold Nanoparticle Enhanced QCM Immunosensor for Detecting C-Reactive Protein. *Sensors Actuators B: Chem.* 188, 1277–1283. doi:10.1016/j.snb.2013.07.099

Dominici, R., Luraschi, P., and Franzini, C. (2004). Measurement of C-Reactive Protein: Two High Sensitivity Methods Compared. *J. Clin. Lab. Anal.* 18, 280–284. doi:10.1002/jcla.20038

Dong, S., Zhang, D., Cui, H., and Huang, T. (2019). ZnO/porous Carbon Composite from a Mixed-Ligand MOF for Ultrasensitive Electrochemical

Immunosensing of C-Reactive Protein. *Sensors Actuators B: Chem.* 284, 354–361. doi:10.1016/j.snb.2018.12.150

Eissa, S., and Zourob, M. (2017). Competitive Voltammetric Morphine Immunosensor Using a Gold Nanoparticle Decorated Graphene Electrode. *Microchim. Acta* 184, 2281–2289. doi:10.1007/s00604-017-2261-9

Etorki, A. M., Massoudi, F. M. N., and Abuein, M. M. (2012). X-ray Photoelectron Spectroscopy Study of Surface Complexation between Trace Metal Ions and Self-Assembled Monolayers. *Adv. Sci. Lett.* 17, 87–100. doi:10.1166/asl.2012.4240

Fabre, B., and Hauquier, F. (2017). Boronic Acid-Functionalized Oxide-free Silicon Surfaces for the Electrochemical Sensing of Dopamine. *Langmuir* 33, 8693–8699. doi:10.1021/acs.langmuir.7b00699

Fakanya, W., and Tothill, I. (2014). Detection of the Inflammation Biomarker C-Reactive Protein in Serum Samples: Towards an Optimal Biosensor Formula. *Biosensors* 4, 340–357. doi:10.3390/bios4040340

Gruian, C., Vanea, E., Simon, S., and Simon, V. (2012). FTIR and XPS Studies of Protein Adsorption onto Functionalized Bioactive Glass. *Biochim. Biophys. Acta (Bba) - Proteins Proteomics* 1824, 873–881. doi:10.1016/j.bbapap.2012.04.008

Gupta, R. K., Periyakaruppan, A., Meyyappan, M., and Koehne, J. E. (2014). Label-free Detection of C-Reactive Protein Using a Carbon Nanofiber Based Biosensor. *Biosens. Bioelectron.* 59, 112–119. doi:10.1016/j.bios.2014.03.027

Hansson, G. K. (2005). Inflammation, Atherosclerosis, and Coronary Artery Disease. *N. Engl. J. Med.* 352, 1685–1695. doi:10.1056/NEJMra043430

Hu, W. P., Hsu, H.-Y., Chiou, A., Tseng, K. Y., Lin, H.-Y., Chang, G. L., et al. (2006). Immunodetection of Pentamer and Modified C-Reactive Protein Using Surface Plasmon Resonance Biosensing. *Biosens. Bioelectron.* 21, 1631–1637. doi:10.1016/j.bios.2005.11.001

Iucci, G., Polzonetti, G., Infante, G., and Rossi, L. (2004). XPS and FT-IR Spectroscopy Study of Albumin Adsorption on the Surface of Aπ-Conjugated Polymer Film. *Surf. Interf. Anal.* 36, 724–728. doi:10.1002/sia.1747

Kang, F., Qu, X., Alvarez, P. J. J., and Zhu, D. (2017). Extracellular Saccharide-Mediated Reduction of Au3+to Gold Nanoparticles: New Insights for Heavy Metals Biomineralization on Microbial Surfaces. *Environ. Sci. Technol.* 51, 2776–2785. doi:10.1021/acs.est.6b05930

Kim, D.-M., Moon, J.-M., Lee, W.-C., Yoon, J.-H., Choi, C. S., and Shim, Y.-B. (2017). A Potentiometric Non-enzymatic Glucose Sensor Using a Molecularly Imprinted Layer Bonded on a Conducting Polymer. *Biosens. Bioelectron.* 91, 276–283. doi:10.1016/j.bios.2016.12.046

Korin, E., Froumin, N., and Cohen, S. (2017). Surface Analysis of Nanocomplexes by X-ray Photoelectron Spectroscopy (XPS). *ACS Biomater. Sci. Eng.* 3, 882–889. doi:10.1021/acsbiomaterials.7b00040

Kowalczyk, A., Sęk, J. P., Kasprzak, A., Poplawska, M., Grudzinski, I. P., and Nowicka, A. M. (2018). Occlusion Phenomenon of Redox Probe by Protein as a Way of Voltammetric Detection of Non-electroactive C-Reactive Protein. *Biosens. Bioelectron.* 117, 232–239. doi:10.1016/j.bios.2018.06.019

Lebugle, A., Rovira, A., Rabaud, M., and Rey, C. (1996). XPS Study of Elastin-Solubilized Peptides Binding onto Apatite in Orthopaedic Biomaterials. *J. Mater. Sci. Mater. Med.* 7, 223–226. doi:10.1007/BF00119734

Libby, P., Ridker, P. M., and Maseri, A. (2002). Inflammation and Atherosclerosis. *Circulation* 105, 1135–1143. doi:10.1161/hc0902.104353

Liu, G., Qi, M., Zhang, Y., Cao, C., and Goldys, E. M. (2016). Nanocomposites of Gold Nanoparticles and Graphene Oxide towards an Stable Label-free Electrochemical Immunosensor for Detection of Cardiac Marker Troponin-I. *Analytica Chim. Acta* 909, 1–8. doi:10.1016/j.aca.2015.12.023

Lv, Y., Wu, R., Feng, K., Li, J., Mao, Q., Yuan, H., et al. (2017). Highly Sensitive and Accurate Detection of C-Reactive Protein by CdSe/ZnS Quantum Dot-Based Fluorescence-Linked Immunosorbent Assay. *J. Nanobiotechnol* 15, 1–10. doi:10.1186/s12951-017-0267-4

Makaraviciute, A., and Ramanaviciene, A. (2013). Site-directed Antibody Immobilization Techniques for Immunosensors. *Biosens. Bioelectron.* 50, 460–471. doi:10.1016/j.bios.2013.06.060

Maya Girón, J. V., Vico, R. V., Maggio, B., Zelaya, E., Rubert, A., Benítez, G., et al. (2016). Role of the Capping Agent in the Interaction of Hydrophilic Ag Nanoparticles with DMPC as a Model Biomembrane. *Environ. Sci. Nano* 3, 462–472. doi:10.1039/c6en00016a

Moreno-Guzmán, M., Ojeda, I., Villalonga, R., González-Cortés, A., Yáñez-Sedeño, P., and Pingarrón, J. M. (2012). Ultrasensitive Detection of Adrenocorticotropin Hormone (ACTH) Using Disposable Phenylboronic-Modified Electrochemical Immunosensors. *Biosens. Bioelectron.* 35, 82–86. doi:10.1016/j.bios.2012.02.015

Naumkin, A. V., Kraut-Vass, A., Gaarenstroom, S. W., and Powell, C. J. (2012). NIST X-ray Photoelectron Spectroscopy Database. *Meas. Serv. Div. Natl. Inst. Stand. Technol.* 20899, 20899. doi:10.18434/T4T88K

Nxele, S. R., Mashazi, P., and Nyokong, T. (2015). Electrode Modification Using Alkynyl Substituted Fe(II) Phthalocyanine *via* Electrografting and Click Chemistry for Electrocatalysis. *Electroanalysis* 27, 2468–2478. doi:10.1002/elan.201500212

Parra, M. D., Tuomola, M., Cabezas-Herrera, J., and Cerón, J. J. (2005). Use of a Time-Resolved Immunofluorometric Assay for Determination of Canine C-Reactive Protein Concentrations in Whole Blood. *Am. J. Vet. Res.* 66, 62–66. doi:10.2460/ajvr.2005.66.62

Pepys, M. B., and Hirschfield, G. M. (2003). C-reactive Protein: a Critical Update. *J. Clin. Invest.* 111, 1805–1812. doi:10.1172/jci1892110.1172/jci200318921

Quershi, A., Gurbuz, Y., Kang, W. P., and Davidson, J. L. (2009). A Novel Interdigitated Capacitor Based Biosensor for Detection of Cardiovascular Risk Marker. *Biosens. Bioelectron.* 25, 877–882. doi:10.1016/j.bios.2009.08.043

Qureshi, A., Gurbuz, Y., and Niazi, J. H. (2012). Biosensors for Cardiac Biomarkers Detection: A Review. *Sensors Actuators B: Chem.* 171-172, 62–76. doi:10.1016/j.snb.2012.05.077

Rajesh, V., Sharma, V., Tanwar, V. K., and Biradar, A. M. (2010). Electrochemical Impedance Immunosensor for the Detection of C-Reactive Protein in Aqueous Solution. *Sens. Lett.* 8, 362–369. doi:10.1166/sl.2010.1278

Repo, T., Paine, D. H., and Taylor, A. G. (2002). Electrical Impedance Spectroscopy in Relation to Seed Viability and Moisture Content in Snap Bean (Phaseolus vulgaris L.). *Seed Sci. Res.* 12, 17–29. doi:10.1079/ssr200194

Rodriguez, M. C., Kawde, A.-N., and Wang, J. (2005). Aptamer Biosensor for Label-free Impedance Spectroscopy Detection of Proteins Based on Recognition-Induced Switching of the Surface Charge. *Chem. Commun.*, 4267–4269. doi:10.1039/b506571b

Rong, Z., Chen, F., Jilin, Y., and Yifeng, T. (2019). A C-Reactive Protein Immunosensor Based on Platinum Nanowire/Titania Nanotube Composite Sensitized Electrochemiluminescence. *Talanta* 205, 120135. doi:10.1016/j.talanta.2019.120135

Song, S. Y., and Yoon, H. C. (2009). Boronic Acid-Modified Thin Film Interface for Specific Binding of Glycated Hemoglobin (HbA1c) and Electrochemical Biosensing. *Sensors Actuators B: Chem.* 140, 233–239. doi:10.1016/j.snb.2009.04.057

Songjaroen, T., Feeny, R. M., Mensack, M. M., Laiwattanapaisal, W., and Henry, C. S. (2016). Label-free Detection of C-Reactive Protein Using an Electrochemical DNA Immunoassay. *Sensing Bio-Sensing Res.* 8, 14–19. doi:10.1016/j.sbsr.2016.03.003

Sonuç Karaboğa, M. N., and Sezgintürk, M. K. (2018). Determination of C-Reactive Protein by PAMAM Decorated ITO Based Disposable Biosensing System: A New Immunosensor Design from an Old Molecule. *Talanta* 186, 162–168. doi:10.1016/j.talanta.2018.04.051

Vashist, S. K., and Luong, J. H. T. (2018). *Antibody Immobilization and Surface Functionalization Chemistries for Immunodiagnostics*. Elsevier, 19–46. doi:10.1016/B978-0-12-811762-0.00002-5

Verma, S., and Yeh, E. T. H. (2003). C-reactive Protein and Atherothrombosis-Beyond a Biomarker: an Actual Partaker of Lesion Formation. *Am. J. Physiology-Regulatory, Integr. Comp. Physiol.* 285, R1253–R1256. doi:10.1152/ajpregu.00170.2003

Vilian, A. T. E., Kim, W., Park, B., Oh, S. Y., Kim, T., Huh, Y. S., et al. (2019). Efficient Electron-Mediated Electrochemical Biosensor of Gold Wire for the Rapid Detection of C-Reactive Protein: A Predictive Strategy for Heart Failure. *Biosens. Bioelectron.* 142, 111549. doi:10.1016/j.bios.2019.111549

Vogt, S., Su, Q., Gutiérrez-Sánchez, C., and Nöll, G. (2016). Critical View on Electrochemical Impedance Spectroscopy Using the Ferri/Ferrocyanide Redox

Couple at Gold Electrodes. *Anal. Chem.* 88, 4383–4390. doi:10.1021/acs.analchem.5b04814

Wang, J., Guo, J., Zhang, J., Zhang, W., and Zhang, Y. (2017). RNA Aptamer-Based Electrochemical Aptasensor for C-Reactive Protein Detection Using Functionalized Silica Microspheres as Immunoprobes. *Biosens. Bioelectron.* 95, 100–105. doi:10.1016/j.bios.2017.04.014

Whelan, C. M., Ghijsen, J., Pireaux, J.-J., and Maex, K. (2004). Cu Adsorption on Carboxylic Acid-Terminated Self-Assembled Monolayers: A High-Resolution X-ray Photoelectron Spectroscopy Study. *Thin Solid Films* 464-465, 388–392. doi:10.1016/j.tsf.2004.06.041

Yang, J., He, X., Chen, L., and Zhang, Y. (2016). The Selective Detection of Galactose Based on Boronic Acid Functionalized Fluorescent Carbon Dots. *Anal. Methods* 8, 8345–8351. doi:10.1039/c6ay02530g

Yang, Y.-N., Lin, H.-I., Wang, J.-H., Shiesh, S.-C., and Lee, G.-B. (2009). An Integrated Microfluidic System for C-Reactive Protein Measurement. *Biosens. Bioelectron.* 24, 3091–3096. doi:10.1016/j.bios.2009.03.034

Yu, J., and Wang, B. (2010). Effect of Calcination Temperature on Morphology and Photoelectrochemical Properties of Anodized Titanium Dioxide Nanotube Arrays. *Appl. Catal. B: Environ.* 94, 295–302. doi:10.1016/j.apcatb.2009.12.003

Zhang, B., Tang, D., Liu, B., Chen, H., Cui, Y., and Chen, G. (2011). GoldMag Nanocomposite-Functionalized Graphene Sensing Platform for One-step Electrochemical Immunoassay of Alpha-Fetoprotein. *Biosens. Bioelectron.* 28, 174–180. doi:10.1016/j.bios.2011.07.016

Zhang, X., Hu, R., Zhang, K., Bai, R., Li, D., and Yang, Y. (2016). An Ultrasensitive Label-free Immunoassay for C-Reactive Protein Detection in Human Serum Based on Electron Transfer. *Anal. Methods* 8, 6202–6207. doi:10.1039/c6ay01464j

Zhou, F., Lu, M., Wang, W., Bian, Z.-P., Zhang, J.-R., and Zhu, J.-J. (2010). Electrochemical Immunosensor for Simultaneous Detection of Dual Cardiac Markers Based on a Poly(dimethylsiloxane)-Gold Nanoparticles Composite Microfluidic Chip: A Proof of Principle. *Clin. Chem.* 56, 1701–1707. doi:10.1373/clinchem.2010.147256

Conflict of Interest: The authors declare that the research was conducted in the absence of any commercial or financial relationships that could be construed as a potential conflict of interest.

frontiers in Chemistry

ORIGINAL RESEARCH
published: 05 August 2021
doi: 10.3389/fchem.2021.643578

I-V Curves of an Apigenin Dye and Their Analysis by a New Parabolic Function

Kayode Sanusi[1]*, Olukayode S. Ajayi[1], Adegoke O. Borisade[2], Regina B. Elusiyan[1], Yusuf Yilmaz[3] and Ümit Ceylan[4]

[1]Department of Chemistry, Obafemi Awolowo University, Ile-Ife, Nigeria, [2]Centre for Energy, Research and Development, Obafemi Awolowo University, Ile-Ife, Nigeria, [3]NT Vocational School, Gaziantep University, Gaziantep, Turkey, [4]Department of Medical Services and Techniques, Vocational High School Health Services, Giresun University, Giresun, Turkey

A new parabolic function for I-V curves' analysis has been proposed. The new "analytical tool" provides a simple way to describe photophysical processes at an approximately monolayer surface of a dye-sensitized solar cell. It may now be possible to estimate factors such as hole–electron recombination, surface defects, and electron diffusion at the semiconductor layer. The theoretical approach that was previously reported by our group for predicting the photovoltaic performance of potential dye sensitizers has also been validated. The experimental photovoltaic and DFT/TD-DFT data of apigenin and those of the highly rated black dyes were used for the validation.

Keywords: ***Hibiscus rosa-sinensis*, renewable energy, photovoltaic cell, black dye, open-circuit voltage**

Edited by:
Shivani Mishra,
University of South Africa, South Africa

Reviewed by:
Daniel Tudor Cotfas,
Transilvania University of Braşov, Romania
Amiya Kumar Panda,
Vidyasagar University, India

***Correspondence:**
Kayode Sanusi
sosanusi@oauife.edu.ng
orcid.org/0000-0003-0358-8666

Specialty section:
This article was submitted to Physical Chemistry and Chemical Physics,
a section of the journal Frontiers in Chemistry

Received: *21 December 2020*
Accepted: *22 June 2021*
Published: *05 August 2021*

Citation:
Sanusi K, Ajayi OS, Borisade AO, Elusiyan RB, Yilmaz Y and Ceylan Ü (2021) I-V Curves of an Apigenin Dye and Their Analysis by a New Parabolic Function.
Front. Chem. 9:643578.
doi: 10.3389/fchem.2021.643578

INTRODUCTION

For more than 3 decades, scientists have been continuously and intensely engaged in the search for suitable dye systems to be used as sensitizers in the fabrication of highly efficient dye-sensitized solar cells (DSSCs) (Mehmood et al., 2014; Muchuweni et al., 2020). The target DSSCs are expected to produce overall efficiency of similar magnitudes as those of silicon-based solar cells (SBSCs) (Kwon et al., 2016; Gong et al., 2017). This, however, has not been achieved as most of the already-synthesized dye systems lacked the optical property require to produce an equivalent photoelectrical efficiency as those of the conventional SBSCs (Nazeeruddin et al., 2001; Mehmood et al., 2014; Kwon et al., 2016; Gong et al., 2017; Muchuweni et al., 2020). Of the already-synthesized plethora of dyes, the tricarboxy–terpyridyl ruthenium complex, commonly known as the black dye, is still the best photosensitizer (Nazeeruddin et al., 2001). The overall efficiency of the black dye in DSSC, nonetheless, is still far less than the conventional SBSCs.

Power generation has been a major challenge to global communities on account of the cost and negative impacts of activities that culminate into an eventual power production. Hundreds of thousands of research reports have been published since Thomas Edison's first power plant was commissioned in 1882 (Luo et al., 2015). The results of these research efforts have led to the development of various power generation technologies available today (Breeze, 2010; Luo et al., 2015). It is interesting to note that most of these technologies have associated heavy financial and/or environmental cost, making us to realize that power generation is not cheap (Breeze, 2010). Sources based on fossil materials or nuclear substances are few examples that show how financially and environmentally costly power production could be. Hydro, wind, ocean wave, and solar sources are now being considered as safe, alternative sources. Although, for most of the global communities, the accessibility of these new sources is still very low due to the cost of installation.

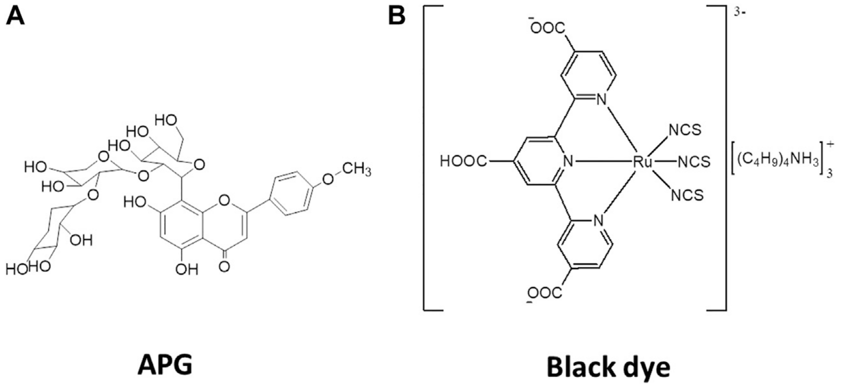

FIGURE 1 | Isolated dye molecule with chemical name: Apigenin-4′-methylether-8C-β-D-glucosyl-(1′→6)-2″-O-β-[xylopyranosyl-[1′′′′→ 2‴)-O-β-xylopyranosyl **(A)**, and 2*D*-structure of the black dye **(B)**.

The sun appears to be the easiest and the most accessible source of renewable energy amongst the identified sources. It is inexhaustible, quiet, and adjustable to enormous applications (Ludin et al., 2014; ByranvandMalekshahi, 2016). The amount of solar energy that gets into the Earth's surface at any moment has been estimated to have convertible power of about 120,000 TW; approximately 8,000 times higher than the present rate of the global energy consumption per year (Yin et al., 2012). Consequently, photovoltaic (PV) technology has been viewed as an important means of attaining a healthy environment and a sustainable global economy. It has the potential to offer a solution for the dwindling fossil energy reserves, as well as the current issues of climate change.

Despite the potential advantages that PVs offer, the cost of conventional highly crystalline silicon-based PVs is limiting the solar energy usage. Therefore, the harvesting and conversion of solar energy into electricity at low cost using abundantly available raw materials remains a major research focus. Chemistry is therefore expected to make valuable contributions in this regard, by providing environmentally friendly solutions, one of which is the "organic PVs" (OPVs). OPVs employ organic dyes for light harvesting and sensitization to produce electrical power (O'Regan and Grätzel, 1991; Grätzel, 2001; Grätzel, 2003; Grätzel, 2005; Yella et al., 2011).

The development of new organic dye OPVs has been dominated by natural photosensitizers, mostly because of their low cost, abundant supply, and sustainability (Gao et al., 2000; Hao et al., 2006; Fernando and Senadeera, 2008). The technology can be scaled up without running into raw material supply problem, giving it an advantage over the currently used silicon-based PVs, which uses inorganic materials that require highly specialized skill to fabricate. One of the earliest deployed natural dyes is 8′-apo-β-caroten-8′-oic acid bound to TiO_2 (Gao et al., 2000). OPVs based on these dyes are expected to produce an overall efficiency of similar magnitudes as those of the conventional SBSCs (Gao et al., 2000; Tryk et al., 2000; Hao et al., 2006; Fernando and Senadeera, 2008).

Notably, most of the dyes isolated or synthesized so far have not been quite successful in giving the required optical property that could produce equivalent photoelectrical efficiency as those of the known SBSCs. We have, therefore, in this article, tried to provide explanation on why the majority of dyes previously used have not given the desired photovoltaic response; knowing that the performance efficiency of OPVs depend majorly on the applied dye sensitizer. This effort has further helped validate our previously published theoretical model (Sanusi et al., 2019), which can act as a viable tool for predicting dyes' photovoltaic efficiencies.

In this study, an apigenin (APG) derivative isolated from the leaf extracts of *Hibiscus rosa-sinensis* plant was employed as the source of our test natural dye (**Figure 1A**). *Hibiscus rosa-sinensis* plant is known to constitute considerable amount of dye pigments and had been used in organic solar cells' fabrication previously (Fernando and Senadeera, 2008; Vankar and Shukla, 2011; Mansa et al., 2014). Comparisons between the computed and experimental photovoltaic properties of APG and the known tricarboxy–terpyridyl ruthenium complex (black dye = BD) have been made, as shown in **Figure 1B** (Nazeeruddin et al., 2001). To establish the relationship between theory and experiment, we used the computed and experimental photovoltaic data of APG and black dyes. While the experimental photovoltaic data of APG were obtained for this study, similar data for BD were taken from the literature (Nazeeruddin et al., 2001). The use of BD as the standard in this study was because it is currently the best synthetic photosensitizer for OPV cells (Wei et al., 2008; Hagfeldt et al., 2010; Feng et al., 2011; Akhtaruzzaman et al., 2013).

EXPERIMENTAL SECTION

Materials

Equipment and Methods

Electronic absorption spectrum of the isolated dye was collected on a Shimadzu UV-1800 spectrophotometer. ^1H and ^{13}C NMR data were collected on a Bruker Avance III 400 MHz spectrometer in DMSO-d_6. Infrared (FT-IR) spectrum was recorded on a PerkinElmer Spectrum 100 FT-IR spectrometer. The cells' I-V characteristics were determined using an intensity of ~35.7 W cm^{-2}, from a Newport 66245 Oriel lamp, which was coupled with a Kelthley 2400 multimeter. All solvents were distilled before use. TiO_2 paste was prepared with a mixture of 95% ethanol and 15% acetic acid at a volume ratio of 1:1. The iodide/triiodide redox solution employed was prepared by weighing 10 g of KI in 100 ml of distilled water, after which 15% acetic acid solution of iodine (obtained with pure iodine crystals) was slowly added. The resulting solution was filtered and the filtrate was kept in a tightly stoppered amber bottle. Five cell samples (1–5) were fabricated with the APG dye at different concentrations of the dye. The dye solutions were prepared in 1:1 volume of 95% ethanol and 15% acetic acid.

Structures of APG and BD dyes are depicted in **Figures 1A**,**B**, respectively. Both the ground and excited state calculations on the structures were performed using the Gaussian 09 package (Frisch et al., 2010). Ground state optimization and vibrational frequency of APG were carried out using B3LYP hybrid functional with the 6-311 g(d) basis set. Mixed basis sets with effective core potential LANL2DZ and 6-311 g(d) for C, H, N, O, and S atoms were used for BD at the B3LYP level. TD-DFT vertical excitation energies and the oscillator strengths were computed for the two dyes at the same level of theory employed for their optimization and frequency calculations. Solvent effects were incorporated in both the DFT and TD-DFT calculations using the integral equation formalism polarizable continuum model (IEF-PCM) (Tomasi et al., 2005) with acetonitrile (AcCN) and ethanol (EtOH) as solvents. Theoretical photovoltaic and photophysicochemical parameters of the two dyes were estimated as described in our previous article (Sanusi et al., 2019). The experimentally determined TiO_2 conduction band (CB) edge reported by Xu and Schoonen (2000) was employed in the determination of the LUMO-TiO_2 CB (δ_p) gap as described previously (Sanusi et al., 2019).

RESULTS AND DISCUSSION

Structural Characterization of the Isolated Dye Molecule

The APG molecule (412 mg) was isolated as a yellow amorphous powder. The ^1H NMR and ^{13}C NMR spectra exhibited signals due to aromatic systems and sugar moieties. The ^1H NMR spectrum of APG showed a pair of ortho-related protons, indicating the AA'BB' aromatic ring system due to ring B of flavonoid. The ^1H NMR spectrum of APG suggests one flavone unit with signals corresponding to many sugar moieties and one methoxy (-OCH_3) group. It also exhibited one down field peak at δ_H 13.33 ppm for chelated-OH, a pair of doublets (J = 8.8 Hz each) indicating *para* substituted ring B, and a singlet at δ 6.79 ppm due to H-3 on ring C. We observed another singlet at δ 6.48 ppm, which was assigned to H-6. A singlet observed at δ_H 3.87 ppm confirmed the presence of a methoxy (–OCH_3) group and was assigned to position 4′ on ring B of the flavone unit. The anomeric proton of the first sugar unit appeared as a broad signal at δ_H 4.87 ppm (J = 7.2 Hz, indicating *β*-configuration), while the remaining sugar protons appeared between δ 3.13 and 4.20 ppm. The ^{13}C NMR spectrum of this dye revealed two separate singlets corresponding to C-3 and C-6 positions of flavone nucleus, indicating a substituted C-8. The absence of meta-related coupling suggested a C-8 substituted flavone. Correlation between the anomeric proton δ_H 4.92 of the first glucose sugar unit and C-6 (δ_C 104.9) of the aglycone confirmed the attachment of the anomeric sugar carbon to the C-6 position of the flavone nucleus. Based on the 1D-NMR data and comparison of the data given in the literature (Nawwara et al., 2014), it could be concluded that the structure of APG is a 4′-methoxy derivative of vitexin (apigenin-4′-methylether-8C-glucopyranoside). The proton and carbon-13 NMR results have been summarized in **Table 1**.

It has been reported that specific functional groups are required for dyes to be effectively adsorbed onto the TiO_2 thin film (Chang et al., 2013). A previous study by Ahmad and Nafarizal (2010) also reported that some functional groups such as hydroxyl groups (–OH) and carbonyl groups (–CO) are important in providing points of attachment to the TiO_2 surface. **Table 2** shows the FT-IR spectra with diagnostic absorption bands within the wave band of 4,000–400 cm^{-1}. The FT-IR of the APG isolated from the *Hibiscus rosa-sinensis* leaf extract revealed the presence of CH_3 and CH_2 vibrations at 2,930 and 2,634 cm^{-1}, respectively. Moreover, vibrations of C=O at 1716 cm^{-1}, C–O at 1,043 cm^{-1}, C=C at 1,651 cm^{-1}, and O–H at 3,311 cm^{-1} were also observed. Calculated IR data for the APG is presented in **Figure 2** alongside the measured data. The computed IR data are in good agreement with the experiment, suggesting that the theoretical method adopted is suitable in the description of the molecular structure.

New Parabolic Function for Analyzing I-V Curves

Initially, it was thought that the experimental photovoltaic parameters (J_{sc} and V_{oc}) and the overall efficiencies ($\%PCE_{expt}$ and $\%\eta_{global}$) of the fabricated APG cells would increase with increasing dye concentration. Interestingly, what was observed was different from this expectation (**Table 3**). There was no clear trend in the observed photovoltaic data with respect to concentration. To explain this observation, a parabolic model, from which could be obtained certain physical parameters that may be useful in understanding the underlining photoelectrical processes, was proposed (**Eq. 1**).

$$J_{eff} = \gamma + \beta V - \delta V^{\alpha}, \tag{1}$$

$$V_{eff} = \beta V - \delta V^{\alpha}. \tag{2}$$

The representative experimental I-V profiles for the APG-based cells are presented in **Figure 3**, with the solid line representing the fitting curve. The graphs were fitted to the parabolic function described in **Eq. 1**. The model assumes that the effective potential (V_{eff}), **Eq. 2**, is a function of some intrinsic potential V, and some variable factors, *α*, *β*, and *δ*. The intrinsic potential V has been assumed to depend on dye electron injection efficiency (φ_{inj}), velocity of charge transport on the semiconductor medium (*ω*), and the amount of dye that is available (*n*) for sensitization. Both J_{eff} and V_{eff} in this case

TABLE 1 | ^{1}H (400 MHz, DMSO- d_6) and ^{13}C (100 MHz, DMSO- d_6) NMR data of isolated dye molecule (APG) and vitexin from the literature.

APG			**[a]Vitexin 2″-O-β-[xylosyl-(1⁗→2‴)-O-β-xylopyranosyl] from the literature**	
Position	**1H (ppm) *J* (Hz)**	**^{13}C (ppm)**	**1H (ppm) *J* (Hz)**	**^{13}C (ppm)**
2		164.3		163.72
3	6.79 s	102.7	6.76, s	102.44
4		182.3		182.00
5	13.33 s, (5-OH)	161.3		161.20
6	6.48 s	98.1	6.25, s	98.30
7		163.5		161.69
8		104.9		103.80
9		155.3		156.50
10		104.7		104.53
1′		121.7		121.50
2′	8.03, d, (8.8)	129.1	7.95, d, (8.0)	128.78
3′	6.91, d, (8.4)	115.9	6.98, d, (8.0)	115.98
4′		161.5		
5′	6.91, d, (8.4)	115.9	6.98, d, (8.0)	115.98
6′	8.03, d, (8.8)	129.1	7.95, d, (8.0)	128.78
4-(OCH3)	3.87 s	56.7		
Glucosyl signals				
1″	4.72, d, (8.4)	71.4	4.62, d, (8.5)	71.22
2″		82.9		83.26
3″		78.4		79.30
4″		69.9		69.80
5″		81.9		82.44
6 ″		61.3		61.95
Xylosyl signals				
1‴	4.87, d, (7.2)	96.4	4.80, d, (7.0)	97.73
2‴		81.8		83.51
3‴		73.1		73.25
4‴		67.8		68.13
5‴		64.4		65.45
Xylosyl signals				
1⁗	4.92, d, (9.2)	104.2	4.87, d, (7.0)	103.86
2 ⁗		74.4		73.80
3 ⁗		76.8		77.31
4 ⁗		69.2		68.12
5 ⁗		69.3		68.46

[a]*Data for vitexin derivative were obtained from reference (Nawwara et al., 2014).*

TABLE 2 | IR absorption band of APG isolated from *Hibiscus rosa-sinensis*.

Functional group	**APG absorption bands (cm^{-1})**
O-H	3,311
C=C	1,651
(sp^3) C-H	2,893, 2,634
C=O	1716
C-O	1,043

are unit-less values that describe charge and force factors, respectively. The variables, α, β, γ, and δ, which were obtained by fitting **Eq. 1** to the experimental I-V curves (**Figure 3**), may be described as the diffusion, hole–electron recombination, charge transfer, and surface defect factors, respectively, with all of them influencing the overall efficiencies of the DSSCs (%PCE and %η_{global}). γ was found to be 1×10^6 fold higher in magnitude than the experimental short circuit current (J_{sc}) for each of the cells 1–5. The diffusion factor α was observed to increase proportionally with the dye concentration (**Table 3**). The maximum effective charge factor ($J_{\text{max,eff}}$) was estimated by assuming that the intrinsic potential has a magnitude equivalent to that of V_{oc}, that is, the experimental V_{oc} was taken as V in **Eq. 1**. $J_{\text{max,eff}}$ values were found to vary with α, β, γ, and δ. The cell's overall efficiencies were found to depend on the $J_{\text{max,eff}}$ values (**Table 3**). As indicated in **Table 3**, cell 4 composing of $4.2 \times 10^{-2}\,\text{mol}\,\text{dm}^{-3}$ of APG produced the highest $J_{\text{max,eff}}$ value and global efficiency of 0.061 and 1.98%, respectively. A slight decrease in the value of β was also found to result in a significant increase in the $J_{\text{max,eff}}$ values (**Table 3**).

The fit factors α, β, γ, and δ, especially, were shown to affect the power conversion (%PCE), and the global (%η_{global}) efficiency values of the cells which have generally followed a noticeable trend for which the values in cell 2 < cell 5 < cell 1 < cell 3 < cell 4. It is worthy of note that cell 5 which contained the highest amount of dye gave a δ value of 3.744. This value is the highest of the five cells (**Table 3**), suggesting that it has the highest degree of surface defects, which could explain why it has one of the lowest power efficiencies. This high degree of surface defects might have

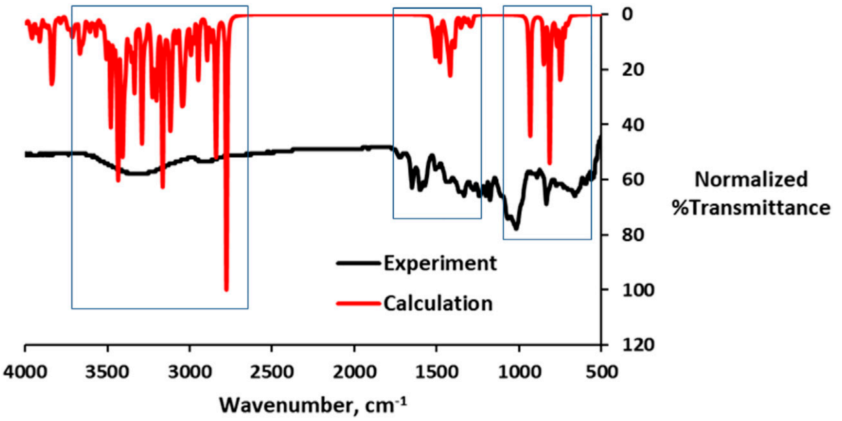

FIGURE 2 | Overlay of the calculated and experimental IR data (red = computed and black = experiment).

TABLE 3 | Experimental photovoltaic properties of the APG-based DSSCs at different concentrations as compared to the properties of the reported BD-based DSSC.

Cells	APG in EtOH at various conc. [mol. dm^{-3}]	J_{sc} [μA/cm^2]	V_{oc} [V]	%PCE_{expt}	%η_{global}	γ	α	β	δ	$J_{max,eff}$
1	1.1×10^{-2}	0.125	0.899	3.96×10^{-7}	1.49	0.125	5.50	4.53×10^{-2}	0.285	0.007
2	2.1×10^{-2}	0.141	1.000	1.65×10^{-7}	0.84	0.141	9.33	1.83×10^{-5}	0.088	0.053
3	3.2×10^{-2}	0.141	0.820	4.58×10^{-7}	1.53	0.141	9.54	1.96×10^{-5}	0.720	0.033
4	4.2×10^{-2}	0.129	0.842	7.46×10^{-7}	1.98	0.129	10.02	0	0.379	0.061
5	6.2×10^{-2}	0.128	0.880	3.09×10^{-7}	1.46	0.128	29.68	1.84×10^{-5}	3.744	0.045
^{a}BD	$\sim 2.0 \times 10^{-4}$	20.5×10^3	0.720	—	10.4	—	—	—	—	—

^{a}*Data for BD was obtained from reference (Nazeeruddin et al., 2001). $J_{max,eff}$ is the maximum effective charge factor that influence the power output of the DSSC assuming that the intrinsic potential has a magnitude equivalent to the V_{oc}. **1–5** represents the cells fabricated using different dye concentrations.*

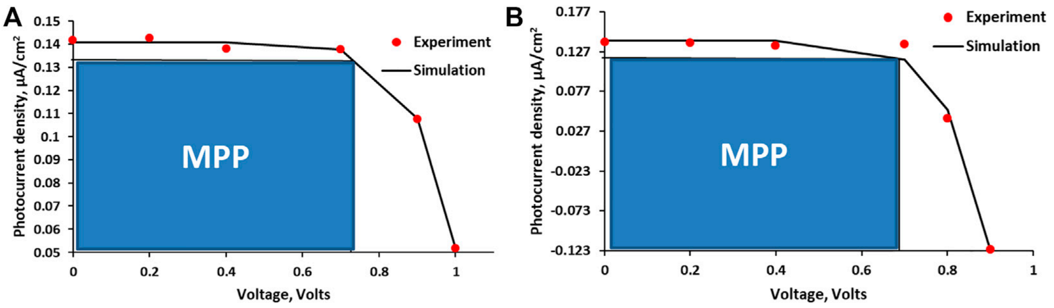

FIGURE 3 | I-V profiles (experimental and simulated) for cell 2 **(A)** and cell 3 **(B)** as representatives (MPP, maximum power point). The solid line represents the fitting curve obtained with **Eq. 1**.

resulted from the aggregation of dye molecules due to increasing dye concentration. With these fitting parameters, it may now be possible to explain I-V curves of different DSSCs.

Validation of Previous Theoretical Model

The observed electronic absorption property of the APG in Ethanol (EtOH) is depicted in **Figure 4** along with those obtained by TD-DFT methods in the gas phase, EtOH, and acetonitrile (AcCN). The observed spectrum showed a broad absorption band covering between 320 and 350 nm and peaked at ~340 nm (λ_{max}). The computed solution-phase electronic spectra showed similar pattern with the experiment but with slight blue-shifting compared to the latter. The agreement between the solution-phase electronic properties obtained *via*

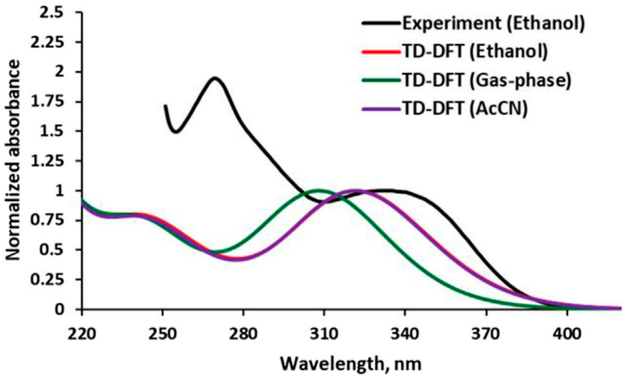

FIGURE 4 | Experimental (conc. ~1.10×10^{-5} mol/dm^3) and calculated electronic absorption spectra of APG in different media.

computation and the one by experiment indicates that the computational method employed is suitable. Solvent effects are noticeable in the computed λ_{max} when comparing APG in gas and solution phases (**Figure 4**). The superimposed computed spectra of APG in EtOH and AcCN are red-shifted relative to the gas phase.

It is understood that the lack of sufficient chromophoric groups in the isolated APG would put it at disadvantage for the proposed application, which requires high extinction coefficient over a wide spectral range, covering the visible to the near infrared region. Nonetheless, APG was an ideal choice of sample to validate the previous theoretical model for the prediction of dye's photovoltaic properties prior to the use of the dye (Sanusi et al., 2019). On the other hand, the BD which has shown relatively higher extinction coefficients (Nazeeruddin et al., 2001), spanning from the visible to the infrared region, is expected to show superior photovoltaic responses compared to APG, and so could serve as a suitable positive reference to validate the theoretical method (Sanusi et al., 2019). The experimental photovoltaic data showed that BD is in manifold better as a photosensitizer than the APG, with the overall efficiency ($\%\eta_{global}$) value being 5.25 times higher than that of the best APG-based cell (cell 4) (**Table 3**).

The computed absorption–emission spectral curves presented in **Figure 5** show the longer spectrum range covered by both absorption and emission curves of BD when compared to APG in

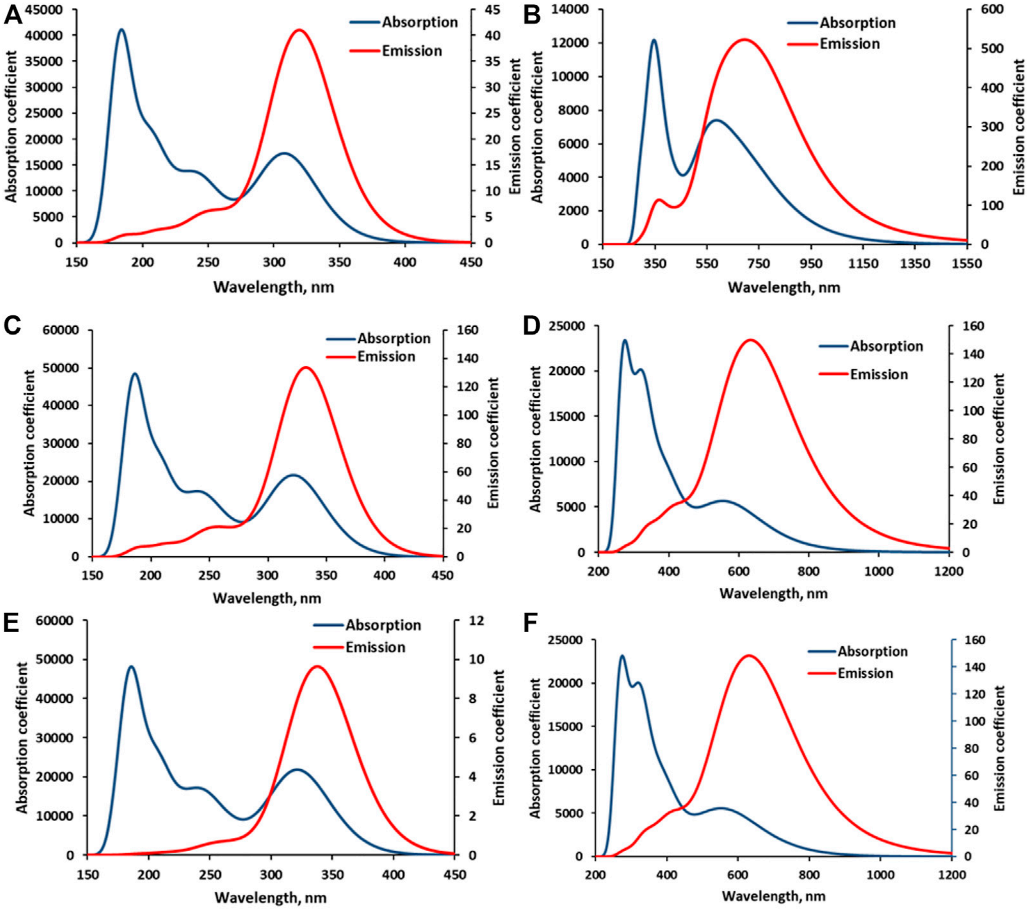

FIGURE 5 | Calculated electronic absorption and emission spectra of APG and BD in various media. **(A)** = APG in the gas phase, **(B)** = BD in the gas phase, **(C)** = APG in EtOH, **(D)** = BD in EtOH, **(E)** = APG in AcCN, and **(F)** = BD in AcCN.

TABLE 4 | Computed photophysicochemical and photovoltaic parameters of the APG and BD in gas and solution phases.

Sample	$f \times 10^{-3}$	LHE	ΔG_{inj}	$\varphi_{\text{inj}} \times 10^{-4}$	δ_p (eV)	$IPCE_{\text{calc}} \times 10^{-15}$	$\eta_c \times 10^{-12}$
APG in the gas phase	8.90	0.0203	−1.445	9.86	2.23	3.16	158
BD in the gas phase	93.7	0.194	−7.375	628	7.69	159	13.1
APG in EtOH	88.7	0.185	−1.574	26.7	2.12	1.76	3.57
BD in EtOH	135	0.267	−1.187	111	1.69	16.4	5.52
APG in AcCN	87.1	0.182	−1.577	34.6	2.11	6.46	10.3
BD in AcCN	137	0.271	−1.112	111	1.62	51.8	17.3

the three media—gas, EtOH, and AcCN. The calculated photovoltaic parameters, which include light-harvesting (LHE), electron injection efficiency (φ_{inj}), and incident photon conversion efficiency (IPCE) are mostly higher in BD than APG in the three media, except in the gas phase where the charge collection efficiency (η_c) is higher for APG. The δ_p term (potential gap) which is excessively high for BD in the gas phase could be responsible for the lower η_c. It may thus imply that the excited state BD is highly unstable in the gas phase, but much more stable in solution (**Table 4**). Overall, the conclusions from the computed data (**Table 4**) that BD is a better sensitizer for DSSCs do compare favorably with those of experiments (**Table 3**). This study, by comparing the experimental I-V data of APG and BD, to those predicted by our previously reported theoretical method, has confirmed the validity of the theoretical method. The method predicted that BD is a better sensitizer compared to APG, just as the experiments have done for the considered media phases, except in the gas phase. It is, however, worthy of note that there is no experimental gas phase photovoltaic data for these two sensitizers yet; hence, it would be impossible to know the validity of the theoretical result that shows APG as a better sensitizer in terms of η_c in the gas phase. The free-energy of injection (ΔG_{inj}) is generally negative for both dyes in the three media, suggesting that their electron injection from the LUMO to the TiO_2 CB edge would be spontaneous (**Table 4**).

CONCLUSION

A natural dye, an APG derivative, has been isolated from the leaf extracts of *Hibiscus rosa-sinensis* plant. The full structure of the isolated dye molecule has been elucidated by ^1H and ^{13}C NMR, FT-IR, and UV spectroscopic techniques. The I-V characteristics of the dye have also been measured, with further interpretation of the data given by the use of a new parabolic function. Activities at an approximately monolayer semiconductor surface, such as hole–electron recombination, surface defects, charge transfer, and electron diffusion factors could be determined from this model. The theoretical approach previously reported by our group for the prediction of dyes' photovoltaic performance has been validated. The experimental photovoltaic data obtained for the APG- and BD-based cells, together with the TD-DFT data of these dyes, were employed in the method validation.

DATA AVAILABILITY STATEMENT

The original contributions presented in the study are included in the article/Supplementary Material; further inquiries can be directed to the corresponding author.

AUTHOR CONTRIBUTIONS

KS: conceptualization, provision of research materials, supervision, results analysis, and wrote the article. OA: supervision, results analysis, and wrote the article. AB: technical engineer/technologist. RE: student (carried out the research) YY–NMR and IR data acquisition, ÜC–NMR data acquisition, and DFT/TD-DFT calculations.

FUNDING

This work was supported by the Federal Government of Nigeria Tertiary Education Trust Fund (FGN-TETFund) (Grant code: TETFUND/DESS/OAU/ILE-IFE/IBR/VOL.I).

REFERENCES

Ahmad, M. A. R., and Nafarizal, N. (2010). "Study on TiO_2 Film for Dye-Sensitized Solar Cell Using Natural Dyes," in Proceedings of the International Conference on Enabling Science and Nanotechnology (ESciNano '10), 1–2.

Akhtaruzzaman, Md., Islam, A., Karim, M. R., Hassan, A. K. M., and Han, L. (2013). Improving the Spectral Response of Black Dye by Cosensitization with a Simple Indoline Based Dye in Dye-Sensitized Solar Cell. *Hindawi Publ. Corp. J. Chem.* 2013, 1–5. doi:10.1155/2013/910527

Breeze, P (2010). *The cost of power generation: The current and future competitiveness of renewable and traditional technologies*. Business Insights.

ByranvandMalekshahi, M. (2016). Recent Development of Carbon Nanotubes Materials as Counter Electrode for Dye-Sensitized Solar Cells. *J. Nanostruct.* 6 (1), 1–16.

Chang, H., Kao, M., Chen, T., Chen, C., Cho, K., and Lai, X. (2013). Characterization of Natural Dye Extracted from Wormwood and Purple Cabbage for Dye-Sensitized Solar Cells. *Intern. J. Photoenerg* 2013, 8. doi:10.1155/2013/159502

Feng, Q., Wang, H., Zhou, G., and Wang, Z-S. (2011). Effect of Deoxycholic Acid on Performance of Dye-Sensitized Solar Cell Based on Black Dye. *Front. Optoelectron. China* 4 (1), 80–86. doi:10.1007/s12200-011-0209-y

Fernando, J. M. R. C., and Senadeera, G. K. R. (2008). Natural Anthrocyanins as Photosensitizers for Dye-Sensitized Solar Devices. *Curr. Sci.* 95 (5), 663–666.

Gao, P. G., Bard, A. J., and Kispert, I. D. (2000). Photocurrent Generated on a Carotenoid-Sensitized TiO_2 Nanocrystalline Mesoporous Electrode. J. Photochem. Photobiol. *A.* 130, 49–56. doi:10.1016/s1010-6030(99)00193-8

Gaussian, 09, Revision, C.01, Frisch, M. J., Trucks, G. W., Schlegel, H. B., Scuseria, G. E., et al. (2010). , Gaussian, Inc., Wallingford CT: Gaussian, Inc.

Gong, J., Sumathy, K., Qiao, Q., and Zhou, Z. (2017). Review on Dye-Sensitized Solar Cells (DSSCs): Advanced Techniques and Research Trends. Renew.*Renewable Sustainable Energ. Rev.* 68, 234–246. doi:10.1016/j.rser.2016.09.097

Grätzel, M. (2003). Dye-sensitized Solar Cells. *J. Photochem. Photobiol. C: Photochem. Rev.* 4, 145–153. doi:10.1016/s1389-5567(03)00026-1

Grätzel, M. (2001). Photoelectrochemical Cells. *Nature* 414, 38–344. doi:10.1038/35104607

Grätzel, M. (2005). Solar Energy Conversion by Dye-Sensitized Photovoltaic Cells. *Inorg. Chem.* 44, 6841–6851. doi:10.1021/ic0508371

Hagfeldt, A., Boschloo, G., Sun, L., Kloo, L., and Pettersson, H. (2010). Dye-sensitized Solar Cells. *Chem. Rev.* 110, 6595–6663. doi:10.1021/cr900356p

Hao, S., Wu, J. H., Huang, Y., and Lin, J. (2006). Natural Dyes as Photosensitizers for Dye-Sensitized Solar Cells. *Sol. Energ.* 80, 209–214. doi:10.1016/j.solener.2005.05.009

Kwon, J., Im, M. J., Kim, C. U., Won, S. H., Kang, S. B., Kang, S. H., et al. (2016). Two-terminal DSSC/silicon Tandem Solar Cells Exceeding 18% Efficiency. *Energy Environ. Sci.*, 1–9. doi:10.1039/c6ee02296k

Ludin, N. A., Al-Alwani Mahmoud, A. M., Bakar Mohamad, A., Sopian, K., and Abdul Karim, N. S. (2014). Review on the Development of Natural Dye Photosensitizer for Dye-Sensitized Solar Cells. *Renew. Sust. Energ. Rev.* 31, 386–396. doi:10.1016/j.rser.2013.12.001

Luo, X., Wang, J., Dooner, M., and Clarke, J. (2015). Overview of Current Development in Electrical Energy Storage Technologies and the Application Potential in Power System Operation. *Appl. Energ.* 137, 511–536. doi:10.1016/j.apenergy.2014.09.081

Mansa, R. F., Govindasamy, G., Farm, Y. Y., Bakar, H. A., Dayou, J., and Sipaut, C. S. (2014). Hibiscus Flower Extract as a Natural Dye Sensitizer for a Dye-Sensitized Solar Cell. *J. Phys. Sci.* 25 (2), 85–96.

Mehmood, U., Rahman, S.-u., Harrabi, K., Hussein, I. A., and Reddy, B. V. S. (2014). Recent Advances in Dye Sensitized Solar Cells. *Adv. Mater. Sci. Eng.* 2014, 1–12. doi:10.1155/2014/974782

Muchuweni, E., Martincigh, B. S., and Nyamori, V. O. (2020). Recent Advances in Graphene-Based Materials for Dye-Sensitized Solar Cell Fabrication. *RSC Adv.* 10, 44453–44469. doi:10.1039/d0ra08851j

Nawwara, M., El-Mousallamib, A., Husseina, S., Hashema, A., Mousaa, M., Lindequistc, U., et al. (2014). Three New Di-o-glycosyl-c-glucosyl Flavones from the Leaves of *Caesalpinia Ferrea* Mart. *Z. Naturforsch* 69c, 357–362. doi:10.5560/ZNC.2014-0113

Nazeeruddin, M. K., Péchy, P., Renouard, T., Zakeeruddin, S. M., Humphry-Baker, R., Comte, P., et al. (2001). Engineering of Efficient Panchromatic Sensitizers for Nanocrystalline TiO_2-Based Solar Cells. *J. Am. Chem. Soc.* 123 (8), 1613–1624. doi:10.1021/ja003299u

O'Regan, B., and Grätzel, M. (1991). A Low-Cost, High-Efficiency Solar Cell Based on Dye-Sensitized Colloidal TiO_2 Films. *Nature* 353, 737–740.

Sanusi, K., Fatomi, N. O., Borisade, A. O., Yilmaz, Y., Ceylan, Ü., and Fashina, A. (2019). An Approximate Procedure for Profiling Dye Molecules with Potentials as Sensitizers in Solar Cell Application: A DFT/TD-DFT Approach. *Chem. Phys. Lett.* 723, 111–117. doi:10.1016/j.cplett.2019.03.028

Tomasi, J., Mennucci, B., and Cammi, R. (2005). Quantum Mechanical Continuum Solvation Models. *Chem. Rev.* 105, 2999–3093. doi:10.1021/cr9904009

Tryk, D. A., Fujishima, A., and Honda, K. (2000). Recent Topics in Photoelectrochemistry: Achievements and Future Prospects. *Electrochim. Acta* 45, 2363–2376. doi:10.1016/s0013-4686(00)00337-6

Vankar, P. S., and Shukla, D. (2011). Natural Dyeing with Anthrocyanins from *Hibiscus Rosa-Sinensis* Flowers. *J. Appl. Polym. Sci.* 122, 3361–3368. doi:10.1002/app.34415

Wei, D., Unalan, H. E., Han, D., Zhang, Q., Niu, L., Amaratunga, G., et al. (2008). A Solid-State Dye-Sensitized Solar Cell Based on a Novel Ionic Liquid Gel and ZnO Nanoparticles on a Flexible Polymer Substrate. *Nanotechnol* 19, 424006–424010. doi:10.1088/0957-4484/19/42/424006

Xu, Y., and Schoonen, M. A. A. (2000). The Absolute Energy Positions of Conduction and Valence Bands of Selected Semiconducting Minerals. *Am. Min.* 85, 543–556. doi:10.2138/am-2000-0416

Yella, A., Lee, H. W., and Tsao, H. N. (2011). Porphyrin-sensitized Solar Cells with Cobalt (II/III)-based Redox Electrolyte Exceed 12 Percent Efficiency. *Science* 334, 629–634. doi:10.1126/science.1209688

Yin, J.-F., Velayudham, M., Bhattacharya, D., Lin, H.-C., and Lu, K.-L. (2012). Structure Optimization of Ruthenium Photosensitizers for Efficient Dye-Sensitized Solar Cells – A Goal toward a "Bright" Future. *Coord. Chem. Rev.* 256, 3008–3035. doi:10.1016/j.ccr.2012.06.022

Conflict of Interest: The authors declare that the research was conducted in the absence of any commercial or financial relationships that could be construed as a potential conflict of interest.

frontiers in Chemistry

ORIGINAL RESEARCH
published: 07 December 2021
doi: 10.3389/fchem.2021.633547

Poly-Phthalocyanine–Doped Graphene Oxide Nanosheet Conjugates for Electrocatalytic Oxidation of Drug Residues

*Prince Chundu, Edith Dube, Ngceboyakwethu P. Zinyama, Mambo Moyo and Munyaradzi Shumba**

Department of Chemical Sciences, Midlands State University, Gweru, Zimbabwe

Donor and acceptor phthalocyanine molecules were copolymerized and linked to graphene oxide nanosheets through amidation to yield electrocatalytic platforms on glassy carbon electrodes. The platforms were characterized using transmission electron microscopy (TEM), scanning electron microscopy (SEM), Fourier-transform infrared (FTIR) spectroscopy, UV/Vis spectroscopy, cyclic voltammetry, and electrochemical impedance spectroscopy. The fabricated electrochemical catalytic surfaces were then evaluated toward electrocatalytic detection of ascorbic acid and tryptophan. These were characterized by a wide linear dynamic range and low limits of detection and quantification of 2.13 and 7.12 μM for ascorbic acid and 1.65 and 5.5 μM for tryptophan, respectively. The catalytic rate constant was 1.86×10^4 and $1.51 \times 10^4\ M^{-1}s^{-1}$ for ascorbic acid and tryptophan, respectively. The Gibbs energy for catalytic reactions was –17.45 and –14.83 $kJ\ mol^{-1}$ depicting a spontaneous reaction on the electrode surface. The sensor platform showed an impressive recovery when applied in real samples such as fresh cow milk, in the range 91.71–106.73% for both samples. The developed sensor therefore shows high potential for applicability for minute quantities of the analytes in real biological samples.

Keywords: spontaneous reaction, real biological samples, amidation, poly-phthalocyanines, simultaneous electrodetection

Edited by:
Tebello Nyokong,
Rhodes University, South Africa

Reviewed by:
Abolanle Saheed Adekunle,
Obafemi Awolowo University, Nigeria
Lokesh Koodlur Sannegowda,
Vijayanagara Sri Krishnadevaraya University, India

****Correspondence:***
Munyaradzi Shumba
shumbamunya@staff.msu.ac.zw

Specialty section:
This article was submitted to Electrochemistry, a section of the journal Frontiers in Chemistry

Received: *25 November 2020*
Accepted: *04 October 2021*
Published: *07 December 2021*

Citation:
Chundu P, Dube E, Zinyama NP, Moyo M and Shumba M (2021) Poly-Phthalocyanine–Doped Graphene Oxide Nanosheet Conjugates for Electrocatalytic Oxidation of Drug Residues.
Front. Chem. 9:633547.
doi: 10.3389/fchem.2021.633547

INTRODUCTION

The electrocatalytic behavior of non-precious metals is enhanced when incorporated in macrocyclic ensembles such as phthalocyanines and porphyrins (Nyokong and Khene, 2016). These macrocyclics are very flexible to structure manipulation through different substituent introduction. The substituent can either pump or pull out electron density to or from the metal center. On the contrary, we have recently shown that the inclusion of carbon-based nanomaterials has resulted in improved electron flow and enhanced redox capabilities of the metal center in the macrocyclic ensemble (Shumba and Nyokong, 2016a). The approaches such as nanosizing and polymerization alike discourage aggregation which is prominent in phthalocyanines. Nanosizing encourages breaking down of the macrocyclics into smaller aggregates, while polymerization may not necessarily result in perfectly planar platforms, hence disrupting close proximity of subsequent layers in which cases aggregation is discouraged. The less aggregated the macrocyclics are, the more available the central metal is for electrocatalysis. Though polymerized phthalocyanines have been reported before (Nyokong and Khene, 2016; Liu et al., 2010;

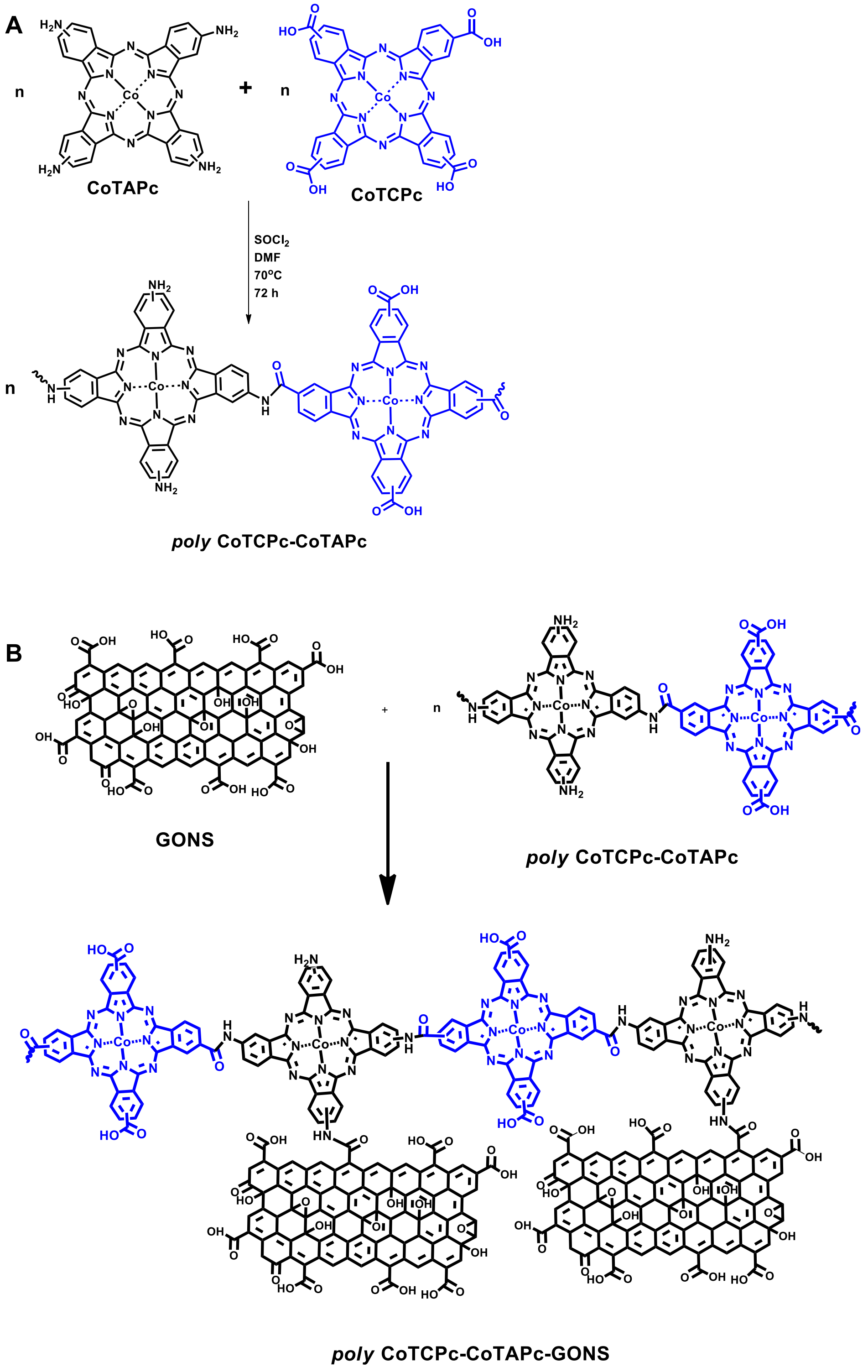

SCHEME 1 | Prepolymerization of CoTAPc and CoTCPc **(A)**; conjugation of polymeric phthalocyanines to graphene oxide nanosheets **(B)**.

Sekhosana et al., 2017), this work explores for the first time prepolymerization of differently substituted phthalocyanines. This was achieved through amidation of carboxylate- and amine-terminated phthalocyanines as described before (Moyo et al., 2016; Shumba and Nyokong, 2017), **Scheme 1A**. Poly-phthalocyanines (Pcs) are thought to have a higher concentration of the electroactive metal center, hence an enhanced electrocatalytic performance compared to monophthalocyanines (MPcs) (Nyokong and Khene, 2016). The amine-terminated phthalocyanines and prepolymerized Pcs were further covalently linked to graphene oxide nanosheets before being used as electrode modifiers, **Scheme 1B**. It is noteworthy that the linear representation of the polymers in **Scheme 1B** is for convenience and does not rule out the most probable random coupling of the MPcs. Amidation linkage between metallophthalocyanines and carbon-based nanomaterials has recently been reported to form highly stable electrocatalysts compared to pristine phthalocyanines (Liu et al., 2013). Electropolymerized phthalocyanines and their subsequent application as electrocatalysts have been reported before (Griveau et al., 2002; Nyoni et al., 2015; Nemakal et al., 2019; Sajjan et al., 2019), and here, we report for the first time the prepolymerized phthalocyanines for the same purpose. The uniqueness in the present paper is that the monomeric forms are different unlike in previously reported electropolymerization steps where one monomeric form was utilized.

Electrochemical detection of different analytes is gaining popularity due to its fastness, simplicity, reproducibility, less simple preparation protocol, and inexpensive nature. The only challenge is the lack of meaningful sensitivity and high detection potentials characteristic of conventional electrodes. This has prompted the need to look for better electrocatalysts to improve the performance of conventional electrodes. One prerequisite of such modifiers should be their inexpensiveness and availability, hence the popularity gained by carbon-based nanomaterials.

We have reported the use of polymer-appended phthalocyanines (Mafuwe et al., 2018) and carbon nanotube–appended phthalocyanines (Shumba and Nyokong, 2017) among other manipulations, and we have shown how these can be used as electrode modifier materials. Normally, push–pull effects have been reported with respect to asymmetric phthalocyanines (Erdem et al., 2008; Dumrul and Yuksel, 2013), but we hereby demonstrate the same effects *via* copolymerized symmetric phthalocyanines with different sets of substituents. Amine- and carboxyl-terminated phthalocyanines are co-linked to form polymer phthalocyanines and/or linked to graphene oxide nanomaterials. In essence, we explore the effect of substituent groups on the electrocatalytic behavior of phthalocyanines.

Tryptophan and ascorbic acid, as small biomolecules, are used as test analytes because of their presence in most biological environments. Their simultaneous detection becomes critical since they coexist in physiological environments. The detection of these molecules is important for their biomedical chemistry, neurochemistry, and both diagnostic and pathological research (Kałużna-Czaplińska et al., 2019) since out-of-range concentrations are associated with some physiological disorders (Filik et al., 2016).

EXPERIMENTAL

Materials

Chemicals used in this study were of pure analytical grade and used directly without further purification unless stated. Potassium ferrocyanide {$K_4[Fe(CN)_6]$}, potassium ferricyanide {$K_3[Fe(CN)_6]$}, sodium hydroxide (NaOH), dimethylformamide (DMF), potassium chloride (KCl), hydrochloric acid (HCl), ascorbic acid ($C_6H_8O_6$), L-tryptophan, cobalt chloride ($CoCl_2.6H_2O$), and potassium bromide (KBr) were obtained from ACE; methanol (CH_3OH) and ethanol (C_2H_5OH) were purchased from Glassworld; and trimellitic acid anhydride ($C_9H_4O_5$), ammonium chloride (NH_4Cl), urea [$CO(NH_2)_2$], nitrobenzene ($C_6H_5NO_2$), hydrochloric acid (HCl), thionyl chloride ($SOCl_2$), tetrahydrofuran (THF), potassium dihydrogen phosphate (KH_2PO_4), ammonium molybdate [$(NH_4)_2MoO_4$], sodium nitrate ($NaNO_3$), potassium permanganate ($KMnO_4$), hydrogen peroxide (H_2O_2), graphite flakes, sulfuric acid (H_2SO_4), and distilled water were locally prepared in the laboratory. The carboxylate-terminated (CoTCPc) and amine-terminated (CoTAPc) phthalocyanines (Moyo et al., 2016; Shumba and Nyokong, 2017) and graphene oxide nanosheets were synthesized as reported in the literature.

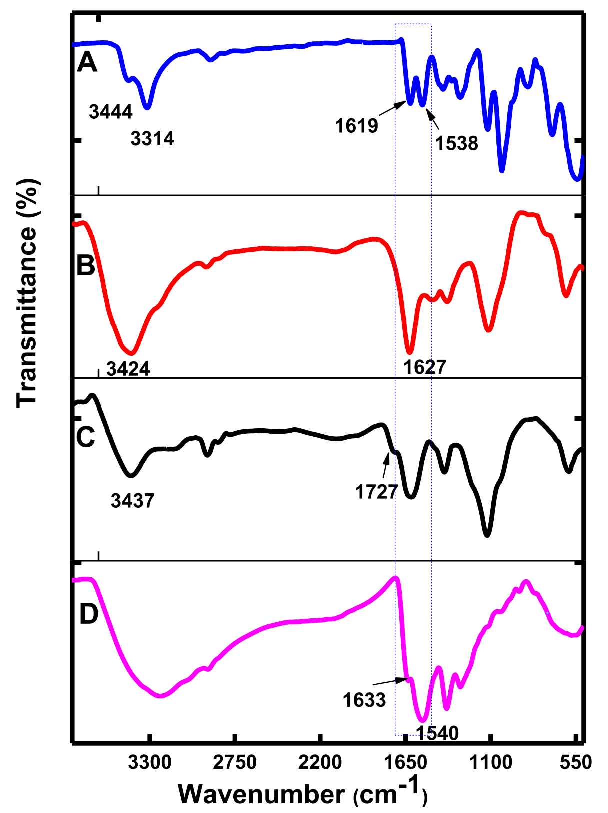

FIGURE 1 | FT-IR spectra of CoTAPc **(A)**, CoTAPc-GONS **(B)**, GONS alone **(C)**, and poly-CoTCPc-CoTAPc-GONS **(D)**.

Equipment

Transmission electron microscopy (TEM) images were obtained from a Zeiss Libra TEM 120 model operated at 90 kV. Scanning electron microscopy (SEM) images of modified glassy carbon plates (Goodfellow, UK) were obtained using a TESCAN Vega TS 5136LM electron microscope.

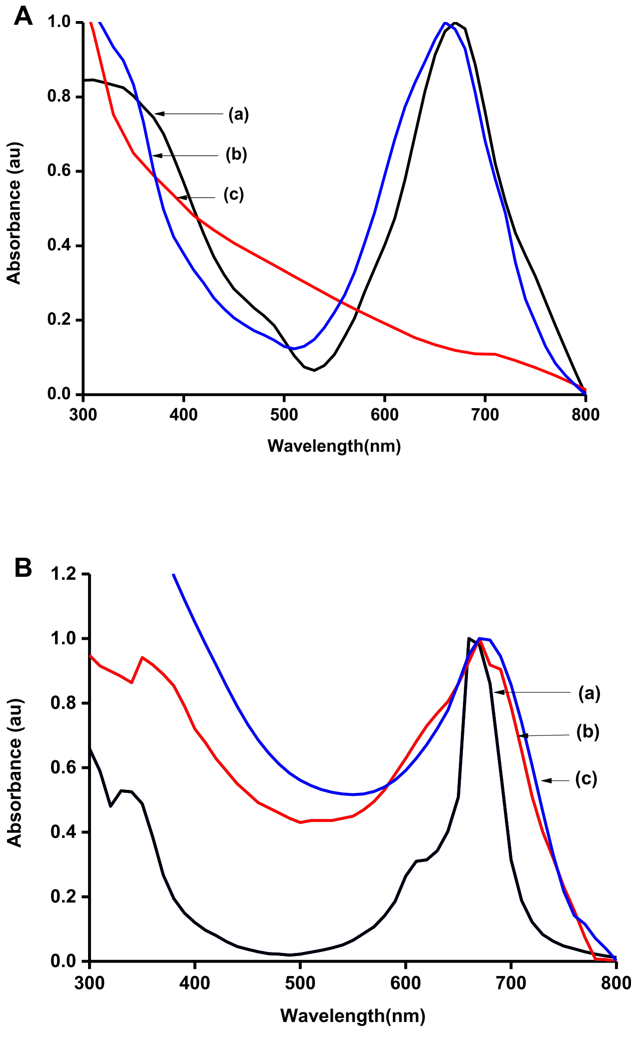

FIGURE 2 | Normalized UV/Vis spectra of electrode modifiers: **(A)** CoTAPc (a), CoTAPc-GONS (b), and GONS (c); **(B)** CoTCPc (a), poly-CoTCPc-CoTAPc (b), and poly-CoTCPc-CoTAPc-GONS (c) in DMSO.

The ground-state electronic absorption was measured using a Shimadzu UV-2550 spectrophotometer.

Fourier-transform infrared (FTIR) spectroscopy (Nicolet 6700 model) was used in IR characterization.

All electrochemical work was done on an Autolab potentiostat PGSTAT 302N equipped with NOVA version 1.10 software and encompassed with three electrochemical cells comprising of a glassy carbon working electrode (GCE), platinum wire auxiliary electrode, and saturated Ag|AgCl reference electrode.

Synthesis

Poly-CoTAPc-CoTCPc, poly-CoTAPc-CoTCPc-GONS, CoTAPc-GONS, CoTAPc, and GONS were covalently linked *via* an amide bond as reported before with minor modifications (**Scheme 1**) (Shumba and Nyokong, 2017). A mass of 0.02 g CoTAPc and 0.01 g GONS was added to 3 ml $SOCl_2$ and 6 ml DMF, and the mixture was stirred at 70°C for 72 h. The resulting mixture was allowed to cool to room temperature and then centrifuged for 20 min at 4,000 rpm, and the supernatant was decanted. The CoTAPc-GONS solid was washed with tetrahydrofuran several times and then with ethanol to remove the tetrahydrofuran. The CoTAPc-GONS solid was dried at room temperature. Poly-CoTCPc-CoTAPc and poly-CoTCPc-CoTAPc-GONS were synthesized by adopting the just described procedure with equal amounts of each Pc and used as electrode modifiers. These were utilized to modify glassy carbon

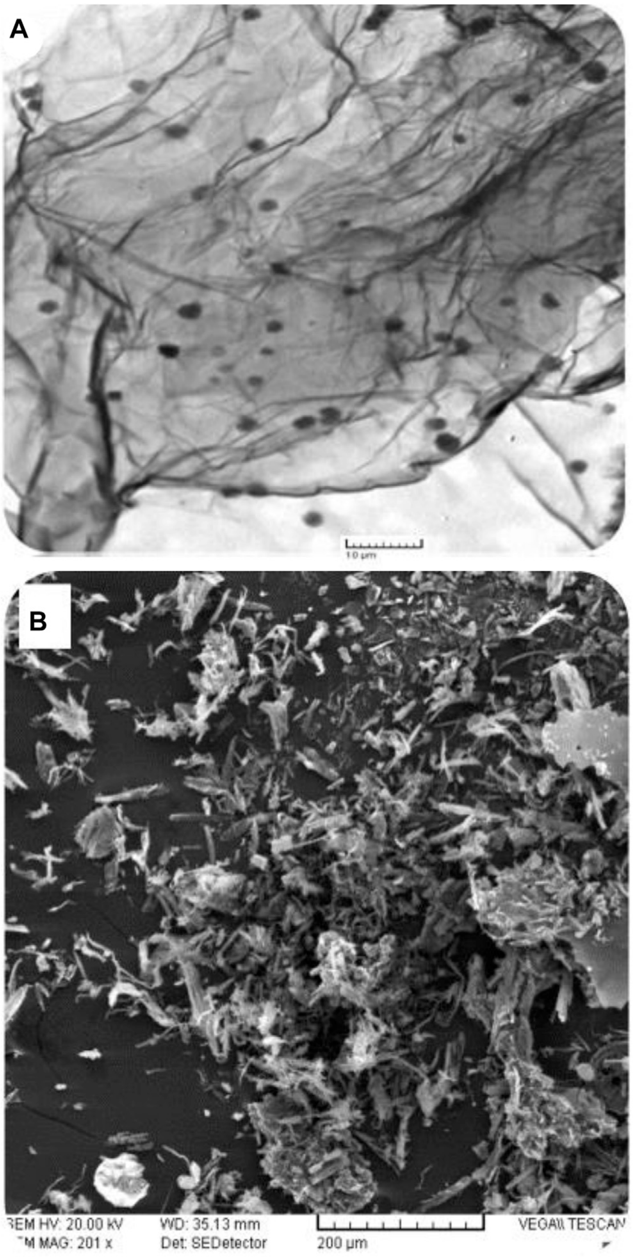

FIGURE 3 | Microscopic characterization: **(A)** TEM micrograph of poly-CoTAPc-CoTCPc-GONS; **(B)** SEM image of poly-CoTAPc-CoTCPc-GONS/GCE.

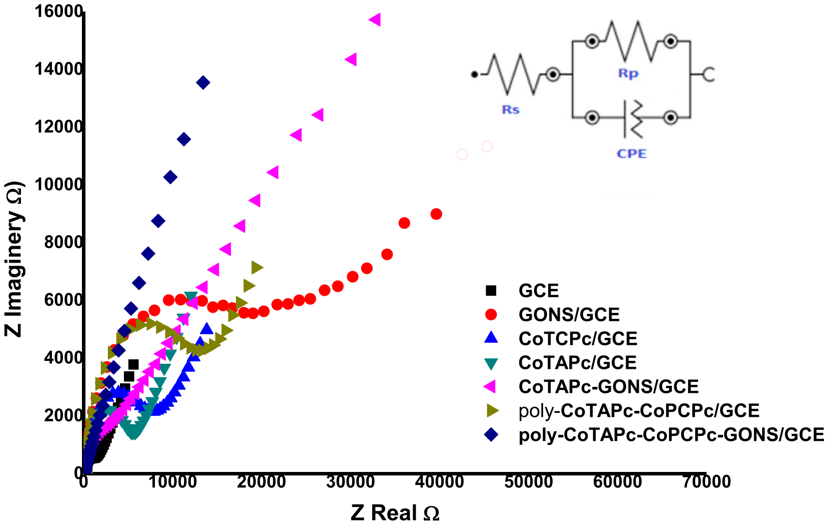

FIGURE 4 | Nyquist plots for the modified glassy carbon plots in a 0.2 mM $Fe^{2+/3+}$ redox system at 0.3 V (inset: Randles equivalent circuit).

electrodes as described before, and the resultant electrodes were named GO/GCE, CoTAPc/GCE, CoTCPc/GCE, poly-CoTAPc-CoTCPc-GCE, poly-CoTAPc-CoTCPc-GONS/GCE, and CoTAPc-GONS/GCE.

RESULTS AND DISCUSSION

Characterization

Spectroscopic Characterization

Fourier-Transform Infrared Spectra

The FTIR spectra (**Figure 1**, using CoTAPc, CoTAPc-GONS, GONS, and poly-CoTCPc-CoTAPc-GONS, and **Supplementary Figure S1**, using CoTCPc and poly-CoTCPc-CoTAPc) were employed to prove amide bond formation between CoTAPc and GONS, CoTAPc and CoTCPc, and poly-CoTCPc-CoTAPc and GONS. The spectrum of CoTAPc alone (**Figure 1A**) displayed peaks at 3,444 and 3,314 cm^{-1} and split peaks at 1,619 and 1,588 cm^{-1}, characteristic of primary amines. The spectrum of GONS (**Figure 1C**) displayed a peak at 3,437 cm^{-1} (OH) and shoulder peak at 1727 cm^{-1} (C=O) due to the presence of hydroxyl and carboxylic acid groups, respectively (**Scheme 1B**). Similar functional groups were displayed by CoTCPc when alone (**Supplementary Figure S1A**). The disappearance of the primary amine twin peaks and the appearance of the secondary carbon amide (O=C-NH) band which overlaps with the carbonyl group peak at around 1,627 cm^{-1} for CoTAPc-GONS (**Figure 1B**), and at 1,532 cm^{-1} for CoTCPc-CoTAPc (**Supplementary Figure S1B**), confirm the linkage of the carboxylic acid–functionalized complexes to amine-functionalized phthalocyanines through an amide bond. The spectra of poly-CoTCPc-CoTAPc-GONS (**Figure 1D**) show the secondary carbon amide peak at 1,540 cm^{-1} and hydroxyl and carboxyl groups at 3,300 and 1,633 cm^{-1}, respectively.

Ground-State Absorption Spectra

Ground-state absorption spectra were also run for the polymers and the carbonaceous materials (**Figures 2A,B**). The graphene materials produced a featureless spectrum that has been reported elsewhere (Ikram et al., 2020). MPcs were characterized by two main absorption regions, one around 300 nm (B-band) and the other above 600 nm (Q-band). The Q-band is attributed to the transition from the HOMO a_{1u} to the LUMO e_g, while the B-band is attributed to the transition from the HOMO a_{2u} to the HOMO e_g in monomer units of the MPcs (Kaya et al., 2015). The B-band was however swamped in the presence of graphene sheets. Metallophthalocyanines are well known for their tendency to form aggregates in solution, and hence, a shoulder is observed alongside the Q-band (Choi et al., 2019; Ghazal et al., 2019). The Q-band for poly-CoTCPc-CoTAPc (**Figure 2B(b)**) is split probably because the polymer is made from two Pcs with different Q-band positions that slightly overlapped on polymerization.

Microscopic Analyses

The nature of electrode modification determines the surface area available for interface between the analyte and the redox platform. As such, electrode surface morphology plays a very vital role in electrochemical reactions. It is noteworthy though that morphology only becomes vital given the fabricated platform's electron exchange capability. To this effect, scanning electron microscopy becomes a prerequisite to augment surface coverage determinations as a way to explore the nature of the sensing platform that ensues from such studies. The TEM micrograph shows the sheet structure of the graphene oxide nanosheets that are decorated by poly-phthalocyanines revealing as black spots spread over the sheet (**Figure 3A**). The SEM images show a rolled-up, flaked, and crumpled rough surface (**Figure 3B**). The rough structure of poly-CoTAPc-CoTCPc-GONS/GCE provides a high specific surface

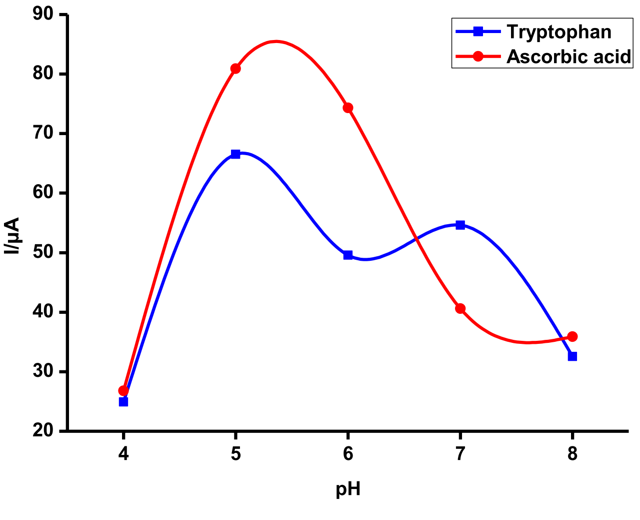

FIGURE 5 | Detection current variation with changes in pH on poly-CoTCPc-CoTAPc-GONS/GCE in the buffer solution at a scan rate of 100 mV/s.

area and high electron transfer rate, confirmed by the higher electroactive electrode surface area as determined above.

Electrochemical Characterization

The developed probes were characterized by electrochemical impedance spectroscopy. $[Fe(CN)_6]^{3-/4-}$ solution was chosen as the medium due to its well-known ease redox behavior. The potential at which to perform EIS studies was determined by cyclic voltammetry to be 0.3 V. The EIS parameters were obtained by fitting the Randles equivalent circuit (inset in **Figure 4**) to the experimental data and performing complex non-linear least-squares procedures available in an EIS data fitting computer program. The behavior of probes under electrochemical impedance studies is known to exhibit two sections: the circular part which is associated with resistance to charge transfer behavior and the straight line component associated with diffusion of redox materials toward the electrode surface (Wu et al., 2015). The higher the radius of the circle, the higher the difficulty with which the probe can facilitate redox reactions. The designed electrodes displayed different abilities to act as electron exchange platforms. The R_{CT} values in the above media varied in the following order: GONS/GCE (2.611 kΩ) > poly-CoTCPc-CoTAPc/GCE (2.207 kΩ) > CoTCPc/GCE (2.084 kΩ) > CoTAPc/GCE (1.901 kΩ) > CoTAPc-GONS/GCE (1.616 kΩ > GCE (1.179 kΩ) > poly-CoTCPc-CoTAPc-GONS/GCE (1.061 kΩ) (**Figure 4**). Similar results were obtained when the same investigation was done by cyclic voltammetry under the same conditions (figure not shown). The Bode plots also confirmed the modification of the glassy carbon electrodes, with phase angle shifting from 75° for GCE to 55° for poly-CoTCPc-CoTAPc-GONS/GCE and corresponding frequency decrease (**Supplementary Figure S2**), confirming efficient electron transfer and electrocatalysis after modification (Teo et al., 2021). It can be noted that the combination of the two differently substituted phthalocyanines in the absence of the electron-rich GONS compromised the electron transfer ability of the resultant electrodes, comparing poly-CoTCPc-CoTAPc/

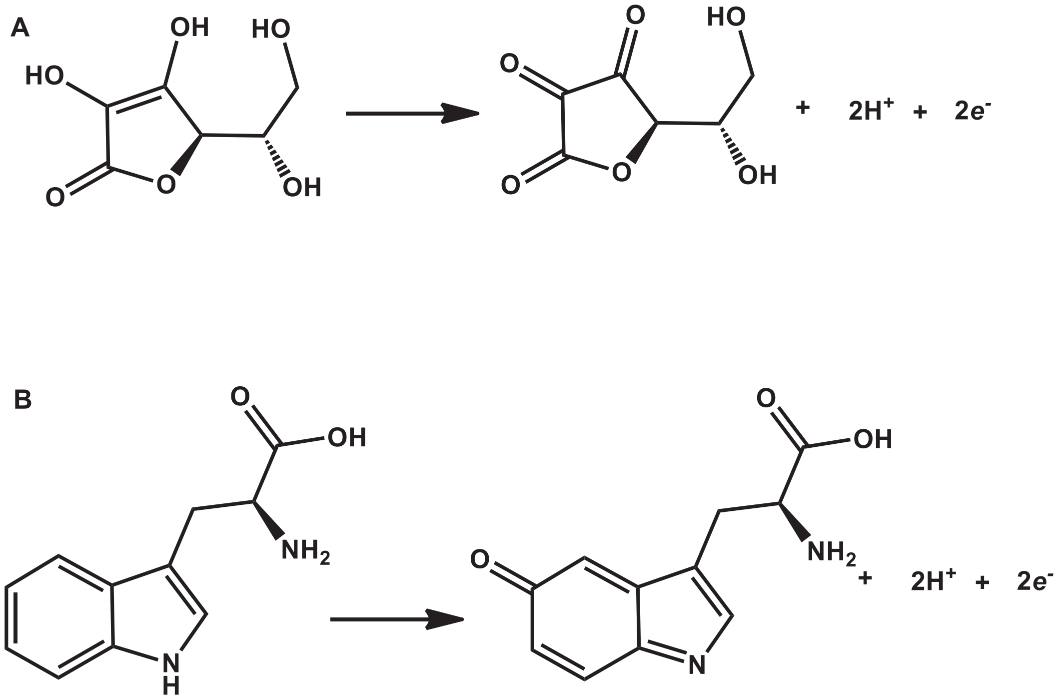

SCHEME 2 | Mechanism of detection of ascorbic acid **(A)** and tryptophan **(B)** on poly-CoTCPc-CoTAPc-GONS/GCE, respectively.

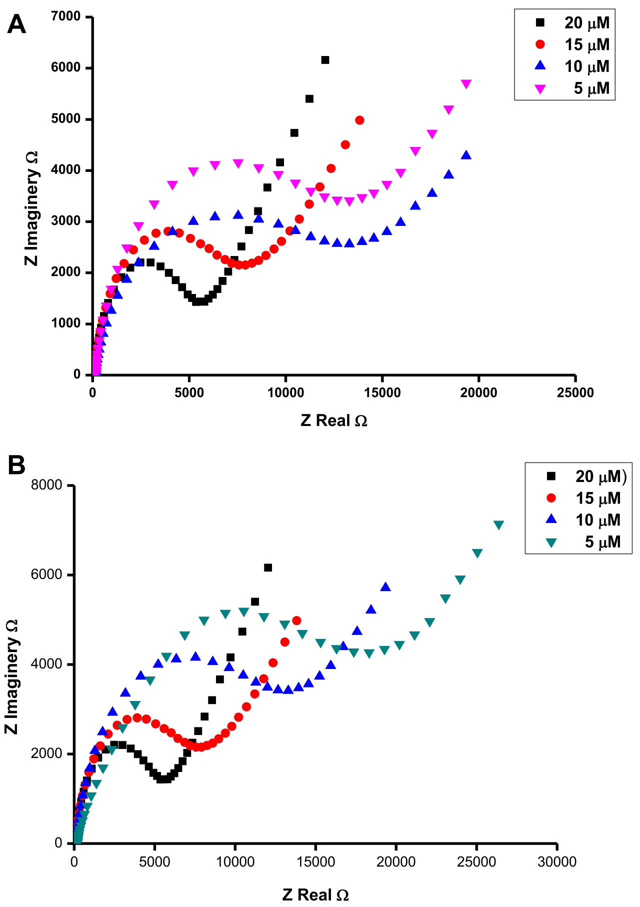

FIGURE 6 | Nyquist plots for ascorbic acid at 0.37 V **(A)** and tryptophan at 0.72 V **(B)** in different concentrations of respective analytes on the surface of poly-CoTCPc-CoTAPc-GONS/GCE at pH 5.

GCE (2.207 kΩ) with CoTCPc/GCE (2.084 kΩ) or CoTAPc/GCE (1.901 kΩ). The introduction of the graphene oxide moiety resulted in an improved electron transfer ability, comparing CoTAPc/GCE (1.901 kΩ) with CoTAPc-GONS/GCE (1.616 kΩ) and poly-CoTCPc-CoTAPc/GCE (2.207 kΩ) with poly-CoTCPc-CoTAPc-GONS/GCE (1.061 kΩ). This is attributable to the availability of abundant delocalized pi electron systems in sp^2 carbon skeletons, for electrical conductivity (Nkhahle et al., 2019). Carboxy-terminated phthalocyanines have a poor electron transfer ability compared to amine-terminated counterparts. This shows that the pull (electron withdrawing) effect of the carboxyl group reduces the availability of the pi electron system on the central metal (redox center) for redox participation or otherwise for amine-terminated macrocycles as observed elsewhere (Nkhahle et al., 2019). To further explore the nature of the modified electrode surfaces, the effective electroactive surface was determined in the same media because of a favorable electron exchange ability and established as follows: GONS/GCE 0.076 cm^2, poly-CoTCPc-CoTAPc/GCE 0.093 cm^2, CoTCPc/GCE 0.096 cm^2, CoTAPc/GCE 0.099 cm^2, CoTAPc-GONS/GCE 0.116 cm^2, and poly-CoTCPc-CoTAPc-GONS/GCE 0.134. These are improved surface areas from the geometrical area of a bare GCE of 0.071 cm^2, showing a highly improved electroactive area for poly-CoTCPc-CoTAPc-GONS/GCE. For this reason, the latter is going to be studied in depth for the remainder of this work.

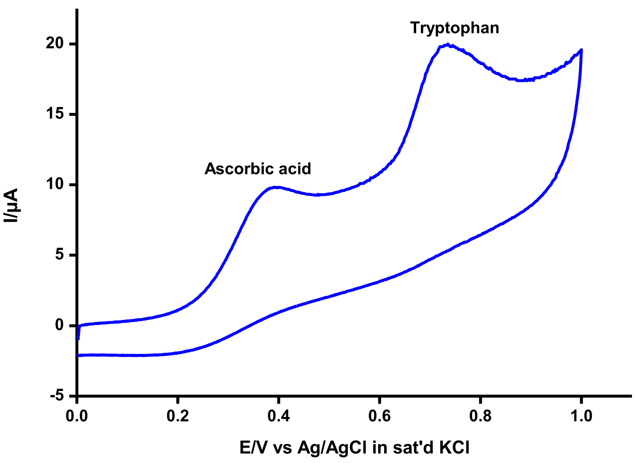

FIGURE 7 | Simultaneous detection of ascorbic acid and tryptophan by cyclic voltammetry on poly-CoTCPc-CoTAPc-GONS/GCE at pH 5. Scan rate, 100 mV/s.

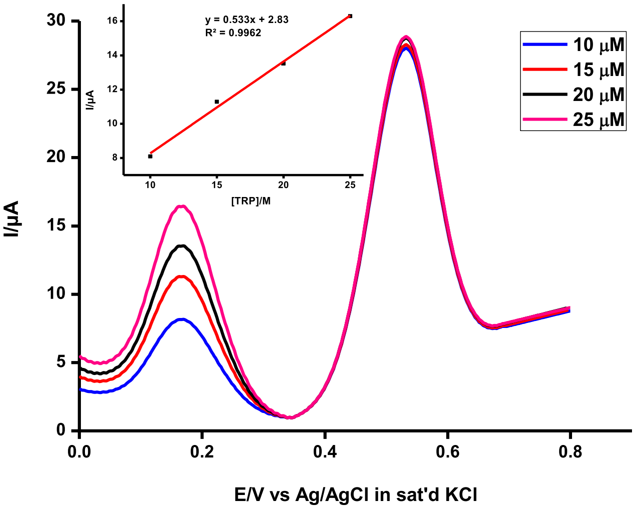

FIGURE 8 | Simultaneous detection of a range of concentrations of ascorbic acid at a constant tryptophan concentration at pH 5 on poly-CoTCPc-CoTAPc-GONS/GCE. Scan rate, 100 mV/s.

Electrocatalytic Detection

Electrocatalytic detection (redox reactions) is usually a subject of a number of factors including pH, the amount of electrode modifier, and the method of modification among others. It is therefore apparent that these factors have to be interrogated

TABLE 1 | Comparison of performance of poly-CoTCPc-CoTAPc-GONS/GCE with other electrodes reported in the literature.

Electrode	Analyte	Detection limit (μM)	Linear range (μM)	References
AzA/MWCNTs/AuNPs	Tryptophan	0.3	1–100	Filik et al. (2016)
$NiCoO_2$/C/GCE	Tryptophan	5.7	0–943.4	Yang et al. (2015)
PSA/GCE	Tryptophan	0.0068	0.05–10	Ba et al. (2013)
CVD graphene	Tryptophan	0.1	0.25–75	Wang et al. (2017)
Poly-CoTCPc-CoTAPc-GONS/GCE	Tryptophan	1.65	5.5–80	This work
AzA/MWCNTs/AuNPs	Ascorbic acid	16	300–1000	Filik et al. (2016)
$NiCoO_2$/C/GCE	Ascorbic acid	3.3	0–943.4	Yang et al. (2015)
CVD graphene	Ascorbic acid	1.58	5–1500	Wang et al. (2017)
Poly-CoTCPc-CoTAPc-GONS/GCE	Ascorbic acid	2.1	7.12–100	This work

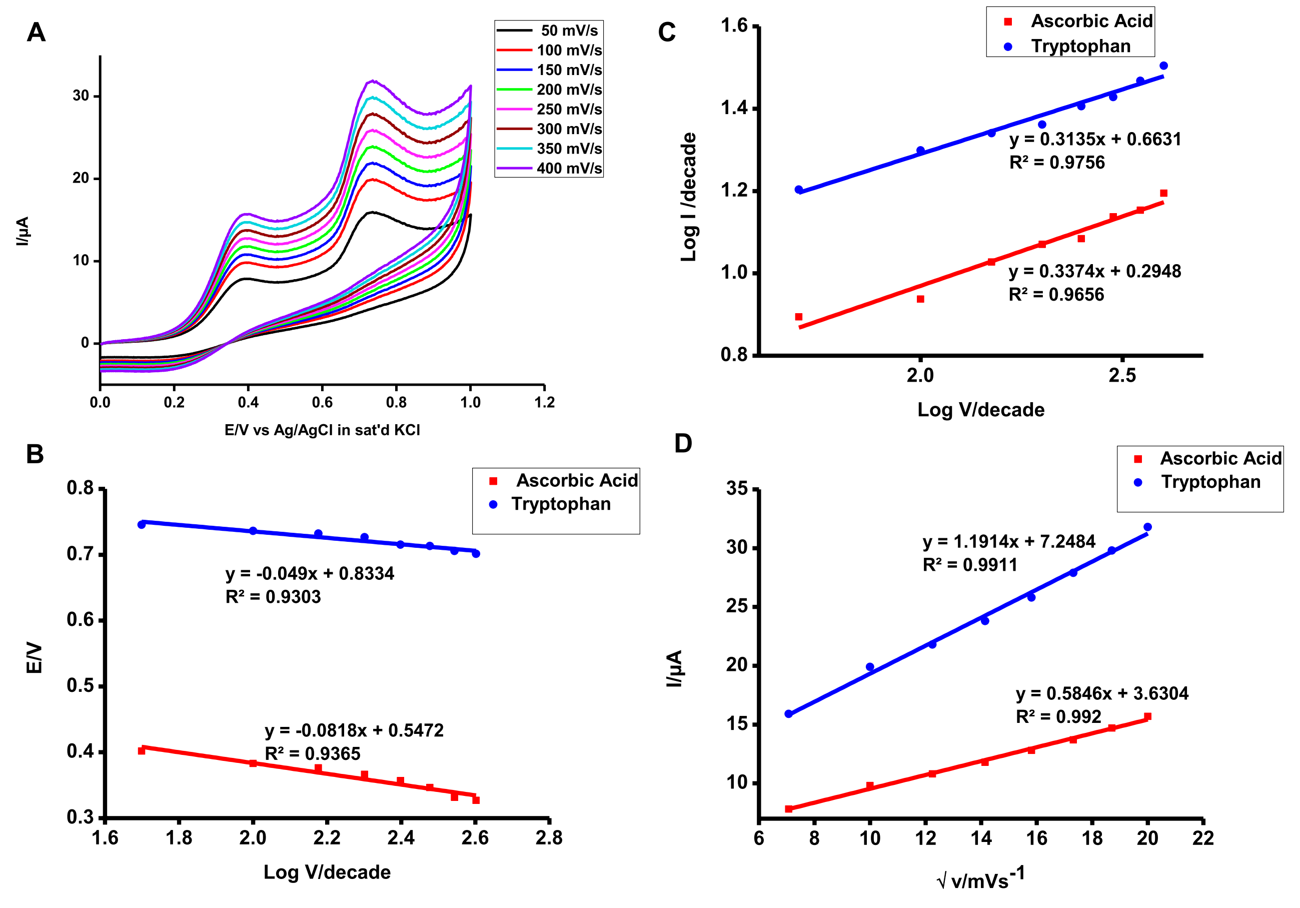

FIGURE 9 | Scan rate of poly-CoTCPc-CoTAPc-GONS/GCE in 1 mM ascorbic acid and tryptophan from 50 to 400 mV **(A)**, V vs. log v **(B)**, log I vs. log E **(C)**, and plot of Ipa vs. √v **(D)**.

thoroughly and optimized. The amount of modifier was optimized at 5 µL of 1 mg/ml of DMF using the drop dry method under inert conditions. The effect of pH was investigated in the range 4–8 as guided by previous investigations (Filik et al., 2016; Kumar Gupta et al., 2018). There was a significant variation of the background current and detection potentials in the detection of both ascorbic acid and tryptophan during the development of the sensor platform in this range of pH. Variations in pH values normally determine the extent of protonation or deprotonation of the analyte, hence its ease of oxidation or reduction which subsequently brings a signal of its presence or absence setting the basis of detection and quantification. Among other important parameters to consider, the kinetics, thermodynamics, and sensitivity of such reactions on the fabricated platform deserve much attention and set a good basis for the evaluation of the potential sensor. Robustness and stability of any sensor cannot be overlooked, and as such, this has to be addressed. A good detection platform

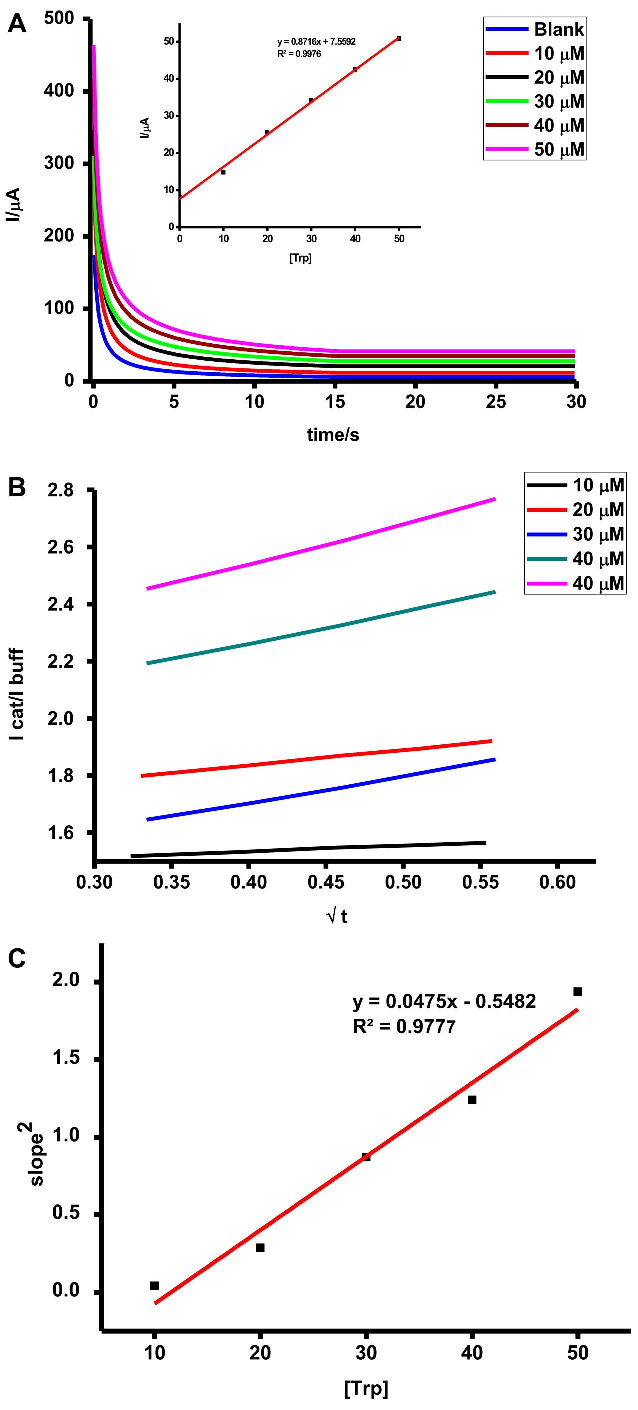

FIGURE 10 | (A) Chronoamperometric scans (inset = dependence of tryptophan concentration on current); **(B)** plot of I_{cat}/I_{buf} vs. $t^{1/2}$; **(C)** plot of concentration of tryptophan vs. square of slopes on **(B)** determined using chronoamperometry for the poly-CoTAPc-CoTAPc-GO/GCE electrode.

has to be selective and free from common interferences for it to be of any practical relevance which is also a preoccupation of this work.

pH Optimization

Tryptophan and ascorbic acid were both detected at varying pHs, and the variation of both background detection currents and potentials was noted. The optimum detection currents were at pH 5 (**Figure 5**) for both tryptophan and ascorbic acid using a composite (poly-CoTCPc-CoTAPc-GONS/GCE) electrode due to its superior performance as established already in an efficient redox medium $Fe^{2+/3+}$. Both analytes displayed a similar trend also observed elsewhere (Chihava et al., 2020) with other analytes: peak potentials decrease as the pH increases due to a proton transfer process. **Scheme 2** shows the mechanism of detection of ascorbic acid and tryptophan on poly-CoTCPc-CoTAPc-GONS/GCE, respectively.

Both reactions display readiness to oxidation as observed on the poly-CoTCPc-CoTAPc-GONS/GCE platform. While the fabricated platforms are good candidates for the detection of the two residues, the poly-CoTCPc-CoTAPc-GONS/GCE platform has significantly improved background currents and energetically feasible detection potentials at pH 5 for both residues; hence, we report its performance here onward.

Quantification of Tryptophan and Ascorbic Acid

Very little work has been done in which EIS has been employed as a quantifying tool for the analyte. Electrochemical impedance spectroscopy utilizes the conductivity response of an electrolyte to the concentration of the conducting species, hence its beauty in analyte quantification. The assumption is that, within a certain range of concentrations, the conductivity should be proportional to the number of conducting species (Yang et al., 2014). The potential at which EIS studies were carried out was determined by cyclic voltammetry (**Figure 7**) as the corresponding oxidation peak. The EIS parameters were obtained by fitting the Randles equivalent circuit (inset in **Figure 4**) to the experimental data and performing complex non-linear least-squares procedures available in an EIS data fitting computer program. The resistance to charge transfer (R_{CT}) for tryptophan on different sensor platforms varied in the following order: GONS/GCE (4.657 kΩ) > GCE (3.712 kΩ) > CoTAPc-GONS/GCE (2.842 kΩ) >CoTCPc/GCE (2.695 kΩ) > CoTAPc-GONS/GCE (2.561 kΩ) > poly-CoTCPc-CoTAPc/GCE (2.191 kΩ) > poly-CoTAPc-CoTAPc-GONS/GCE (1.254 kΩ) (**Figure 6**). A similar trend was also observed with the Bode plots and was characterized by varying phase angles and frequencies indicative of varying levels of effectiveness of electrode modification as shown in **Supplementary Figure S3**, for ascorbic acid as an example. The same order was also observed for the detection of ascorbic acid confirming the redox behavior established in $Fe^{2+/3+}$ media; hence, poly-CoTAPc-CoTAPc-GONS/GCE will be utilized for further studies. Since this electrode showed very low resistance to charge, it was then used to study the response to concentration variation. Investigations showed that the resistance to charge linearly decreased with an increase in the concentration of the analyte in the range 0–20 μM of the analyte. This is evidence

TABLE 2 | Determination of ascorbic acid and tryptophan in milk and urine samples using poly-CoTCPc-CoTAPc-GONS/GCE.

Sample	Electrode	Analyte	Original (μM)	Spiked (μM)	Found (μM)	Recovery (%)
Milk	CoTAPc-CoTCPc-GONS-GCE	Ascorbic acid	1.5	10	11.6	106.7
			3	20	22.9	96.7
*Urine	Nafion/AuNPs/AzA/MWCNTs-GCE	Tryptophan	6	30	35.7	95.0
			—	500	498.6	99.72
			2	10	12.1	105.0
			4	20	23.9	97.5
*Urine	Nafion/AuNPs/AzA/MWCNTs-GCE		6	30	35.5	91.7
**Aminoven 10%	Nafion/AuNPs/AzA/MWCNTs-GCE		190	50	240	100
	GNP/CILE		—	10	10.1	101
			100	40	143.9	100.6

**Filik et al. (2016); **Liu et al. (2020).*

TABLE 3 | Validation parameters.

Analytical method	RSD	SE of slope	SE of intercept	Accuracy
Chronoamperometry	6.56	2.86E-08	9.48E-07	97.37 ± 6.38
Tryptophan	3.67	3.26E-09	1.08E-07	116.98 ± 4.30
Ascorbic acid				
DPV at constant	3.12	2.50E-08	4.59E-07	99.85 ± 3.12
Tryptophan	1.55	5.24E-08	9.63E-07	99.60 ± 1.55
Ascorbic acid				

that the analyte is the source of current as a result of its oxidation.

Differential pulse and cyclic voltammetry were also employed to detect and quantify tryptophan at around 0.72 V and ascorbic acid at 0.37 V, respectively, similar to values reported elsewhere for independent and/or simultaneous detection of the analytes (Filik et al., 2016; Kumar Gupta et al., 2018; Govindasamy et al., 2019). The two analytes could be adequately detected simultaneously at significantly different potentials by both techniques as illustrated using cyclic voltammetry (**Figure 7**). Tryptophan and ascorbic acid are common residues in human physiological systems, hence the beauty of a platform such as poly-CoTAPc/CoTCPc/GONS/GCE reported in this work with the ability to detect the residues at significantly different potentials.

This makes the probe very applicable in biological media since the two analytes coexist in physiological environments (Wu et al., 2015). To further ascertain non-interference between the two, the concentrations of the two were independently varied and the results were observed (**Figure 8**). The concentration of one analyte was increased, while the other was kept constant and vice versa, and the probe picked the difference with impressive sensitivity.

The developed sensing platform can therefore be used for simultaneous detection and quantification of the two analytes with reasonable reliability. It is also very important to establish the limits of detection and quantification of a sensing platform as biological molecules usually occur in minute concentrations. This was done using the 3δ and 10δ notations. The limit of detection and limit of quantification were found to be 2.1×10^{-6} and 5.5×10^{-6} M, respectively, for ascorbic acid and 1.65×10^{-6} and 5.5×10^{-6} M for tryptophan when the two analytes coexist comparable to reported values (Filik et al., 2016; Yao et al., 2020). These values have practical significance since they closely relate to physiological concentrations which lie in the range 28–99 mM for ascorbic acid (Hagel et al., 2018), and up to 95% of tryptophan is taken up by the kynurenine pathway (Kałużna-Czaplińska et al., 2019). **Table 1** shows a comparison of poly-CoTCPc-CoTAPc-GONS/GCE with other reported electrodes (Ba et al., 2013; Yang et al., 2015; Filik et al., 2016; Wang et al., 2017) for simultaneous detection and shows its potential in application to real samples.

Kinetics

Since the probe under investigation could satisfactorily detect and quantify both analytes in a single solution, the behavior of detection was investigated at different scan rates simultaneously. For both analytes, it was observed that the peak position shifted with the change of scan rates indicative of an irreversible reaction (Sajjan et al., 2019). Irreversible reactions are governed by the following equation:

$$E_p = \frac{b}{2}\log v + k, \tag{1}$$

where b is the Tafel slope, v is the scan rate, and k is a constant. Tafel slopes of 162 and 98 mV/decade were obtained for ascorbic acid and tryptophan, respectively. Tafel slopes above 120 mV/decade imply slower reactions (Liu et al., 2020; Mooni et al., 2020), while those below are suggestive of diffusion-controlled reactions. Log v against log I were plotted and characterized by straight lines of curves of slopes below 0.5 further suggesting diffusion-controlled reactions for both ascorbic acid and tryptophan oxidation (**Figure 9**). Adsorption-characterized reactions have slopes close to unity, while gradients below 0.5 are characteristic of diffusion-controlled reactions (Shumba and Nyokong, 2016b). Diffusion-controlled reactions are facile by nature and hence characterized by very high slopes of the plots of peak current versus the square root of scan rate. **Figures 9A–C** shows such plots, and it is apparent that the developed probe is more facile during the oxidation of tryptophan than it is for ascorbic acid [slope 1.19 μA/

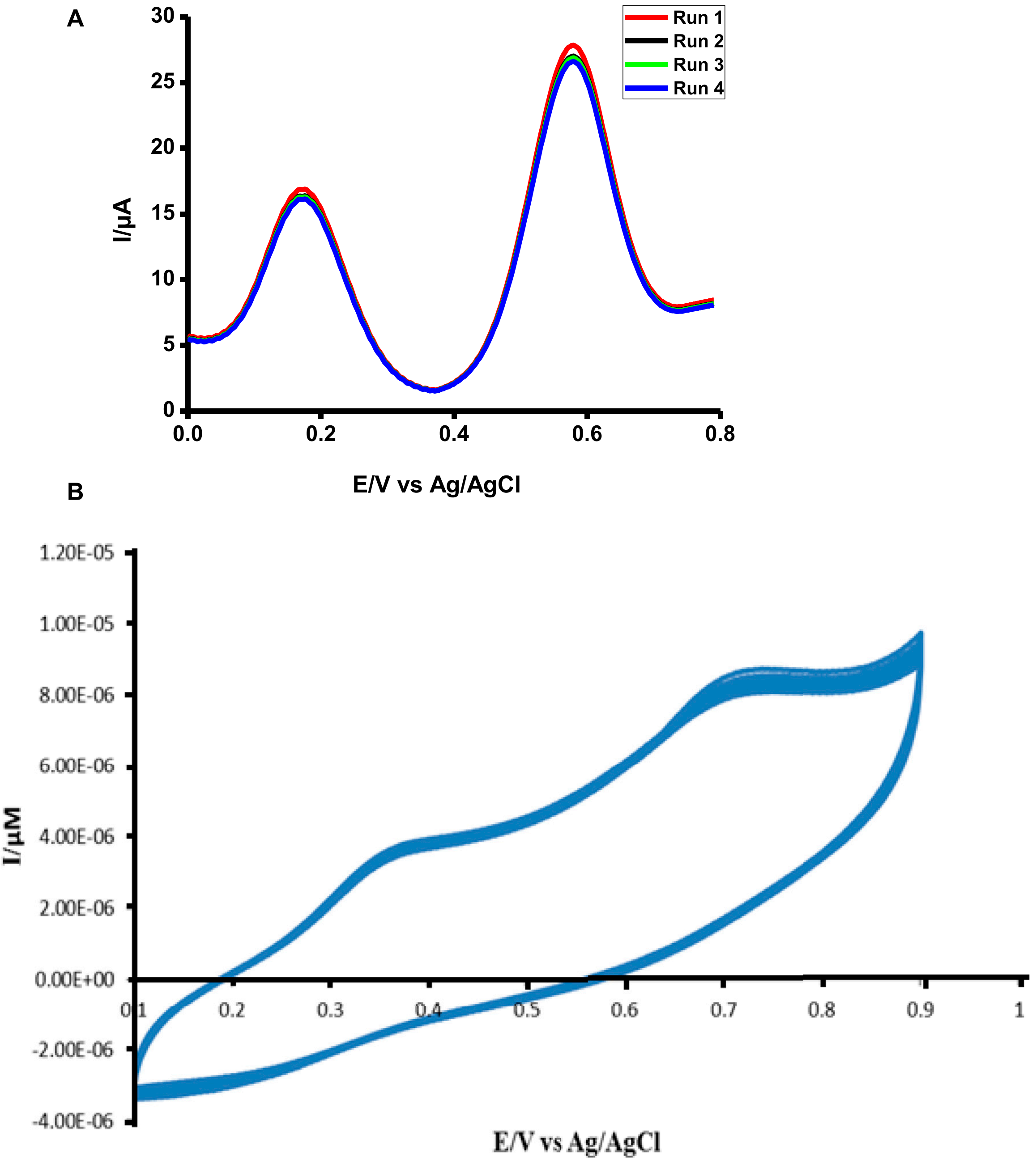

FIGURE 11 | Stability study of poly-CoTCPc-CoTAPc-GONS/GCE in 1 mM ascorbic acid and tryptophan in pH 5 buffer solution using DPV **(A)** and CV **(B)**.

$(\mathrm{mVs}^{-1})^{1/2}$ against 0.58 $\mu\mathrm{A}/(\mathrm{mVs}^{-1})^{1/2}$] despite it having a higher activation energy as depicted by its detection potential.

The plots of Ipa vs. $\sqrt{v}$ gave a linear plot evidence of diffusion-controlled reactions. Diffusion-controlled reactions are facile in nature indicative of a highly catalyzed reaction. The slope of the plot is indicative of how facile the reaction is. Tryptophan detection is more facile and readily feasible as shown by a higher slope in **Figure 9D**.

The Langmuir adsorption theory was applied to confirm the feasibility of the two oxidative reactions as reported earlier (Shumba and Nyokong, 2016c). The Gibbs free energy obtained was −17.45 and −14.83 kJ mol^{-1} for ascorbic acid and tryptophan, respectively, depicting a spontaneous reaction on the electrode surface. These values are comparable to those reported elsewhere for high Tafel slopes (Adekunle et al., 2011; Shumba and Nyokong, 2016c).

Catalytic Rate Constants

Catalyzed reactions are characterized by improved reaction rates and low energy consumption reactions. The initial stages during chronoamperometric scans are characterized by rapid current decays before a constant signal is observed. This can be attributed to the oxidation of a high concentration of tryptophan or ascorbic acid as a result of adsorption followed by a steady diffusion-controlled step which reflects the actual concentration of the test analyte, hence higher currents for higher concentrations as shown in **Figure 10**. Oxidation of tryptophan and ascorbic acid on poly-CoTAPc-CoTCPc-GONS/GCE showed different sensitivities of 0.9 and 0.1 AM^{-1}, respectively. A similar trend was also observed under DPV with the analyte detection giving sensitivities of 0.6 and 0.2 AM^{-1}, respectively. This shows that the developed sensing platform is more responsive to tryptophan compared to ascorbic acid though the latter is detected at a more favorable potential.

Rate constants can be evaluated using

$$\frac{I_{cat}}{I_{buf}} = \frac{\gamma^{\frac{1}{2}}\left[\pi^{\frac{1}{2}} erf\left(\gamma^{\frac{1}{2}}\right) + \exp\left(-\gamma\right)\right]}{\gamma^{\frac{1}{2}}}, \tag{2}$$

where I_{cat} and I_{buf} are the currents on poly-CoTAPc-CoTCPc-GONS/GCE in the presence and absence of the test analyte, respectively, and erf is the error function. At values of γ above 2, the error function is approximately equal to 1, and **Eq. 2** reduces to

$$\frac{I_{cat}}{I_{buf}} = \gamma^{\frac{1}{2}}\pi^{\frac{1}{2}} = \pi^{\frac{1}{2}}\left(kC_o t\right)^{\frac{1}{2}}, \tag{3}$$

where k is the catalytic rate constant, t is the time elapsed, and $\gamma = kC_o t$ (C_o is the bulk concentration of the test analyte). The plot of $\frac{I_{cat}}{I_{buf}}$ against $t^{\frac{1}{2}}$ therefore gives a slope of πk, and the catalytic rate constant can therefore be deduced from the plot of square of the above plot against concentration. The equations of the plots are represented as

$$y = 0.0475\left[Trp\right]\frac{s^{-1}}{\mu M} + 0.582, \tag{4}$$

$$y = 0.0585\left[AA\right]\frac{s^{-1}}{\mu M} - 1.634. \tag{5}$$

These translate to catalytic rate constants of 1.512×10^4 and $1.862 \times 10^4\ \mathrm{M}^{-1}\mathrm{s}^{-1}$ for tryptophan and ascorbic acid on the modified electrode, respectively. Such values are attractive and pose the probe as a potential candidate for practical applications.

Practical Application of the Probes

Most probes usually work well in synthetic solutions but simply get poisoned or lose selectivity once in real samples. The prepared probe was tested for selectivity in the presence of other interferences and in milk samples. The standard addition method was used to investigate the recoveries of ascorbic acid in milk samples and tryptophan in urine samples, **Table 2**. The recoveries were quite impressive: 95–106.7% for ascorbic acid and 91.7–105% for tryptophan comparable to and even better than the values reported elsewhere (Govindasamy et al., 2019), implying that the developed probe is a promising candidate for the sensing of these biomolecules. With very high accuracy above 97%, low relative standard deviation below 6%, and standard error in the nanorange (**Table 3**), the probe provides a high potential as a sensor platform for both tryptophan and ascorbic acid in real samples. The probes show no interferences of potentially electroactive molecules in milk samples, as shown in **Figure 11**.

The probe was very stable after repetitive scans for both analytes (**Figure 11**). This is a very good sign showing that the probe can be used several times without signal loss; hence, it is a perfect candidate for practical use. While DPV shows stability over a period of 6 months when kept at 4°C and dry conditions, CV shows stability against repetitive scans.

CONCLUSION

Polymerization of phthalocyanine entities has resulted in electron redistribution patterns within the modifiers due to the different electron withdrawal affinities resulting from the new bonding patterns. This has significantly improved the electrocatalytic behavior of the designed sensor posing a very promising multi-analyte platform for the detection of coexisting pollutants. The need for minimal to no sample preparation is a very positive aspect in the field of sensor development. Coupled with low detection limits, resistance to fouling, robustness, and high selectivity, the developed sensor has high potential as a practical solution to environmental pollution monitoring.

DATA AVAILABILITY STATEMENT

The raw data supporting the conclusion of this article will be made available by the authors, without undue reservation.

AUTHOR CONTRIBUTIONS

PC was responsible for synthesis and characterization of practical work. MS, a principal researcher, was responsible for experimental design. MM, also a principal researcher, was responsible for electrocatalytic work. MS and MM analyzed the data. ED, a synthetic chemist, performed organic synthesis and reaction optimization. NZ, an inorganic synthetic chemist, performed manuscript assembly.

SUPPLEMENTARY MATERIAL

The Supplementary Material for this article can be found online at: https://www.frontiersin.org/articles/10.3389/fchem.2021.633547/full#supplementary-material

REFERENCES

Adekunle, A. S., Mamba, B. B., Agboola, B. O., and Ozoemena, K. I. (2011). Nitrite Electrochemical Sensor Based on Prussian Blue/Single-Walled Carbon Nanotubes Modified Pyrolytic Graphite Electrode. *Int. J. Electrochem. Sci.* 6, 4388–4403.

Ba, X., Luo, L., Ding, Y., and Liu, X. (2013). Determination of L-Tryptophan in the Presence of Ascorbic Acid and Dopamine Using Poly(sulfosalicylic Acid) Modified Glassy Carbon Electrode. *Sensors Actuators B: Chem.* 187, 27–32. doi:10.1016/j.snb.2012.09.018

Chihava, R., Apath, D., Moyo, M., Shumba, M., Chitsa, V., and Tshuma, P. (2020). One-Pot Synthesized Nickel-Cobalt Sulfide-Decorated Graphene Quantum Dot Composite for Simultaneous Electrochemical Determination of Antiretroviral Drugs: Lamivudine and Tenofovir Disoproxil Fumarate. *J. Sensors* 2020, 1–13. doi:10.1155/2020/3124102

Choi, J., Wagner, P., Gambhir, S., Jalili, R., Macfarlane, D. R., Wallace, G. G., et al. (2019). Steric Modification of a Cobalt Phthalocyanine/Graphene Catalyst to Give Enhanced and Stable Electrochemical CO2 Reduction to CO. *ACS Energ. Lett.* 4, 666–672. doi:10.1021/acsenergylett.8b02355

Dumrul, H., and Yuksel, F. (2013). Synthesis and Characterization of Novel Symmetrical and Asymmetrical Substituted Zn(II) Phthalocyanines. *Polyhedron* 63, 83–90. doi:10.1016/j.poly.2013.07.015

Erdem, S. S., Nesterova, I. V., Soper, S. A., and Hammer, R. P. (2008). Solid-Phase Synthesis of Asymmetrically Substituted "AB3-type" Phthalocyanines. *J. Org. Chem.* 73, 5003–5007. doi:10.1021/jo800536v

Filik, H., Avan, A. A., and Aydar, S. (2016). Simultaneous Detection of Ascorbic Acid, Dopamine, Uric Acid and Tryptophan with Azure A-Interlinked Multi-Walled Carbon Nanotube/gold Nanoparticles Composite Modified Electrode. *Arabian J. Chem.* 9, 471–480. doi:10.1016/j.arabjc.2015.01.014

Ghazal, B., Husain, A., Ganesan, A., Durmuş, M., Zhang, X.-F., and Makhseed, S. (2019). Exceptionally Effective Generation of Singlet Oxygen in Aqueous media via Iodinated Zinc-Phthalocyanine. *Dyes Pigm.* 164, 296–304. doi:10.1016/j.dyepig.2019.01.036

Govindasamy, M., Wang, S.-F., Pan, W. C., Subramanian, B., Ramalingam, R. J., and Al-lohedan, H. (2019). Facile Sonochemical Synthesis of Perovskite-type SrTiO3 Nanocubes with Reduced Graphene Oxide Nanocatalyst for an Enhanced Electrochemical Detection of α-amino Acid (Tryptophan). *Ultrason. Sonochem.* 56, 193–199. doi:10.1016/j.ultsonch.2019.04.004

Griveau, S., Albin, V., Pauporté, T., Zagal, J. H., and Bedioui, F. (2002). Comparative Study of Electropolymerized Cobalt Porphyrin and Phthalocyanine Based Films for the Electrochemical Activation of Thiols. *J. Mater. Chem.* 12, 225–232. doi:10.1039/b106817b

Hagel, A. F., Albrecht, H., Dauth, W., Hagel, W., Vitali, F., Ganzleben, I., et al. (2018). Plasma Concentrations of Ascorbic Acid in a Cross Section of the German Population. *J. Int. Med. Res.* 46, 168–174. doi:10.1177/0300060517714387

Ikram, M., Raza, A., Imran, M., Ul-hamid, A., Shahbaz, A., and Ali, S. (2020). Hydrothermal Synthesis of Silver Decorated Reduced Graphene Oxide (rGO) Nanoflakes with Effective Photocatalytic Activity for Wastewater Treatment. *Nanoscale Res. Lett.* 15, 95–11. doi:10.1186/s11671-020-03323-y

Kaya, E. N., Basova, T., Polyakov, M., Durmuş, M., Kadem, B., and Hassan, A. (2015). Hybrid Materials of Pyrene Substituted Phthalocyanines with Single-Walled Carbon Nanotubes: Structure and Sensing Properties. *RSC Adv.* 5, 91855–91862. doi:10.1039/C5RA18697H

Kałużna-Czaplińska, J., Gątarek, P., Chirumbolo, S., Chartrand, M. S., and Bjørklund, G. (2019). How Important Is Tryptophan in Human Health? *Crit. Rev. Food Sci. Nutr.* 59, 72–88. doi:10.1080/10408398.2017.1357534

Kumar Gupta, V., Shamsadin-azad, Z., Cheraghi, S., and Agarwai, S. (2018). Electrocatalytic Determination of L-Cysteine in the Presence of Tryptophan Using Carbon Paste Electrode Modified with MgO Nanoparticles and Acetylferrocene. *Int. J. Electrochem. Sci.* 13, 4309–4318. doi:10.20964/2018.05.53

Liu, G., Wang, B., Ding, P., Wei, W., Ye, Y., Wang, L., et al. (2020). *In-situ* Synthesis Strategy for CoM (M = Fe, Ni, Cu) Bimetallic Nanoparticles Decorated N-Doped 1D Carbon nanotubes/3D Porous Carbon for Electrocatalytic Oxygen Evolution Reaction. *J. Alloys Compd.* 815, 152470–153294. doi:10.1016/j.jallcom.2019.152470

Liu, L., Guo, L.-p., Bo, X.-j., Bai, J., and Cui, X.-j. (2010). Electrochemical Sensors Based on Binuclear Cobalt Phthalocyanine/surfactant/ordered Mesoporous Carbon Composite Electrode. *Analytica Chim. Acta* 673, 88–94. doi:10.1016/j.aca.2010.05.019

Liu, Y., Wu, Y.-Y., Lv, G.-J., Pu, T., He, X.-Q., and Cui, L.-L. (2013). Iron(II) Phthalocyanine Covalently Functionalized Graphene as a Highly Efficient Non-precious-metal Catalyst for the Oxygen Reduction Reaction in Alkaline media. *Electrochim. Acta* 112, 269–278. doi:10.1016/j.electacta.2013.08.174

Mafuwe, P. T., Moyo, M., Mugadza, T., Shumba, M., and Nyoni, S. (2018). Cobalt Oxide Nanoparticles Anchored Polyaniline-Appended Cobalt Tetracarboxy Phthalocyanine, Modified Glassy Carbon Electrode for Facile Electrocatalysis of Amitrole. *J. Solid State. Electrochem.* 23, 285–294. doi:10.1007/s10008-018-4131-8

Mooni, S. P., Kondamareddy, K. K., Li, S., Zhou, X., Chang, L., Ke, X., et al. (2020). Graphene Oxide Decorated Bimetal (MnNi) Oxide Nanoflakes Used as an Electrocatalyst for Enhanced Oxygen Evolution Reaction in Alkaline media. *Arabian J. Chem.* 13, 4553–4563. doi:10.1016/j.arabjc.2019.10.003

Moyo, P., Mugadza, T., Mehlana, G., and Guyo, U. (2016). Synthesis and Characterization of Activated carbon-ethylenediamine-Cobalt(II) Tetracarboxyphthalocyanine Conjugate for Catalytic Oxidation of Ascorbic Acid. *Res. Chem. Intermed.* 42, 6511–6529. doi:10.1007/s11164-016-2477-z

Nemakal, M., Aralekallu, S., Mohammed, I., Swamy, S., and Sannegowda, L. K. (2019). Electropolymerized Octabenzimidazole Phthalocyanine as an Amperometric Sensor for Hydrazine. *J. Electroanal. Chem.* 839, 238–246. doi:10.1016/j.jelechem.2019.03.050

Nkhahle, R., Sekhosana, K. E., Centane, S., and Nyokong, T. (2019). Electrocatalytic Activity of Asymmetrical Cobalt Phthalocyanines in the Presence of N Doped Graphene Quantum Dots: The Push-pull Effects of Substituents. *Electroanalysis* 31, 891–904. doi:10.1002/elan.201800837

Nyokong, T., and Khene, S. (2016). “Modification of Electrode Surfaces with Metallo Phthalocyanine Nanomaterial Hybrids,” in *Electrochemistry of N4 Macrocyclic Metal Complexes* Switzerland: Springer International Publishing, 225–275. doi:10.1007/978-3-319-31332-0_6

Nyoni, S., Mashazi, P., and Nyokong, T. (2015). Electrode Modification Using Nanocomposites of Electropolymerised Cobalt Phthalocyanines Supported on Multiwalled Carbon Nanotubes. *J. Solid State. Electrochem.* 20, 1075–1086. doi:10.1007/s10008-015-2985-6

Sajjan, V. A., Mohammed, I., Nemakal, M., Aralekallu, S., Hemantha Kumar, K. R., Swamy, S., et al. (2019). Synthesis and Electropolymerization of Cobalt Tetraaminebenzamidephthalocyanine Macrocycle for the Amperometric Sensing of Dopamine. *J. Electroanal. Chem.* 838, 33–40. doi:10.1016/j.jelechem.2019.02.042

Sekhosana, K. E., Shumba, M., and Nyokong, T. (2017). Electrochemical and Non-linear Optical Behavior of a New Neodymium Double-Decker Phthalocyanine. *Polyhedron* 138, 154–160. doi:10.1016/j.poly.2017.09.033

Shumba, M., and Nyokong, T. (2016a). Development of Nanocomposites of Phosphorus-Nitrogen Co-doped Graphene Oxide Nanosheets and Nanosized Cobalt Phthalocyanines for Electrocatalysis. *Electrochim. Acta* 213, 529–539. doi:10.1016/j.electacta.2016.07.079

Shumba, M., and Nyokong, T. (2017). Effects of Covalent versus Non-covalent Interactions on the Electrocatalytic Behavior of Tetracarboxyphenoxyphthalocyanine in the Presence of Multi-Walled Carbon Nanotubes. *J. Coord. Chem.* 70, 1585–1600. doi:10.1080/00958972.2017.1303679

Shumba, M., and Nyokong, T. (2016b). Electrocatalytic Activity of Nanocomposites of Sulphur Doped Graphene Oxide and Nanosized Cobalt Phthalocyanines. *Electroanalysis* 28, 3009–3018. doi:10.1002/elan.201600226

Shumba, M., and Nyokong, T. (2016c). Electrode Modification Using Nanocomposites of boron or Nitrogen Doped Graphene Oxide and Cobalt (II) Tetra Aminophenoxy Phthalocyanine Nanoparticles. *Electrochim. Acta* 196, 457–469. doi:10.1016/j.electacta.2016.02.166

Teo, L., Subramanian, V. R., and Schwartz, D. T. (2021). Dynamic Electrochemical Impedance Spectroscopy of Lithium-Ion Batteries: Revealing Underlying Physics through Efficient Joint Time-Frequency Modeling. *J. Electrochem. Soc.* 168, 010526. doi:10.1149/1945-7111/abda04

Wang, X., Gao, D., Li, M., Li, H., Li, C., Wu, X., et al. (2017). CVD Graphene as an Electrochemical Sensing Platform for Simultaneous Detection of Biomolecules. *Sci. Rep.* 7, 1–9. doi:10.1038/s41598-017-07646-2

Wu, D., Xin, X., Pang, X., Pietraszkiewicz, M., Hozyst, R., Sun, X. g., et al. (2015). Application of Europium Multiwalled Carbon Nanotubes as Novel Luminophores in an Electrochemiluminescent Aptasensor for Thrombin Using Multiple Amplification Strategies. *ACS Appl. Mater. Inter.* 7, 12663–12670. doi:10.1021/acsami.5b03381

Yang, F., Xie, Q., Zhang, H., Yu, S., Zhang, X., and Shen, Y. (2015). Simultaneous Determination of Ascorbic Acid, Uric Acid, Tryptophan and Adenine Using Carbon-Supported NiCoO2 Nanoparticles. *Sensors Actuators B: Chem.* 210, 232–240. doi:10.1016/j.snb.2014.12.120

Yang, Y., Pan, J., Hua, W., and Tu, Y. (2014). An Approach for the Preparation of Highly Sensitive Electrochemical Impedimetric Immunosensors for the Detection of Illicit Drugs. *J. Electroanal. Chem.* 726, 1–6. doi:10.1016/j.jelechem.2014.04.022

Yao, W., Guo, H., Liu, H., Li, Q., Wu, N., Li, L., et al. (2020). Highly Electrochemical Performance of Ni-ZIF-8/N S-CNTs/CS Composite for Simultaneous Determination of Dopamine, Uric Acid and L-Tryptophan. *Microchem. J.* 152, 104357. doi:10.1016/j.microc.2019.104357

Conflict of Interest: The authors declare that the research was conducted in the absence of any commercial or financial relationships that could be construed as a potential conflict of interest.

The handling Editor declared a past co-authorship with one of the authors MS.

Publisher's Note: All claims expressed in this article are solely those of the authors and do not necessarily represent those of their affiliated organizations, or those of the publisher, the editors, and the reviewers. Any product that may be evaluated in this article, or claim that may be made by its manufacturer, is not guaranteed or endorsed by the publisher.

Advantages of publishing in Frontiers

OPEN ACCESS
Articles are free to read
for greatest visibility
and readership

FAST PUBLICATION
Around 90 days
from submission
to decision

HIGH QUALITY PEER-REVIEW
Rigorous, collaborative,
and constructive
peer-review

TRANSPARENT PEER-REVIEW
Editors and reviewers
acknowledged by name
on published articles

Frontiers
Avenue du Tribunal-Fédéral 34
1005 Lausanne | Switzerland

Visit us: www.frontiersin.org
Contact us: frontiersin.org/about/contact

REPRODUCIBILITY OF RESEARCH
Support open data
and methods to enhance
research reproducibility

DIGITAL PUBLISHING
Articles designed
for optimal readership
across devices

FOLLOW US
@frontiersin

IMPACT METRICS
Advanced article metrics
track visibility across
digital media

EXTENSIVE PROMOTION
Marketing
and promotion
of impactful research

LOOP RESEARCH NETWORK
Our network
increases your
article's readership